TIDAL AND WIND FORCED FLOW IN CLODE SOUND: OBSERVATIONS AND NUMERICAL MODELLING

PATRICK GEORGE TIMKO

Tidal and Wind Forced Flow in Clode Sound: Observations and Numerical Modelling

by

Patrick George Timko

A thesis submitted to the

School of Graduate Studies

in partial fulfilment of the

requirements for the degree of

Doctor of Philosophy

Department of Physics and Physical Oceanography

Faculty of Science

Memorial University of Newfoundland

Abstract

Clode Sound is a small fjord on the east coast of Newfounland that contains a shallow sill and coinciding contraction. Studies of the hydrographic properties and currents in Clode Sound, Newfoundland during the summers of 1996 and 1997 indicate that considered as a two-layered model the tidally forced flow over the sill is supercritical during spring tides. Supercritical flow may lead to the formation of internal bores or internal hydraulic jumps that increase the vertical mixing as they propagate away from seaward side of the sill. Within the inner basin, there is little evidence of mixing below the level of the sill and the inner basin water, formed during the winter months, remains trapped. Fresh water inflow from the Northwest River is low but the combination of mixing and the input of solar radiation leads to the formation of a well-defined surface layer in which the water column is thermally stratified. On the seaward side of the sill, the surface layer extends below the level of the sill, within the inner basin the depth of the surface layer is limited by the depth of the sill.

The model used to simulate the circulation of Clode Sound is based upon the Princeton Ocean Model (POM). Attempts to simulate the three-dimensional circulation using a static density field reveal that such a model is not capable of reproducing the tidal currents with Clode Sound. Models with a static density field show no significant difference to a model with constant density. The inability of the model to reproduce the tides leads to an imbalance of forces when wind stress is applied to the model. Further simulations in which temperature and salinity evolve within the model provide a much better result for the main tidal constituents. The inclusion of temperature and salinity mixing required very strong relaxation of the scalar fields and the model performance is

evaluated with both a constant background density field and an evolving background density field. Wind stress applied to the mixing model leads to the rapid onset of numerical instability limiting the length of the model simulations. A comparison of the model simulations to the observations of 1996 and 1997 indicate that with both tidal and wind stress forcing the model, the model is able to reproduce the variability of the residual circulation but is unable to reproduce the observed velocity field.

Acknowledgments

I wish to thank my supervisor, Brad de Young, for his patience, continual support and encouragement in the completion of this work. I would also like to thank my parents, who are also blessed with patience and also provided support and encouragement. Finally I would like to thank Bunny and other assorted friends who were always there when I needed them.

Financial support for this work was provided by an ongoing NSERC Discovery Grant (B. de Young) and an NSERC Strategic Grant (B. de Young, J. Helbig, et. al.)

Table of Contents

List of Tables

List of Figures

Page

List of Appendicies

Chapter 1 Introduction

Alice was beginning to get very tired of sitting by her sister on the bank and of having nothing to do: once or twice she had peeped into the book her sister was reading, but it had no pictures or conversations in it, 'and what is the use of a book,' thought Alice, 'without pictures or conversations?'

- Lewis Carroll
Alice's Adventure in Wonderland

Coastal seas and inlets have, historically, played an important role in the relationship between people and the ocean. Activities such as fishing have always been dependent on favourable conditions within the ocean. The sea-state is largely dependent on the forcing produced by tides and winds. Tidal forcing may create large daily or twice daily changes in the volume of coastal harbours and bays and also promote vertical mixing, breaking down the local stratification of the oceanic waters (Pickard and Emery, 1990, p. 277). Strong winds may produce rough seas that reduce the safety and limit the opportunities for activities taking place on the ocean. Severe storms, such as hurricanes, may also produce storm surges along coastlines bounded by shallow water. Such storm surges together with spring tides and ocean waves may have disastrous consequences as coastal areas may become severely flooded resulting in wide scale infrastructure damage and loss of life (Bowden, 1983, pp. 142-149). Steady, but lighter winds, may drive ocean currents near the surface. Steady winds blowing parallel to a coastline may produce upwelling or downwelling as the Ekman transport is directed away from or towards the coast. In turn, these surface currents may alter the local properties (temperature and salinity) along coastal regions by advecting water to and from a given region. The response of the ocean to tidal forcing was observed by the ancient Greeks (Russell and

Macmillan, 1954), although they did not understand the nature of the tide-generating force. Our present understanding of tide-generating forces builds upon the work of Newton who presented his theory in his "Principia" in 1687 (Darwin, 1898).

Since the time of Newton our knowledge and understanding of tides has greatly increased. Today, observations and predictions of tides within the ocean have become an almost "routine computer operation" (Cartwright, 1999, p. 268). Less routine and more difficult to obtain are regular observations of hydrographic properties and ocean currents (including tidal currents) at a particular location. Most observations of sub-surface temperature, salinity and currents within the ocean are done for short periods with a specific purpose in mind.

Waters on the east coast of Newfoundland have long been subjected to intensive fishing activities (Lear, 1998). Despite this, regular observations of the hydrographic properties of this region did not really begin until after WW-II when regular year round observations were recorded at such places as Station 27 (47° 33′ N, 52° 35′ W) off St. John's, Newfoundland. Ocean waters off the east coast of Newfoundland are dominated by the influence of the Labrador Current (Figure 1.1). The Labrador Current, a combination of Hudson Strait outflow, the east Baffin Island Current and the west Greenland Current advects cold, low-salinity water from the Arctic region down along the east coast of Labrador and Newfoundland (Colbourne, 2004). The cold (-1 to 2 °C), low salinity (32.5-33.5 PSU) arctic waters represent approximately 20% of the total volume of the Labrador Current, the remaining 80% originates in the Irminger Sea and is warmer (3-4 °C) and more saline (~34.9 PSU) brought around the southern coast of Greenland by the East and West Greenland Currents (Lazier, 1982). The Labrador current, which can have an average velocity (near surface) of up to 0.3 ms^{-1}, is diverted seaward just south of Bonavista Bay but has a smaller branch which travels south towards the Avalon Pennisula and Station 27 (Petrie and Anderson, 1983). The inshore branch carries approximately 15% of the total transport along the eastern coast of Newfoundland towards the Avalon Pennisula (Lazier and Wright, 1993).

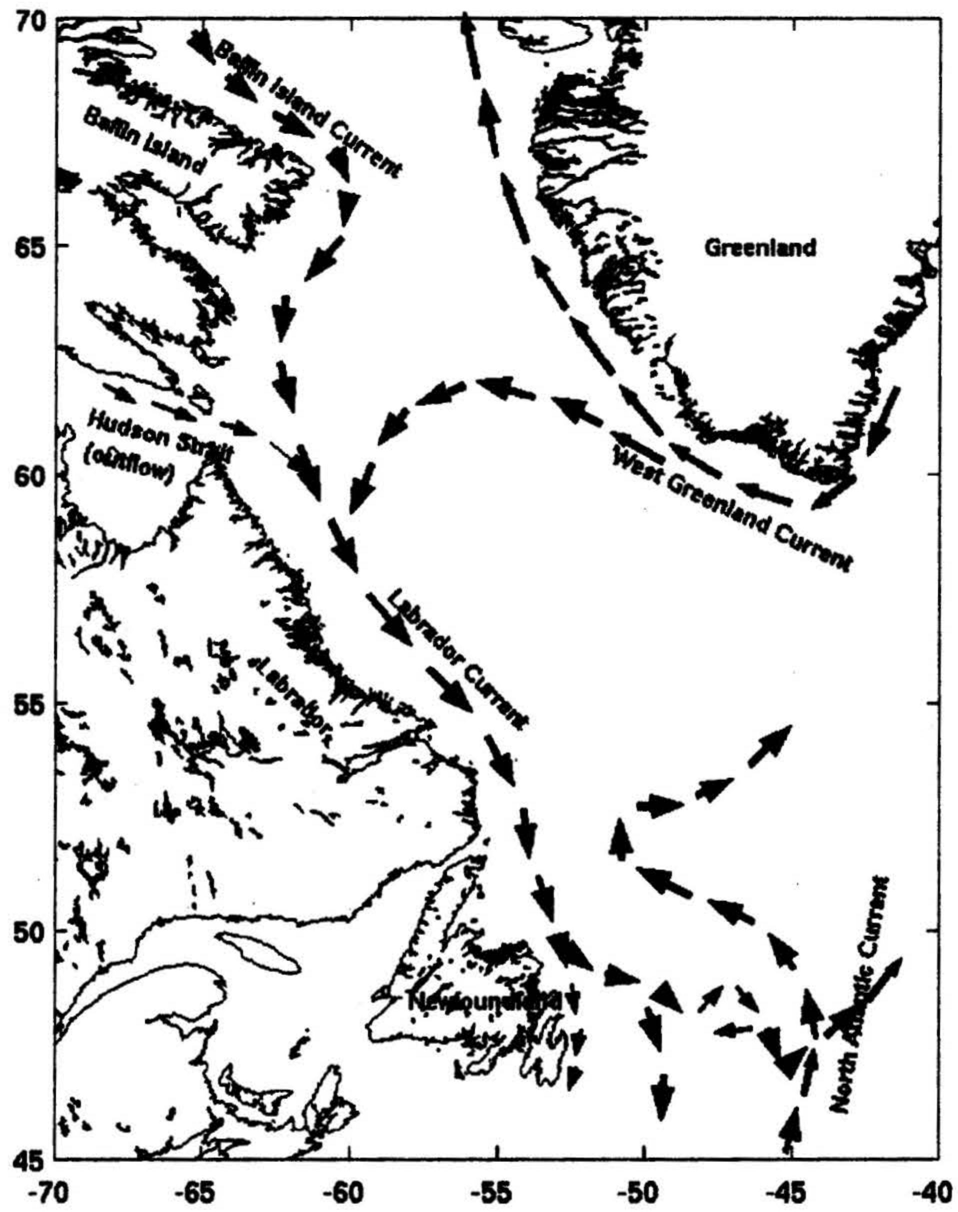

Figure 1.1 Major Ocean Currents influencing the Newfoundland shelf region. Arrows indicating the major ocean currents that influence the Newfoundland Shelf region. Shown are the West Greenland Current, the Baffin Island Current, The Hudson Bay Outflow (through the Hudson Strait). These three currents combine to form the Labrador Current which flows southwards along the East Coast of Newfoundland.

On the eastern shore, from the Northern Peninsula to the Bonavista Peninsula, north of the separation into the inshore and offshore branches, maximum temperature values are achieved around Year Day 232 (August 20) while at Station 27 maximum values for temperature are achieved around day 242 (August 20). Surface salinity values attain a maximum between days 34 (February 4) to 88 (March 29) (Petrie *et al.*, 1991).

During winter months, waters may be covered with ice, however the range of sea surface temperature is approximately 13° C from August to March (Thompson et al, 1988). Minimum surface salinity values are found between mid-August to mid-September and surface salinity has an annual range of 31 to 32.5 ppt (Petrie and Anderson, 1983). Sub-surface water (depths 50-200m) located over the continental shelf in summer are generally found to be colder and less saline (-1.5° to 0° C, 32-33 PSU) than water located over the continental slope (3°-4°, 34-35 PSU) separated by strong gradient near the shelf break (Narayanan et. al., 1991).

In addition to these seasonal variations, temperature and salinity along the east coast of Newfoundland also exhibits variation on a decadal time scale. Colbourne (2004) demonstrates that mean temperatures calculated over a 10 year period at station 27 were warmest during the 1950's and 1960's and below average for the 1970's, 80's and 90's when compared to 30-year normal calculated from 1961-90. Colbourne also shows that both vertically averaged temperature and upper-layer averaged salinity exhibit large amplitude fluctuations with a period of approximately 10 years. Salinity cycles generally preceding colder temperature cycles by 2-5 years.

Small coastal inlets and bays are common along the east coast of Newfoundland. Typically these inlets have served as the centres of human activity. In recent years there has been a growing interest in the cultivation of fish and shellfish through farming activities as the decline of fish stocks has reduced or stopped the harvesting of various species. The decline and collapse of the groundfish stocks has been attributed to overfishing, as well as environmental changes in the ocean along the Newfoundland Shelf (Lear, 1998) The development of viable fish or shellfish farms will depend on the suitability of the chosen site. Many marine species are known to be sensitive to the temperature and salinity of the water (Webber and Thurman, 1991 pp 22-27). For any given inlet or estuarine system, physical factors such as the characteristic salinity and temperature, the amount of available oxygen and the likelihood of contamination from pollution or parasites may influence the success or failure of an aquaculture industry.

The salinity, temperature and available oxygen are dependent on the residence time of the water and the amount of mixing that occurs. Without regular renewal of water from the ocean, the characteristics of the water within a particular system may depart significantly from those found on the continental shelf. The amount of vertical mixing that occurs will greatly influence the salinity and temperature of deeper waters. Factors that may influence the magnitude and depth of vertical mixing include the amount of fresh water run-off, the existence of large topographic features such as a sill, and the amount of energy available from wind stress and tides.

Based upon topographic features, estuaries may be classified into three main groups (Pritchard, 1952). These groups are coastal plain estuaries, fjords and bar-built estuaries. Coastal plain estuaries and bar-built estuaries have topographic features similar to those of river valleys. Generally they are wide compared to their depth and widen towards the mouth where the estuary meets the ocean. Bar-built estuaries differ from coastal plain estuaries by the formation of a bar across the mouth formed by the deposit of sediment. Both coastal plain estuaries and bar-built estuaries may have rivers flowing into them; the amount of sediment discharge associated with the river flow and the ability of the currents within the system to remove this sediment are significant factors in determining if a bar may form with a particular estuary.

The formation of fjords is attributed to the scouring of river valleys by glacial ice during the Pleistocene era (Dyer, 1973). One characteristic feature of fjords is the existence of one or more shallow sills that may restrict water flow entering or leaving the system. These sills may be quite shallow when compared to the depth of the main body of water. Fjords are generally quite narrow when compared to the length and often deepen quickly away from the coastline providing an almost rectangular cross section.

Two principal forces that drive the circulation within a fjord are tides and wind stress. Tidal forces act throughout the entire water column and are, generally, predictable for long periods of time based upon observations and knowledge of the tide generating forces. Wind stress is dependent upon local meteorological conditions. The forcing due to wind stress is restricted to the surface; however, winds may drive deeper currents as momentum from the surface is transferred downwards. Although observations of wind speed and direction may exist for extended periods of time, the strength and direction of the wind field cannot, typically, be forecast for more than a few days in advance. As a result of the unpredictability of the wind field, it is not possible to completely determine the forces that will act upon an estuarine system at any given time. The circulation within a given estuarine system may vary significantly in response to similar tidal forcing due to the force imparted onto the surface by the wind during the tidal cycle. Despite this, aggregate annual averages of the local wind field may provide sufficient information to determine the expected wind stress that may act upon the body of water and thus permit some predictability on the dynamical structure of a specific inlet.

The shallowness of the sill in a fjord directly influences the hydrographic properties and dynamics of the system. A shallow sill may block deep-water circulation preventing renewal of the water within the inner basin. Renewal of the deep inner basin water trapped below the level of the sill can only occur when the water outside of the sill has a density, at or above sill depth, which exceeds the density of the inner basin water. The time scale of deep water renewal can range from tidal periods to years (Pickard and Emery, 1990, p. 285). Gade and Edwards (1980) showed that the timing of renewal may be controlled by the depth of the sill relative to the depth of minimum density variation. Fjords with a sill depth shallower than the minimum density variation were found to renew during the winter, while those with a sill depth below the minimum density variation were found to renew in summer. In between successive renewal events, the water trapped behind the sill may become anoxic and its characteristic temperature and salinity may differ significantly from the temperature and salinity of the water on the seaward side of the sill.

During periods of deep water renewal, the water displaced at depth may establish an exchange flow across the sill with less dense surface water at the surface flowing outwards against the incoming denser water at the bottom. Armi (1986), Armi and Farmer (1986) and Farmer and Armi (1986) study the hydraulic control of two-layer exchange flow at a sill and contraction and also through a combined sill and contraction when subjected to barotropic forcing. They demonstrate that strong tidal forcing may overcome the hydraulic control imposed by either a sill or contraction (or combination of both) such the magnitude of the exchange flow may be controlled by the tidal cycle. If barotropic forcing is strong enough, the exchange flow may be arrested and replaced with a single-layer flow.

Some of the energy input into a fjord from the barotropic tide is lost due to frictional forces. The dominant energy balance over a tidal cycle for a barotropic tide acting at the mouth of an estuary is given by (Freeland and Farmer, 1983):

$$-\int_{mouth} \overline{gH\vec{u}\zeta} \cdot \vec{n}ds = \int_{area} \overline{\vec{F} \cdot \vec{u}dA},$$

where $\vec{u}$ is the velocity, ζ is the surface elevation, H is the depth and $\vec{F}$ is an arbitrary function representing frictional forces. Frictional forces may act in the form of side wall or bottom friction, or energy loss due to the action of internal waves or mixing. Tinis and Pond (2001) studied the energy dissipation over the shallow sill (~15m depth) of Sechelt Inlet, British Columbia. They found that the frictional dissipation rate was comparable in magnitude to the tidal energy flux of 100 MW. Inlets with relatively deep sills, such as Knight Inlet, typically have frictional dissipation accounting for less than 5% of the tidal energy flux.

Freeland and Farmer (1980) showed that the dominant process for tidal energy loss in Knight Inlet was internal wave drag at the sill. This provides a mechanism whereby tidal energy is transferred into *"intense wave-like disturbances and hydraulic jumps to dominate the mixing processes in the inlet"* (Freeland and Farmer, 1983). The transfer of energy into the mixing process through internal wave activity is most likely not isolated to Knight Inlet.

Tidal currents flowing over the sill may also generate internal waves that propagate along the fjord or break to enhance vertical mixing. Internal waves generated at a sill may contribute to the mixing process further up or down inlet from the location of the sill. As these waves propagate away from the location of the sill in the form of an internal wave train, the location of the mixing in the vertical axis may depend on the modal structure and stratification of the inlet (Freeland and Farmer, 1983; Gargett, 1980). Mode 1 waves enhance the entrainment of deeper more saline water into the surface layer, while for mode 2 waves the majority of mixing is found to occur below the main pycnocline.

When these internal waves oscillate at tidal frequencies they are commonly referred to as internal tides. As internal tides are generated at the sill, nonlinearities can move energy into higher harmonics of the forcing frequency (Bell, 1975). Blackford (1978) and Stigebrandt (1980) discuss the role of nonlinearities in transferring energy into the even (attributed to Bernoulli effects) and odd (attributed to friction) harmonics. It has also been hypothesized that the breaking of internal tides may supply turbulent energy for mixing (Stigebrandt, 1976 and 1980).

During periods of strong tidal forcing, Allen and Simpson (2002) concluded that in the strongly stratified Upper Loch Linnhe, the M_2 tide gave rise to a dominant 1st mode internal tide that behaved as a standing wave. Closer to the sill, denser water advected across the sill during a flood tide as a single layer created an anticlockwise circulation attributed to the tidal jet which entered the inner basin off centre of the main axis of the along channel direction. Denser water entering Upper Loch Linnhe was observed to pushed towards the head of the inner basin creating a depression in the density field near the sill. Allen and Simpson (2002) also identified three possible scenarios, dependent upon the density difference between the flood waters and inner basin waters, that may regulate the renewal of inner basin water. When flood waters are significantly denser than the existing inner basin water, the input rate of new waters into the inner basin will be high as the incoming water sinks below the sill replacing the existing waters which are removed from the inner basin during the subsequent ebb tide. If the flood waters have a density close to the existing surface waters of the inner basin, the system may be considered as a two layered model and the rate of water renewal will be low as the incoming waters mix with the existing surface waters, evacuating the inner basin on the ebb tide. During periods when the incoming waters sink only to mid-depths, leading to the formation of the observed density depression, the flushing rate of the inner basin will be "dependent on the amount and mechanics of the mixing associated with the depression formation". The upstream propagation of hydraulic jumps or internal bores is known to be dependent on the height of the sill. When the height of the sill, h_m (measured from the bottom), increases above a critical height, h_c (at which the flow becomes critical at the obstacle crest), in a stably stratified shear flow, the flow may become supercritical and hydraulic jumps or internal bores may propagate upstream against the flow changing the incoming velocity and density to a new steady state (Baines, 1988). Hibiya (1986) examined the generation of internal waves over a sill forced by strong, moderate and weak tides revealing that the generation of internal waves at a sill "are formed in response to a time variation of tidal flow". The formation of nonlinear internal structures, such as hydraulic jumps and internal solitary waves of the Korteweg-de Vries genre, in response to the interaction of velocity field with topography depends upon appropriate balances between nonlinearities, dissipation and dispersion which may be a function of the forcing mechanism and local stratification. Consequently, such nonlinear structures may exist frequently, occasionally or not at all for a particular location. When such structures do form they may contribute significantly to the amount of vertical mixing in the neighbourhood of the sill region. The dissipation of internal solitary waves has been shown to enhance vertical mixing in the lee of the propagation solitary wave (Timko, 1995; Timko and Swaters, 1997).

The two primary mixing processes found in estuaries are entrainment and diffusion. Entrainment is the process in which slower moving, less turbulent water is drawn into a faster moving, more turbulent layer. The rate of entrainment is dependent on the velocity difference of the two water masses; as the velocity difference increases the amount of slower moving water that is entrained into the faster moving layer also increases. The mixing which results from entrainment is a one-way process. Water is drawn into the faster moving, more turbulent layer, thereby increasing the volume of this layer. Diffusion is a two way process, it requires the existence of turbulence in both layers. As a result of diffusion, there is no net gain or loss in volume, however the characteristic properties (such as salinity) of the two water masses are exchanged resulting in a reduction in the gradient of these properties across the interface.

Within a fjord system, both types of mixing may occur. Surface layers, where there exists high shear in the velocity field will be dominated by mixing due to entrainment. Where as deeper water, where velocities and velocity gradients are smaller may be dominated by the diffusion process. Entrainment may also dominate the mixing process in regions of significant topographic variation such as those that occur in the region of a sill. As the tide flows over a sill or through a constriction, the water will accelerate forming a jet into the centre of the channel. The resulting shear will entrain surrounding water into this jet. As a result of this entrainment, deeper water may be drawn up above the level of the sill or away from the sides of the channel. The loss of mass at depth or along the channel walls may result in a counter-current as water flows against the jet to replace the missing mass. In regions where surface currents are too strong for a counter-current to set up along the channel walls, significant upwelling may occur to replenish the surface waters drawn into the tidal jet.

The influence of wind stress on the mixing process that occurs within an inlet is also dependent upon the stratification of the water column. In an inlet with continuous stratification and no well defined surface layer, the energy applied to the surface by the wind may be readily transferred down into the water column. The effect of winds blowing over a region with a well defined surface layer, however, are restricted to only acting within the surface layer as the pycnocline separating the two layers prevents the wind stress from influencing the bottom layer.

Analytical models of ocean circulation are difficult to obtain. Typically analytical solutions are restricted to idealized domains and/or forcing functions. While such solutions may provide some insight into the mechanics and processes of the circulation they can seldom be directly applied to the real environment where bathymetry, coastlines and applied forces often differ significantly from the idealized situations that permit analytical solutions.

Numerical models of oceans and coastal seas are necessary to provide solutions to the circulation in the real world. There is a wide variety of numerical models currently used for modeling oceanic circulation. The algorithms used by various models differ in a multitude of ways including the discretization of the domain, the integration scheme and the physical processes being modeled.

Discretization of the domain may be classified into two broad categories: structured and unstructured grids. Unstructured grids are generally associated with the finite element method while the structured grid techniques are associated with finite difference techniques. The unstructured grids used in the finite element method permit the modeler to fit the computational grid to complex geometries. This is advantageous in the modeling of coastal seas where the coastline may be very irregular. The unstructured grid also allows for a large degree of variation in the horizontal resolution. This variability may be used to generate localized regions of high resolution where necessary to provide a greater amount of detail in regions of interest to the modeler. Lynch et. al. (1996) used a finite element model using a wave-continuity equation method to study the circulation in the Gulf of Maine. However, Kantha and Clayson (2000) point out that the wave-continuity equation method has been found to suffer with difficulties in local mass conservation and neither is it clear that the propagation of scalars is conservative without careful construction of the finite element grid.

Structured grids associated with the finite difference method include both uniform and non-uniform grid schemes. Non-uniform grid schemes such as curvilinear orthogonal grid schemes, telescoping grids and nested grids may be employed to improve the ability of the structured grid to accommodate complex geography while reducing the overall size of the computational grid. However, the development of such grids is not necessarily trivial and very little literature appears discussing the generation and magnitude of numerical errors associated with such grid schemes.

If a model is to represent three-dimensional flow then the representation of the vertical coordinate may also vary. Two methods of representing the vertical coordinate are the z-level and sigma level approaches. The z-level method uses fixed reference levels that are independent of the depth of the water column to represent the vertical coordinate while the sigma-level method uses a fixed ratio to determine the location of the vertical coordinate dependent on the depth of the water column. The two different methods both have advantages and disadvantages that must be taken into account when using the model that is appropriate for a given application. A well-known disadvantage of the sigma coordinate system is the pressure gradient error (Haney, 1991, Mellor et. al. 1994). This error does not occur with the z-level model, however, the application of the bottom boundary condition in the z-level model is more difficult and such a grid scheme is subject to "continuity" problems when the bottom layer terminates in the presence of large topographic features (Adcroft et. al. 1997). In the sigma coordinate system, the number of vertical layers remains constant throughout the domain providing a much easier method for applying the bottom boundary condition. The CANDIE model (Sheng et. al., 1998) uses a z-level scheme to represent the vertical coordinate while the sigma-level scheme is used by the Princeton Ocean Model (POM) (Blumberg and Mellor, 1987).

Another significant difference in ocean models is the treatment of the surface boundary layer. Dependent upon the interest needs of the application a model may either use a "rigid-lid" approximation for the surface or a free surface. Often treatment of the ocean surface as a rigid lid is sufficient, however, in coastal waters and in particular in regions where tidal forcing is a dominant feature the ocean surface may not be treated as a rigid lid and a model that uses a free surface must be employed to accurately reflect the dynamical forces present. (DieCAST (Dietrich et. al., 1987) and CanDIE are rigid lid model, POM is free surface models. Lu et. al. (2001) have developed a free surface implementation of DieCAST).

Many ocean models also assume that the pressure is defined by the hydrostatic equation (hydrostatic approximation). In regions of the ocean where mixing is enhanced or where non-linearities are strong, such as in oceanic jets, the hydrostatic assumption may be invalid. Non-hydrostatic models are computationally expensive so the use of such models for modeling oceanic flows is quite limited. An application of a nonhydrostatic model for a limited region in the North Atlantic was presented by Mahadevan and Archer (1998). More recently Bourgault and Kelley (2004, submitted) have developed a laterally averaged nonhydrostatic ocean model. A Laterally averaged model has been used to study the circulation of Knight Inlet (Stacey et. al., 1995). A laterally averaged model, which integrates along the centre of the channel axis, makes an implicit assumption that the channel is symmetric about the centre of the inlet and that the velocity field acts as a plane wave across the entire domain. While laterally averaged models are, typically, computationally inexpensive and can be applied to situations where the aforementioned assumptions are reasonable, it is not obvious that such models are appropriate when the local coastline geometry is asymmetric making the choice of the along channel axis ambiguous.

Open boundary conditions pose a challenge for most models of oceanic flow. On an open boundary, the governing equations may form an ill-posed problem (Oliger and Sundstrom, 1978, Browning et. al. 1990) that requires the modeler to impose velocity and hydrographic conditions in an attempt to match the internal solution to a known external solution. The choice of the open boundary conditions applied to a model is dependent on the needs of the modeler and the specific application. Often it is necessary to apply a variation of a Sommerfeld radiation condition (Chapman, 1985) or a sponge layer to prevent outgoing waves being reflected back into the interior of the model domain. If the model requires specification of velocity at the open boundaries, it is not uncommon to derive the boundary velocities using the thermal wind equations to determine the geostrophic balance in the open ocean. In coastal regions, where tidal forces may be significant, specification of surface elevation may be necessary. Boundary velocities may then be derived as the barotropic tidal velocity.

A 2-dimensional, laterally averaged variant of the Princeton Ocean Model (POM) (Blumberg and Mellor, 1987) has been applied by: Stacey et. al. (1995) to model Knight Inlet; Stacey and Gratton (2001) to model Sagueney Fjord; and Tinis and Pond (2001) to model Sechelt Inlet. Cummins (2000) applied a laterally averaged version of the POM model to study the stratified flow over the sill in Knight Inlet. Afanasyev and Peltier (2001a,b) applied a nonhydrostatic model to the same region to study the influence of inflow velocity and topographic height to the breaking of internal waves. Das, et. al. (2000) used POM as a 2-dimensional depth averaged barotropic model to study the residual circulation of Sydney Harbour. ECOM and ECOM-si (Blumberg and Mellor, 1987, Casulli and Cheng, 1992), variants of the Princeton Ocean Model have been used to study New York Harbor (Blumberg et. al., 1999) and the tidal circulation in Cobscook Bay (Brooks, et. al., 1999). With each of these models the authors identify horizontal resolutions of (approximately): 170 metres to 8 kilometers (Stacey et. al., 1995); 150 metres (Das, et. al., 2000); 100 metres to 50 kilometres (Blumberg et. al., 1999) and 255 metres (Brooks, et. al., 1999). Given these results, the Princeton Ocean Model appears to be an appropriate choice for studying Clode Sound, a small estuary on the east coast of Newfoundland. Clode Sound contains both a sill and a coincident contraction; at its narrowest point, Clode Sound the width of the inlet reduces to approximately 500 metres. To provide a reasonable resolution to the region of the sill, the model will require a horizontal resolution of 50 metres, this will allow the region of the contraction (and the sill) to be represented by approximately 10 grid points.

This thesis will focus on observations collected in Clode Sound, Newfoundland during the summers of 1996 and 1997 as well as modelling of the inlet and comparison to the observations to verify the model. Chapter 2 will present the observed hydrographic properties and currents of Clode Sound during the observation periods. The focus of the analysis in Chapter 2 will be on the variations across the sill and the internal response generated at the sill. Velocities recorded at the sill indicate that the flow at the sill may become supercriticial during spring tides. During neap tides, wind stress may drive a weak exchange flow across the sill. A spectral analysis of the fluctuating kinetic energy is presented to determine the balance between the wind stress and tidal forcing at the mooring locations. Finally a discussion of selected mixing is presented to explain the various causes of mixing across the sill.

Chapter 3 presents the necessary modifications made to the Princeton Ocean Model (POM) in order to execute this model at a horizontal resolution of 50 metres in Clode Sound. In addition to the development of the domain and model boundary conditions code changes within the model to correct numerical errors that arise as a consequence of the land/sea masking will also be discussed. A simplistic scheme to permit the evolution of background temperature and salinity in the presence of strong tidal forcing will also be presented.

Chapter 4 evaluates the model's performance when the model is forced with tidal elevations and wind stress using a statically stratified fluid and compares the results to the observational data. It is shown that the tides and residual circulation are poorly represented when density field is held constant. With the addition of wind stress to the model simulations, the inability of the statically stratified models to reproduce the tidal forcing contributes to an imbalance of the forces that drive the residual circulation. Models with a static density field do not vary significantly from a 3-dimensional barotropic model forced by winds and tides.

In Chapter 5 simulations in which temperature and salinity are allowed to mix using the relaxation scheme presented of Chapter 3 are presented. Compared to the results of Chapter 4, the model is able to provide a reasonable representation of the tidal flow in the outer channel (seaward of the sill) however, when wind stress is applied the model is found to be numerically unstable resulting in simulations of approximately 10 days duration. An attempt is made to analyze the balance of forces with wind stress applied to the model, however, the results are very inconclusive as the shorter 10 days simulations have a large degree of uncertainty. When the model is forced with wind stress and tides, the resulting residual circulation is shown to have greater variability than when the model is executed with the static density fields of Chapter 4. Even though the model is able to reproduce some of the variability found in the observed residual flow at the mooring locations, it is not able to reproduce the recorded signals. Chapter 6 summarizes the results of the previous chapters discusses the suitability of the model to this application and its limitations. Unresolved issues in modeling this domain are also presented with suggestions to those who may wish to pursue the subject further.

Chapter 2 Observations

So she was considering, in her own mind (as well as she could, for the hot day made her feel very sleepy and stupid), whether the pleasure of making a daisy-chain would be worth the trouble of getting up and picking the daisies, when suddenly a White Rabbit with pink eyes ran close by her.

- Lewis Carroll
Alice's Adventure in Wonderland

Clode Sound is a small glacial carved fjord with a single sill located on the east coast of Newfoundland (Figure 2.1). Measured along the centre of the inlet from head to mouth, the length of the inlet is approximately 30 kilometres. Outside of the sill, the inlet has an average width of approximately 2 kilometres, narrowing to 0.5 kilometres at the sill. The inner basin is rectangular in shape with a dome shaped bottom, the lateral extent of the inner basin is approximately 7 kilometres with a width of about 3 kilometres. The depth of the inlet varies from over 200 metres at the mouth decreasing to between 15-20 metres at the sill. The inner basin has an average depth of approximately 25 metres with a maximum of about 60 metres.

During the summers of 1996 and 1997 a series of observations were conducted to measure variations in temperature, salinity and velocity within the inlet (Timko et al., 1998a,b). These observations were supplemented by measurements of the wind field collected at Gander, Newfoundland (48° 57′ N, 54° 34′ W) by the Atmospheric Environment Service of the government of Canada, and also daily river flow data on the Northwest River that flows into the head of the inlet (HYDAT 2000). A series of CTD stations were located along the centre of the inlet and fixed submerged moorings were located in the region of the sill. The configuration of the CTD and mooring stations for both the 1996 and 1997 observations are shown in Figures 2.2 and 2.3 respectively. In addition to the CTD and mooring data collected during the summer of 1997, ADCP data was also collected over three days during the month of June 1997 (Timko et al., 1998b).

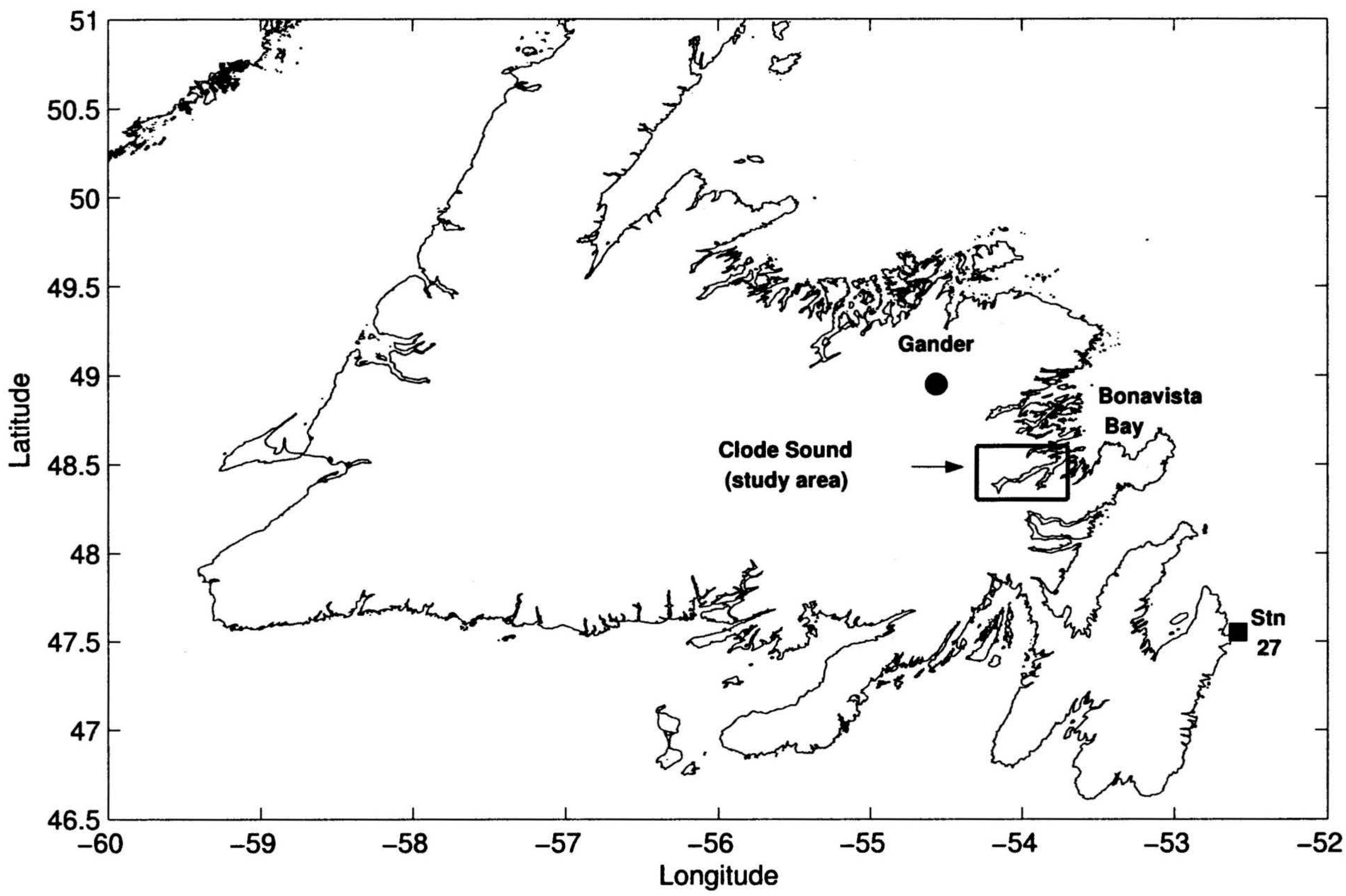

Figure 2.1: Map of Newfoundland identifying the study area Clode Sound (square box), the location of Gander (48° 57′ N, 54° 34′ W) and the location of hydrographic station 27 (47° 33′ N, 52° 35′ W).

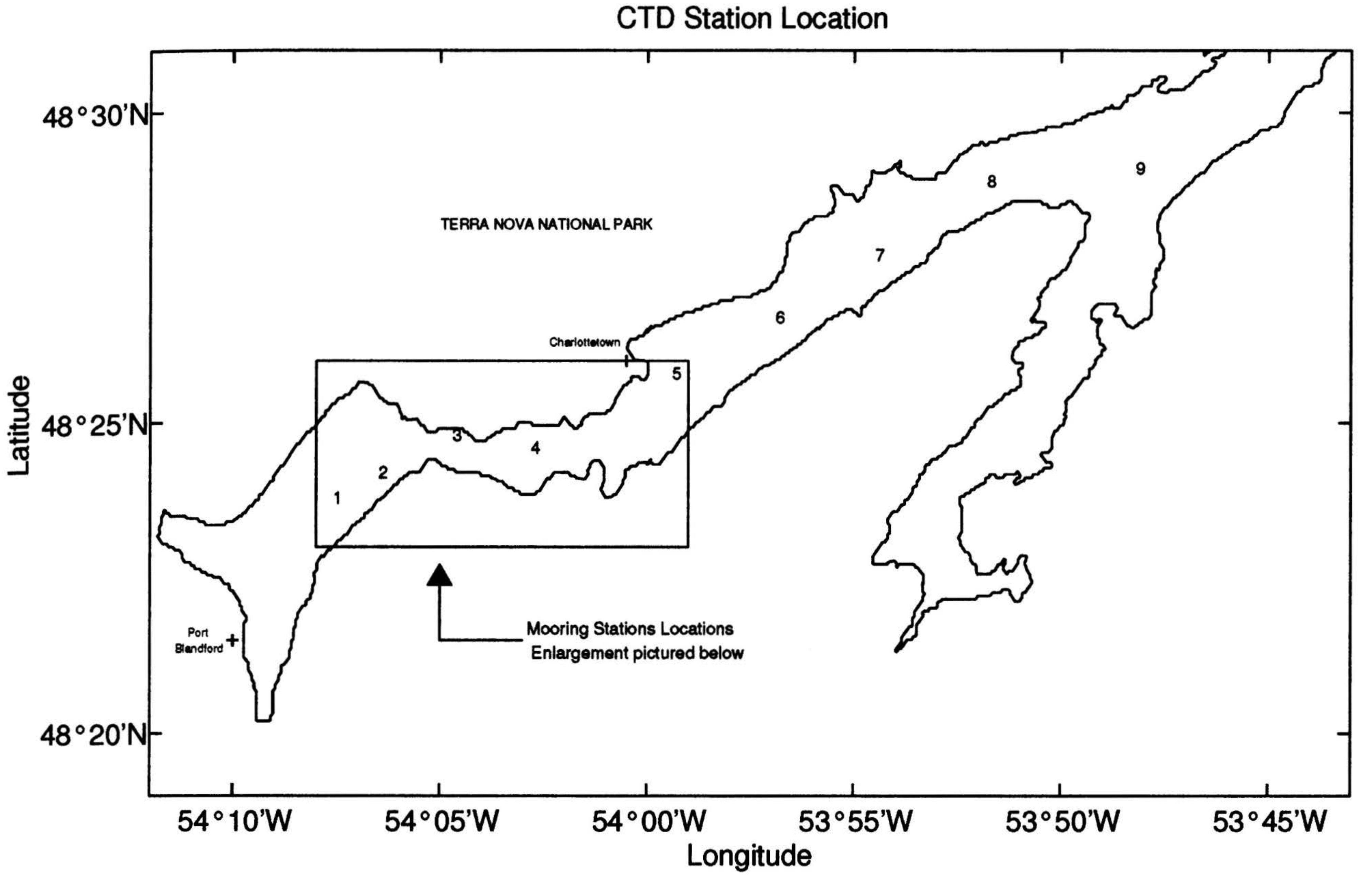

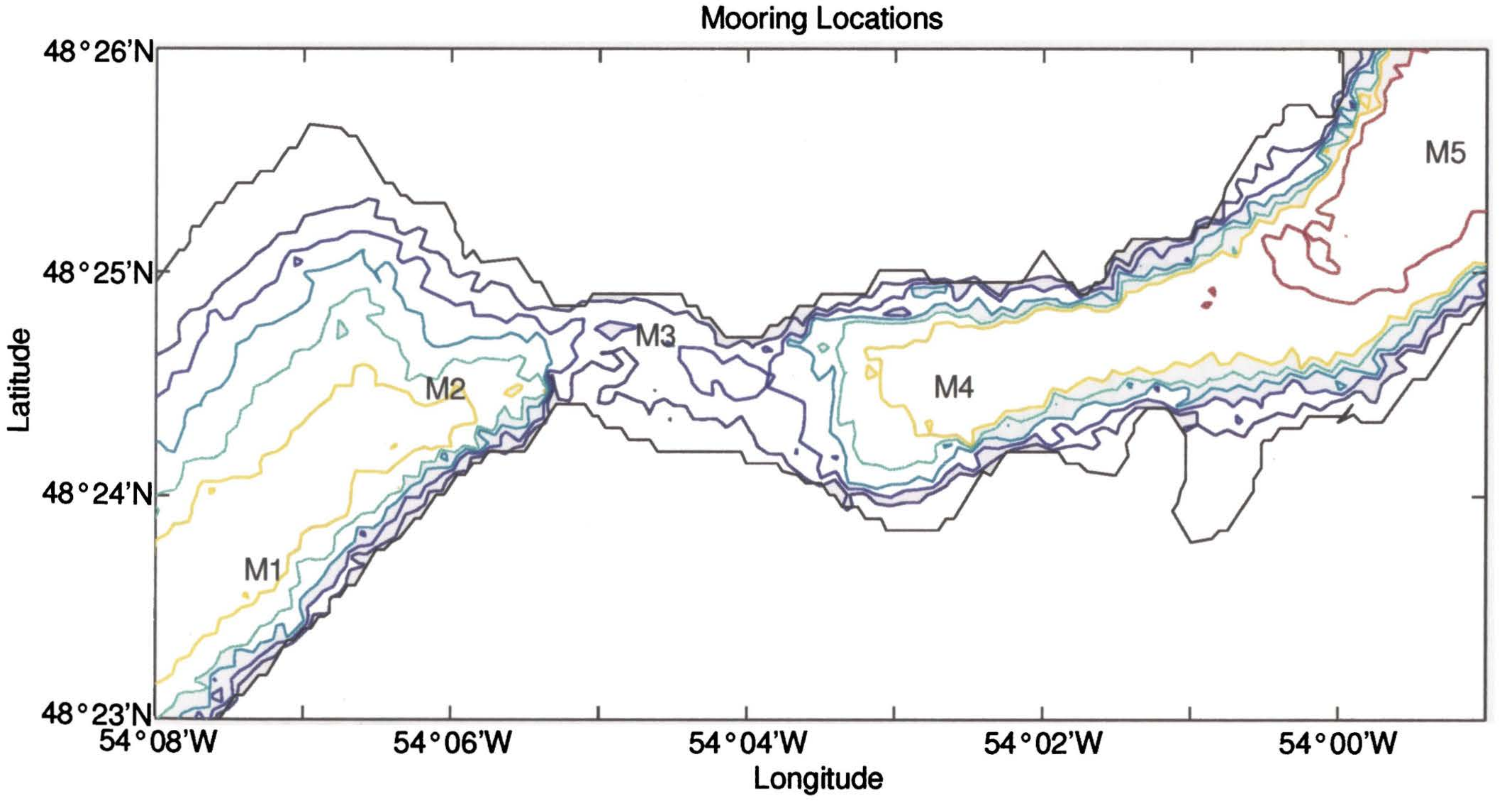

Figure 2.2: Top: Map of Clode Sound showing CTD station locations for the 1996 survey. Bottom: Mooring locations deployed during 1996, depth contours are drawn at 10, 20, 30, 40 and 50 m.

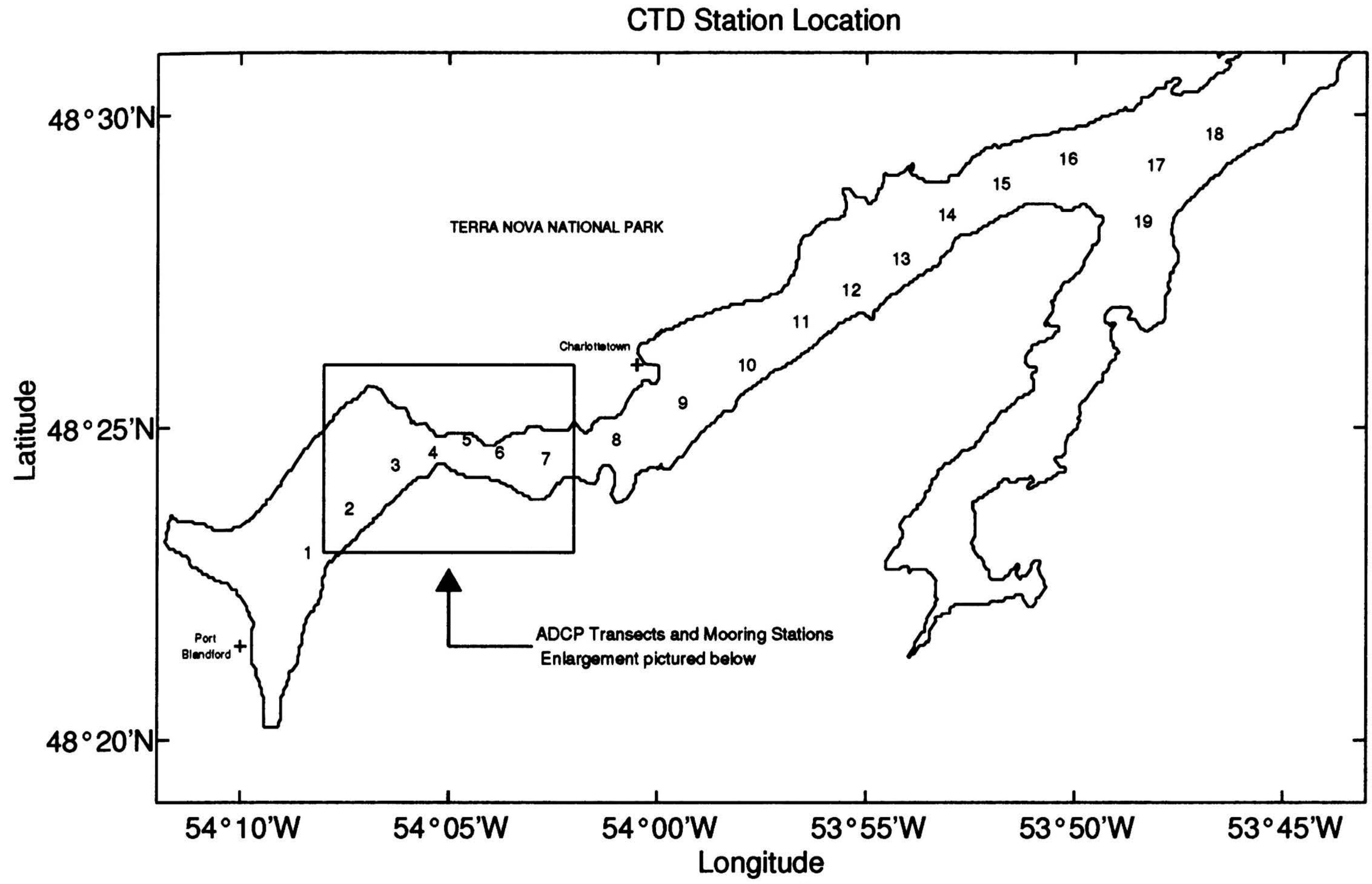

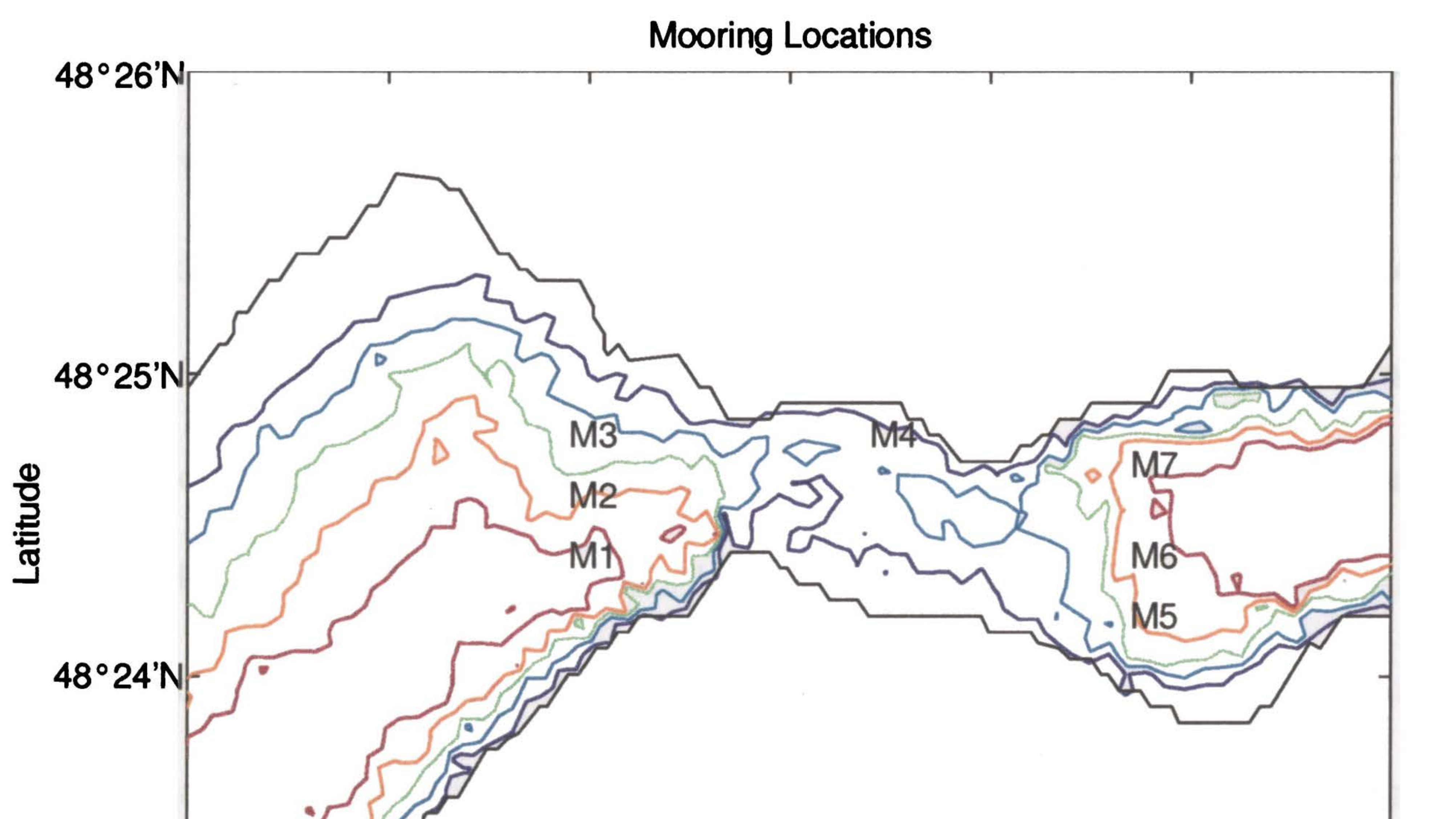

Figure 2.3: Top: Map of Clode Sound showing CTD station locations for the 1997 survey. Bottom: Mooring locations deployed during 1997, depth contours are drawn at 10, 20, 30, 40 and 50 m

2.1. *Temperature and Salinity*

Both the 1996 and 1997 mooring data reveal an increase in temperature as well as a decrease in salinity typical of the summer season. The summer time trends in temperature and salinity values may be partially attributed to the seasonal harmonic on the east coast of Newfoundland. At station 27 (47° 33′ N, 52° 35′ W, Figure 2.1), the annual harmonic of temperature (salinity) reaches a maximum value on Julian day 242 (day 88 for salinity) along the east coast of Newfoundland. Between 100 metres and the surface, the annual harmonic for temperature (salinity) accounts for 50-94% (53-71%) of the total variance in the temperature (salinity) signal (Petrie et al., 1991). Observations of temperature and salinity in Clode Sound covered only 60 days in 1996 (Julian Days 185-245) and 100 days in 1997 (Julian Days 170-270). Due to the short observation periods it is not possible to determine if any such annual harmonic exists. However, the observation periods from 1996 records attain a maximum temperature value between days 236-237 in the top 20 metres. Instruments located below this depth indicate a temperature signal that increases continuously over the entire observation period. During 1997, maximum temperature values were attained between days 240-243 at the sill and seaward of the sill above 20 metres depth. Below 20 metres, the maximum temperatures were attained between days 244-253 with deeper instruments lagging those closer to the surface. Within the inner basin, the temperature records above 20 metres depth show maximum temperatures lagging those seaward of the sill by approximately 5 days with the maximum temperatures occurring between days 247-248. Below 20 metres, the temperature records indicate that the bottom temperatures continue to rise over the entire 100 days of observation.

2.1.1 Gradients, Rates of Change and Vertical Mixing

The average rate of change in the temperature and salinity was determined for each instrument by a least squares fit to a straight line (Tables A.1-A.4). The annual harmonic with frequency ω may be described as a function of the form: $A_i cos(\omega t- \phi_i)$ where A_i and ϕ_i are the amplitude and the phase (occurence of maxima in Julian days) of the temperature signals (Petrie et al., 1991). The average rate of change of the harmonic based upon the values provided by Petrie et al. over the period of observations for 1996 (days 185 to 245) and 1997 (days 170 to 270) are provided in Table A.5. Comparison of Tables A.1-A.5 (Figure 2.4) shows that during both the 1996 and 1997 observation periods, the rates of change in temperature above the sill (7.5-10 m) are 2-3 times greater than the rates of change calculated from the harmonic. Near the depth of the sill (15-20 m) there is a two- to three-fold increase in the rate of temperature change at both the sill and in the outer channel. At this depth, the inner basin water in 1996 shows a temperature gradient only 1.5 times greater than the harmonic while the data from 1997 shows an increase almost equal to the rate of change calculated from the harmonic.Below the sill (at depths greater than 30 m), the water temperature within the inner basin increases at a slower rate than that of the annual harmonic. In 1996 the rate of increase in temperature is 70-80% of the harmonic while in 1997 the change is only 50-70%. Seaward of the sill, the temperature gradients are generally higher than those of the harmonic for depths between 30 to 50 metres. The greatest departures from the harmonic are seen during 1996 when there is an increase of about 80% and at mooring M7-97 (30 m) where the increase is approximately 60% greater. The CTD casts along the channel axis from 1996 and 1997 (Figure 2.6) show the influence of the differences in heating rates of the water column over the course of the 1997 season.

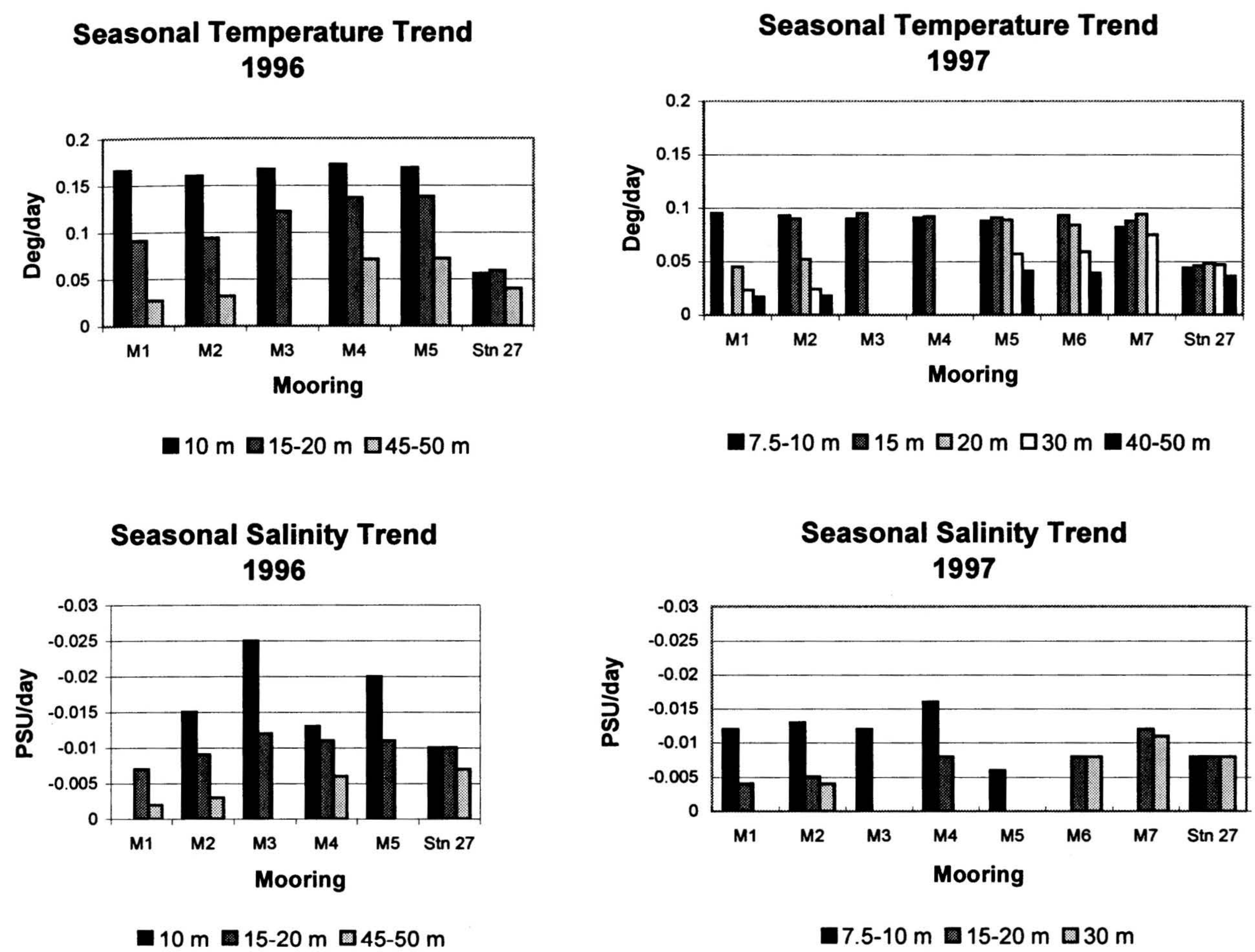

Figure 2.4: Rates of Change of Temperature and Salinity in Clode Sound 1996 and 1997.

A comparison of the rates of change of salinity reveals a similar trend to that found in the temperature signals. Above the level of the sill, the rates of change in salinity are from 30-200% greater than the rates of change calculated from the harmonic. The greatest rate of change is found at the sill. Near the depth of the sill, the rates of change of salinity are about 10-30% lower in 1996 and 37-50% lower in 1997 than the rates of change predicted from the harmonic. During 1996 the instrument located at the sill (M3-96) shows a salinity gradient which is approximately 20% higher than that of the harmonic while in 1997 the rates of change in the centre of the channel (M4-97 and M6-97) are similar to the harmonic. There is a noticeable increase in the rate of change in salinity for those instruments located to the north and south of M6-97. Moorings M5-97 and M7-97 show a salinity gradient that is 1.5 to

1.75 times greater than that predicted from the harmonic and also calculated from the data collected at the sill (M4-97) and in the centre of the outer channel (M6-97).

Below the depth of the sill, the 1997 data indicates that the rate of change of salinity is similar to the rate of change of salinity closer to sill depth. However, the 1996 data indicates that salinity within the inner basin decreases at a rate which is 57-71% lower than the rate of decrease indicated by the harmonic for station 27. The data from the outer channel in 1996 (M4-96 and M5-96) are almost in agreement with the harmonic with a slightly lower (0-14%) rate of decrease in salinity values.

The information contained in Figure 2.4 and Tables A.1-A.5 also reveal that although the rates of change across the sill are very similar in the surface layer (7.5-10m), there is a substantial difference in the rate of change in both temperature and salinity across the sill for those instruments located at or below the depth of the sill (approximately 20m). In particular, the temperature data from 1996 reveals that, at the sill (mooring M3-96) and seaward of the sill (moorings M4-96 and M5-96), the rate of change in temperature at sill depth (15-20m) is about 1.5 times the rate of change in temperature for those instruments located within the inner basin (moorings M1-96 and M2-96). The difference in temperature gradients is even greater at 45 m depth, with those instruments located seaward of the sill showing a temperature gradient approximately 2-3 time greater than those located within the basin. The data from 1997 reveals a similar trend in temperature gradients. One noticeable difference is that the rates of change remain reasonably constant down to a depth of 15 metres. This is most easily explained by the greater proximity of the instruments to the sill during the 1997 study.

The rates of change cannot be meaningfully interpreted without a comparison of the average temperature and salinity values at the mooring locations. Averages of temperature and salinity for all instruments as well as those observations taken at Station 27 during the study periods are provided in Figure 2.5 and Tables A.6-A.10. The average temperatures for those instruments located above the level of the sill are typically lower than the temperatures recorded at 10 metres depth at Station 27. The average temperatures recorded at Clode Sound are typically 10-20% lower with the exception of the instrument located at 7.5 m depth at mooring M7-97. For those instruments located close to the depth of the sill (15-20 m) the average temperature are significantly different for those instruments located within the inner basin when compared to those located in the outer channel. Instruments located within the inner basin at 20 metres depth (just below the level of the sill) show average temperatures which are between 35-60% lower than those temperatures recorded at the same depth at Station 27. It is evident that the sill blocks the exchange of water at this depth because the instruments located at 15 metres depth and at 20 m depths in the outer channel differ from the Station 27 data by only 5-20%. A similar pattern is seen for those instruments located in deeper water. During the 1996 study, the average temperature at 45 metres depth within the inner basin is in good agreement with the data at Station 27, however, in the outer channel, the average temperature is 75-100% higher. This could only be possible if warmer water from the surface layers is being mixed downwards in the region seaward of the sill. The 1997 data supports this hypothesis. The data from 1997 shows that temperatures within the inner basin at 30 metres depth are 55-70% lower than recorded values at Station 27. At the same depth in the outer channel, the temperature values are 10-50% higher.

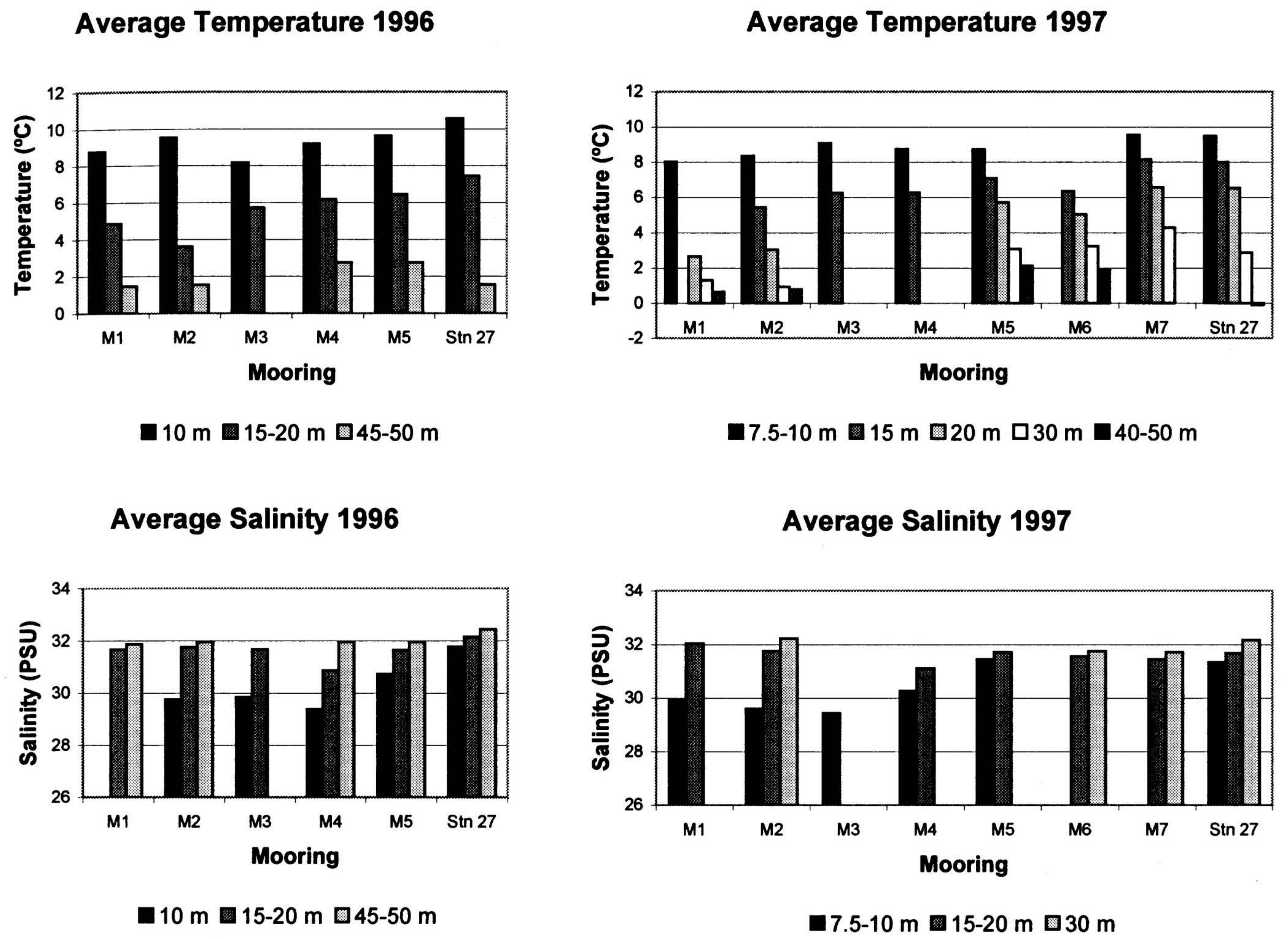

Figure 2.5: Average Temperature and Salinity recorded in Clode Sound during the observations of 1996 and 1997

2.1.2 Formation of the Inner Basin Water and The Mixed Layer

A comparison of the average temperature and salinity values within the inner basin also reveals that the water below the sill is colder and more saline in 1997 than the water that was resident there during the 1996 study. This suggests that the inner basin water renewed between the observation periods. By comparing the temperature and salinity values of the water located within the inner basin to those at 20 m of depth at Station 27 (Figure 2.8) it is apparent that the renewal took place between February and March 1997. Figure 2.8 clearly shows that the density of the water located at 30 metres depth at Station 27 is much less

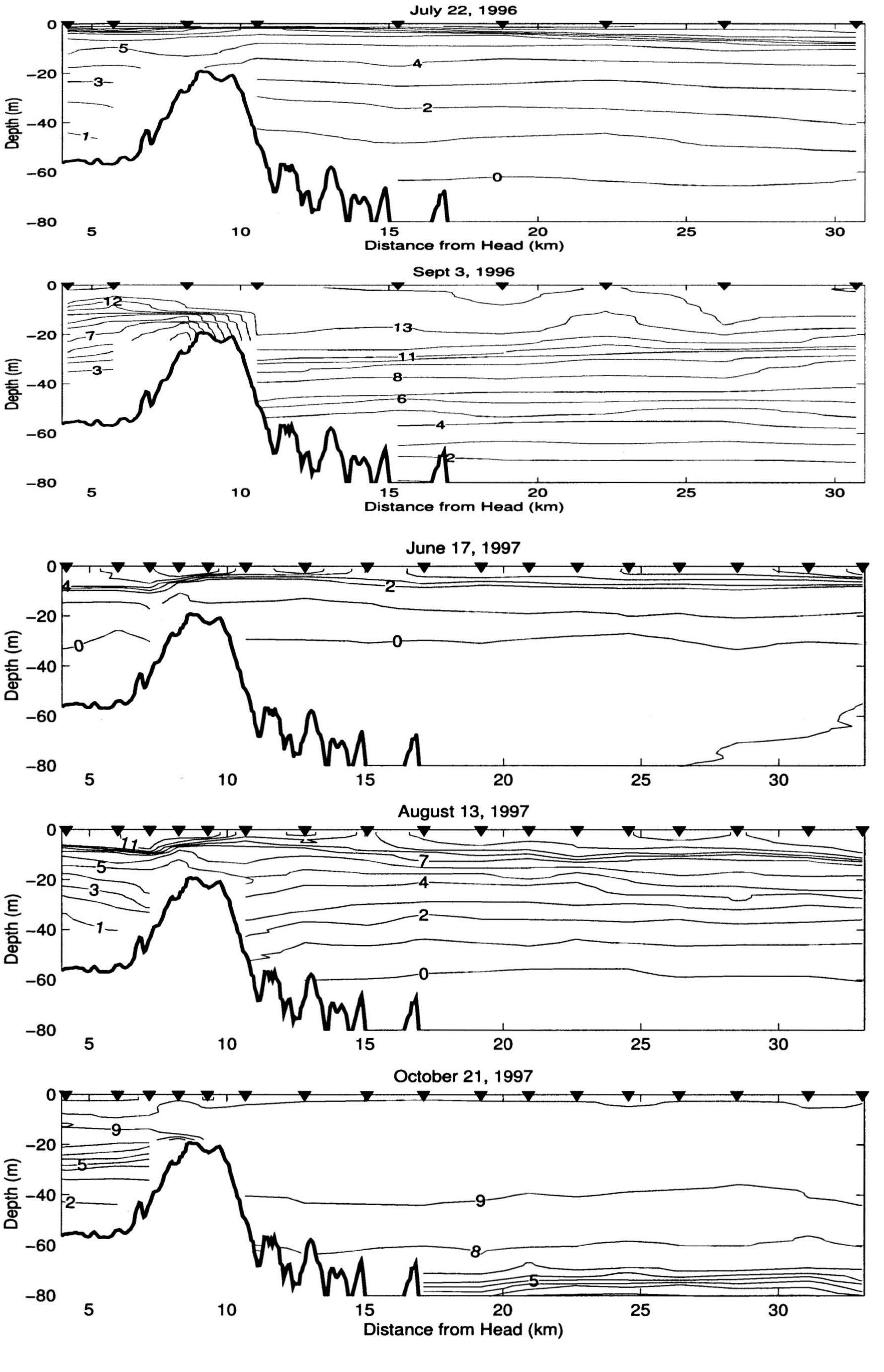

Figure 2.6 Top: Temperature data from the CTD casts on July 22 and September 3, 1996 (panels 1 & 2); **June 17, August 13 and October 21, 1997** (panels 3, 4 & 5).

(almost 1kgm^{-3}) during the month of December 1996. The difference in density during January 1997 is within 0.5 kgm^{-3} but the water is still less saline. Unfortunately there are no data for February and March 1997 at Station 27 but by April 1997 the water types appear similar. A similar comparison of the 1996 inner basin water to the data at Station 27 reveals a similar trend in the data (Figure 2.7). One noticeable difference between the Station 27 data in 1996 and 1997 is that the denser water persists until May 1997 while in 1996 the densest water appears to occur in April.

Below the sill, the inner basin water is trapped during the summer months. Figure 2.7 indicates that there is very little variation in either the temperature or salinity at 45 metres depth. With the input of heat during the summer months, the surface layer deepens and in the absence of any significant fresh water input the entire inlet should become thermally stratified. The resulting stratification may be represented by a two-layer fluid, the depth of the surface layer increasing as the water is warmed by the input of solar radiation at the surface.

The amount of mixing that occurs on either side of the sill may be a consequence of hydraulic control at the sill. Figure 2.9 shows the average depth, width and volume across the sill from M2-96 to M4-96. The total area of the inner basin is approximately 1.94×10^7 m^2. A spring tide with a range of 1.5 metres would require approximately 2.91×10^7 m^3 of water to flow over the sill and through the contraction over a time of 6.21 hours during a flood or ebb tide (assuming the tidal period is M_2). This would require an average flow rate of, approximately, 1.3×10^3 m^3/s over the sill from low water to high water or vice-versa.

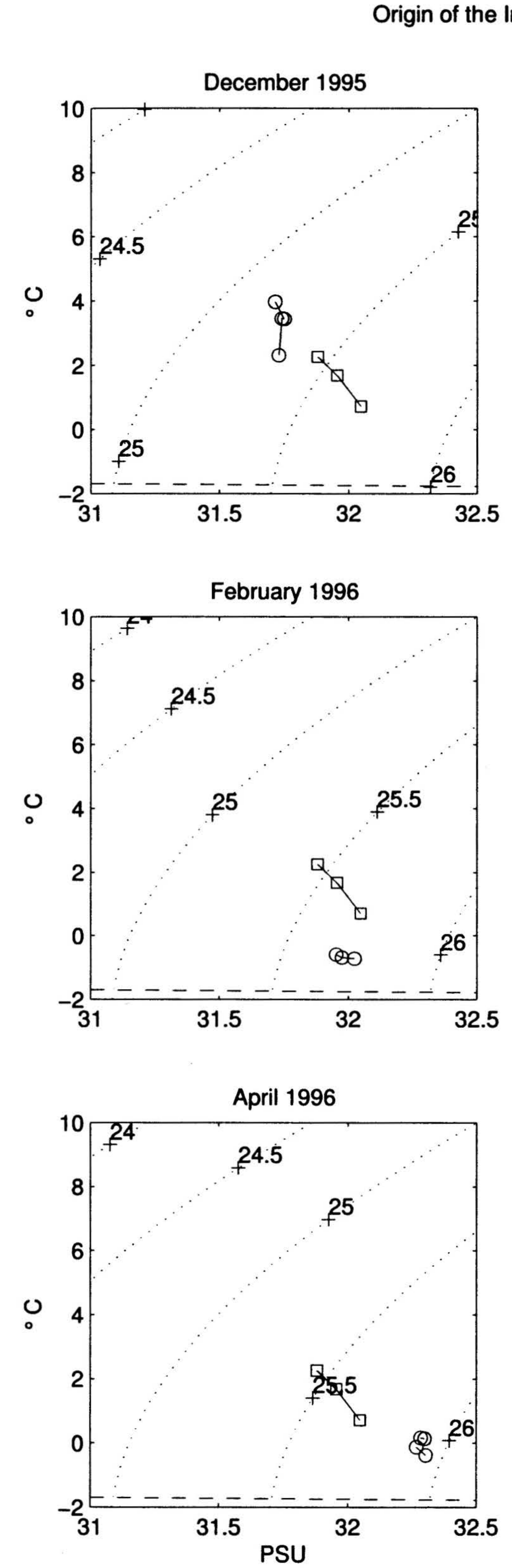

Figure 2.7: T-S Diagram comparing the Inner Basin water at 45 metres depth (M2-96) in 1996 (squares) to the record at Station 27 (circles) between December 1995 and April 1996.

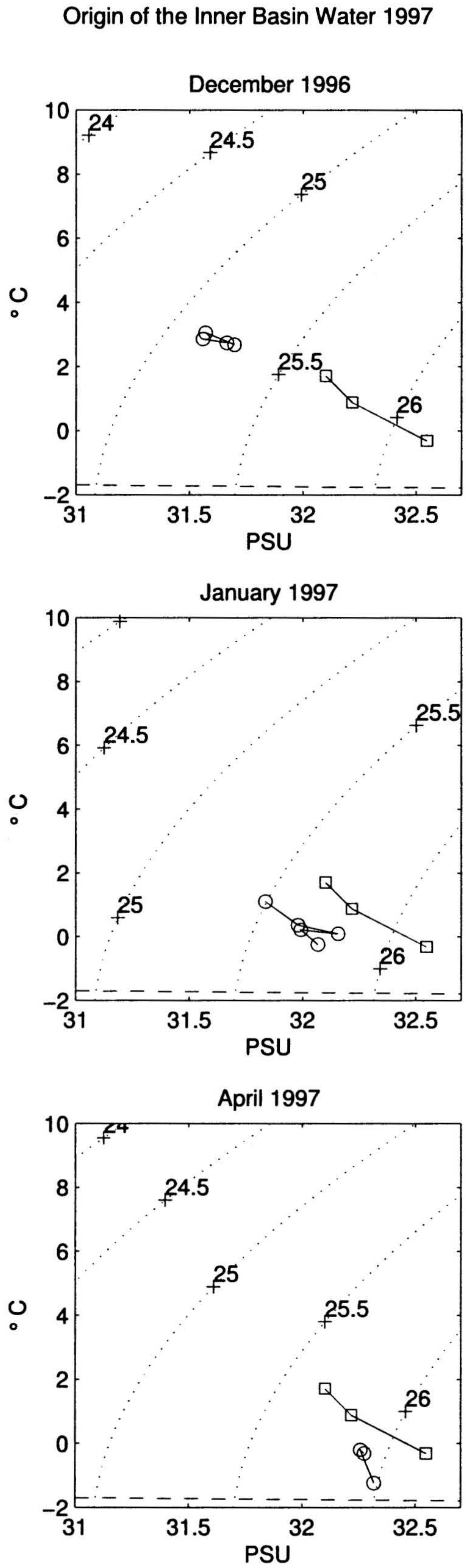

Figure 2.8: T-S Diagram comparing the Inner Basin water at 30 metres depth (M2-97) in 1997 (squares) to the record at Station 27 (circles) between December 1996 and April 1997.

The minimum cross-sectional area (Figure 2.9) is approximately $1.0x10^4$ m^2 so we should anticipate an average current speed of approximately 0.13 m/s. The average along channel speed, on both flood and ebb tides, measured at 10 metres depth is approximately 0.12 m/s in good agreement with this estimate. Considered as a barotropic fluid and a single layer, the Froude number for a single fluid would be given by $F_r=U/(gH)^{1/2}$ where U is the speed of the fluid, $g=9.81m/s^2$ is the acceleration due to gravity and H is the depth of the sill. For U=0.12 m/s and H=15 m, clearly $F_r<<1$, along current velocities measured at the sill moorings where bounded between -0.50 m/s $<= U <=$ 0.60m/s so the barotropic mode will always remain subcritical.

The CTD cast from August 13, 1997 (Figure 2.6) indicates a well-defined surface layer of approximately 10 metres depth. If we consider a two-layer fluid with a surface layer of depth h_1 and a lower layer of depth h_2 such that $h_1+h_2=H$. The interfacial Froude number is then given by $Fr_i=U_i/(g'h_i)^{1/2}$, where $g'=g(\rho_i- \rho_m)/ \rho_m$ is the reduced gravity, U_i is the velocity in the i^{th} layer. Assuming that temperature and salinity measurements recorded at 10 metres (7.5 metres) depth in 1996 (1997) are representative of the surface layer and that the temperature and salinity records at deeper instruments are representative of the lower layer, it is possible to calculate the amount of buoyancy (indicated by the reduced gravity, g') at various locations throughout the inlet.

The average and extreme values for the bouyancy parameter, g' are provided in Table 2.1. From both 1996 and 1997 we see a clear indication that the mean value of g' decreases as the distance from the head of the inlet (and also the source of fresh water) increases. The fresh water that is available is most likely mixed into the surface waters near the head of the inlet before moving seaward and across the sill. Unfortunately the absence of any surface salinity measurements at M1-96 makes verification of the decreasing salinity towards the head impossible within the inner basin.

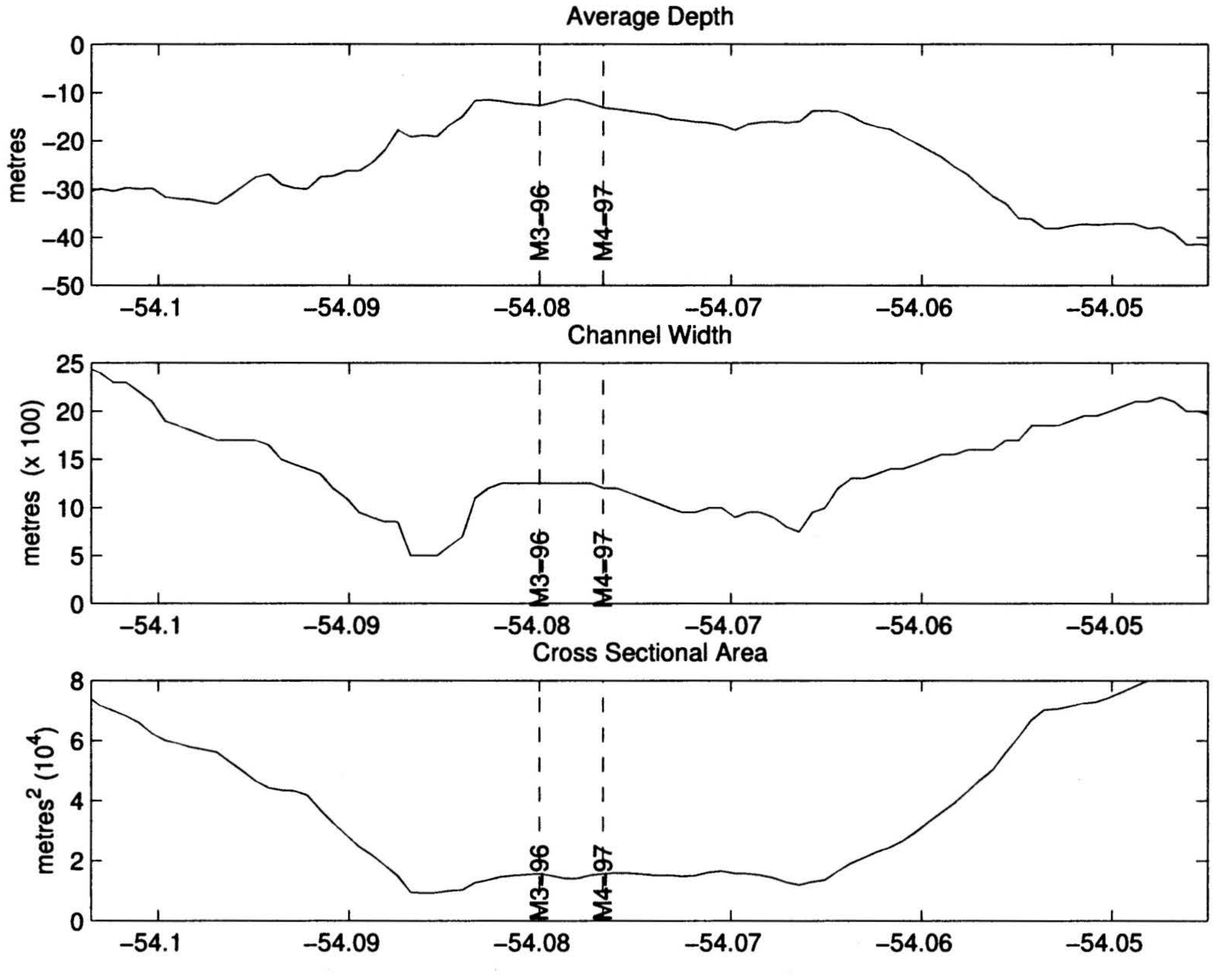

Figure 2.9: Average Depth, Width and Cross Sectional Area across the sill. Mooring locations M3-96 and M4-97 are indicated as vertical lines. Mooring location M2-96 is located on the left-hand side of the figure; location M4-96 is located on the right-hand side.

Table 2.1: Bouyancy parameter (reduced gravity) for two-layer representation of the inlet estimated from the mooring locations assuming that the surface instruments were representative of the surface layer and instruments located at greater depth are representative of a lower layer.

	Bouyancy ($g' = g(\rho - \rho_m)/\rho_m$)		
Location	**Mean**	**Minimum**	**Maximum**
Inner Basin:			
(M2-96)	0.023	0.012	0.034
(M1-97)	0.023	0.010	0.034
(M2-97)	0.023	0.011	0.033
Sill:			
(M3-96)	0.017	0.010	0.026
(M4-97)	0.010	0.002	0.024
Outer Channel:			
(M4-96)	0.015	0.010	0.028
(M5-96)	0.012	0.005	0.023
(M5-97)	0.006	0.000*	0.020

At the sill, the buoyancy parameter g' had a mean value of approximately 0.017 ranging between 0.010 to 0.026 during 1996 while in 1997 the mean value of g' was found to be 0.010 with a values ranging from 0.002 to 0.024. The low value of g'=0.002 in 1997 was recorded in June when the surface layer was clearly confined to the top few meters of the water column as can be seen in the CTD temperature data for June 1997(Figure 2.6). The combination of a contraction and the shallower water at the sill may lead to supercritical flow at the sill during both flood and ebb tides. Figure 2.10 shows the distribution of the along channel velocities (rotated to the principle axis as in section 2.5) along with the location of the line Fr_i=1.0 as a function of layer depth h_i and velocity U_i indicating the transition from subcritical to supercritical flow for values of g'=0.01, 0.02, 0.03 and 0.04. The flow is supercritical for all velocities lying below the line Fr_i=1.0. Clearly supercritical flow may occur at the sill even if the value of g'=0.04. Typical values at the sill for g' were between 0.02 to 0.03, approximately 10% of the velocities recorded at the sill were found to be supercritical when g'=0.02. The most obvious time of occurrence of supercritical flow would be during spring tides as this would be when maximum flow over the sill (and hence maximum velocities) would occur.

Supercritical flow at the sill may lead to the formation of internal bores and hydraulic jumps on either side of the sill (Klemp et. al., 1997). The geometry of the coastline, changes in depth and the buoyancy parameter may all play significant roles in determining if an internal bore or hydraulic jump may form. During a supercritical flood tide we may anticipate the formation of an internal bore forming seaward of the sill and a hydraulic jump forming within the inner basin. Seaward of the sill, the internal bore may propagate upstream against the flow into a region of decreasing buoyancy and increasing depth if the rate of decrease in buoyancy is able to compensate for the increasing depth and slight widening of the inlet (Figures 2.2 and 2.3). This would increase the mixing along the interface and deepen the mixed layer. Within the inner basin, however, the buoyancy increases, the depth and width of the inlet increase more rapidly than the region on the seaward side of the sill. A hydraulic jump (if it was able to form) would likely become stationary as it balances against increasing buoyancy towards the head of the inlet. This may create a region of high local mixing in the vicinity of the sill, but would not significantly increase the overall depth of the mixed layer within the inner basin as the mixing would be confined very closely to the sill. During an ebb tide, the newly mixed water close to the sill would be advected across the sill and an internal bore may not even form within the inner basin as the advancing density gradient from the head of the inlet would increase the buoyancy on the upstream side of the sill. If an internal bore is able to form within the inner basin, increasing buoyancy towards the head of the inlet would prevent it from propagating upstream against the flow. On the seaward side of the sill, a hydraulic jump may propagate downstream away from the sill into a region of decreasing buoyancy if the decrease in buoyancy was able to compensate for the slower change in depth and width found in this region. This propagating internal wave would also enhance the mixing seaward of the sill. The enhanced mixing seaward of the sill, may slowly create a deeper surface layer on the seaward side of the sill, this deepening of the mixed layer would continue until such time as the surface layer of the outer channel was deep enough to completely block the lower layer flow from crossing the sill. Such a processs may help to explain the temperature distribution found in the CTD data for September 3, 1996 (Figure 2.6).

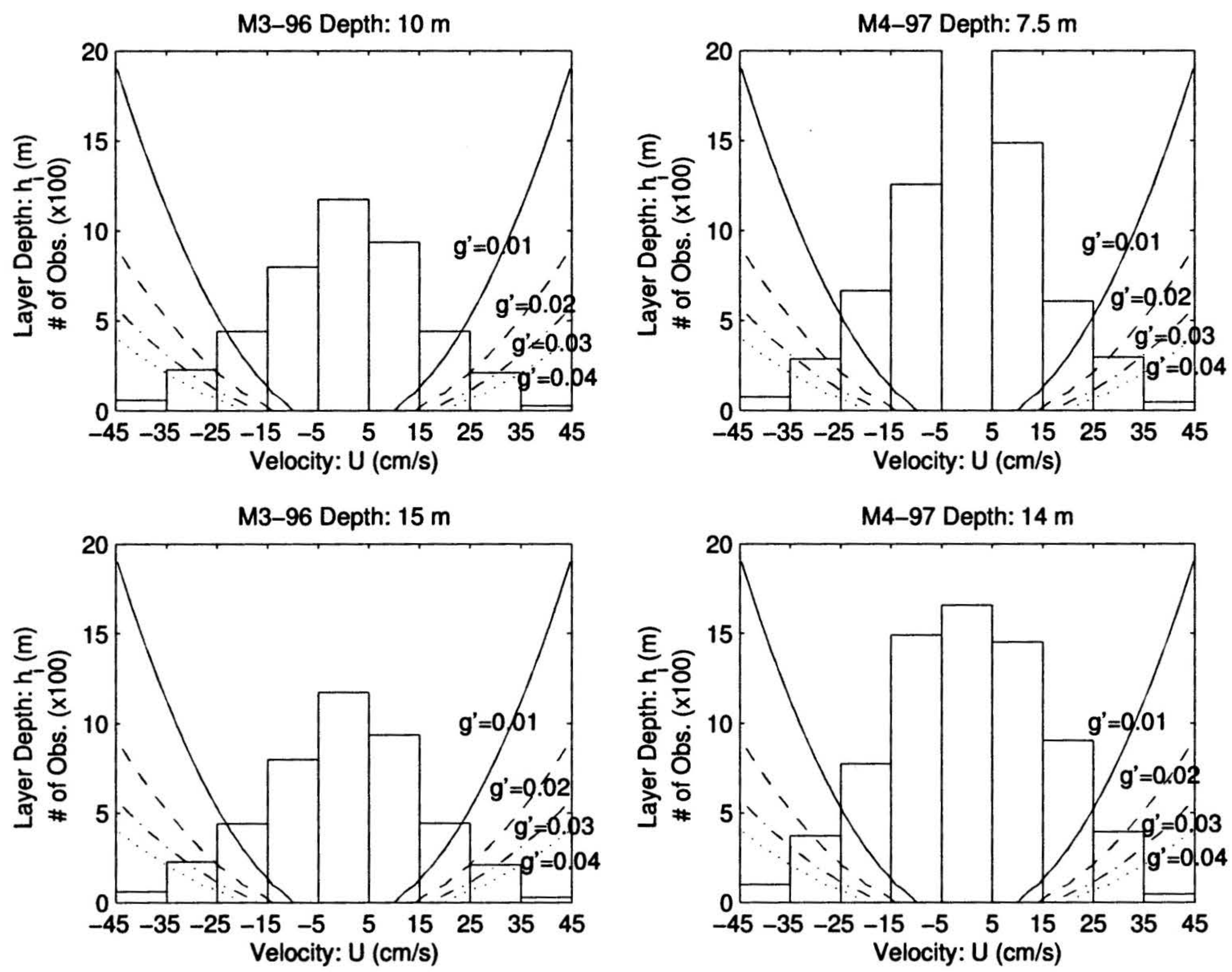

Figure 2.10: Distribution of the along channel velocity at the sill and the dependency of the interfacial Froude number as a function of depth and velocity. Fr_i=1. is shown for the values of g′=0.01,0.02,0.03 and 0.04. Region below each line is the region of supercritical flow (Fr_i>1).

Enhanced mixing east (seaward) of the sill should increases the depth of the mixed layer for that region. This mixing would decrease the density of the water at all depths and eventually cut off the exchange of deeper water. T-S diagrams can be used to determine the approximate time when the surface layer of the outer channel begins to deepen below the surface layer depth of the inner basin. Figure 2.11 shows the evolution of de-tided temperature and salinity near the depth of the sill (20 metres) and below sill depth (30-45 metres) at 10-day intervals. During both the 1996 and 1997 observations, we find that the density of the water at 45 metres (1996) and 30 metres (1997) depth decreases until it becomes significantly less dense than water at the same depth within the inner basin while the change in density near the depth of the sill is approximately equal. In both 1996 and

1997, the timing of the deepening of the surface layer in the outer channel below the level of the sill is between Julian Days 211 and 220 (the first week of August). As will be shown in the section on tidal analysis (section 2.5.1), the timing of the development of the surface layer seaward of the sill coincides with a change in the amplitude of the dominant semi-diurnal tides.

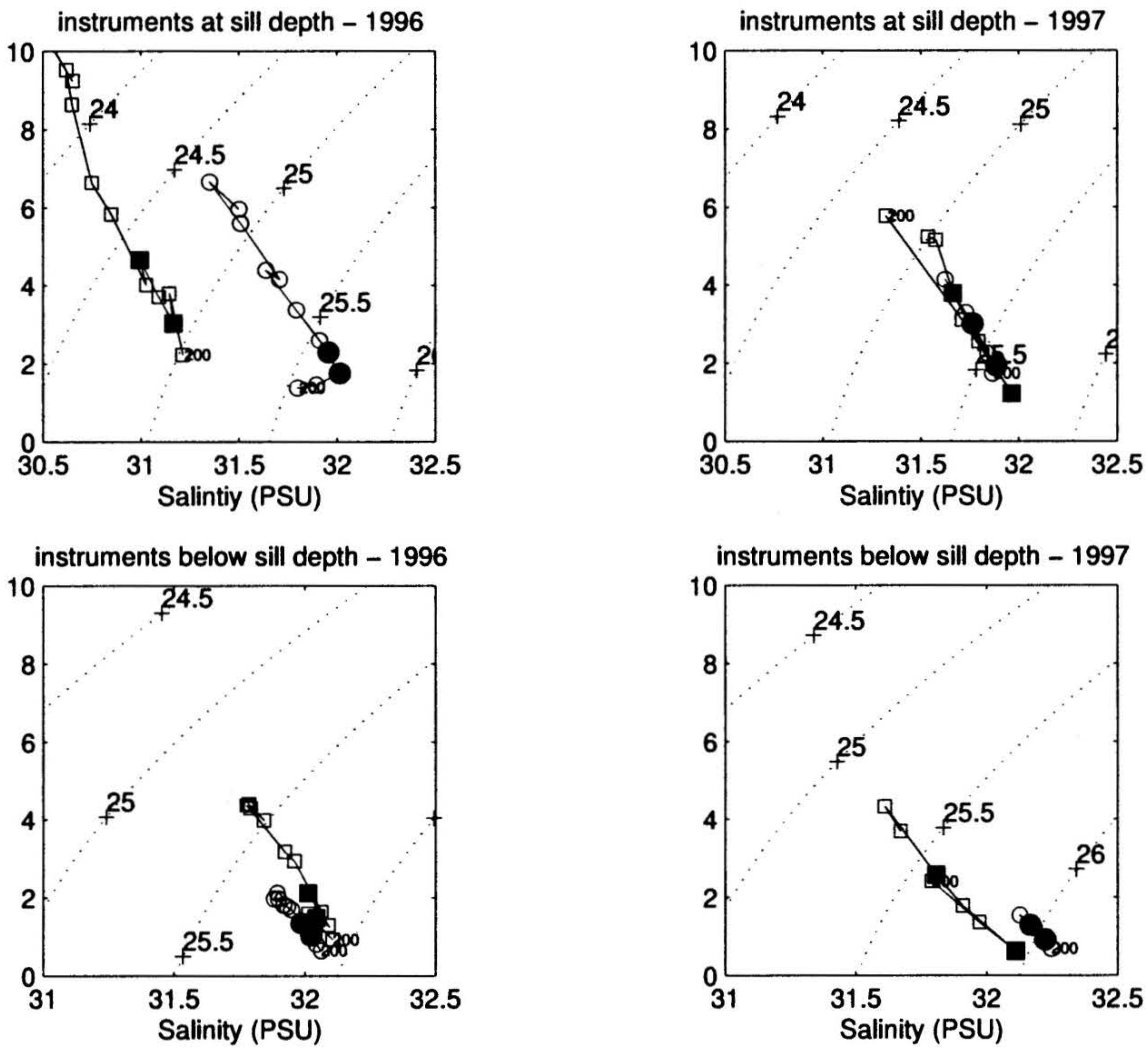

Figure 2.11: T-S diagram showing the temporal evolution at the inner basin M2-96 and M2-97 (circles) and the outer channel M4-96 and M6-97 (squares) at 10 day intervals from 1996. The filled points represent Julian days 210 and 220.

2.1.3 Fluctuations in Temperature

The temperature signals were also subjected to harmonic analysis to determine the amplitude and the phase of the major diurnal (K_1) and semi-diurnal (M_2) fluctuations. The results of the harmonic analysis (Pawlowicz et al, 2002) are given in Tables A.11 to A.14 and the amplitudes of the signals at each mooring are shown graphically in Figures 2.12 and 2.13. The harmonic analysis reveals that at the sill there is an increase in both the K_1 and M_2

temperature fluctuations with depth. This is only possible if there is a continuous vertical displacement of the thermoclines in response to the tidal forcing, suggesting that deeper water is continuously being lifted up onto the sill permitting it to mix with the waters nearer the surface. Seaward of the sill, there is an increase in the amplitude of the temperature fluctuations at the K_1 tidal frequency between 10 and 25 metres depth; this increase is not seen within the inner basin. The 1996 data shows that this increase in amplitude extends to mooring M4-96 but not to M5-96. Since the major forcing of the sill occurs at the M_2 frequency, we should anticipate that internal waves will be generated at the sill at twice the M_2 frequency (Blackford, 1978). These internal waves should be generated on both sides of the sill. The amplitude of the temperature fluctuations at the K_1 frequency suggests that these internal waves may propagate only seaward of the sill but not into the inner basin. The energy associated with these structures is dissipated by the time it reaches M5-96 suggesting that these waves may contribute to the mixing process seaward of the sill.

To determine if the vertical temperature fluctuations varied during the period of observations the temperature data was divided into 29-day windows and each window was again subjected to harmonic analysis. Examples of this analysis are show in contour plots of the diurnal and semi-diurnal frequencies bands (Figures 2.14 – 2.19). Although the signals are very noisy (with signal to noise ratios less than 1.0) there appear to be some consistent results worth noting.

Within the inner basin at M2-96 (Figure 2.14) and M2-97 there is evidence that the peak diurnal fluctuations in the near surface (10 metres and 7.5 metre depth) do not occur at K_1 but occur at higher frequencies such as OO_1 (approximately 0.045 cyc/hr). This frequency does not appear to dominate the diurnal frequency band at the sill (Figures 2.15) or seaward of the sill (Figures 2.16). During 1997 these fluctuations appear to dissipate after Julian Day 220 but reappear in deeper water (depth 20-25 metres) suggesting that the surface layer has become well-mixed and that the strongest mixing occurs below the sill after day 230. These temperature fluctuations may represent an internal tide within the inner basin. At the frequency of approximately ω=0.045 cyc/hr and estimating the length of the inner basin to be L=7.0 km the propagation speed of such a signal would be $c \sim 2L\omega = 0.175$ m/s. This wave speed corresponds to the midpoint of the range of values found for the first baroclinic mode (section 2.2).

At the sill (moorings M3-96 and M4-97) the diurnal fluctuations differ between the two studies. The peak of the temperature fluctuation of the diurnal bands is centered about K_1 during 1997 but during 1996 it occurs at higher frequencies the same as those located in the inner basin and only beyond Julian day 220. This may be a response to the depth of the mixed layer which was well-defined in 1997 but not so well defined in 1996 (section 2.2 and Figure 2.20).

In the outer channel (moorings M4-96 and M6-97) the strongest diurnal fluctuations occurring during 1996 appear to be confined to the surface with the largest amplitude fluctuations either above or below the K_1 frequency. The 1997 data suggests that the strongest mixing in the diurnal bands again occurs at frequencies above K_1 but does not appear until after day 230. The 1996 data is consistent with some evidence of an increase in the fluctuations at these frequencies occurring after day 225. The timing of this is coincident with the blocking of the lower layer by the sill as the mixed layer deepens.

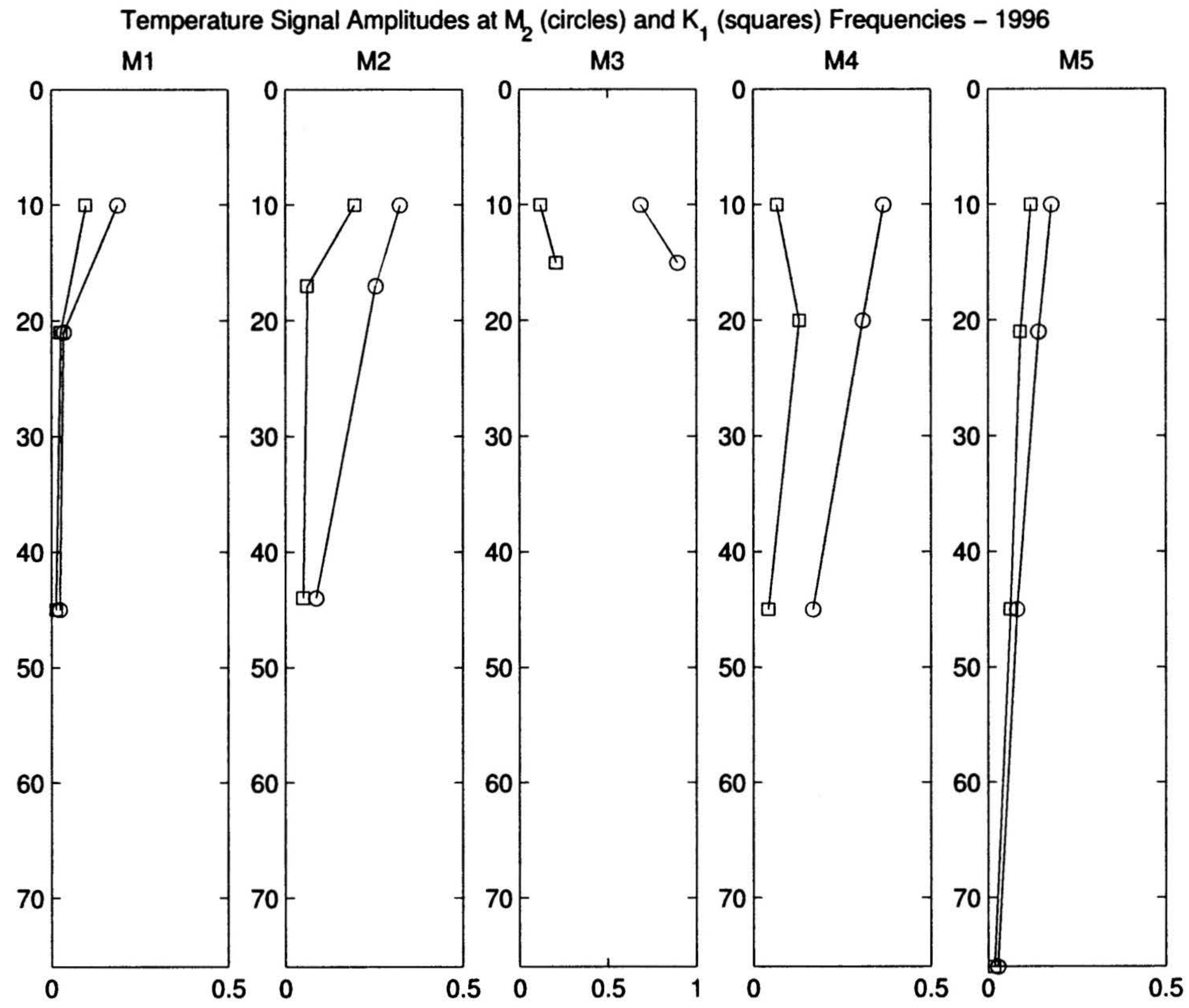

Figure 2.12: Amplitude (°C) of Temperature Fluctuations (x-axis) vs. Depth (y-axis, metres) at M_2 and K_1 frequencies recorded during 1996.

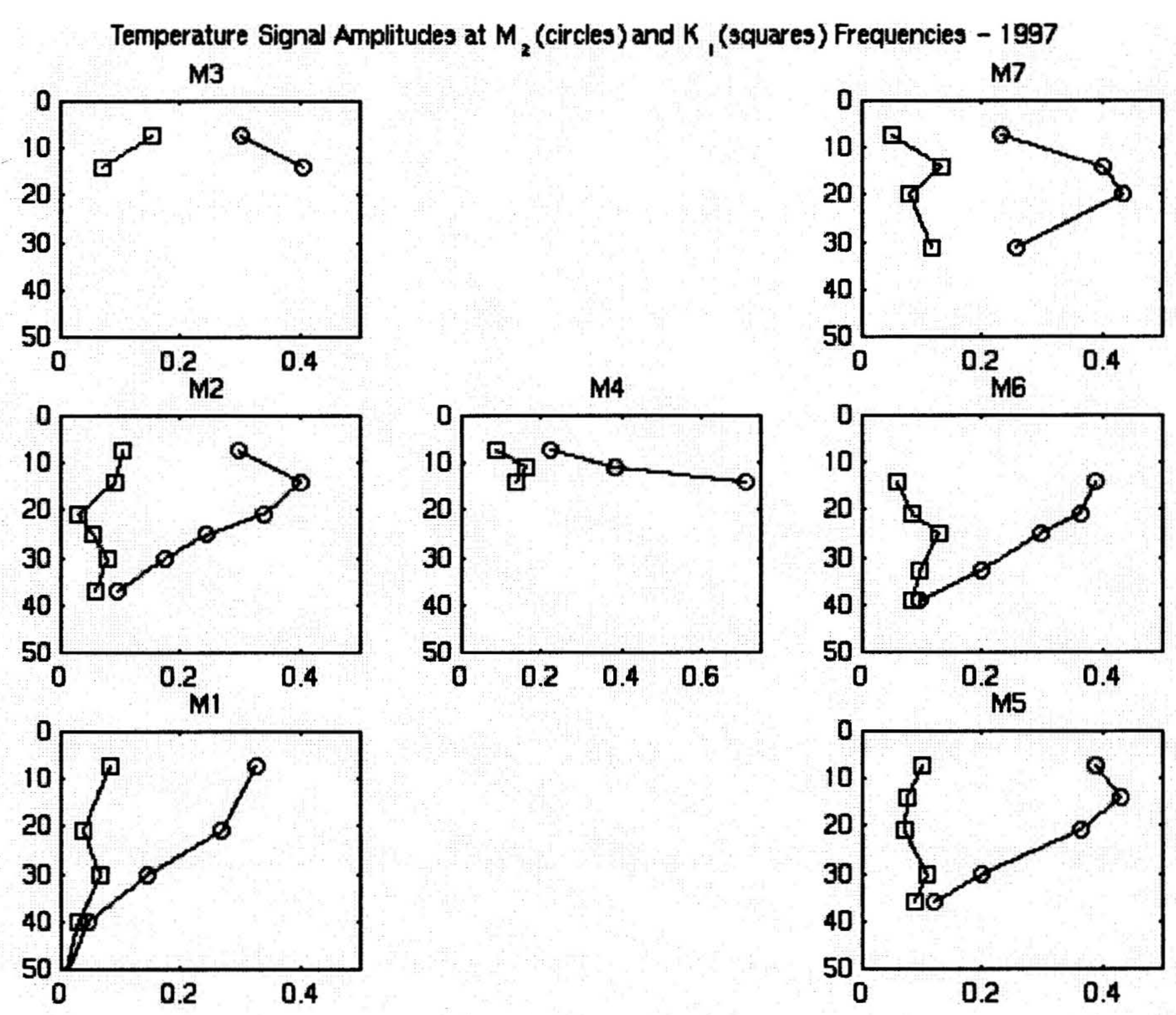

Figure 2.13: Amplitude of Temperature Fluctuations (x-axis, °C) vs. Depth (y-axis, metres) at M_2 and K_1 frequencies recorded during 1997.

As expected the fluctuations in the semi-diurnal frequency bands are much stronger. Within the inner basin, the highest temperature fluctuations are centered at M_2 however, the strength of the M_2 fluctuations appears to weaken near the surface and strengthen at depth during both the 1996 and 1997 studies. As in the case of the diurnal fluctuations, this suggests that the surface layer is becoming well-mixed and the majority of the mixing energy is shifting downwards through the water column where the temperature gradient is the greatest. The only exception to this is at 44 metres of depth at mooring M2-96, where the strongest M_2 fluctuations occur in the early part of the study.

At the sill, the semi-diurnal temperature fluctuations are strongest at 15 metres depth. During 1997, the fluctuations at all depths diminish as the season progresses and a well-mixed surface layer is formed during August. During 1996, strong mixing appears to continue at a depth of 15 metres. This may result from the lack of a uniform surface layer during the 1996 observation period. The CTD data of September 3, 1996 reveal a surface layer that increases with depth as it crosses the sill while the CTD casts of August 13, 1997 show a more uniform surface layer with the main thermocline located between 10 and 15 metres depth (Figure 2.6).

Seaward of the sill, the largest fluctuations in temperature are also located around M_2. During 1996, the mixing appears to grow stronger as the season progresses throughout the entire water column while the frequency band at which the mixing occurs appears to broaden. The 1997 data indicates that after the formation of the surface layer in August the amount of mixing increases though the entire water column from 21 metres to 39 metres almost simultaneously. The mixing is weaker at depth, but the timing of the increase at all depths starts around day 225.

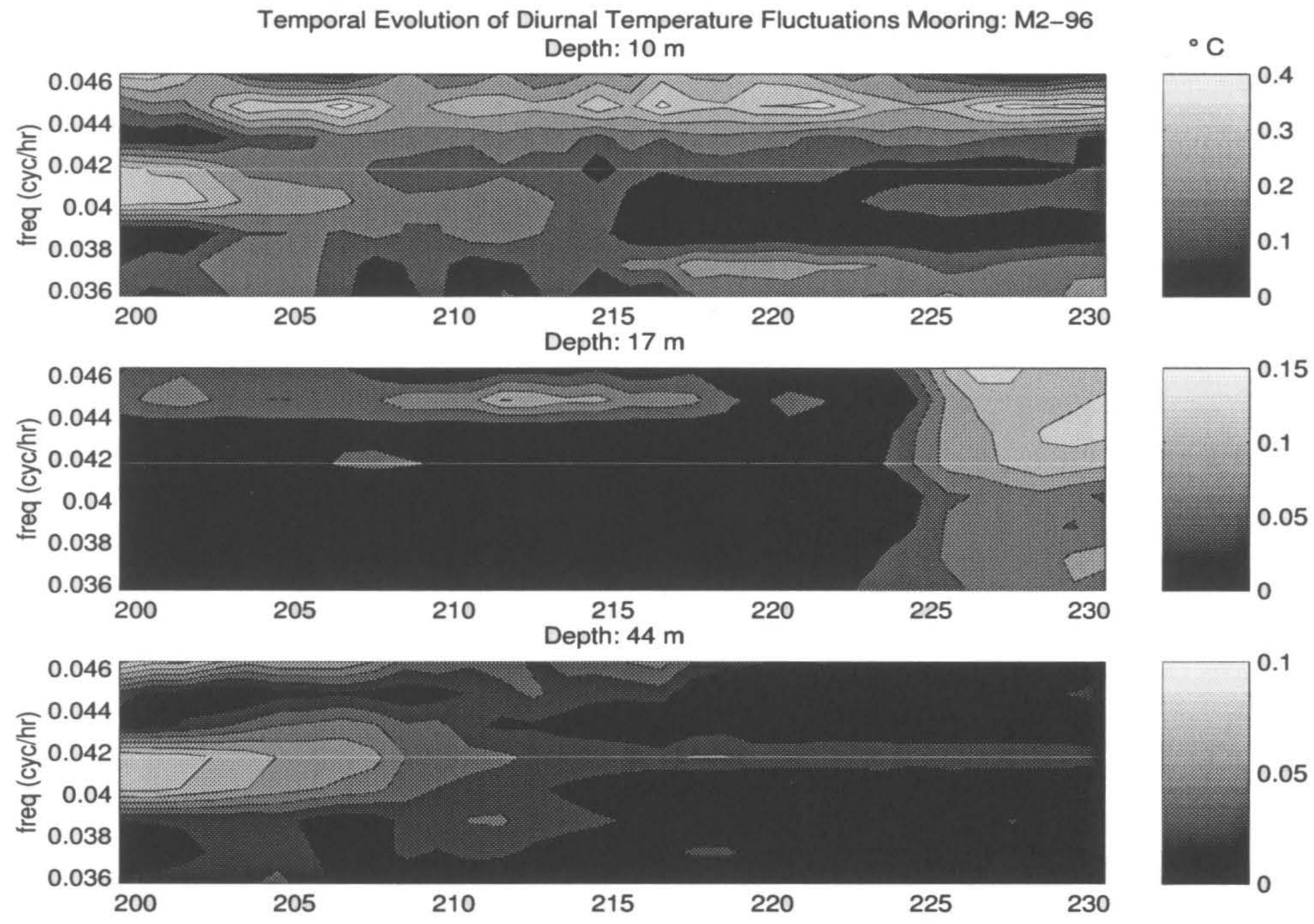

Figure 2.14: Temporal Evolution of the Diurnal Temperature Fluctuations within the inner basin (M2-96). Temperature signal reveals a strengthening of the diurnal frequency band after day 220 when the main pycnocline has dropped below the level of the sill. The white line through the image represents the frequency of K_1

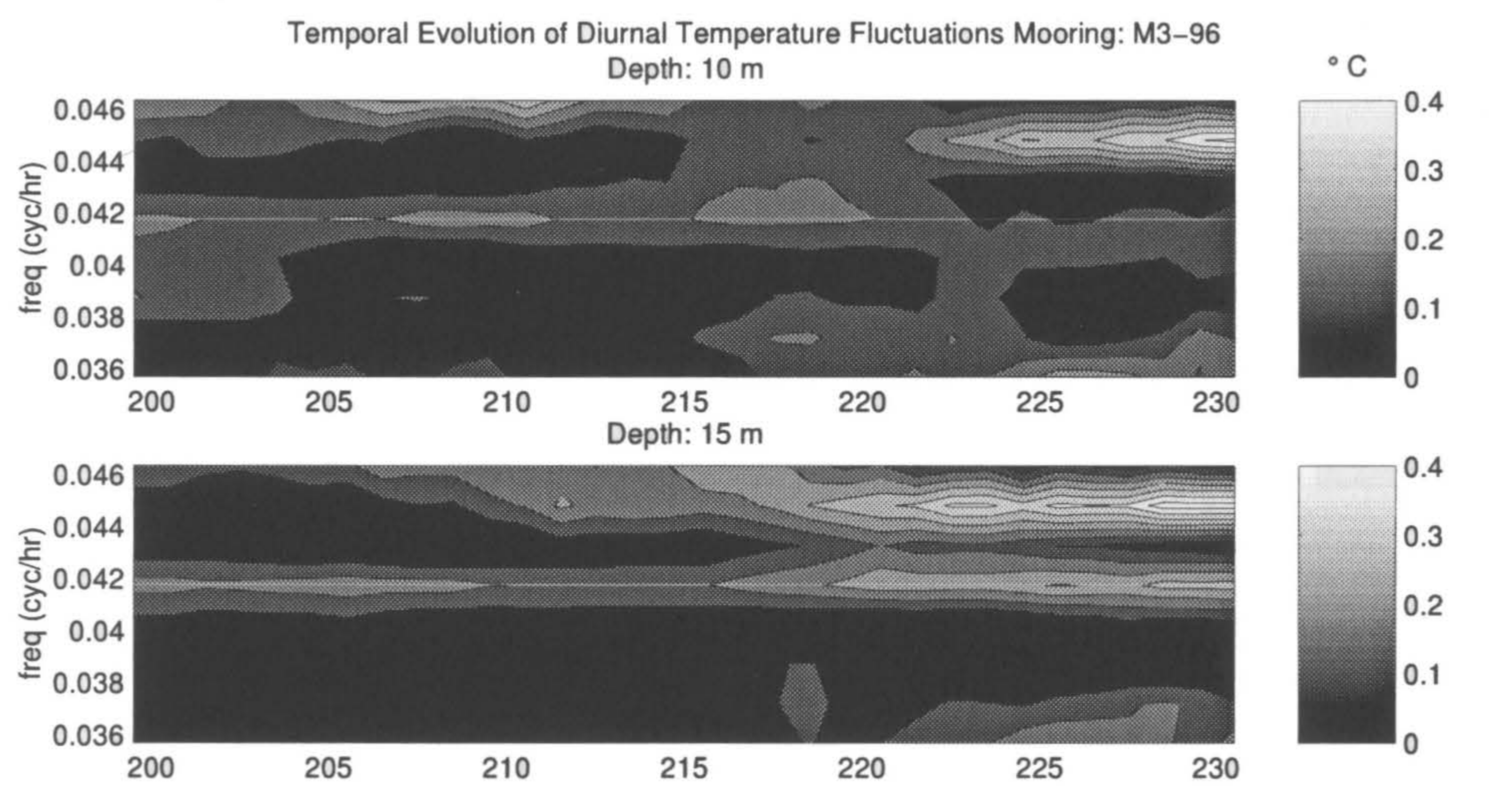

Figure 2.15: Temporal Evolution of the Diurnal Temperature Fluctuations at the sill (M3-96). Temperature signal reveals a strengthening of the diurnal frequency band after day 220 when the main pycnocline has dropped below the level of the sill. The white line through the image represents the frequency of K_1

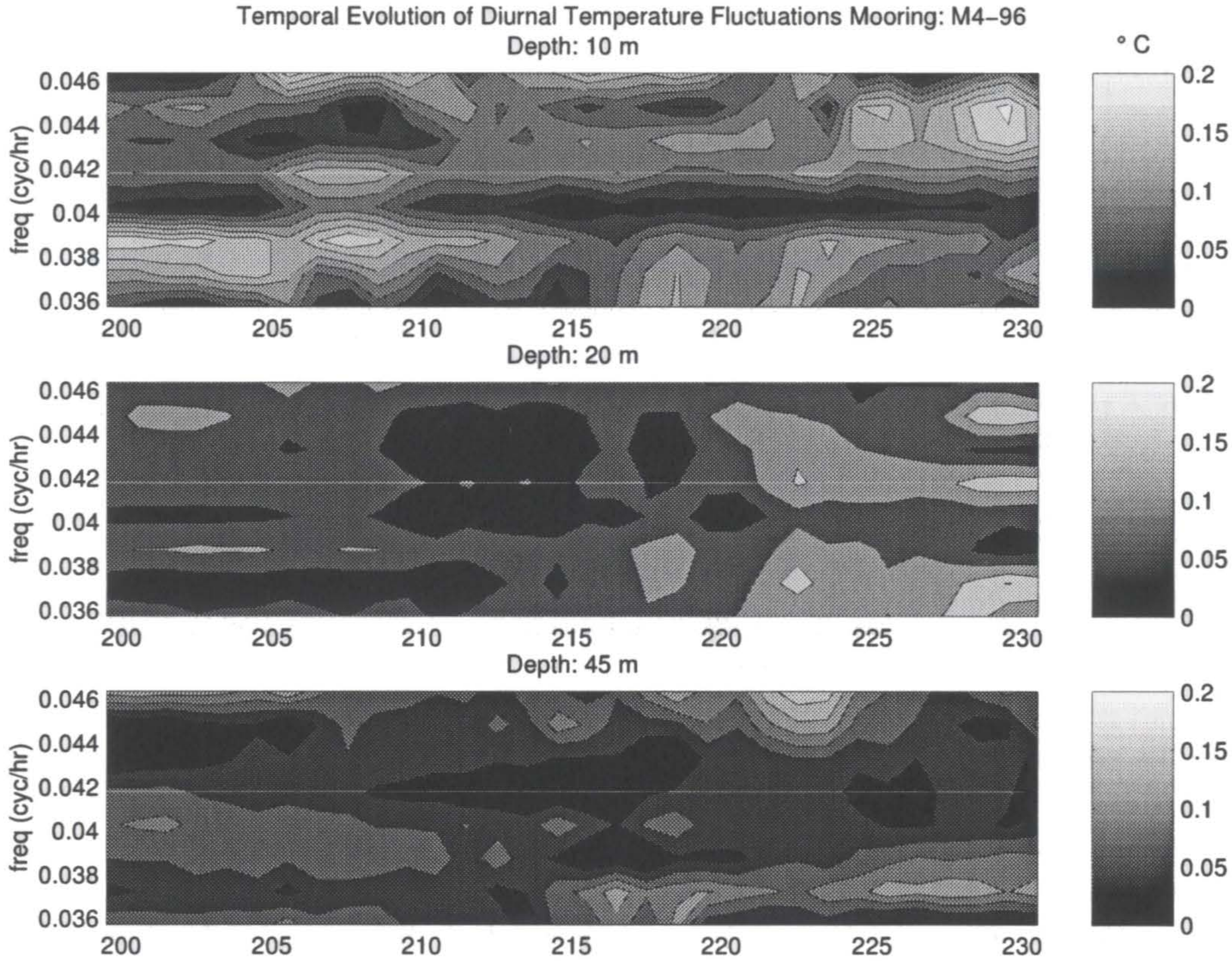

Figure 2.16: Temporal Evolutions of the Diurnal Temperature Fluctuations Seaward of the Sill (M4-96) during 1996. The white line through the image represents the frequency of K_1. Maximum temperature fluctuations at 10 m depth are bounded away from K_1. At 20 m, the maximum temperature fluctuations remain small until after day 220 when the main pycnocline drops below sill depth.

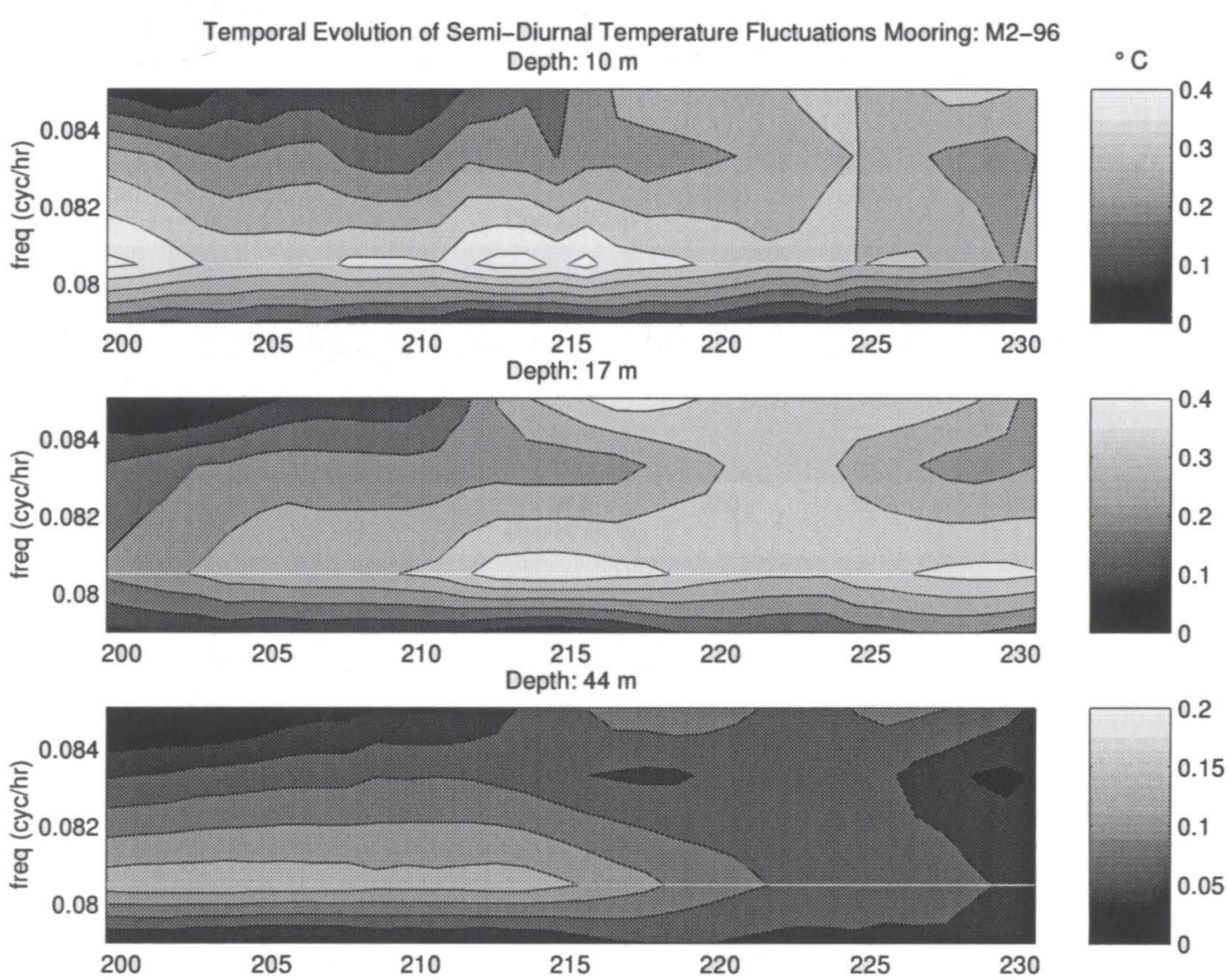

Figure 2.17: Temporal Evolution of the semi-diurnal temperature fluctuations of the inner basin 1996. See Figure 2.18 for explanation.

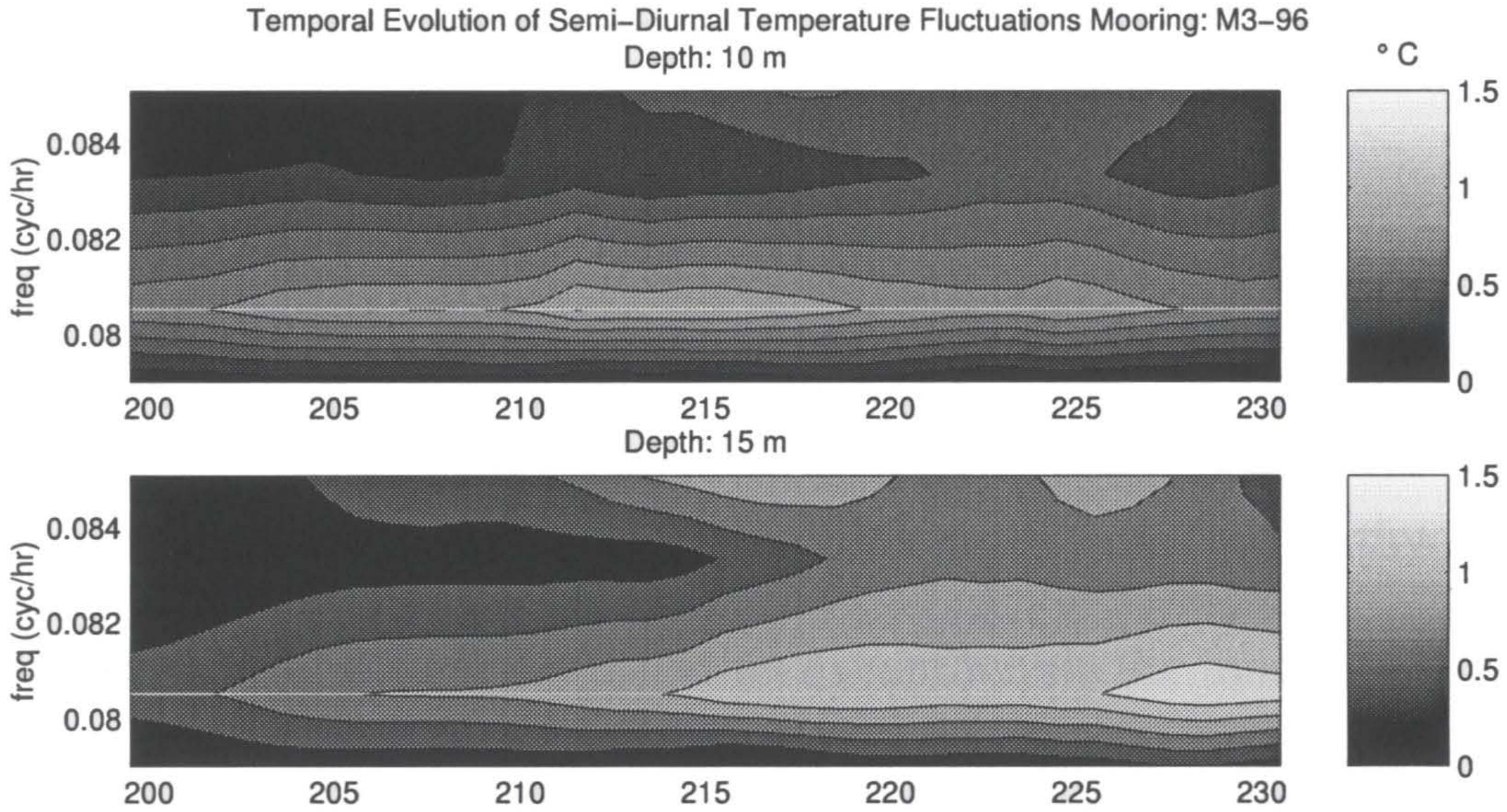

Figure 2.18 Temporal evolution of the semi-diurnal temperature fluctuations at the sill during 1996. The white line through the image represents the frequency of M_2. Within the inner basin (Figure 2.17 above) and at the sill, the temperature fluctuations at 17 and 15 metres depth become stronger as the main pycnocline deepens. After day 220, when the main pycnocline drops below the level of the sill in the outer channel, the temperature fluctuations at 45 metres depth in the inner basin (Figure 2.17) grow weaker, even though the temperature fluctuations at 17 metres depth grow stronger. The tidal energy within the inner basin appears to create little mixing as waves appear to propagate along the interface between the surface and bottom layers.

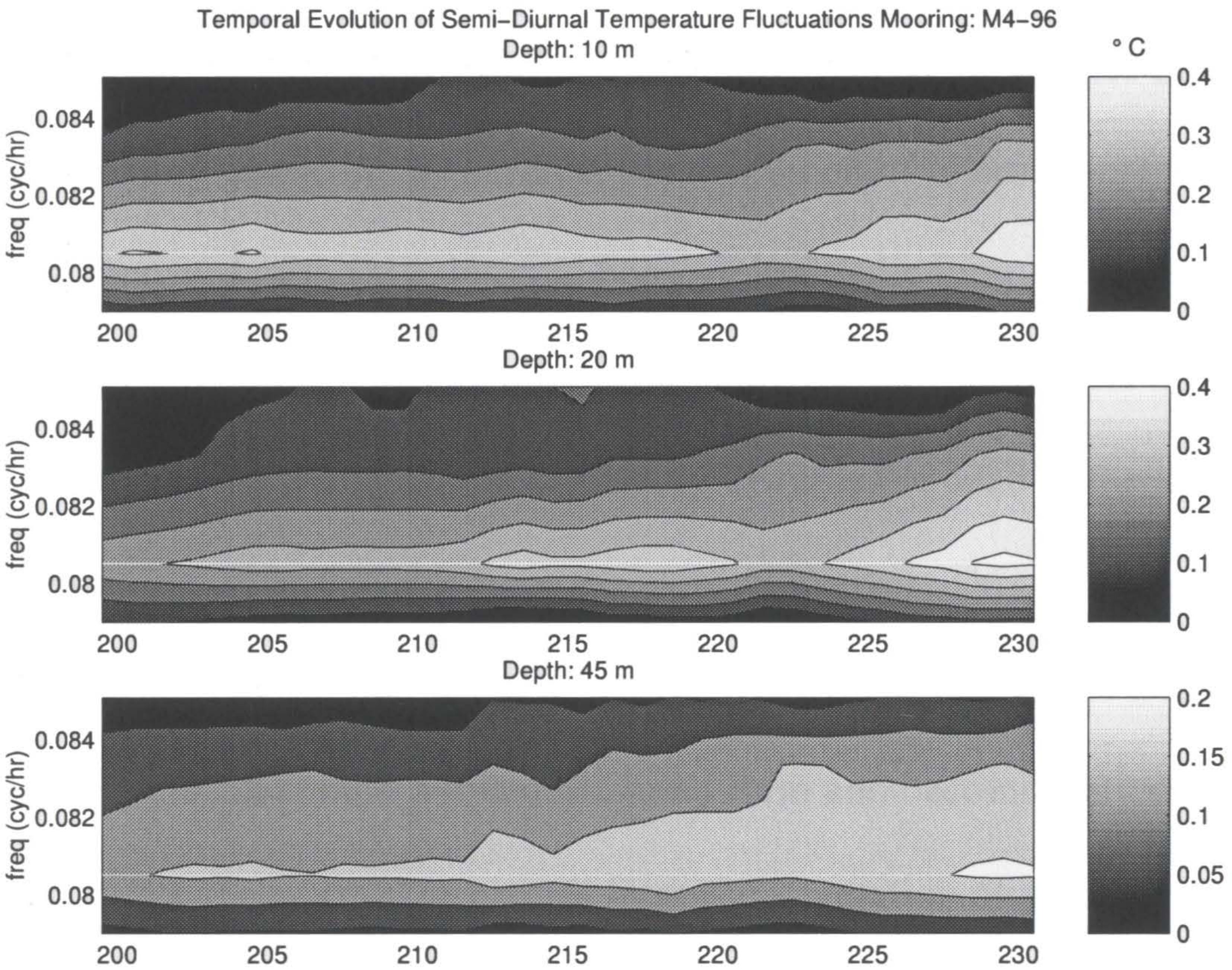

Figure 2.19: Temporal Evolution of the Semi-Diurnal Temperature Fluctuations Seaward of the Sill during 1996. The white line through the image represents the frequency of M_2. Seaward of the sill, the temperature fluctuations increase throughout the water coloumn to at least 45 metres depth as the main pycnocline drops below the level of the sill after day 220.

The analysis of the temperature and salinity signals from Clode Sound indicates that mixing is stronger on the seaward side of the sill than it is in the inner basin. During the summer months, incoming solar radiation heats the surface layer and may produce a thermally stratified water column throughout the inlet while a small amount of fresh water normally flows into the head of the inlet. Typical flow rates from the Northwest River are too small to contribute significantly to stratification except within the inner basin. The mixing of fresh water within the inner basin decreases the surface density thereby increasing the buoyancy gradient for that region of Clode Sound. Two possible explanations for the increase in mixing seaward of the sill have been presented. When flow at the sill is supercritical, an increase in temperature in the surface layer should help to increase the stability of the water column. However, the deepening surface layer decreases the depth of the lower layer at the sill increasing the chance of supercritical flow. It follows that as the surface layer deepens in response to the input of heat from the surface, the likelihood of internal bores or hydraulic jumps increases. Seaward of the sill, internal bores or hydraulic jumps may propagate away from the region of formation as the buoyancy gradient weakens. Within the inner basin, the buoyancy gradient is found to increase significantly towards the head of the inlet most likely the result of the mixing of fresh water from the Northwest river. This increase in buoyancy does not permit the upstream propagation of internal bores and may create a local region of intense mixing near the sill should a hydraulic jump form and become stationary.

Another source for mixing may result from the generation of internal waves at the sill in response to the strong semi-diurnal forcing. Examination of the fluctuations in the temperature signal in response to the tidal forcing indicates that a diurnal internal tide may exist within the inner basin at a frequency bounded away from the main K_1 forcing. This internal tide may be forced by the generation of internal waves during a flood tide. At the sill and seaward of the sill, diurnal fluctuations (tidal frequency K_1) in temperature appear to reach a maximum around sill depth, suggesting that internal waves may be generated at the sill in response to the M_2 tidal forcing at the sill. The increase in the K_1 temperature fluctuations at sill depth at M4-96 (seaward of the sill) suggests that the waves may propagate towards the mouth of the inlet but appear to dissipate as there is no evidence of an increase in the diurnal fluctuations in temperature at M5-96. The dissipation of these internal waves as they propagate towards the mouth may also contribute to the mixing process of the region immediately seaward of the sill. Both the generation of internal waves and the propagation of internal bores and/or hydraulic jumps on the seaward side of the sill may contribute to the deepening of the mixed layer. The surface layer will continue to deepen in response to the input of surface heat flux until such time that the sill blocks the lower layer. Once the lower layer becomes blocked the surface layer may continue to deepen on the seaward side of the sill, but obtains a maximum depth within the inner basin approximately equal to the sill depth.

Water below the depth of the sill is found to undergo very little mixing. The inner basin water at 30-45 metres depth appears to form during the winter months and remain resident throughout the summer. The response within the inner basin to large external events (non-tidal) will depend on the depth of the mixed layer at the time of the event. If the surface layer is deep enough that the lower layer is blocked by the sill, these events may result in significant mixing and deepening of the mixed layer seaward of the sill, while leaving the inner basin relatively unchanged.

2.2. The Vertical Modes

Within the inner basin the CTD data indicates two different density profiles for the 1996 and 1997 season. During the 1996 season, the density structure is primarily exponential while the density profile during the 1997 season shows a well-developed surface layer similar to a 2-layer model (Figure 2.20).

The Brundt-Väisälä frequency, $N(z)$, is given by:

$$N^2(z) = -\frac{g}{\rho}\frac{d\rho}{dz} \tag{2.2.1}$$

where g is the acceleration due to gravity and $\rho \equiv \rho(z)$ is the vertical density structure. The estimates of the mean vertical profiles of the Brundt-Väisälä frequency, within the inner basin are shown for 1996 and 1997 in Figure 2.20. The vertical profiles indicate that the maximum buoyancy frequency occurs at a depth of approximately 15 metres in 1997 and extends through the surface layer in 1996.

The determination of the Brundt-Väisälä frequency allows one to calculate the vertical modes of the inner basin determined from the Sturm-Liouville problem:

$$\frac{d^2 Z_n}{dz^2} + \frac{N^2}{c_n^2} Z_n = 0, \tag{2.2.2a}$$

$$Z_n(0) = Z_n(-H) = 0. \tag{2.2.2b}$$

where: $N^2 = N^2(z)$ as defined above, $Z = Z(z)$ is the vertical structure of the vertical velocity, and $-H$ is the depth of the fluid column. For a continuously stratified fluid there exist an infinite number of eigenvalues, c_n, and eigenfunctions, Z_n, which satisfy the above equation.

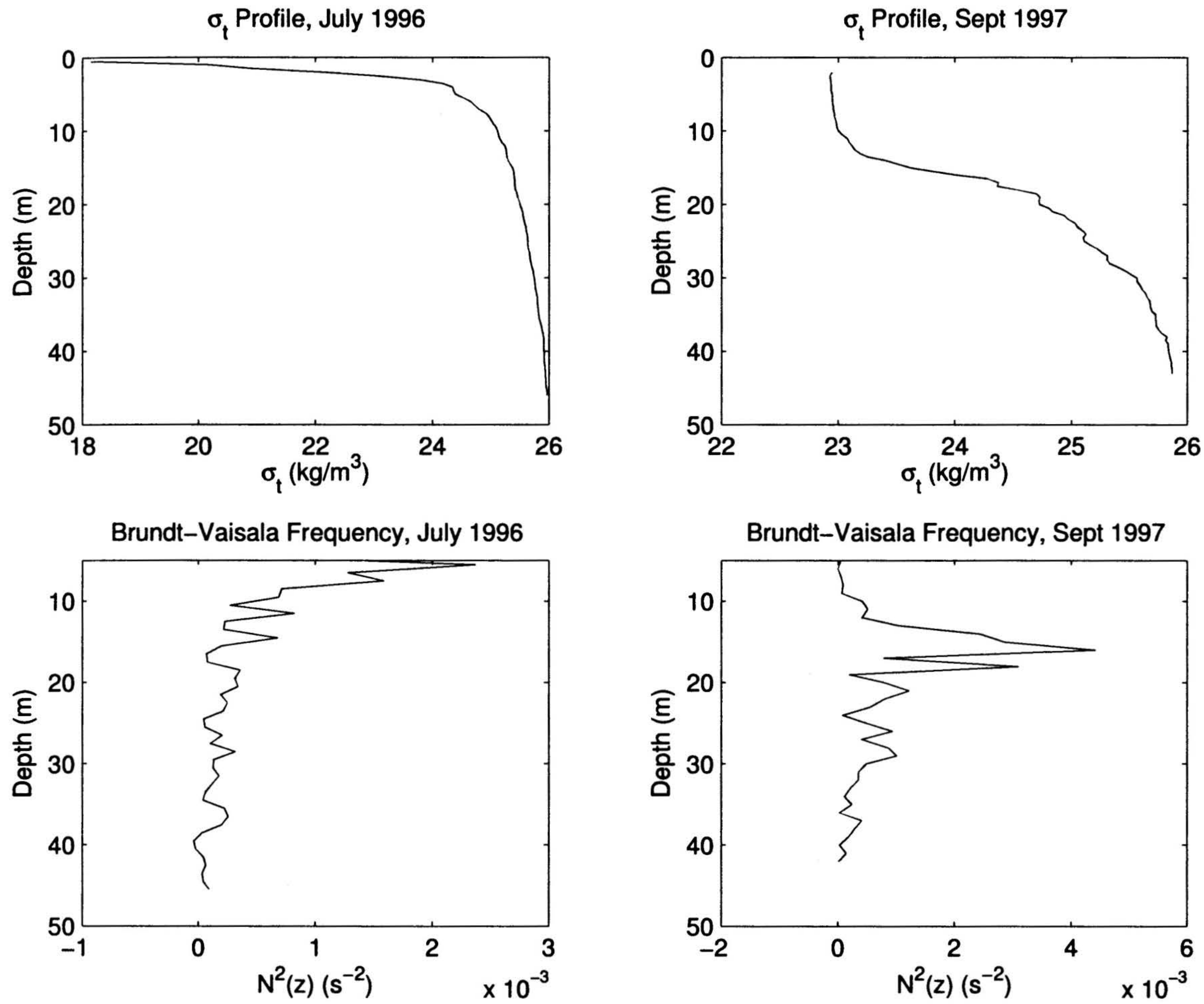

Figure 2.20: Sigma-t and Brundt-Vaisala frequency within the inner basin during 1996 and 1997

The eigenvalues represent the speed of the i^{th} mode while the eigenfunctions represent the vertical structure corresponding to the i^{th} mode. The vertical structure of the horizontal velocity (pressure perturbation) may be computed from: $p' = \rho_0 c_n^2 \frac{dZ_n}{dz}$ where ρ_0 represents the mean density. The solution of (2.2.2a,b) was determined numerically from the available CTD data. The first three eigenvalues were found to lie in the ranges: c_0*=28-48 cm/s*, c_1*=15-20 cm/s*, c_2*=8-12 cm/s*. It follows that the period of the internal tides (T_i=2L/c_i) corresponding to the first three modes must lie between *8.1-13.9, 19.4-25.9* and *32.4-48.6* hours respectively. The period of the gravest mode overlaps with the semi-diurnal tides while the period of the first baroclinic mode overlaps with the diurnal tides. The eigenfunctions corresponding to the vertical velocity structure and horizontal velocity structure for July 1996 and August 1997 are shown in Figure 2.21. The internal Rossby radii ($R_n = c_n/f$, $f = 1.09 \cdot 10^{-4}$ at $48.4°$ latitude) corresponding to the gravest and first baroclinic modes are: $R_o = 3.5\ km$ and $R_1 = 1.6\ km$. The width of the inner basin is approximately $3\ km$; rotation may play role in determining the nature of the flow within the basin but is unlikely to influence the flow at the sill or in the outer channel where the channel width is narrower.

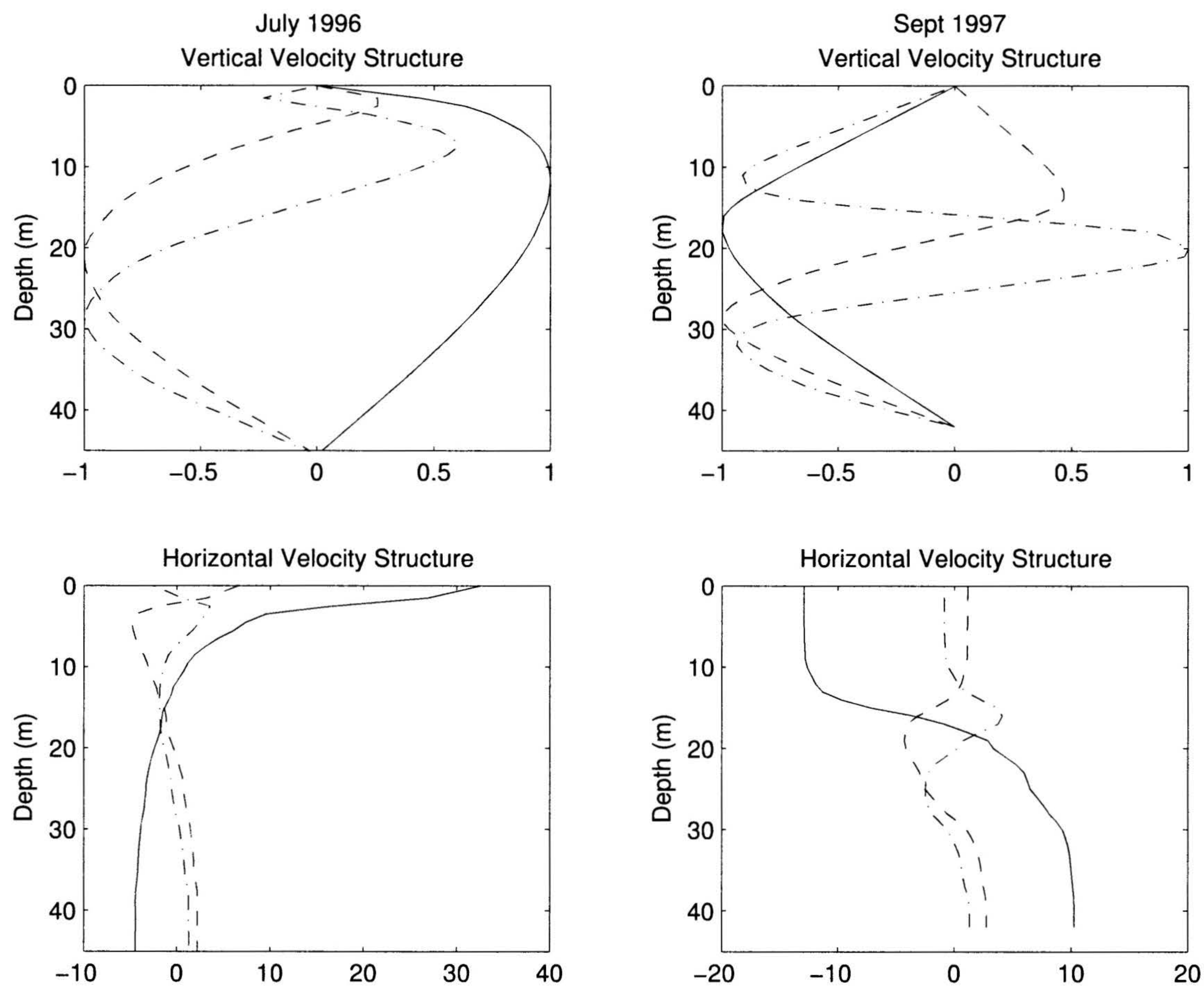

Figure 2.21: Eigenfunctions corresponding to the first three vertical modes derived from 1996 and 1997 density profiles. The top two panels show the eigenfunctions for the vertical velocity structure. The bottom two panels show the eigenfunctions for the horizontal velocity structure.

2.3. *Distribution of Fluctuating Kinetic Energy*

The power spectra of the current records were estimated using Welch's method. The signal was subdivided into 15-day windows that were allowed to overlap by 7.5 days (50% overlap). For the 1996 data, the 60-day signal provides a total of 7 overlapping windows from which the power spectrum was estimated. For 1997, the 100-day signal provides 13 windows for the estimation of the power spectrum. The degrees of freedom for K non-overlapping windows should be 2K, however as the windows overlap the actual number of degrees of freedom will be less as the samples cannot be considered independent. The mean current was removed prior to the analysis so that the estimated spectrum represents the energy distribution of the fluctuating current profile. Subdividing the spectrum and identifying low frequency (less than 0.8 cpd) and high frequency (0.8 cpd to 36 cpd) regions of the power spectrum, we are able to calculate the proportion of energy in each of the frequency bands. We may further subdivide the frequency bands to determine the amount of energy that may be attributed to tidal (semi-diurnal and diurnal), inertial, and synoptic scale meteorological events (such as the passing of low pressure systems). The percentage of the total fluctuating kinetic energy in the meteorological band (0.10 to 0.50 cpd); the diurnal band (0.80 to 1.20 cpd); the inertial band (1.20 to 1.70 cpd); and the semi-diurnal band (1.70 to 2.11 cpd) are summarized in Tables 2.2 and 2.3. Also included in the tables are the percentage of the total kinetic energy found in the low and high frequency regions of the spectrum as well as the percentage of high frequency energy which is unexplained.

The results of the spectral analysis for the near surface flow in 1996 (Figure 2.22) show a distinct peak in the meteorological band at 0.3 cpd. There is little evidence of this signal in the along channel flow at the sill. In the outer channel, this peak appears to have shifted to a frequency of 0.35-0.4 cpd. At the lower end of the meteorological band between 0.1 and 0.2 cpd there is evidence of a broad band of energy, this low frequency energy is not as evident within the inner basin suggesting that the source may be from outside of the inlet. Semi-diurnal forcing is clearly dominant at all moorings with the strongest signal appearing at the sill. Energy in the diurnal band appears to be quite evenly distributed over the entire diurnal band except at the sill where there is a very distinct peak of energy. The broad distribution of the fluctuating kinetic energy in the diurnal frequency band agrees well with the observations of the temperature fluctuations which suggested that energy in the diurnal band is turned in mixing energy at frequencies other than the primary tidal constituent K_1. At mooring M1-96, located almost halfway along the length of the inner basin, there appears to be approximately 10% of the energy associated with the inertial band throughout the entire water column (Table 2.2). Mooring M2-96, also located with the inner basin, indicates an increasing amount of energy in the inertial band with increasing depth. Seaward of the sill, inertial energy accounts for 7% of the total energy, but this energy decreases with depth.

Generally, for all locations, the meteorological band accounts for 60-75% of the low frequency energy (< 0.8 cpd) found in the observed currents. The influence of meteorological events (wind stress) is seen to decrease substantially below 21m of depth, suggesting that the Ekman depth lies somewhere between 20 and 30m. The influence of the tide is strongest in the region of the sill where there is a strong tidal jet formed due to topographic effects. Inertial effects represent approximately 5-10% of the total fluctuating energy, the effect is strongest in the surface layer at all locations except within the inner basin during 1996 where the energy of the inertial band appears to increase or at least remain relatively constant with depth. At the sill, the inertial band accounts for less than 2% of the total energy, the region of the sill is very narrow (approximately 0.5-1.0 km) so it is not surprising that rotational effects are least significant in this region. Previously (section 2.2), it was shown that the internal Rossby radii for the first two modes were approximately 3.5 and 1.6 km. The internal Rossby radius for the gravest mode is comparable to the typical width (3 km) of the inner basin at the location of moorings M1-96 and M2-96 while the internal Rossby radius corresponding to the first baroclinic mode is approximately ½ the typical width of the inner basin.

Table 2.2: Distribution (percent of total) of the Fluctuating Kinetic Energy in 1996. Values in table represent the percent of the total Fluctuating Kinetic Energy for the following frequency bands: low (0.0-0.80 cpd), meteorological (0.10-0.50 cpd), diurnal (0.80-1.20 cpd), inertial (1.20-1.70 cpd) and semi-diurnal (1.70-2.10 cpd). Also shown are the percentage of low frequency energy associated with meteorological frequencies and the amount of high frequency energy which remains unexplained.

Mooring	Depth (m)	low %	met %	Met/low %	high %	diurnal %	inertial %	semi %	% of high freq energy unexpl.
M1	**10**	32	19	61	68	7	7	20	50
	21	30	18	60	70	23	11	8	40
	45	14	6	42	86	13	9	43	24
M2	**10**	40	27	67	60	9	4	19	47
	17	49	35	71	51	12	5	11	47
	44	19	12	62	81	8	9	18	56
M3	**10**	18	11	64	82	7	2	46	33
	15	33	25	75	67	4	2	37	37
M4	**10**	31	21	66	69	8	7	10	63
	20	45	35	77	55	4	4	11	64
	45	17	9	57	83	4	5	13	74
M5	**10**	52	39	76	48	11	7	10	44
	21	60	40	67	40	6	5	11	47
	45	43	30	69	57	8	5	13	55

2.3.1 Energy Distribution at the Sill

In the region of the sill (mooring M3-96 and mooring M4-97), 65-70% of the total fluctuating kinetic energy is located in the low (<0.1 cpd), meteorological (0.1-0.5 cpd), inertial, diurnal and semi-diurnal frequency bands. Approximately 40 - 60% of the total fluctuating energy is found in the diurnal and semi-diurnal frequency bands (3 – 7% diurnal;

35 – 55% semi-diurnal) while less than 2% is associated with the inertial band. The proportion of energy attributed to the tides decreases with depth by about 10-15%, the observations at approximately 15 metres of depth are close to the bottom of the inlet so this decreasing proportion of energy may be attributed to increasing friction near the bottom. Altogether the tidal frequencies account for about 60-70% of the high frequency energy at the sill. The large amount of energy associated with the semi-diurnal band is readily

Table 2.3: Distribution (percent of total) of the Fluctuating Kinetic Energy in 1997. Values in table represent the percent of the total Fluctuating Kinetic Energy for the following frequency bands: low (0.0-0.80 cpd), meteorological (0.10-0.50 cpd), diurnal (0.80-1.20 cpd), inertial (1.20-1.70 cpd) and semi-diurnal (1.70-2.10 cpd). Also shown are the percentage of low frequency energy associated with meteorological frequencies and the amount of high frequency energy which remains unexplained.

Mooring	Depth (m)	low %	met %	Met/low %	high %	diurnal %	inertial %	semi %	% of high freq energy unexpl.
M1	**7.5**	28	16	57	72	7	5	22	52
	21	24	15	61	76	10	4	15	62
M2	**7.5**	27	16	58	73	7	7	26	44
	21	51	36	70	49	5	4	14	54
M3	**7.5**	20	11	56	80	4	7	37	40
M4	**7.5**	18	13	71	82	3	2	56	25
	14	40	31	76	60	2	1	39	29
M5	**7.5**	28	19	66	72	6	3	29	48
	21	30	18	62	70	3	5	25	54
M6	**33**	32	24	75	68	6	3	10	72
M7	**7.5**	29	16	54	71	7	6	22	50
	31	21	13	62	79	5	6	24	56

explained by the formation of a tidal jet as the tidal currents must pass through the shallow and narrow region of the sill. There is a distinct peak in the diurnal band for this location, however, the energy associated with this band is only 5-15% of the energy associated with the semi-diurnal band. This is consistent with the harmonic analysis of the tidal heights (Section. 2.5, Tables 2.6-2.9) that indicates the ratio of the sum of the diurnal constituent heights to the sum of the semi-diurnal is approximately 0.25 to 0.3. At 15 metres depth, 25 – 30 % of the energy is associated with the meteorological band as compared to 10-15% closer to the surface (7.5-10 m). This apparent increase in the meteorological forces is easily accounted for by the decreasing strength of the tidal energy levels.

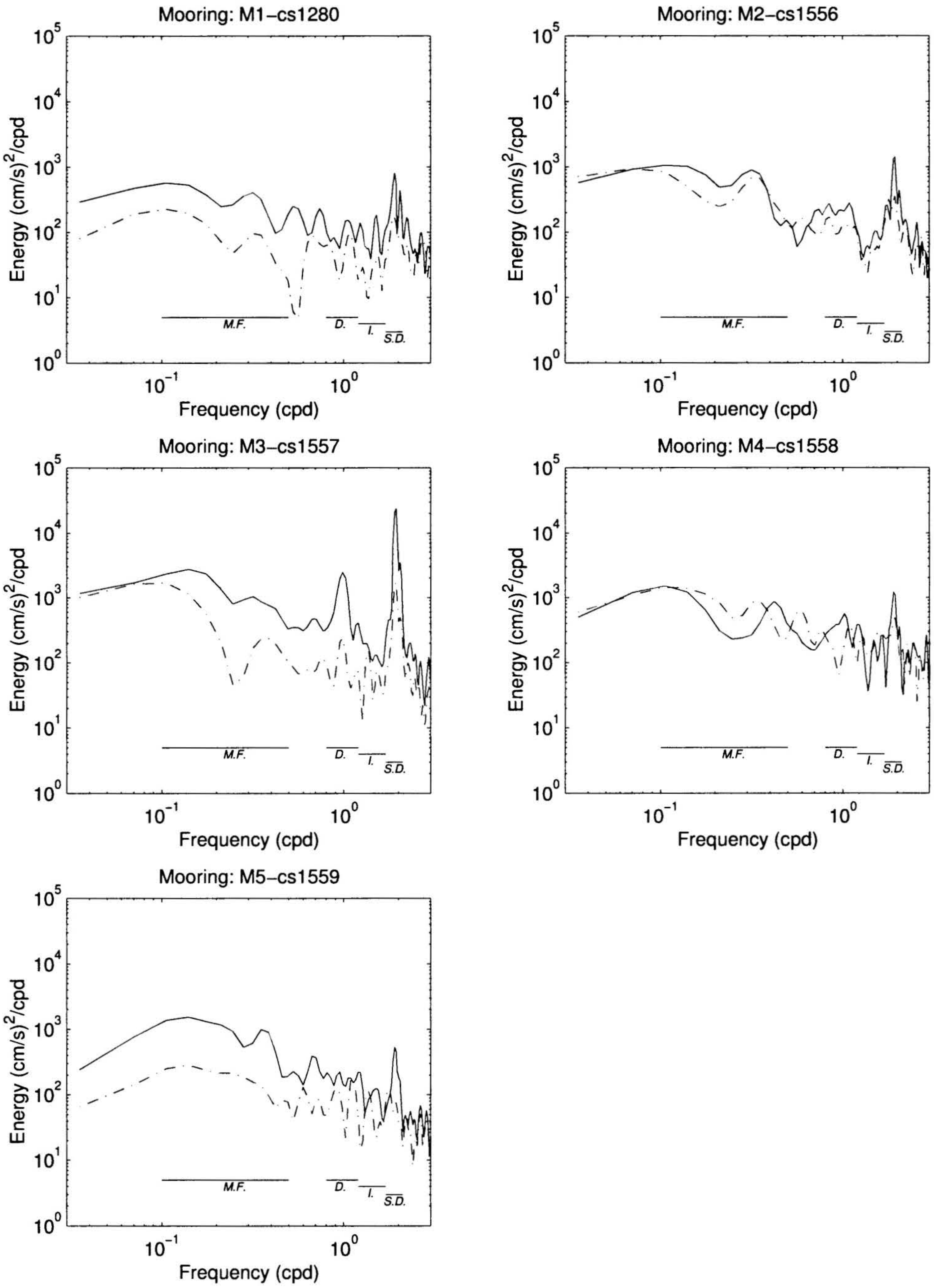

Figure 2.22: Spectrum of the fluctuating kinetic energy at surface moorings during 1996. Along channel flow (solid line) and cross channel flow (dashed line) are depicted. Also shown are the frequency bands used to determine the distribution of the energy: M.F. (meteorological frequencies), D (diurnal), I (inertial) and S.D. (semi-diurnal).

2.3.2 Distribution of Energy within The Inner Basin

For the year 1996, moorings M1 and M2 were located along the centreline of the inner basin (Figure 2.2). For the year 1997, moorings M1, M2 and M3 were located across the channel a short distance (less than 0.5 km) from the sill (Figure 2.3). For the region of the inlet inside of the sill, 50-60% of the energy of the surface currents may be associated with the previously defined frequency bands (with 10 – 15% of the energy being associated with the extremely low frequency oscillations of less than 0.1 cpd). The tidal frequencies account for approximately 25-35% of the energy (20 - 25% semi-diurnal and 5 – 10% diurnal) with the exception of the surface current located at mooring M3 in the 1997 field year. The strong semi-diurnal component of energy (35% of the total energy) at this mooring is likely due to the location almost directly in line with the strong tidal jet flowing over the sill. The inertial band accounts for 5 - 10% of the energy within the inner basin which is 2-3 times greater than the energy of this band in the sill region. Typically, the meteorological band accounts for 15-20% of the total energy with the exceptions of mooring M3 in the 1997 data (10% of the total energy) and mooring M2 in 1996 (over 25% of the total energy). The low proportion of kinetic energy associated with the meteorological band at mooring M3 in the 1997 data may be a consequence of the higher proportion of energy in the tidal frequencies. The reason for the increased proportion of energy in the meteorological band at mooring M2-96 may indicate the existence of a large eddy circulation as it appears to be associated with the cross channel component of velocity (Figure 2.22) which is much stronger compared to other locations.

At mid-level depths (~20m), mooring M2 for both the 1996 and 1997 data indicates that approximately 50% of the total energy may be found in the low frequency bands (< 0.8

cpd). Of this low frequency energy, the majority (~70%) is found in the meteorological band. Mooring 2 (M2-96 and M2-97) was located near the centre of the inlet just inside the sill during both studies. For three of the four instruments located at mid-depths, 60% of the total energy may be accounted for as belonging to either the meteorological, tidal or inertial bands. The exception to this is mooring M1 during the 1997 field study. Almost 50% of the energy for this instrument lies in the high frequency band (> 2.11 cpd). The large amount of energy located in the high frequency part of the spectrum is most likely noise as over 50% of the measured velocities at this instrument were tied-low possibly due to instrument error. The increase in the fluctuating kinetic energy along the inlet in 1996 indicates that diurnal currents are relatively strong at this depth. Despite the strength of these currents, the semi-diurnal temperature fluctuations at 20 m depth do not increase (Section 2.1, Table A.11). Although the increase in diurnal current energy suggests the possible existence of internal tides within the inner basin, there is no evidence that these internal tides contribute to the mixing.

During the 1996 study two instruments were located at approximately 45m of depth to measure the currents near the bottom of the inner basin. The percentage of energy located in the meteorological band is weakest at this depth accounting for only 5-10% of the total energy. The inertial band also accounts for about 10% of the energy indicating some influence of rotational effects. The percentage of energy within the semi-diurnal band is greater at 45m of depth than at 20m; while the opposite is true for the diurnal band. The percentage of power located in the high frequency portion of the spectrum is large on mooring M2-96 because the data recorded at this location is sparse with current speed being recorded only during spring tides. For the remainder of the observation period the instrument is tied-low. The lack of significant bottom currents clearly indicates that the bottom water within the inner basin remains relatively undisturbed during the period of observations.

2.3.3 Distribution of Energy in The Outer Channel

On the seaward side of the sill (moorings: M4 and M5 for 1996; M5, M6 and M7 for 1997), the meteorological band represents approximately 20% of the energy found in the near surface currents with the exception of M5 in 1996 where 40% of the energy is located in this band. It is not clear why there is a larger percentage of energy in the meteorological band at all depths on this mooring. The semi-diurnal and diurnal tides each account for approximately 10% of the total energy in the 1996 data. The larger proportion (20-30%) of the energy attributed to the semi-diurnal band in the 1997 data may be due to the proximity to the sill region where the tidal jet may still have some influence on the local currents. The inertial band accounts for 3-7% of the total energy similar to the proportion of energy found in this frequency band for those instruments located within the inner basin.

Moorings at 20m depth show a distribution of energy similar to those near the surface. The instruments located at depths below 30m reveal a decrease in the meteorological energy. The large amount of energy distributed to the high frequency bands for those instruments located below 30m depth is most likely an indication of noise in the signal as opposed to a significant amount of turbulent energy as currents measured at these depths were close to instrument threshold values.

With the high frequency band sub-divided into diurnal, inertial and semi-diurnal frequency bands the proportion of high frequency energy that remains unexplained must lie above the semi-diurnal frequency. Some of this energy may be identified to lie within particular shallow water frequencies generated by the tidal interaction while the rest will be available for mixing through turbulence. If we assume that the amount of energy that goes into mixing is proportional to the amount of unexplained high frequency energy, then the greatest mixing should occur where the greatest amount of high frequency energy is unexplained. An examination of Table 2.2 and 2.3 indicates that the lowest amount of unexplained high frequency is located at the sill with only 25-35% of the energy remaining unexplained. This is consistent with a coherent and strong tidal jet transporting a well-mixed fluid across the sill. The greatest amount of unexplained high frequency energy (approximately 65-75%) is located at M4-96 and M6-97. These are the two moorings that lie seaward of the sill where the analysis of temperature and salinity indicated that the greatest amount of mixing occurred. The amount of unexplained high frequency energy is found to increase with depth at M4-96 although, as previously mentioned, the weak currents at 45 metres depth suggests that the large amount of unexplained high frequency energy may be associated with a small signal to noise ratio. Within the inner basin, at M2-96 and M2-97, only 45-55% of the high frequency energy remains unexplained even though the moorings located within the inner basin are a similar distance from the sill to those seaward of the sill. Table 2.22 also indicates that the greatest amount of turbulence and mixing seaward of the sill may occur in the centre of the channel as only 45-55% of the high frequency energy remains unexplained at M5-97 and M7-97.

2.4. Winds and Wind stress

Wind data was not recorded at Clode Sound during either of the studies, however, the weather station at Gander International Airport (48 57 N, 54 35 W), approximately 70 km from Clode Sound should provide a good approximation for the wind field (Brown and Swail, 1988). During the months from June to September, typical winds, measured at Gander

International Airport, are predominantly from the southwest (Figure 2.23) with an average wind speed of 17-19 km/hr (Environment Canada, 1998). The average wind speed for the period of observation in 1997 was 17 km/hr. The hourly records of wind speed and direction were low-pass filtered (Timko et al, 1998a&b); the filtered time series for 1997 is shown in Figure 2.24 as east-west and north-south components and a vector plot sub-sampled at twelve-hour intervals.

To determine the influence of the wind on the currents and density structure of the inlet, the records for wind and currents were rotated to determine the along channel and cross channel components. The angle of rotation for each mooring was determined by estimating the angle (from true north) of the coastline for the region surrounding the instrument. The wind stress was calculated according to:

$$\vec{\tau} = \rho_a C_D \left|\vec{w}\right| \vec{w} \qquad (2.3.1)$$

where, $\rho_a=1.26kg/m^3$, $C_D=1.5 \cdot 10^{-3}$, $w=(u,v)$, and u,v represent the along channel and cross channel rotated wind (Gill, 1982). Cross-spectral analysis was then performed between the wind stress and rotated currents and density records (sub-sampled at hourly intervals). Coherence and phase lags for the cross-spectral analysis were also computed. Figure 2.25 shows a sample of this analysis.

The surface currents for the 1996 data were found to be coherent with the wind stress for frequencies 0.2-0.3 cpd, suggesting that weather systems passing over with periods ranging from 3 to 5 days influence the surface flow. The surface currents lag the wind stress by approximately 45°, or 9 to 15 hours after the onset of the wind. Further down the water column the currents of the same frequency lag the wind stress by 90° or 18 to 30 hours. It is evident that the wind is driving these surface currents and that frictional forces act downwards through the water column to drive deeper currents. There appears to be little coherence between the wind stress and currents at a depth of 45m where the direct influence of the wind is no longer measurable.

The 1997 data reveals coherence between the wind stress and surface currents at 7.5m of depth. However, the currents lag the wind by 90° or 18 to 30 hours after the onset of the wind. It is not clear why the wind stress should require 18 to 30 hours to establish the near surface currents in 1997 when they appeared 9 to 15 hours after the onset of the wind in 1996, although the proximity of the moorings to the sill may be partially responsible. The inner basin moorings M1-96 and M2-96 were located near the centre of the channel away from the influence of the coastline. During 1997, the inner basin moorings M2-97 and M3-97 were located in water that was shallower (depths 41m and 26m, respectively) than the depths of the inner basin moorings in 1996 (approximately 55 metres depth). Another difference that may partially account for the increased lag between the currents and the wind stress is the alignment that moorings M2-97 and M3-97 have with the sill where the tidal signal is expected to be much stronger. Seaward of the sill, the moorings locations in 1997 were also in shallower water (approximately 40 metres depth) than the closest instrument in 1996 (M4-96 located in a region of 75 metres depth). Shallower water, proximity to the sill and coastline may all help to explain the increasing lag between the wind stress and currents recorded during 1997.

There appears to be little coherence between the wind stress and currents for instruments located at 20m of depth and below in 1997. In addition to the influence of topography and bathymetry, it is possible that the stratification within the inlet during 1997 inhibited the wind effects from reaching the same depths as in 1996. The stratification during the 1997 field study indicates a well-developed surface layer down to a depth of 10-15 metres, the vertical density profile resembling a two-layer system; the stratification during the 1996 field year shows an exponential profile (Figure 2.20). It is possible that surface wind stress is not able to transmit any significant energy through the interface between the upper and lower layers.

While surface wind stress may contribute to the mixing of water in the near surface region, the distribution of energy within the observed currents (section 2.3; Tables 2.2 and 2.3) indicates that the influence of the wind is greatly reduced at the sill. We should anticipate that surface currents driven by the wind will be separated by the strong tidal flow at the sill especially during spring tides as it is highly unlikely that surface wind stress is strong enough to overcome the strong tidal jet at the sill. During slack water it is possible that surface wind stress may help to drive a weak exchange flow across the sill. Figure 2.26 indicates the frequency of occurrence (number of observations) for exchange flow across the sill in 1996 from Julian days 185 to 245. The total number of observations of exchange flow across the sill represents 16% of the total number of observations (20 minute intervals).

During intervals of exchange flow, the velocities across the sill are generally quite small and the flow remains subcritical, the mean velocity across the sill during periods of exchange flow was found to be only 5 cm/s for both the inflowing and outflowing water although the maximum current speed measured was in excess of 25 cm/s at 10 metres depth and 20 cm/s at 15 metres depth. From Figure 2.26 we see that exchange flow with surface water flowing outwards ($U_1>0$) occurs frequently between days 185 and 205 with almost 45 percent of the observed episodes occurring in the first 20 days of observations. A closer examination of the period from days 185 to 200 (Figure 2.27) reveals that the exchange events typically occur during slack water. This may be an indication of estuarine circulation with fresh water at the surface flowing outwards being replaced by more saline water at depth. Flow rates for the Northwest River during this time period average 28 m^3/s. This would amount to approximately 1.25 10^6 m^3 of fresh water being added to the inner basin during the period of the M_2 tide which is approximately 4% of the volume flux associated with a spring tide (6% for a neap tide). The exchange flow from days 235 to 240, however does not appear to be driven by an abundance of fresh water at the surface. During this period of time, the flow rate of the Northwest river was less than 5 m^3/s which would add less than 1% to the volume of water in the inner basin even during a neap tide. It is possible that this period of exchange flow is driven by surface winds. Strong southwesterly winds during that appear during this time may drive the surface waters of the inner basin towards and over the sill.

Episodes with exchange flow during which the surface flow was seaward represent only 30% of the total observed exchange flow across the sill. The other 70% of the observations of exchange flow across the sill represent periods during which the flow at 10 metres depth was directed inwards while the flow at 15 metres depth was directed seaward. From Figure 2.26 we see that periods during which the exchange flow across the sill was reversed occur most frequently during neap tides. This flow cannot represent the classical estuarine circulation as water nearer the surface is driven towards the source of fresh water while the denser water at 15 metres depth is flowing seaward. Figure 2.28 displays a closer look at the period of exchange flow between days 185 to 200. During a 24-hour period from day 190.7 to 191.7, 57% of the current observations at M3-96 indicated that the surface flow (10 metres depth) was directed towards the inner basin while the deeper water (at 15 metres depth) was moving seaward. The data was explored for correlation between the wind stress and the currents at both 10 and 15 metres depth. The only significant correlation that was found was between the currents at 15 metres depth and the east-west component of the wind stress. From days 190 to 192, the east-west currents at 15 metres depth at the sill and the east-west component of the wind stress had a correlation coefficient of –0.34 with a p-value (t-statistic) of 0.03 (0.05 representing 95% confidence interval) with 19 degrees of freedom. For the period from days 185 to 245, the correlation coefficient for this type of exchange flow with the east-west component of the wind with the current at 15 metres depth was –0.11 with a p-value (t-statistic) of 0.02. Since the velocity at 15 metres depth was chosen to be positive to represent outflowing water over the sill, it would appear that this circulation may be driven by weak but relatively steady easterly winds.

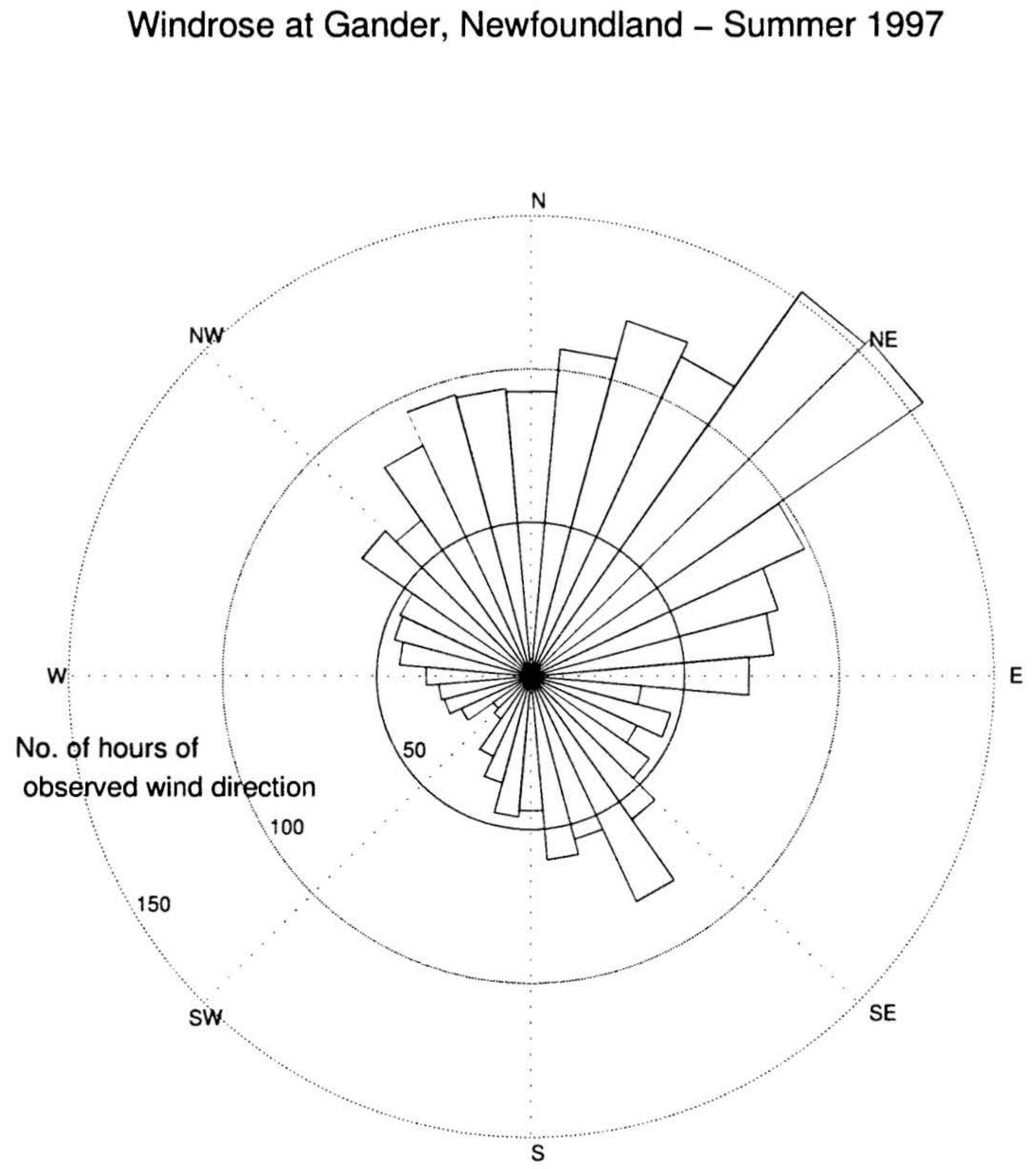

Figure 2.23: Distribution of the wind measured at Gander International Airport during 1997. Wind direction is shown in the oceanographic sense in that the wind direction is identified as the direction that the wind is blowing into.

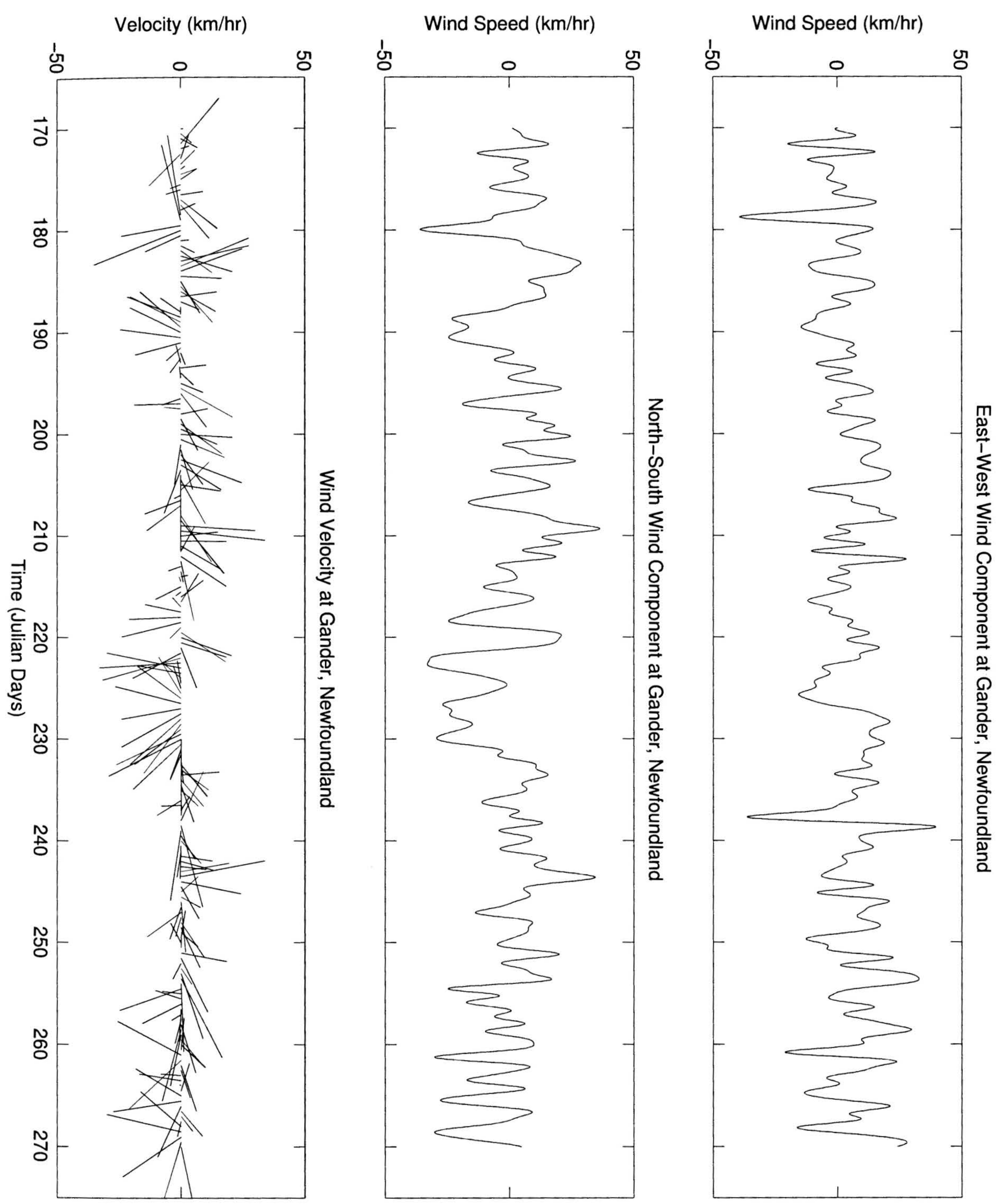

Figure 2.24: North-South and East-West components of the Wind Speed (km/hr) as recorded at Gander International Airport during the period of observations in 1997. North and East are assumed to be the positive directions.

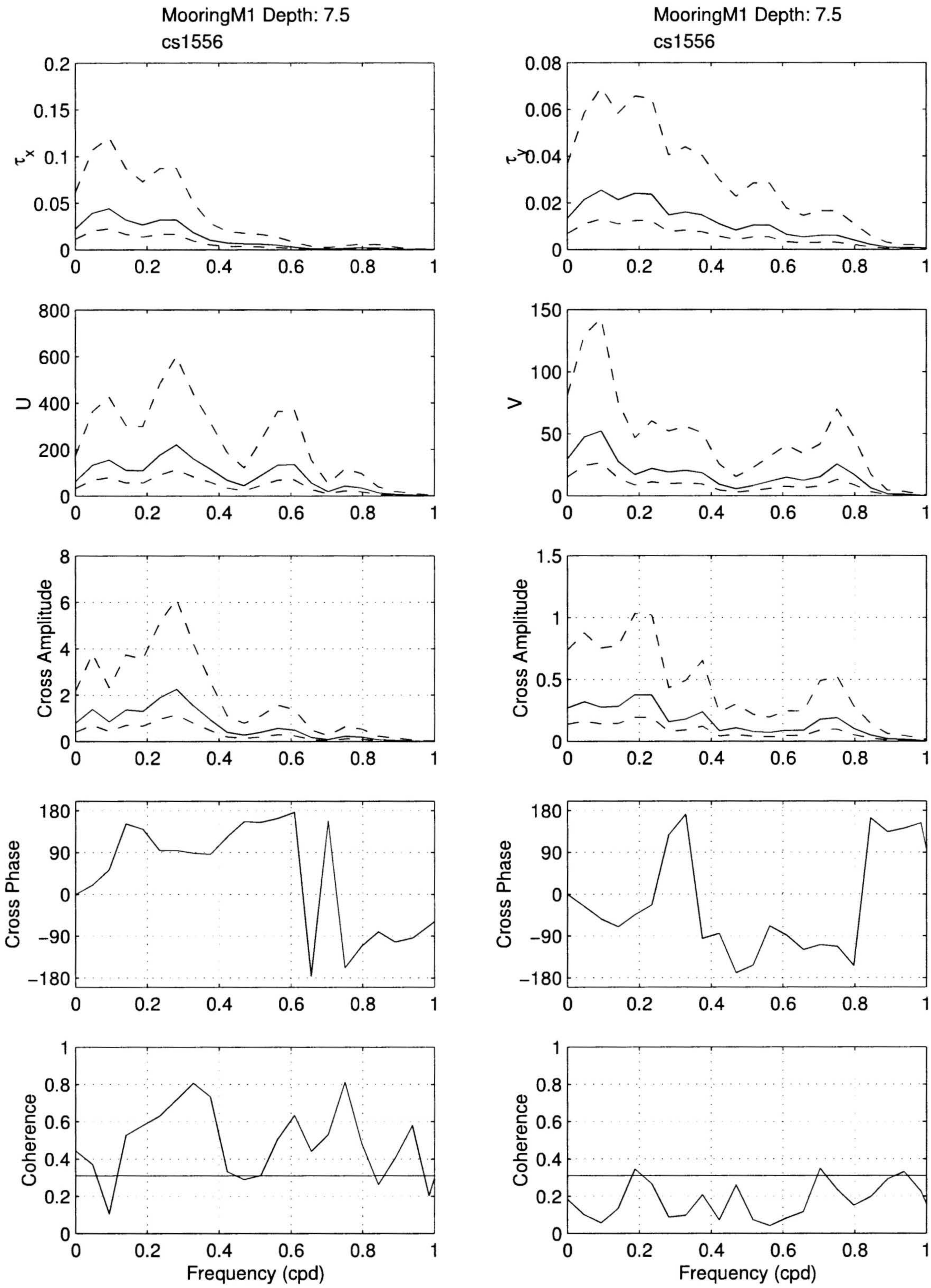

Figure 2.25: Cross Spectrum between the windstress and surface currents at mooring M1-97 using 15 day windows overlapping by 7.5 days. With 100 days of data, nonoverlapping windows would have approximately 13 degrees of freedom, the degrees of freedom will be less for overlapping windows. The dashed lines in the top six panels represent 95% confidence intervals, the horizontal line in the bottom two panels represents the 95% significance level for coherence.

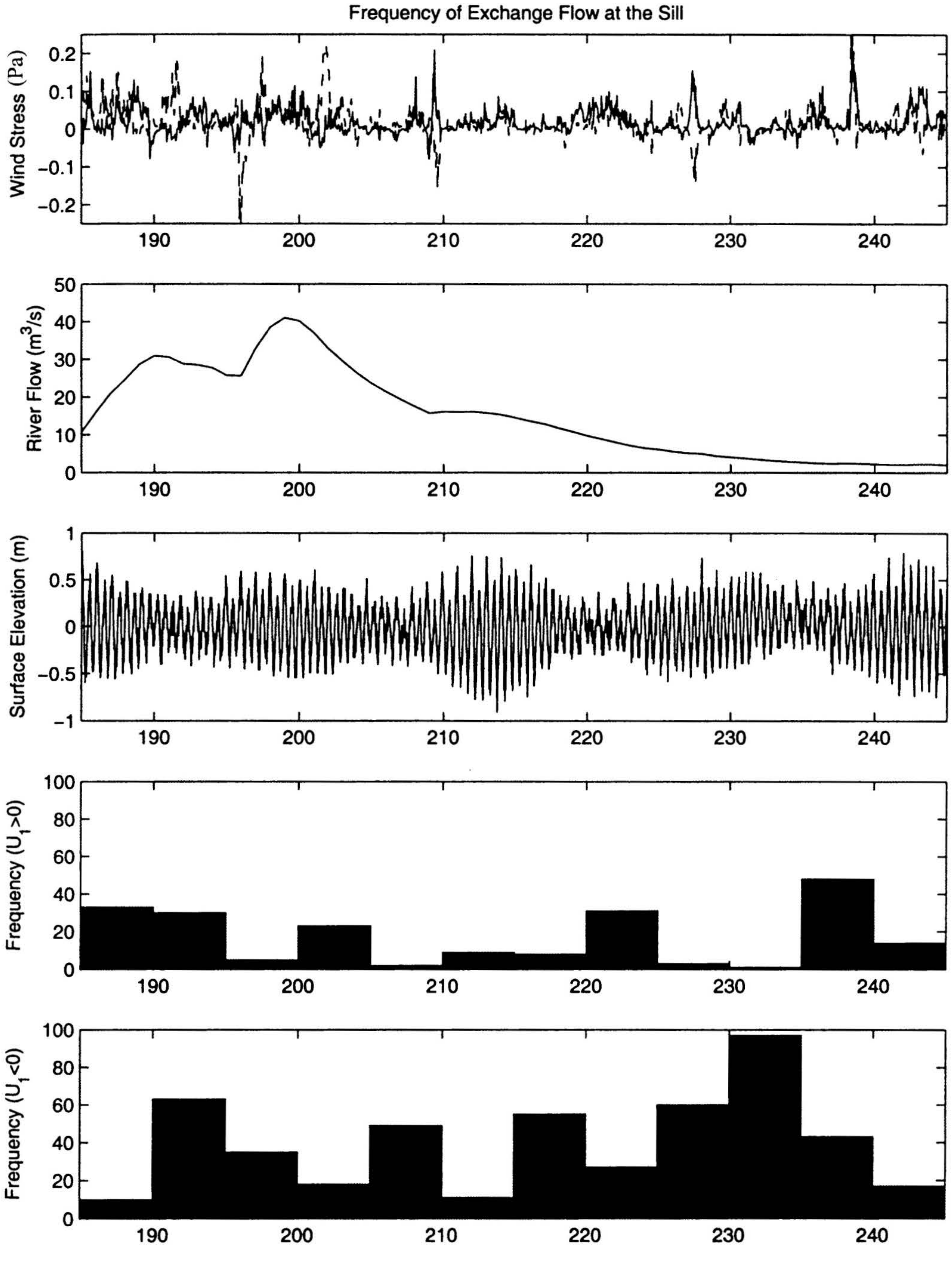

Figure 2.26: Frequency of Occurrence for exchange flow across the sill. Top: North-South (solid) and east-west (dashed) wind stress; **Second Panel:** Flow rate of the North-West River; **Third Panel:** Surface elevations recorded during 1996; **Fourth Panel:** Number of observations of exchange flow with surface waters flowing seaward; **Bottom Panel:** Number of observation of exchange flow with surface waters flowing inwards.

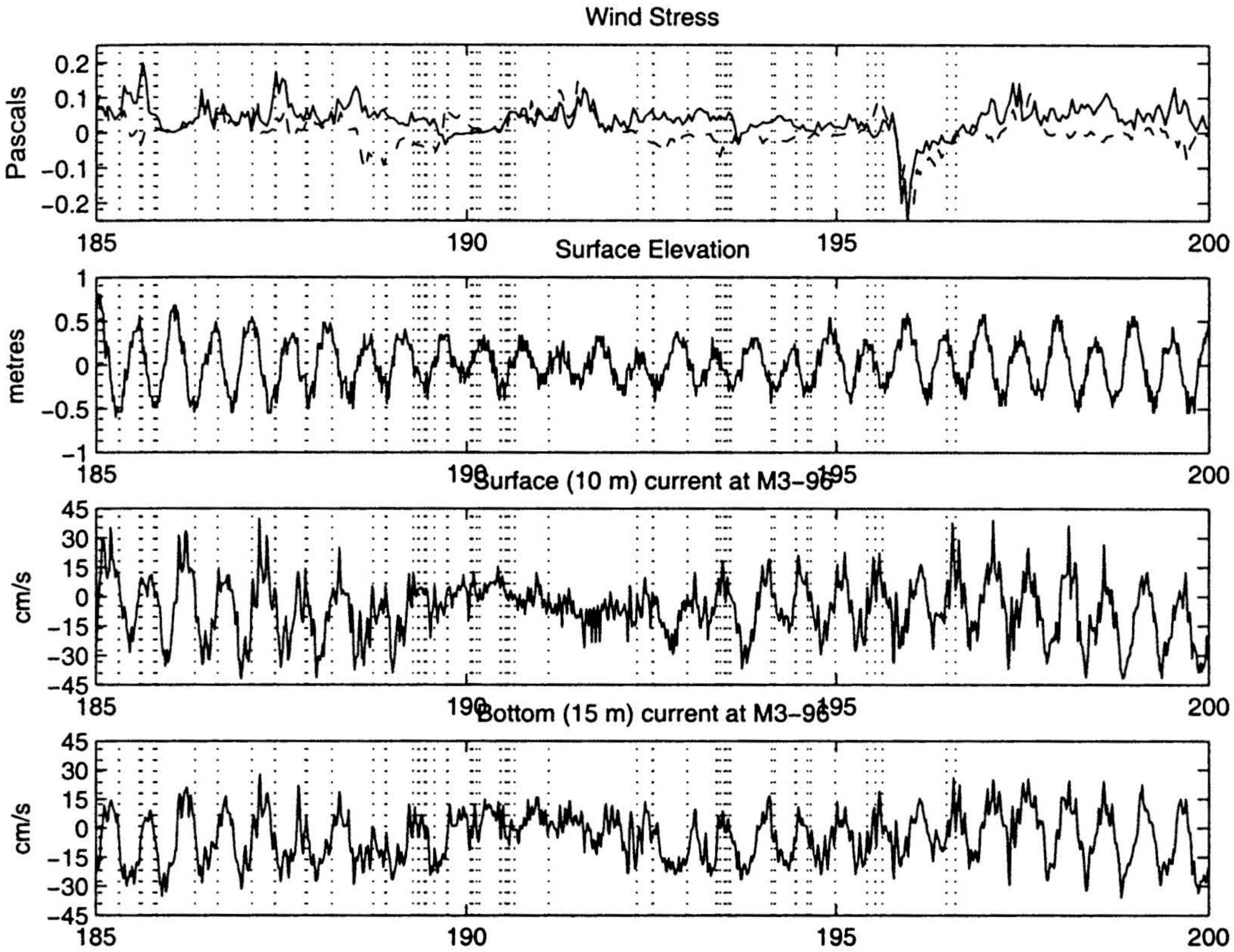

Figure 2.27: Occurrence of exchange flow with surface waters moving seaward. The dashed lines indicate the time of observed exchange flow. Top panel indicates the wind stress, panel 2 shows the surface elevation while panels 3 and 4 show the velocity of the currents measured at 10 and 15 metres depth at the sill.

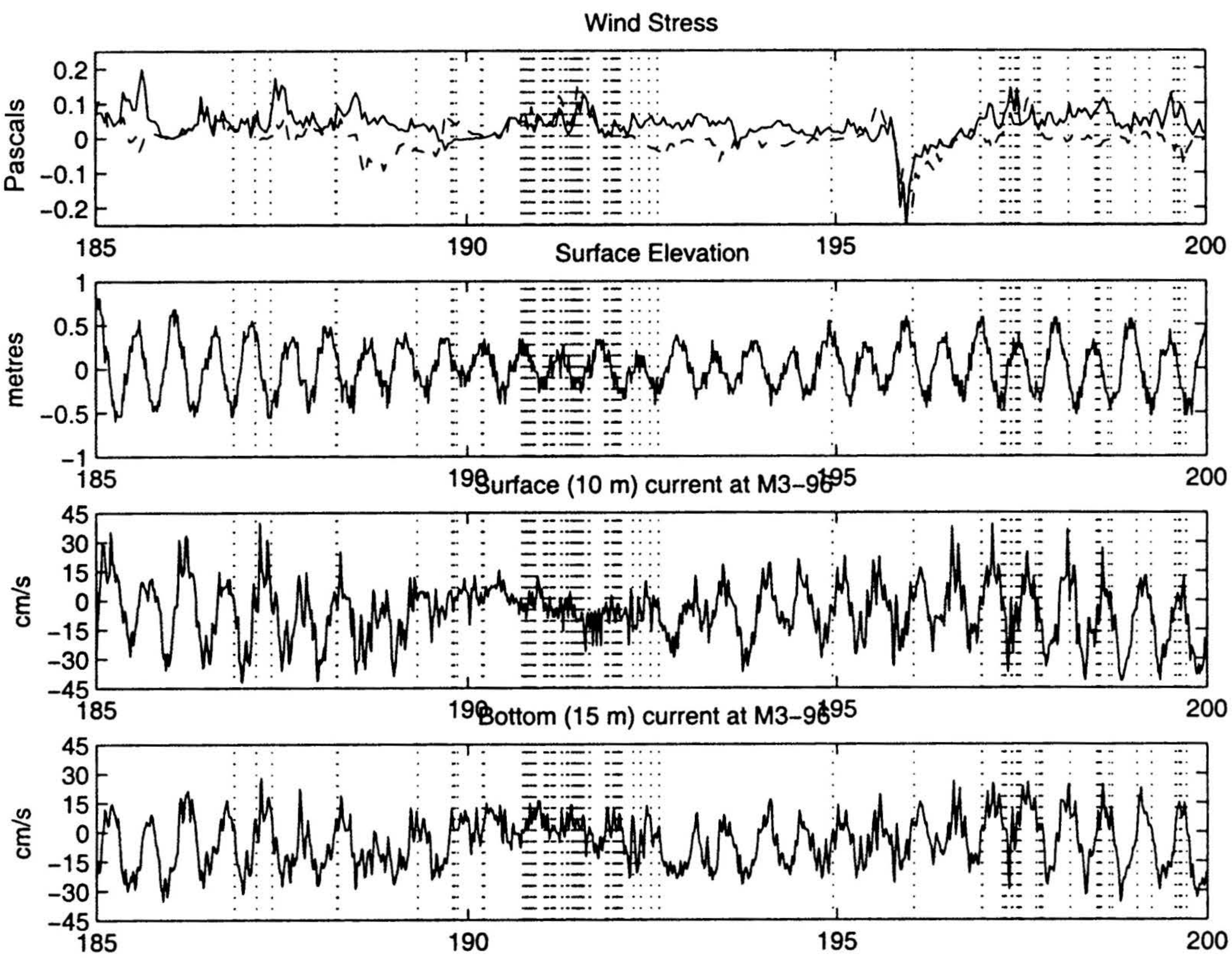

Figure 2.28: : Occurrence of exchange flow with surface waters moving inwards. The dashed lines indicate the time of observed exchange flow. Top panel indicates the wind stress, panel 2 shows the surface elevation while panels 3 and 4 show the velocity of the currents measured at 10 and 15 metres depth at the sill.

2.5. *Tidal Heights and Currents*

The tidal current records, with a sampling interval of 20 minutes, were analyzed to determine the principle axes. The principle axis is oriented at an angle, θ, determined by (Emery and Thomson, 1997):

$$\theta = \frac{1}{2}\arctan(\frac{2u'v'}{u'^2 - v'^2}) \tag{2.5.1}$$

where u'^2, v'^2, $u'v'$ are the components of the covariance matrix. The angle of rotation for each instrument can be found in the Tables 2.4 and 2.5 and plotted in Figure 2.29. As can be seen in Figure 2.29, the principle axes are generally aligned with the coastline or bathymetric contours.

Table 2.4: Orientation of the Principle Axis (degrees) 1996. Axis orientation measured with east representing zero degrees, positive angles are measured in a counter-clockwise direction.

Depth (m)	M1 (deg)	M2 (deg)	M3 (deg)	M4 (deg)	M5 (deg)
10	44	18	-10	28	45
15-20	41	19	-18	12	55
45	43	-7	-	23	51
76	-	-	-	-	61

Table 2.5 Orientation of the Principle Axis (degrees) 1997 Axis orientation measured with east representing zero degrees, positive angles are measured in a counter-clockwise direction.

Depth (m)	M1 (deg)	M2 (deg)	M3 (deg)	M4 (deg)	M5 (deg)	M6 (deg)	M7 (deg)
7.5	35	17	-16	-18	-9	-	14
15-21	30	17	-	-12	-26	-	-
30-35	-	-	-	-	-	-18	13

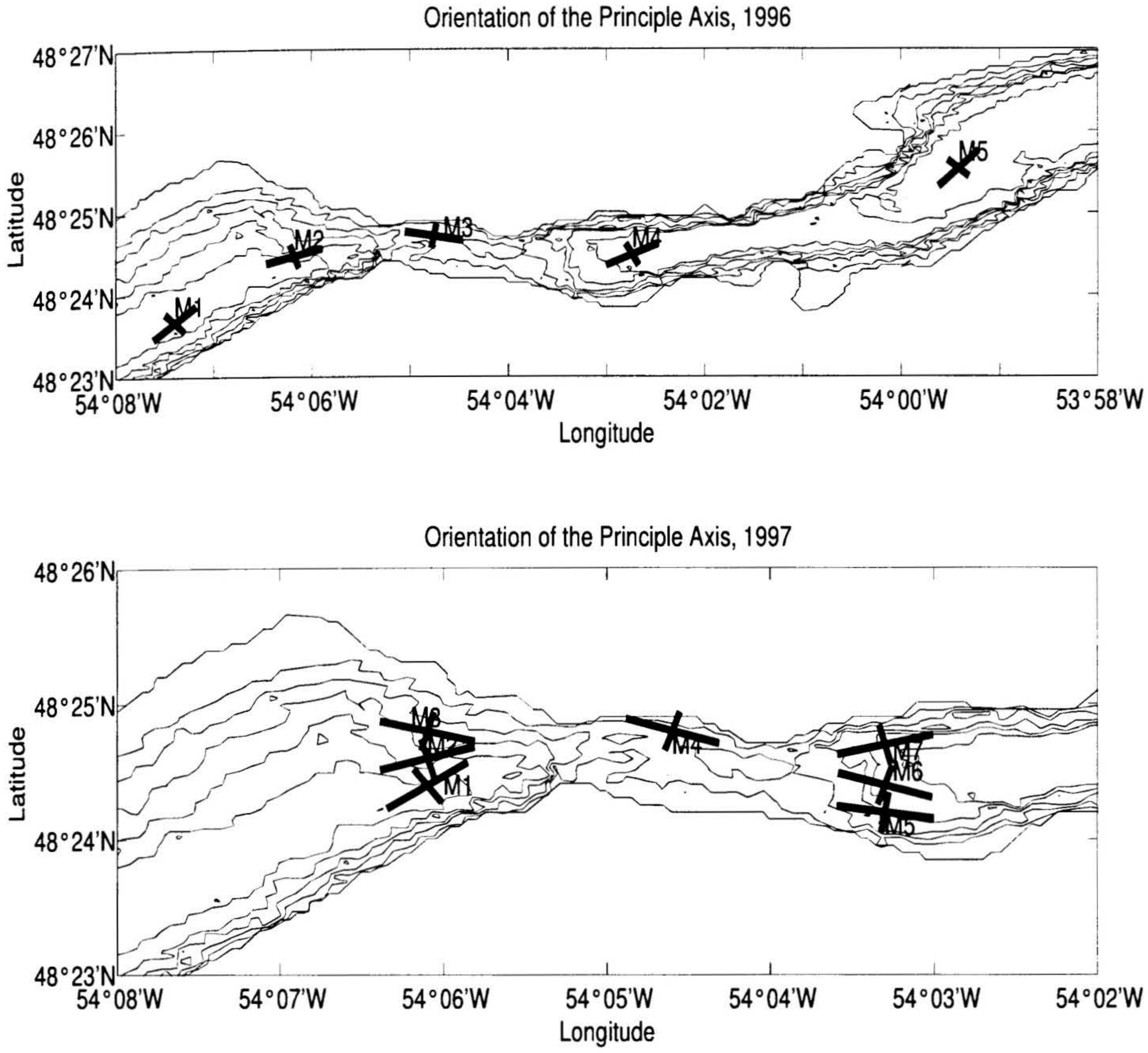

Figure 2.29: Orientation of the Principle Axis evaluated from the recorded currents at 10 metres depth in 1996 (top) and 7.5 metres depth in 1997 (bottom).

After rotation to the principle axes the recorded velocities were analyzed for tidal constituents following Pawlowicz et al (2002). Amplitudes of the tidal height constituents were also computed. The amplitudes and Greenwich phase of the tidal heights, along with the 95% confidence intervals may be found in Tables 2.6-2.9. Apart from MSF, only the main diurnal and semi-diurnal tidal constituents are provided along with M_2 harmonics with a signal to noise ratio greater than four.

The classification of tides found in estuaries may be determined using the form number, F, given by:

$$F = \frac{K_1 + O_1}{M_2 + S_2} \tag{2.5.2}$$

where, K_1, O_1, M_2 and S_2 represent the amplitudes of the tidal heights for the specified constituents (the ratio of the sum of the amplitudes of the main diurnal constituents to the sum of the amplitudes of the main semi-diurnal constituents). For the pressure sensors in both the 1996 and 1997 data, the form number was estimated to be approximately 0.36. A form number between 0.25 and 3.0 is considered to represent a mixed tide (Foreman, 1977)

Table 2.6: Tidal Height Constituents 1996 Mooring: M2-96. Estimated from the pressure gauge located within the inner basin.

Constituent	Amplitude (cm)	Phase (deg)	Signal / Noise
MS_f	2.5 ± 3.1	164 ± 82	0.6
O_1	6.4 ± 0.9	125 ± 8	45.0
K_1	8.8 ± 0.8	180 ± 6	120.0
μ_2	2.5 ± 1.2	271 ± 27	4.2
N_2	7.2 ± 1.1	294 ± 10	39.0
M_2	29.8 ± 1.1	306 ± 2	740.0
S_2	14.1 ± 1.2	358 ± 5	130.0
M_6	1.5 ± 0.4	237 ± 16	11.0

Table 2.7: Tidal Heights Constituents 1996 Mooring: M4-96. Estimated from the pressure gauge located in the outer channel.

Constituent	Amplitude (cm)	Phase (deg)	Signal / Noise
MS_f	6.8 ± 10.9	137 ± 122	0.4
Q_1	2.2 ± 0.7	103 ± 20	8.6
O_1	4.9 ± 0.7	135 ± 9	50.0
K_1	7.9 ± 0.6	180 ± 5	170.0
J_1	1.7 ± 0.7	170 ± 26	5.9
μ_2	2.8 ± 1.3	295 ± 27	4.6
N_2	6.8 ± 1.2	306 ± 11	32.0
M_2	26.3 ± 1.2	313 ± 3	490.0
S_2	11.6 ± 1.3	7 ± 6	81.0

Table 2.8: Tidal Heights Constituents 1997 Mooring: M4-97. Estimated from the pressure gauge located at the sill

Constituent	Amplitude (cm)	Phase (deg)	Signal / Noise
MS_f	1.9 ± 3.0	306 ± 107	0.4
O_1	6.8 ± 0.7	123 ± 6	86
K_1	8.5 ± 0.6	176 ± 5	180
μ_2	3.1 ± 0.8	266 ± 14	16
N_2	7.0 ± 0.8	299 ± 6	70
M_2	29.9 ± 0.9	307 ± 1	1100
S_2	14.3 ± 0.7	359 ± 4	410
M_3	0.9 ± 0.2	225 ± 17	17
M_6	1.2 ± 0.4	226 ± 17	12
M_8	0.6 ± 0.2	158 ± 17	11

Table 2.9: Tidal Heights Constituents 1997 Mooring: M6-97. Estimated from the pressure gauge located in the outer channel.

Constituent	Amplitude (cm)	Phase (deg)	Signal / Noise
MS_f	0.45 ± 1.0	130 ± 157	0.2
O_1	6.8 ± 0.8	122 ± 6	80
K_1	8.8 ± 0.6	177 ± 4	200
μ_2	2.7 ± 0.6	264 ± 16	18
N_2	7.1 ± 0.7	303 ± 6	98
M_2	30.9 ± 0.8	308 ± 1	1600
S_2	14.9 ± 0.6	359 ± 3	560
M_3	0.9 ± 0.2	228 ± 14	20
M_4	0.2 ± 0.1	122 ± 21	6.8
M_6	1.0± 0.3	238 ± 16	12
M_8	0.4 ± 0.1	144 ± 21	7.1

although the tidal signal is clearly dominated by the semi-diurnal constituents. The range of a typical spring tide in Clode Sound is approximately 120 cm, but can reach 150 cm; the range of a typical neap tide is 60 cm. The principal lunar semi-diurnal constituent, M_2, has an amplitude of 29 cm and a Greenwich phase lag of 309°; S_2, the principal solar semi-diurnal constituent, has an amplitude 14 cm and a phase lag of 1°. The semi-diurnal lunar elliptic constituent, N_2, was found to have an amplitude of 7 cm and Greenwich phase lag of 300°. The lunar diurnal constituent, O_1, and the luni-solar diurnal constituent, K_1, have amplitudes of 6 and 8 cm and phase lags of 126° and 178°; respectively.

The tidal current information for the dominant semidiurnal (M_2) and diurnal (K_1) for 1996 are provided in Tables 2.10 and 2.11. The tables provide information on the length of the semi-major and semi-minor axis (cm/s) as well as the orientation of the tidal ellipse and the Greenwich phase. A negative value for the semi-minor axis indicates that the current rotates about the tidal ellipse in a clockwise manner. The analysis was done after rotation to the principle axis so the major axis and minor axis may be considered to represent along channel and cross channel flow.

Table 2.10: M_2 Tidal Current: Major and Minor Axis (cm/s), Phase and Inclination (relative to the principal axis) of the tidal ellipse 1996

	M1-96		**M2-96**		**M3-96**		**M4-96**		**M5-96**	
Depth (m)	**maj (cm/s)**	**Min (cm/s)**	**maj (cm/s)**	**min (cm/s)**	**maj (cm/s)**	**min (cm/s)**	**maj (cm/s)**	**min (cm/s)**	**maj (cm/s)**	**Min (cm/s)**
10	1.8	0.1	3.4	0.1	14.4	0.2	2.9	-0.9	2.0	0.1
15-20	0.7	0.3	1.5	0.1	12.0	-0.3	1.3	0.1	1.8	0.1
45	2.4	-0.2	1.1	0.0	-	-	1.0	0.2	1.0	0.1
76	-	-	-	-	-	-	-	-	0.8	-0.1

	M_2 Tidal Current Phase (deg)					**M_2 Tidal Ellipse Inclination (deg)**				
Depth (m)	**M1**	**M2**	**M3**	**M4**	**M5**	**M1**	**M2**	**M3**	**M4**	**M5**
10	95	84	232	64	88	8	0	180	2	6
15-20	44	72	49	231	238	4	4	0	172	176
45	332	284	-	356	33	2	1	-	2	5
76	-	-	-	-	205	-	-	-	-	16

Table 2.11: K_1 Tidal Current: Major and Minor Axis (cm/s), Phase and Inclination (relative to the principal axis) of the tidal ellipse 1996

	M1-96		**M2-96**		**M3-96**		**M4-96**		**M5-96**	
Depth (m)	**Maj (cm/s)**	**Min (cm/s)**	**maj (cm/s)**	**min (cm/s)**	**maj (cm/s)**	**min (cm/s)**	**maj (cm/s)**	**min (cm/s)**	**maj (cm/s)**	**min (cm/s)**
10	0.4	0.2	0.9	0.6	3.7	-0.5	0.8	-0.1	0.5	-0.3
15-20	1.1	-0.2	1.0	0.0	2.4	-0.1	0.3	0.1	0.5	-0.2
45	0.8	0.0	0.4	0.0	-	-	0.2	0.1	0.4	0.0
76	-	-	-	-	-	-	-	-	0.3	0.0

	K_1 Tidal Current Phase (deg)					**K_1 Tidal Ellipse Inclination (deg)**				
Depth (m)	**M1**	**M2**	**M3**	**M4**	**M5**	**M1**	**M2**	**M3**	**M4**	**M5**
10	274	121	288	173	87	27	167	1	168	85
15-20	286	355	110	300	114	11	2	179	8	168
45	348	344	-	283	277	177	180	-	2	16
76					306					171

The tidal heights for the M_2 tidal constituent in 1996 indicate that the phase of the M_2 constituent is 309°. Assuming a barotropic tide, we should anticipate that the phase of the tidal currents and tidal heights should differ by 90° with maximum currents occurring half way between the time of high water and low water. The tidal currents estimated from the 1996 data vary significantly from this expected phase shift. Within the inner basin, both friction and internal tides likely contribute to tidal currents. Examination of the current meter data at 20 and 45 metres depth for the K_1 constituent shows an amplification of the along channel current by a factor of two compared to the along channel current of K_1 in the outer channel. There is also evidence of internal tides at 45 metres for the M_2 constituent that shows a large increase in amplitude from mooring M2-96 to M1-96. At 10 metres depth both K_1 and M_2 show the effect of shoaling as the amplitude increases then decreases across the sill. In the outer regions of the inlet (seawards of the sill), the difference from the barotropic tide is likely due to friction and the influence of the shoaling topography. Within the inner basin, the maximum M_2 current at mid-level depths (near 20m) occurs prior to the maximum current at the surface. The difference in phase between the near surface current (10m depth) and the current at mid depths (20 m) ranges from 12° at M2-96 to 51° at M1-96, indicating that the amount by which the surface currents lag those at mid-depths varies from mooring to mooring.

Comparison of the tidal heights and currents from the 1996 data set, indicate that the flow over the sill may be responsible for producing M_2 harmonics within the inner basin. Comparison of the tidal height data from moorings M2-96 (inner basin) and M4-96 (seaward of the sill), reveal that constituents M_4 and M_8 are amplified by a factor of 70-100 after crossing the sill (Table 2.12). During the 1997 observations, tidal height data was collected at the sill (mooring M4-97) and outside the sill (mooring M6-97), no tidal height data was collected within the inner basin. From the 1997 there is no evidence of the amplified overtides in the tidal heights at the sill (M4-97) this suggests that the amplification of the M_2 harmonics occurs only within the inner basin. A review of the tidal height data from 1996 (Tables 2.6 and 2.7) indicates that all of the main diurnal and semi-diurnal constituents show an increase in height from the outer channel (M4-96) to the inner basin (M2-96) of between 10-30%. Based upon the 95% confidence intervals included with the analysis, only the 13% amplification of M_2 appears to be significant with clearly distinct confidence intervals. The 11% increase in the amplitude of K_1 does not appear to be significant with confidence intervals that clearly overlap. There is also a 20-30% increase found in S_2 and O_1, however, the analysis is inconclusive with confidence intervals overlapping by approximately 0.1cm/s. It does appear however that there may be some amplification of the tidal heights as the tide crosses the sill into the inner basin.

Table 2.12: Amplitude (tidal height) and Greenwich phase of the M_2 constituent and harmonics

Station	M_2 height (cm)	M_2 phase °G	M_4 height (cm)	M_4 phase °G	M_8 height (cm)	M_8 phase °G
M2-96	30.41	307	0.87	81	0.57	153
M4-96	31.74	308	0.0089	69	0.0082	183
M4-97	30.37	308	0.0031	172	0.061	158
M6-97	31.35	309	0.0021	119	0.0039	143

Following Jay and Musiak (1996), the tidal currents in the 1996 observations were investigated for internal tidal asymmetry. Internally generated overtides should exhibit the following factors:

1.) along channel currents stronger than can be justified by the barotropic surface tide,

2.) a 180° phase reversal in the vertical,

3.) a decrease in current amplitude at the upstream limits of salinity intrusion.

From Table 2.13, normalized current amplitudes ranging from 3 to 20 suggest that nonlinearities play an important role in the tidal currents within the inner basin. We see a significant decrease in the current amplitudes at 10 metres and 20 metres between moorings M1-96 and M2-96. M1-96 is closer to the head of the channel where fresh water from the Northwest River enters the inlet. M1-96 also shows a change in the relative phase of 194° between 10m and 21m.

Table 2.14 shows a comparison of the M_2 and M_4 tidal currents for the 1997 data. Moorings M1-97, M2-97 and M3-97 represent those locations within the inner basin from south to north, M4-97 is the mooring located at the sill, and M5-97, M6-97 and M7-97 are located south to north seaward of the sill. Within the inner basin, the M_2 current increases from 2.5 cm/s at M1-97 (south) to 5.4 cm/s at M3-97 (north) and exhibits a phase change of approximately 180°. Seaward of the sill, there is a difference in the M_2 current amplitude across the basin of approximately 1cm/s, however, the lack of velocity data at M6-97 located in the centre of the channel does not permit us to conclude if the current increases steadily across the inlet or has a maximum in the centre of the channel. There is also a phase change of about 200° across the outer channel. Given the orientation of the inner basin with the sill and the changes across the inner basin can probably be attributed to the geometry of the coastline. Moorings M2-97 and M3-97 are located more directly in line with the sill (Figure 2.3). The tidal jet from the sill appears to flow towards these locations and possibly recirculates around and back to M1-97 in a large eddy. Such a tidally induced residual circulation may explain the phase change across the channel on both sides of the sill.

Table 2.13: Data from 1996 used to investigate Internal Tidal Asymmetry within the inner basin. Tidal heights measured at M2-96 were substituted for the tidal heights of M1-96 as there was no pressure sensor located at M1-96.

Station	Depth (m)	M_2 height (cm)	M_4 height (cm)	M_8 height (cm)	M_2 current (cm/s)	M_2 phase (deg)	M_4 current (cm/s)	M_4 phase (deg)	Normalized amplitude (M_4 cur./ht.) / (M_2 cur./ht.)	Relative Phase $2M_2$-M_4
M1-96	**10**	30.4	0.9	0.6	1.9	97	0.2	16	3.5	177
M1-96	**21**	30.4	0.9	0.6	0.7	43	0.2	103	7.8	-17
M1-96	**45**	30.4	0.9	0.6	2.6	333	0.1	359	1.7	307
M2-96	**10**	30.4	0.9	0.6	3.4	85	0.6	315	6.6	-145
M2-96	**17**	30.4	0.9	0.6	1.6	74	0.2	303	4.8	-154
M2-96	**44**	30.4	0.9	0.6	1.1	107	0.6	294	19.9	-79

Table 2.14: M_2 and M_4 currents across the channel measured in 1997. The values used for the currents represent the semi-major axis of the tidal ellipse. The data indicates a large variation across the inner basin for both M_2 and M_4. Between M1-97 and M3-97, the phase difference in M_2 is 180° indicating an eddy at 7.5 metres depth. Seaward of the sill, the M_2 current also indicates a phase difference of approximately 200° at 7.5 metres depth, the strength of the M_2 current in the outer channel also varies across the channel but the variation is significantly smaller than the variation found within the inner basin. The incoming tide clearly does not behave as a plane wave in the vicinity of the sill.

Station	Depth (m)	M_2 current (cm/s)	M_2 phase (deg)	M_4 current (cm/s)	M_4 phase (deg)
M1-97	**7.5**	2.5	58	0.1	246
	21	0.9	355	0.1	31
M2-97	**7.5**	4.6	75	0.7	359
	21	1.2	24	0.2	19
M3-97	**7.5**	5.4	240	0.8	133
M4-97	**7.5**	12.2	231	0.9	200
	14	11.4	221	0.4	30
M5-97	**7.5**	3.0	241	0.3	27
M6-97	**33**	0.5	15	0.1	333
M7-97	**7.5**	2.3	39	0.2	158
	31	1.4	360	0.2	56

2.5.1 Temporal Evolution of the M_2 and K_1 constituents

The time series from the current meters was subdivided into intervals of 29 days, with each 29-day window overlapping the previous window by 28 days. Each of the 29-day windows was then analyzed to calculate the main tidal constituents to determine if there was any temporal dependence on the tidal currents over the period of observation. Prior to the harmonic analysis the velocity data was rotated to the principle axis calculated from the complete observation record for each year. Figure 2.30 shows the evolution of the M_2 tidal current (magnitude (cm/s) of the semi-major axis of the tidal ellipse) and phase at the sill compared to the evolution of the density (at sill depth) for the inner basin, sill and outer channel for both 1996 and 1997. The phase of the M_2 current (Figure 2.30 panels 2 and 4) remained almost constant over the observation period, the 180° "jump" in the phase representing the orientation of the tidal ellipse as the semi-major axis rotates through the principle axis.

During 1996, the surface M_2 tidal current (Figure 2.30 top panel) is found to decrease steadily after day 218 at a rate of approximately 0.13 cm/s/day reaching a minimum of 13.8 cm/s around day 230 (Figure 2.31), representing the end of the available data. This is a decrease of approximately 10% in the second half of the observation period compared to the average of current of 15.2 cm/s from days 200 to 218. The M_2 current at 15 metres depth undergoes a similar transition, however the maximum current of 13.6 cm/s is achieved about day 212 after which the current steadily decreases at a rate of approximately 0.15 cm/s/day to achieve a minimum of 11.0 cm/s at day 230; a 17% decrease when compared to the average 13.2 cm/s current from days 200 to day 212. Comparison (Figure 2.30, top panel) of the M_2 currents at the sill to the density of the water from 15-20 metres depth at moorings M2-96 (dashed line), M3-96 (dotted line) and M4-96 (dash dot line) suggests that this change in current speed may be correlated with the decrease in density at the sill from days 212 to 220 even though the density gradient across the sill from moorings M4-96 to M2-96 remains relatively constant. However, the correlation was not found to be statistically significant.

Analysis of the 1997 data (Figure 2.30, panel 3) also reveals a decrease in the M_2 current after day 216 at 7.5 metres depth while the current at 14 metres depth remains relatively constant until after day 225 when it also begins to decrease (Figure 2.31). After day 216 the current at 7.5 metres depth decreases at approximately 0.12 cm/s/day and this decrease continues until around day 230 (Figure 2.31). The maximum current speed achieved in 1997 is 13.2 cm/s and the minimum is 11.5, the decrease from days 216 to 230 represents a decline in the current speed of approximately 13%. However, the maximum current at day 216 appears as if it may be an anomaly, from days 185 to 212 the M_2 tidal current showed very little variation with a mean of 12.3 cm/s. The current was then found to increase rapidly over 4 days at a rate of 0.23 cm/s/day. Again there appears to be a correlation between the change in current speed and the change in density at the sill (dotted line) and also seaward of the sill at M6-97 (Figure 2.30, panel 3). Between days 214 to 222 in 1997, however, the density at the sill is less than the density at either M2-97 located within the inner basin (dashed line) or M6-97 located in the outer channel (dash dot line). Unlike the observed density from the 1996 data, when the density gradient remained relatively constant across the sill, the density gradient during the 1997 observations increases from the sill towards both the inner basin and outer channel.

The timing of this change in the M_2 current coincides with the timing of the surface layer in outer channel beginning to reach below the level of the sill (Section 2.1.2 Figure

2.11). In both 1996 and 1997, these events occur when the tidal amplitudes are significantly greater than a neap tide (not necessarily a spring tide but more of a spring tide than a neap tide). The data also suggests that the timing of the deepening of the surface layer seaward of the sill may be seasonal occurring only after a sufficient amount of thermal energy has entered from the surface. However, many more years of observations would be required along with a measurement of the net surface heat flux to draw any real conclusion with regards to the coincident timing of this event in both 1996 and 1997.

The temporal evolution of the M_2 current at M4-96 (Figure 2.31) indicates that the M_2 current at 10 metres depth exhibits a weak oscillatory behaviour and slowly increases by approximately 1 cm/s from days 200 to 230. At 20 metres depth, the M_2 current also exhibits a weak oscillation but does not indicate any obvious increase or decrease in strength. At 45 metres depth, the current is found to decrease by approximately 0.5 cm/s between days 200-230. There was no significant change in the phase of the M_2 tide at M4-96 either (Figure 2.32).

The decrease in density and current speed at the sill exhibited by M_2 suggests that the amount of kinetic energy associated with this tidal constituent is decreasing. Defining a kinetic energy density (kinetic energy per unit volume) as:

$$\mathrm{K}(t) = \frac{1}{2}\rho(t) * U(t)^2 \qquad (2.5.3)$$

where $\rho(t)$ is the density (kg/m^3) of the water and U(t) is the velocity along the semi-major axis of the M_2 tidal ellipse we may estimate the loss of kinetic energy per unit volume of water recorded at the sill. Figure 2.35 shows the kinetic energy density at the sill (top panel) and seaward of the sill at M4-96 (bottom panel). The maximum value of K(t) at the sill was found to be 1.2 10^5 and 9.4 10^4 N/m^3 at 10 and 15 metres depth respectively while the minimum values (at day 230) were found to be 9.8 10^4 and 6.2 10^4 N/m^3 at 10 and 15 metres depth. At M4-96, the energy density function K(t) at 10 metres depth increases until approximately day 215 at which time it oscillates about 6.0 10^3 N/m^3 while at 20 metres depth the energy density function is relatively constant around 1.0 10^3 N/m^3. The only indication of energy loss at the M4-96 occurs at 45 metres depth where the energy density function decreases from 1.4 10^3 N/m^3 to 6.7 10^2 from days 212 to day 230. The phase of the M_2 current at M4-96 remains almost constant over the entire observation period (Figure 2.33) so the incoming M_2 signal does not appear to undergo any significant reflection that may account for this change in amplitude. The coincident timing of the surface layer beginning to deepen below the level of the sill suggests that the energy which is extracted from the M_2 tide at the sill and at 45 metres depth at M4-96 is used for mixing and subsequent deepening of the surface layer.

Within the inner basin, there is also evidence that the M_2 signal is modulated, the clearest example being exhibited at mooring M2-97 where both the amplitude (Figure 2.33) and the phase (Figure 2.34) of the M_2 signal exhibit a "wave-like" graph. The period of modulation is approximately 55-60 days or about twice the period of the lunar monthly constituent M_M; although it may be non-tidal. There is some indication of this type of oscillatory behaviour at M1-96 and M2-96 (Figures 2.31 and 2.32) but the shorter 60-day record from 1996 makes any confirmation impossible. This weak oscillatory behaviour is not statistically significant at the 95% confidence level. A longer current meter record may help to determine if this apparent modulation is real or merely a consequence of the tidal analysis.

There is little evidence of any such modulation of the M_2 amplitudes in the outer channel, the modulation appears as the tidal signal crosses over the sill. The near surface moorings (depth 7.5 m) M1-97 and M3-97 show little evidence of M_2 being modulated at this frequency (Figures 2.36 and 2.37) but at 20 m depth, M1-97, the modulation is still apparent (not shown). Although weaker, K_1 amplitudes at 7.5 metres depth exhibit similar modulation as the tide crosses the sill (Figure 2.38) although the modulation extends to M1-97. At the sill (M4-97) the K_1 amplitude also shows a significant decrease in the similar in magnitude to those found in the M_2 amplitudes, representing a much larger percentage decrease (as much as 75%) between days 200 to day 255.

On the northern side of the outer channel, the M_2 tidal current amplitude at M7-97 increases by approximately 2 cm/s from day 170 to day 230 while on the southern side the current remains almost constant. On the northern boundary, the currents in the inner basin (M3-97) decrease by approximately 3 cm/s during the development of the surface layer which initiates around Julian day 215. The greatest decrease in the current amplitudes occurs after day 230 suggesting that the surface layer may also be forming on the northern boundary within the inner basin.

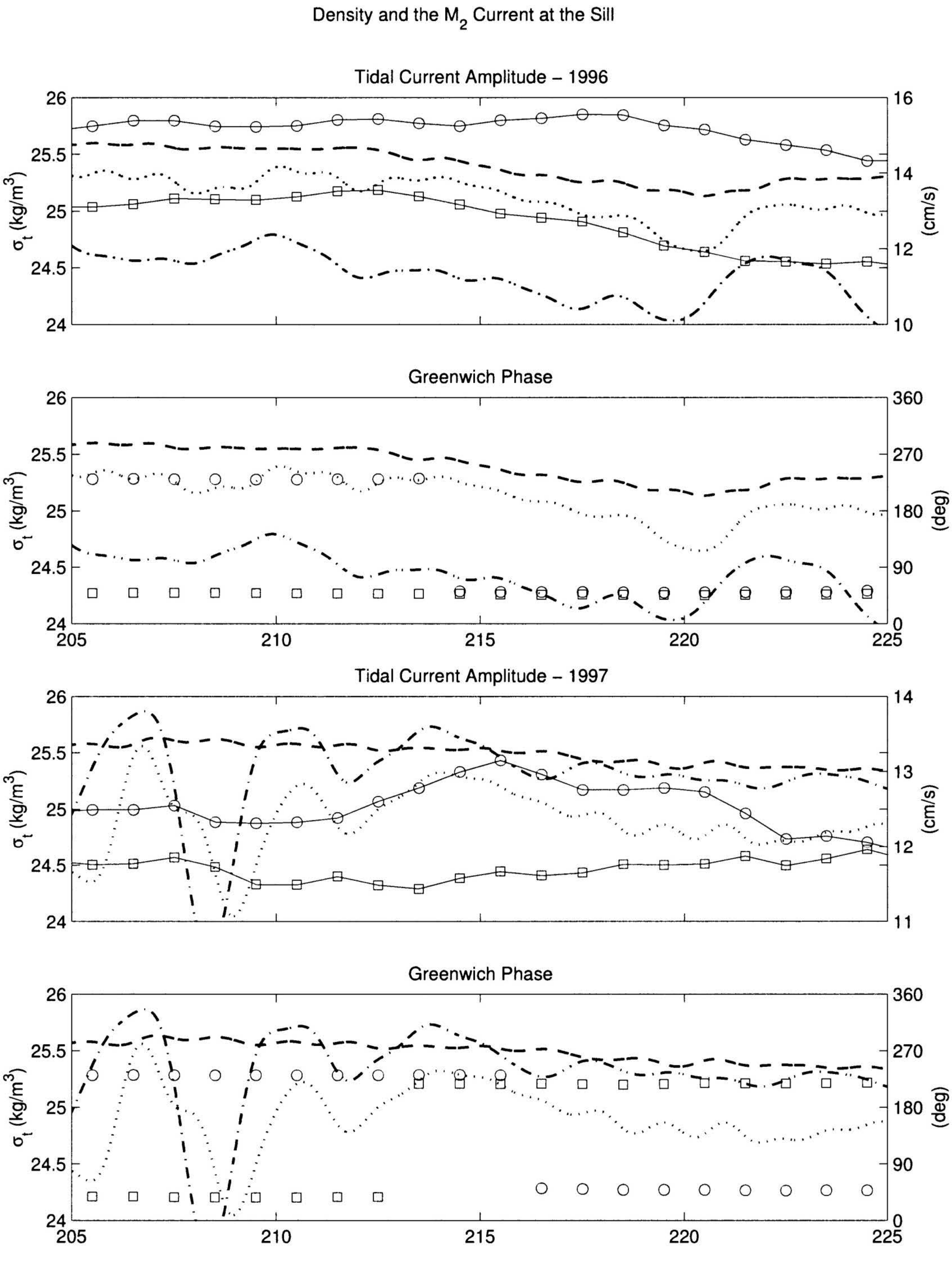

Figure 2.30: Comparison of the M_2 current amplitude (semi-major axis) and phase with density. M_2 current amplitude (phase) near the surface (circles) and at 15 metres depth (squares). Density (sigma-t) of inner basin (dashed), sill (dotted) and outer channel (dash-dot) for 1996 (panels 1 and 2) and 1997 (panels 3 and 4). Time is represented as Julian Days along the x-axis.

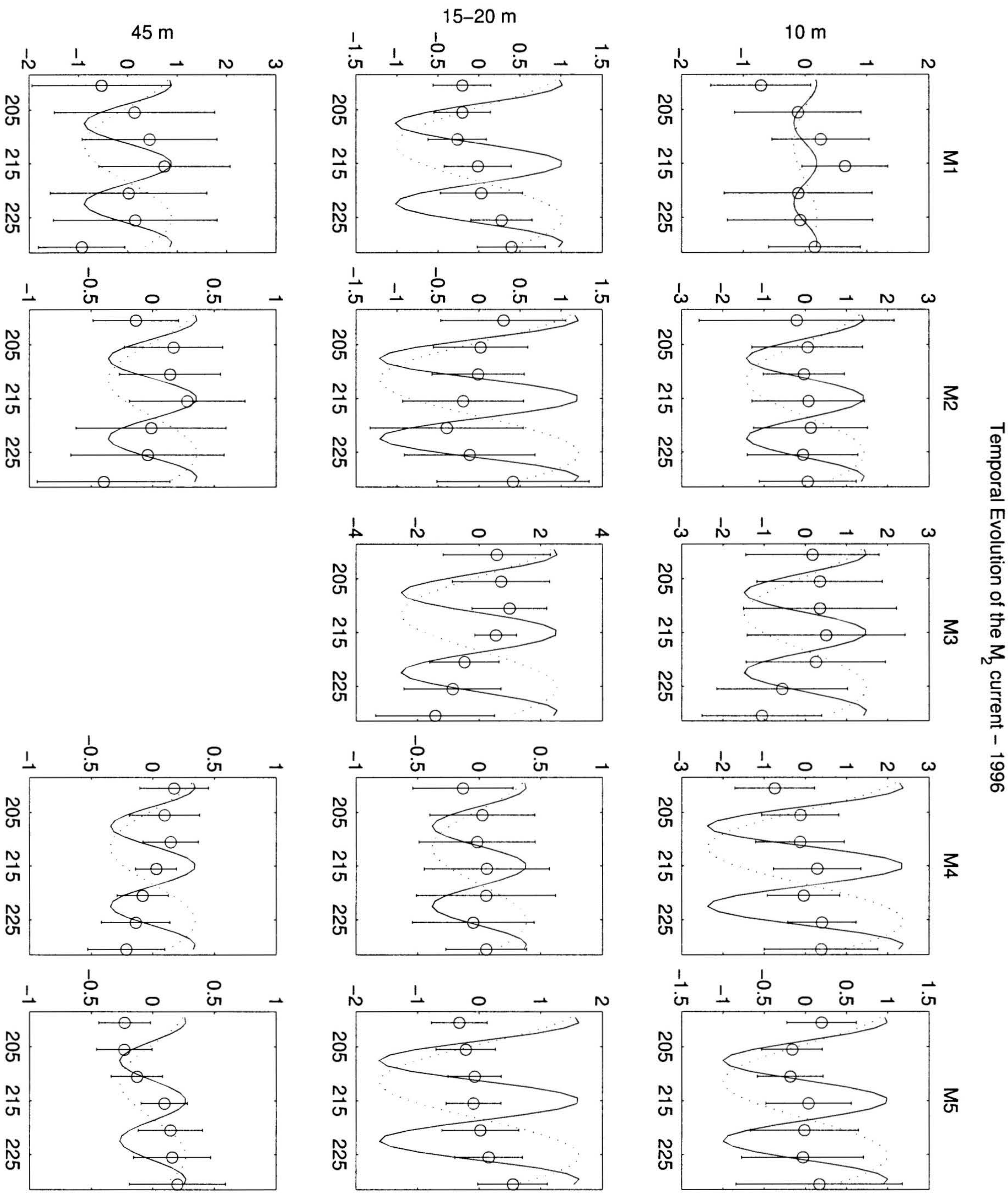

Figure 2.31: Temporal Evolution of the M_2 current amplitude (semi-major axis) 1996 with 95% confidence intervals shown as error bars. Amplitudes (cm/s) plotted as the difference from the M_2 current amplitude estimated from the 60-day signal. Solid line indicates the MS_f current calculated from the 60-day signal; dotted line represents the M_M current calculated from the 60-day signal. Time is represented as Julian Days along the x-axis

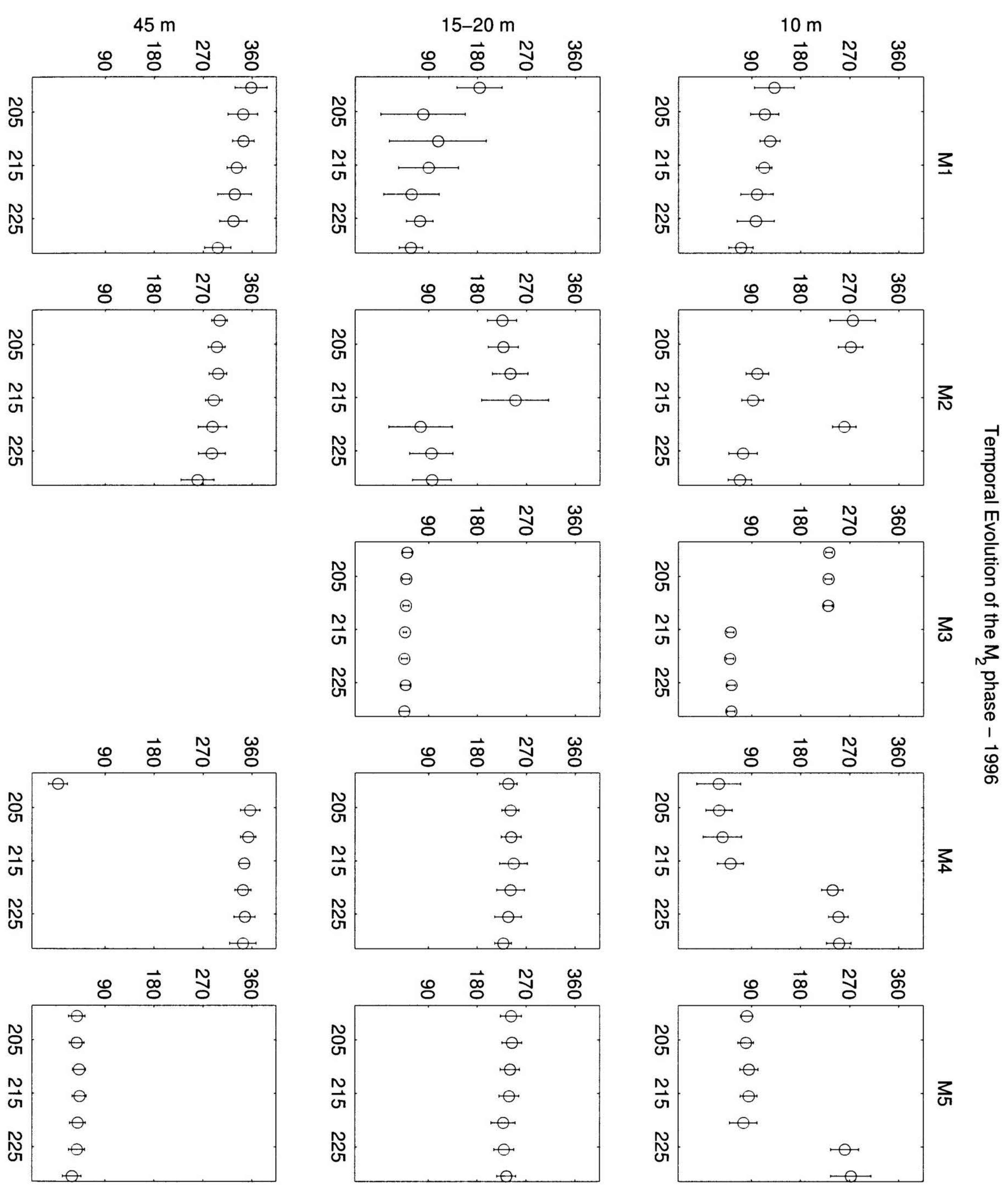

Figure 2.32: Temporal Evolution of the M_2 current phase 1996 with 95% confidence intervals shown as error bars. "Jumps" of 180 degree indicate a change in the orientation of the semi-major axis of the tidal ellipse as it passes through the principal axis. Time is plotted as Julian Days along the x-axis.

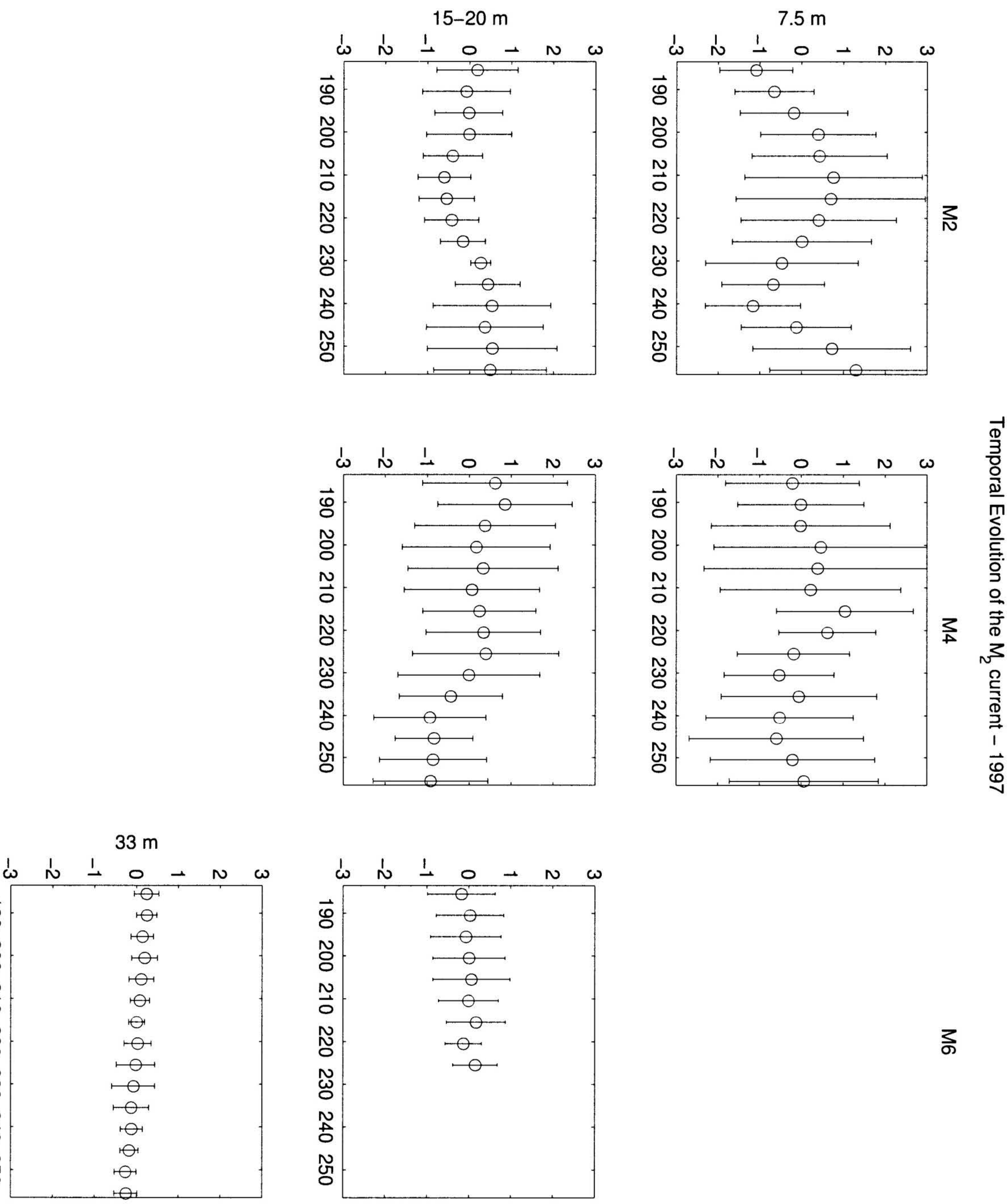

Figure 2.33: Temporal Evolution of the M_2 current amplitude (semi-major axis) across the sill in 1997, Moorings M2-97 (inner basin), M4-97 (sill) and M6-97 (outer channel) with 95% confidence intervals shown as error bars. Amplitudes (cm/s) plotted as the difference from the current amplitude estimated from the 100-day signal. Time is plotted as Julian Days along the x-axis.

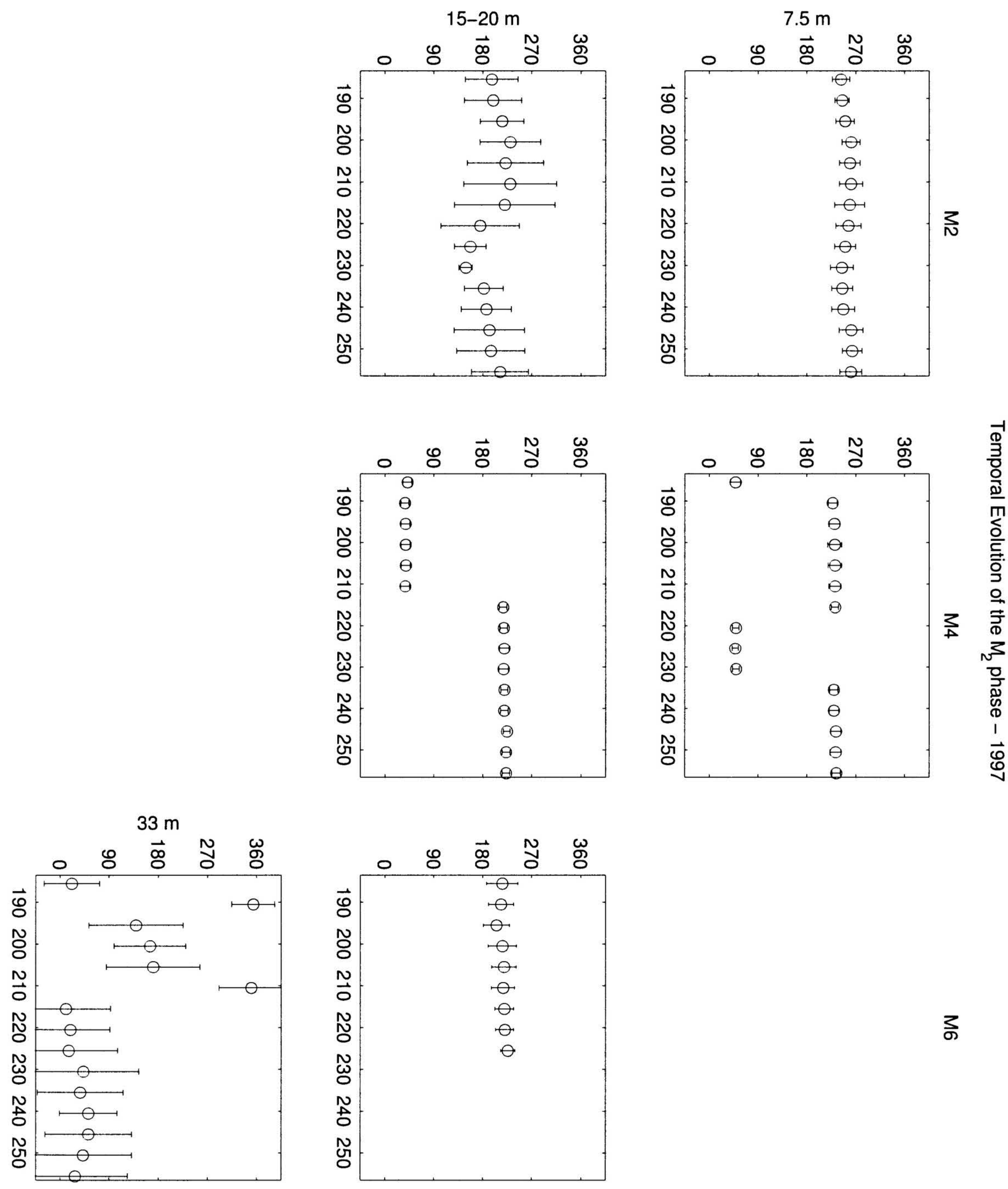

Figure 2.34: Temporal Evolution of the M_2 current phase across the sill in 1997 at moorings M2-97 (inner basin), M4-97 (sill) and M6-97 (outer channel) with 95% confidence intervals shown as error bars. . "Jumps" of 180 degree indicate a change in the orientation of the semi-major axis of the tidal ellipse as it passes through the principal axis. Time is plotted as Julian Days along the x-axis.

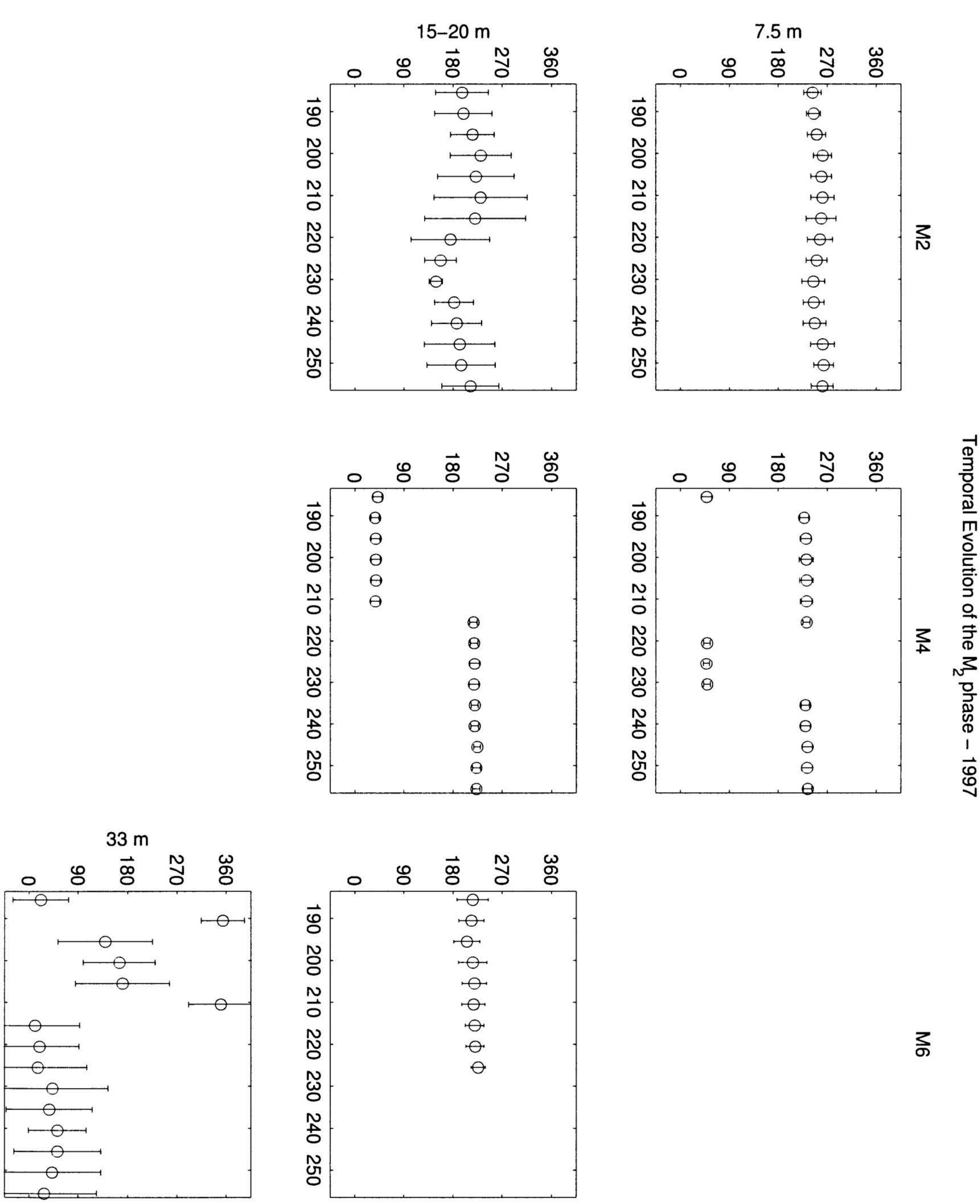

Figure 2.34: Temporal Evolution of the M_2 current phase across the sill in 1997 at moorings M2-97 (inner basin), M4-97 (sill) and M6-97 (outer channel) with 95% confidence intervals shown as error bars. . "Jumps" of 180 degree indicate a change in the orientation of the semi-major axis of the tidal ellipse as it passes through the principal axis. Time is plotted as Julian Days along the x-axis.

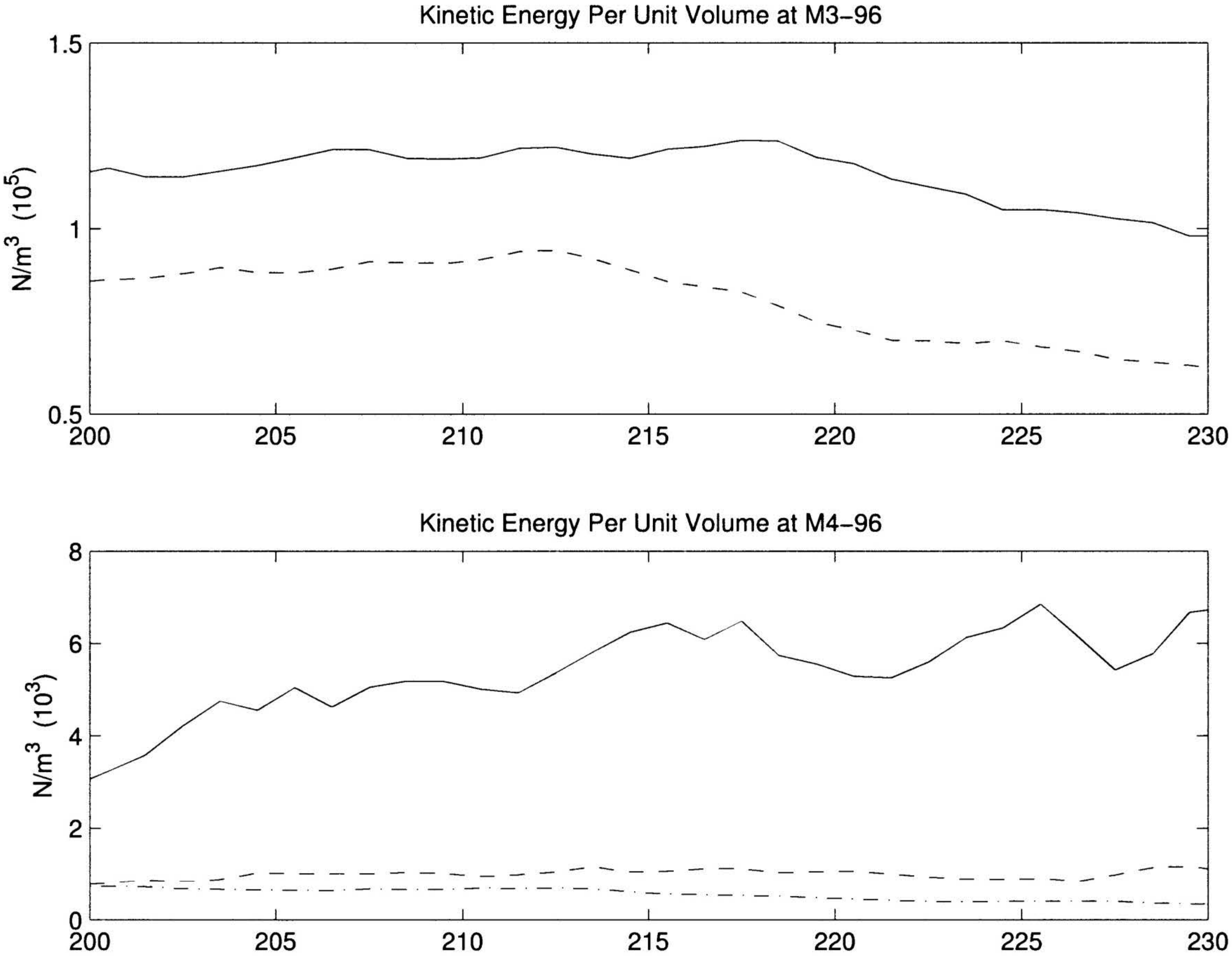

Figure 2.35: Top: Kinetic Energy Density at the sill at depths of 10 metres (solid line) and 15 metres (dashed line). Bottom: Kinetic Energy Density of the outer channel at M4-96 at depths of 10 metres (solide line), 20 metres (dashed line) and 45 metres (dash-dot line).

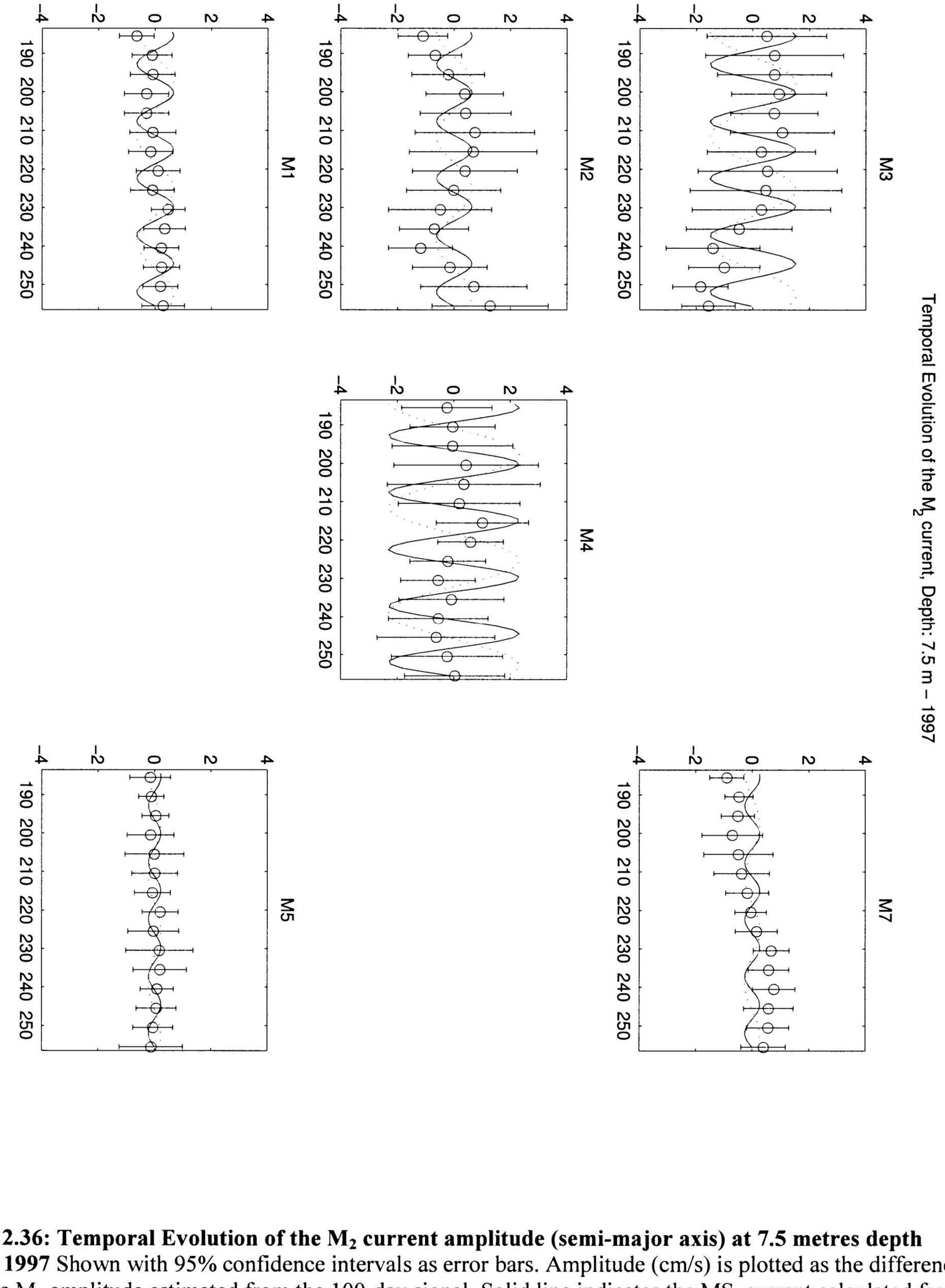

Figure 2.36: Temporal Evolution of the M_2 current amplitude (semi-major axis) at 7.5 metres depth during 1997 Shown with 95% confidence intervals as error bars. Amplitude (cm/s) is plotted as the difference from the M_2 amplitude estimated from the 100-day signal. Solid line indicates the MS_f current calculated from the 100-day signal, dotted line indicates the M_M current calculated from the 100-day signal. Time is indicated as Julian Days along the x-axis.

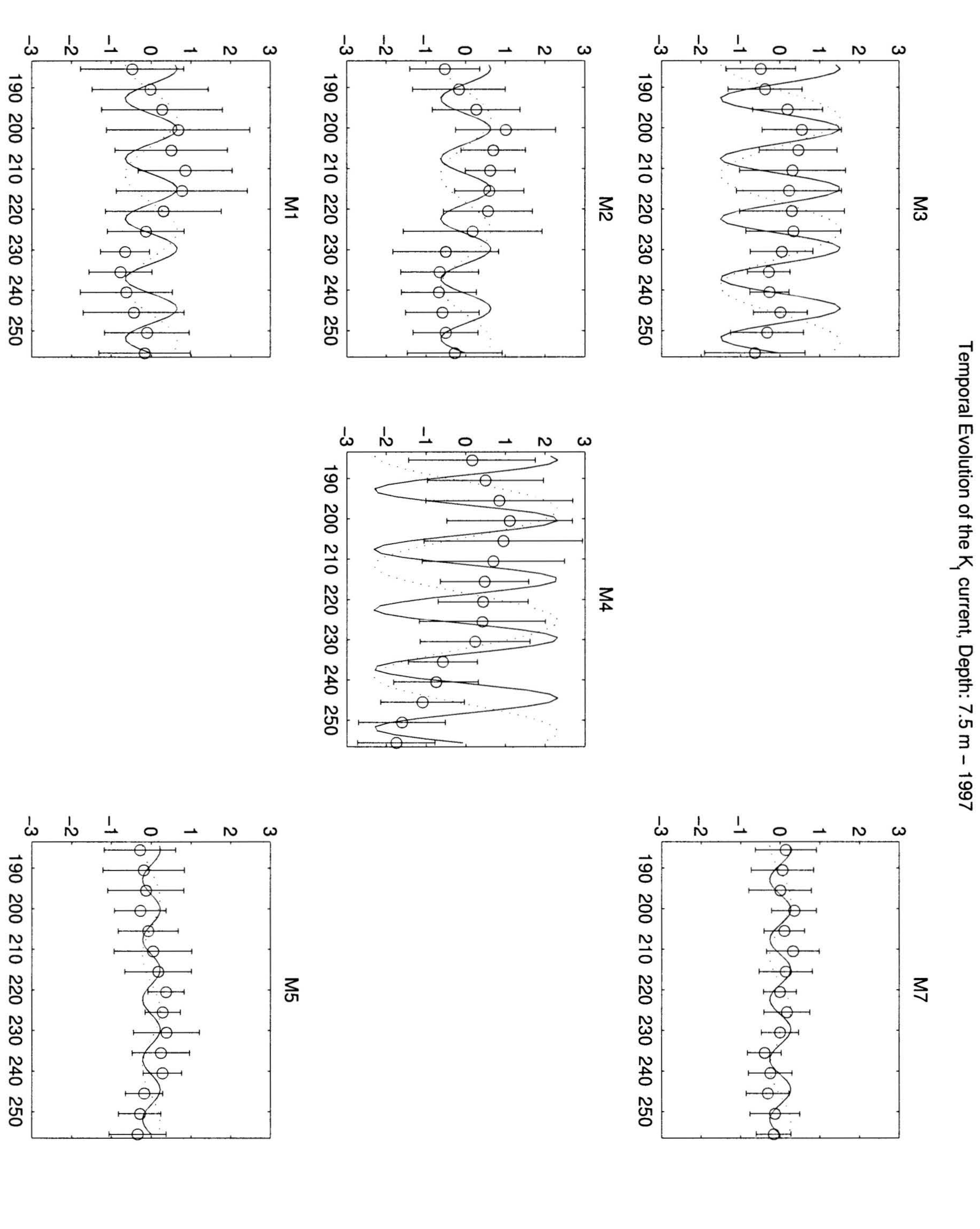

Figure 2.38: Temporal Evolution of the K_1 current amplitude (semi-major axis - cm/s) at 7.5 metres depth in 1997 with 95% confidence intervals shown as error bars. Solid line indicates the MS_f current calculated from the 100-day signal; dotted line represents the M_M current calculated from the 100-day signal. Time is represented as Julian Days along the x-axis.

2.6 The Residual Circulation

The 20-minute records for temperature, salinity, u and v were de-tided to remove diurnal and semi-diurnal fluctuations. The de-tided data represent low frequency changes in velocity, temperature and salinity. Both the 1996 and 1997 temperature and salinity data reveal seasonal trends with increasing temperature and decreasing salinity (Tables A.1-A.4). The net result of these seasonal changes in temperature and salinity is a seasonal decrease in density with values ranging between $\sigma_t=21$ at the surface to $\sigma_t=27$ at 45 metres depth. Also present in the de-tided records is evidence of low frequency nonlinear events (Figures 2.40-2.42).

A comparison of the density signals at the three moorings indicates that the density structure at mooring M2-97, located within the inner basin (Figure 2.40) is subjected to significantly fewer nonlinear events than moorings M4-97, located at the sill (Figure 2.41) and M6-97, located in the outer channel (Figure 2.42). Two possible explanations for this difference are:

1.) Fresh water mixed downwards at the sill is advected away from the inlet;
2.) Changes in stratification beyond the mouth of the inlet are introduced to the system but are blocked by the sill and do not transmit energy into the inner basin.

The first process requires that fresh water be available for mixing at the sill. The primary source of fresh water in Clode Sound is the Northwest River flowing into the head of the inlet near the northern shore. River flow data (HYDAT 2000) for the Northwest River (Figure 2.39) indicate that the mean flow was 15 m^3/s in 1996 with a minimum flow of 2 m^3/s occurring on day 245 and peak flow of 41 m^3/s on day 199. The river flow during the

1997 study had a mean of 8 m^3/s in 1997 with peak flow of 37 m^3/s occurring on day 252 and a minimum of 3 m^3/s on day 209.

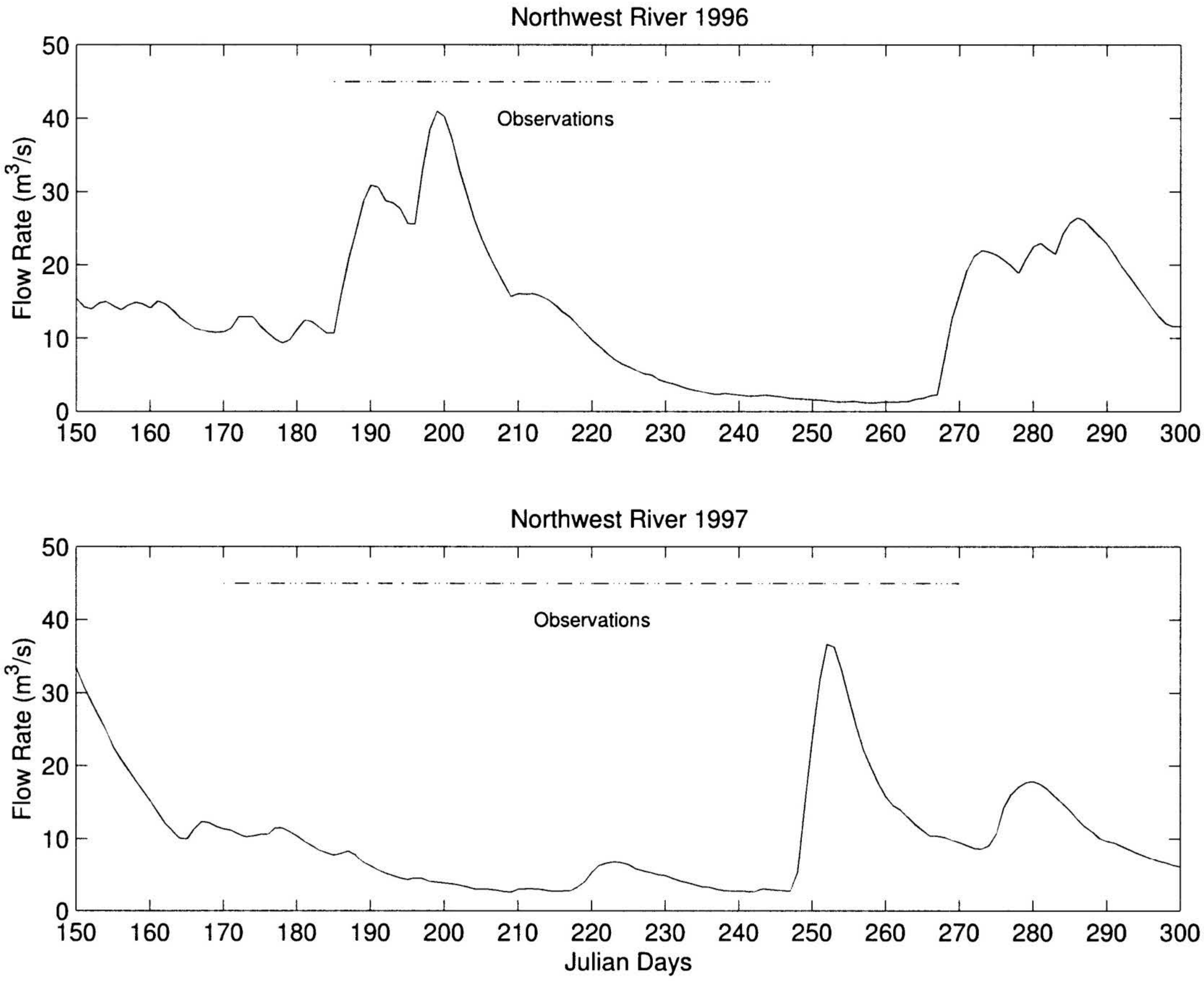

Figure 2.39: Flow rate of the Northwest River during 1996 (top) and 1997 (bottom). The dash-dotted line above the measured flow rate (solid black line) indicates the period of observations.

The second process depends on the stratification of the water at the mouth where Clode Sound is connected to Bonavista Bay. Changes in stratification within Bonavista Bay such as upwelling due to wind stress may bring cold saline waters to the surface that may then be advected into Clode Sound. Sudden changes in density may also be introduced by Kelvin waves propagating around Bonavista Bay creating a pulse into the inlet as the wave passes across the mouth.

Figures 2.40-2.42 show the time series of the detided velocity and density for three instruments at moorings M2-97, M4-97 and M6-97 at 21, 14 and 33m depths respectively.

Mooring M2-97 and M4-97 clearly show a large cold saline front (increasing density) associated with large inwards flow (negative U) between Julian days 245-250. The only source for cold saline water would be outside of the inlet and may be the result of an upwelling event followed by wind advection. Mooring M6-97 also reveals strong outward currents associated with dropping density at Julian days 175, 195, 208, 225, 230 and 250.

The current records, oriented along the north-south and east-west axis (u, v), were rotated to the principle axis into along channel, U, and cross channel, V, coordinates. In the rotated coordinate system, positive values of U indicate outward flow, while positive values of V indicate flow towards the northern coastline. Cross-spectral analysis was performed between the rotated (U, V) velocities and density fields, the phase lags and coherence of the cross-spectrums were analyzed. The statistical hypothesis for the coherence to be nonzero with 95% confidence was determined following Koopmans (1974), the result being critical (significantly different from zero) for coherence of 0.48 for the 1996 data and 0.31 for the 1997 data. The difference in critical values for the two data sets is the result of the differing record lengths.

For both the 1996 (Figure 2.43) and 1997 data (Figure 2.44) it was found that low frequency (0.1-0.3 cpd) along channel currents at 15-25 metres depth lag fluctuations in the density by 90° (2.5 to 0.6 days). This suggests that some low frequency circulation may be driven by density gradients. The density gradients possibly set up by the advection of water masses by the tides and winds.

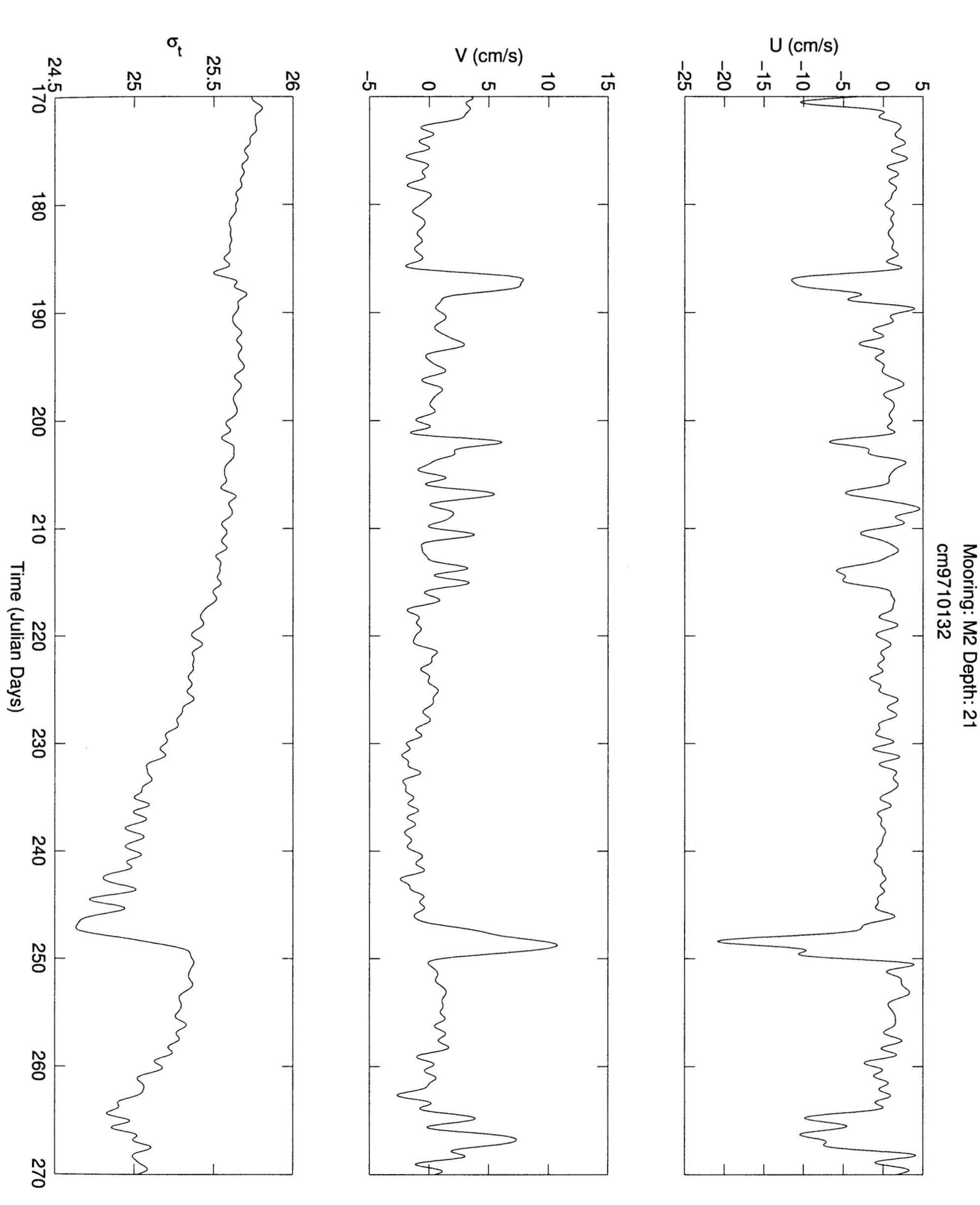

Figure 2.40: De-tided East-West and North South Velocity along with density (sigma-t) at 21 metres depth at mooring M2-97.

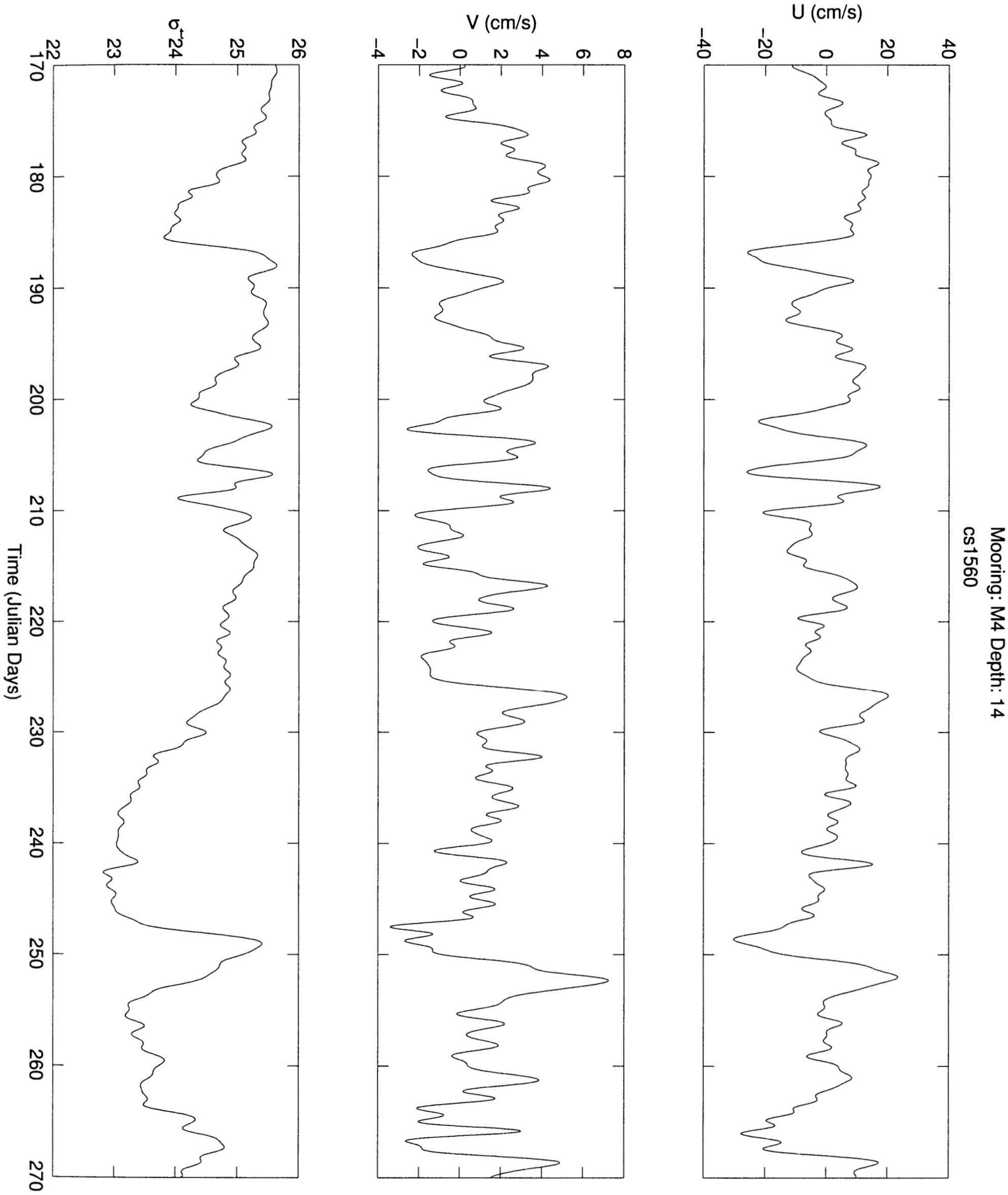

Figure 2.41: De-tided East-West and North South Velocity along with density (sigma-t) at 14 metres depth at mooring M4-97.

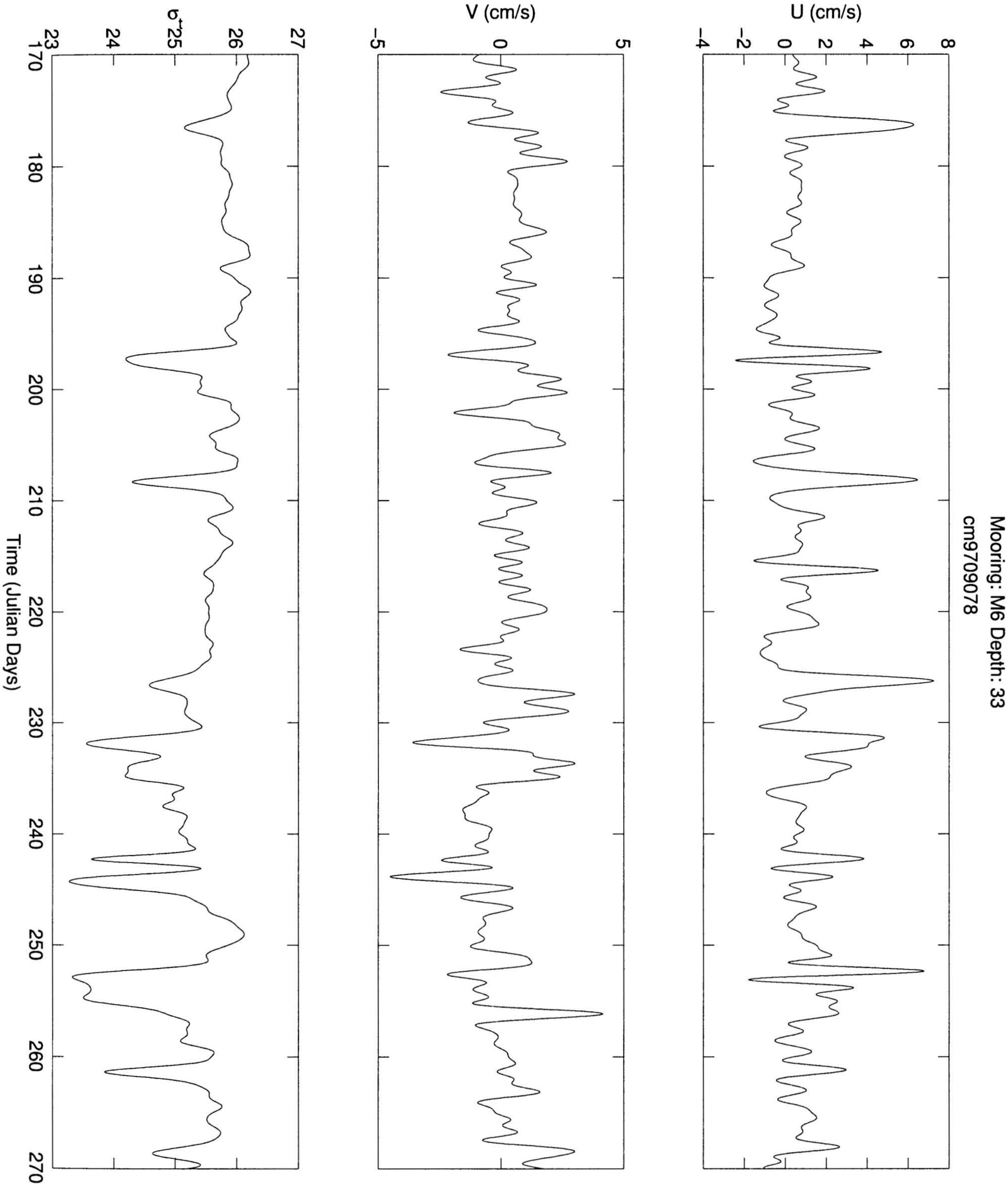

Figure 2.42: De-tided East-West and North South Velocity along with density (sigma-t) at 33 metres depth at mooring M6-97.

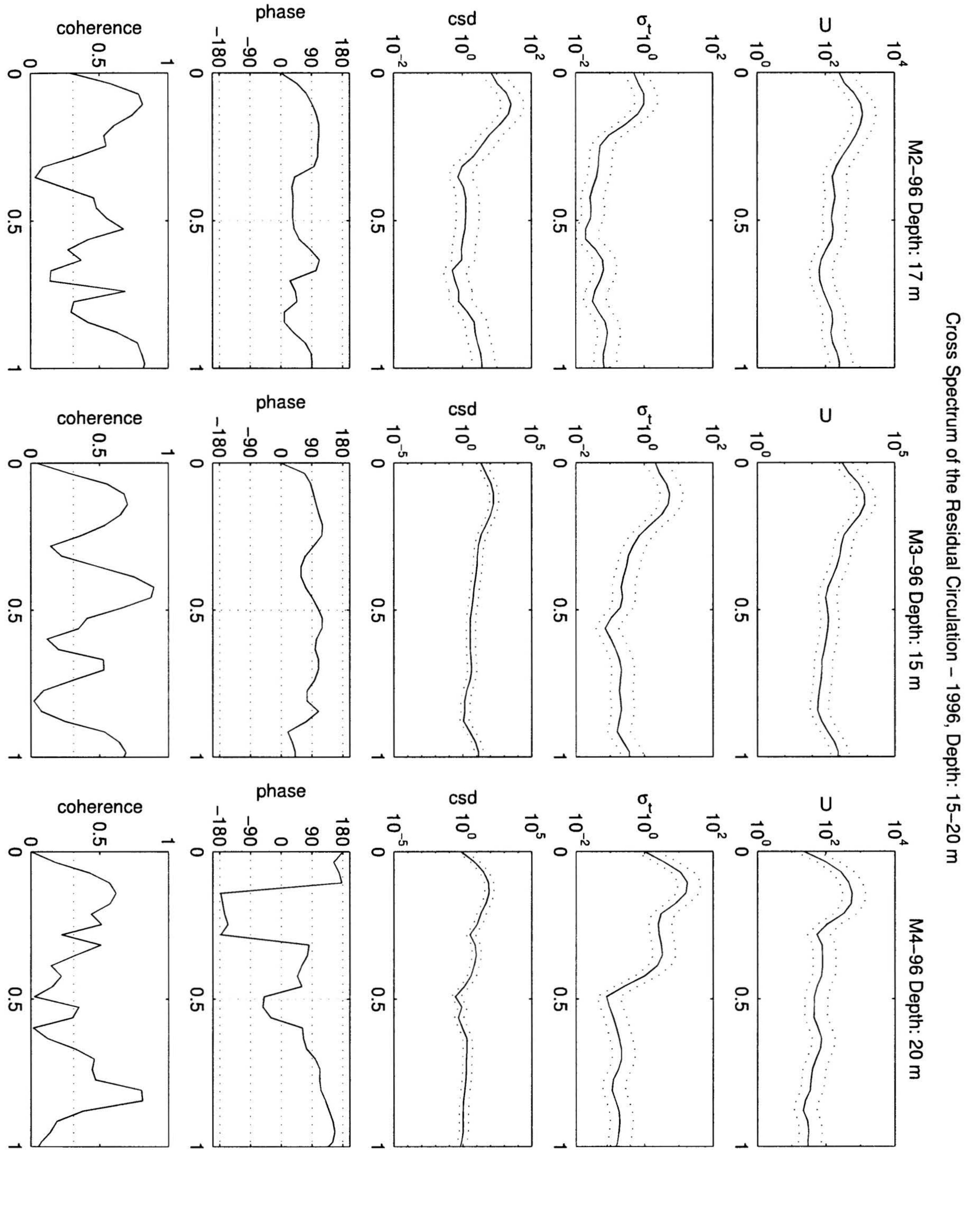

Figure 2.43: Cross Spectrum of along channel velocity with density across the sill during 1996. Estimated with 15 day windows overlapping by 7.5 days. The dotted lines in the power spectrum indicates the 95% confidence intervals for non-overlapping windows. The dashed line in the plot of coherence (bottom row) indicates the critical value (significantly different than zero). Frequency is represented as cycles per day along the x-axis.

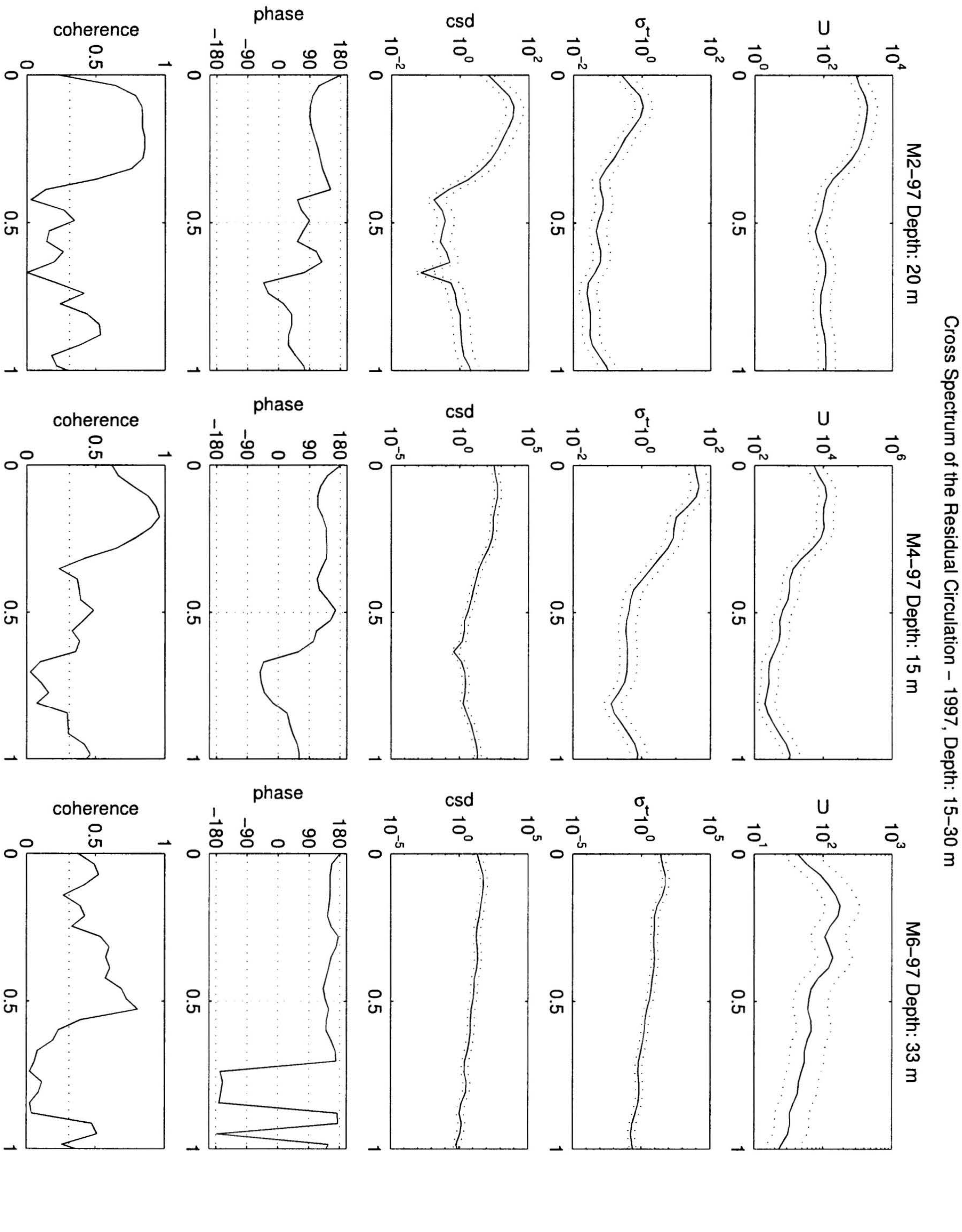

Figure 2.44: Cross Spectrum of along channel velocity with density across the sill during 1997. Estimated with 15 day windows overlapping by 7.5 days. The dotted lines in the power spectrum indicates the 95% confidence intervals for non-overlapping windows. The dashed line in the plot of coherence (bottom row) indicates the critical value (significantly different than zero). Frequency is represented as cycles per day along the x-axis.

To investigate the role that fresh water, wind stress and non-tidal external forcing may have on the residual circulation we examine a couple of events from each year of observation when there was a significant internal response. During 1996, there was a sudden increase in fresh water run-off between days 180 and 210 that occurred during a spring tide (Figure 2.45). This increase in available fresh water resulted in a rapid decrease in the salinity of the outer channel as fresh water was mixed downwards as it crossed over the sill. Mooring M4-96 (outer channel) shows a decrease in density of approximately 1.5 kg/m^3 between days 195 and 197 (panel 3) compared to a change in density less than 1 kg/m^3 at the sill (M3-96) and within the inner basin (M2-96) The rapid change in density initiates a strong inward flow within the inner basin. The current is enhanced and reaches almost 20 cm/s as the density in the outer channel is quickly restored (probably with water from Bonavista Bay). While there is little response at the sill or in the outer channel to this as density is restored either, the inner basin responds with a large amplitude internal wave. From peak to peak, the period of this response is approximately 48-55 hours. There was no salinity data available at mooring M1-96, however the signal does appear in the temperature readings recorded at this location. A comparison of temperature signals showed that the amplitude of the temperature fluctuations was smaller at M1-96 when compared to those at M2-96. The signal at M1-96 lagged the signal at M2-96 by approximately 5 hours, indicating propagation into the inlet with a speed of about 20 cm/s. From peak to peak the period of this wave measured at M1-96, located closer to the head of the inlet, was only 43 hours suggesting that this internal wave propagated to the head of the inlet and reflected.

Also during 1996 from days 219 to 229 there is an opportunity to study the internal response when mixing of fresh water occurs within the inner basin. From day 220 to 221 there is a decrease in density of about 1 kg/m^3 at M2-96 (Figure 2.45 panel 4), associated with this decrease is a steady but small increase in the density in the outer channel and at the sill. The surface flow associated with the mixing at M2-96 is outwards, oriented towards the sill. Water mixed within the inner basin is apparently moving towards denser water. There are steady southwesterly winds of about 5-7 m/s during this period that may help to explain the surface flow at this time. The sudden rise in the density appears as the winds ease. It is possible that winds are advecting fresher water at the surface towards the sill increasing the amount of fresh water available for mixing at this location. This mixing event occurs during a neap tide and is identified as a period of exchange flow across the sill (section 2.4, Figure 2.26) which appears to be driven by wind stress. This may explain why the event appears only within the inner basin as the tide may not have enough energy to mix at the sill. As the tide changes from neap to spring during days 223 to 229 the density at all 3 locations decreases, with the outer channel leading the density change at the sill and within the inner basin by about 1.5 days. There is no evidence of these events at 20 m depth at mooring M2-96 suggesting that these mixing events are restricted to the near surface of the inner basin. In the outer channel, the signal for these two mixing events does appear at 20 metres depth but the signature is significantly weaker.

In 1997 (Figure 2.46), there is evidence of strong mixing of fresh water between days 170 to 190 (panel 3). This signal appears within the inner basin, at the sill and in the outer channel. The source of fresh water for this mixing is not clear. Over a period of about 60 days (Julian days 90 to 150) the flow rate of the Northwest River was in excess of 30 m^3/s. Other instances of peak river flow indicate that the mixing events lag the increase in the fresh water flux by only 1-2 days. It is possible that this event is related to this large and steady influx of fresh water from days 90 to 150 but this would require the fresh water to remain resident in the system for up to 40 days. The mixing event from days 170 to 190 is interesting because its initial stages are similar to the mixing event from days 195 to 205 in 1996. We see a large decrease in density at all instrument locations, followed by a rapid restoration of denser water in the outer channel which produces a large inflow (10 cm/s) within the inner basin. However, during 1997, there is no large amplitude response within the inner basin.

There is another large mixing event from days 195 to 210 (Figure 2.46 panel 4) when there appears to be a large amplitude response (density variations in excess of 1 kg/m^3 over a 24-48 hour period) at all three locations. During both these events, winds are relatively mixed so it is unlikely that wind is responsible for the two different responses. Both events occur during a spring tide so the cause of the differing responses is not obvious.

From days 245 to 260 in 1997 there is another large influx of fresh water from the Northwest River. Curiously there is a rise in salinity values just prior to the increase in fresh water availability. The rise in salinity propagates inwards suggesting an external source. Once additional fresh water is made available, the salinity values decrease quite rapidly. At the sill there is strong inflow of up to 30 cm/s followed by a strong outflow of about 20 cm/s (Figure 2.41). Within the inner basin near 20 metres of depth there is strong inflow followed by weak outflow (Figure 2.40). It is clear that this intrusion of cold saline water from Bonavista Bay was reflected at the sill and had little influence on the deeper circulation of the inner basin. It is not clear if the increase in the availability of fresh water for mixing shortly after the arrival of this cold saline water was a significant factor in the rapid decrease of salinity values. This large pulse of energy may be partially responsible for the mixing recorded by the CTD casts between August 13, 1997 and October 21, 1997 (Figure 2.6). An examination of the temperature signals recorded at M6-97 shows that cold saline water from a depth of 39 metres lifted as high as 14 metres on the seaward side of the sill. Assuming a density of 1025 kg/m^3, the amount of work to lift one cubic metre of water over 25 metres would be 2.5 10^5 N. Sustained over a period of 2 days this may provide the missing kinetic energy which results in the increase of potential energy when the surface layer on the seaward side of the sill deepens to 80 metres depth (Figure 2.6).

The events described from the 1996 and 1997 observations indicate that fresh water, when available may lead to large vertical mixing on either side of the sill. During a spring tide, downwards mixing of fresh water appears to initiate on the seaward side. As density is restored on the seaward side, the inner basin may respond with a internal wave which propagates towards the head of the inlet. This may help to thicken the interface between the surface and bottom layers by increasing the mixing or may merely propagate as an interfacial wave with little mixing. The evolution of temperature and salinity below the depth of the sill suggests that little mixing does occur within the inner basin and that these events travel as interfacial waves. Surface wind stress may help to mix fresh water downwards during periods of neap tide. The surface winds may also drive a weak exchange flow across the sill, allowing fresher, less saline water to escape while deeper water is transported across the sill as volume must be conserved.

The intrusion of cold saline water from the mouth of the inlet may also result in large mixing events that occur on the seaward side of the sill. The intrusion of cold saline water is blocked by the sill and is unable to influence the bottom water within the inner basin. Although the cause of such a large intrusion of cold saline water from outside of the inlet is not clear, it is evident that these events do occur and may significantly influence the stratification of the inlet on the seaward side of the sill.

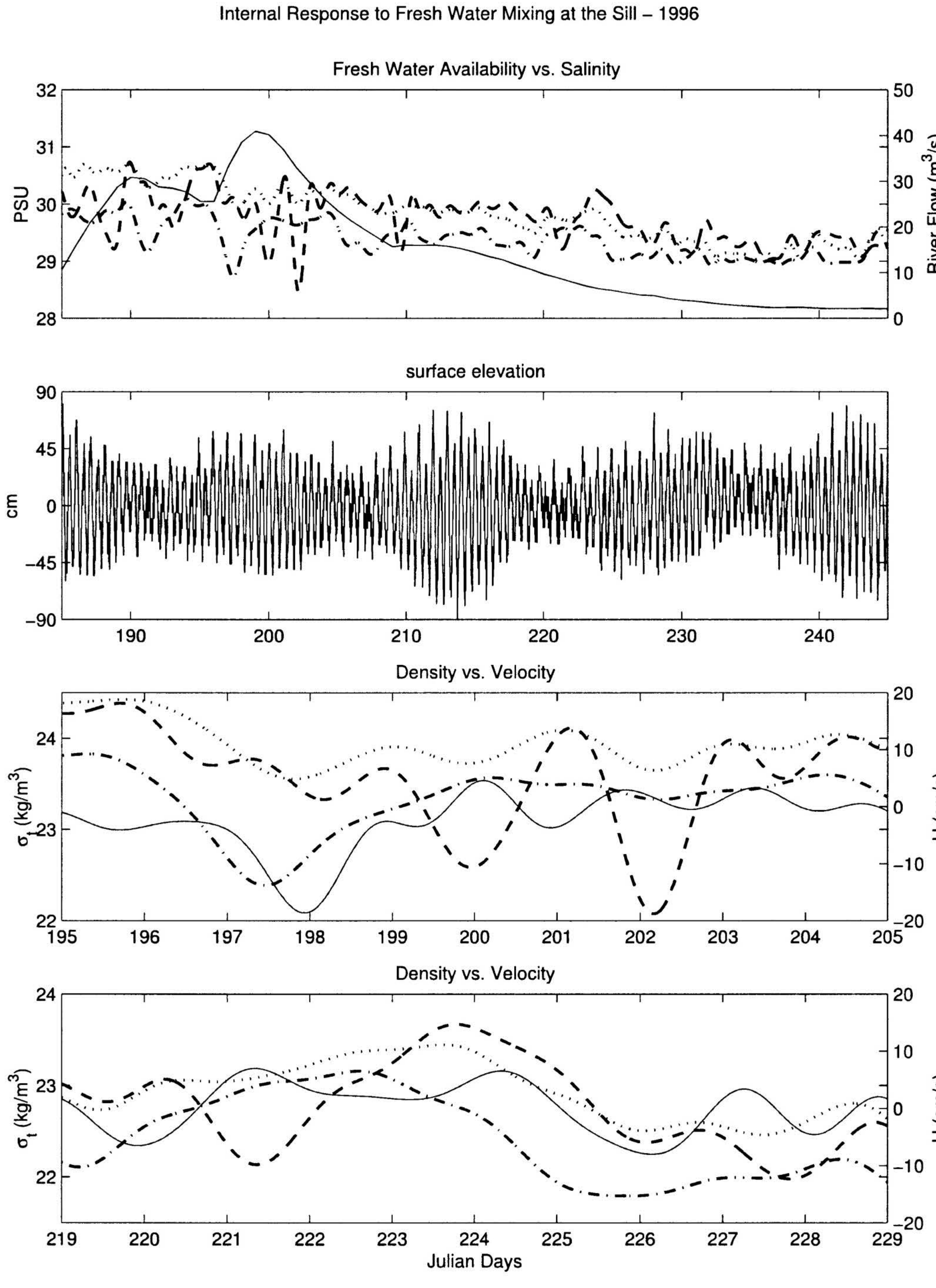

Figure 2.45: 1996 -Top: Flow rate of the Northwest River (solid line) and salinity at 10 metres depth of inner basin (dashed line), sill (dotted line) and outer channel (dash-dot line); **Panel 2:** Surface Elevation; **Panels 3&4:** Along channel velocity at 10 metres of the inner basin (solid line) and density of the inner basin (dashed line), sill (dotted line) and outer channel (dash-dot line).

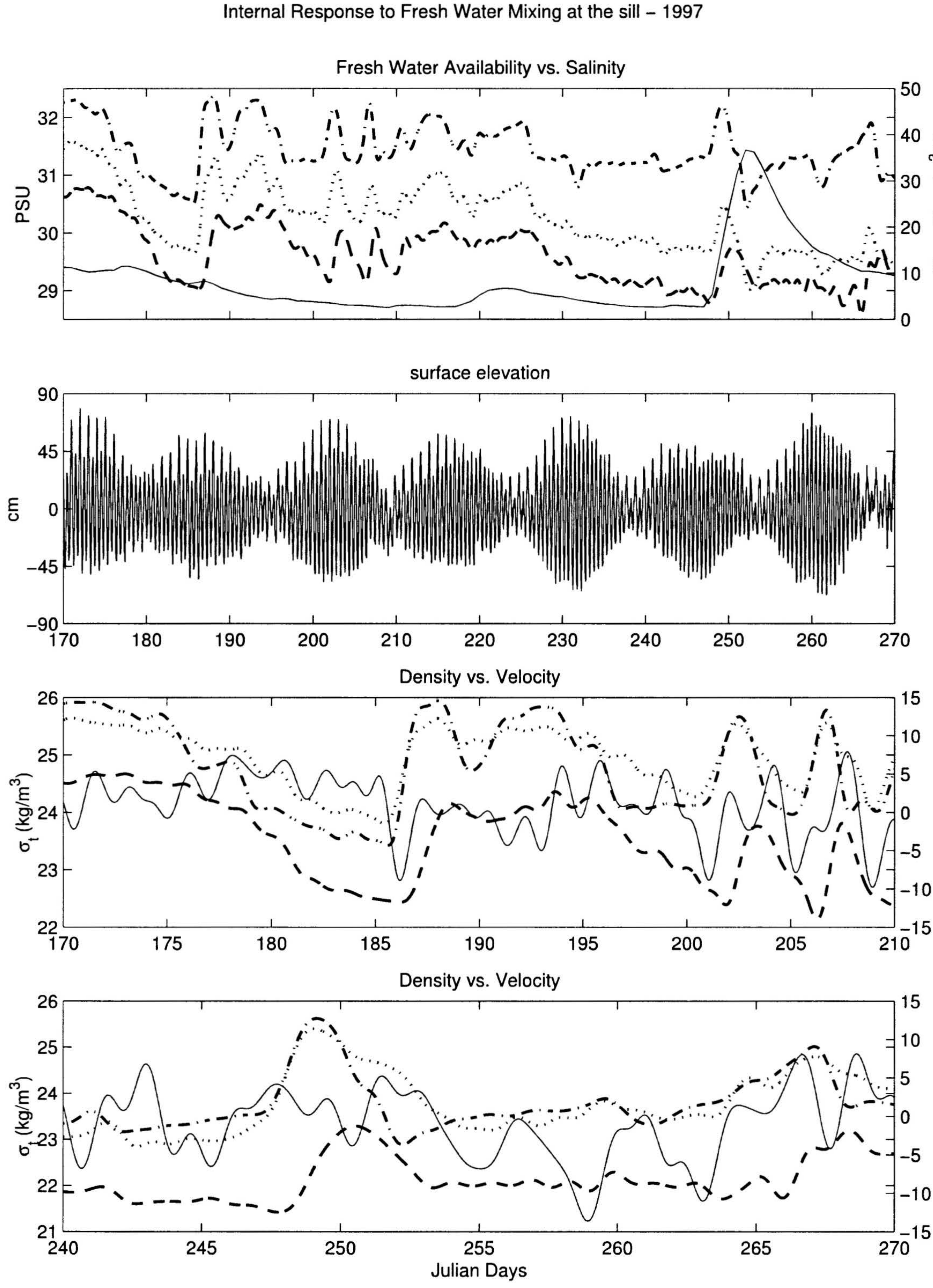

Figure 2.46: 1997 -Top: Flow rate of the Northwest River (solid line) and salinity at 7.5 metres depth of inner basin (dashed line), sill (dotted line) and outer channel (dash-dot line); **Panel 2:** Surface Elevation; **Panels 3&4:** Along channel velocity at 7.5 metres of the inner basin (solid line) and density of the inner basin (dashed line), sill (dotted line) and outer channel (dash-dot line).

Mixing in Clode Sound is concentrated in the region of the sill. Analysis of the temperature and salinity signals indicates that most of the mixing occurs on the seaward side of the sill while the inner basin water remains relatively unmixed. Formation of the water of the inner basin has been shown to occur during the winter months. The water which forms in the inner basin during the winter months remains trapped by the sill with very little if any mixing with surface waters.

At the sill, the along channel flow may become supercritical during a spring tide, this supercritical flow may lead to the formation of internal bores and hydraulic jumps. It is evident that the formation and propagation of these internal structures may be partially responsible for the increase in mixing that occurs on the seaward side of the sill. Within the inner basin, fresh water from the Northwest river may increase the stratification of the water column towards the head of the inlet. The increase in the amount of stratification may inhibit the propagation of internal bores and/or hydraulic jumps within the inner basin. This may create a region of localized mixing close to the sill while leaving the rest of the inner basin water relatively unmixed.

Internal waves generated at the sill may also force internal tides within the inner basin that result in a diurnal rise and fall of the main pycnoclines with little energy being transformed into mixing. On the seaward side of the sill, internal waves appear to enhance the mixing process as they propagate towards the mouth while dissipating their energy.

Surface winds may also be responsible for mixing in the near surface layer, the advection of water by the wind may result in periods of weak exchange flow across the sill. However, this exchange flow does not extend below the level of the sill resulting in only the top 20 metres of the inner basin water to undergo the exchange process.

To properly study the mixing process across the sill in Clode Sound, it is very clear that first priority must be given to properly modeling the tides across the sill. Supercritical flow at the sill during spring tides appears to be one of the most significant factors in determining the amount of mixing that occurs. Modeling such flow with a hydrostatic model will be difficult. In chapters 4 and 5 we will investigate the influence of tides and winds on the circulation of Clode Sound. As will be shown in chapter 4, when the stratification of the inlet is held constant, the depth of the surface layer appears to have little influence on the tidally forced circulation. In the absence of mixing, tidal forces appear to be inhibited and modeled tides are unable to match the observed tides. Chapter 5 will demonstrate the necessity of allowing temperature and salinity to mix in order to provide a more accurate simulation of the tidal flow in Clode Sound. The influence of wind stress will also be investigated in chapter 4 and 5. The tidal forcing within the inner basin is much weaker than expected and the energy balance between the wind and tides does not reflect the energy distribution discussed in section 2.3.

Chapter 3 The model

The rabbit-hole went straight on like a tunnel for some way, and then dipped suddenly down, so suddenly that Alice had not a moment to think about stopping herself before she found herself falling down what seemed to be a very deep well.

- Lewis Carroll
Alice's Adventure in Wonderland

The model used is based upon the Princeton Ocean Model (POM). POM is an explicit, finite difference, primitive equation model with a vertical sigma coordinate system and a free surface (Blumberg and Mellor, 1987; Mellor, 1998). Turbulence calculations are accomplished through a Mellor-Yamada closure scheme (Mellor and Yamada, 1982). Horizontal grid spacing for the Clode Sound domain was set at 50m and ten equally spaced vertical levels were specified. The grid scheme and model algorithm must be taken into account when developing the model domain. The sigma co-ordinate system imposes numerical constraints that restrict the ability of the model to accurately reflect the bathymetry in Clode Sound. Lateral boundary conditions must be established to allow for proper calculation of the surface elevation and velocity in grid cells along the coastline as well as fluxes through the solid boundaries. The first lateral boundary condition is accomplished through the introduction of partial cells; the latter condition is accomplished by adjusting the land masking procedure established within the original model code. This chapter discusses the aspects of the algorithm that must be taken into account while establishing the computational grid for the model domain as well as the boundary conditions used for computing the solutions presented in later chapters. Most of the numerical issues raised in this chapter appear as a result of the high horizontal resolution. If the horizontal resolution of the model is increased to 500 metres or 1 km without any changes to the bathymetry, the level of numerical noise in the model decreases and the model can be run without most of the code changes that follow.

3.1. Developing the Domain

The vertical coordinate system used by POM is a sigma coordinate system. The vertical coordinate, σ, is specified as $\sigma = (z-\eta)/(H+\eta)$ where z is the depth of the cell, η is the elevation of the free surface and H is the depth of the water column. Unfortunately, when complex topographic features such as sills are present, the ability of the coordinate system to accurately reflect the true bathymetry of the domain is limited by the requirement of hydrostatic consistency (Janjić, 1997; Beckmann and Haidvogel, 1993). It is necessary that the bathymetry be smoothed to guarantee convergence of the finite difference scheme. For twenty evenly spaced levels the constraint of hydrostatic consistency requires that $\Delta H/H^* < 1/20$ (Mellor et al, 1994) where ΔH is the change in depth between neighbouring grid cells and H^* is the minimum depth of the depth of the two cells.

The design of the numerical grid for Clode Sound required a balance between this constraint with the desire to accurately reflect the true bathymetry. Bathymetric data supplied by the Department of Fisheries and Oceans, Canada (DFO) was interpolated onto a horizontal grid with a 50 metre resolution, then smoothed to yield a maximum slope of approximately 8% between neighbouring grid cells. This will allow for a minimum of at least 10 evenly spaced vertical levels (the model is executed with 10 evenly distributed sigma levels). The smoothing algorithm searches for gradients such that $\Delta H/H > 1/n$ for $1 \leq n \leq 12$ then reduce the gradient by increasing the minimum depth to $H^*=H_{max}-[1/(n+3)]H_{max}$. The grid is passed in four directions and on each pass it iterates from n=1 to n=12 to adjust the depth. After passing the grid in each direction the grid is search again to determine if any neighbouring cells still violate the condition for consistency. The process of searching and smoothing repeats until all grid points within the domain satisfy the necessary condition. Contour plots (Figure 3.1) of the data before and after the smoothing reveal the results.

The Courant-Friedrichs-Levy (CFL) condition for computational stability on the external mode (vertically integrated) of the model requires that (Mellor, 1998):

$$\Delta t_E \leq \frac{1}{C_t}\left|\frac{1}{\delta x^2}+\frac{1}{\delta y^2}\right|^{-1/2} \tag{3.1.1}$$

where Δt_E is the time step of the external mode; δx, δy are the horizontal grid spacing; and $C_t=2(gH)^{1/2}+U_{max}$ with U_{max}, the maximum velocity, g the acceleration due to gravity and H the depth of the water column.

At the mouth, the depth of Clode Sound exceeds 200 metres. At a 50 metre horizontal resolution with H=200 metres and U_{max}=1.0 m/s the CFL criteria requires that $\Delta t_E \leq 0.4$ seconds. The only data collected below 50 metres of depth in Clode Sound was recorded at mooring M5-96 at a depth of 76 metres. In order to improve the execution time of the model the maximum depth of the domain was set to 100 metres so that the CFL criteria was $\Delta t_E \leq 0.55$ seconds; minimum depth was set to 10 metres with the coastline established at the 3 metre contour. The choice of 100 metres for the maximum depth does not permit the entire inlet to be included in the computation domain. The purpose of this study was to examine the dynamics in the vicinity of the sill. The choice of 100 metres for the maximum depth still provides enough of the inlet to be included to permit such a study. Even by truncating the domain when the majority of the depths exceed 100 metres the cartesian grid required to cover the domain still requires 392 by 136 grid points. With 10 vertical levels the grid scheme is able to satisfy the constraint of hydrostatic consistency while retaining a reasonable vertical resolution in the deepest part of the domain. Small coves were eliminated and smoothed to reduce numerical noise. At the mouth of the domain (Figure 3.2), the bathymetry was linearly increased to a maximum depth of 100m to form a rectangular channel with a length of approximately 3 km (an additional 60 grid points in the along channel direction (total 452)). The decision to add this channel to the mouth of the domain simplified the implementation of the open boundary conditions as discussed below. One final addition to the code was made in the interest of reducing the computational cost of such a large domain. As indicated in Figure 3.1, there is a large number of grid points for which no computation will be necessary as they correspond to land. The number of points that actually correspond to water represent only 33% of the grid. The execution time is greatly reduced by restricting the calculations in the cross channel axis to the water points. Hence for almost all loops in the code the statement:

```
DO I=1,IM
```

is replaced by the statement:

```
DO I=ISTART(J),ISTOP(J)
```

where ISTART(J) and ISTOP(J) are integers representing the southern most and northern most coastline point, respectively, on the grid.

The horizontal grid was oriented at a 30° angle from the east-west axis (Figure 3.1). The orientation of the horizontal grid was chosen to align with the coastline seaward of the sill. With this grid orientation, the velocity vectors at the mouth become along

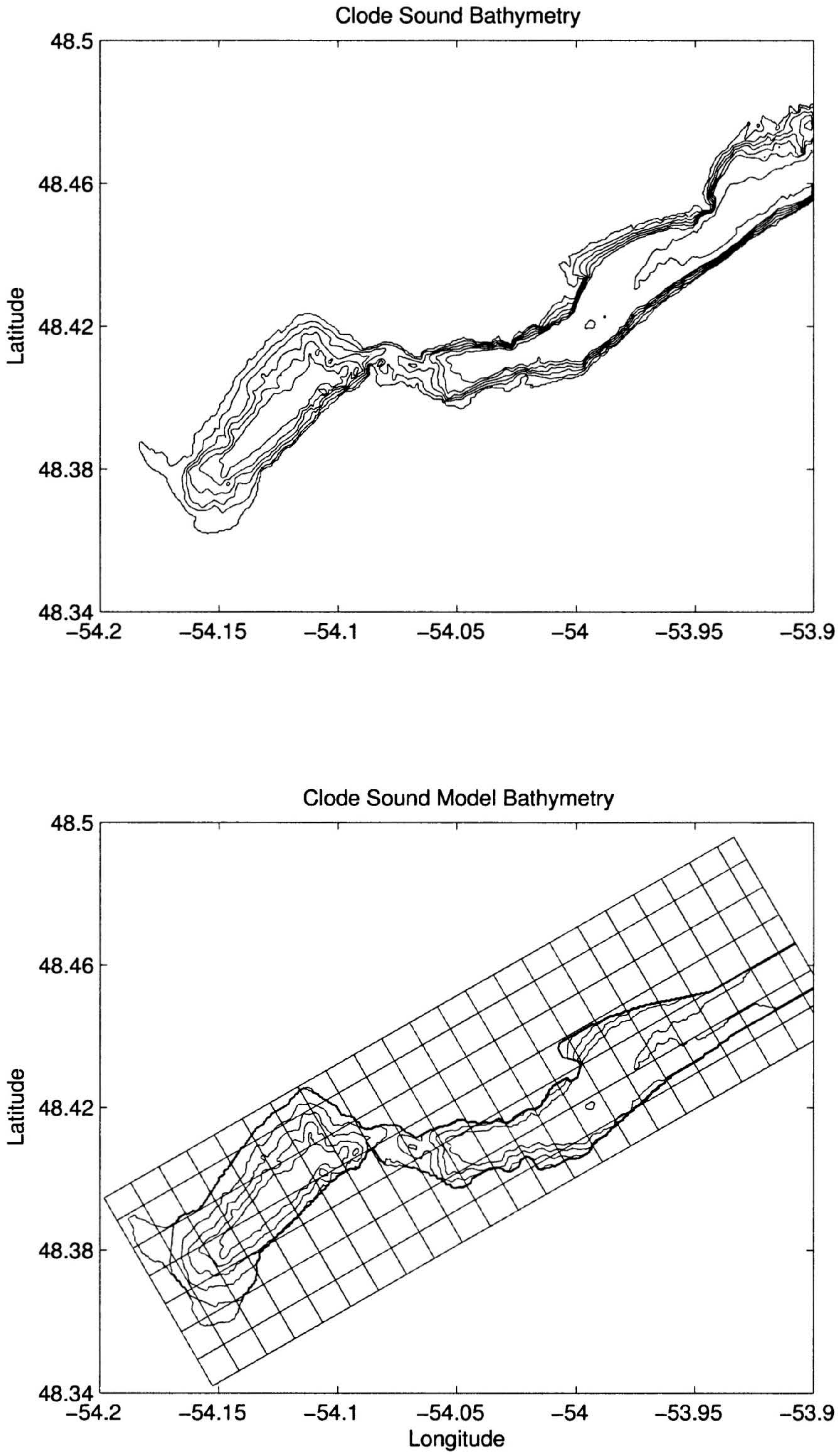

Figure 3.1: Top: Bathymetry of Clode Sound derived from data supplied by Department of Fisheries and Ocean, Governmen of Canada. **Bottom:** The smoothed bathymetry used by the model. Computational grid is shown at intervals of 20 grid cells. Contours drawn at 10, 20, 30, 40, 50 and 100 metres in both figures.

channel (u) and cross channel (v) components of the calculated velocity. At the open mouth, it is then assumed that the cross channel component of velocity is identically zero ($v \equiv 0$) so that only the along channel component of velocity needs be calculated at the open mouth (King and Wolanski, 1996). Given the geographical orientation of Clode Sound, the number of grid cells necessary to cover the inlet are also greatly reduced by this choice of along channel and cross channel directions. A detailed discussion of the open boundary conditions follows in the next section.

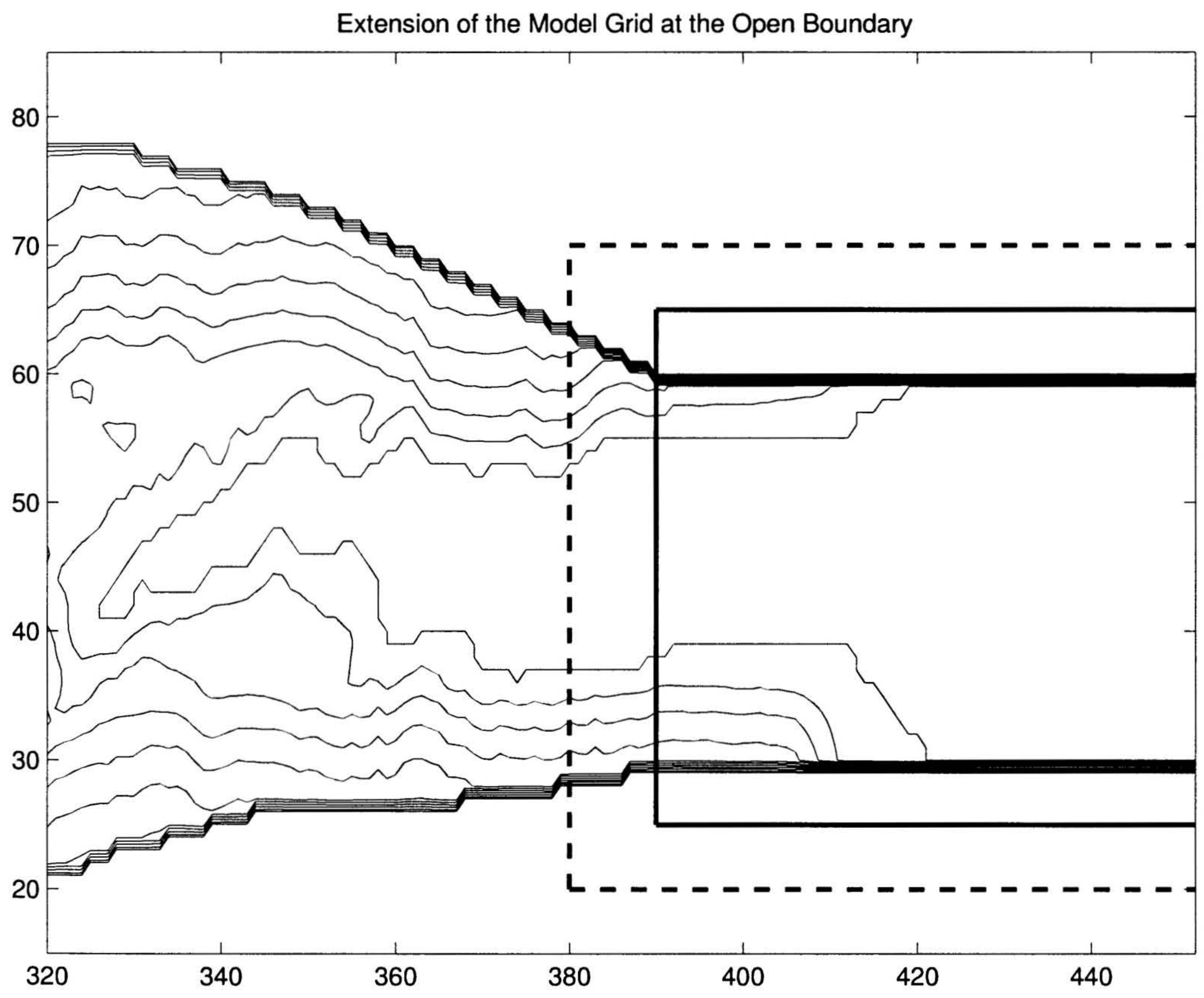

Figure 3.2: The mouth of the model domain. Depth contours are drawn at intervals of 10 metres. The area enclosed in the box with solid lines represents the region where bathymetry is linearly interpolated to a uniform depth of 100m. The region enclosed in the box with dashed lines represents the region where temperature and salinity are relaxed on the grid to damp outward propagating internal waves (section 3.5).

3.2. *Open Boundary Conditions*

As mentioned above, the orientation of the grid along the coastline of the inlet provides a basis for a simplified open boundary condition. With no velocity data collected near the location of the open mouth, the tidal forcing at the open mouth is specified by the surface elevation, η, derived from the tidal data collected from the moorings located further up inlet. It is assumed that the value of the surface elevation does not vary across the open mouth,

$$\eta(IM,j,t)=f(t)\ \forall\, j \in [1,..,JM] \tag{3.2.1}$$

The specification of surface elevation requires that velocity be calculated. Since velocity is divided into an external and internal mode, both modes must be calculated for each velocity component.

Given the orientation of the grid, it is reasonable to assume that the cross channel component of the velocity (V) is negligible so the appropriate boundary condition is:

$$V_{ext}(IM,j) \equiv V_{int}(IM,j,k) \equiv 0,\ \forall\, j,k \in [1,..,JM;\ 1,..,KB] \tag{3.2.2}$$

The along channel component of velocity (U) must satisfy two conditions:

1.) It must accurately reflect the barotropic current generated by the surface elevation,

2.) It must allow for seaward travelling internal waves to escape and not be reflected back into the domain.

With a horizontal resolution of 50 metres there should be no significant changes in the external mode (forced by surface elevation), it follows that the appropriate boundary condition for the external mode is a zero gradient condition given by:

$$U_{external}(IM,j) = U_{external}(IM-1,j)\ \forall\, j \in [1,..,JM] \tag{3.2.3}$$

where IM is the index of the boundary cell. To allow for the outward propagation of internal waves, the internal mode is calculated using a Sommerfeld Radiation boundary condition given by (Orlanski, 1976):

$$\text{uf(IM,j,k)=(ub(IM,j,k)*(1.-}c_I\text{)+2.*}c_I\text{*u(IM-1,j,k))/(1.+}c_I\text{)} \;\forall\, j,k \in [1,..,JM;\ 1,..,KB] \tag{3.2.4}$$

where u, uf and ub are the values of the velocity at the current, forward and backwards time steps and c_I ($0 \leq c_I \leq 1$) is the phase speed of the outgoing wave,

$$c_I = \frac{\text{(ub(IM-1,j,k)-uf(IM-1,j,k))}}{\text{(uf(IM-1,j,k)+ub(IM-1,j,k)-2.*u(IM-2,j,k))}} \;\forall\, j,k \in [1,..,JM;\ 1,..,KB]. \tag{3.2.5}$$

3.3. Lateral Boundary Conditions

Along the coastline, the differencing scheme of the model must:

1.) Avoid the inclusion land points into calculations for surface elevation

2.) Calculate zero mass and momentum flux across solid boundaries.

3.) Correct for changes in surface area of the grid cell in both velocity and surface elevation.

4.) Apply frictional dissipation to velocity terms near the coastline.

The first two requirements listed above may be accomplished by making use of the masking variables for velocity and scalars (variables DUM, DVM and FSM). The third requires the introduction of partial cells along the coastline to adjust the volumes of those grid cells along the coast. Frictional dissipation is accomplished with a biharmonic operator which applies a drag coefficient which decays exponentially as a function of the number of grid cells increases from the closest land cell. The dissipation term is simplistic but appears to be necessary for numerical stability; a dissipation term with a better physical interpretation is desirable.

3.3.1. Surface Elevation Correction

The original code calculated the surface elevation as follows:

```
      FLUXUA(I,J)=.25E0*(D(I,J)+D(I-1,J))*(DY(I,J)+DY(I-1,J))*UA(I,J)
      FLUXVA(I,J)=.25E0*(D(I,J)+D(I,J-1))*(DX(I,J)+DX(I,J-1))*VA(I,J)

      ELF(I,J)=ELB(I,J)
     1    -DTE2*(FLUXUA(I+1,J)-FLUXUA(I,J)+FLUXVA(I,J+1)-FLUXVA(I,J))
     2    /ART(I,J)
```

where D(I,J) is the total depth of the water column (bathymetric depth plus surface elevation); DX(I,J), DY(I,J) and ART(I,J) are the dimensions of the grid cell [ART(I,J)=DX(I,J)*DY(I,J)]; and UA(I,J) and VA(I,J) are the velocities of the external mode calculation.

If D(I,J) is the first element inside the domain then D(I-1,J) and D(I,J-1) will represent the first land point of the boundary. Assuming a uniform horizontal grid such that DX(I,J) and DY(I,J) are constant for all I, J, the above calculation assumes that the volume of the grid cell along the coastline is ½ the volume of the next grid cell inside the domain, but that the area of the grid cell remains constant. The result is that the flux at (I,J) is ½ the flux at (I+1,J) [or (I,J+1)] while the area remains constant. Essentially, it clamps the surface elevation along the coastline to zero. Over a large distance the error in the calculation may be small resulting in some noise but at a high resolution (DX, DY=50m) the error becomes very significant. For a tidal signal with amplitude of 0.5

metres the result is a change in surface elevation of 0.5 metres over a distance of 50 metres setting up a very large surface driven current.

It is not desirable to establish a false depth along the coastline to allow for a volume correction; this would be inconsistent with the Arakawa C-grid requiring U and V to both equal zero at such a point and may create difficulties with calculations involving other scalars. The remaining choice is to redefine the horizontal distance to be consistent with effective depth of the cell along the coastline used in the flux calculation. The horizontal distance along the coastline may be redefined as:

```
dx1(i,j)=DX(i,j)*(dum(i,j)+fsm(i,j)+dum(i+1,j))/3.0
dy1(i,j)=DY(i,j)*(dvm(i,j)+fsm(i,j)+dvm(i,j+1))/3.0
```

(3.3.1)

where: dum(i,j), dvm(i,j) and fsm(i,j) are the calculation masks of the u and v velocities and surface elevation (scalars) respectively (e.g. fsm(i,j)=0 for land and fsm(i,j)=1 for water).

The calculation of surface elevation then becomes:

```
 FLUXUA(I,J)=.25E0*(D(I,J)*DUM(I,J)*DUM(I+1,J)
1              +D(I-1,J)*DUM(I-1,J)*DUM(I,J))
1              *(DY1(I,J)+DY1(I-1,J))*UA(I,J)

 FLUXVA(I,J)=.25E0*(D(I,J)*DVM(I,J)*DVM(I,J+1)
1              +D(I,J-1)*DVM(I,J-1)*DVM(I,J))
1              *(DX1(I,J)+DX1(I,J-1))*VA(I,J)


ELF(I,J)=ELB(I,J)
1   -DTE2*(FLUXUA(I+1,J)-FLUXUA(I,J)+FLUXVA(I,J+1)- FLUXVA(I,J))
2   /ART1(I,J)
```

where ART1(I,J)=DX1(I,J)*DY1(I,J).

The new horizontal coordinate reduces the error in the surface elevation to less than 10^{-6} metres and allows the surface elevation along the coast to rise and fall with the same magnitude as the interior points of the domain. The additional factors of dum(i,j) and dvm(i,j) balance the algorithm between all four possible boundaries.

3.3.2. Velocity Correction

While it was possible to correct the surface elevation by examining only the external mode of the model, the correction necessary to address the error associated with the velocities required investigation into the three dimensional structure of the model. If the model is run with the above correction as a two dimensional model utilizing only the external mode calculations, the calculated velocities are not unreasonable when compared to the available data, however there is no frictional drag associated with the coastlines. Ignoring Coriolis terms, corrections for time splitting and baroclinic components the original calculation for velocity in the external mode appears below:

```
      UAF(I,J)=ADVUA(I,J)
     1         +.25E0*GRAV*(DY(I,J)+DY(I-1,J))
     2         *(D(I,J)+D(I-1,J))*(EL(I,J)-EL(I-1,J))
     3         +ARU(I,J)*( WUSURF(I,J)-WUBOT(I,J) )

       UAF(I,J)=((H(I,J)+ELB(I,J)+H(I-1,J)+ELB(I-1,J))*ARU(I,J)*UAB(I,J)
     1         -4.E0*DTE*UAF(I,J))
     2         /((H(I,J)+ELF(I,J)+H(I-1,J)+ELF(I-1,J))*ARU(I,J))


       VAF(I,J)=ADVVA(I,J)
     1         +.25E0*GRAV*(DX(I,J)+DX(I,J-1))
     2         *(D(I,J)+D(I,J-1))*(EL(I,J)-EL(I,J-1))
     3         + ARV(I,J)*( WVSURF(I,J)-WVBOT(I,J) )

       VAF(I,J)=((H(I,J)+ELB(I,J)+H(I,J-1)+ELB(I,J-1))*VAB(I,J)*ARV(I,J)
     1         -4.E0*DTE*VAF(I,J))
     2         /((H(I,J)+ELF(I,J)+H(I,J-1)+ELF(I,J-1))*ARV(I,J))
```

UAB, VAB and UAF, VAF are the backwards and forwards velocities (in time). ADVUA and ADVVA are the advection terms calculated elsewhere in the model, GRAV is the acceleration due to gravity, ARU, ARV are the areas of the grid cells for U and V. ELB, EL and ELF are the surface elevation at the previous, current and future time steps, H is the bathymetric depth and D=H+EL is the total depth of the water column at the current time step. WVSURF and WUSURF are the surface boundary conditions associated with wind stress; WVBOT and WUBOT are the bottom boundary conditions associated with bottom friction.

Assume that U represents east-west velocity and that V represents north-south velocity. Let grid indices I and J increase from west to east and from south to north, respectively. The code above reveals that the calculated value of U will never take into account any change in the surface elevation across an eastern boundary. In the same manner V will never take into account a northern shore. Another point of concern is the manner in which the velocity masks are calculated. The current convention is to calculate them as:

```
DUM(I,J)=FSM(I,J)*FSM(I-1,J)
DVM(I,J)=FSM(I,J)*FSM(I,J-1)
```

If (I, J) represent an interior point on a north-western corner then:

```
FSM(I,J)=1; DUM(I,J)=0; DVM(I,J)=1
```

The boundary on the C-grid is shown in Figure 3.3. With the current configuration of the masks, the velocity at U(I+1,J) does not recognize that U(I,J) is equal to zero and when calculating the component of the velocity driven by the surface elevation. Since H(I,J) has now been corrected above to avoid a large barotropic component, there is no communication between U(I,J) and U(I+1,J) (Figure 3.3). Prior to the change in the calculation of the surface elevation, there was communication between the two points because the surface elevation at H(I,J), was forced towards zero. This resulted in a decrease in the velocity at U(I+1,J) which no longer exists. Essentially the correction to the surface elevation removes the boundary condition on the western shore.

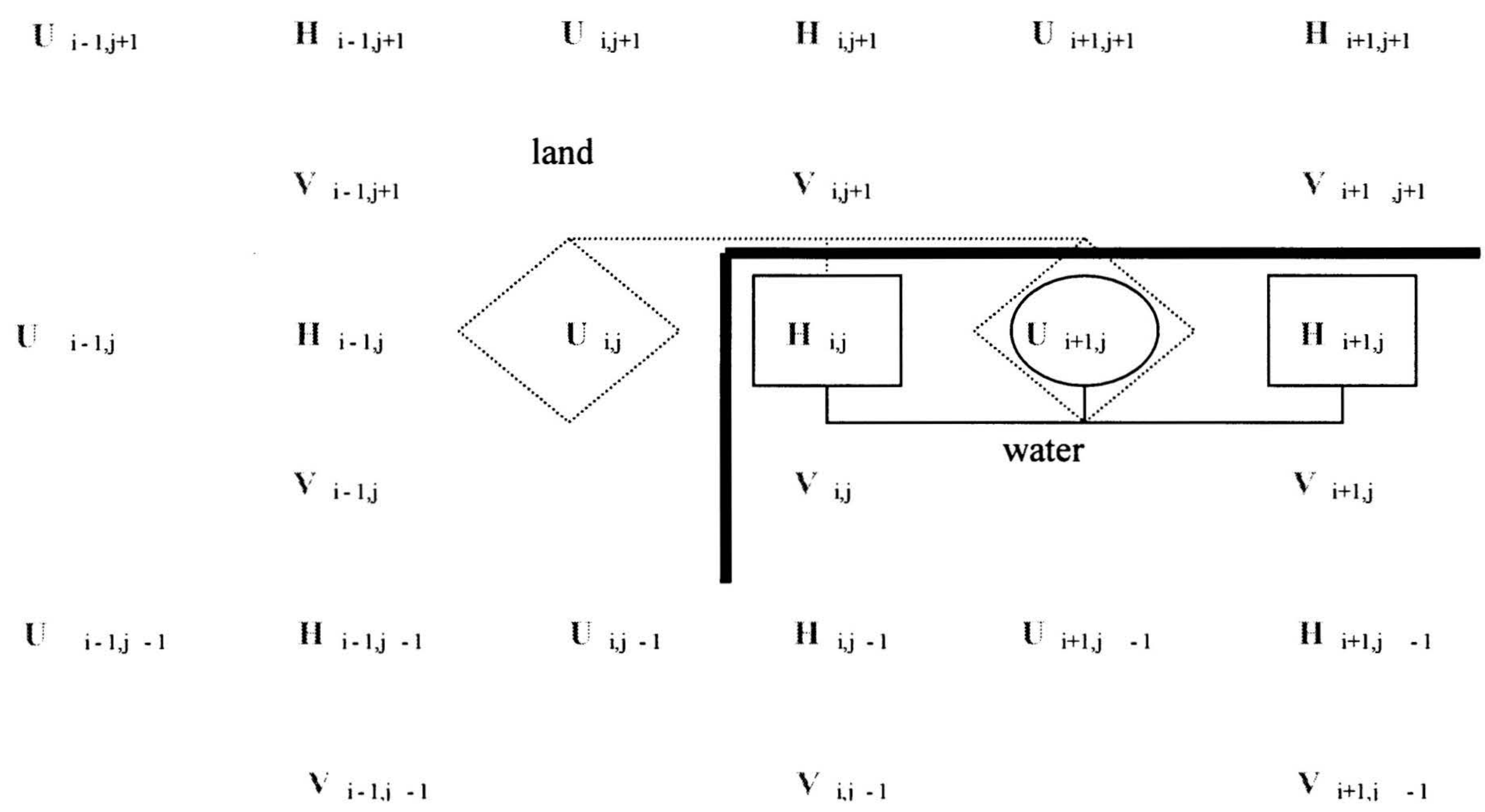

Figure 3.3 Calculation of UAF(I+1,J) (circles) depends upon the surface heights located at H(I,J) and H(I+1,J) (squares). The correction to H(I,J) specified in the text eliminates the communication between U(I+1,J) and U(I,J) (diamonds) by increasing the value of at H(I,J) to match values in the interior. The result is that U(I+1,J) now acts as an interior point and does not recognize that it is approaching a boundary.

Similar situations exist for all corners. It is possible to communicate the boundary condition with the following changes to the code:

```
UAF(I,J)=ADVUA(I,J)  +.25E0*GRAV*(DY1(I,J)+DY1(I-1,J))
3         (D(I,J)*DUM(I,J)*DUM(I+1,J)+D(I-1,J)*DUM(I-1,J)*DUM(I,J))
4         *(EL(I,J)-EL(I-1,J))
5         +DRX2D(I,J)
6         +ARU1(I,J)*( WUSURF(I,J)-WUBOT(I,J) )

 UAF(I,J)=
1         ((H(I,J)+ELB(I,J)+H(I-1,J)+ELB(I-1,J))*ARU1(I,J)*UAB(I,J)
2         -4.E0*DTE*UAF(I,J))
3         /((H(I,J)+ELF(I,J)+H(I-1,J)+ELF(I-1,J))*ARU1(I,J))

 VAF(I,J)=ADVVA(I,J)   +.25E0*GRAV*(DX1(I,J)+DX1(I,J-1))
3         (D(I,J)*DVM(I,J)*DVM(I,J+1)+D(I,J-1)*DVM(I,J-1)*DVM(I,J))
4         (EL(I,J)-EL(I,J-1))
5         +DRY2D(I,J)
6         + ARV1(I,J)*( WVSURF(I,J)-WVBOT(I,J) )
```

```
      VAF(I,J)=
     1      ((H(I,J)+ELB(I,J)+H(I,J-1)+ELB(I,J-1))*VAB(I,J)*ARV1(I,J)
     2      -4.E0*DTE*VAF(I,J))
     3      /((H(I,J)+ELF(I,J)+H(I,J-1)+ELF(I,J-1))*ARV1(I,J))
```

With this correction the boundary is now communicated to the velocity at the first interior point through a reduction in the cross sectional area and depth associated with the velocity calculation as opposed to a reduction in the surface elevation. As in the surface elevation correction, the velocity masks are also used to balance the code on all four boundaries.

The calculation of the internal velocity field requires the same corrections as stated above for the external velocity. The changes are the same with UAF(I,J), VAF(I,J) in the above discussion replaced with uf(i,j,k) and vf(i,j,k) respectively.

3.3.3. Flux Correction

The advection of U and V is calculated by first calculating fluxes at grid points located in between those points associated with velocity. This method works quite well in both the interior and along the coastlines of the domain except at those points where there is a corner along the grid.

Ignoring viscosity in the calculation of the advection of U the flux calculation in the original code is:

```
 FLUXUA(I,J)=.125E0*((D(I+1,J)+D(I,J))*UA(I+1,J)
1             +(D(I,J)+D(I-1,J))*UA(I,J))
2             *(UA(I+1,J)+UA(I,J))

 FLUXVA(I,J)=.125E0*((D(I,J)+D(I,J-1))*VA(I,J)
1             +(D(I-1,J)+D(I-1,J-1))*VA(I-1,J))
2             *(UA(I,J)+UA(I,J-1))
```

Where FLUXUA and FLUXVA are the fluxes associated with U and V respectively. The advection is then determined as the difference of the fluxes:

```
ADVUA(I,J)=FLUXUA(I,J) - FLUXUA(I-1,J)
1             +FLUXVA(I,J+1) -FLUXVA(I,J)
```

As shown in Figure 3.4, the y-flux operator of U-advection leaves the component FLUXVA(I,J) nonzero even though it is associated with a land point where no flux is possible. Similar situations exist at all corners of the grid and this result in an error in the advection term at all corners. Depending on the corner and the sign of the error, it may either be dissipative or additive to the advection term. A simple correction can be made by creating a mask for the flux using the existing velocity mask. The correction is given below:

```
ADVUA(I,J)=FLUXUA(I,J)*dum(i,j)*dum(i+1,j)
1             -FLUXUA(I-1,J)*dum(i-1,j)*dum(i,j)
1             +FLUXVA(I,J+1)*dum(i,j+1)*dum(i,j)
1             -FLUXVA(I,J)*dum(i,j)*dum(i,j-1)
```

This type of error also occurs in the calculation of V-advection and a similar correction may be introduced into the calculation :

```
ADVVA(I,J)=FLUXUA(I+1,J)*dvm(i+1,j)*dvm(i,j)
1             -FLUXUA(I,J)*dvm(i,j)*dvm(i-1,j)
1             +FLUXVA(I,J)*dvm(i,j+1)*dvm(i,j)
1             -FLUXVA(I,J-1)*dvm(i,j)*dvm(i,j-1)
```

The above corrections have also been applied to the velocity calculations of the

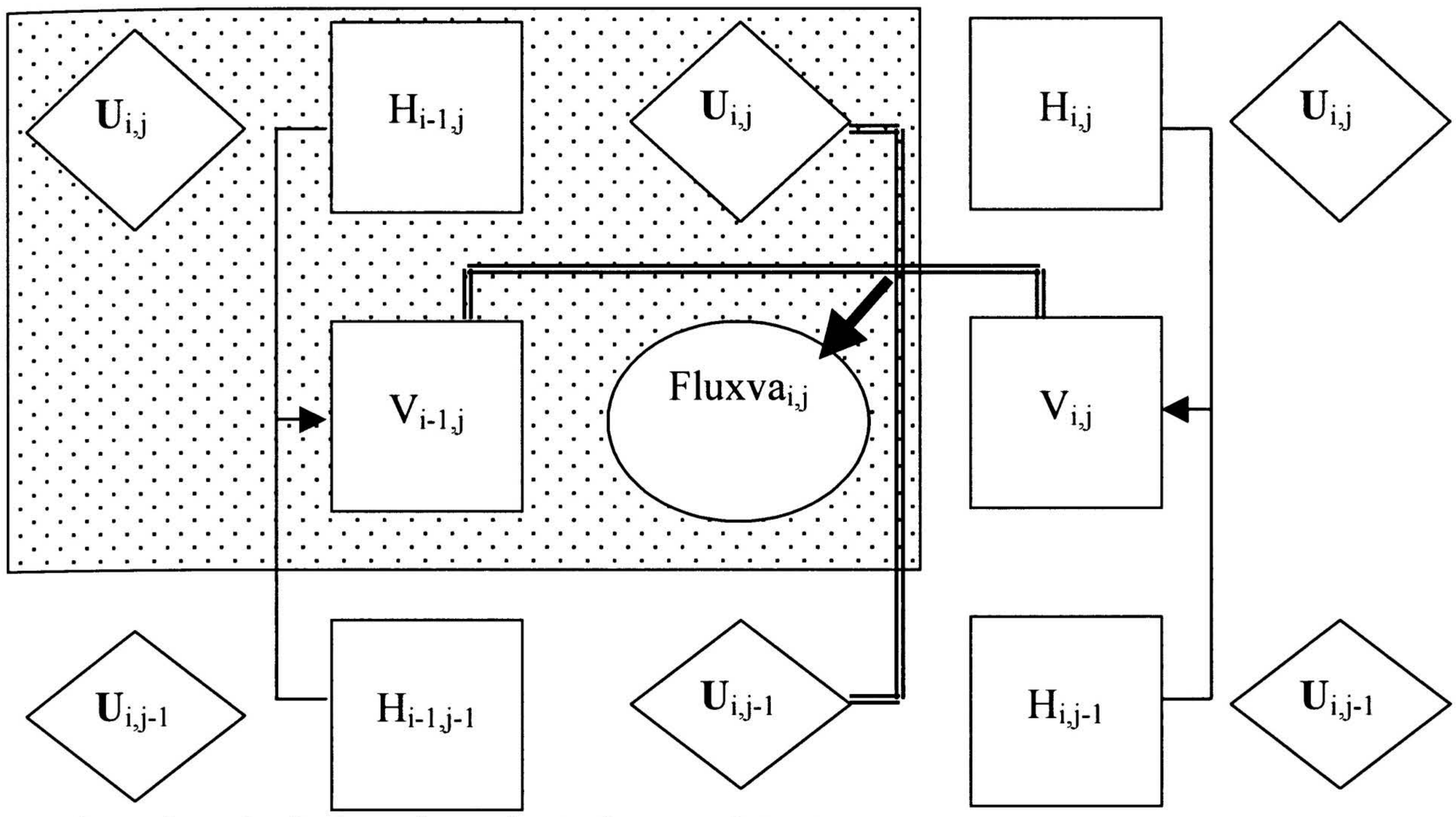

internal mode calculations in order to be consistent.

Figure 3.4: The y-flux operator used in the calculation of the u velocity advection scheme. The shaded portion represents land. The value of Fluxva(i,j) depends on the sum of the depths, H, multiplied by the value of V respective to each column. These two sums are added then multiplied by the sum of the values of U in the center column. U(i,j-1) and the result from the fourth column are both nonzero resulting in a nonzero flux on the land.

3.3.4. Lateral Friction

In order to maintain stability in models where temperature and salinity was held constant it was found necessary to introduce a dissipative biharmonic operator to reduce the noise level generated by the nonlinear terms along the coastline. The operator is added to both the external mode and internal mode velocity calculations; it is actually a dissipative term (U_{xx} or V_{yy}) and helps to reduce the noise generated by the nonlinear terms. It acts as friction along the coastline by extending into the first land point on the grid. As the velocity on a land point is identically equal to zero, the magnitude of the dissipative term increases and acts as a frictional force. The code is implemented as follows:

```
 UAF(I,J)=ADX2D(I,J)+ADVUA(I,J)
1        + ARU1(I,J)...

8   +4.0*mu_u(i,j)*aru1(i,j)*0.5
9   *(D(i,j)*dum(i+1,j)*dum(i,j)+D(i-1,j)*dum(i,j)*dum(i-1,j))
0   *(uab(i+1,j)-4.*uab(i,j)+uab(i-1,j)+uab(i,j+1)+uab(i,j-1))

 VAF(I,J)=ADY2D(I,J)+ADVVA(I,J)
1        +ARV1(I,J)...

8   +4.0*mu_v(i,j)*arv1(i,j)*0.5
9   *(D(i,j)*dvm(i,j+1)*dvm(i,j)+D(i,j-1)*dvm(i,j)*dvm(i,j-1))
0   *(vab(i+1,j)-4.*vab(i,j)+vab(i-1,j)+vab(i,j+1)+vab(i,j-1))
```

where mu_u(i,j), mu_v(i,j) are dimensionless coefficients which decrease exponentially as 2^{-n} where n=0 is the first velocity grid cell neighbouring the coastline, with

$$\text{mu\_u}|_{n=1} = \text{mu\_v}|_{n=1} = 0.02. \tag{3.3.2}$$

Values of mu_u and mu_v decay for n=0 to n=7 and are then held constant across the domain. It appears necessary to maintain some a nonzero coefficient across the entire domain in order to prevent noise from appearing across the cell face where the dissipative term ends. Although the dissipative coefficients appear quite high in value, it was found through numerical tests that the terms did not greatly influence the velocities within the center of the domain. Lower values for the coefficients did not adequately damp out numerical noise and generated solutions would not maintain numerical stability.

3.4. Surface Boundary Condition (Wind Stress)

Surface wind stress values for the barotropic mode are tapered along the coastline in a manner similar to the algorithm for the lateral dissipative operator. Along the coastline, the surface wind stress, τ, was calculated as:

$$\tau_n = \tau \sin(\frac{n\pi}{14}), n = 1,..,7 \qquad (3.4.1a)$$

$$\tau_n = \tau, n \geq 8 \qquad (3.4.1b)$$

where n represents the grid cell which is n cells from the coastline.

A consequence of the sigma-coordinate system is that the depth of the surface layer varies as the depth of the water column in a grid cell. For the present configuration of the model, the surface layer varies from a depth of approximately 1.2 m to 12 metres. The data analysis of the previous chapter suggests that the Ekman depth is between 25 to 30 metres. In the baroclinic mode, the surface wind stress is applied to the surface layer of the model. This means that all of the energy which would normally be distributed over a depth of 25 to 30 metres is deposited in a layer which is only 1 to 10 metres deep. Numerically, this creates a large shear in the velocities, particularly when the water column in the model domain is only 10 metres deep (surface layer ~ 1 metre), which leads to numerical instability when strong wind forcing is introduced. Recent changes to the algorithm for the turbulence calculations (subroutine PROFQ) to allow for the breaking of surface waves (Mellor and Blumberg, 2004) may address this issue, however this new algorithm has not been implemented in the model used here.

To overcome this issue, the surface wind stress in the baroclinic mode is assumed to act over the entire Ekman layer. The proportion of wind stress supplied to the surface layer is calculated as the windstress supplied to the barotropic mode multiplied by ratio of the depth of the surface layer to the Ekman depth, i.e.,

$$\tau_{k=1} = \tau \frac{\Delta z_1 H_{i,j}}{D_E} \qquad (3.4.2)$$

where τ is the windstress applied to the barotropic mode, $\tau_{k=1}$ is the wind stress applied to the surface layer, Δz_1 is the normalized depth of the surface layer, $H_{i,j}$ is the depth of the water column at the i^{th}, j^{th} coordinate and D_E is the Ekman depth. For the Clode Sound domain, D_E was assumed to be 30 metres.

Pond and Pickard (1991, Introductory Dynamical Oceanography, 2nd edition) give:

$$D_E = \frac{4.3W}{\sin(|\varphi|)^{1/2}} \tag{3.4.3}$$

where W is the wind speed in m/s and φ is the latitude. With an average wind speed of 17-19 km/hr (~5 m/s) at 45 degrees $\sin(\pi/4)=2^{-1/2}$ we get $D_E \sim 25$ m

There is limited data available for which to estimate the depth of the Ekman layer. Only in the 1996 data is velocity recorded below 30 metres depth. From Table 2.21, the Fluctuating Kinetic Energy indicates that within the inner basin, meteorological forces produce approximately 20% of the fluctuating kinetic energy at 10 and 20 metres depth, but only 6% of the fluctuating kinetic energy at 45 metres depth for mooring M1-96. At M2-96, meteorological forces produce between 27-35% of the fluctuating kinetic energy at 10 and 17 metres depth at M2-96 and only 12% at 45 metres depth. On the seaward side of the sill, 21-35% of the fluctuating kinetic energy appears in the meteorological band at 10 and 20 metres depth, while only 9% is found in this frequency band at 45 metres depth. It is only at M5-96 that we find 30% of the fluctuating kinetic energy at 45 metres depth, which may indicate that the Ekman Depth could possibly be adjusted along the inlet. The usage of $D_E = 30$ metres appears to be reasonable for the outer channel and inner basin given the data and the estimate from Pond and Pickard. At the sill, the fluctuating kinetic energy from 1996 and 1997 indicates that between 11-13% of the fluctuating kinetic energy originates from meteorological forces but at 15 metres depth we find that 25-31% of the fluctuating kinetic energy is associated with the meteorological forces. Even though meteorological forces do not appear to be that strong in the near surface at the sill, there is, evidence that meteorological forces may be significant at greater depths. Admittedly 30 metres depth is below the maximum depth of the sill so that meteorological forces may be weaker than necessary at the sill within the model.

3.5 Mixing of Temperature and Salinity

The mixing of temperature and salinity at a resolution of 50 metres in regions of rapid bathymetric changes is problematic. Small numerical errors are found to lead to the rapid onset of numerical instability as the numerical scheme for the calculation of temperature and salinity used by the Princeton Ocean Model appears unable to compensate for the errors. Numerical experimentation revealed that the model algorithm produces upwelling along the coastline. This upwelling produced a large non-physical baroclinic front along the coastline.

Another area of concern for the temperature and salinity calculations was identified in the region of the sill for the Clode Sound domain. There were two separate problems identified in the sill region; each problem required a separate distinct solution to the model algorithm. The solutions proposed here in order to maintain numerical stability are found to be necessary for the calculation of temperature and salinity for the Clode Sound domain. It is not known how the model would behave in other domains at a similar horizontal resolution so the algorithmic changes used may not be general enough to be suitable for other domains.

The first problem identified at the sill is similar to the problem of upwelling along the coastline. In the region of the sill, large horizontal velocity gradients produced large vertical velocities resulting in either overmixing of temperature and salinity or large upwelling events which in turn produced baroclinic fronts that lead to the onset of numerical instability. While it is possible that some of these upwelling events may actually be physical, the model algorithm was unable to maintain numerical stability. Flow in the region of the sill was shown to be supercritical, it seems likely that the model error may partially result from an attempt to model a non-hydrostatic regime with a hydrostatic model.

The second problem identified at the sill was found to be caused by the adiabatic boundary condition used in the vertical diffusivity calculation of subroutine PROFT. Although it is not understood why, the bottom boundary condition was found to be unable to maintain reasonable values for temperature and salinity on the inner basin slope leading to the sill. Even in the absence of any thermal energy being input or extracted from the model, the existing adiabatic boundary condition was found to decrease temperatures in the bottom layer by as much as 20 degrees in a 24-hour simulation . This error appeared to be isolated to the slope region of the sill. The source of the error was traced to the first few time steps of the model, where small numerical differences were found. These differences of order 10^{-6} appear to grow unbounded as the model simulation progresses. The result of this error is a large pool of very cold water forming on the slopes of the sill. This is clearly non-physical as the model has no heat sink and normally water wouldn't even be in liquid form at –20 degrees. The calculation for salinity, which uses the same algorithm for the vertical diffusivity calculation, was also found to produce errors in the salinity values. Salinity values were found to increase by as much as 55 PSU over the same 24-hour period as the temperature decreased.

The upwelling that occurs along the coastline and in the region of the sill can be compensated for by relaxation of the temperature and salinity values to a stable background field. The rate of relaxation necessary to maintain numerical stability was found to be equal to ¼ of the period of the dominant tidal frequency used to force the model. As shown in chapter 2, the dominant tidal frequency in Clode Sound was M_2 having a period of 12.42 hours. It follows that the rate of relaxation necessary to achieve numerical stability was 3.105 hours. From a physical point of view, the rate of relaxation corresponds to the time of maximum deflection of the thermoclines and haloclines from their initial positions when the model is forced by specification of a simple sinusoidal function for the surface elevation at the open boundary. The relaxation necessary to maintain numerical stability is very strong. In consequence of this strong relaxation the model is expected to inhibit mixing and nonlinear interactions as temperature and salinity fields are not permitted to depart significantly from the background fields imposed on the model.

Even with the strong relaxation described above, the bottom boundary layer in the region of the sill was found to generate heat and salt. To eliminate this problem, the adiabatic boundary condition used in subroutine PROFT was replaced with a simple statement so that the temperature and salinity in the bottom layer are held constant. In view of the weak rates of change in temperature and salinity recorded in Clode Sound at

45 metres depth during 1996 (Chapter 2, section 2.1) this does not appear to be a unreasonable compromise for most of the model domain. Although far from ideal, this solution does prevent the loss of heat and generation of salt in the region of the sill.

Finally it was found that the outwards propagation of internal waves had a tendency to produce numerical instability at the open boundary. Even with an Orlanski Radiation Boundary condition for temperature and salinity, the model algorithm was found to be unable to maintain stability for temperature and salinity calculations. To avoid the propagation of internal waves at the mouth of the inlet, the temperature and salinity values were relaxed on the grid back to the background temperature and salinity fields. The area used for the relaxation was extended 20 grid points (1 km) beyond the region that had been used to linearly interpolate the depths (Figure 3.2).

The extension of the relaxation zone beyond the ramping error was found necessary to damp out persistent numerical errors that appeared on the corners where the Clode Sound domain met the ramping region. The relaxation in the region of the open mouth was done in addition to the relaxation performed over the entire domain. The advantage of this grid based relaxation is that it produces a sponge layer near the open boundary where outgoing internal waves can be damped before an attempt is made to radiate them outwards using an Orlanksi Radiation Boundary condition.

To summarize the code changes found necessary to maintain numerical stability in the model when temperature and salinity evolve:

1.) The entire temperature and salinity fields are relaxed back to stable background fields (normally background fields are considered to be the initial state) after the calculation of the open boundary condition.

```
      DO K=1,KB
        DO J=1,JM
          DO I=1,IM

            TF(I,J,K)=TF(I,J,K)-(DTI2/(3.105D0*3600.D0))
     1                          *(TB(I,J,K)-TCLIM(I,J,K))
            SF(I,J,K)=SF(I,J,K)-(DTI2/(3.105D0*3600.D0))
     1                          *(SB(I,J,K)-SCLIM(I,J,K))
           ENDDO
         ENDDO
       ENDDO
```

Above TF, SF are the values of temperature and salinity at new time step, DTI2 is twice internal time step (in seconds) of the model and TCLIM and SCLIM are the background temperature and salinity fields.

2.) The adiabatic boundary condition is commented out in subroutine PROFT and replaced with the bottom layer being set equal to the background value in the bottom boundary (which remains constant).

```
      DO 102 J=1,JM
C        DO 102 I=1,IM
        DO 102 I=ISTART(J),ISTOP(J)

C           F(I,J,KBM1)=((CD(I,J,KBM1)*GGD(I,J,KBM2)-F(I,J,KBM1)
C     1        +DBLE(DT2)*(RAD(I,J,KBM1)-RAD(I,J,KB))
C     1        /DBLE(DH(I,J)*DZ(KBM1)))
C     2        /(CD(I,J,KBM1)*(1.D0-EED(I,J,KBM2))-1.D0))

            F(I,J,KBM1)=FCLIM(I,J,KBM1)

  102 CONTINUE
```

Where F and FCLIM represent either temperature and salinity and the appropriate background field. The code which is commented out is the adiabatic boundary condition.

3.) The temperature and salinity are relaxed towards the mouth of the grid back to the background field

```
      DO K=1,KB
        DO J=380,JM
          DO I=1,IM

            TF(I,J,K)=TF(I,J,K)+(1.D0-DFLOAT(JM-J)/DFLOAT(JM-
380))
     1                        *(TCLIM(I,J,K)-TF(I,J,K))

            SF(I,J,K)=SF(I,J,K)+(1.D0-DFLOAT(JM-J)/DFLOAT(JM-
380))
     1                        *(SCLIM(I,J,K)-SF(I,J,K))

          ENDDO
        ENDDO
      ENDDO
```

The algorithm is specific to the Clode Sound domain extending in the along channel direction from grid point J=380 to grid point JM=452.

It may be possible to partially compensate for the strong relaxation schemes imposed by the first correction by permitting the background temperature and salinity fields to slowly evolve in time. As it is not generally known what state the temperature and salinity will evolve to an appropriate background field must be calculated from the existing state variables. The approach used to permit the evolution of the background temperature and salinity fields in the model is rather simplistic. The model calculates the average of temperature salinity values over the period of the M_2 tide at every grid point.

$$T_{avg}(x,y,z) = \frac{1}{\mathrm{T}_M}\int_0^{T_M} T(x,y,z,t)dt \tag{3.5.1}$$

Where: T_{avg} is the average temperature (salinity) T_M represents the averaging period and T is the current value of temperature (salinity). The thermoclines and haloclines are expected to rise and fall in response to the change in surface elevation. By averaging over an M_2 period the average should be zero if we assume a purely sinusoidal motion. The background scalar fields are then updated to the time averaged temperature and salinity once per tidal period. The averaging operator is strongly dissipative and should permit the background temperature and salinity to evolve slowly over time.

The additions to the code are highlighted in bold font below, the averaging period used by the model is actually 12.5 hours (corresponding to 3000 time steps (variable IINT) which is slightly longer than the period of M_2.

```
      CALL ADVT(TB,T,TCLIM,DTI2,TF)

      CALL ADVT(SB,S,SCLIM,DTI2,SF)

C     CALCULATE VERTICAL PROFILES OF T & S

      CALL PROFT(TF,WTSURF,SWRAD,TSURF,TCLIM,1,DTI2)

      CALL PROFT(SF,WSSURF,SWRAD,SSURF,SCLIM,1,DTI2)

      CALL MYBCOND(4)

      DO 355 K=1,KBM1
        DO 355 J=1,JM
          DO 355 I=ISTART(J),ISTOP(J)

            T(I,J,K)=T(I,J,K)+.50D0*SMOTHD*(TF(I,J,K)
     1        +TB(I,J,K)-2.D0*T(I,J,K))
            S(I,J,K)=S(I,J,K)+.50D0*SMOTHD*(SF(I,J,K)
     1        +SB(I,J,K)-2.D0*S(I,J,K))

            TB(I,J,K)=T(I,J,K)
            T(I,J,K)=TF(I,J,K)
            SB(I,J,K)=S(I,J,K)
            S(I,J,K)=SF(I,J,K)

  355 CONTINUE

      DO K=1,KB
        DO J=1,JM
          DO I=1,IM

            T_AVG(I,J,K)=T_AVG(I,J,K)+TF(I,J,K)
            S_AVG(I,J,K)=S_AVG(I,J,K)+SF(I,J,K)

          ENDDO
        ENDDO
      ENDDO
```

```
IF(MOD(IINT,3000).EQ.0) THEN

  DO K=1,KB
    DO J=1,JM
      DO I=1,IM

        T_AVG(I,J,K)=T_AVG(I,J,K)/3000.D0
        S_AVG(I,J,K)=S_AVG(I,J,K)/3000.D0
        TCLIM(I,J,K)=0.5D0*(TCLIM(I,J,K)+T_AVG(I,J,K))
        SCLIM(I,J,K)=0.5D0*(SCLIM(I,J,K)+S_AVG(I,J,K))
        T_AVG(I,J,K)=0.D0
        S_AVG(I,J,K)=0.D0

      ENDDO
    ENDDO
  ENDDO

  CALL DENSD(SCLIM,TCLIM,RMEAND)

ENDIF

CALL DENSD(S,T,RHOD)
```

In the above code: T, TF, TB are the current, forwards and backwards values for temperature. S, SF, SB are the current, forwards and backwards values for salinity. TCLIM and SCLIM represent the background temperature and salinity fields. T_AVG and S_AVG are temporary values used in the averaging process for temperature and salinity. The additional call to DENSD after the averaging process updates the background density field RMEAND, which is required for consistency as the background density field must evolve with the background temperature and salinity fields.

This is a very simple attempt at implementing a numerical scheme that permits the evolution of a background scalar field to avoid imposing an initial state that may not be physically consistent with the actual evolving scalars fields. It was specifically designed to work within the existing model algorithm. Other methods of allowing the background fields to evolve were not investigated and may lead to different results than those presented in Chapter 5. To reduce the possibility of sudden changes in the background field, the average temperature and salinity fields are averaged with the background field of the previous averaging process to form the new background field. It is not obvious that the chosen M_2 period used for the averaging process is the appropriate time scale. It was chosen because M_2 is the dominant tidal frequency for Clode Sound. The algorithm is tested and the results presented in Chapter 5 where they are compared to the results of the model in which the background is held at the initial state.

The advantage and disadvantage of permitting the background scalar fields for temperature and salinity are quite obvious. In regions of the domain where there is a large amount of mixing, the scalar fields will now be able evolve away from the initial state. However, the time scale of the averaging process will be significant in determining the evolution of the background field. The background field lags the actual temperature and salinity fields giving the fluid a memory of its previous state. If the averaging process is too long, the scalar fields will be restrained back to the previous state and may not evolve quickly enough. If the averaging process is too short, the strong relaxation used may create episodic sources and sinks in the grid, again preventing the proper evolution of the scalar fields. For example consider the case where the temperature is averaged over a flood tide so that thermoclines are rising and temperature is dropping. If the tide has a period of M_2 and the averaging is done over one half the M_2 period, then the background field used for the next averaging period will represent the average between the initial temperature and the minimum temperature achieved with the rising thermocline. As the tide begins to ebb and the thermoclines begin to move downwards, the temperature field would be continually relaxed back to the average temperature of the rising tide even though the thermoclines should be sinking and temperature rising. This is the reason why the averaging time was chosen to be equal to approximately the period of the dominant tidal frequency. As previously mentioned, the average of a sinusoidal curve over one complete period should be equal to zero. If the evolution of temperature and salinity at a particular location are such that the average over the dominant tidal period is significantly different than zero, than it seems appropriate that to adjust the background field towards the average temperature or salinity field calculated by the model.

The evolution of the background temperature and salinity fields should also permit the introduction of a surface heat flux and/or a fresh water source such as a river. Without the evolution of the background field, the model temperature and salinity fields would be continually relaxed back towards the initial state regardless of the amount of heat or fresh water input. In the case of a surface heat flux, the relaxation back to the initial state would create a sink for the thermal energy and the water column would not warm at the expected rate. By updating the background temperature field as indicated above, the background temperature field would slowly increase as thermal energy is introduced in the model. The averaging of the average temperature and the old background field to create the new background fields may be a little excessive for such a scenario.

3.6 The Influence of High Horizontal Resolution

As mentioned in the introduction of this chapter, the code changes listed above appear to be necessary due to the high horizontal resolution (50m) used in the domain. In section 3.3.1 a correction was introduced for the calculation of surface elevation along the coastline. This correction was found necessary to correct an error found in the surface elevation along the coastline that generated a large barotropic force. In the absence of this correction and at a coarser resolution (greater than 1 km), an error in the surface elevation may generate noise along a coastline, however, it seems that this noise remains bounded and does not adversely effect the solution to any large degree or this issue would most likely have been addressed in past releases of the code.

The effects of horizontal resolution on the tolerance of the model to numerical noise should not be under estimated. If we consider a typical finite difference in which the algorithm requires the division by length or area the tolerance level of the model to noise decreases as resolution increases. Suppose that $F = F_i^n + \varepsilon$ is a function located at the ith grid point on a 1-dimensional grid at time step, n, with error, ε. Let Δx and represents the length of the grid cell. The solution to the wave equation:

$$\frac{\partial F}{\partial t} = c\frac{\partial F}{\partial x}, \tag{3.6.1}$$

using upstream differencing with leap-frog in time, becomes:

$$\begin{aligned} F_i^{n+1} &= \frac{2c\Delta t}{\Delta x}\left[F_i^n + \varepsilon - (F_{i-1}^n + \varepsilon)\right] + F_i^{n-1} + \varepsilon \\ &= \frac{2c\Delta t}{\Delta x}\left[F_i^n - F_{i-1}^n\right] + F_i^{n-1} + \varepsilon\left[\frac{4c\Delta t}{\Delta x} + 1\right] \end{aligned} \tag{3.6.2}$$

where it has been assumed that errors of order ε should be added to represent the maximum possible error. The error, ε, may propagates as $\varepsilon\left[\frac{4c\Delta t}{\Delta x} + 1\right]$ in the calculation. For numerical stability the CFL criteria requires that $\alpha = c\Delta t/\Delta x < 1$, so that the propagation of the error may be written as $(4\alpha+1)\varepsilon$. If $c=(gH)^{1/2}$ then for an ocean basin with H~1km, c~99 m/s and with Δx~1km we find that Δt~10 s, so that an error of order 10^{-7} may propagate as $(4\alpha+1)\cdot 10^{-7}$ for a single time step. If H~100m, c~31m/s and with Δx~50m we find that Δt~1.6s and again the error propagates as $(4\alpha+1)\cdot 10^{-7}$ for a single time step. However, while the larger scale model can achieve a time step of 10 s amplifying the error only once. The smaller scale model requires at least 6 iterations to achieve the same advance in time. As a result, over a period of 10 seconds representing one time step of the larger scale model, an the smaller scale model with 6 time steps may amplify the same error as $(4\alpha+1)^6 \cdot 10^{-7}$.

Similar results may be obtained for the advection equation and also for a one-dimensional equation representing the advection of scalars:

$$\frac{\partial F}{\partial t} = U\frac{\partial F}{\partial x} \tag{3.6.3}$$

If $U = U_i^n + \varepsilon,\ F = F_i^n + \varepsilon$ then for upstream differencing with leap-frog in time we have:

$$\begin{aligned} F_i^{n+1} &= \frac{2\Delta t}{\Delta x}\left(U_i^n + \varepsilon\right)\left[F_i^n + \varepsilon - (F_{i-1}^n + \varepsilon)\right] + F_i^{n-1} + \varepsilon \\ &= \frac{2\Delta t}{\Delta x}\left(U_i^n + \varepsilon\right)\left[F_i^n - F_{i-1}^n + 2\varepsilon\right] + F_i^{n-1} + \varepsilon \\ &= \frac{2\Delta t}{\Delta x}U_i^n\left(F_i^n - F_{i-1}^n\right) + F_i^{n-1} + \varepsilon\left[\frac{2\Delta t}{\Delta x}\left(F_i^n - F_{i-1}^n + 2U_i^n\right) + 1\right] + O(\varepsilon^2) \end{aligned} \tag{3.6.4}$$

The error propagation associated with the advection of a scalar indicates that the propagation of the error is dependent on the spatial difference of the scalar. For a sigma coordinate system, changes in depth of neighbouring cells may produce salinity or temperature gradients that promote the growth of the error. This is particularly true in coastal regions where changes in depth may result in the sigma layer passing through an interface such as the interface at the bottom of a surface layer. This may help to explain why the calculations of temperature and salinity require such strong relaxation in the presence of rapidly changing bathymetry. It follows that for simulations with a high horizontal resolution, small errors in the solution have the potential to lead to the rapid onset of instability even if the simulation time is kept short.

Chapter 4 Model Performance with a Statically Stratified Fluid

"Mine is a long and a sad tale!" said the Mouse, turning to Alice, and sighing.

"It is a long tail, certainly," said Alice, looking down with wonder at the Mouse's tail: "but why do you call it sad?"

- Lewis Carroll
Alice's Adventure in Wonderland

4.1 Model Input and Output

The model domain used in the simulation of Clode Sound consisted of a rectangular grid with each cell having dimensions of 50 metres by 50 metres. The maximum depth used in the simulation was 100 metres. In order to satisfy the Courant-Friedrichs-Levy (CFL) condition for numerical stability the time step of the external mode must satisfy Equation 3.1.1. With $C_t=2(gH)^{1/2}+U_{max}$. For $U_{max} << (gH)^{1/2}$ the time step for the external mode is primarily determined by the maximum depth, H_{max}, of the domain. Given $H_{max} = 100$ and $\delta x = \delta y = 50$. The maximum time step allowed is approximately $\Delta t_E = 0.56$ seconds. However, the model was found to be numerically unstable for time steps in excess of 0.3 seconds. For this reason, all simulations discussed in this chapter used an external time step of $\Delta t_E = 0.3$ seconds. The internal mode was set to 15 seconds (*ISPLIT=50*) for all simulations. Larger values of the internal mode time step were also found to lead to numerical instability.

In order to evaluate the magnitude of the pressure gradient error, the model was executed for 5-days with zero external forcing and constant stratification. Only those runs for which the pressure gradient error was identically zero were found to remain stable during the 5-day simulation. The pressure gradient error was zero for the choice of 10 sigma levels or fewer, this is not unexpected given the criteria for smoothing the bathymetry as discussed in Chapter 3.

The model was also tested with zero external forcing during which temperature and salinity were allowed to evolve. All of these initialization tests failed to execute for even 48 hours of simulation when only 10 sigma levels were chosen. The error associated with the advection of temperature and salinity as well as the bottom adiabatic boundary condition for the vertical diffusivity the source of the numerical instabilities.

Examination of the CTD data collected during the 1996 and 1997 observation periods (Figures 2.6) reveals that the sill may act to divide the domain into distinct regions of stratification. In spring and early summer (July 1996, June and August 1997), the stratification from the head to the mouth of Clode Sound is almost constant with the main pycnocline located at or above sill depth. In late summer and into the autumn (September 1996 and October 1997) there are two very distinct stratification regimes. Within the inner basin, the main pycnocline remains very close to the depth of the sill, while in the outer channel the main pycnocline is significantly below the depth of the sill.

Given the different states of the stratification found within Clode Sound, the model was initialized with 3 different stratifications (Figure 4.1):

1.) Main pycnocline located above sill depth (~ 10 m) throughout the domain,
2.) Main pycnocline located at sill depth (~ 15 m) throughout the domain,
3.) Main pycnocline located at sill depth (~ 15 m) within the inner basin and below sill depth (~30 m) in the outer channel.

The model was forced with the tidal signal from the moorings located in the outer channel. The width of Clode Sound at the location of these moorings was found to be approximately the same as the width used at the mouth in the model domain. As discussed in Chapter 2, the shallow water constituents and harmonics of the main tidal signals are much weaker at these locations making this choice of a tidal function reasonable.

Wind data collected by Atmospheric Environment Service (AES) at Gander International Airport was used to simulate the wind field. The wind field was filtered with a low pass filter (cut-off frequency of 12 hours) prior to being applied to the model. Higher frequency variations in the wind data lead to numerical instability.

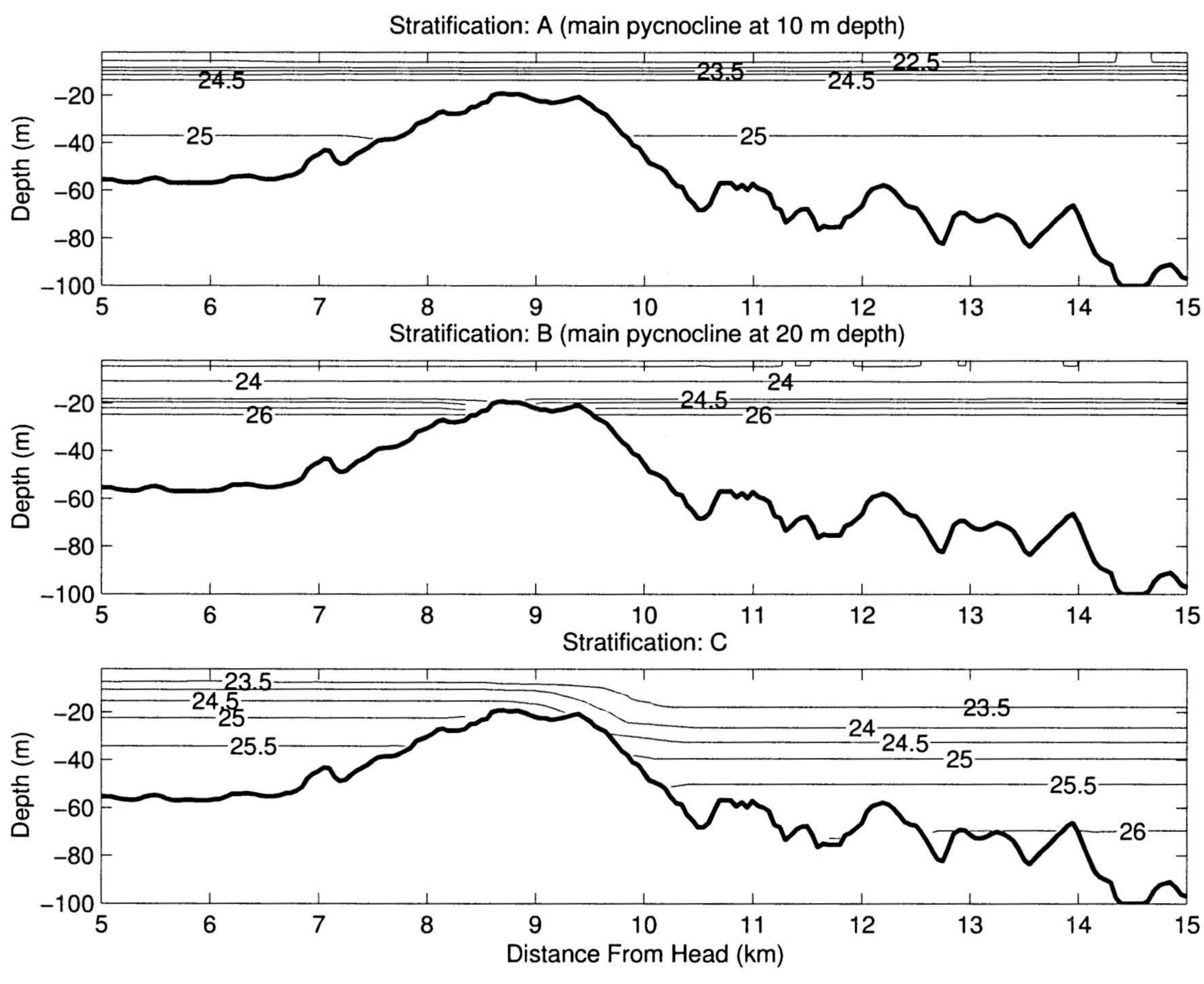

Figure 4.1: Stratification of the Model Domain: The stratification used to initialize the model. Density contours are given in units of σ_t, contour intervals at 0.5 kg/m^3. Top: Stratification A, pycnocline at 10 m depth; Middle: Stratification B, pycnocline at 20 m (sill) depth; Bottom: Stratification C, pycnocline deepening over the sill.

Model output was concentrated on regions where data was available for comparison. A plan view (Figure 4.2) shows the regions where the model data was saved for analysis, the output consisted of velocities, advective terms, and diffusivities as calculated for the model runs. Model output consisted of cross sections of the domain that passed through the mooring locations, as well as specific outputs for the model grid points nearest to the actual mooring locations. Additional output consisted of the external mode velocities and advection over the entire domain.

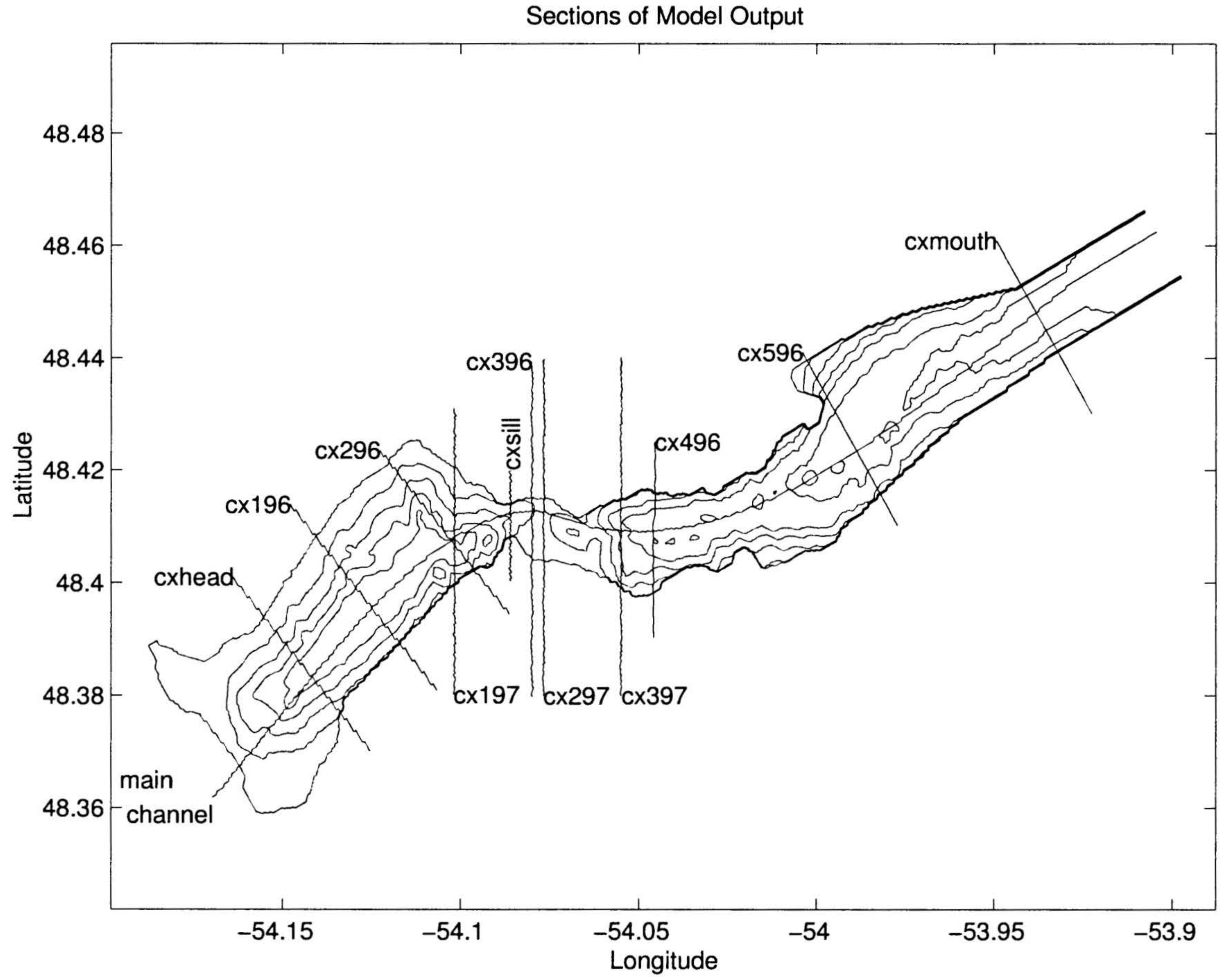

Figure 4.2: Model Output: Graphic depiction of the locations of model output, the line passing from the head of the inlet to the open mouth passes through the mooring locations of the 1996 observations. Channel cross-sections cx196 to cx596 intersect the main channel at mooring locations from 1996. Cross sections cx197 and cx397 pass through the North-South lines of the mooring array used in 1997 while cx297 passes through the mooring located at the sill during 1997 (slightly displaced from the 1996 sill mooring). Additional cross sections were used to monitor the model behaviour at: the head (cxhead); the narrowest point of the sill (cxsill); and at the mouth (cxmouth).

4.2Statically Stratified Fluids Forced by a Tide

4.2.1 Linear and Nonlinear Model of a Barotropic Fluid

Initial tests of the model were performed with a barotropic fluid to determine if there were significant differences with depth to justify the need for a three dimensional nonlinear model. The model was run in both a linear and nonlinear mode forced with the tidal signal from 1997 to evaluate the tide as it propagated over the sill. The tidal currents were calculated at the mooring locations for 1996 and 1997 and compared to the data collected during the observation period. The results of this analysis are tabulated in Tables B.1-B.4 and shown graphically in Figures 4.3-4.4. A quick inspection of the graphs reveals that the tidal velocities located at the sill (M3-96 and M4-97) are poorly represented. This is partially a consequence of the algorithm used to smooth the grid and also the introduction of the lateral friction boundary conditions. A comparison of model bathymetry to actual bathymetry in the region of the sill (Figure 3.1) reveals that the actual sill has a deep channel of about 15-20 metres depth located along the northern coastline; the southern region of the sill region has a typical depth less than 5 metres. The smoothing required to guarantee hydrostatic consistency for the model domain resulted in a deepening of the southern portion of the sill by broadening the narrow channel situated along the northern coast. Smoothing increases the volume of the sill disproportionately to the volume increase of the rest of the domain. Integrating around the region of the inner basin, the sill and outer channel indicates that the volume increase, due to smoothing, of the inner basin and outer channel was approximately 15% while the volume increase of the sill region was approximately 35%. Careful reconstruction of the sill region, establishing the coastline along the 10-metre depth contour, should help to correct for the increase in volume that occurs in this region. To date, attempts to correct the volume at the sill have been numerically unstable for a tides more energetic than a simple M_2 harmonic with amplitude of 30 cm.

In addition to this volume increase at the sill, the moorings located at the sill during 1996 and 1997 were located in the deeper channel and close to the northern coastline. When placed on the model grid, both locations are close to the coast and subjected to damping associated with the lateral dissipation term described in Chapter 3. The additional damping and the broadening of the channel at the modelled sill reduces the velocities at the model cells which represent the mooring locations. Despite this misrepresentation, the actual tidal signal located at the sill does reach velocities that are closer to those measured. However, this maximum is generally located closer to the centre of the model domain (to the south of the actual mooring location). For the nonlinear barotropic model, the maximum tidal signals located along the cross sections cx297 and cx396 were: O_1 1.09 ± 0.12 cm/s; K_1 1.91 ± 0.10 cm/s; M_2 10.13 ± 2.11 cm/s; S_2 3.51 ± 2.02 cm/s. For the linear barotropic model, the maxima were: O_1 0.66 ± 0.06 cm/s; K_1 1.43 ± 0.06 cm/s; M_2 8.86 ± 1.03 cm/s; S_2 3.69 ± 1.08 cm/s.

Tidal analysis of the observations from 1996 and 1997 indicates that tidal currents at 10 and 7.5 metres depth have a large uncertainty compared to the measured value, this may be a consequence of wind forcing within the inlet during the period of observation. The tidal currents calculated by the barotropic model are significantly lower than the observed values (generally only 20-50% of those observed). However, due to the large amount of noise in the observations, the tidal currents generated by the model generally lie within the estimated error for the observations. The data in Tables B.1-B.4 suggests

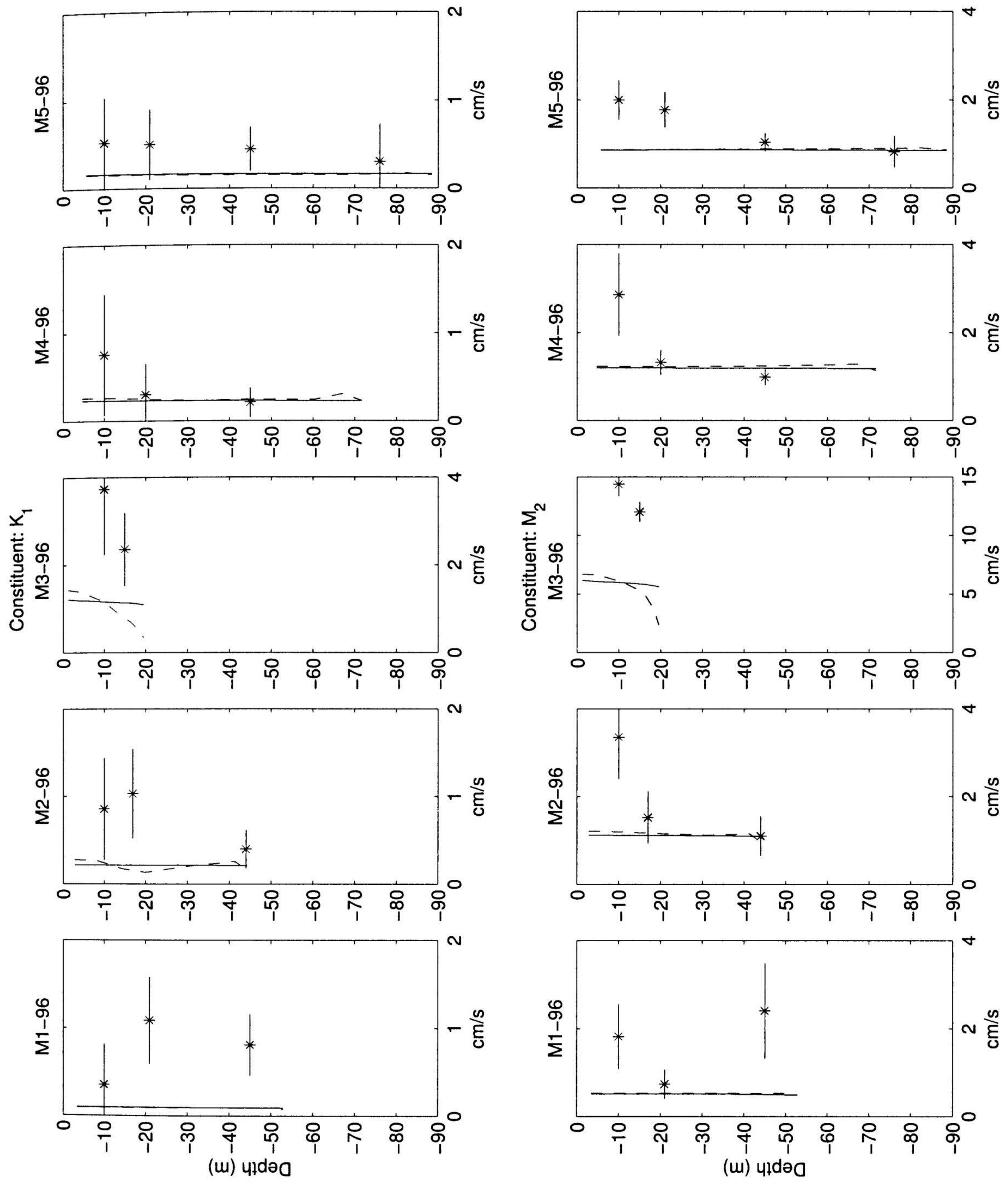

Figure 4.3: Comparison of main diurnal and semidiurnal tidal constituents for a barotropic fluid. Linear model output is represented by a solid line, **nonlinear model** output is represented by a dashed line. Data collected during the 1996 **observation** period is represented by an asterisk, the bar represents the error as calculated in Pawlowicz et al. (2002).

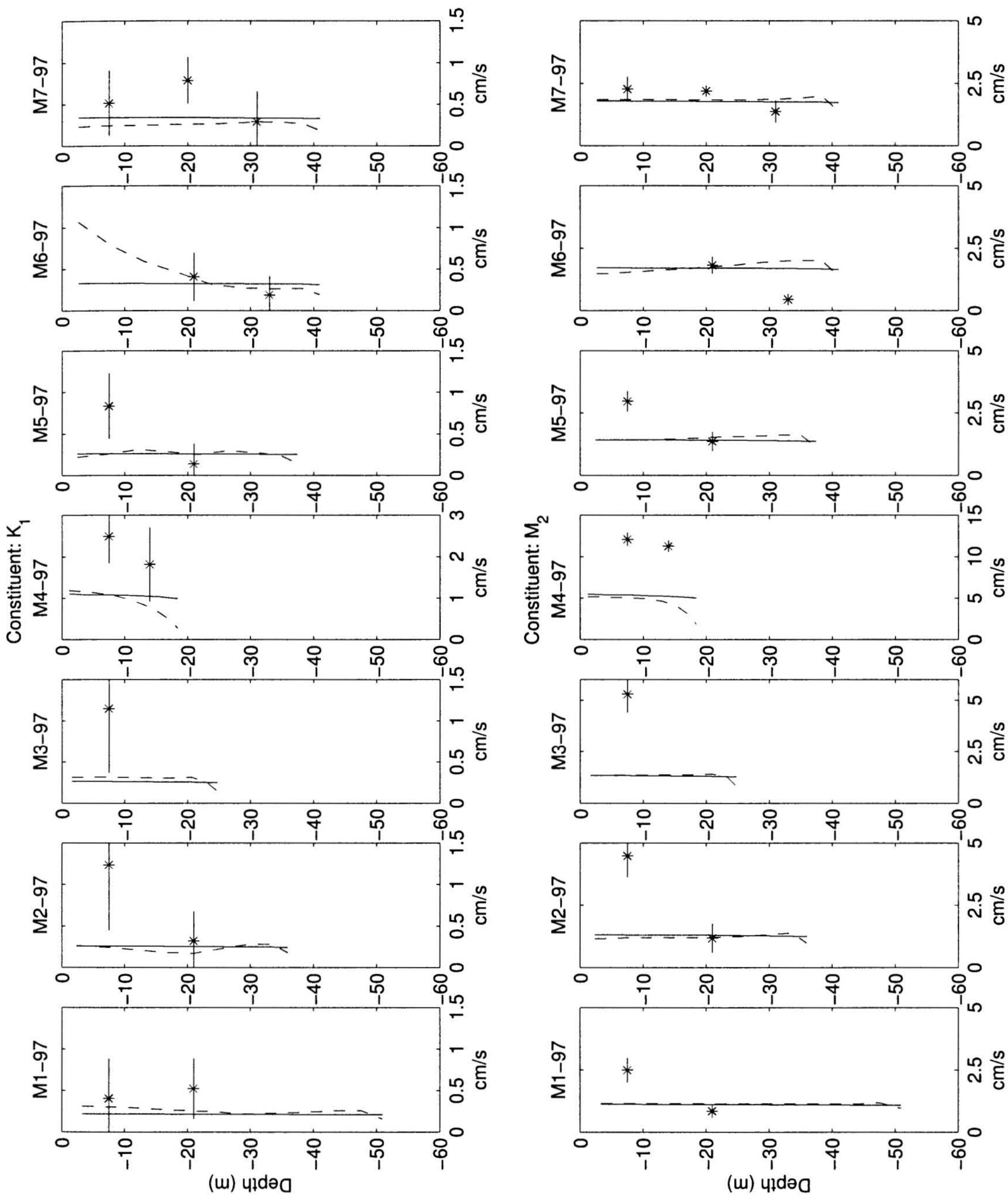

Figure 4.4: Comparison of main diurnal and semidiurnal tidal constituents for a barotropic fluid. Linear model output is represented by a solid line, **nonlinear model** output is represented by a dashed line. Data collected during the 1997 **observation** period is represented by an asterisk, the bar represents the error as calculated in Pawlowicz et al. (2002).

most of the energy is lost as the tide is forced over the sill. Modelling the flow over the sill required significant numerical damping to maintain stability. It is likely that too much energy extracted by the model. The lateral dissipation is relatively strong over the sill. At its narrowest, the sill is represented by only 10 grid points (lateral dissipation depends upon the number of grid points from the coastline (Section 3.3.4)). Unfortunately, the model would not permit forcing with the observed tide without becoming numerically unstable in the sill region without this damping.

The model output at the mooring locations for the barotropic model provides little justification for use of a nonlinear model in analyzing the circulation for Clode Sound. Apart from the sill locations (M3-96 and M4-97) and M6-97, nonlinearities have little influence on the tidal flow. However, inspection of the cross section data at cx197, cx297 and cx397 indicates that the a jet forms in the nonlinear model during a spring tide. Figures 4.5-4.7 reveal the strength of the nonlinear terms for a barotropic fluid in the vicinity of the sill during a spring tide. Within the inner basin (cx197, Figure 4.5), the nonlinear model produces a 500 m wide jet with a core velocity up to 10cm/s which does not exist in the linear model. At the sill (cx297, Figure 4.6), the nonlinearities increase the velocity by up to 10cm/s during a flooding spring tide; the core of the tidal jet at the sill moves southwards at the sill but this may be a consequence of the lateral dissipation. Seaward of the sill, (cx397, Figure 4.7) the formation of a 500 m wide jet in the center of the channel and core velocity of 10cm/s is also present in the nonlinear model. The existence of this jet suggests strong mixing will occur in the vicinity of the sill as a result of nonlinear interaction of the lunar and solar tidal constituents. In the next section the influence of the depth of the main pycnocline on the structure of the tide is investigated.

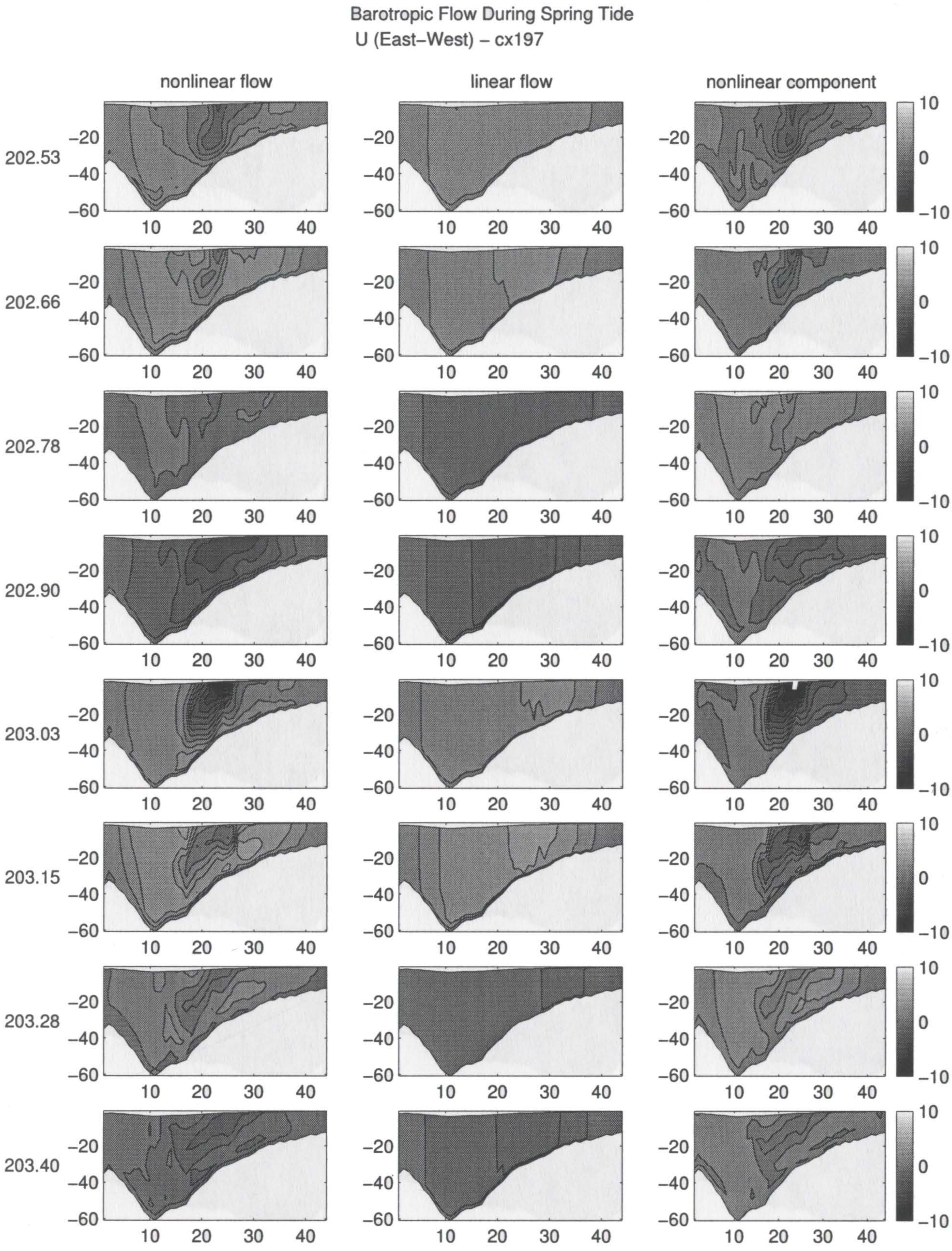

Figure 4.5: Linear vs. Nonlinear flow at cx197 (inner basin) during a spring tide. First column shows the tidal flow during a spring tide for the nonlinear model, the second column shows the tidal flow at the same time for the linear model. The difference between the two model runs is shown in the third column. Contour intervals are drawn at 1cm/s. Time (Julian days) for each row is listed downwards along the left side of the figure. X-axis represents grid points, one grid point represents 50 metres. Y-axis represents depth in metres.

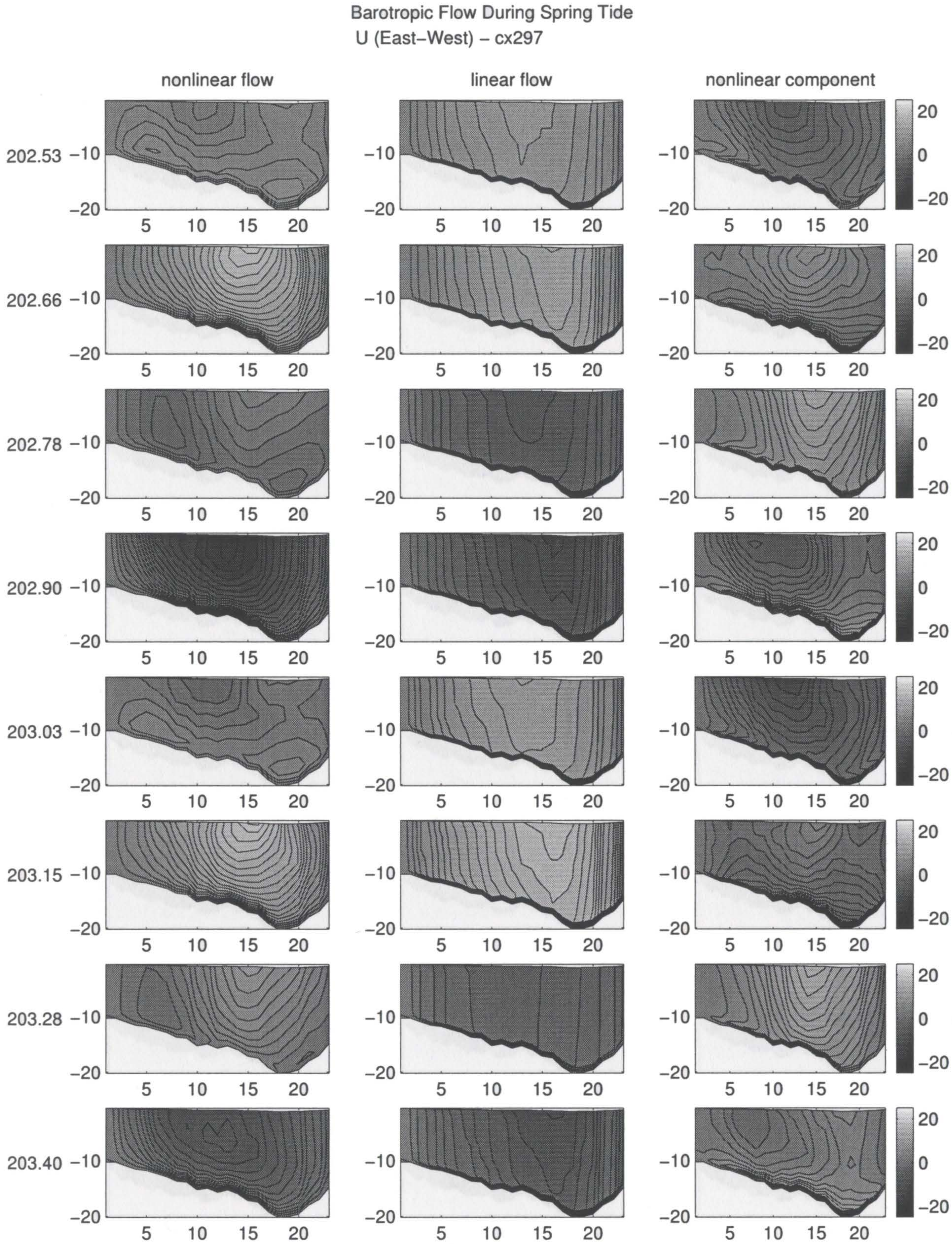

Figure 4.6: Linear vs. Nonlinear flow at cx297 (the sill) during a spring tide. First column shows the tidal flow during a spring tide for the nonlinear model, the second column shows the tidal flow at the same time for the linear model. The difference between the two model runs is shown in the third column. Contour intervals are drawn at 1cm/s. Time (Julian days) for each row is listed downwards along the left side of the figure. X-axis represents grid points, one grid point represents 50 metres. Y-axis represents depth in metres.

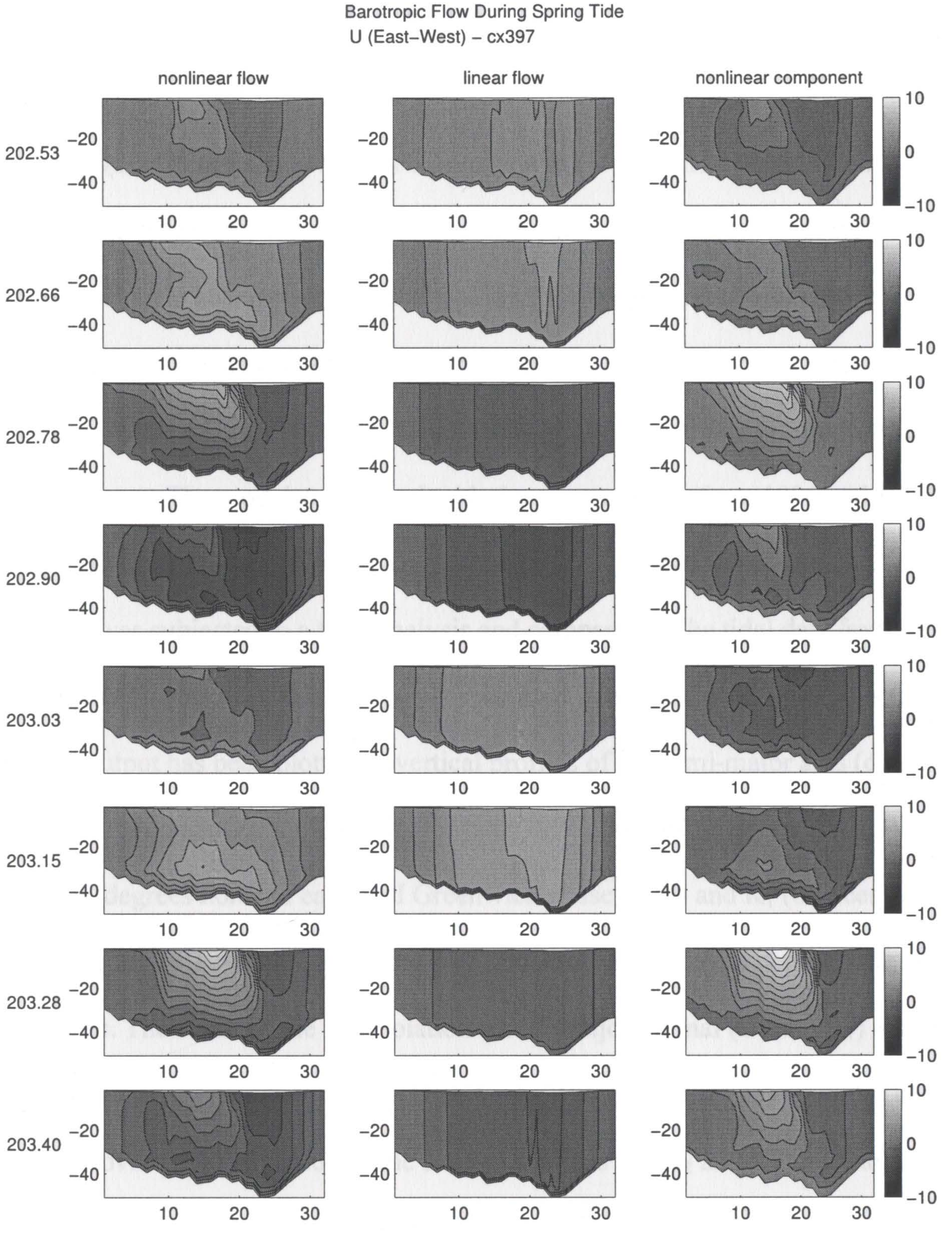

Figure 4.7: Linear vs. Nonlinear flow at cx397 (seaward of the sill) during a spring tide. First column shows the tidal flow during a spring tide for the nonlinear model, the second column shows the tidal flow at the same time for the linear model. The difference between the two model runs is shown in the third column. Contour intervals are drawn at 1cm/s. Time (Julian days) for each row is listed downwards along the left side of the figure. X-axis represents grid points, one grid point represents 50 metres. Y-axis represents depth in metres.

4.2.2 The Tides of a Stratified Fluid

4.2.2.1 The Main Tidal Constituents

Han (2000), in a study of tidal currents on the Newfoundland shelf using the model ECOM-si (a POM variant) finds that tidal currents in shallow areas were sensitive to stratification. He also reports that that phase of the tidal currents in sensitive to the stratification. A comparison of the diurnal and semi-diurnal tidal constituents to determine what if any influence stratification has on the tidal flow as it propagates along the inlet follows. The model was forced with the observed tide from 1996 and 1997 to produce a 30-day simulation for each stratification as described in section 4.1. The hourly model data was subjected to a tidal analysis and compared to the tidal data from the observations. The result of this analysis is presented in two different ways. Graphically, the model output has been plotted as vertical profiles of the semi-major axis (cm/s) of the tidal ellipse for constituents M_2 and K_1 for both 1996 and 1997 (Figures 4.8-4.9). The inclination (degrees north of east) and Greenwich phase of M_2 and K_1 (degrees) are shown in Figures 4.10-4.13. The output was also interpolated to the depth of the mooring observations. The result of the interpolation for the major diurnal (O_1 and K_1) and semi-diurnal (M_2 and S_2) constituents is given in Tables B.5-B.8 (semi-major axis). Tables B.9-B.10 provide the inclination of the semi-major axis for M_2 and K_1 and Tables B.11-B.12 the Greenwich phase for M_2 and K_1.

At mooring M1-96, the introduction of stratification makes little difference to the amplitude of the tidal currents with the exception of O_1. The amplitude of O_1, at 10 metres depth, increases from close to zero in the barotropic fluid (Table B.1, nonlinear model) to reach an amplitude of 0.1 cm/s for all three stratifications (Table 4.5). This increase in amplitude makes the modelled tide consistent with the observed tidal signal at 10 metres depth for mooring M1-96. However, the observed O_1 tide increases with depth, this behaviour is not replicated by the model.

At M2-96 the tidal constituent O_1, when compared to the nonlinear barotropic model remains relatively constant at 10 metres depth and decreases by almost 50% near 20 metres depth (the actual depth of this observation was 17 metres) (Tables B.2 and B.5). Although the O_1 current amplitude is still weak compared to the observed value at 10 metres depth, the observed value has a large uncertainty associated with it; the 95% confidence interval having the same magnitude as the estimated value from the data. The decrease of 50% in the estimated value near 20 metres depth brings the modelled tide into agreement with the observed value. Constituent K_1 is poorly represented by both the barotropic and stratified models. The K_1 current increases between 25-50% for stratification A at the 10 metre level (Tables B.1 and B.5) but the model value of 0.3 cm/s for stratification A (Table 4.5) is still only 30% of the observed value for this tidal constituent at this depth. Near 20 metres depth, stratifications A and C both show an increase of between 50%-100% with the K_1 current doubling from 0.1 cm/s to 0.2 cm/s. The observed value at this depth is 1.0 cm/s, however, so the K_1 current is poorly represented at M2-96.

The lunar semi-diurnal constituent, M_2, decreases by approximately 15% with the introduction of stratification into the model when compared to the model run with a barotropic fluid (Tables B.7, B.1 and B.2). The observed value is 3.4 cm/s much greater than the typical value of 1.2 cm/s at 10 metres depth for the model runs. There is good agreement between the observed and modelled values of the M_2 current at 17 metres and

44 metres with all modelled values lying within the 95% confidence interval of the observed values. Stratification has also reduced the M_2 current at 17 metres depth by approximately 5-10% compared to the model output from a barotropic fluid Tables B.1 and B.2). The solar semi-diurnal constituent, S_2, shows no significant changes at the 10 metre depth at mooring M2-96 when compared to the barotropic model run and only achieves approximately 35% of the observed values for this location. The values of the S_2 tidal current have increased by approximately 5-10% at 17 metres depth but remain much weaker than the observed values. The model values of 0.5 cm/s achieving only 50% of the observed value of 1.0 cm/s. The S_2 tidal current of the model runs is representative of the observed values at 44 metres of depth where there is close agreement.

At the sill, M3-96, all tidal currents, with the exception of constituent O_1 at 15 metres depth, are still too weak when compared to the observations achieving, at best, 65% of the observed values. When compared to the model run for a barotropic fluid (Tables B.1 and B.2), however, there is some improvement. Specifically, at 10 metres depth, O_1 increases by 50%; K_1 increases by approximately 15% for stratifications A and B. M_2 increases between 10%-15% for all stratifications, the smallest increase occurs for stratification C and the greatest increase in stratification B. S_2 increases between 25%-35%, stratification C having the smallest increase and stratification B showing the greatest improvement. At 15 metres depth, constituent O_1 increases by 100% and is now in agreement with the observations. Although the amplitude of K_1 increases by 100% for stratifications A and B and 85% for stratification C it is still only 50%-60% of the observed values for 1996. Graphically (Figure 4.9) we see that the increase in amplitude associated with stratification A and B produce a maximum tidal current at 15 metres depth. The strongest tidal current, M_2, increased by 40% at this location (M3-96, 15 metres depth) compared to the barotropic model, but still only achieves 65% of the observed value. Apart from the agreement for O_1 at this location, the M_2 tide at this depth represents the best agreement found for the tidal currents over the sill. The principal solar semi-diurnal constituent S_2 increases by 75%-90% (stratification A weakest improvement, stratification C strongest improvement) when compared to a barotropic fluid but this improvement still leaves the modelled S_2 tidal current representing only 45%-55% of the observed values.

Seaward of the sill (moorings M4-96 and M5-96) stratification appears to have little effect on the tidal currents with the model. There is no significant difference between the tidal currents for the model runs with a stratified fluid and those of a barotropic fluid. In this region of the model domain, we find that the modelled values for O_1 at 10 metres depth are only 10% of the observed 1.1 cm/s current at M4-96 and approximately 15% of the observed 0.6 cm/s at M5-96. There is closer agreement for the O_1 tidal currents at 20 and 45 metres depth at M4-96 and M5-96 with the modelled values of 0.1-0.2 cm/s within the 95% confidence intervals of the observed 0.2-0.3 cm/s O_1 currents.

K_1 currents from the model also fail to represent the tide at the 10 metres depth. Although the observed K_1 tidal signal is relatively noisy at all depths, with the 95% confidence interval almost equal to the amplitude of the signal, the currents at 10 metres depth for M4-96 are only 25% of the observed value of 0.8 cm/s. At 20 and 45 metres depth, both the model and the observed currents range from 0.2-0.3 cm/s. At M5-96 the

K_1 tidal currents generated by the model only achieve 40%-50% of the observed values 0.4-0.5 cm/s at all depths.

Generally, the introduction of stratification in the inlet is found to have a direct influence on the tidal structure at the sill and within the inner basin. Seaward of the sill, the tidal structure, generated by the model, is not greatly influenced by the depth of the main pycnocline. Clearly stratification has a significant role in the dynamics in the region of the sill. The influence of stratification at the sill on the tide results in a change in the tidal flow within the inner basin. Seaward of the sill, the tide is dominated by the barotropic tide as it enters inlet from the mouth with stratification having little influence on the tidal currents in this region of the inlet.

The response of the tidal structure to stratification in the vicinity of the sill may be analysed in greater detail by comparison of the mooring data from 1997 and corresponding model output (Tables B.6 and B.8). Within the inner basin, mooring M1-97 is located towards the southern coastline. Tidal analysis from M1-97 reveals that the O_1 current at 7.5 metres depth decreases by 50% when the main pycnocline drops below the level of the sill in the outer channel (Table B.6, stratification C). When the main pycnocline lies at or above sill depth (Table B.6, stratifications A and B), the strength of the O_1 current (7.5 metres) is the same strength as the tidal current for a barotropic fluid (Table B.3). The maximum current achieved by the model is only 50% of the observed value but does fall within the 95% confidence interval of the observation due to the amount of noise present in the measurements. Stratification does not appear to influence the strength of the O_1 tide below the sill (21 metres depth) which remains at least 50% weaker than the observed value.

Stratification appears to have little influence on constituent K_1 at the 7.5 metre depth when compared to the tidal signal calculated from the barotropic model (Table B.3). The magnitude of the K_1 current at 7.5 metres depth is in good agreement with the observed values for all model runs. At 21 metres of depth, the models indicate that the K_1 tidal current is weakest when the pycnocline lies above the sill (Table B.6, stratification A) decreasing from 0.3 cm/s to 0.2 cm/s. For all model runs the K_1 tidal currents at this location are approximately 50% weaker than observations. For the main lunar semi-diurnal constituent M_2 the tidal currents generated by the model are similar in amplitude to those of a barotropic fluid although slightly weaker at both 7.5 and 21 metres depth when the main pycnocline is located at sill depth (stratification B).

The modelled M_2 current (Table B.8) is also 50% weaker than the observed value at 7.5 metres depth and approximately 50% stronger than the observed current at 21 metres depth. The prinicipal solar semi-diurnal constituent S_2 decreases by about 20% when the pycnocline is located either above the sill depth (Table B.8, stratification A) or below the sill depth in the outer channel (Table B.8, stratification C). The amplitude of modelled S_2 tide is in good agreement with the observations at 21 metres depth but only 50% of the amplitude of the observed value at 7.5 metres depth.

Mooring M2-97 is located near the centre of a north-south line drawn across the inner basin. It is at this location where we see the greatest influence of stratification on the tidal structure of the inner basin. At M2-97, the O_1 tidal current in the stratified model runs is 25% weaker than the barotropic O_1 current at 7.5 metres depth (Table 4.3). All of the modelled O_1 tides were no more than 50% of the amplitude of the observed 7.5 metre O_1 current (which was a very noisy signal). At 21 metres depth the model runs and observations are in relatively good agreement for the O_1 constituent. The amplitude of the O_1 current increases by approximately 65% when the main pycnocline is located above the depth of the sill (Table B.6, stratification A) compared to those model runs when the main pycnocline was located at or below sill depth (stratifications B and C).

The K_1 tidal current at 7.5 metres depth decreases approximately 25% when stratification is introduced into the model (Tables B.3 and B.6). All model runs, including the barotropic model, produced K_1 tidal currents at this location of no more than 25% of the observed values. At 21 metres depth, modelled currents were in good agreement with observed values with the best agreement occuring when the pycnocline was located either above the sill or below the sill in the outer channel (Table B.6, stratifications A and C). The amplitude of the K_1 current for these model runs increases by approximately 50% compared to the K_1 tidal currents for the barotropic model (Table B.3).

The lunar semi-diurnal current, M_2 is poorly represented at 7.5 metres depth, the strongest tidal current produced by the models was 1.5 cm/s (Table B.8, stratifications A and C) compared to an observed M_2 tidal current of 4.5 cm/s. Below the depth of the sill, at 21 metres depth, the observed current (1.2 cm/s) is in close agreement, although slightly weaker than the modelled tidal currents of 1.4 cm/s, 1.3 cm/s and 1.5 cm/s for stratifications A, B and C respectively (Table B.8). The barotropic modelled M_2 tidal current was 1.3 cm/s (Table B.3).

Stratification was not found to produce any significant difference in the modelled tides for the principal lunar semi-diurnal constituent, S_2. Similar to the results of the M_2 current, the modelled S_2 currents were in good agreement with the observed value of 0.6 cm/s below the level of the sill (21 metres depth) while much too weak at 7.5 metres depth where the maximum current produced by the model was only 25% of the observed value of 2.2 cm/s (Table B.8). The barotropic model also produced an S_2 tidal current between 0.5-0.6 cm/s at both observation levels (Table B.3).

To the northern side of the inner basin, only one current observation was available for comparison to the model. This current meter was located at 7.5 metres depth. Similar to the model output at other locations in the model domain, the near surface flow is poorly represented. Stratification appears to have little influence on the tidal currents at this location, with all model runs producing tidal currents of similar amplitude, all of which are approximately 25% of the observed values for all four of the tidal constituents: O_1, K_1, M_2 and S_2.

At the sill, mooring M4-97, the comparison of the model output to the observed values is very similar to the results at mooring M3-96, this is not surprising given the proximity of these locations to each other in the observations programs of 1996 and 1997 and in the model domain, separated by only a few grid points.

For constituent O_1 the stratified model runs produced an O_1 tidal current of 0.8 cm/s at 14 metres depth when the main pycnocline is located at or above sill depth (Table B.6, stratifications A and B). This is a significant improvement compared to the 0.4 cm/s current produced by the barotropic model (Table B.4) and agrees with the observed value of 0.8 cm/s. The is no significant change in the tidal currents at 7.5 metres depth between all model runs and the observed O_1 current of 2.0 cm/s is at least 3 times stronger than the model currents of 0.6-0.7 cm/s.

When the main pycnocline is located at the depth of the sill (stratification B), constituent K_1, at 7.5 metres depth, is approximately 30% stronger compared to the K_1

current generated by the model when the main pycnocline is located above or below the sill (stratifications A and C) (Table B.6). The barotropic model produced a K_1 tide of 1.2 cm/s. The K_1 tide appears to decrease when the main pycnocline lies either above or below the sill. At 21 metres depth, stratification B (main pycnocline at sill depth) produces a K_1 current 35% stronger than the barotropic model. The observed values for the K_1 current at both 7.5 and 14 metres depth are, typically, 2 to 2.5 times stronger than those currents produced by the model.

The M_2 tidal currents observed are also at least 2 times stronger than the currents produced by the model. There are some differences in the M_2 tidal currents as stratification is introduced. At 7.5 metres depth, the M_2 current is found to be strongest, 5.5 cm/s when the main pycnocline lies above the level of the sill (Table B.8, stratification A), the strength of the M_2 current is equal to the strength of the barotropic model.. As the main pycnocline drops to the depth of the sill and below (stratifications B and C) the amplitude of the M_2 current at 7.5 metres depth is decreases by almost 10%. At 14 metres depth, the introduction of stratification into the model increases the M_2 tidal currents to 5.0-5.2 cm/s compared to the barotropic M_2 tide of 4.4 cm/s, approximately 10-15%.

Constituent S_2 is also influenced by the presence of stratification in the model. The amplitude of the S_2 current is strongest (2.1-2.4 cm/s at 14 and 7.5 m respectively) when the main pycnocline is located at sill depth (stratification B), with this stratification the S_2 tidal current is in good agreement with the barotropic model (1.8-2.5 cm/s at 14 and 7.5 m, respectively). For the model runs where the main pycnocline was located either above or below the depth of the sill, the S_2 tidal current (1.7-1.9 cm/s) was found to be 25%-30% weaker at 7.5 metres depth and approximately 10% weaker (1.7 cm/s) at 14 metres depth.

The modelled M_2 and S_2 tidal currents suggest that the sill acts as a filter for the main semi-diurnal tidal currents, with the stratification playing a significant role in determining the allowed frequencies through the sill. The M_2 is strongest when the main pycnocline is located above or below the sill and decreases as the depth of the main pycnocline increases. The S_2 current is found to be strongest when the main pycnocline is located at the same depth as the sill and significantly weaker when the main pycnocline is located either above or below this depth.

Seaward of the sill, the model output from moorings M5-97, M6-97 and M7-97 indicates that stratification does influence the tidal structure. At M4-96, located approximately 0.5 kilometres further from the sill, stratification appears to have little influence on the tide generated by the model.

Towards the southern coastline, model data from mooring M5-97 (Table B.6) indicates that the introduction of stratification decreases the O_1 tidal current at 7.5 metres depth (0.1 cm/s) by approximately 50% when compared to the barotropic model (Table 4.3). The modelled O_1 tidal current is only 20% of the observed values at 7.5 metres depth (0.1 cm/s modelled vs. 0.5 cm/s observed). When the main pycnocline is located above the depth of the sill, the O_1 current at 21 metres depth increases from 0.1 cm/s to 0.2 cm/s; almost in agreement with the observations (0.3 cm/s) at this level.

K_1 tidal currents at 7.5 metres depth at M5-97 are found to decrease as the depth of the main pycnocline increases. The model output shows a decrease from 0.3 cm/s for the barotropic model and stratification A compared to 0.2 cm/s for stratifications B and

C. At 21 metres depth, all of the model runs produce a K_1 tidal current of approximately 0.3 cm/s, three time stronger than the observed value of 0.1 cm/s. The 95% confidence interval of the observation was ±0.3 cm/s indicating a high degree of uncertainty.

The tidal currents of the principal lunar and principal solar semi-diurnal constituents M_2 (1.5-1.6 cm/s) and S_2 (0.5-0.7 cm/s) generated by the model runs at 7.5 metres depth are 50% weaker than the observed 3.0 cm/s M_2 current and 1.3 cm/s S_2 current. At 21 metres depth, modelled currents at M5-97 for both M_2 (1.6-1.7 cm/s) and S_2 (0.5-0.6 cm/s) agree well with the observations (M_2: 1.4 cm/s; S_2: 0.4 cm/s). Similar to the model output at M4-97 the modelled S_2 tide at M5-97 was strongest when the pycnocline was located at the same depth of the sill. Compared to the barotropic model (Tables B.3 and B.4), there were no significant changes to the modelled M_2 tide when stratification was introduced.

Mooring M6-97 is located in the centre of a north-south line across the inlet and may be considered to be most directly in line with flow across the sill. Unfortunately, due to an instrument failure there are no observations to compare the tidal currents at 7.5 metres depth for the particular mooring. As a result a comparison to observations may only be conducted for depths below that of the sill. At M6-97, the modelled O_1 tidal current agrees with the observations (0.3 cm/s) at both 21 and 33 metres depth when the main pycnocline is located above or at the depth of the sill (Stratifications A and B). When the main pycnocline was located below the depth of the sill (stratification C), the O_1 current increases by 65% to 0.5 cm/s. This increase occurs at both 21 and 33 metres depth.

Graphically (Figure 4.10) we see that the amplitude of the K_1 current is relatively constant through all depths when the main pycnocline is located above the depth of the sill (Stratification A) increasing only slightly near the surface. The graph also reveals that stratification B and C have a maximum near 30 metres depth and surface currents of approximately 0.6 cm/s.

The K_1 tidal current increases at M6-97 as the depth of the main pycnocline increases. As the main pycnocline deepens (from 10 metres depth in stratification A to approximately 25-30 metres depth in stratification C), the amplitude of the K_1 current increases from 0.4 cm/s to 0.6 cm/s. This increase occurs at both 21 and 33 metres depth and suggests that the deepening of the main pycnocline may result in an increase in the amount of energy associated with the incident K_1 current that is reflected at the sill. While the modelled K_1 current (0.4-0.6 cm/s) at 21 metres depth is in good agreement with the observed value of 0.5 cm/s, the modelled currents at 33 metres depth (0.4-0.6 cm/s) were two to three times stronger than the observed value of 0.2 cm/s (Table B.6).

The M_2 tidal currents generated by the model at 33 metres depth are much stronger than the observed values. All modelled runs produced a M_2 tide with an amplitude between 2.0-2.1 cm/s while the observed values indicated an M_2 current of 0.5 cm/s (Table B.8). At 21 metres depth, the model and the observations agree with an M_2 tide of approximately 1.8-1.9 cm/s. The depth of the main pycnocline does not appear to influence the amplitude of the M_2 tide at this location below the depth of the sill. However; the barotropic M_2 tide (2.1 cm/s at 21 metres depth) is approximately 15% stronger (Table B.4) suggesting that some energy may be extracted from the tide in the presence of stratified flow.

The S_2 current at 33 metres depth was observed to be 0.2 cm/s while the modelled S_2 current was four times stronger (0.7-0.9 cm/s). There is good agreement of the S_2 tide at 21 metres of depth with both observations and models indicating amplitudes of 0.7-0.8 cm/s. The model output again shows that the S_2 current is strongest when the main pycnocline is located at the depth of the sill (Stratification B) with the S_2 current amplitude increasing from 0.7 cm/s to 0.8 cm/s at 21 metres depth and also increasing from 0.7 cm/s to 0.9 cm/s at 33 metres depth (Table B.8).

Towards the northern coastline, mooring M7-97 shows that the modelled O_1 currents of 0.1 cm/s are relatively weak compared to the observed values of 0.3 cm/s at both 7.5 and 31 metres depth (Table B.6). The O_1 currents are weakest when the main pycnocline lies below the depth of the sill. At 33 metres depth, the modelled currents for this particular stratification (stratification C) are less than 0.05 cm/s (recorded in Table 4.6 as 0.0 cm/s). There is good agreement between the observed and modelled K_1 current (0.3 cm/s) at 33 metres depth. The modelled K_1 currents are 50% weaker than observed values at 7.5 metres depth (0.2-0.3 cm/s vs. 0.5 cm/s).

Compared to the large errors found in the model currents near the surface (7.5 cm/s) at other mooring locations, the amplitude of the M_2 tidal current (2.0-2.1 cm/s) at mooring M7-97 agrees very well with the observations (2.3 cm/s). Figure 4.9 indicates that this agreement extends down to approximately 20 metres. However, the tidal observations at the 20 metre level are questionable due to an instrumentation error that produced a 30 day gap in the velocity measurements, the tidal analysis presented in the figure was evaluated over the longest period of continuous data (about 30 days out of the

100 day record). At 33 metres depth the modelled M_2 current (2.0 cm/s) are 40% stronger than the observed value (1.4 cm/s).

Modelled tidal currents for S_2 again reveal that location of the main pycnocline may influence the strength of this current within the inlet. The strongest S_2 tide is found when the pycnocline is located at the same depth as the sill (Table B.8, stratification B). However, the observed value of 1.3 cm/s at 7.5 metres depth is almost 1.5-2.0 times as strong as the modelled currents (0.7-0.9 cm/s). At 33 metres depth, model output from stratifications A and C reveal an S_2 tide of approximately 0.7 cm/s compared to the observed value of 0.6 cm/s. Stratification B, which has an increased value of the S_2 current (0.9 cm/s) at this location appears to be too strong.

A comparison of the model output to the data for the inclination and phase will not account for the influence of the wind that may influence the orientation of the tidal ellipse near the surface. It is not possible to remove the unknown wind effects from the observations so the comparison of the observations to the model output with only tidal forcing in the near surface regions may not be in very good agreement. The influence of the wind should be most notable in those currents with the weakest amplitude, we anticipate that the tidal current ellipses near the surface for the K_1 currents observations may therefore have a large amount of error associated with both the inclination and the phase. The M_2 tidal currents will be less influenced by the wind due to their greater amplitude.

The inclination (Table B.9, Figure 4.10) and phase (Table B.11, Figure 4.12) of the K_1 tidal ellipses at M1-96 indicates that the observed K_1 current rotates in a clockwise manner from the surface to the bottom (from 70° to 40°), while the current ellipse in the model rotates in a counter-clockwise manner (40° to 50°). This change in the rotational direction of the current ellipses is most likely due to wind forcing; the error associated with the orientation of the tidal ellipse (inclination error) is significantly larger at 10 metres (± 89°) than at 21 (± 29°) and 45 metres depth (± 23°). The phase (Table B.11) of the K_1 current at M1-96 also has a large error (± 116°) associated with the near surface observations. Despite this large error there is good agreement between the phase of the observed tide (~280°) and the modelled tide (~300°) at this location except at 45 metres depth where there is a phase difference of approximately 130 degrees between the observed value (170°) and the model (300°).

At M2-96, the orientation of the tidal ellipses for the observed and modelled K_1 tide agree reasonably well at all depths. The inclination of the observed (modelled) tidal ellipse(s) rotate from 5° (10°-20°) at the surface through the principle axis to 170° (155°-160°) at 45 metres depth. Both the observed tide and the modelled tide rotate in a clockwise direction from 17 to 44 metres depth. The model output indicates that the K_1 current rotates in a clockwise direction from the surface to the bottom while the observed K_1 current rotates in a counter clockwise direction from 10 to 17 metres depth. The large error (± 87°) associated with the observed inclination of the tidal ellipse at 10 metres depth suggests (as with M1-96) that wind may be influencing the orientation of the current. There is a significant difference in the phase (Table B.11, Figure 4.12) between the observed values for K_1 and the modelled values. The observed phase difference of 90° between 20 and 44 metres depth is absent in the model output. The modelled tide appears barotropic while the observed tide indicates an internal response at 44 metres depth.

At M3-96 and M4-96 both the inclination and phase of K_1 agree quite well between the observations (inclination: 160°-170°; phase: 110°) and the model (inclination: 170°-175°; phase: 110°-125°). Mooring M3-96 is located at the sill in a region sheltered from the influence of the wind. Given the narrowness of the channel and the reduced wind forcing at this location it is not surprising that the modelled tide (without wind forcing) agrees favourably with the observed values. Mooring M4-96 is also located in a region where the influence of the wind on the observed tide should be reduced or at least directed in the along the channel direction due to local topographic features such as high surround cliff walls. The phase of the modelled K_1 (300°-310°) agrees well with the observed phase (290°-300°) at 20 and 45 metres depth while the surface currents show a phase difference of approximately 60° with the observed phase of 355° at 10 metres depth. The apparent "jump" in the phase of the K_1 tide at 50 metres depth shown in Figure 4.12 is a consequence of the tidal ellipse rotating through the principle axis as revealed in Figure 4.11.

At M5-96, model output suggests that the K_1 tide at this location is nearly barotropic with both the inclination (50°) and the phase (300°) of the modelled K_1 current remaining constant throughout the water column. The observations suggest otherwise, with the observed K_1 tide rotating in a clockwise manner (130° to 40°) from 10 to 21 metres depth then reversing and rotating in a counter clockwise direction (40° to 70°) from 21 to 45 metres depth. The large change in the phase (90° to 290°) of the K_1 tide from 10 to 21 metres is not as great as the values might suggest at first. When calculating the Greenwich Phase of the tide, the phase is measured from the principal semi-major axis of the tidal ellipse which changes from a north-westerly to a north easterly direction as the orientation of tidal ellipse rotates through 180° back to 0°. The tidal ellipses rotate through 90° between these levels so the actual change in the phase is only 90°.

The comparison of the orientation of the M_2 tidal ellipses at all moorings from 1996 is very good with only small variations found in the inclination of the semi-major axis (Figure 4.10, Table B.9). However, there exist differences in the phase of the M_2 tide that should be noted.

The observed tide at M1-96 shows a phase lag of approximately 50° from the instrument located at 21 metres depth and the instrument located at 10 metres depth. There is an additional phase lag of approximately 70° between the instrument located at 45 metres depth and the instrument located at 21 metres depth. The data suggests that the tide arrives first at depth and later at the surface of the inlet at this location. This behaviour is noticeably absent in the model with the phase of the M_2 tidal currents remaining constant (80°) throughout the entire water column.

At M2-96 the M_2 tide arrives first at a depth of 17 metres, then at the near surface depth of 10 metres, lagging the arrival time at 17 metres depth by 12°, the arrival time at 44 metres lags the arrival of time at 17 metres depth by 32°. The model does not reflect this behaviour, in the model runs, for all three stratifications tested, the tide is found to arrive at 44 metres depth first, the time of arrival at 10 and 17 metres depth is almost identical lagging the bottom current by approximately 20°. The Greenwich Phase of the model output and observations at 10 metres depth are almost equal (varying between 82°-85°); the model, which is statically stratified, fails to accurately reflect the internal tidal structure.

At M3-96 the observed tide has a Greenwich Phase lag of approximately 230° and is reasonably constant over the water column differing only by 4° from 10 to 15 metres depth. The model reflects the near constant phase quite well, but lags the observation by approximately 35°, having a Greenwich Phase lag ranging from 259° to 268°.

At M4-96 and M5-96, located seaward of the sill, there is a difference in the arrival time of the M_2 tide throughout the water column. From the observations we find that the M_2 tide arrives earliest at 45 metres depth, at 20 metres depth the tide at M4-96 lags the tide at 45 metres depth by 56° while at M5-96 the tide lags the arrival time at 45 metres depth by 25°. The surface tide lags the tide at 20 metres depth by another 13° at M4-96 and by 30° at M5-96. In all of the model runs the phase of the tide at M4-96 and M5-96 is found to be nearly constant at all depths with a Greenwich phase lag of 81°-85° at M4-96 and 82°-83° at M5-96.

The inability of the model to reflect the internal structure of the M_2 tide may be associated with the static stratification of the model. With stratification held constant, it is not possible for internal waves to propagate through the domain. Mixing of temperature and salinity should permit a greater amount of internal structure to form within the model. If the model is able to propagate internal waves it may improve the ability of the model to accurately reflect the tidal structure of Clode Sound. The effect of mixing on the tidal structure of Clode Sound is investigated in Chapter 5.

In the vicinity of the sill (1997 observation program), the K_1 tidal ellipses are found to rotate in a clockwise direction with increasing depth at M1-97 for both the observed and modelled tides. However, the observed tidal ellipses are oriented further to the north east (35°-40°) than the modelled tides (0°-10°). The phase of the observed tide and the modelled tide are found to be in good agreement (Figure 4.13); the difference in the phase of the model run for stratification A (main pycnocline above sill depth) may be accounted for by the 180° difference in the orientation of the principal axis of the tidal ellipse.

At M2-97, both stratification A and B in the model runs indicate that the K_1 tide rotates in a clockwise direction with depth (A: 22° to 13°; B: 15° to 8°). However, the observations and the model run for stratification C indicate a tidal current that rotates in a counter clockwise direction with depth (C: 12° to 17°, obs.: 179° to 19°). It is not clear from the model output that the wind may account for the change in the orientation of the tidal ellipse with depth, stratification may also contribute to the direction of the tide at this location. The observations also indicate that the Greenwich phase of the tide differs by approximately 60° between 7.5 and 21 metres depth (Table B.10 and B.12), this phase difference is not reproduced by the models where the largest phase difference between the two levels was only 20° (Table B.12, stratification A).

There is good agreement between the observations and modelled tide at M3-97 where the observed tidal ellipse is oriented at 165° compared to the 175°-180° of the modelled K_1 tide. The phase of the K_1tide at this location was observed to be 81° and the modelled K_1 tides have amplitudes of 115°-125°. The modelled tides lag the observed tide by as much as 40°.

At the sill (M4-97), both the orientation of the tidal ellipse (110°-125°) and the phase (165°-175°) of the K_1 tide are in good agreement. As this mooring is located close to M3-96 so we should expect little influence by the wind at this location. Seaward of the sill, all of the modelled tides are found to rotate in a clockwise manner with increasing depth with the exceptions of the model runs for stratification A and B at mooring M5-97. The orientation of the K_1 tide remains constant for stratification A at M5-97 between 7.5 and 21 metres depth indicating that the direction of the tide above and below the main pycnocline (located near 10 metres depth) remains constant. Stratification B rotates in a counter clockwise direction with depth although the change in direction is relatively weak (only 4°) which is not significantly different once the 95% confidence intervals are taken into account. The observed K_1 tidal ellipses also appear to lie almost in the same orientation with only a 2° difference between the ellipse orientation (176°-178°) at 7.5 and 21 metres depth. The observed Greenwich Phase of K_1 at M5-97 varies between 100° (21 m) and 130° (7.5 m) and almost completely encompasses the 95°-115° phases of the modelled K_1 tides.

The observed K_1 tide at M6-97 rotates 45° in a counter clockwise direction (150° to 18°) between 21 and 33 metres depth. The modelled K_1 tides rotate clockwise and are almost constant in direction with the change in orientation of the ellipses no more than 10°. Taking into account the change in the ellipse orientation as it passes through the east-west axis, the phase of K_1 for both the observed and modelled tides ranges between 310°-320°.

At M7-97 there is good agreement between the orientation and phase of the K_1 tide. At this location the near surface tidal ellipses were observed to be oriented at 27°, the range of orientations produced by the model was 22°-29°. Mooring M7-97 is located close to the northern coastline, the agreement of the tidal ellipse orientation between the observed and modelled tides may be easily explained by the proximity of the mooring to the coastline. It is most probable that the currents in this location are steered by the local bathymetry. The phase of the modelled tides at this location (245°-255°) also agree well with the observed Greenwich Phase of 252° at 7.5 metres depth.

In the region of the sill studied during 1997 the agreement between the orientation of the observed M_2 tidal ellipses and the M_2 tidal ellipses generated by the model is quite good (Table B.10, Figure 4.11). However, the model consistently fails to achieve the proper phase variation with depth that is seen in the 1997 observations. In the case where the main pycnocline is located at sill depth (stratification B), the model produces a phase lag which is consistently different than the phase lag calculated for the M_2 tide for the other statically stratified model runs and also distinctly different than the observed tide (Figure 4.13). Within the inner basin, stratification B consistently produces a Greenwich Phase lag that differs from the phase calculated for the other model runs by approximately 120°. This difference must be a consequence of the choice of stratification because the only difference between the model runs was the temperature and salinity profiles used to initialize the model runs.

Specifically, at M1-97, the M_2 tide was found to have a Greenwich Phase of 318°-319° for stratification B while stratification A and C indicate a Greenwich Phase of 79°-83°. The Greenwich Phase lag calculated for the observations was 354° at 21 metres depth preceding the near surface tide that has a phase lag of 58°. At M2-97, stratification B has a phase lag of 328°-333° as opposed to the phase lag for stratifications A and C of 92°-95°. The is a 54° difference in the phase of the M_2 tide at 21 metres depth and 7.5 metres depth with the tide at greater depth arriving first (Greenwich Phase 21°) followed by the surface tide (Greenwich Phase 75°). At M3-97 there was no data available to determine any differences in the vertical phase of the M_2 tide due to an instrument failure.

However, at 7.5 metres depth the observed tide had a Greenwich Phase of 239° which compares well with the Greenwich Phase lag of 262° for stratifications A and C but not with the 139° phase lag for stratification B.

At the sill the Greenwich Phase of the model, 253°-267°, for stratification A and C differs by approximately 35° from the observed values of 220°-231°. This is very close to the difference found in the model runs for 1996. At this location, stratification B produced a Greenwich Phase of 130°-144°. At M4-97 the phase lag between the bottom current and the surface current calculated by the model (A: 14°; B: 14°; C: 6°) is quite good when compared to the observed lag (11°).

Seaward of the sill, at M5-97 the M_2 tide observed at 21 metres depth (206°) precedes the tide at 7.5 metres depth (240°) by 34°. All of the model runs indicate that the phase difference between the currents at these locations is only 5°-6°. Stratifications A and C lag the observed tide by approximately 30° while stratification B precedes the observed tide by between 66° (21 metres) and 104° (7.5 metres). At M6-97, the observed tide at 33 metres depth precedes the tide at 21 metres depth by 36°. The vertical phase difference in the model was only 2°-6°. There is a phase difference of 90°-95° degrees between the observed tide (180°) and the modelled tide at 33 metres depth for stratification A (269°) and stratification C (275°). The tide generated by the model for stratification B precedes the observed tide by approximately 50°. Towards the northern coastline at M7-97, there is a phase difference (70°) between the observed M_2 tide at 31 metres depth (359°) and model runs A and C (69°-70°). Model run B again precedes the observed value by approximately 50° having a phase lag of 307° at 31 metres depth.

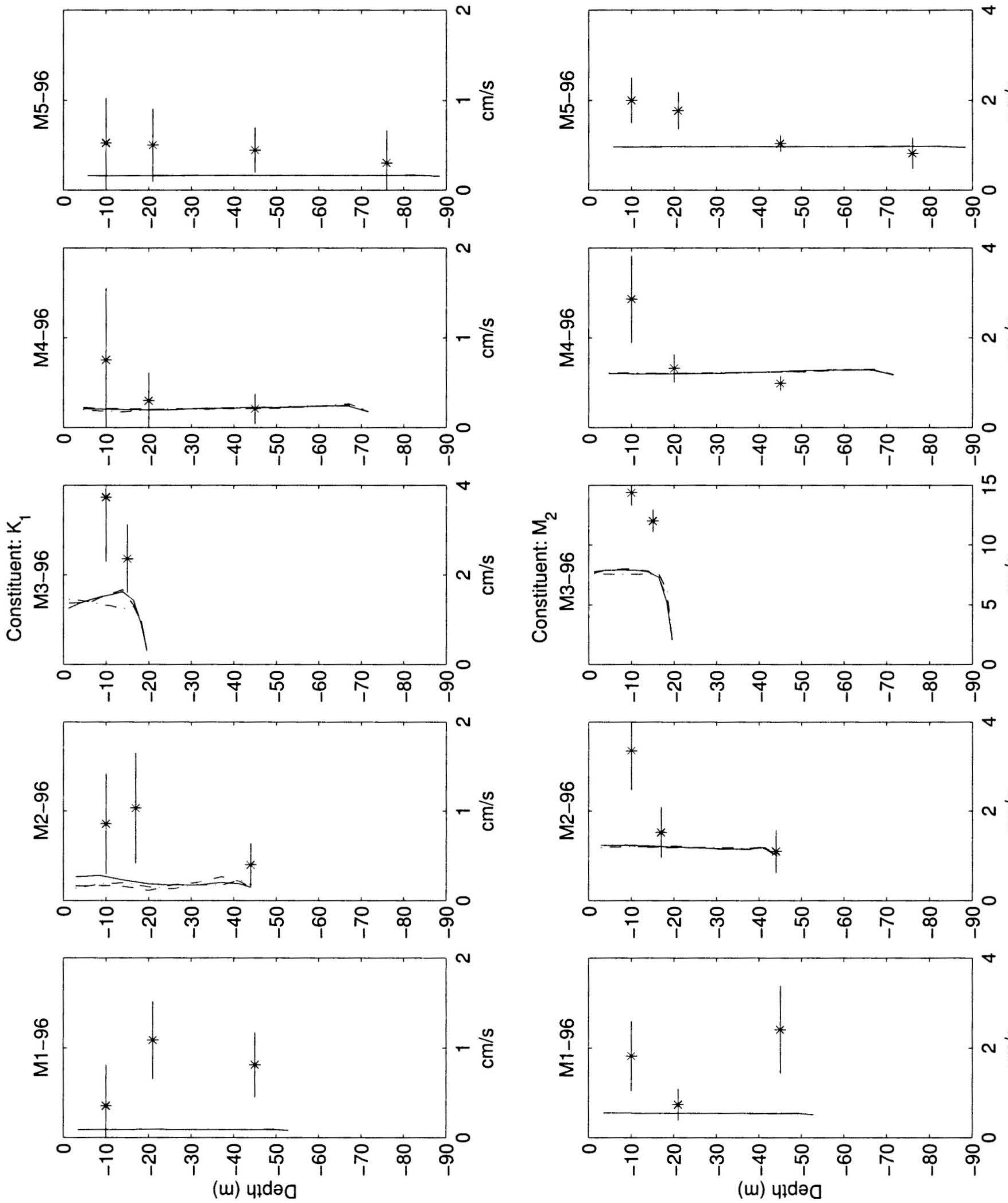

Figure 4.8 Main Diurnal and Semi-Diurnal Constituents for Stratified flow 1996: Graphs represent the semi-major axis (cm/s) of the tidal ellipses for K_1 (left) and M_2 (right). **Stratification A** (solid line), **Stratification B** (dashed line) and **stratification C** (dash-dot line). **Observations** (*) plotted with error bars representing the 95% confidence interval.

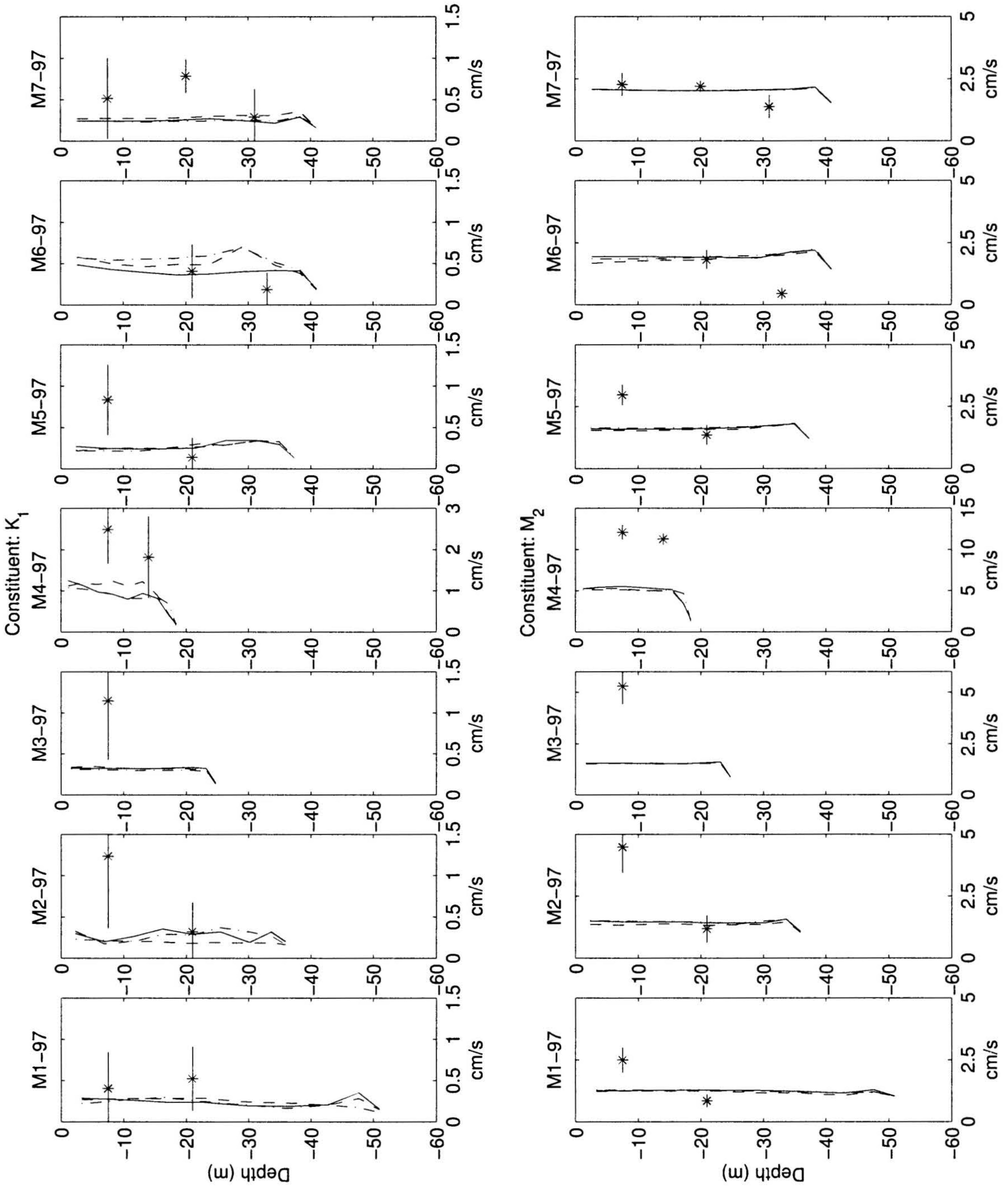

Figure 4.9: Main Diurnal and Semi-Diurnal Constituents for Stratified flow 1997: Graphs represent the semi-major axis (cm/s) of the tidal ellipses for K_1 (left) and M_2 (right). **Stratification A** (solid line), **Stratification B** (dashed line) and **stratification C** (dash-dot line). **Observations (*)** plotted with error bars representing the 95% confidence interval.

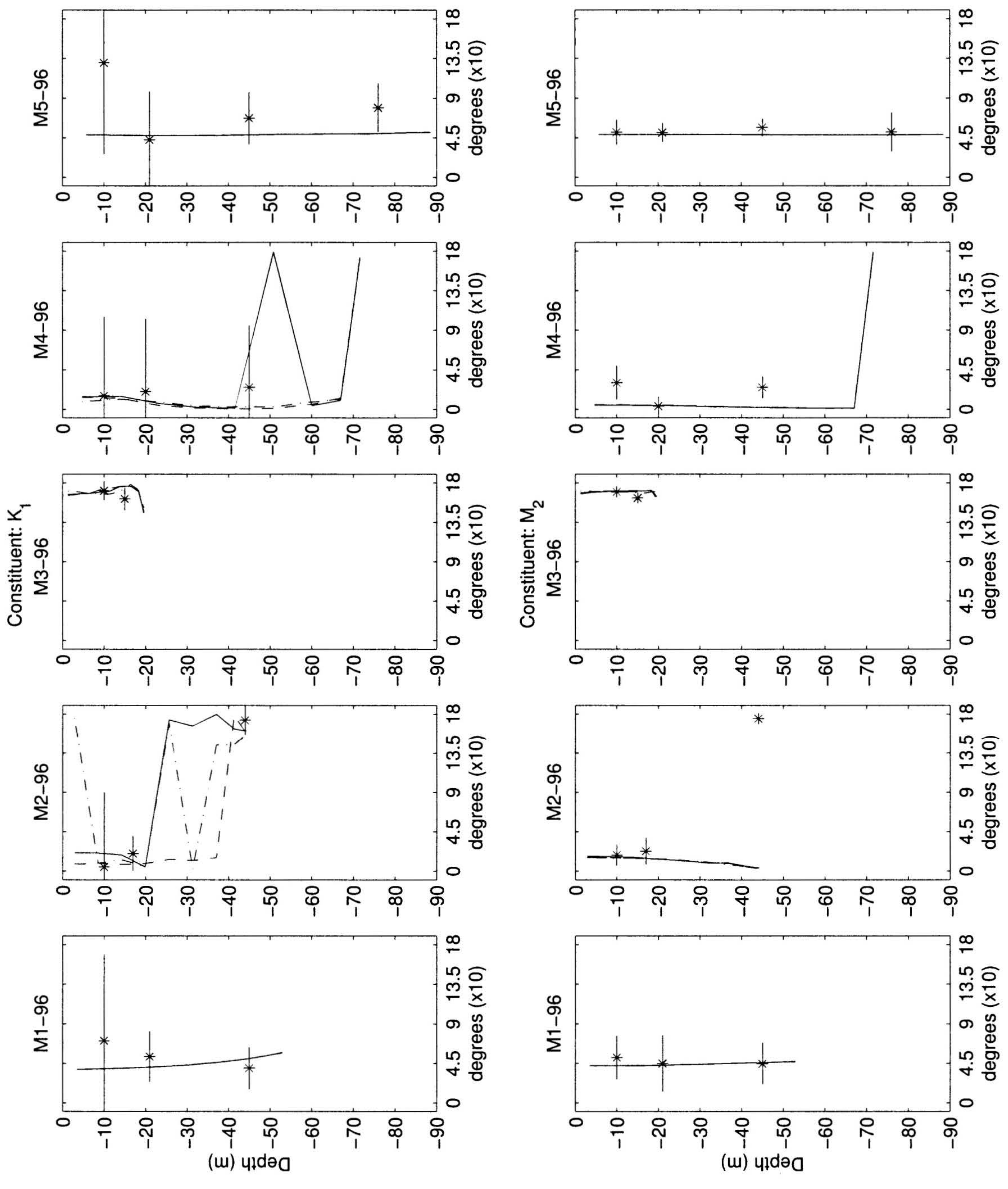

Figure 4.10 Inclination of the tidal ellipses 1996. The inclination of the $\mathbf{K_1}$ (left) and $\mathbf{M_2}$ (right) tidal ellipses for the stratified model runs. **Stratifications: A** (solid line); **B** (dashed line) and **C** (dash dot line) along with the **observed values** (*) from 1996. The error bars associated with the observations represent 95% confidence intervals. Sudden jumps from 0 to 180 degrees indicates the transition of the tidal ellipse through 0 degrees, the orientation of the tidal ellipse always being calculated as the position of the semi-major axis directed towards the north.

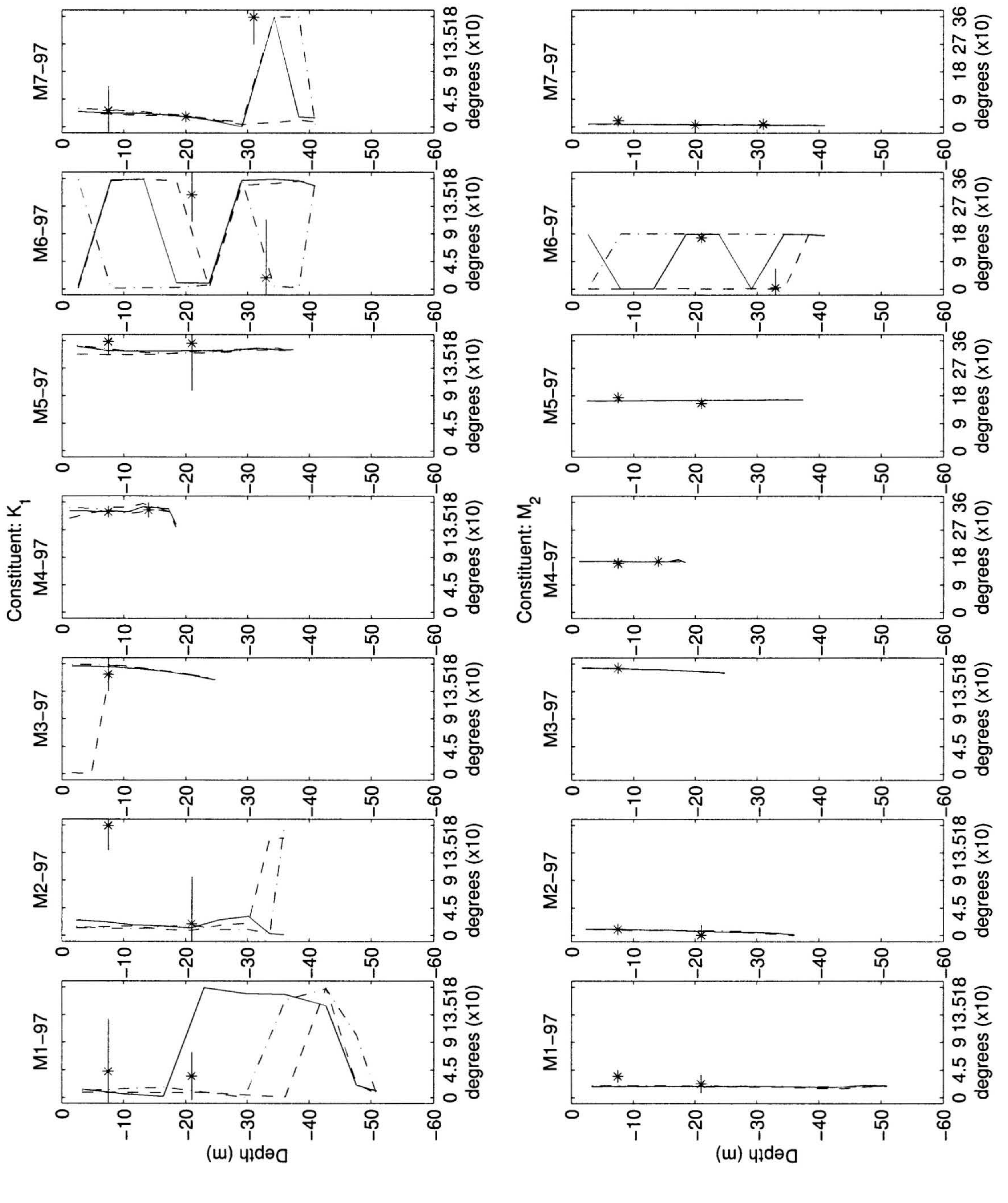

Figure 4.11 Inclination of the tidal ellipses 1997. The inclination of the tidal $\mathbf{K_1}$ (left) and $\mathbf{M_2}$ (right) ellipses for the stratified model runs. **Stratifications: A** (solid line); **B** (dashed line) and **C** (dash dot line) along with the **observed values** (*) from 1996. The error bars associated with the observations represent 95% confidence intervals. Sudden jumps from 0 to 180 degrees indicates the transition of the tidal ellipse through 0 degrees, the orientation of the tidal ellipse always being calculated as the position of the semi-major axis directed towards the north.

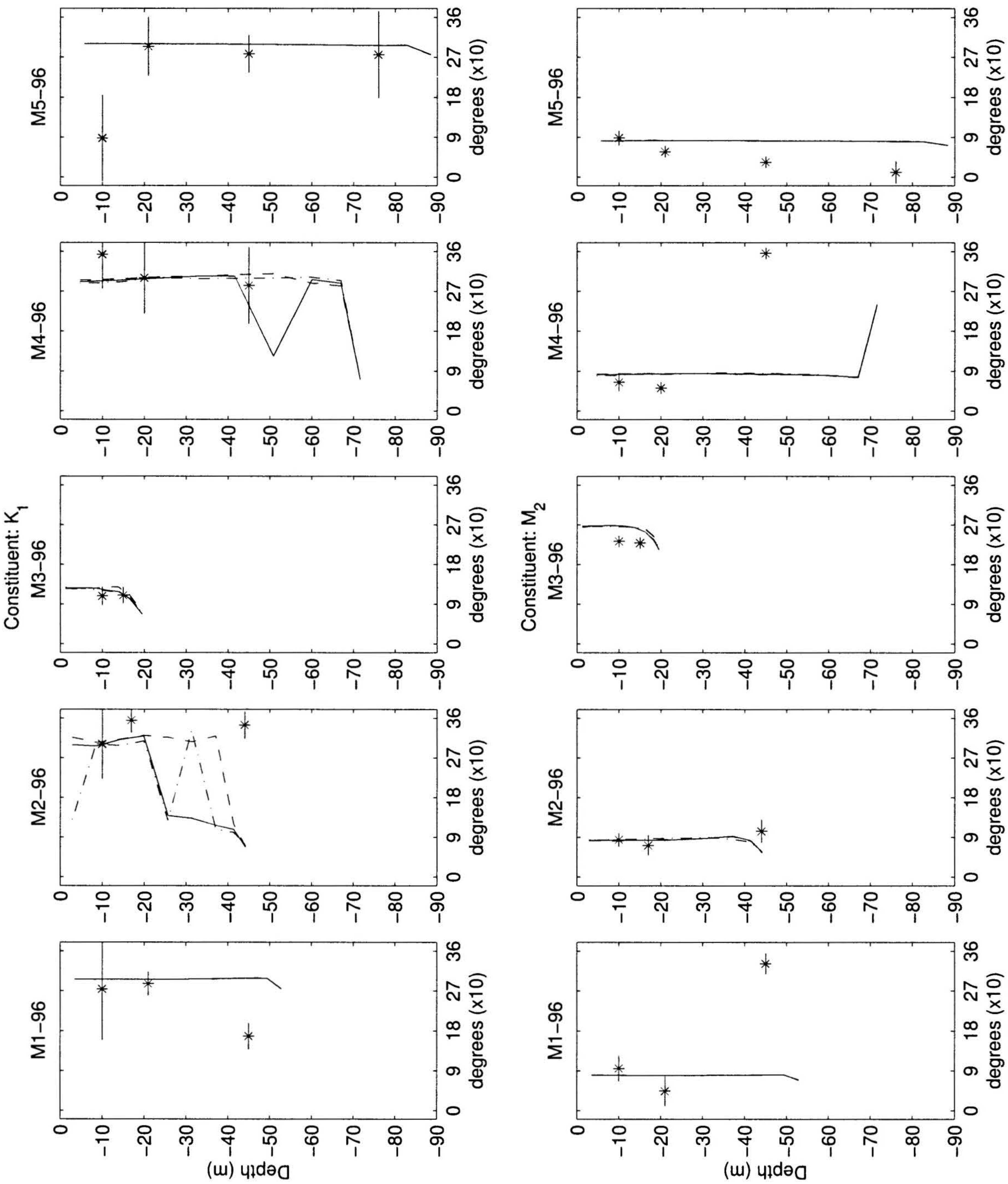

Figure 4.12 Greenwich phase of the K_1 (left) and **M_2** (right) **tidal constituents 1996. Stratifications: A** (solid line); **B** (dashed line) and **C** (dash dot line) along with the **observed values** (*). The error bars associated with the observed values represent 95% confidence intervals.

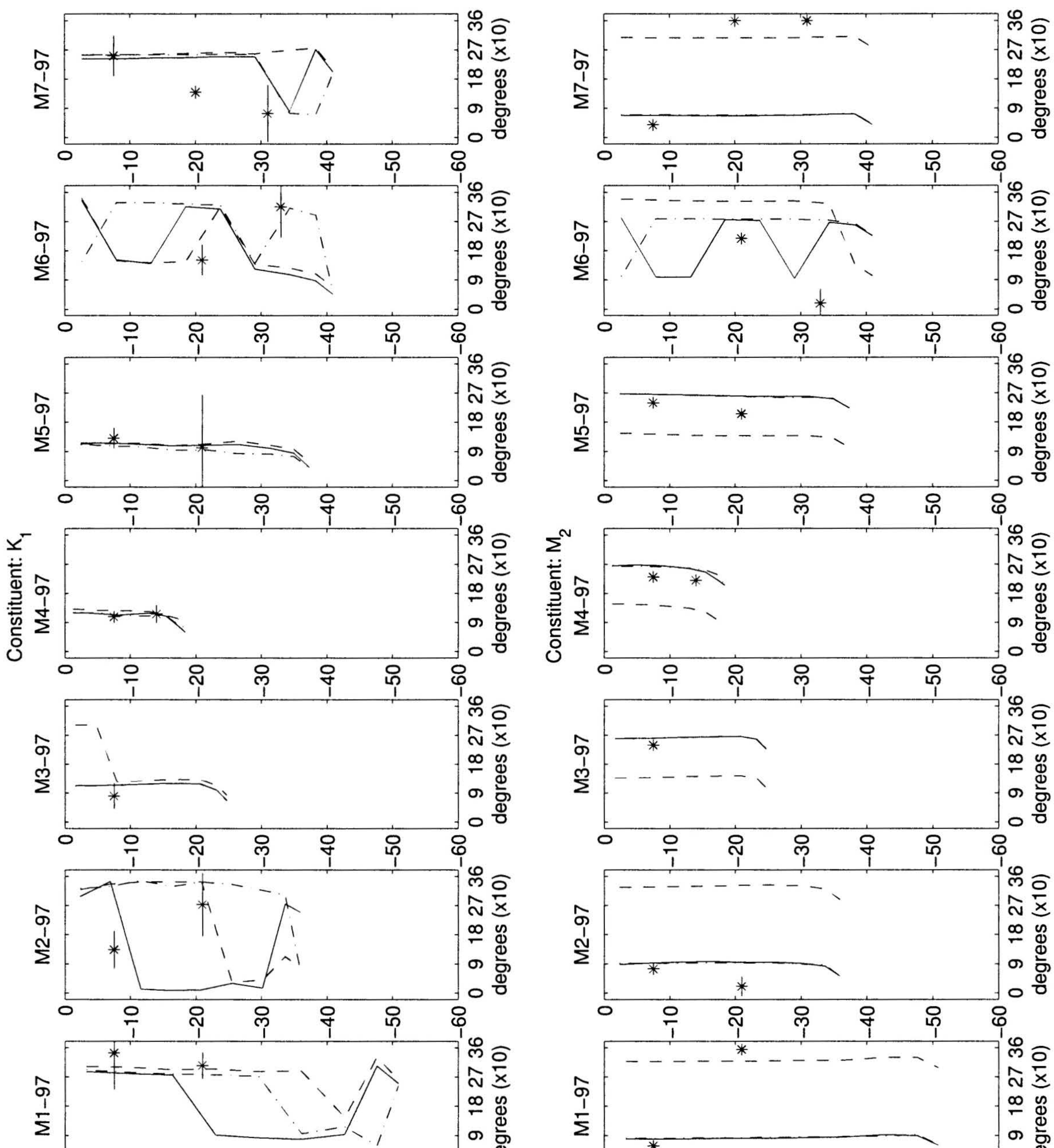

Figure 4.13 Greenwich phase of the K_1 (left) and **M_2** (right) **tidal constituents 1997. Stratifications: A** (solid line); **B** (dashed line) and **C** (dash dot line) along with the **observed values** (*). The error bars associated with the observed values represent 95% confidence intervals.

4.2.2.2 Nonlinear Tidal Constituents

The effects of nonlinearities on the main diurnal and semi diurnal constituents may be evaluated following Godin (1972). For one-dimensional flow the nonlinear term *udu/dx* may be evaluated for $u(x,t)=u_1(x)\sin(\omega_1 t)+u_2(x)\sin(\omega_2 t)$ where u_1, u_2 are velocities at frequencies ω_1, ω_2 respectively. Substituting this form of $u(x,t)$ into the nonlinear term gives (Godin, 1972):

$$u\frac{\partial u}{\partial x}=\frac{1}{2}\Big[\left(1-\cos(2\omega_1 t)\right)u_1u_1' + \left(1-\cos(2\omega_2 t)\right)u_2u_2' + (u_1u_2' + u_1'u_2)[\cos((\omega_1-\omega_2)t)-\cos((\omega_1+\omega_2)t)]\Big] \qquad (4.3.1)$$

It follows that the nonlinearity will provide a response at the additional frequencies: $2\omega_1$, $2\omega_2$, $\omega_1+\omega_2$, $\omega_1-\omega_2$. For the main diurnal (O_1 and K_1) and semidiurnal (M_2 and S_2) frequencies, the combinations that are possible are tabulated in Table 4.1.

Table 4.1: Nonlinear interaction of tidal constituents: The tidal constituents which are generated as a result of the advection term of the equations of motion. The constituents generated by the difference are respresented in the lower left corner, the upper right corner of the table represents the summation of the tidal frequencies.

		ω_2		$\omega_1+\omega_2$	
	ω_1	O_1	K_1	M_2	S_2
$\omega_1-\omega_2$	O_1	O_2	M_2	MO_3	SO_3
	K_1	M_f	K_2	MK_3	SK_3
	M_2	K_1	O_1	M_4	MS_4
	S_2	SO_1	P_1	MS_f	S_4

For a 30-day simulation with hourly data as output, not all of the above constituents may be calculated, however several of the combinations listed in the table may be found in a tidal analysis of the model output. By comparing the tidal analysis of the model output to the observations, the degree of nonlinearities in the simulations may be quantified. For the 30 day simulations, the nonlinear tidal constituents M_4, S_4, MS_f, and MS_4 are available for comparison.

Generally, the nonlinear terms are significantly weaker than those observed. Away from the sill at moorings M1-96, M2-96, M4-96 and M5-96 the amplitude of the nonlinear tidal constituents M_4, MS_4, and S_4 generated by the model were found to have amplitudes less than 0.05 cm/s (Figures 4.14-4.15). With such weak interactions in the model, no meaningful comparison is possible for these terms. Only MS_f was strong enough to permit a meaningful comparison of the nonlinear terms in the inner basin (M1-96 and M2-96) and the outer channel (M4-96 and M5-96).

At M1-96, the amplitude of MS_f (Table B.13) is much weaker than those observed at M1-96. At 10, 20 and 45 metres depth, the observed value of MS_f is 1.0, 0.3, and 0.4 cm/s compared to values of 0.1 cm/s or less generated by the model at all depths (Figure 4.14). In consideration of the relative weakness of the M_2 tides at this location in the model data (Table B.7), the weakness of MS_f is not unexpected.

At M2-96, (Figure 4.14) the surface observations are much stronger than the model output, although there is a noticeable increase in the amplitude of the tide as the main pycnocline deepens. When the main pycnocline lies at 10 metres depth (stratification A), the MS_f amplitude is weakest (0.1 cm/s). As the main pycnocline deepens to 20 metres (stratification B), then deepens seaward of the sill to 30 metres (stratification C) we find that the amplitude of the MS_f tide increases to 0.2 and 0.4 cm/s. Clearly the stratification must influence the amount of interaction which exists between the M_2 and S_2 tides. There is, clearly, a lack of interaction missing in the near surface region with the observed amplitude being 1.6 cm/s. At 17 metres depth, we find a similar trend with the amplitude of the MS_f tide increases from 0.2 to 0.5 cm/s. The model values are consistent with the observed value (0.4) cm/s at this depth. At 45 metres depth, the observed amplitude of MS_f is 0.3 cm/s marginally stronger than the model amplitudes of 0.1-0.2 cm/s. There is no evidence of any dependence on stratification at this depth.

Seaward of the sill (M4-96, M5-96), the amplitude of the model MS_f constituent 0-0.2 cm/s) is much weaker than the observed tidal current (0.3-0.9 cm/s). The model is unable to replicate the nonlinear interaction between the main tidal constituents at these locations. The tide seaward of the was barotropic in the model simulations (Tables B.7 and B.11). The model is unable to reproduce the baroclinic nature of the tide on the seaward side of the sill and also fails to reproduce the nonlinear interaction between the main semi-diurnal constituents. This is most noticeable near the surface layers where MS_f was estimated between 0.6-0.9 cm/s from the 1996 data compared to the model MS_f of only 0.1 cm/s (Figure 4.14).

In the vicinity of the sill (Table B.14, Figure 4.16), the model produces an MS_f tide at M1-97 with constant amplitude of 0.2 cm/s between 7.5 and 21 metres depth. This value agrees with the observed amplitude of 0.2 cm/s at 21 metres depth but is significantly weaker than the observed MS_f amplitude of 0.8 cm/s at 7.5 metres depth. Graphically (Figure 4.16), we see the amplitude of this tidal constituent increases with depth with a maximum value of approximately 0.8 cm/s near 45 metres depth for stratifications A and B and a maximum of 0.6 cm/s for stratification C.

At M2-97, stratification A generates the largest MS_f amplitude (0.8 cm/s) at 21 metres depth compared to 1.2 cm/s for the observed value. Stratification B and C only have amplitudes of 0.5 cm/s at this depth. Near the surface (7.5 metres depth) stratification B produces the strongest interaction between the M_2 and S_2 tides with MS_f amplitude of 0.5 cm/s. Stratification A produces a slightly weaker 0.4 cm/s MS_f amplitude. Both of these values are significantly weaker than the observed 1.0 cm/s MS_f amplitude. Figure 4.16 indicates that the MS_f amplitude at M2-97 varies with depth and that the variation is dependent upon the stratification. Stratification A produces a distinct maximum MS_f current near 20 metres of the depth. Stratification B has a maximum current surface near 7 metres depth and the current remains almost constant for the top 20 metres. Stratification C produces a current steadily increasing from, approximately, 0.2 cm/s at the surface to a maximum value of 0.6 cm/s at 25 metres depth.

The surface MS_f current (0.3 cm/s) at M3-97 is much weaker than the observed value of 1.4 cm/s. There is no evidence that the amplitude of MS_f at this location is dependent upon stratification. Figure 4.16 reveals no significant variation in the vertical structure of the MS_f current that was identified at M2-97.

On the seaward side of the sill, at M5-97, stratification C produces the strongest MS_f current (0.3 cm/s). At 7.5 metres depth, stratifications A has a MS_f amplitude of 0.2 cm/s. Both of these values agree well with the observed MS_f amplitude (0.3 cm/s). Stratification B produces a much weaker (0.1 cm/s) MS_f tide. The modelled currents at 21 metres depth are to weak having amplitudes of only 0.1-0.2 cm/s compared to the observed current of 0.6 cm/s. At M6-97, the best agreement between the observed amplitude of 0.8 cm/s for MS_f at 21 metres depth is stratification C which has an amplitude of 0.7 cm/s. Stratifications A and B have amplitudes of only 0.5 cm/s. At 33 metres depth the observed MS_f tidal current is much weaker having amplitude of only 0.1

cm/s. This decay in the strength of the current is not reproduce by the model run except in the bottom sigma layer. The results in a MS_f current at 33 metres depth in the model runs which is much stronger than expected. At M7-97 there is no significant difference in the MS_f tide between the model runs. All of the model runs produce an MS_f current of 0.5 cm/s at all depths. This agrees with the observed MS_f current (0.4 cm/s) at 31 metres depth of 0.4 cm/s but is much weaker than the observed 1.3 cm/s at 7.5 metres depth.

At the sill, the observed MS_f tide at M3-96 (Table B.13, Figure 4.14) and M4-97 (Table B.14, Figure 4.16) indicate two very different profiles for MS_f even though the mooring locations lie very close to each other. At M3-96 the observed tide has amplitude of 2.1 cm/s at 10 metres depth and amplitude of 0.6 cm/s at 15 metres depth. The modelled tide with amplitude of 0.5-0.7 cm/s at 10 metres depth is much weaker than the observed tide. At 15 metres depth, the model MS_f amplitude 0.4-0.6 cm/s at 15 metres depth compares reasonably well with the observed value (0.6cm/s).

At M4-97 the observed MS_f signal is very noisy. At 7.5 metres depth, the observed MS_f was 0.8 ± 2.6 cm/s. The observed value of 0.8 cm/s is much weaker than the observed 2.1 cm/s at 10 metres depth at M3-96, but does agree with the modeled values of 0.6-0.8 cm/s. At 14 metres depth, the observed MS_f amplitude (4.2 ± 4.9cm/s) seems unreasonably large compared to the value of 0.6 ± 2.6 cm/s in 1996. The observed value for the amplitude of the MS_f tide at this location should probably be rejected. All three stratified models produce MS_f amplitudes of 0.4 cm/s that are consistent with the observed value (0.6 cm/s) and model output (0.4-0.6 cm/s) from M3-96.

At the sill locations M3-96 and M4-97, the other nonlinear constituents M_4, MS_4 and S_4 generated by the model, have large enough amplitudes to permit a comparison to the observed values (Tables B.15 and B.16, Figures 4.14-4.17). Constituent M_4 has observed amplitudes of 0.9-1.0 cm/s and 0.4-0.6 cms/ at the surface (7.5-10 metres depth) and bottom (14-15 metres depth), respectively. The surface M_4currents generated by the model are much weaker having amplitude of only 0.2-0.3 cm/s. At 15 metres depth, the model M_4 current (0.2-0.4 cm/s) at M3-96 are slightly weaker than the observations (0.6 $\pm$ 0.4 cm/s) but all values lie within the 95% confidence interval. The modelled amplitude of 0.1 cm/s at M4-97 is weaker than observations (0.4 $\pm$ 0.2 cm/s) and does not lie within the 95% confidence interval. Stratification influences the strength of the M_4 tide with the greatest amplitudes at the sill being produced when the main pycnocline is located at 10 metres depth in the model.

The surface MS_4 currents generated by the model (0.1-0.2 cm/s) are much weaker than the amplitudes for MS_4 estimated from the observations (0.7-0.9 cm/s). At the bottom, the currents produced by the model are also weaker (0.0-0.3 cm/s) than the observed amplitudes (0.4-0.5 cm/s). From the model data it is evident that the nonlinear interactions decrease when the depth of the main pycnocline increases.

Constituent S_4 is almost too weak in both the observed values and the modelled values to provide any meaningful comparison. The amplitude of the S_4 tidal constituent is found to be nearly constant with depth having a amplitude of (0.2-0.3 cm/s). The model produces S_4 amplitudes in the range of (0.0-0.2 cm/s) with at least one-half of the amplitudes less than 0.05 cm/s (indicated by the value of 0.0 in the table).

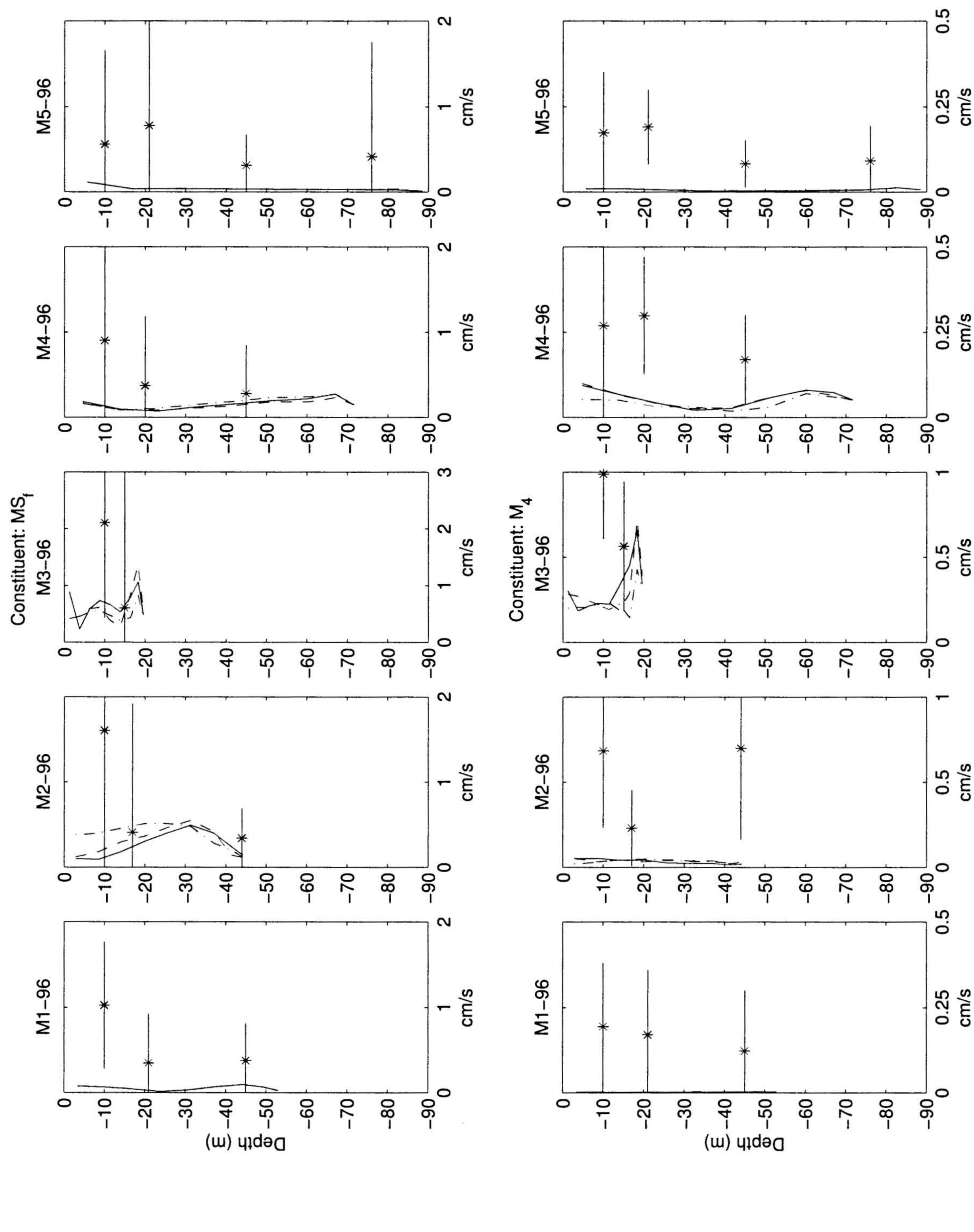

Figure 4.14 Amplitude (semi-major axis) of the Nonlinear Tidal Currents MS_f and M_4 1996. The amplitude (cm/s) of the semi-major axis. **Stratifications: A** (solid line); **B** (dashed line) and **C** (dashed dot line) along with the **observed values** (*). The error bars associated with the observations represent 95% confidence intervals

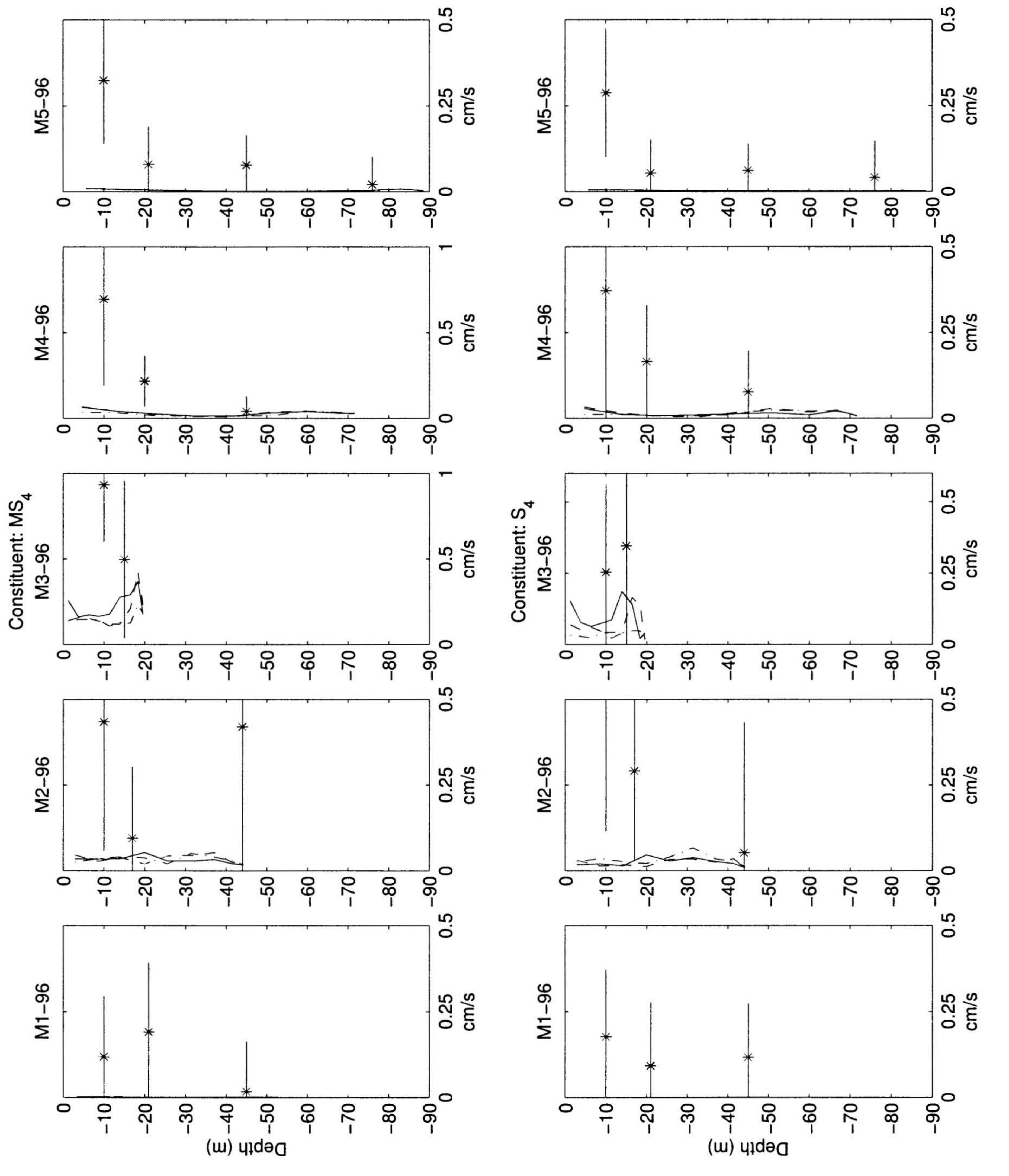

Figure 4.15Amplitude (semi-major axis) of the Nonlinear Tidal Currents MS_4 and S_4 1996. The amplitude (cm/s) of the semi-major axis. **Stratifications: A** (solid line); **B** (dashed line) and **C** (dashed dot line) along with the **observed values** (*). The error bars associated with the observations represent 95% confidence intervals

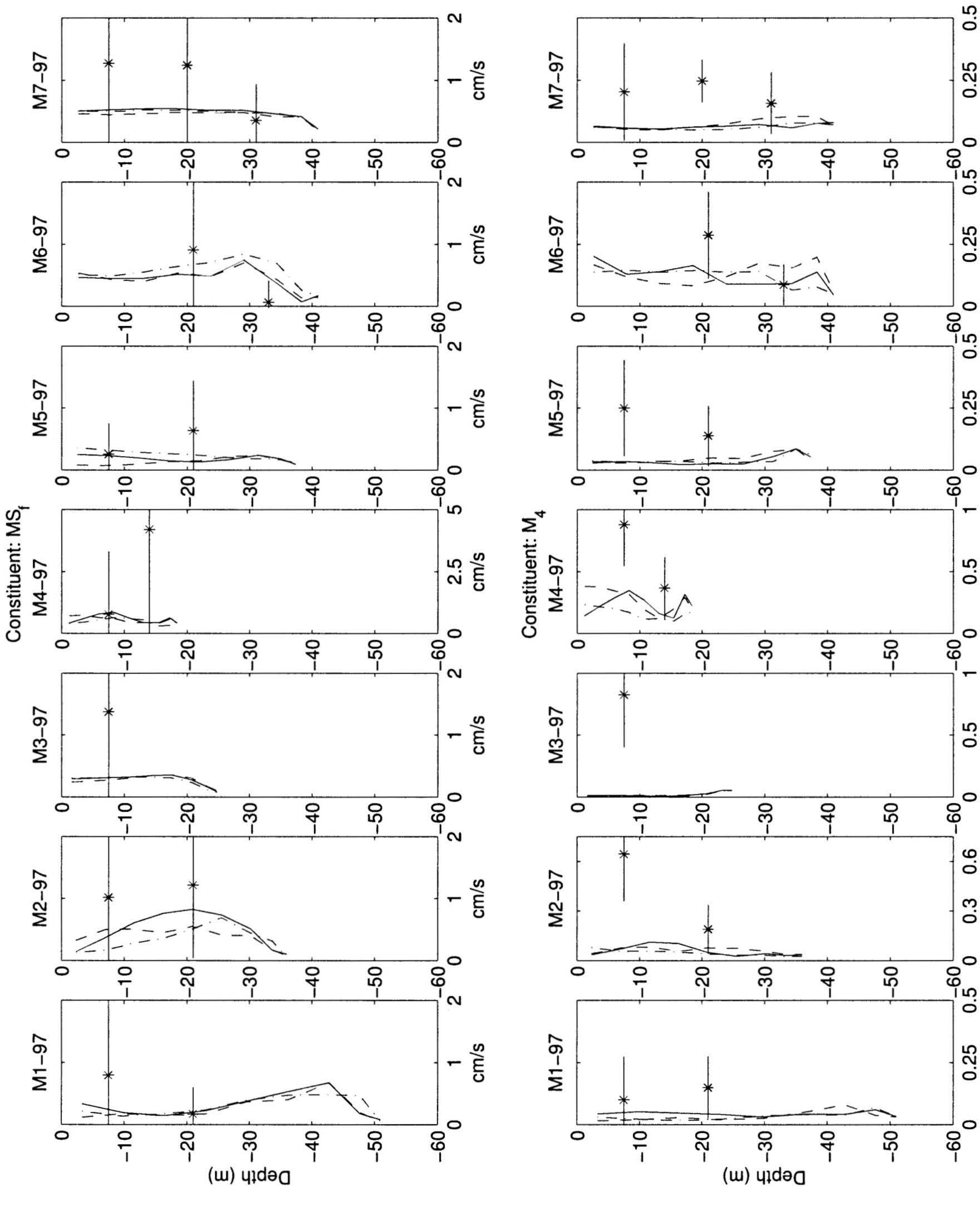

Figure 4.16 Amplitude (semi-major axis) of the Nonlinear Tidal Currents MS_f and M_4 1997. The amplitude (cm/s) of the semi-major axis. **Stratifications: A** (solid line); **B** (dashed line) and **C** (dashed dot line) along with the **observed values (*)**. The error bars associated with the observations represent 95% confidence intervals

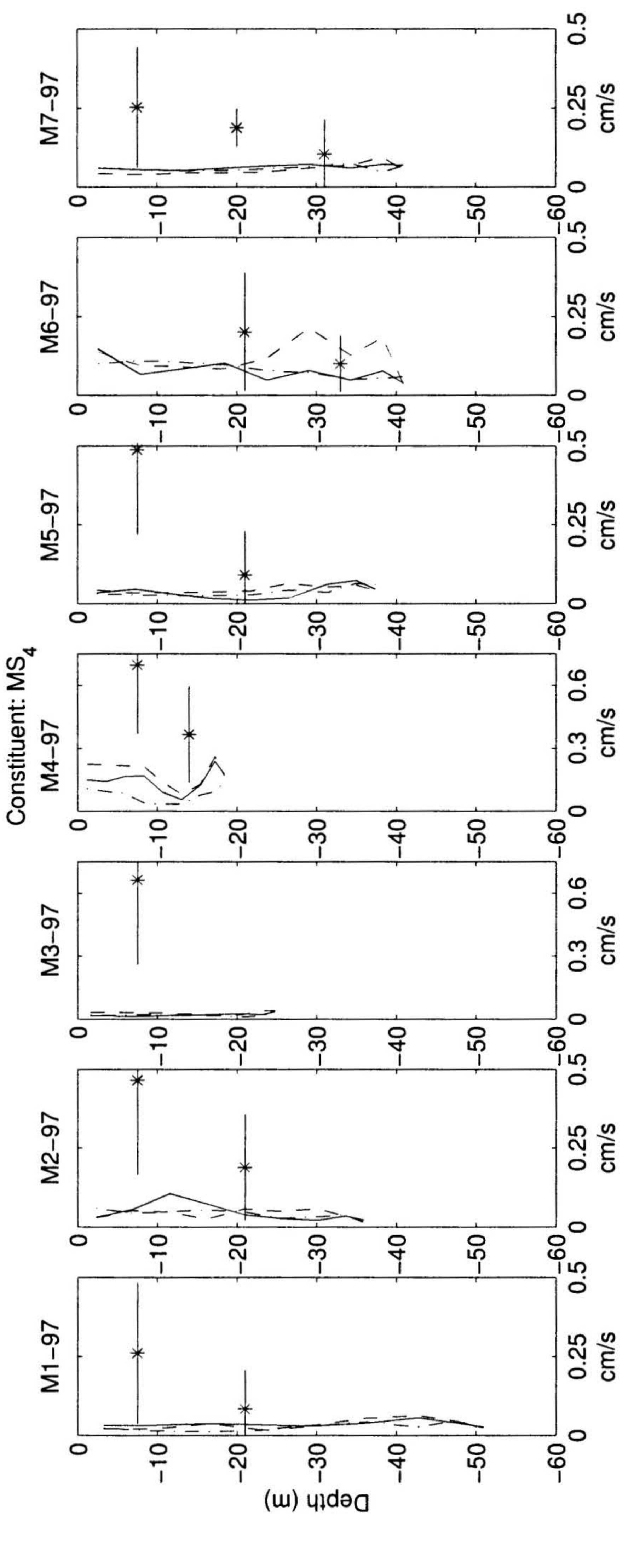

Figure 4.17 Amplitude (semi-major axis) of the Nonlinear Tidal Currents MS_4 and S_4 1996. The amplitude (cm/s) of the semi-major axis. **Stratifications: A** (solid line); **B** (dashed line) and **C** (dashed dot line) along with the **observed values** (*). The error bars associated with the observations represent 95% confidence intervals

4.2.2.3 Frictional Tidal Constituents

Other shallow water constituents worthy of consideration for comparison are those which are generated due to friction. In response to forcing by harmonic constituents, friction will act to introduce new harmonics into the system. The harmonics introduced when the forcing function is a combination of the tidal harmonics M_2 and S_2 are (Godin, 1972) M_6, S_6, $2MS_6$, $2SM_6$, $2MS_2$ and $2SM_2$.A comparison these frictional harmonics with those found in the tidal analysis of the data will help to establish the influence of friction on the tidal flow generated by the model.

For the 30-day simulations generated by the model, only the constituents M_6, $2MS_6$, and $2SM_6$ are available for comparison. Away from the sill these tidal constituents are very weak so a meaningful comparison is difficult. The observed amplitudes of these three constituents at moorings located away from the sill in 1996 was 0.1-0.3 cm/s, however the model was seldom able to achieve amplitudes in excess of 0.05 cm/s at these locations (Figures 4.18-4.19). Clearly the model underestimates the strength of these tidal constituents.

Those moorings not located at the sill in 1997 also have, typically, observed frictional constituent amplitudes in the range of 0.1-0.3 cm/s. At these locations, the model was able to produce slightly larger amplitudes than those found at the 1996 mooring locations. Typical amplitudes produced by the model were between 0.0-0.1 cm/s. Constituent M_6 in the analysed model output for 1997 was found to have amplitude of 0.1 cm/s at almost all instrument locations, weaker than the 0.3-0.5 cm/s M_6 observed at the surface but consistent with the observed 0.1-0.2 cm/s at 20 and 30 metres depth. The largest amplitude for the $2MS_6$ was generated with stratifications A and C amplitudes ranging from 0.05-0.15 cm/s are quite weak but consistent (within the 95% confidence interval) with the observed $2MS_6$ current (0.1-0.2 cm/s) as opposed to typical amplitudes of less than 0.05 cm/s for stratification B. Constituent $2SM_6$ has greatest amplitude (0.05-0.15 cm/s) with stratification B compared that are consistent with the observed $2SM_6$ (0.1-0.2 cm/s) while the $2SM_6$ current generated with stratifications B and C are less than 0.05 cm/s. Although the model signals are very weak, the position of the main pycnocline in relation to the depth of the sill (above, at or below) appears to play a role in the generation of both $2MS_6$ and $2SM_6$.

At the sill (Tables B.17-B.18), the observed M_6 have amplitude was 1.3-1.4 cm/s in 1996 and 1.0-1.2 cm/s in 1997. This does not seem unreasonable as friction should be one of the dominant forces in the across the sill. All of the model runs failed to produce M_6 amplitudes close to these values despite friction being deliberately increased at the sill to damp out numerical instabilities generated in the model. The largest amplitude found for M_6 in the model runs was 0.4 cm/ occurred at M4-97 with stratification B.

For constituent $2MS_6$, the observed values ranged from 0.1-0.6 cm/s. The model performed best at M4-97 producing amplitudes of 0.1-0.2 cm/s compared to the observed values of 0.1-0.3 cm/s, the poorest performance of the model was at 15 metres depth, M3-96 where the observations indicated (a very noisy) 0.6 cm/s compared to the modelled amplitudes of 0.1 cm/s. The observed values for $2SM_6$ were slightly stronger than those of $2MS_6$ ranging from 0.4-0.6 cm/s, the model was unable to replicate this producing maximum values of only 0.2 cm/s.

In the presence of a statically stratified fluid, the statically stratified model fails to be able to reproduce the effects of nonlinearities and friction on the tidal flow. The importance of temperature and salinity mixing on the amplification of nonlinear and frictional interactions of the main diurnal and semi-diurnal constituents will be studied further in chapter 5.

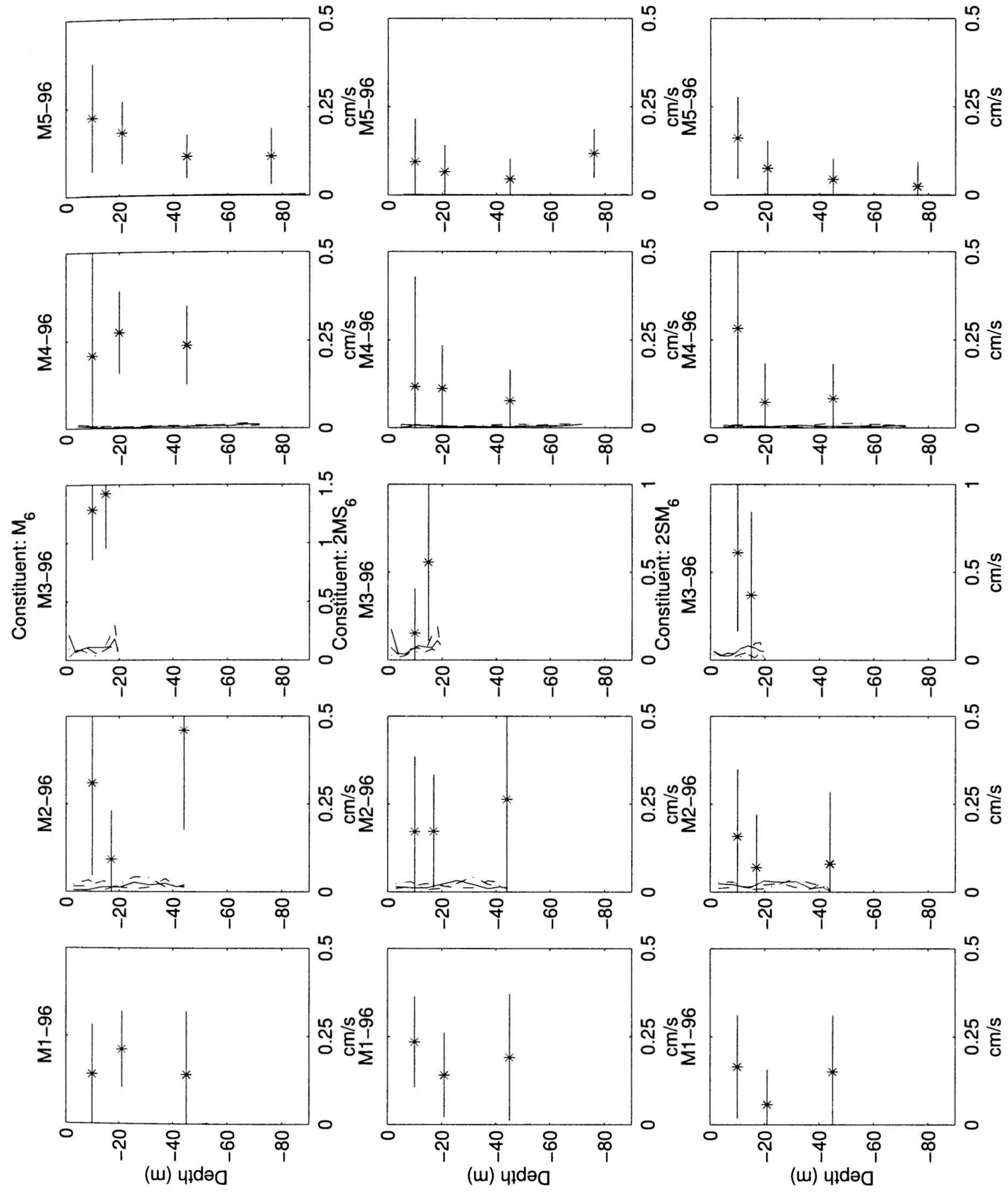

Figure 4.18 Amplitude (semi-major axis) of the Frictional Tidal Currents M_6 and $2MS_6$ and $2SM_6$ 1996. The amplitude (cm/s) of the semi-major axis: **Stratifications: A** (solid line); **B** (dashed line) and **C** (dashed dot line) along with the **observed values** (*). The error bars associated with the observations represent 95% confidence intervals

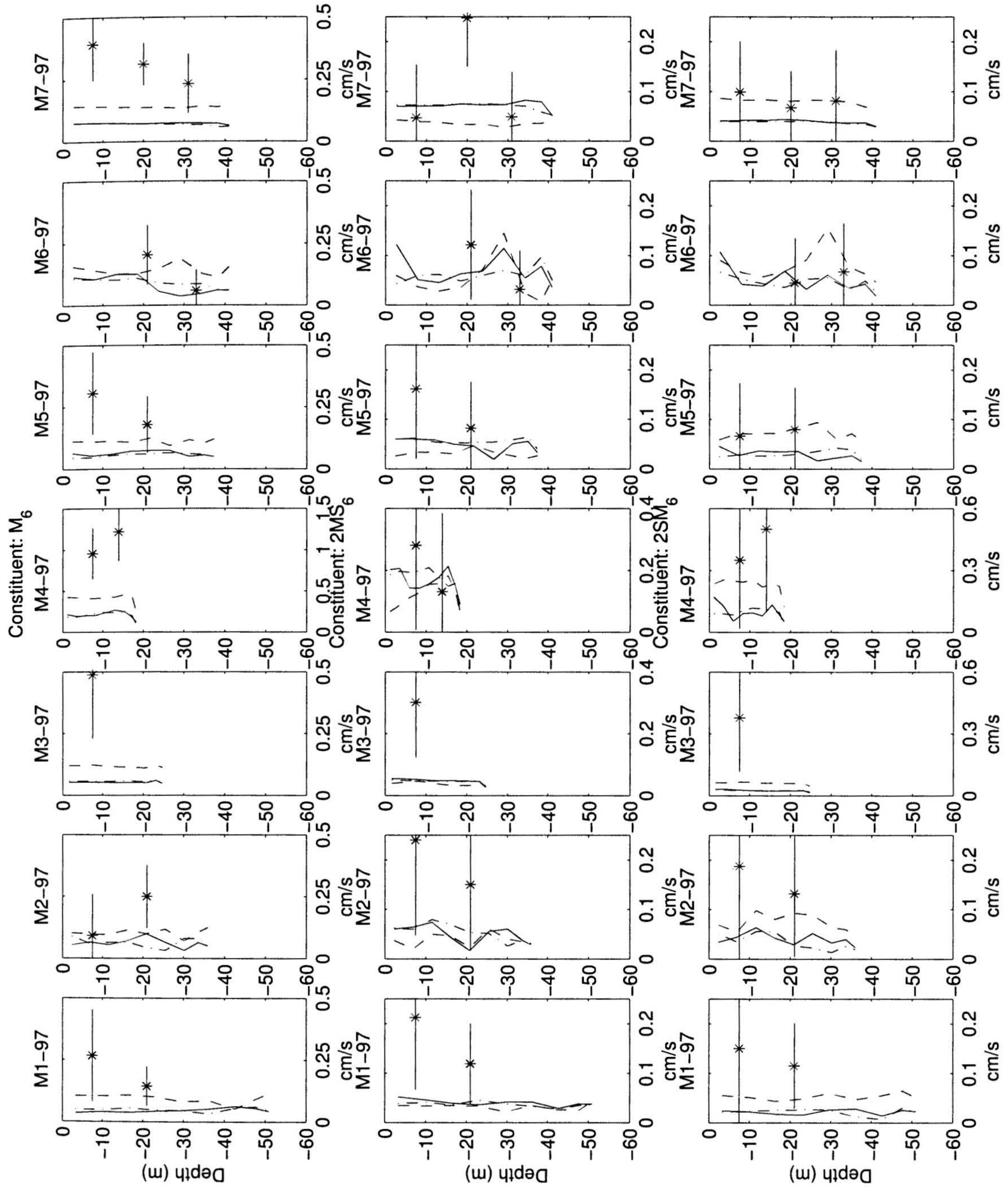

Figure 4.19 Amplitude (semi-major axis) of the Frictional Tidal Currents M_6 and $2MS_6$ and $2SM_6$ 1997. The amplitude (cm/s) of the semi-major axis: **Stratifications: A** (solid line); **B** (dashed line) and **C** (dashed dot line) along with the **observed values** (*). The error bars associated with the observations represent 95% confidence intervals

4.2.3 Volume Flux and Work Done by the Tides

Stratification appears to have little influence on the main diurnal and semi-diurnal constituents. Figures 4.20–4.22 provide a comparison of the amplitude of the M_2 current (semi-major axis) in the region of the sill. The cross sections from CX-197 and CX-397 (Figure 4.2) also show that the main semi-diurnal forcing is located towards the northern coastline on either side of the sill, with very little difference in the distribution of the tidal signal as the main pycnocline deepens from above the sill (Strat. A) to below the sill (Strat. C.). Across the sill, however, there is evidence that the tidal jet through the constriction and across the sill weakens from a maximum value of about 10 cm/s to a maximum value of about 8 cm/s as the main pycnocline deepens. This suggests that as the surface layer deepens seaward of the sill, the volume flux across the sill during the summer season would see a small reduction that would reducing the tidal action within the inner basin. The maximum flux associated with each of the diurnal and semi-diurnal constituents may be estimated by projecting the semi-major axis of the tidal ellipse onto the normal vector of the cross section. For a tidal ellipse with an angle of inclination given by θ measured from the normal to the cross section. The velocity normal to the cross section is given by:

$$U_n = U \cos\theta \tag{4.3.2}$$

where U is the velocity along the semi-major axis of the tidal ellipse and U_n is the velocity normal to the cross section. Ignoring the phase of the tidal current, the maximum volume flux possible through the cross section is then given by:

$$F_{\max} = \int_{-h}^{0}\int_{0}^{B} U_n \, dy dz\,, \tag{4.3.3}$$

where: F_{max} is the maximum flux through the cross section, $-h$ is the depth along the cross section and B is the width. This flux value does not account for the possibility of a counter current through the section. However, if the tidal current is considered to be unidirectional it does provide an estimate of the flow rate associated with each of the main constituents. In the region of the sill, the maximum volume flux was calculated at CX-197, CX-297 and CX-397 (Figure 4.2) for each of the density profiles as well as the barotropic density profile. The calculated flux values at each of the cross sections for the constituents O_1, K_1, M_2, and S_2 are provided in Table 4.2.

As the pycnocline deepens from Stratification A to Stratification C, the flux associated with the diurnal constituents O_1 and K_1 at CX-197 reduces by 11% and 4%, respectively, while the flux associated with the semi-diurnal constituents remains relatively constant (changing less than 1%). The volume flux at CX-297 (the sill) and CX-397 (outer channel) remain almost constant for all tidal constituents. At CX-297, M_2 indicates a very small (~0.6%) decrease as the pycnocline deepens. At CX-397 there is a small decrease (~2%) of the flux associated with O_1 when the main pycnocline is located at or below the sill (stratification B and C) and a small increase (~2%) associated with K_1 when the main pycnocline is located below the sill (stratification C).

The distribution of the tidal currents (semi-major axis) K_1 are shown in Figures 4.23-4.25. At CX-197, there is a noticeable decay in the maximum tidal current located along the northern side (right hand side of Figure 4.23) as the pycnocline deepens. At CX-397 there is a distinct maximum located at approximately 30 metres of depth once the main pycnocline drops below the level of the sill (Stratification C). The decrease within the inner basin and the formation of the maxima seaward of the sill indicates that the sill acts as a filter for the diurnal tide with stratification seaward of the sill a controlling factor.

Table 4.2: Volume Flux Through Model Cross Section. The volume (m^3/s) flux associated with each of the main tidal constituents for each of the model runs. For identification of the cross sections see Figure 4.2

Maximum Volume Flux through Cross Section (M^3/s) - Tidal Forcing

	O_1				K_1			
	Baro	**Strat. A**	**Strat. B**	**Strat. C**	**Baro**	**Strat. A**	**Strat. B**	**Strat. C**
Cx197	96	95	86	84.	146	142	137	136
Cx297	88	90	88	89	151	153	153	152
Cx397	96	97	95	95	185	176	176	180

	M_2				S_2			
	Baro	**Strat. A**	**Strat. B**	**Strat. C**	**Baro**	**Strat. A**	**Strat. B**	**Strat. C**
Cx197	763	761	760	760	258	253	250	255
Cx297	905	913	911	907	303	305	304	304
Cx397	959	957	956	955	329	326	324	322

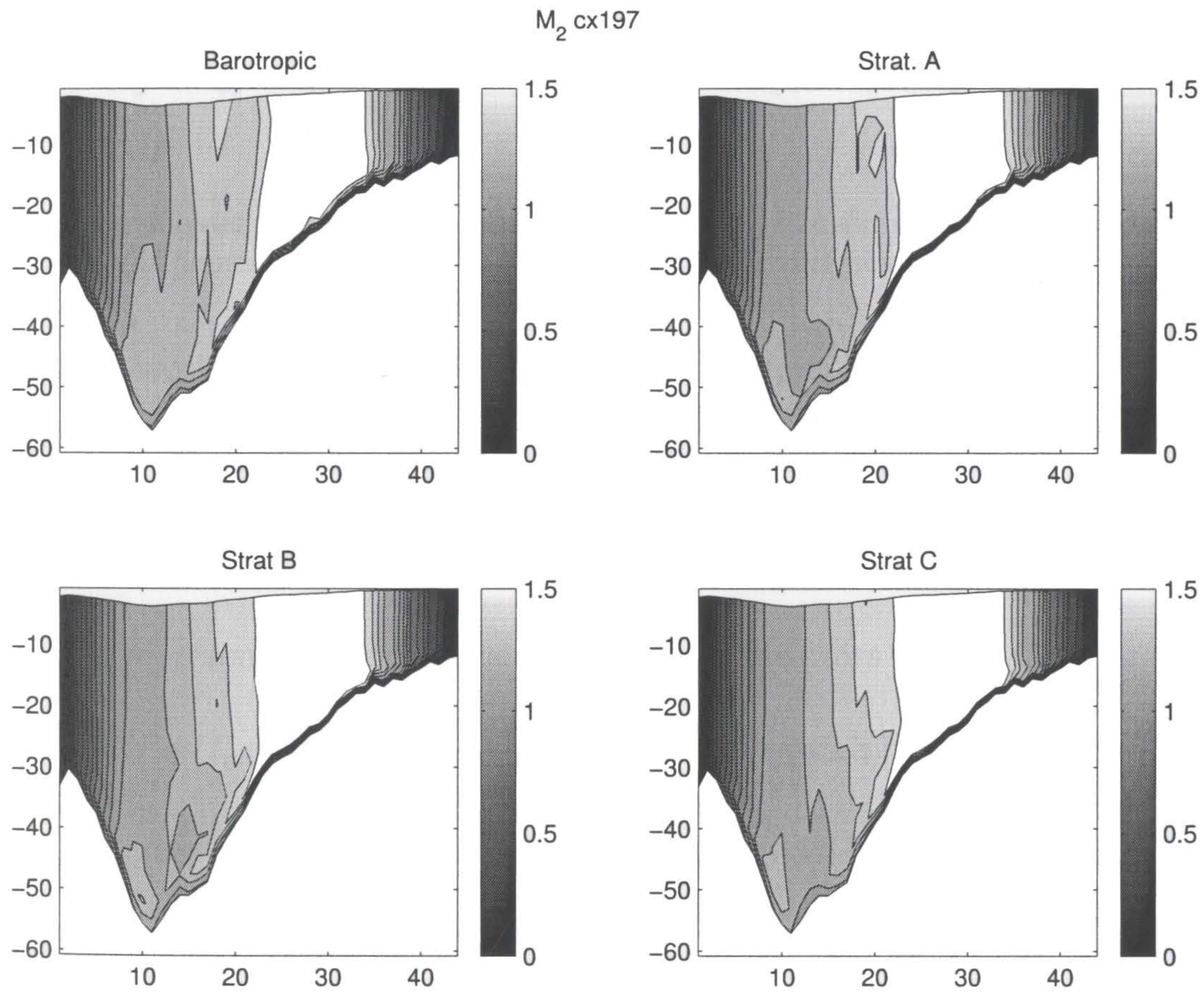

Figure 4.20: Semi-diurnal (M_2) tide within the inner basin. Units are in cm/s, contour intervals drawn at 0.1 cm/s. X-axis indicated by grid points, one grid points equals 50 metres. Y-axis represents metres.

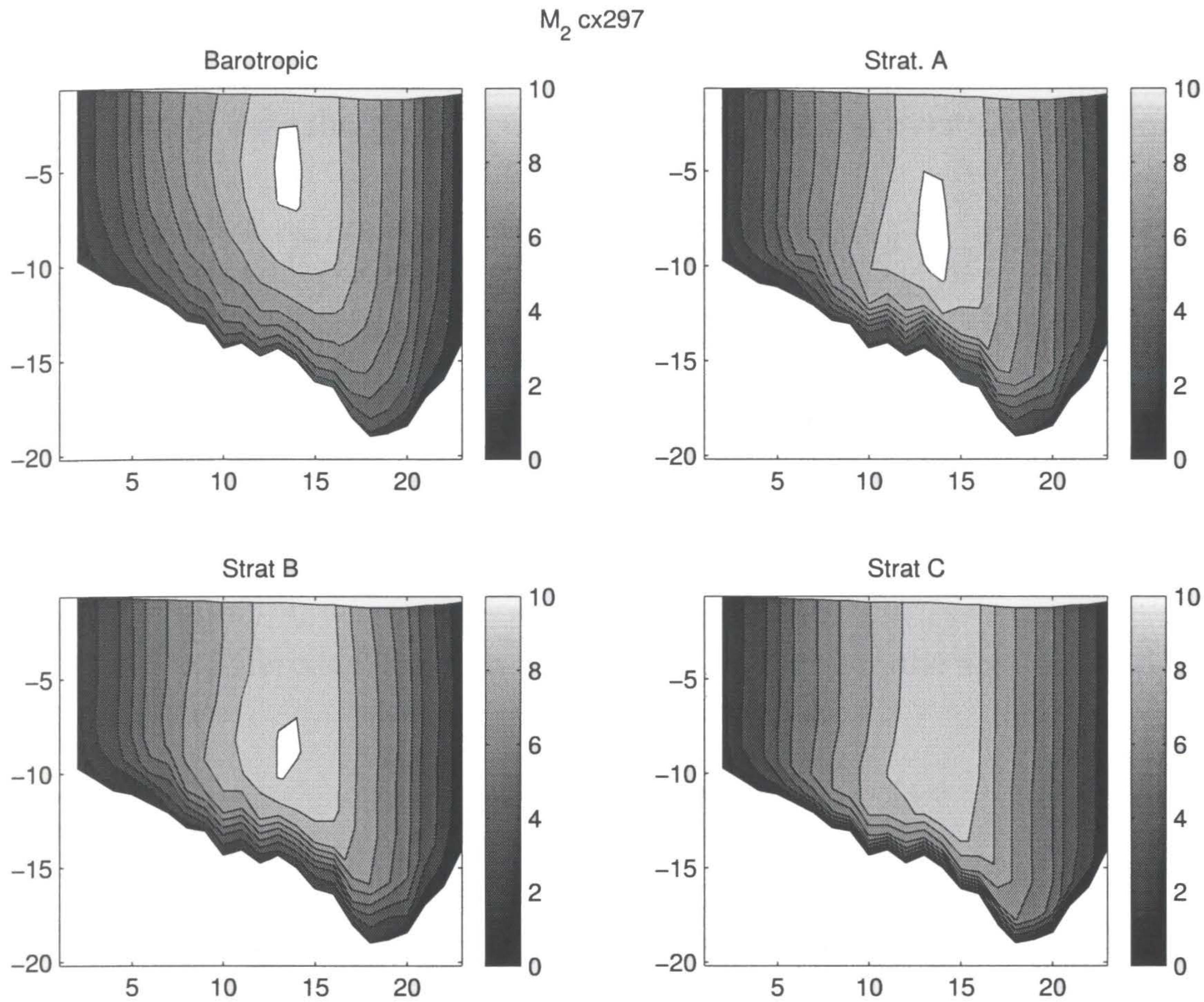

Figure 4.21: Semi-diurnal (M_2) tide at the sill. Units are in cm/s, contour intervals drawn at 1 cm/s. X-axis indicated by grid points, one grid points equals 50 metres. Y-axis represents metres.

To estimate the work done by the tide as it propagates along the inlet we assume that the surface height is constant across the inlet so that it may be represented as:

$\eta = \eta_0 \cos(\sigma t - g_1)$, where sigma is the frequency of the tide and g_1 is the Greenwich phase lag. If U represents the current perpendicular to the cross section then we may also represent U as $U = U_0 \cos(\sigma t - g_2)$. Where g_2 is the Greewich phase lag associated with the current. The rate of work across the section is then given by (Proudman, 1953):

$$W = g\rho \int_{-H}^{\eta} \int_{0}^{L} \eta U dy dz . \qquad (4.3.4)$$

Substitution of the two expression for η and U into this last equation and integrating over a tidal cycle of period $2\pi/\sigma$ the average work across the section over a tidal period is:

$$W_T = \frac{1}{2} g\rho \int_{-H}^{\eta} \int_{0}^{L} \eta_0 U_0 \cos(g_1 - g_2) dy dz \tag{4.3.5}$$

For each cross section through the 1996 mooring locations, CX-196 to CX-596 (Figure 4.2), the average work done by the tide for a barotropic fluid (*ρ=1025*) is presented in Table 4.3. The amount of dissipation of tidal energy between two neighbouring sections must be equal to the difference between the work done between the sections and is provided in Table 4.4.

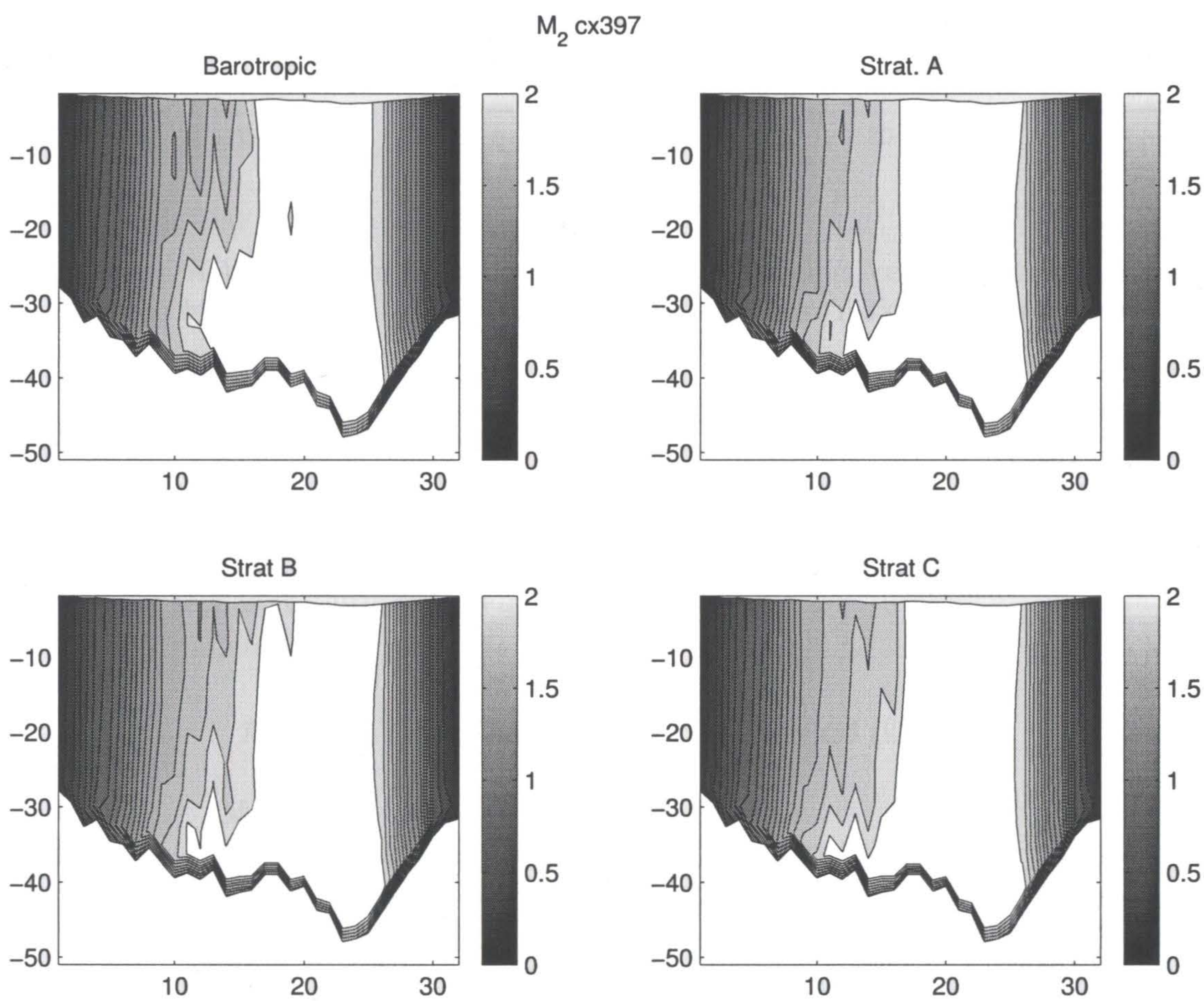

Figure 4.22: Semi-diurnal tide seaward of the sill. Units are in cm/s, contour intervals drawn at 0.1 cm/s. X-axis indicated by grid points, one grid points equals 50 metres. Y-axis represents metres.

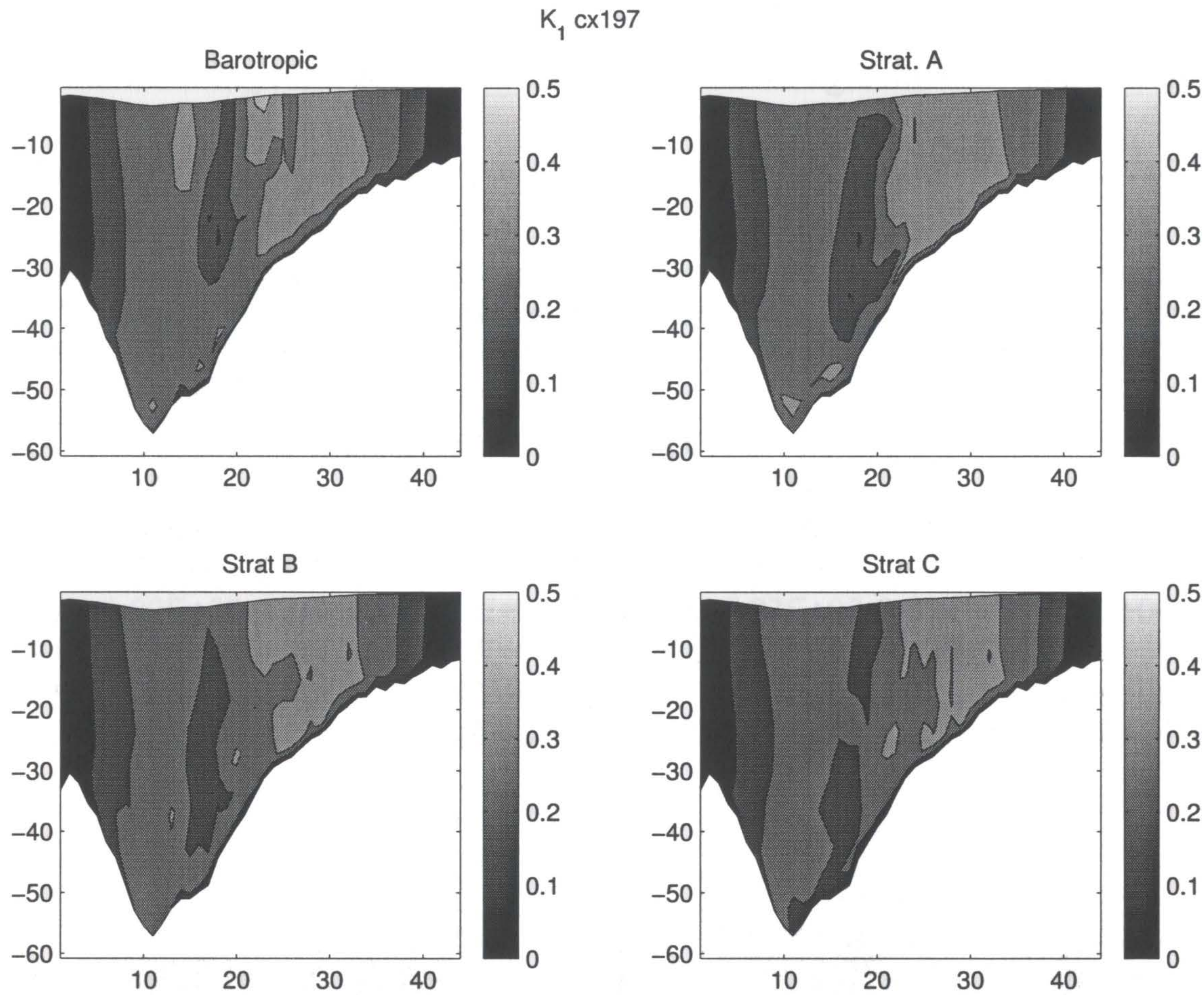

Figure 4.23: Diurnal (K_1) tide within the inner basin. Units are in cm/s, contour intervals drawn at 0.1 cm/s. X-axis indicated by grid points, one grid points equals 50 metres. Y-axis represents metres.

Table 4.3 Average Work Done by the Tide Through a Cross Section. Observed values are calculated by assuming that the tide measured at the moorings is uniform across the entire channel, the model results are calculated by estimating the tidal currents and amplitudes at each grid point in the model cross section. The location of each cross section is illustrated in Figure 4.2.

	Average Work Done over a Tidal Period (kW)							
	M2		S2		O1		K1	
Section	**Obs**	**Mod**	**obs**	**mod**	**obs**	**Mod**	**obs**	**mod**
cx196	2.12E+05	1.63E+04	5.42E+04	1.90E+03	9.43E+03	7.00E+02	1.99E+04	1.70E+03
cx296	1.27E+05	1.34E+04	3.27E+04	1.80E+03	6.25E+03	1.20E+03	3.25E+04	5.00E+02
cx396	2.67E+04	1.45E+04	4.61E+03	1.20E+03	8.80E+02	3.00E+02	2.41E+03	6.00E+02
cx496	9.82E+03	2.90E+03	3.30E+03	3.00E+02	8.10E+02	3.00E+02	1.37E+03	3.00E+02
cx596	3.52E+04	3.01E+04	8.86E+03	3.90E+03	8.50E+03	1.30E+03	8.27E+03	3.30E+03

From Table 4.3, the amount of work done at CX-596 in both the observations and the data for the main M_2 tidal constituent are very close to agreement with a difference of only 510kW. However, at CX-496 the work done by the tide through the cross section

Table 4.4: Dissipation of Tidal Energy Between Cross Sections. Values in kiloWatts represent the difference in the Average Work between neighbouring cross section as indicated in Table 4.21. The calculated values indicate the loss of tidal energy to friction or turbulence. The area bounded by the cross sections may be determined from Figure 4.2.

Tidal Dissipation Along the Inlet (kW)

	M2		S2		O1		K1	
	Obs	**mod**	**obs**	**mod**	**obs**	**mod**	**obs**	**Mod**
|cx196-cx296|	8.55E+04	2.90E+03	2.15E+04	1.00E+02	3.18E+03	5.00E+02	1.26E+04	1.20E+03
|cx296-cx396|	1.00E+05	1.10E+03	2.81E+04	6.00E+02	5.37E+03	9.00E+02	3.01E+04	1.00E+02
|cx396-cx496|	1.68E+04	1.16E+04	1.31E+03	9.00E+02	7.00E+01	0.00E+00	1.04E+03	3.00E+02
|cx496-cx596|	2.54E+04	2.72E+04	5.56E+03	3.60E+03	7.69E+03	1.00E+03	6.90E+03	3.00E+03
Total	2.28E+05	4.28E+04	5.65E+04	5.20E+03	1.63E+04	2.40E+03	5.06E+04	4.60E+03

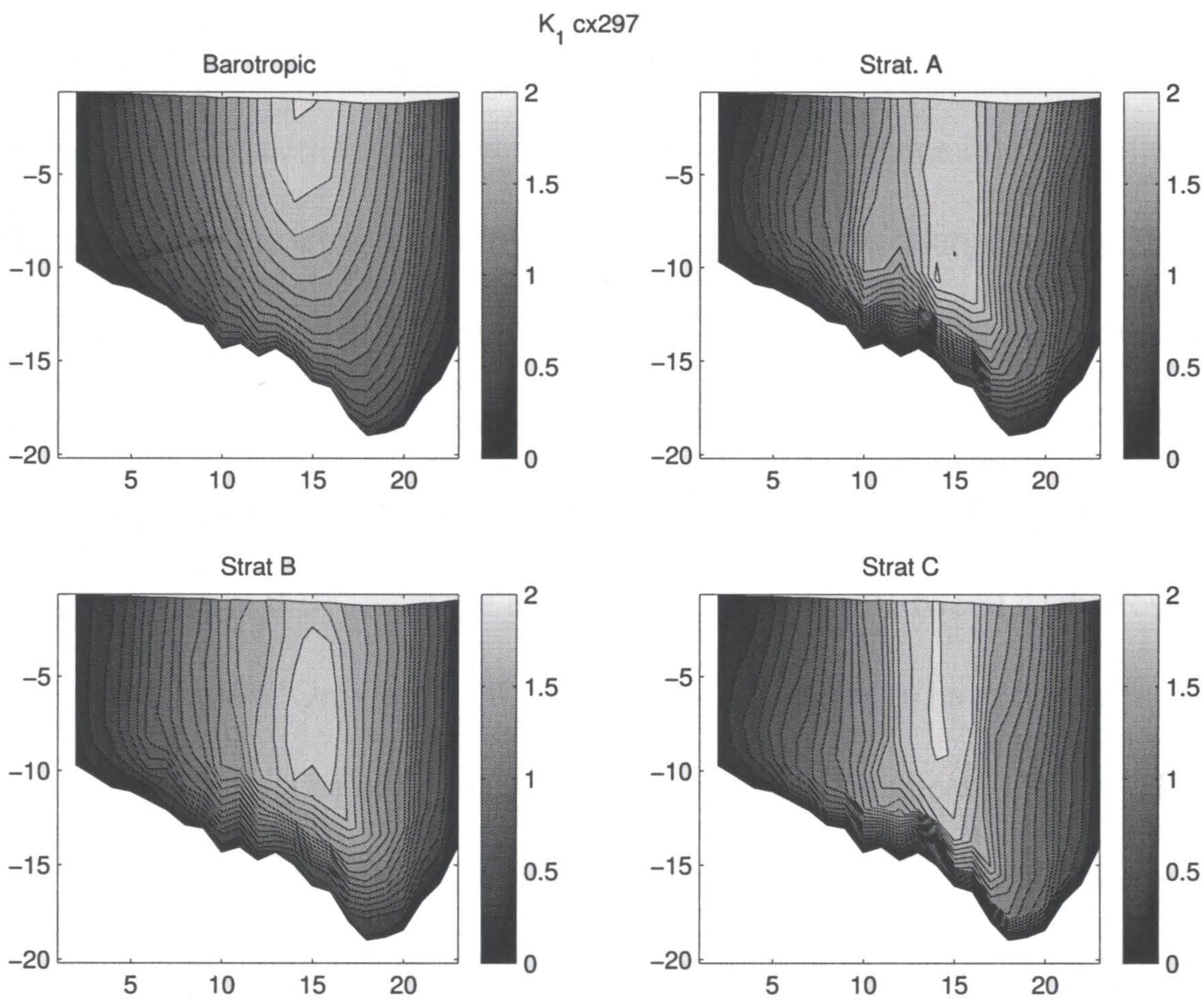

Figure 4.24: Diurnal (K_1) tide at the sill. Units are in cm/s, contour intervals drawn at 0.1 cm/s. X-axis indicated by grid points, one grid points equals 50 metres. Y-axis represents metres.

within the model of 2900 kW is significantly lower than the observed value of 9820 kW. This difference indicates that the energy dissipated between the two sections in the model (27,200 kW) is 10% greater than the observed energy loss (25,400 kW).

As the tide crosses the sill (CX-396), the work done by the tide in the model is only 50% of the observed value. Within the inner basin, the average work done over a tidal period through sections CX-196 and CX-296 when calculated from the mooring observations is greater than the work done within the model by an order of magnitude; the model values no more than 10% of the observed values. Clearly not enough tidal energy is transmitted through the inner basin of the model. Some of the difference may be attributed to the calculation of the average work done that used only one value integrated across the entire width of the channel as opposed to integrating the tidal signal calculated at all grid points in the section. However, given the large difference in the amplitude of the tidal signals at the mooring locations, it is clear that there is a large energy loss in the model that does not agree with the observed loss of energy. The energy loss experienced by the model as the tide crosses the sill is most likely due to the high friction and lateral dissipation found necessary to maintain numerical stability in the region of the sill.

Table 4.5 shows the percentage of the total energy lost between each cross section from CX-196 to CX-596. Only the tidal constituent O_1 appears to have the correct proportional energy loss. The other main tidal constituents all indicate that only 10%-20% of the total energy loss in the observations occurs seaward of the sill; the remaining 80%-90% of the dissipation occurs within the inner basin. Conversely, the model indicates that the 85%-90% of the energy loss at the semi-diurnal frequencies M_2 and S_2 occurs in the outer channel. The diurnal frequency K_1 also exhibits that 65% energy dissipation occurs in the outer channel of the model compared to the 60% dissipated between the sill and cross section CX-296 of the inner basin. These results confirm what had already been seen in the previous tidal analysis. The model extracts too much energy from the forcing function as the signal crosses over the sill. The observational evidence suggests that the majority of tidal energy is lost within the inner basin but this is not replicated by a barotropic model nor with a model of which is statically stratified.

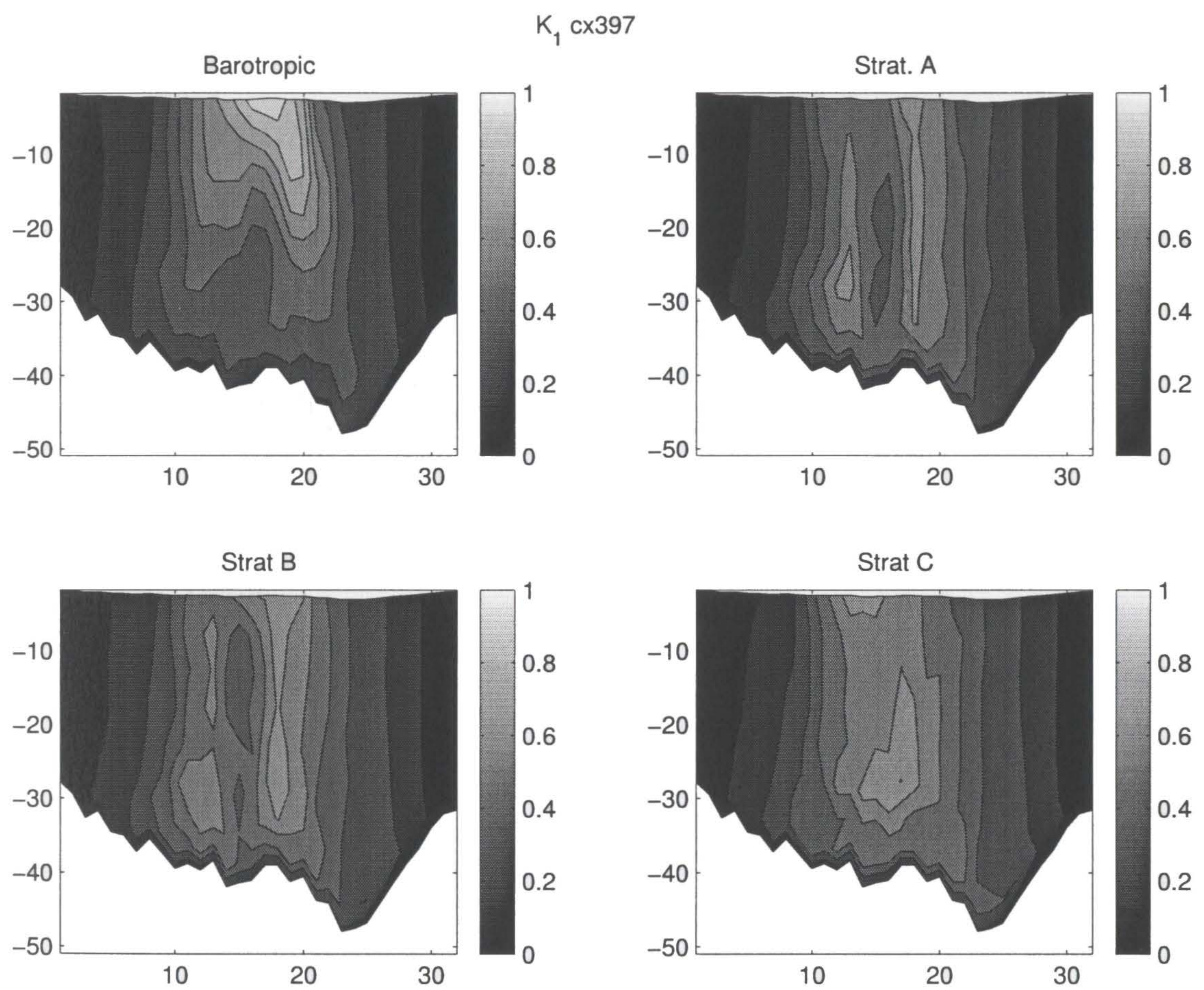

Figure 4.25: Diurnal (K_1) tide within the inner basin. Units are in cm/s, contour intervals drawn at 0.1 cm/s. X-axis indicated by grid points, one grid points equals 50 metres. Y-axis represents metres.

Table 4.5: Percentage of Total Energy Lost by the Tide. Percentage of the total energy lost between cross sections cx596 and cx196 in each region bounded by the model cross-sections. Calculations based upon values in Table 4.22

	Percentage of Total Energy Loss							
	M2		S2		O1		K1	
	obs	mod	obs	mod	obs	Mod	obs	mod
|cx196-cx296| /total	38	7	38	2	19	21	25	26
|cx296-cx396| /total	44	3	50	12	33	38	59	2
|cx396-cx496| /total	7	27	2	17	0	0	2	7
|cx496-cx596| /total	11	64	10	69	47	42	14	65

4.3 Statically Stratified Fluids Forced by Tides and Wind

Keeping in mind that the fluid remains statically stratified, with temperature and salinity fields held constant, it is not possible for this model to introduce any upwelling or vertical mixing of the surface layer which would normally be anticipated in the presence of wind. The focus of this analysis will be on the influence of wind stress on the horizontal velocity fields.

The model runs previously discussed (tidal forcing only) were repeated with the addition of wind stress as described in Section 3.4. The addition of wind stress to the model was complicated by the tendency of the model to become numerically unstable when the applied wind speed exceeded 8 km/hr for extended periods of time. For 1996 the period chosen for comparison to the data was between Julian Days 205 and 235. This choice of days was chose based upon the absence of strong sustained winds in the input field allowing the model to remain numerically stable during this time frame. The results from model will be compared to the distribution of energy between the different frequency bands as described in Section 2.3. A direct comparison to the data over the entire time frame being modelled is difficult because the stratification of the inlet changes (from stratification A to stratification C) with the formation of a deeper mixed layer seaward of the sill between days 211 and 220 (Section 2.1).

Based upon the model output from the 1996 model simulations it was decided to approach the model runs from 1997 differently. Stratifications A and B were run between days 195 and 225 during which time the stratification in the model should be a reasonable approximation to the stratification of Clode Sound for at least the first 20 days. Stratification C was run from day 225 to day 234 at which time high wind stresses in the model input produced a numerical instability. With the deeper mixed layer forming between days 211 and 220, model stratification C should provide a reasonable approximation to the actual stratification in Clode Sound during that time period.

In order to reduce the amount of error that would be introduced due to the variability of the wind field over the entire observations period in 1996 and 1997, subsets of the complete 20-minute records, corresponding to the dates being modelled, were extracted, decimated to hourly observations, then re-analysed for determination of the principal axis and power spectral estimates. For this reason some of the observations listed in Tables 4.6-4.19 may not be in complete agreement with the estimates obtained in Section 2.3.

We begin our comparison with an examination of the principle axis as estimated in section 2.5. The principle axis provides a basis upon which the velocity field may be analyzed in terms of along channel and cross channel flow. Upon rotation to the principle axis, the axis direction corresponding to the maximum variability of the velocity is chosen to represent the along channel velocity. Given the geometric constraints of the bathymetry and coastline, the chosen "along channel" axis is generally aligned with the coastline and bathymetric contours of the inlet.

As shown in Tables 4.6 And 4.7 there is good agreement between the principle axis of the data and the model output with most differences of less than 7° between the model and mooring data. The noticeable exception to this is mooring M4-96 where the difference is very large (45° at 10 metres depth) and as large as 20° at 20 and 45 metres depth. It is possible that the reduced wind stress used by the model permits this mooring to be dominated by the tidal signal that is aligned with the coast. The actual near surface observations may be dominated by the wind.

Table 4.6: Orientation of the Principle Axis for Tidal and Wind Forced Flow 1996. Values (degrees) represent the orientation of the principle axis (See section 2.5) with 0 degrees representing the eastern axis.

Principle Axis (degrees)

	Mooring: M1-96					Mooring: M4-96			
Depth	**Data**	**A**	**B**	**C**	**Depth**	**Data**	**A**	**B**	**C**
10	44	42	45	42	**10**	54	7	7	6
21	38	42	42	39	**20**	21	4	4	6
45	45	37	36	39	**45**	23	2	2	2

	Mooring: M2-96					Mooring: M5-96			
Depth	**Data**	**A**	**B**	**C**	**Depth**	**Data**	**A**	**B**	**C**
10	20	18	20	15	**10**	45	50	49	50
17	22	15	17	14	**21**	55	48	49	49
44	-6	5	4	7	**45**	53	48	48	48

	Mooring: M3-96			
Depth	**Data**	**A**	**B**	**C**
10	-8	-9	-10	-10
15	-15	-9	-9	-10

Table 4.7: Orientation of the Principle Axis for Tidal and Wind Forced Flow 1997. Values (degrees) represent the orientation of the principle axis (See section 2.5) with 0 degrees representing the eastern axis. The first column under the heading "Data" was calculated between Julian days 205-235 (stratifications A and B); the second column between Julian days 220-235 (stratification C).

Principle Axis (degrees)

Mooring: M1-97

Depth	Data		A	B	C
7.5	31	32	21	21	24
21	29	24	24	24	21

Mooring: M5-97

Depth	Data		A	B	C
7.5	-6	-5	-15	-17	-17
21	-22	-24	-13	-13	-13

Mooring: M2-97

Depth	Data		A	B	C
7.5	10	15	8	11	12
21	17	-1	3	3	10

Mooring: M6-97

Depth	Data		A	B	C
21	-6	-5	0	0	-3
33	1	-9	-2	-1	-2

Mooring: M3-97

Depth	Data		A	B	C
7.5	-21	-17	-11	-11	-9

Mooring: M7-97

Depth	Data		A	B	C
7.5	14	9	9	9	10
31	12	10	7	7	8

Mooring: M4-97

Depth	Data		A	B	C
7.5	-19	-14	-12	-13	-12
14	-12	-10	-14	-14	-13

Tables 4.8-4.12 provide a comparison of the percentage of energy in the low (0.0-0.1 cpd), meteorological (0.1-0.5 cpd), diurnal (0.8-1.13 cpd) and semi-diurnal (1.75-2.11 cpd) frequency bands in the along channel direction for 1996. It would be meaningless to compare the energy distribution of the inertial band analyzed in Section 2.3 because the model was run with the Coriolis term set identically equal to zero. Given the low amount of energy attributed to this frequency band in the analysis of Section 2.3, there should be little difference to the amount of energy remaining for distribution into the other frequency bands if this term is ignored.

At mooring M1-96 we find that the majority of the modelled energy is distributed in the meteorological band, with 44%-50% of the total fluctuating kinetic energy at 10 metres depth. The proportion of energy in the meteorological band is much greater than the 11% of the kinetic energy located in the meteorological frequency band of the mooring data. The inability of the model to reflect the proper energy distribution at this location is easily traced back to the weak tidal signals that were found in the model output. The tidal energy has been almost completely dissipated by the model by the time it reaches this far into the inner basin. The wind stress (which has already been reduced by a factor proportional to the ratio of the layer depth to the Ekman depth D_E=30 metres) is still able to dominate the surface flow. The weakness of the tide at this location is also evident at 45 metres depth where the model indicates that approximately 45% of the energy is found in the meteorological band as opposed to the 1% indicated by the data. The importance of the tidal flow at 45 metres depth is indicated in the observations with 83% of the energy is found in the semi-diurnal band where as the model indicates only 35% of the energy lies within this frequency band. Given the large amount of error between the meteorological and semi-diurnal bands at this location, it is doubtful that the model will be able to provide any meaningful conclusions regarding the true nature of the residual circulation in the region of the inlet towards the head of the inner basin.

At 10, 20 and 45 metres depth the observations at M1-96 indicate that a 69%, 60% and 88% of the energy is located in the identified frequency bands. Table 2.17 indicates that approximately 10% of the total energy is found in the inertial band at this particular location, assuming this value holds true for the selected subset of the observations currently under consideration, approximately 20% and 30% of the energy in the observations remains unexplained at 10 and 20 metres depth. Most of this will be high frequency energy available for mixing. Under the constraint of a static stratification, the model is unable to produce any significant amount of high frequency energy for mixing to occur as at M1-96: 96%-98% of the energy lies within the identified frequency bands.

At M2-96, the influence of the meteorological forcing has reduced significantly and now only represents 5%-10% of the identified energy in the model. The upper level observations from 1996 indicate that 20%-25% of the energy lies in the meteorological frequency band. 70%-80% of the energy resides in the semi-diurnal band of the model; more than twice the amount of energy located in the semi-diurnal frequency band in the observations. The model is unable to replicate the required energy distribution. The reduced meteorological forcing in the model may be a consequence of the reduced wind stress that was applied to the surface layer in the model. Unfortunately, without this reduction in the wind stress the model produced a strong vertical shear between the first and second layers in the model that led to numerical instability. There does appear to be an improvement in the amount of high frequency energy (the unexplained energy of the spectrum) that remains available for mixing in the surface layer. The identified frequency bands in the model data indicate that between 10%-15% of the total energy may reside in the upper frequency bands. This is a significant improvement over the 5% available at M1-96 but is still much less than the 30% of the total energy that remains unexplained in the higher frequency bands of the observations.

Mooring M3-96, located at the sill, is dominated by the semi-diurnal nature of the tide. Meteorological forces are responsible for only 5% of the energy found in the observations. The configuration of the wind stress in the model (tapered towards the coastline) reduces the influence of the wind at the sill due to the lack of resolution (number of grid points) that the model uses to represent the sill region. In the absence of wind, the model does not generate any significant amount of high frequency energy to be available for mixing. The total amount of energy identified in the observations indicates that approximately 20% of the total energy available is distributed into the higher frequency bands as opposed to the 2-3% of the total energy available in the simulations.

Seaward of the sill, at M4-96 and M5-96 the amount of energy located in the meteorological band at 10 metres depth for both the observations and the model are in good agreement. Meteorological forces account for only 11% of the energy of the observations at M4-96 while the model indicates 7%-8%. For M5-96 wind stress in the model accounts for 37% of the total energy compared to 30% located in the meteorological band of the observations. At 20 metres depth, the amount of energy located in the meteorological band of the observations represents almost twice the amount of the total energy located in the meteorological band of the model. If we consider the distribution of the sigma coordinate system at a point were the depth of the fluid is 91 metres (M5-96): 10 metres depth lies between the first and second vertical level and 20 metres depth lies between the second and third vertical level. The model appears unable to transfer the wind stress energy from the surface sigma layer into the second layer.

Similar to all of the other mooring locations except M1-96, the velocities generated by the model are dominated by the semi-diurnal frequency band with 80%-85% of the total kinetic energy being located in this frequency band at M4-96 between 10-45 metres depth. At M5-96 the semi-diurnal frequency band accounts for 45%, 70% and 85% of the energy at 10, 20 and 45 metres depth. The identified frequency bands in the model account for 94%-99% of the total energy at both M4-96 and M5-96 the lack of high frequency energy is most noticeable at M4-96 where the identified energy bands account for only 45%-60% of the total energy in the mooring data. The evolution of temperature and salinity discussed in section 2.1, we expect that M4-96 should have the greatest amount of unexplained high frequency energy available for mixing. The available high frequency energy does not exist in a statically stratified model so it is extremely doubtful that the model would provide any insight into the mixing processes associated with flow over the sill without the evolution of temperature and salinity fields.

The lack of energy located in the meteorological band of the model indicates that the model is unable to transmit the energy induced by the wind on the surface layer downwards into the second and third model layers. The inability of the model to produce a proper surface mixed layer may be partially attributed to the lack of vertical layers at the surface. The requirements of hydrostatic consistency prevent an increase in the number of vertical layers to represent the surface flow. There are no significant differences found in the amount of energy located in the meteorological band as the depth of the main pycnocline increases from 10 to 30 metres in the outer channel region. One would normally anticipate that the surface wind stress would increase the amount of energy located in the meteorological band at 20 metres depth as the mixed layer deepens below this level. Recent changes to the POM model to enhance surface mixing and include the effect of wave breaking (Mellor and Blumberg, 2004) have not been included in this implementation of the model to determine if there is any significant improvement at this horizontal scale.

Table 4.8: Distribution of the Energy Associated with the Spectral Frequencies of the Along Channel Flow. Values (percent) indicate the amount of the total energy of the system found in each of the identified frequency bands.

Distribution of Energy
Mooring: M1-96

Low (0.0-0.1 cpd)					Met (0.1-0.5 cpd)				
Depth	**Data**	**A**	**B**	**C**	**Depth**	**Data**	**A**	**B**	**C**
10	12	29	27	24	**10**	11	48	44	49
21	21	14	13	15	**21**	10	42	40	38
45	3	17	16	13	**45**	1	44	45	45

Diurnal (0.8-1.13 cpd)					Semidiurnal (1.75-2.11 cpd)				
Depth	**Data**	**A**	**B**	**C**	**Depth**	**Data**	**A**	**B**	**C**
10	3	1	2	2	**10**	43	18	23	22
21	13	2	2	2	**21**	16	39	42	42
45	1	2	1	2	**45**	83	35	36	37

Table 4.9: Distribution of the Energy Associated with the Spectral Frequencies of the Along Channel Flow. Values (percent) indicate the amount of the total energy of the system found in each of the identified frequency bands.

Distribution of Energy
Mooring: M2-96

Low (0.0-0.1 cpd)					Met (0.1-0.5 cpd)				
Depth	**Data**	**A**	**B**	**C**	**Depth**	**Data**	**A**	**B**	**C**
10	7	5	8	2	**10**	23	6	6	7
17	27	8	8	6	**17**	20	8	7	5
44	4	9	7	9	**44**	2	4	6	5

Diurnal (0.8-1.13 cpd)					Semidiurnal (1.75-2.11 cpd)				
Depth	**Data**	**A**	**B**	**C**	**Depth**	**Data**	**A**	**B**	**C**
10	6	4	4	5	**10**	31	69	69	74
17	5	3	3	6	**17**	13	72	75	72
44	2	3	3	2	**44**	33	79	78	77

Table 4.10: Distribution of the Energy Associated with the Spectral Frequencies of the Along Channel Flow. Values (percent) indicate the amount of the total energy of the system found in each of the identified frequency bands.

Distribution of Energy
Mooring: M3-96

Low (0.0-0.1 cpd)					Met (0.1-0.5 cpd)				
Depth	**Data**	**A**	**B**	**C**	**Depth**	**Data**	**A**	**B**	**C**
10	3	1	0	1	**10**	4	0	0	0
15	12	2	2	1	**15**	7	0	0	0

Diurnal (0.8-1.13 cpd)					Semidiurnal (1.75-2.11 cpd)				
Depth	**Data**	**A**	**B**	**C**	**Depth**	**Data**	**A**	**B**	**C**
10	5	2	2	2	**10**	67	95	96	96
15	2	3	3	3	**15**	60	92	94	95

Table 4.11: Distribution of the Energy Associated with the Spectral Frequencies of the Along Channel Flow. Values (percent) indicate the amount of the total energy of the system found in each of the identified frequency bands.

Distribution of Energy
Mooring: M4-96

Low (0.0-0.1 cpd)					Met (0.1-0.5 cpd)				
Depth	**Data**	**A**	**B**	**C**	**Depth**	**Data**	**A**	**B**	**C**
10	19	5	4	5	**10**	11	7	8	7
20	16	5	5	5	**20**	19	5	5	6
45	3	7	7	6	**45**	4	4	4	5

Diurnal (0.8-1.13 cpd)					Semidiurnal (1.75-2.11 cpd)				
Depth	**Data**	**A**	**B**	**C**	**Depth**	**Data**	**A**	**B**	**C**
10	7	4	4	4	**10**	18	79	80	80
20	6	2	2	2	**20**	18	85	86	85
45	4	3	2	2	**45**	33	84	85	84

Table 4.12: Distribution of the Energy Associated with the Spectral Frequencies of the Along Channel Flow. Values (percent) indicate the amount of the total energy of the system found in each of the identified frequency bands.

Distribution of Energy
Mooring: M5-96

Low (0.0-0.1 cpd)					Met (0.1-0.5 cpd)				
Depth	**Data**	**A**	**B**	**C**	**Depth**	**Data**	**A**	**B**	**C**
10	24	6	7	7	**10**	30	37	37	37
21	16	7	6	4	**21**	37	19	20	18
45	5	3	3	3	**45**	17	9	9	9

Diurnal (0.8-1.13 cpd)					Semidiurnal (1.75-2.11 cpd)				
Depth	**Data**	**A**	**B**	**C**	**Depth**	**Data**	**A**	**B**	**C**
10	6	7	7	6	**10**	15	44	43	46
21	9	2	2	3	**21**	19	69	69	73
45	13	1	1	1	**45**	35	86	85	85

The results of the comparison between the 1996 observations and the model runs indicate that the model performs poorly in regions of the inlet that are removed from the region of the sill. We have established that, for a statically stratified fluid, the tidal forcing is not representative of the observed tidal forcing and this contributes to the differences associated with the velocity field when wind stress is introduced into the model. The comparison of the tidal forcing to the 1997 observations indicated that the tidal forcing in the model was more representative of the observed tide when the focus of the study was restricted to the regions of the inlet in closer proximity to the sill. Wind stress was again applied to the model with tidal forcing from 1997 to determine if any improvement may be found in the distribution of energy when the tidal structure is more representative of the observed tide. The results of the analysis are found in Tables 4.13-4.19.

Within the inner basin, the near surface flow (7.5 metres depth) at mooring M1-97 shows meteorological forces represent 18% or the observed energy between days 195-225 and only 13% of the observed energy between days 220-234. This decrease in the wind stress does not appear to indicate a weakening of the average wind stress, however, because the amount of energy located in the meteorological band at moorings M2-97 and M3-97 is found to increase from 13% to 24% at mooring M2-97 and from 9% to 19% at mooring M3-97. At M1-97 and M2-97, a disproportionately large amount of the energy is located in the semi-diurnal band for stratifications A and B with over 70% of the total energy located in this frequency band at M1-97 and 65%-70% of the energy located in this frequency band at M2-97. The model suggests that the velocity field at this location is dominated by the semi-diurnal tide, however the energy distribution over the same time frame in the observations reveals that only 16% of the total energy is found in the semi-diurnal band at M1-97 and 36% at M2-97. At M3-97, the amount of energy in the semi-diurnal band for the near surface flow is reduced to 53% -54% of the total energy in the model, which is still higher than the 42% of the energy found in this frequency band in the observations but not so disproportionately large to be considered unreasonable.

Stratification C produces a much better distribution of energy within the inner basin. For both stratification C and the observations we find at mooring M1-97 (7.5

metres depth) that 13% of the energy is located in the meteorological band. There also is reasonable agreement for the amount of energy found in the semi-diurnal band with 24% and 31% for the observations and model, respectively. At M3-97, the model reflects the balance of forces found in the observations. At 7.5 metres depth, the proportion of energy located in the semi-diurnal band for the model and the observations differs by only 1%. The difference in the proportion of energy located in the meteorological band for this location is 11% with the model having a greater proportion (30%) of energy located in this frequency band then the observations (19%). The balance of wind stress and tidal forcing at M2-97 is not reproduced in the centre of the inlet. At M2-97, stratification C still has 39% of the total energy located in the semi-diurnal band compared to the 12% located in this frequency band from the mooring data. Only 9% of the energy is located in the meteorological band of the model simulation compared to the observed 24%.

At the sill, the distribution of energy for stratifications A and B in the semi-diurnal band of the model output is disproportionately high (85%) compared to amount of energy observed in this frequency band (40-50%). The amount of energy found within the semi-diurnal band in the model run with stratification C (60%) is significantly less than the amount of energy located in this frequency band for stratifications A and B but does not reflect the reduced energy located in this frequency band (15%-25%) for the corresponding observations. The meteorological band is also much too weak for all model stratifications to accurately reflect the proper balance of forces at the sill.

Seaward of the sill, at moorings M5-97 and M7-97, the energy distribution into the meteorological band for stratification C at 31% and 11%, respectively agrees quite well with the observed values of 27% and 8%. Mooring M6-97 does not reproduce this energy distribution with only 2% of the energy in the model output found in this frequency band compared to 17% from the observations. For stratifications A and B the energy of the meteorological frequency band is much too weak compared to the observations. Semi-diurnal energy still dominates the flow outside the sill for stratifications A and B with 65%-85% of the total energy found at the dominant tidal frequency. Consistent with the results of the inner basin, the semi-diurnal energy for stratification C is much less dominant than that produced by the model for stratifications A and B. Near the surface at moorings M5-97 and M6-97, the model output reveals that only 22% and 57%, respectively, of the total energy resides in the semi-diurnal frequency band compared to the observed values of 11% and 21%. Although this is a significant improvement of the energy distribution found at stratifications A and B, tidal flow will still dominates the flow in these regions in disagreement with the observational evidence. At M6-97, the lack of meteorological energy at 21 metres depth is very evident with only 2% of the total energy being found in this frequency band. Tidal forces (semi-diurnal) dominate for stratification C although they are much weaker (only 40% of the total energy as opposed to 75% of the total energy for stratifications A and B).

With the stratification held constant in the model, the model is unable to move energy into the higher frequency bands to make it available for mixing. The model is, also, unable to transmit energy downwards from the surface layer when wind stress (low-passed filtered with a cut-off frequency of 12 hours to improve model stability) is applied. As a result, a disproportionate amount of the total energy remains in the semi-diurnal frequency band at almost all moorings located in the vicinity of the sill.

Table 4.13: Distribution of the Energy Associated with the Spectral Frequencies of the Along Channel Flow. Values (percent) indicate the amount of the total energy of the system found in each of the identified frequency bands. The first column under the heading "Data" was calculated between Julian days 205-235 (stratifications A and B); the second column between Julian days 220-235 (stratification C).

Distribution of Energy
Mooring: M1-97

	Low (0.0-0.1 cpd)						Met (0.1-0.5 cpd)				
Depth	Data		A	B	C	**Depth**	Data		A	B	C
7.5	19	10	4	5	13	**7.5**	18	13	7	6	13
21	8	8	7	12	26	**21**	13	8	12	12	26

	Diurnal (0.8-1.13 cpd)						Semidiurnal (1.75-2.11 cpd)				
Depth	Data		A	B	C	**Depth**	Data		A	B	C
7.5	11	8	4	4	11	**7.5**	16	24	73	72	31
21	21	14	3	3	2	**21**	5	8	64	59	29

Table 4.14: Distribution of the Energy Associated with the Spectral Frequencies of the Along Channel Flow. Values (percent) indicate the amount of the total energy of the system found in each of the identified frequency bands. The first column under the heading "Data" was calculated between Julian days 205-235 (stratifications A and B); the second column between Julian days 220-235 (stratification C).

Distribution of Energy
Mooring: M2-97

	Low (0.0-0.1 cpd)						Met (0.1-0.5 cpd)				
Depth	Data		A	B	C	**Depth**	Data		A	B	C
7.5	9	39	12	7	16	**7.5**	13	24	4	6	9
21	13	21	10	6	10	**21**	26	3	4	3	13

	Diurnal (0.8-1.13 cpd)						Semidiurnal (1.75-2.11 cpd)				
Depth	Data		A	B	C	**Depth**	Data		A	B	C
7.5	12	2	3	2	5	**7.5**	36	12	66	70	39
21	7	4	4	8	6	**21**	12	15	62	59	32

Table 4.15: Distribution of the Energy Associated with the Spectral Frequencies of the Along Channel Flow. Values (percent) indicate the amount of the total energy of the system found in each of the identified frequency bands. The first column under the heading "Data" was calculated between Julian days 205-235 (stratifications A and B); the second column between Julian days 220-235 (stratification C).

Distribution of Energy
Mooring: M3-97

	Low (0.0-0.1 cpd)						Met (0.1-0.5 cpd)				
Depth	Data		A	B	C	**Depth**	Data		A	B	C
7.5	10	20	26	25	24	**7.5**	9	19	10	11	30

	Diurnal (0.8-1.13 cpd)						Semidiurnal (1.75-2.11 cpd)				
Depth	Data		A	B	C	**Depth**	Data		A	B	C
7.5	5	4	2	2	3	**7.5**	42	27	54	53	28

Table 4.16: Distribution of the Energy Associated with the Spectral Frequencies of the Along Channel Flow. Values (percent) indicate the amount of the total energy of the system found in each of the identified frequency bands. The first column under the heading "Data" was calculated between Julian days 205-235 (stratifications A and B); the second column between Julian days 220-235 (stratification C).

Distribution of Energy
Mooring: M4-97

Low (0.0-0.1 cpd)					
Depth	**Data**		**A**	**B**	**C**
7.5	9	30	1	1	9
14	13	41	0	0	5

Met (0.1-0.5 cpd)					
Depth	**Data**		**A**	**B**	**C**
7.5	12	17	0	0	1
14	25	27	0	0	2

Diurnal (0.8-1.13 cpd)					
Depth	**Data**		**A**	**B**	**C**
7.5	5	2	3	2	4
14	3	1	3	3	5

Semidiurnal (1.75-2.11 cpd)					
Depth	**Data**		**A**	**B**	**C**
7.5	52	27	85	85	57
14	41	16	82	82	60

Table 4.17: Distribution of the Energy Associated with the Spectral Frequencies of the Along Channel Flow. Values (percent) indicate the amount of the total energy of the system found in each of the identified frequency bands. The first column under the heading "Data" was calculated between Julian days 205-235 (stratifications A and B); the second column between Julian days 220-235 (stratification C).

Distribution of Energy
Mooring: M5-97

Low (0.0-0.1 cpd)					
Depth	**Data**		**A**	**B**	**C**
7.5	11	8	8	10	24
21	30	25	5	7	7

Met (0.1-0.5 cpd)					
Depth	**Data**		**A**	**B**	**C**
7.5	23	27	12	9	31
21	17	40	6	6	18

Diurnal (0.8-1.13 cpd)					
Depth	**Data**		**A**	**B**	**C**
7.5	5	10	1	1	1
21	3	3	2	2	1

Semidiurnal (1.75-2.11 cpd)					
Depth	**Data**		**A**	**B**	**C**
7.5	29	11	66	66	22
21	19	8	78	74	52

Table 4.18: Distribution of the Energy Associated with the Spectral Frequencies of the Along Channel Flow. Values (percent) indicate the amount of the total energy of the system found in each of the identified frequency bands. The first column under the heading "Data" was calculated between Julian days 205-235 (stratifications A and B); the second column between Julian days 220-235 (stratification C).

Distribution of Energy
Mooring: M6-97

Low (0.0-0.1 cpd)					
Depth	**Data**		**A**	**B**	**C**
21	19	37	3	3	41
33	5	14	2	3	37

Met (0.1-0.5 cpd)					
Depth	**Data**		**A**	**B**	**C**
21	26	17	2	2	2
33	26	49	3	3	2

Diurnal (0.8-1.13 cpd)					
Depth	**Data**		**A**	**B**	**C**
21	3	4	4	5	4
33	8	1	4	3	6

Semidiurnal (1.75-2.11 cpd)					
Depth	**Data**		**A**	**B**	**C**
21	19	10	75	76	38
33	5	6	78	78	40

Table 4.19: Distribution of the Energy Associated with the Spectral Frequencies of the Along Channel Flow. Values (percent) indicate the amount of the total energy of the system found in each of the identified frequency bands. The first column under the heading "Data" was calculated between Julian days 205-235 (stratifications A and B); the second column between Julian days 220-235 (stratification C).

Distribution of Energy
Mooring: M7-97

Low (0.0-0.1 cpd)					
Depth	**Data**		**A**	**B**	**C**
7.5	15	4	4	4	7
31	19	14	4	4	11

Met (0.1-0.5 cpd)					
Depth	**Data**		**A**	**B**	**C**
7.5	12	8	2	2	11
31	22	11	1	1	13

Diurnal (0.8-1.13 cpd)					
Depth	**Data**		**A**	**B**	**C**
7.5	7	9	1	1	4
31	4	11	1	1	3

Semidiurnal (1.75-2.11 cpd)					
Depth	**Data**		**A**	**B**	**C**
7.5	27	21	84	84	57
31	18	18	84	84	55

4.4 Residual Circulation

In a uniform channel, the action by the tide should be equal in both the flood and ebb. In the presence of large bathymetric features, however, the tide may induce a background mean flow. To determine the background mean flow induced by the tide, the velocity field over the entire domain for the model runs forced by a tidal signal only was averaged for the 30-day model runs. The result shown in Figure 4.26, indicating that the tidal forcing across the sill induces a residual circulation in the neighbourhood of the sill. However, bearing in mind the smoothing algorithm used to produce the model domain, it is not entirely obvious that the tidally induced circulation is very representative of the true circulation that would be produced by tidal action over the sill. The most obvious potential difference between the modelled residual flow and the actual circulation is the existence of a large clock-wise rotating eddy directly over the sill. As previously noted, the southern half of the sill is actually a region of very shallow water with a depth of approximately 5 metres. The smoothing used to produce the model domain has deepened this region to a depth of between 15-20 metres widening the deeper channel that exists along the northern coastline. With a narrower channel along the northern coastline and a much shallower region to the south, one would normally anticipate that the circulation over the sill would be more rectilinear, travelling back and forth across the sill as opposed to forming such a large eddy.

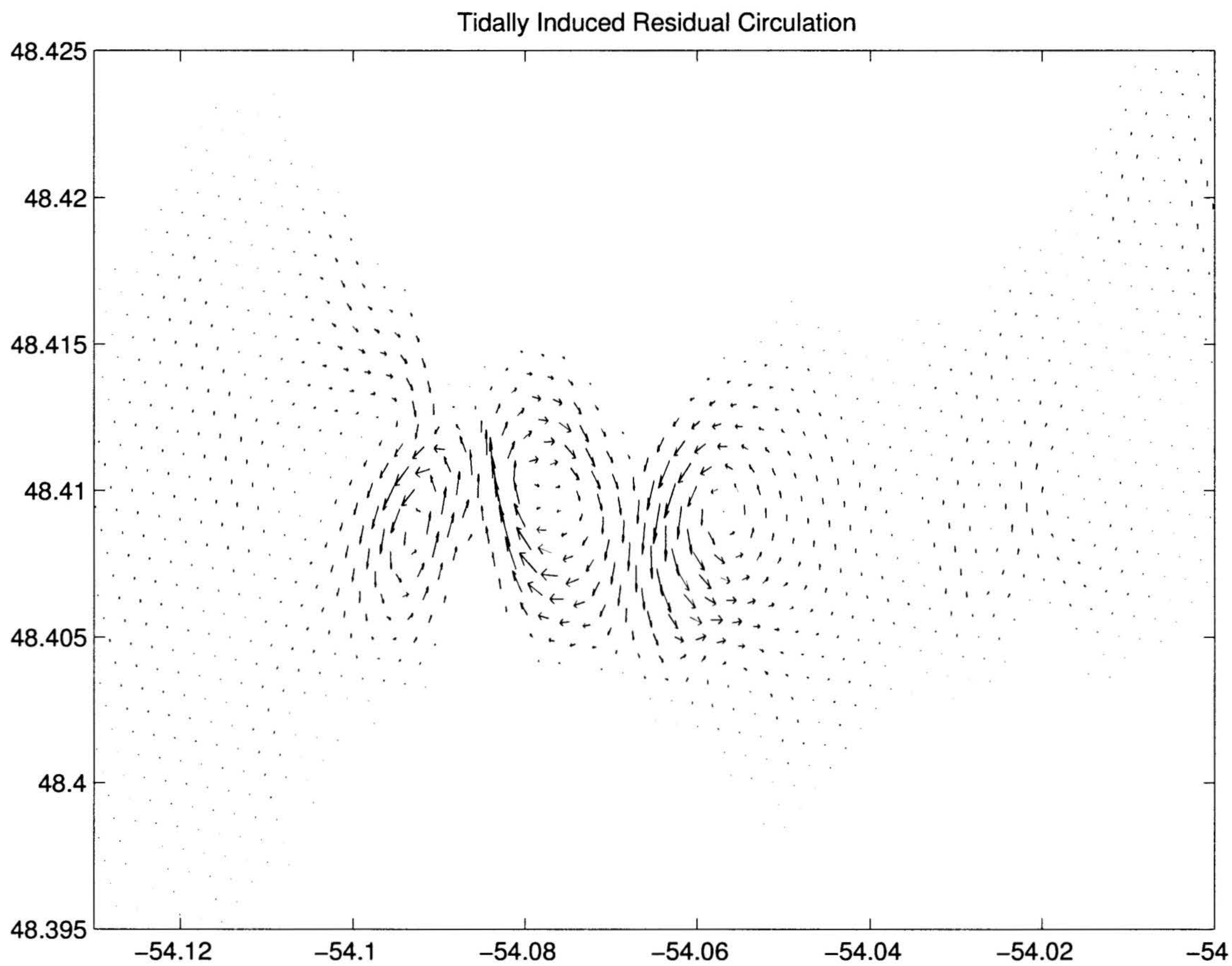

Figure 4.26 Tidally Induced Residual Circulation at the Sill. Tidally driven eddies are produced by the model on either side of the sill. The cross channel phase shift in the M_2 estimated from the mooring data of 1997 indicated that these eddies may exist. The eddy formed by the model on the sill may be a consequence of the widening and deepening used to create the model bathymetry.

Winds in Newfoundland are predominantly southwesterly, by averaging the model data over the entire 30-day simulation the residual circulation for the circulation induced by the winds and the tides may be determined. As noted above tidal forcing alone is able to induce a residual flow in the neighbourhood of the sill, to determine the residual flow induced by the wind field, we can calculate the difference between the model runs forced by both wind and tides and those forced by tides alone. Images of the residual circulation from tidal and wind forced flow and the residual circulation induced by the wind are shown in Figures 4.27 and 4.28. Note that the wind-induced circulation is dominant in the inner basin. Over the long term, the wind induced residual circulation establishes a clockwise eddy circulation with the strongest flow along the northern coastline and also a counter clockwise eddy in the southwestern corner near the head of the inlet. Unfortunately, because of the poor representation of the tide within the inner basin it is difficult to have much confidence that this circulation is truly representative of the actual residual circulation of the inner basin.

To assess the performance of the model in producing a true representation of the residual circulation, the observational data and the model data with wind and tide forcing was de-tided using a low pass Butterworth filter to remove the diurnal, semi-diurnal and higher frequencies from the signal. A sample of the de-tided signals for the barotropic and statically stratified fluids along with the observed residual current, corresponding to the model simulations, are shown in Figures 4.29-4.31. Statistically, the residual currents were averaged over the entire model run and corresponding period of observations. The time-averaged currents (vector components) along with the standard deviation of these currents are provided in Tables B.19 and B.20. In the discussion that follows, the residual currents will be described in terms of their mean speed (cm/s) and direction of the flow (degrees) derived from the vector components of the velocity field provided in Tables B.19 and B.20. The orientation of the current will be referenced with the eastern axis representing zero degrees. Positive angles are measured in a counter-clockwise direction.

In 1996 (Table B.19), the mean current speed at mooring M1-96 was 1.7-1.9 cm/s, oriented 18°-25°. The mean current of the barotropic model is only 0.2 cm/s at -27°. The statically stratified models have mean currents of 0.5-0.6 cm/s, moving in the opposite direction of the observed current (-170°). At M2-96, the observed mean flow is 3.5-3.8 cm/s between 141°-166°. The mean currents in both barotropic and stratified models, at M2-96, remain weak at only 0.2-0.4 cm/s and between -108° and -135°.

At the sill (M3-96), the observed mean circulation is very strong, between 5.1-5.4 cm/s, and directed towards the inner basin at 108°-128°. The barotropic model has no mean flow at the sill (<0.05 cm/s) while the stratified models have a mean current of 0.4-0.6 cm/s directed towards the outer channel, 11°-63°.

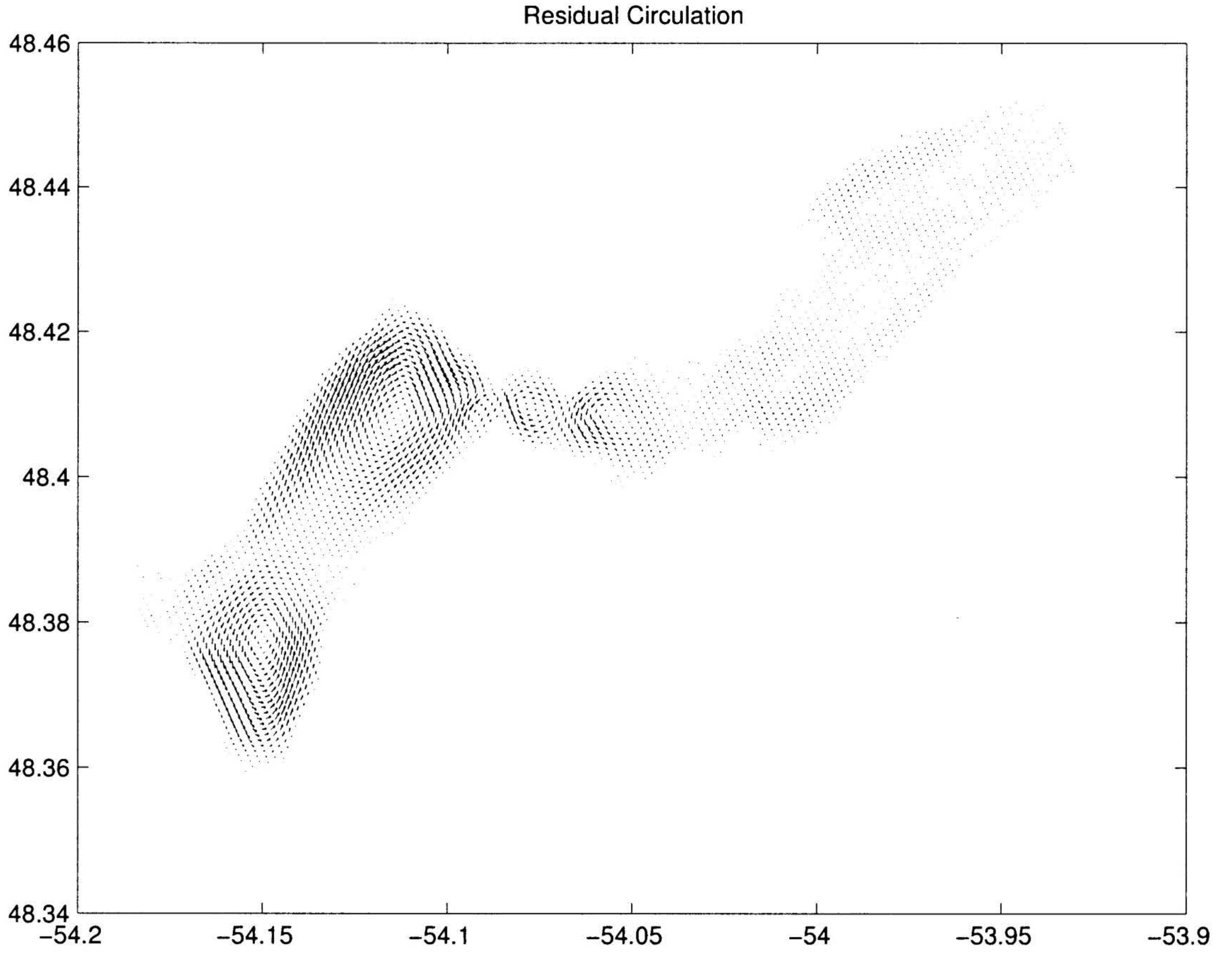

Figure 4.27: Tide and Wind Induced Residual Circulation. Tidal and wind forces combine to generate large eddies in the inner basin of the model. Tidal forcing within the inner basin of the model is weaker than expected. The wind and tidally driven flow may not represent the true circulation of the inner basin.

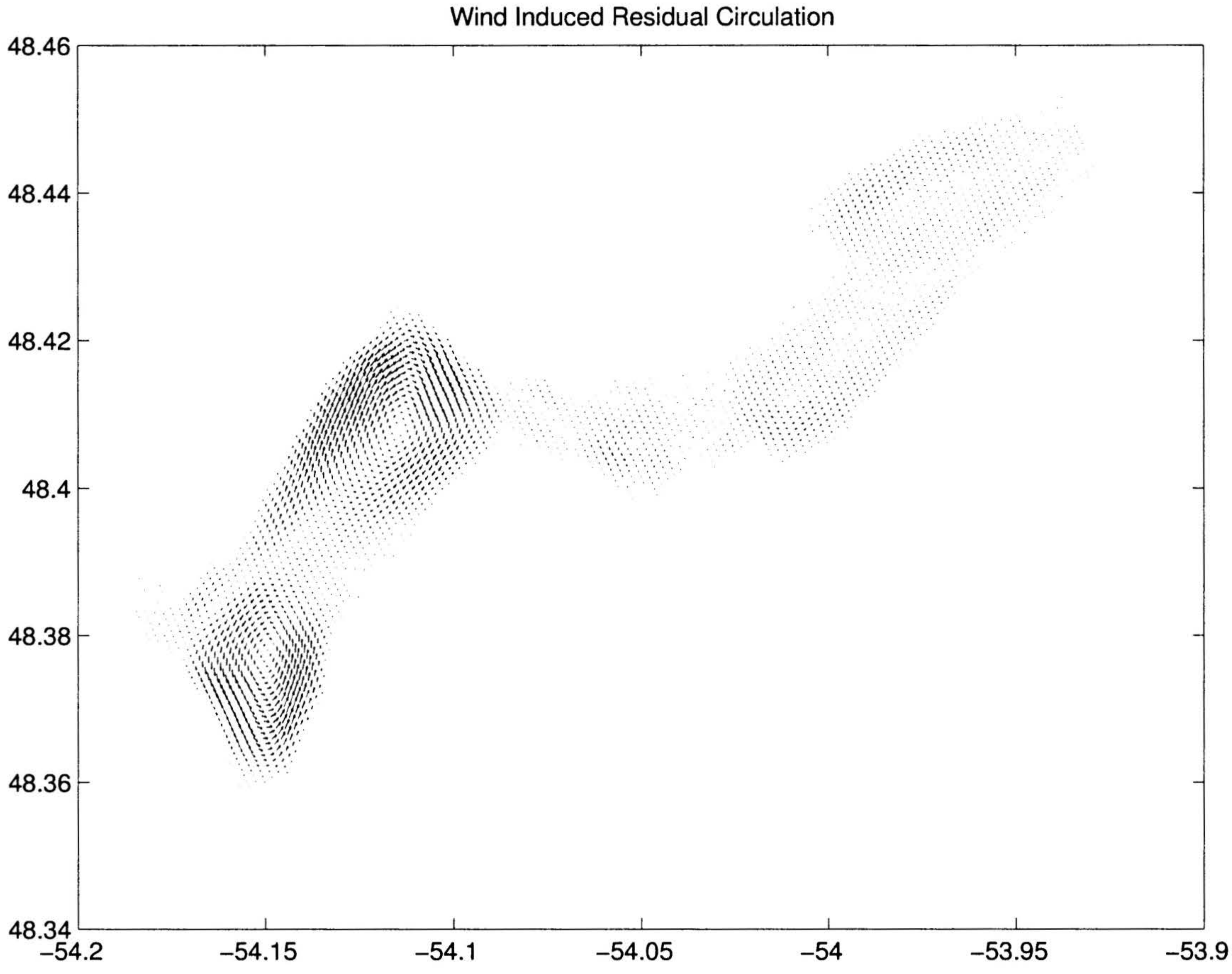

Figure 4.28: Component of the Residual Circulation Induced by the Wind. The residual circulation that is driven by the wind stress in the model indicates the dominance of surface wind stress on the circulation of the inner basin. Surface wind stress as little influence at the sill or in the outer channel.

The model performance did not improve seaward of the sill. At mooring M4-96 the near surface currents were almost due west (177°-178°) at 4.4-4.9 cm/s. The barotropic model indicates a northeasterly residual flow (27°) in the surface region of only 0.4 cm/s. The stratified models produce an even weaker mean current, measuring only 0.1 cm/s, directed either to the north (90°) with stratifications A and B and northeast (45°) with stratification C. At M5-96, the observed mean surface flow was 5.2-5.5 cm/s at -128° (southwest). The barotropic model indicates a mean flow of only 1.1 cm/s at 22°

(northeast). The stratified model runs produce a surface mean current between 0.6-0.7 cm/s at 0° (east).

The comparison between the surface observations and the model from 1997 (Table B.20) is similar to that of the 1996 observations and model simulations. Within the inner basin, at mooring M1-97, the observed mean current varies between 0.8-2.2 cm/s over the time frame used in the model simulations. The direction of this near surface mean flow varies significantly indicating a change in the direction of the wind. Between Julian days 195-240 the mean current is directed towards 104°. Over the shorter time frame used in the model simulations for stratifications A and B (days 195-225), the mean flow is oriented to 156°, while between Julian days 220-235 (stratification C) the direction has changed to 47°. The model is unable to reproduce this mean flow. For all of the simulations, the mean current speed is 0.2-0.3 cm/s. The flow is almost opposite in direction to the observed mean currents varying from -90° in the barotropic model, to between -63° and -72° in the stratified models.

At M2-97, the observed near surface currents were 3.5-4.6 cm/s, west (-177°) between Julian days 195-240. The mean currents in the models are weakest for a barotropic fluid (between Julian days 195-240) at only 0.2 cm/s, due south. For the stratified fluids, the strongest mean currents occur when the main pycnocline is placed below the level of the sill (stratification C), 0.8 cm/s due east (0°). Stratifications A and B have mean currents of 0.5 cm/s between -22° and -11° between days 195-225.

The strongest mean currents in the model are found at mooring M3-97, 1.1-1.6 cm/s; much weaker than the 8.4-9.4 cm/s mean currents calculated from the observations. The observed mean currents not only differ in magnitude, when compared to the model runs, but also in direction. At M3-97 the observed currents flow towards the head of the inner basin (-136 to -150°) while the mean currents produced by the model are directed towards the sill.

At the sill (M4-97), the time averaged surface currents are directed towards the inner basin with an average speed of 3.1-4.9 cm/s from days 195-240. However, between days 220-235, the mean flow is only 2.6 cm/s directed northwards (86°). All of the models indicate that the mean flow at the sill is directed towards the outer channel (8°-22°) and only 0.5-0.8 cm/s. The similarity between all of the model results indicates that the stratification used by the model has little influence on the mean velocity fields in the absence of an evolving temperature and salinity field.

Seaward of the sill, at moorings M5-97 and M7-97 the mean surface flow in the models is also weaker than the observed mean flow. The observed surface flow on the southern mooring, M5-97, was 0.9-1.2 cm/s, the mean flow in the models is only 0.4-0.5 cm/s. The direction of the mean flow in the barotropic model -37° is similar to the observed value of -31° between days 195-240. Stratifications A and B have mean currents directed at -117° which differs observed mean flow, from days 195-225, by 90°. The direction of the observed mean flow at mooring M7-97 (-170° to -171°) agrees very well with the models. The direction of the flow for stratifications A and B was -173°. For the barotropic model and stratification C, the direction of the mean flow was 180°. Although the direction of the mean flow agrees, the modelled current speeds, 0.5-1.0 cm/s are only 10%-20% of the observed 5.2-5.6 cm/s.

At depths below the surface (20-45 metres), there is better agreement between the speed of the observed mean currents and the model results. Observed mean currents, at these depths, are generally weaker than those of the surface layer where wind stress has a greater influence. The model produces currents that are more uniform with depth. Although the time-averaged speeds of the residual currents are in closer agreement, the model is not able to reproduce the direction of the flow.

Tables B.19-B.20 and Figures 4.8-4.13 indicate that the residual circulation in the models also lacks the variability seen in the observations. At the surface, the standard deviation of the observed velocity is, typically, 2-3 times greater than the model. Below the surface, the currents generated by the model and have the required variability, but there is little difference between the barotropic model and the stratified models. Figures 4.29-4.40 indicate that at times when the barotropic model and stratified models coincide, there is little difference in the residual circulation produced by the model.

4.5 Summary

The inability of the model to reproduce the magnitude of the surface mean flow is not that unexpected given the poor representation of the surface tides and the imbalance of forces indicated by the energy spectrum of the simulations. The dissipation of tidal energy on the seaward side of the sill is much too great within the model domain when compared to the observed dissipation rate. As the tidal force enters the inner basin, it lacks the required energy to balance with the wind stress at the surface. Even though the surface wind stress in the model was intentionally reduced when applied to the surface layer of the model's internal mode (Section 3.4), the distribution of the fluctuating kinetic energy clearly indicates that, within the inner basin, meteorological forces are still too strong compared to the available energy of the tide.

An imbalance of energy also exists at the sill, where semi-diurnal tidal forces represent a higher than observed proportion of the total energy. The observed energy distribution at the sill (Section 2.3, Tables 2.2-2.3) does not indicate that meteorological forces are significant in this region where the semi-diurnal tides represent 40%-55% of the total energy. The models indicate (Tables 4.10 and 4.16) that between 80%-90% of the total energy is within the semi-diurnal frequency band. The difference between the amount of energy in the semi-diurnal frequency band of the observations and models indicates that, within the models, the tidal forcing at the sill remains very coherent. This indicates that the model, using a static density field, is unable to extract energy from the tide and move it into higher frequencies where it may be available for mixing. Tables 2.2 and 2.3 indicate that 25%-35% of the high frequency energy at the sill lies outside of the tidal frequency bands. This unidentified energy represents the higher frequencies, such as M_4 and M_6, which represent nonlinear interactions and the effects of friction.

Figures 4.14-4.19 indicate the model suppresses nonlinear interactions and frictional effects at tidal frequencies. Even at the sill, the nonlinear tidal currents (Tables B.15-B.16) and frictional currents (Tables B.17-B.18) are much weaker than the observed tidal currents. Both nonlinear interactions and frictional forces are expected to be strongest at the sill, yet the models are unable to generate any significant interactions in this region. Within the models, the rapid dissipation of tidal energy seaward of the sill (Tables 4.3-4.5) indicates that energy is being extracted by the model at a higher rate than the observed rate of energy dissipation. This energy is not being transferred into shallow water constituents of the tide through nonlinear interactions of frictional forces. The only other energy sink available within the model is the turbulence scheme. The loss of the tidal energy within the model appears to indicate that the turbulence scheme is removing too much energy from the tide. With temperature and salinity held constant, the energy that would normally become mixing energy, cannot mix and appears to be permanently lost within the model domain.

The models discussed throughout this chapter indicate that a linear model of this domain is completely incapable of modelling the observed velocity field. The inclusion of the nonlinear terms into the model equations produces a completely different structure in the velocity field in the neighbourhood of the sill: the formation of a strong jet as the tide passes over the sill. There is some evidence that stratification does influence the nature of the tide and the response to wind forcing although there is little evidence that in a absence of an evolving temperature and salinity field that the location of the main pycnocline has a significant influence on the residual circulation. Generally, it is found that away from the sill, the barotropic model performs as well as the stratified model when compared to the observations collected in 1996 and 1997.

Before the model may be used to study the circulation and mixing within Clode Sound, the representation of the tide must be improved. In Chapter 5, mixing of temperature and salinity will be shown to improve the representation of the tidal forcing. The tide, however, remains very weak towards the head of the inlet and the application of wind stress, in the model, decreases the numerical stability significantly.

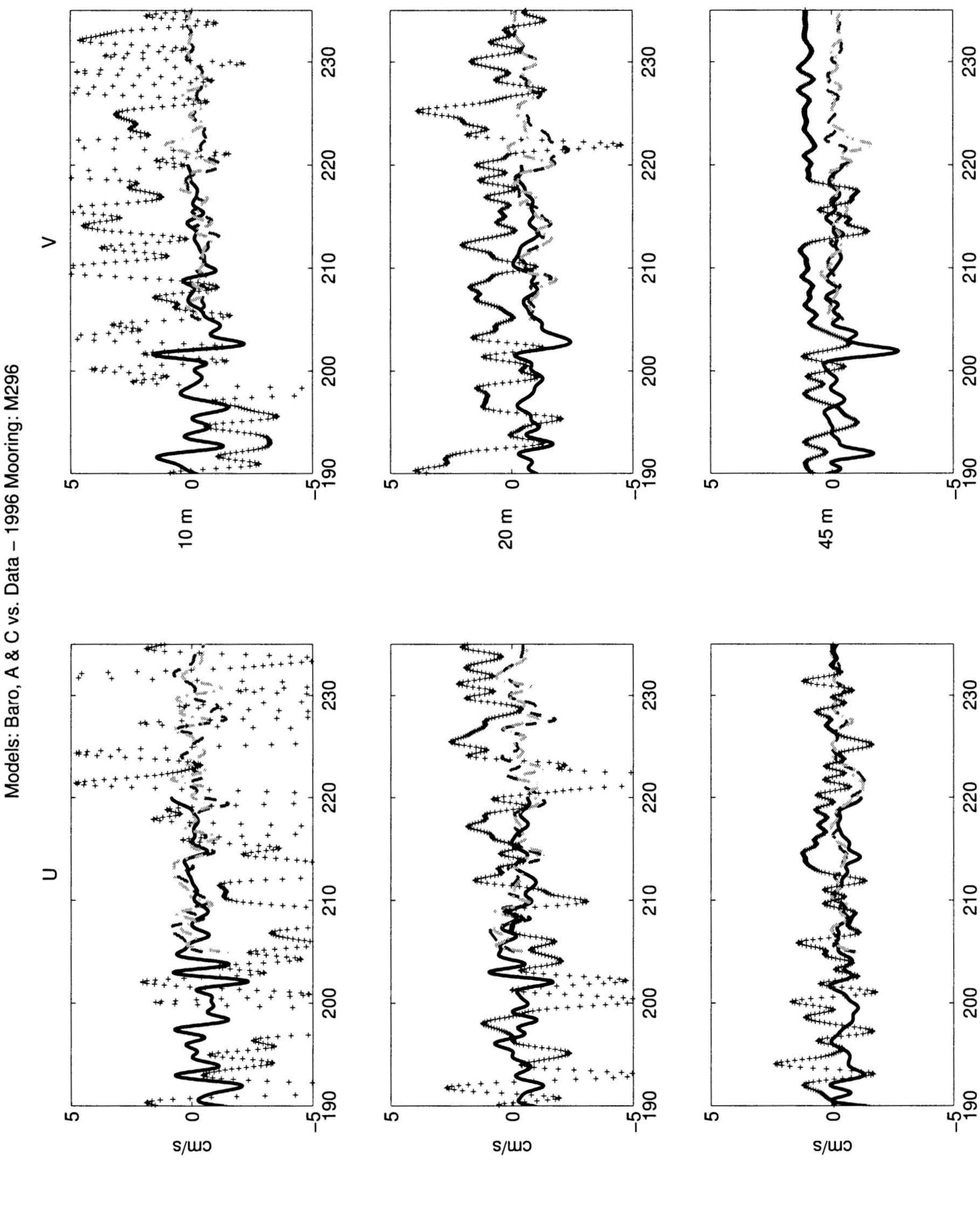

Figure 4.29: Residual Circulation at M2-96 Comparison between the **observed values** (+), **barotropic model** (black solid line), **stratification A** (black dashed line) and **stratification C** (grey dash dot line). Model run with **stratification B** has been omitted for clarity since it did not differ significantly from Stratification A.

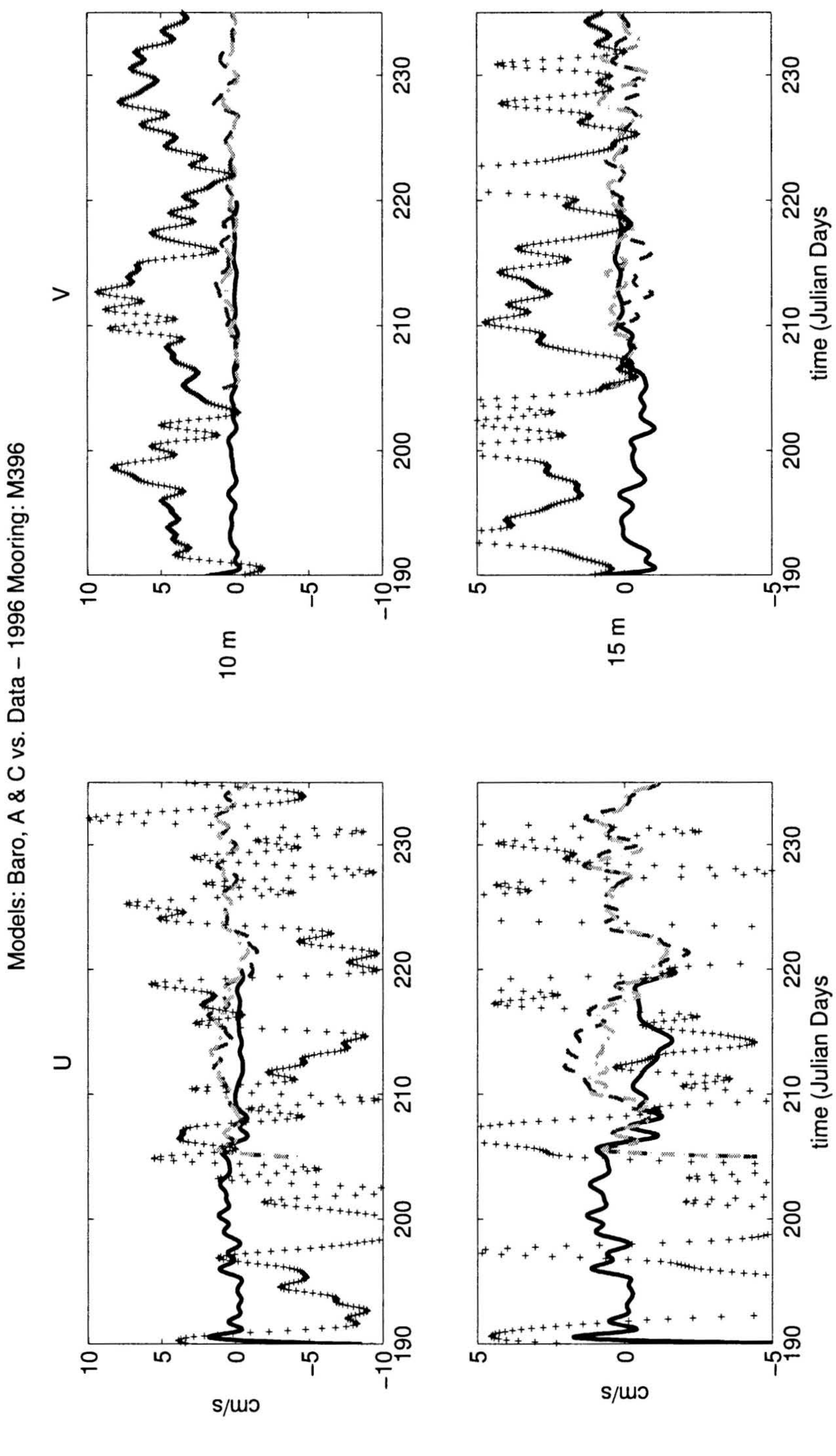

Figure 4.30: Residual Circulation at M3-96 Comparison between the **observed values** (+), **barotropic model** (black solid line), **stratification A** (black dashed line) and **stratification C** (grey dash dot line). Model run with **stratification B** has been omitted for clarity since it did not differ significantly from Stratification A.

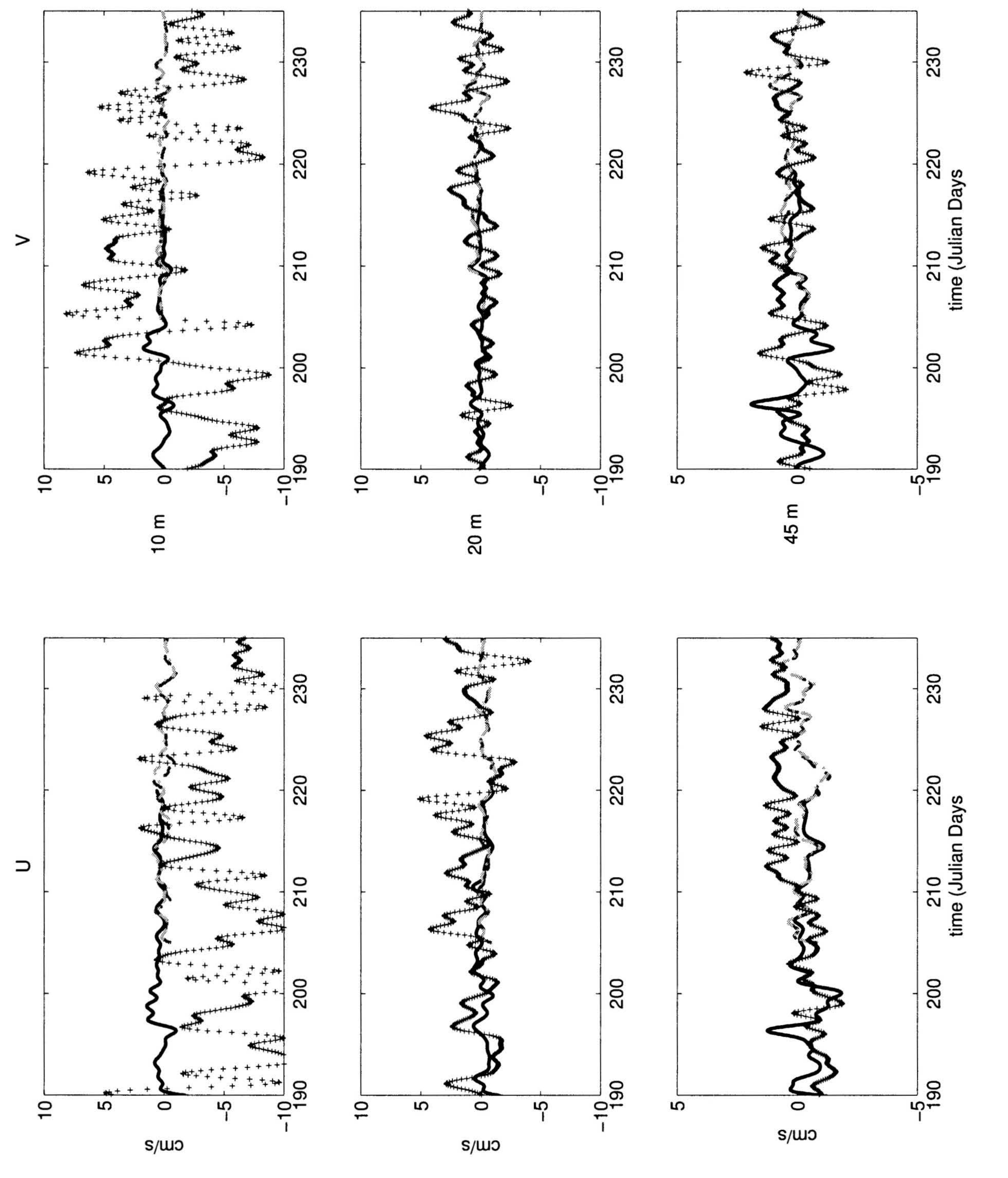

Figure 4.31: Residual Circulation at M4-96 Comparison between the **observed values** (+), **barotropic model** (black solid line), **stratification A** (black dashed line) and **stratification C** (grey dash dot line). Model run with **stratification B** has been omitted for clarity since it did not differ significantly from Stratification A.

Chapter 5 The Influence of Mixing

These words were followed by a very long silence, broken only by an occasional exclamation of "Hjckrrh!" from the Gryphon, and the constant heavy sobbing of the Mock Turtle. Alice was very nearly getting up and saying "Thank you, Sir, for your interesting story," but she could not help thinking there must *be more to come, so she sat still and said nothing.*

- Lewis Carroll
Alice's Adventure in Wonderland

As revealed in Chapter 4, the model fails to produce a reasonable simulation of the tidal forcing when the stratification is held constant. A statically stratified fluid is unable to allow the formation and propagation of baroclinic fronts in the domain. To overcome this, it is necessary to allow temperature and salinity to mix. Steep topographic features within the domain give rise to the formation of baroclinic fronts that are a consequence of the vertical sigma coordinate system as opposed to actual physical processes. These numerical "fronts" lead to the rapid onset of numerical instability making a study of mixing in the Clode Sound domain very difficult. To compensate for the numerical mixing, the temperature and salinity fields may be relaxed back to a background scalar field that may be held constant or evolve on a slower time scale.

This chapter presents a comparison of model runs in which the temperature and salinity fields were allowed to evolve with relaxation of the scalar fields in order to maintain numerical stability. The results of these model runs are compared to the appropriate model runs for a statically stratified fluid to evaluate the significance of mixing as it relates to the tidal structure and distribution of energy.

The required relaxation rate of the temperature and salinity fields was determined through numerical experimentation. It was found that the minimum rate of relaxation needed to guarantee numerical stability for a 30-day simulation was equal to ¼ of the period of the dominant tidal frequency. Physically this is equivalent to a relaxation time that corresponds to the time of maximum amplitude of a sinusoidal wave of period 2π. For Clode Sound, the dominant tidal frequency is M_2 so the relaxation time was chosen to be $12.42/4 \approx 3.11$ hours. This relaxation is very strong but longer relaxation times the model did not remain stable. It is evident that the required relaxation time must be less than or equal to the time of maximum deflection of the thermoclines and haloclines due to the rise and fall of the tide. Of the three density profiles discussed in Chapter 4, only those model runs with a horizontally uniform density structure (Stratification A and B) were stable. Stratification C, for which the main pycnocline drops below sill level as it crosses from the inner basin to the outer channel, was numerically unstable.

Due to the short relaxation time necessary to guarantee numerical stability there will be a tendency for the model to suppress internal mixing and to damp out internal wave structures that may otherwise propagate through the domain. It is possible to compensate for some of this damping by allowing the background scalar fields to evolve over time. The simplest and most direct method to permit the background scalar fields to evolve is to evaluate the temporal average of the scalar over the dominant tidal forcing. For sinusoidal forcing this should result in a stationary background field; the average of a sine function over a period of 2π will be identically zero. The mixing that occurs within the scalar fields allows this averaging process to slowly evolve the background scalar fields corresponding to the evolution of the mean of the field over a tidal period. Another advantage of this averaging method is that it will allow for the introduction of a surface heat flux into the model domain and possibly the introduction of a fresh water source such as a river. The relaxation of the temperature and salinity fields to an evolving background field should permit greater mixing than a model that relaxes towards a constant field.

Model runs discussed in this chapter are identified as follows: 1.) the statically stratified model runs: stratification A (model A), having the main pycnocline located at 10 metres depth, and stratification B (model B) having the main pycnocline located at sill depth; 2.) models with relaxation towards a constant scalar background field: with stratification A (model AR) and stratification B (model BR); 3.) models with relaxation towards an evolving background field (averaged over a tidal cycle) with stratification A (model ARA) and stratification B (model BRA). All model runs were done for a 30-day simulations, only model BRA failed to remain stable for the entire 30-day test period, however, this particular model run did produce a useable 13-day simulation upon which a tidal analysis was conducted for comparison. Attempts to execute the model with a shorter time step did not significantly improve the stability of this model.

5.1 The influence of mixing on the tidal structure

5.1.1 Amplitude of the Diurnal and Semi-diurnal Tidal Currents

The magnitude (cm/s) of the semi-major axis of the tidal ellipses for the main diurnal constituents O_1 and K_1 are given in Tables C.1-C.4. The introduction of the relaxation scheme into the model has little influence on these diurnal constituents of the tide at the centre of the inner basin (mooring M1-96) and at the mouth (mooring M5-96) of the inlet. The O_1 current remains constant (0.1 cm/s), for all model runs at both M1-96 and M5-96. This is consistently weaker than the observed values of 0.1-0.5 cm/s at M1-

96 and 0.1-0.6 cm/s at M5-96. Constituent K_1 also remains constant (0.2 cm/s) for all model runs at M5-96 and weaker than the observed 0.4-0.5 cm/s current. At M1-96, the surface K_1 currents double in strength (from 0.1 cm/s to 0.2 cm/s) with the introduction of relaxation and averaging of the background scalar field (models ARA, BR, and BRA) but remain weaker than the observed, 0.4-1.1 cm/s, K_1 current.

At mooring M2-96 the O_1 current (Table C.1) in model ARA agrees with the observed values at all depths except at the surface (10 metres depth), which is 0.1 cm/s weaker in the model (0.4 cm/s) than in the observations (0.5 cm/s). Models AR and BR have O_1 surface currents of 0.3 cm/s (AR) and 0.7 cm/s (BR). The shorter simulation for model BRA did not permit analysis of the O_1 current. For constituent K_1 (Table C.2), models ARA, BR and BRA have surface currents, 0.5-0.7 cm/s. These are stronger than the K_1 currents in models A and B (0.2-0.3 cm/s) but the strongest surface current (model BRA) is 20% weaker than the observed 0.9 cm/s. All model runs fail to produce a K_1 current at 17 metres depth that attains 50% of the observed K_1 current of 1.0 cm/s at this location. The relaxation schemes and averaging of the background scalar fields have little influence on the strength of the bottom currents.

Seaward of the sill, at mooring M4-96, models AR, BR, and ARA produce stronger O_1 tidal currents than either models A or B. The currents of 0.2-0.4 cm/s in models AR and ARA agree well with the observed value of 0.3 cm/s at 20 metres depth. The surface tidal currents are too weak (0.3 cm/s), less than 30% of the observed 1.1 cm/s at 10 metres depth. K_1 tidal currents are stronger with the introduction relaxation and averaging. When temperature and salinity are relaxed to a constant background profile (models AR and BR), the surface K_1current increases from 0.2 cm/s to 0.4 cm/s if the main pycnocline is located above the sill (AR) and increases from 0.2 cm/s to 0.6 cm/s if the main pycnocline is located at sill depth (BR). Model BR has a vertical profile (Figure 5.2) for the K_1 constituent at M4-96 that is consistent with the observations. At 20 metres depth, model AR produces a tidal current (0.5 cm/s) that is stronger than the surface current (0.4 cm/s) while model BR produces a much weaker (0.2 cm/s) current at this depth. The vertical profile of the K_1 current for model AR (Figure 5.1) indicates a local maximum current near 20 metres depth. The 0.2 cm/s current in model BR is 33% of the surface current for this model run which is very close to the observed ratio, 37.5% between the 10 and 20 metre observations. Models ARA and BRA also produce strong surface currents (0.6 and 0.7 cm/s respectively) that almost agree with the observed K_1 current (0.8 cm/s). Of the two models to include both relaxation and evolving background temperature and salinity fields, model BRA produces the best representation of the observed values (Figures 5.1 and 5.2). The currents at 20 metres depth in model ARA represent 67% of the modelled surface current while 20 metre K_1 currents in model BRA represent only 43% of the modelled surface currents (the observed ratio is 37.5%).

At the sill (M3-96 and M4-97) none of the models are able to reproduce the observed tidal currents near the surface. For constituent O_1 (Table C.1 and C.3) all of the modelled currents are between 0.9-1.2 cm/s at M3-96 and between 0.4-0.7 cm/s at M4-97. The difference in the O_1 current in the models at these locations is surprising given the close proximity (5 grid points) of the corresponding grid cells to each other. This may indicate that the model's smoothed bathymetry is influencing the tidal structure as the observed current is 2.0 cm/s at both of these locations. All of the models except BR indicate that the O_1 currents at 14 metres depth at M4-97 are stronger than the modelled surface currents. Although the magnitude of the observed O_1 current (0.8 cm/s) falls within the range (0.5-0.9 cm/s) of the modelled currents, the vertical structure of the tide is not correct due to the weakness of the surface currents. At M3-96, the introduction of relaxation and averaging (models AR, ARA and BR) for temperature and salinity produces O_1 tidal currents which are much weaker than the tidal currents produced when the scalar fields are held constant (models A and B). Although the currents in models AR, ARA and BRA are weaker (0.6-0.7 cm/s) than the observed values (1.2 cm/s) (with which the statically stratified tides agree), the correct vertical structure of the O_1 tide at M3-96. The observed currents at 15 metres represent 60% of the surface currents (1.2 cm/s); the model runs have currents at 15 metres depth that are 60%-70% of the modelled surface currents.

The diurnal constituents at 1997 moorings (Tables C.3 and C.4) produce stronger currents at most locations once the temperature and salinity are allowed to mix. At M1-97, there is little difference between the model runs with stratification A. Model BR has an O_1 current of 0.3 cm/s at both 7.5 and 21 metres depth. This agrees very well with the observed 0.4 and 0.3 cm/s currents at these depths in contrast to the 0.2 and 0.1 cm/s O_1 currents produced by the other model runs. K_1 currents increase from 0.3 cm/s to 0.5 cm/s and 0.4 cm/s at the surface in models ARA and BRA, in agreement with the observed value of 0.4 cm/s. The depth of the main pycnocline is significant in determining the strength of the K_1 current at 21 metres. The K_1 current in model BRA (0.4 cm/s) is twice as strong as the K_1current in model ARA (0.2 cm/s).

At M2-97, model runs ARA and BR both indicate stronger surface O_1 currents (Table C.3) at 0.6 and 0.8 cm/s, respectively. Models A, AR and B are much weaker (0.3-

0.4 cm/s) then the observed value of 0.8 cm/s. Currents at 21 metres depth in models A and B (0.3-0.5 cm/s) were in agreement with the observed current (0.4 cm/s). Once the static density field is removed, the currents are weaker (0.1-0.2 cm/s). K_1 currents (Table 5.4) increase once temperature and salinity are permitted to mix. With a statically stratified fluid, the surface K_1 current at M2-97 was only 0.2 cm/s for both models A and B. Once temperature and salinity begin to evolve, the K_1 current increases to 0.5 cm/s in model AR and to 0.8 cm/s in models ARA, BR and BRA. This four-fold increase in the surface K_1 current is much closer to the observed 1.2 cm/s. The K_1 current at 21 metres depth remains relatively constant through all model runs at 0.2-0.4 cm/s in agreement with the observed 0.3 cm/s.

At M3-97, the surface O_1current increases from 0.2 cm/s in models A, AR and B to 0.5 cm/s in model ARA but are only 0.3 cm/s in model BR. The K_1 current increases from 0.2-0.3 cm/s in models A, AR and B to 0.5-0.6 cm/s in models ARA, BR and BRA. The diurnal tides in the models are significantly weaker than the observed tidal currents of 0.8 cm/s (O_1) and 1.1 cm/s (K_1) near the surface at M3-97.

Seaward of the sill at M5-97, mixing of temperature and salinity increases O_1 at the surface from 0.1 cm/s (models A and B) to 0.3 cm/s in model BR and 0.5 cm/s in models AR and ARA, which agree with the observed, 0.5cm/s, current. In models A and B, the surface was 0.2-0.3 cm/s, much weaker than the observed value of 0.8 cm/s. With temperature and salinity mixing, models AR and ARA have a K_1 surface current of 1.0 cm/s and 1.3 cm/s, respectively. Models BR and BRA have a K_1 current of 0.5 cm/s and 0.7 cm/s at the surface. This suggests that the depth of the main pycnocline controls the strength of the K_1 current at this location.

The only observations available at M6-97 were located below the depth of the sill. Both O_1 and K_1 currents weaken slightly with the mixing of temperature and salinity. With a static stratification, the O_1 currents at 21 metres depth agreed with the observed values of 0.3 cm/s. Once mixing is introduced into the model, the O_1 current decreases to 0.2 cm/s in model ARA and to 0.1 cm/s in model BR. K_1 currents decrease from 0.4-0.5 cm/s in models A and B to 0.2-0.3 cm/s in all models that include mixing of temperature and salinity.

At M7-97, the O_1 current (Table C.3) at the surface increases from 0.1 cm/s in models A and B to 0.2-0.4 cm/s in models AR, ARA and BR. This increase brings the model into agreement with the observed 0.3 cm/s O_1 current. The strongest modelled O_1 current occurs when the main pycnocline is located near the depth of the sill (BR); the weakest current occurs when the background scalar fields are permitted to evolve (ARA). The response of the O_1 current to temporal evolution of the background scalar fields cannot be assessed at this location as the data from model BRA did not permit the evaluation of the O_1 tidal constituent. The surface K_1 current (Table C.4) in models AR and ARA are 0.5-0.6 cm/s; two to three times stronger than the current in model A and in agreement with the observed 0.5 cm/s current. In models BR and BRA, the surface K_1 currents are 0.7-0.9 cm/s, stronger than the observed current. The difference between models with stratification A and those with stratification B illustrate the dependence of the surface K_1 current on the depth of the main pycnocline. The current in model B is only slightly stronger than model A. With the addition of mixing, the increase in the strength of the surface K_1current is very obvious.

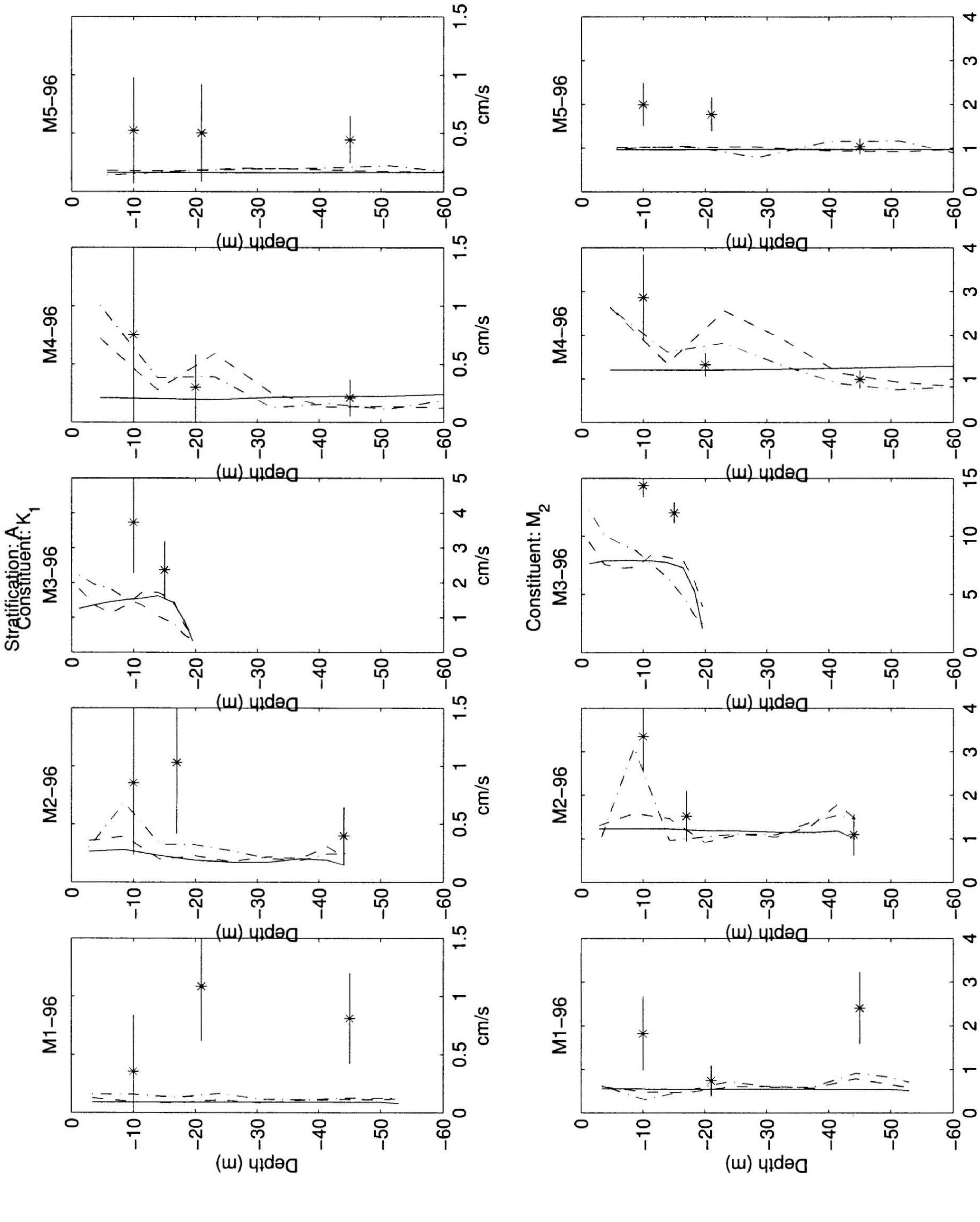

Figure 5.1 Main Diurnal (K_1) and Semi Diurnal (M_2) tidal currents (semi-major axis, cm/s) – 1996
Stratification A: Semi-major axis (cm/s) of the K_1 (left) and M_2 (right) tidal ellipses. The different models are shown as: **Model A** (solid line); **Model AR** (dashed line); **Model ARA** (dash dot line).
Observations (*) plotted with error bars representing the 95% confidence interval.

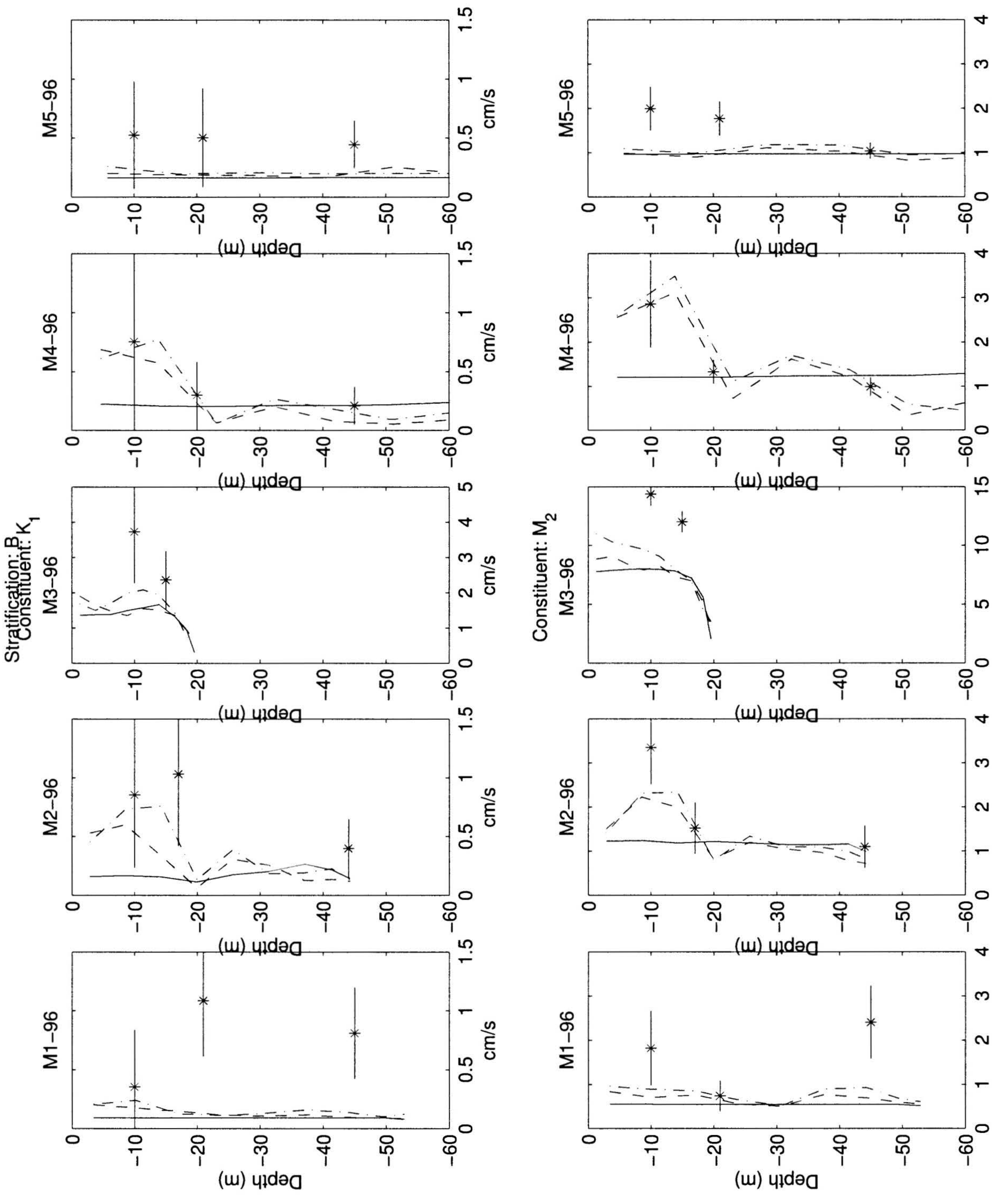

Figure 5.2 Main Diurnal (K_1) and Semi Diurnal (M_2) tidal currents (semi-major axis, cm/s) – 1996
Stratification B: Semi-major axis (cm/s) of the K_1 (left) and M_2 (right) tidal ellipses. The different models are shown as: **Model B** (solid line) **Model BR** (dashed line); **Model BRA** (dash dot line).
Observations (*) plotted with error bars representing the 95% confidence interval.

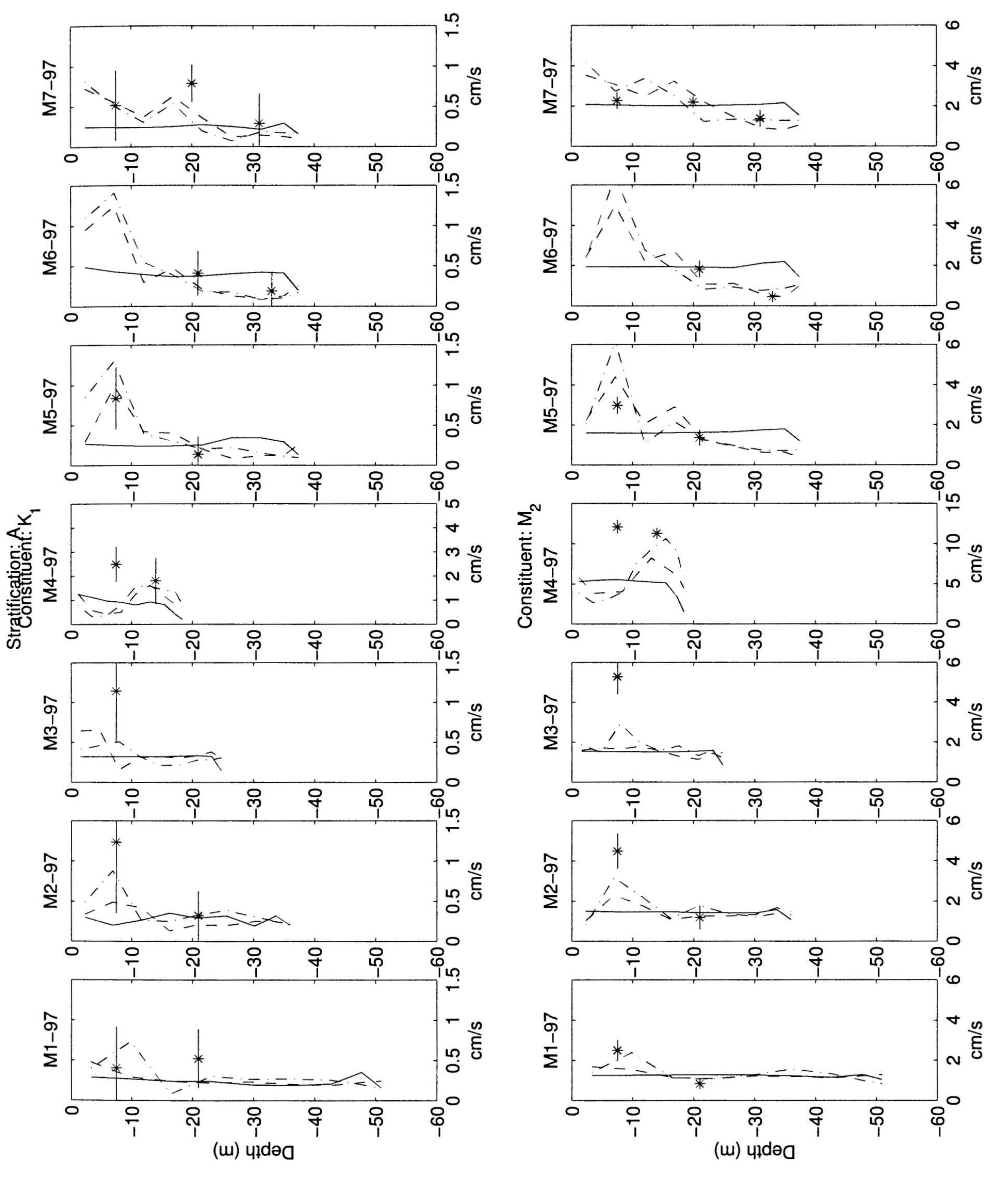

Figure 5.3 Main Diurnal (K_1) and Semi Diurnal (M_2) tidal currents (semi-major axis, cm/s) – 1997
Stratification A: Semi-major axis (cm/s) of the K_1 (left) and M_2 (right) tidal ellipses. The different models are shown as: **Model A** (solid line); **Model AR** (dashed line); **Model ARA** (dash dot line). **Observations** (*) plotted with error bars representing the 95% confidence interval.

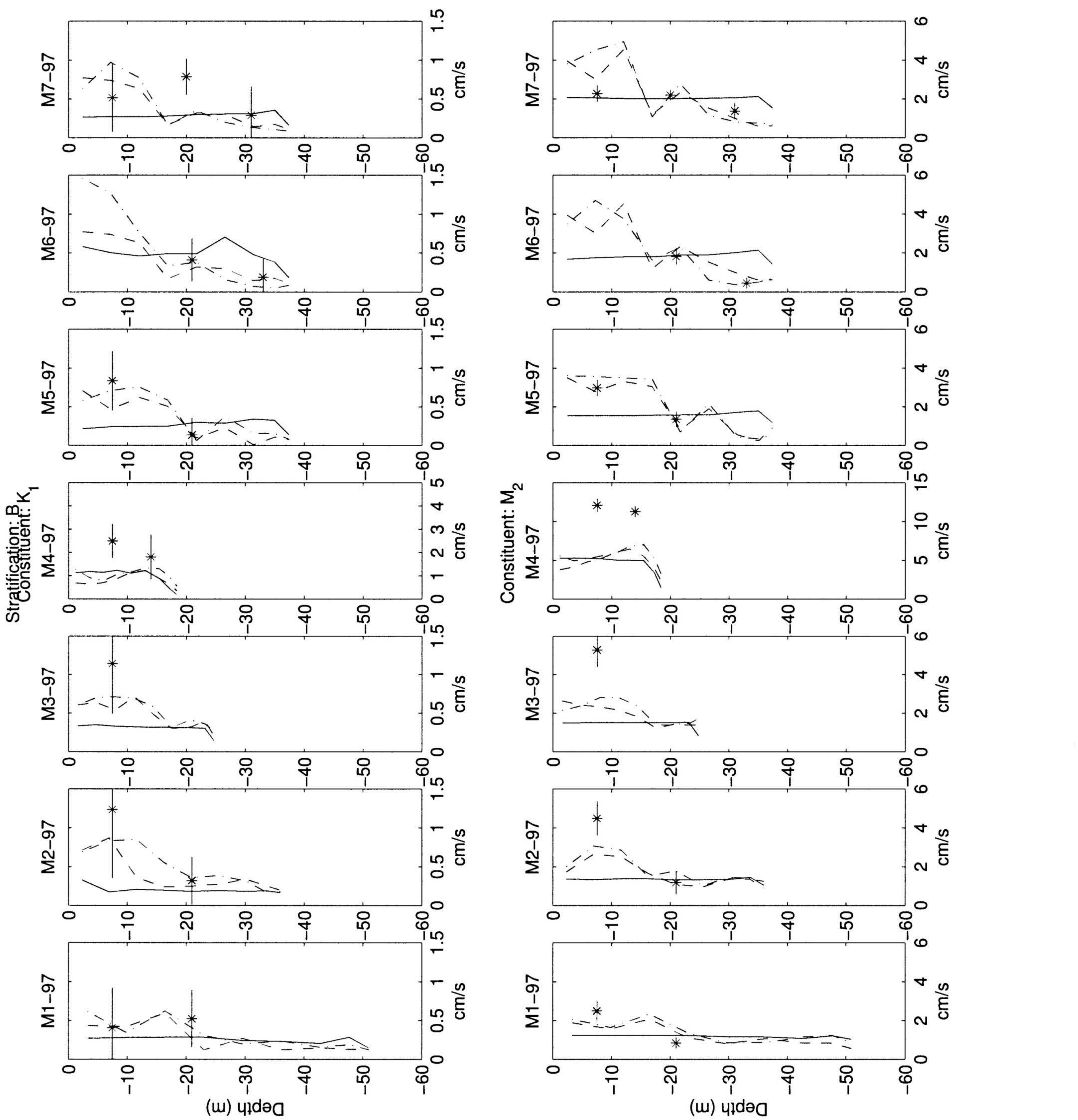

Figure 5.4 Main Diurnal (K_1) and Semi Diurnal (M_2) tidal currents (semi-major axis, cm/s) – 1997
Stratification B: Semi-major axis (cm/s) of the K_1 (left) and M_2 (right) tidal ellipses. The different models are shown as: **Model B** (solid line); **Model BR** (dashed line); **Model BRA** (dash dot line).
Observations (*) plotted with error bars representing the 95% confidence interval.

The semi-diurnal constituents, M_2 and S_2 (Tables C.5-C.8, Figures 5.1-5.4), are influenced by the mixing of temperature and salinity in the model. The most significant differences appear in the vicinity of the sill. There is little evidence of any significant influence of mixing on the tidal signal at the M5-96. To simplify the open boundary condition and also to enhance numerical stability the temperature and salinity fields were relaxed back to a static field over a distance of approximately 5 kilometres from the open boundary. It is very likely that the imposed density field dominates the velocity field at mooring location M5-96, closest to the mouth though outside of the relaxation zone.

Within the inner basin, the addition of mixing in the model has little effect on S_2 currents at M1-96 (Table C.6). The various combinations of stratification and evolving vs. static scalar fields yield different tidal structures for M_2 (Table C.5, Figure 5.1). With the main pycnocline located above sill depth (models AR and ARA), mixing produces bottom currents that are 60-80% stronger than the currents in a statically stratified fluid (models A and B). In contrast to the increase in the bottom currents, surface currents are decrease by 50% in model ARA. With the main pycnocline at sill depth (models B, BR and BRA), the M_2 tidal current increases at all depths. Both surface and bottom currents increase from 0.5-0.6 cm/s to 0.7 cm/s with the introduction of mixing (BR) and to 0.9 cm/s when the background scalar fields are permitted to evolve (BRA). Despite this increase of 50-80% in the strength of the surface and bottom currents, they are too weak compared to the observed 1.8 cm/s current at the surface and the 2.4 cm/s current at the bottom. At mid-depth the increase in the M_2 current in models BR and BRA is only 20-40% in magnitude. The M_2 current of 0.7 cm/s in model BRA agrees with the observed current at 21 metres depth. Even with the mixing of temperature and salinity, the tidal currents remain too weak towards the head of the inlet.

Moving towards the sill, at M2-96 both M_2 and S_2 tidal constituents change as a consequence of mixing. The surface S_2 current (Table C.6) increases 40% to 0.7 cm/s when the main pycnocline is located above the sill (AR). When the main pycnocline is located at sill depth (BR) the S_2 tidal current increases 60% (compared to models A and B) to 1.0 cm/s. If the backgrround scalar fields evolve (ARA) the surface S_2 tide reaches a maximum value of 1.2 cm/s; this is an increase of 140% for the S_2 tide of a statically stratified fluid and the stronger current is quite close to the observed 1.4 cm/s. At 17 metres depth, the modelled currents remain much weaker than the observed value of 1.0 cm/s. For static stratification, the model currents were 0.5 cm/s, there is an increase of 20% to 0.6 cm/s when the main pycnocline is located at sill depth (BR); the currents at 17 metres depth decrease 50% to 0.3 cm/s in model ARA. Near the bottom (45 metres) the modelled currents increase 25-50% in models AR and ARA to 0.5-0.6 cm/s, this agrees very well with the observed 0.6 cm/s S_2 current. With the deeper pycnocline, the bottom currents decrease to 0.3 cm/s: 50% of the observed value.

The near surface M_2 current at M2-96 (Table C.5) is significantly influenced by mixing. With a static stratification, the surface M_2 tidal current was only 1.2 cm/s; much weaker than the observed value of 3.4 cm/s. When temperature and salinity mix, the surface M_2 current increases by 33% to 1.6 cm/s when the main pcynocline is located above the sill (model AR) and increases by 80% to 2.2 cm/s when the main pycnocline is located at sill depth. Evolution of the background scalar fields (ARA and BRA) increases the M_2 tide in model ARA to 2.4 cm/s but has no effect (compared to BR) when the pycnocline was at the same depth of the sill (model BRA). The averaging process increases the strength of the tide in the vicinity of the main pycnocline: located at 10 metres depth in model ARA. The increase in the strength of the M_2 tide suggests that the averaging process may be acting to deepen the surface layer at this location as the surface tide is similar to the tide when the model is initialized with the main pycnocline at the depth of the sill.

At 17 metres depth, mixing reduces the M_2 tide from 1.2 cm/s in model A and B by 10-15% in models AR and ARA but increases the signal 15-30% in models BR (1.4 cm/s) and BRA (1.6 cm/s). This must be related to the depth of the main pycnocline located above17 metres depth in models AR and ARA but very close to the 17 metre level in model BR and BRA. The model results for the M_2 tide in the bottom layer at M2-96 suggest that there may be internal resonance within the inner basin of the model when the main pycnocline is located above the sill. Models AR and ARA show an increase of 50% in the strength of the M_2 current at 44 metres depth. It is not clear that this is a physical phenomena. This stronger bottom tide does not appear in models BR and BRA where the bottom M_2 current is reduced 20-30% to 0.7-0.8 cm/s. M_2 is the dominant tidal constituent within Clode Sound, models BR and BRA provide the best tidal signal, of the six models under consideration. The strength of M_2 tidal current for these models (1.4 and 1.6 cm/s) is in close agreement with the observed current at 17 metres depth (1.5 cm/s) and the bottom currents at 0.7-0.8 cm/s lie within the 95% confidence interval of the observed bottom M_2 current (1.1 cm/s). Surface currents are weaker than expected: 65% of the observed value.

The S_2 tide within the inner basin in 1997 (Table C.8) was almost uniform across at 0.4-0.5 cm/s in model A and 0.5-0.7 cm/s in model B (moorings M1-97, M2-97 and M3-97). When the main pycnocline is located above the depth of the sill and temperature and salinity mix (model AR), the S_2 tidal current increases: 75% to 0.7 cm/s at mooring M1-97, 100% to 1.0 cm/s at M2-97 and 40% to 0.7 cm/s at M3-97. If the main pycnocline is located at the depth of the sill (model BR), the surface S_2 tide is1.3 cm/s at mooring M2-97; an increase of 160% compared to the S_2 for a statically stratified fluid. When background scalar fields are average over a tidal cycle (model ARA) the surface tides are stronger with currents of 0.8, 1.3 and 1.1 cm/s at moorings M1-97, M2-97 and M3-97 respectively. Compared to model AR, the averaging process alone increases the tide by approximately 15% at M1-97, 30% at M2-97 and almost 60% at M3-97. Despite these relatively large increases in the surface S_2 tide, the model results are still much weaker than the observed S_2 tide at M2-97 and M3-97 where the current reaches 2.2 cm/s and 1.9 cm/s, respectively. The observed S_2 tide at M1-97 was only 0.9 cm/s which agrees with the 0.8 cm/s current produced by model ARA.

Across the inner basin at moorings M1-97, M2-97 and M3-97 the M_2 tide (Table C.7) also varies significantly when mixing is introduced into the model. Agreement between the model output and the observed values is best towards the southern coastline at mooring M1-97 (Figures 5.3 and 5.4). Compared to model runs A and B, with constant stratification, models in with mixing increase the M_2 current 25-50% with the greatest increases occuring when mixing is combined with evolving background scalar fields (ARA and BRA). Models ARA and BRA also produce the strongest surface currents at moorings M2-97 and M3-97. At M2-97, the surface M_2 current increases from 1.3-1.5

cm/s in models A and B to 3.0 cm/s in models ARA and BRA, an increase of 100-130% in the strength of the current but only 67% of the observed 4.5 cm/s M_2 current. Without averaging of the background scalar fields, the model M_2 currents are 2.2 cm/s (AR) and 2.6 cm/s (BR). At M3-97, the surface currents increased 75-80% to 2.6-2.7 cm/s in models ARA and BRA; in models AR and BR the M_2 currents are only 1.7 cm/s and 2.3 cm/s respectively. The strongest modelled currents are only 50% of the observed 5.3 cm/s current at M3-97.

At the sill, the behaviour of the model is different between mooring locations M3-96 and M4-97. Neither location is able to reproduce the observed S_2 tidal current. At M3-96, mixing has little influence on the strength of the S_2 current at 10 metres depth. Variation in the strength of the current is only 6% between all models. At M4-97 the S_2 current at 7.5 metres depth decreases with mixing. At 7.5 metres depth the S_2 current decreases from 1.9 cm/s in model A to 1.5-1.6 cm/s in models AR and ARA. When the main pycnocline is located at sill depth, the surface S_2 current decreases from 2.4 cm/s (B) to 2.0 cm/s (BR).

At the 15 metre depth of M3-96, model ARA indicates that the S_2 decreases 30% to 1.9 cm/s compared to the 2.8 cm/s currents in models A and AR. At M4-97, however, the S_2 tidal current at 14 metres depth increases from 1.7 cm/s in model A to 2.8 cm/s in model AR. The current increases to 3.8 cm/s when the background scalar fields are averaged (model ARA). This increase does not appear between models B and BR. The increase in the S_2 current in model ARA at 14 metres depth produces a bottom current over two times stronger than the surface current. This behaviour is not supported by the observed values of the S_2 tide for this location.

At the sill, the M_2 current produced by the models fail to achieve the proper strength. The observed M_2 current at M3-96 and M4-97 is 11-14 cm/s. The maximum surface M_2 current achieved by the model was only 9.4 cm/s in model BRA, only 65%-85% of the observed currents at the sill. The model results at M4-97 indicate an increase in the M_2 current at 14 metres depth not seen in the surface currents. In models AR and ARA this results in an M_2 tide which is 2-3 times stronger at 14 metres depth than it is at 7.5 metres depth. The bottom currents in models BR and BRA are also stronger than the surface currents but the increase from the surface to the bottom is only 20-25%. The current configuration of the model lacks the ability to simulate the main tidal structure at this particular location. It is not known why this occurs at this location of the model but this behaviour is also found in other weaker tidal constituents (such as S_2).

Seaward of the sill, the introduction of mixing into the model enhances the surface S_2 tide while decreasing the S_2 tide at depths below the sill. Comparison to the model runs for a statically stratified fluid indicates that this is the response required to bring the model into agreement with the observed S_2 tidal current. At M5-97, the surface currents produced in models AR and ARA are 1.8 cm/s and 2.3 cm/s respectively, stronger than the observed 1.3 cm/s S_2 current at 7.5 metres depth and 260-360% stronger than the 0.5 cm/s current produced by model A. The S_2 current at 21 metres depth remains almost constant, 0.5-0.6 cm/s, 25-50% stronger than the observed 0.4 cm/s current. Model B produced a current of 0.7 cm/s at both 7.5 and 21 metres depth. Model BR increases the surface current by 57% to 1.1 cm/s and decreases the current at 21 metres depth by 40% to 0.4 cm/s. Compared to the observed values of the S_2 tide for this mooring location (1.3 and 0.4 cm/s at 7.5 and 21 metres depth at M5-97), model BR agrees very well. The large increase in the surface S_2 current in models AR and ARA must depend on the depth of the main pycnocline as this is the only difference between models AR and BR.

No surface observations were available at mooring M6-97. At 21 metres depth, the variation in the S_2 current is limited to 25% between the models. The S_2 currents of 0.6-0.8 cm/s are all reasonable compared to the 0.7 cm/s observed. At 33 metres depth, mixing reduces the S_2 current from 0.7 cm/s in model A to 0.3 cm/s in models AR and ARA. Between models B and BR the current decreases from 0.9 cm/s to 0.4 cm/s. The currents at 33 metres depth remain stronger than the observed 0.2 cm/s fall within the 95% confidence interval of the observed value. Moving towards the northern coastline to M7-97, the surface S_2 current increases 70-85% in models AR and ARA (compared to model A) to 1.2-1.3 cm/s. Model BR produces a S_2 current of 1.2 cm/s, 33% stronger than the 0.9 cm/s current produced by model B. All of the model runs involving mixing agree with the observed value of 1.3 cm/s. Prior to the introduction of mixing into the model, the S_2 tide at M7-97 was uniform with depth at 0.7 cm/s in model A and 0.9 cm/s in model B. With the pycnocline located above the sill, there is no difference in the strength of this current unless the background scalar fields are averaged over a tidal period (ARA) in which case the S_2 current decreases by almost 50% to 0.4 cm/s. When the pycnocline is located closer to the depth of the sill (model BR) the introduction of mixing alone, without the averaging of the scalar fields produces a S_2 current 33% weaker at 0.6 cm/s than the current produce for a statically stratified fluid (model B).

The M_2 current at M5-97 is too strong in models AR and ARA. At 7.5 metres depth, the model currents are 4.3 cm/s (AR) and 5.9 cm/s (ARA), these are 45%-100%

greater than the observed current of 3.0 cm/s and 170-270% than the 1.6 cm/s current produced in model A. Models BR and BRA produce a more reasonable M_2 surface current with 2.8 cm/s in model BR and 3.6 cm/s in model BRA. At 21 metres depth, models AR and ARA have M_2 currents of 1.3-1.4 cm/s that agree with the observed 1.4 cm/s while models BR and BRA are approximately 35% weaker at only 0.9 cm/s. In the centre of the channel, at M6-97, the statically stratified models A and B produced M_2 currents of 1.9 cm/s and 1.8 cm/s at 21 metres depth that agreed well with the observed 1.9 cm/s. These values are consistent with the M_2 tidal currents in models AR and BRA (1.8 cm/s), models ARA and BR produce a weaker M_2 current, 1.3-1.4 cm/s. At 33 metres depth, both models A and B have M_2 currents of 2.0-2.1 cm/s, four times the observed 0.5 cm/s. With the introduction of mixing, all of the models produce much weaker currents. Modelled currents at this depth were reduced 60-67% in models AR and ARA to 0.7-0.8 cm/s. Model BR has a M_2 current of 1.1 cm/s (45% decrease) while BRA produces a current of only 0.4 cm/s (80% decrease). Compared to the available data for this location, model BRA, provides the best fit (Figure 5.4) for the tidal structure at or below the level of the sill. Without any observations available near the surface it is difficult to determine how well this model actually fits the true tide. At M7-97, mixing produces surface currents much stronger than those observed. Models A and B, with static stratification, produce a reasonable 2.1 cm/s current at 7.5 cm/s. The weakest M_2 surface current for a mixing model is 3.0 cm/s in model ARA. Model BRA produces a M_2 tide of 4.3 cm/s, almost double the observed 2.3 cm/s. As with the S_2 tidal current, mixing reduces the currents below the depth of the sill. When the model is statically stratified, it is unable to reproduce the vertical structure in the tidal currents so the currents at 31 metres depth at 2.0 cm/s are almost equal to the 2.1 cm/s currents found at the surface. With the introduction of mixing, all of the models reduce the deeper current by 20-35% so that the modelled M_2 current at 31 metres depth on the northern coastline is 1.3-1.6 cm/s, a reasonable strength for M_2 compared to the observed 1.4 cm/s.

Further from the sill at mooring location M4-96, mixing does not influence the S_2 current as greatly it does closer to the sill. Surface currents increase from 0.5 cm/s (models A and B) to 0.7-0.8 cm/s in models AR and ARA and to 1.1 cm/s in model BR. S_2 surface currents in models AR and ARA are only 50% of the observed 1.6 cm/s current for this location. Model BR is has the most reasonable values for the S_2 tide at this location, however, surface currents are still weaker than observed and bottom currents have also been reduced by 40% from 0.5 cm/s to 0.3 cm/s.

The M_2 current at M4-96 has vertical structure when mixing is introduced that is not seen when the fluid is statically stratified (Figures 5.1-5.2). For models A and B, the M_2 tidal currents are almost constant with depth at 1.2-1.3 cm/s. When temperature and salinity mix, in the model, with the main pycnocline is located above the level of the sill (models AR and ARA), the strength of the M_2 current increases at both 10 and 20 metres depth by 50-67% to 1.6-2.0 cm/s. These increases are not consistent with the observed tide. At 10 and 20 metres depth, the observed M_2 tide was 2.9 cm/s and 1.3 cm/s respectively. The increase in the strength of the M_2 in models AR and ARA is not large enough to match the observed values at 10 metres of depth and is too large to be consistent with the observations at 20 metres depth (Figure 5.1). The performance of models BR and BRA (Figure 5.2) is significantly better than models AR and ARA. Surface M_2 currents in models BR and BRA have increased to 2.8-3.1 cm/s compared to the observed 2.8 cm/s. At 20 metres depth, the M_2 tide in model BR changes only slightly from 1.2 to 1.3 cm/s, consistent with the observed value of 1. 3 cm/s while in BRA the M_2 current increases to 1.8 cm/s and may be considered too strong.

5.1.2 Inclination of the Tidal Ellipses and Phase of the Tide

Mixing may also influence the inclination of the tidal ellipses and phase of the tide. For comparison, we restrict ourselves to the main diurnal constituent, K_1 and the main semi-diurnal constituent, M_2. The inclination and phase associated with the tidal ellipses for the K_1 and M_2 constituents are calculated at the depth of observations for each mooring (Tables C.9-C.16) and the model output at all sigma levels is plotted in Figures 5.5-5.12.

Within the inner basin at mooring M1-96, the tidal ellipse for the main diurnal constituent K_1 (Tables C.9-C.10, Figures 5.5-5.8) rotates in a clockwise direction from the surface to the bottom of the water column. The only exception to this is model ARA where the tidal ellipses rotate counter-clockwise from 10 metres depth to 20 metres depth, then rotate clockwise towards the bottom. There is no significant difference in the orientation of the tidal ellipses (Table C.1) between models A and AR, however, the introduction of mixing into model AR produces a phase difference of 57° between the signal at 10 metres depth and the signal at 45 metres depth (Table C.2). This difference is much greater than the 4° phase difference (which may be considered negligible compared to the 95% confidence intervals of 5°) for constant stratification but only equal to ½ of the phase difference of 106° observed at this location. The orientation of the tidal ellipse at 10 metres depth in model ARA is consistent with models A and AR. At 20 metres depth the orientation of the K_1 tidal ellipses shifts northward in model ARA to 71° compared to

41-47° in models A and ARA. This change in orientation must be a consequence of the averaging process used to permit the background scalar fields of temperature and salinity to evolve. It suggests that the mixing within the inner basin is not uniformly distributed across the inlet resulting in a change of the internal density structure of the model domain. What is not clear, however, is whether this effect is physical or simply a consequence of the distribution of the sigma levels over local bathymetry on the grid.

The phase difference between the surface and bottom levels in model ARA is 103° in agreement with the observed phase difference. However, the observed K_1 tide at 10 metres depth lags the tide at 21 metres depth by 12°; in model ARA, the tide at 21 metres depth leads the surface component by 95°. There is also a difference of approximately 90° in the Greenwich phase of the model and the observed Greenwich phase. Models BR and BRA reveal a significant difference in the orientation of the tidal ellipses compared to model B, however the two models are consistent with each other. Models BR and BRA are consistent with each other, but the orientation of the tidal ellipses indicate that the K_1 tidal ellipse at 10 metres depth is oriented almost due north between 95° (AR) and 85° (ARA), this is a 50° difference from model B (39°) and also from models A, AR and ARA (36°-45° degrees). The phase of the tide in models BR and BRA also indicate that the bottom tide leads the surface tide by approximately 125°, this is larger than the observed value. The tide at 21 metres depth also leads the surface tide by approximately 40°.

At mooring M2-96, most of the K_1 tidal ellipses rotate clockwise with increasing depth. Similar to mooring M1-96, there is little difference in the orientation of the tidal ellipses in models A, AR, ARA and B with the principle axis lying between 9°-31°. The surface tidal ellipses in Models BR and BRA are rotated more northerly, 56°-68° compared to the 5° ellipse orientation observed in 1996. The phase of the observed tide indicates that the surface tide precedes the tide at 17 metres depth by approximate 55°. Models A and B indicate a surface tide preceding the deeper tide by 10°-15° while the models that include mixing all indicate that the surface tide lags the tide at 17 metres by 35°-40°.

Moving from south to north across the inner basin, the mooring locations from 1997 provide the tidal structure across the inlet. At M1-97 the observations and models A, B, AR and ARA indicate that the K_1 tidal ellipse is oriented between 0° and 42°, this orientation aligns the tidal current along the major bathymetric contours. Models BR and BRA, however, indicate a tidal ellipse at 7.5 metres depth oriented towards the northwest at 110° in model BR and 157° in BRA. The observed phase of the K_1 tide indicates that the tide a 21 metres depth precedes the tide at 7.5 metres depth by approximately 40°. Models A and B produce tides that have almost constant in phase through the water column consistent with the lack of internal structure found in these models. Mixing allows the internal structure of the tide is allowed to develop. When the main pycnocline is located above the sill, model AR produces on a phase lag of 10° between the tide at 21 (299°) and 7.5 (290°) metres depth. The addition of an evolving background scalar field (model ARA) increases this phase lag to 53°. With the main pycnocline at sill depth, the phase lag is 76° in model BR while model BRA indicates a surface tide that precedes the tide at 21 metres depth by 77°.

At M2-97, the observed K_1 tide rotates in a counter-clockwise direction with depth. This rotation is only replicated by model ARA, model AR indicates a K_1 tide that changes direction by 135° rotating from 10° to148°. This large change in direction is not found in any of the other models. The tidal ellipses of the other models are oriented between the east and northeast (0°-35°). The observed phase of the K_1 tide indicates that the tide at 21 metres depth, close to the depth of the sill, precedes the surface tide by approximately 40°. With a static stratification, models A and B produced tides in which the surface tide preceded the deeper tide. Mixing of temperature and salinity produced K_1 tides with the tide at 21 metres depth preceding the surface tide by 105° (ARA), 60° (BR) and 75° (BRA).

Towards the northern coastline, both the observed K_1 tide and the modelled tide were oriented towards the northwest. Models A and B produce a more westerly orientation (176°-179°) while models BR and BRA produce tides which lie almost directly northwest (135°-148°). The K_1 tidal ellipse produced by model AR oriented at 159° agrees with the observed value of 163°. None of the models provide a very good representation of the observed Greenwich phase of 81°. The models all produced K_1 tides with a Greenwich phase differing from the observed phase by at least 40° (models A and BR) and by as much as 110° (ARA). Examining the surface tide, the observed K_1 tide progresses across the channel from mooring M3-97 to mooring M1-97, the phase difference between the observed tide at M3-97 and M1-97 being approximately 80° (after adjustment for the orientation of the tidal ellipses). The models do not replicate this behaviour. Models A and B indicate that K_1 tide occurs almost simultaneously at M1-97 and M3-97 with the tide at M2-97 lagging by approximately 60°. Models AR, BR and BRA all indicate that the tide arrives at M1-97 followed by M3-97 and finally M2-97, while model ARA indicates a tide that arrives at M3-97, then M1-97 and finally at M2-

97. The difference between the observed behaviour of the tide and the modelled tide may be a consequence of the broadening and deepening of the channel during smoothing of the domain. Across the sill, the deepening along the southern coastline permits a much stronger current along the southern boundary than is realistic.

At the sill (moorings M3-96 and M4-97), the flow of the tide is restricted by the channel width. With the flow at the sill being nearly rectilinear we should anticipate good agreement in the orientation of the tidal ellipses. Models AR and ARA are oriented slightly more northerly, at M4-97, to between 146°-150° compared to the 165°-170° of the observations and other model runs. In model ARA, the K_1 tidal ellipse is oriented at 4° degrees at 10 metres depth (mooring M3-96); this is a 15°-20° difference from the 165°-173° degrees in the observations and other models. At 10 metres depth for M3-96, the phase of the modelled K_1 tides are 98°-129°, all within the 95% confidence interval of the observed K_1 phase of 109°. At 15 metres depth, models ARA and BRA produce a K_1 tide with a Greenwich phase of approximately 75° significantly different from the 100°-119° Greenwich phase observed and estimated from the other model runs. At M4-97, there is good agreement between the Greenwich phase of the observed K_1 tide and the models except in models B and BRA. In model B, the tide arrives to late (130°-137°) and in model BRA where the tide arrives to early (70°-85°) compared to the with 100° –125° estimated from the observations and other models.

Seaward of the sill at M5-97, the observed K_1 tidal ellipse was oriented at 176°-178° at 7.5 and 21 metres depth. The model produces a more northerly tidal ellipse 146°-164° degrees at 7.5 metres depth. The orientation of the tidal ellipse rotates towards the north when the main pycnocline deepens (models A and B) and also when mixing is introduced (AR and BR) and enhanced by the evolving background scalar fields (ARA, BRA). The observed K_1 tide at 21 metres depth precedes the tide at 7.5 metres depth by approximately 30°. Models A and B do not reflect this behaviour of the tide having a phase that is constant with depth. Models AR and ARA are able to provide the best simulation of the tide at this location. The tide at 21 metres depth precedes the tide at 7.5 metres depth by 17°-18°. The modelled Greenwich phases of 120° (AR) and 114° (ARA) are good agreement with the observed phase of 131° at 7.5 metres depth. The Greenwich phase, at 7.5 metres depth of 129° (BR) and 112° (BRA) agree with the observed value of 131°, the Greenwich phase of the models at 21 metres depth is 34°-38°. This behaviour is not unreasonable and may indicate that the K_1 tide in the model is reflected at the sill.. In models BR and BRA, the main pycnocline is located between 15-20 metres depth, just below the level of the sill. The incoming tide may not be able to push water over the sill resulting in the reflection of the tidal energy back towards the mouth. Although the observed Greenwich phase at 21 metres depth is 102°, the 95% confidence intervals (134°) are very large and allow for the possibility of reflection.

At M6-97 models A and B place the semi-major axis of the K_1 tidal ellipse along the east-west axis. This is not in agreement with the observed 150° at 21 metres depth and 18° at 33 metres depth. The tidal ellipses in the mixing models are aligned in a manner consistent with the observed K_1 tide. The observed phase of the tide at 21 metres depth is 158°, significantly different from the model values that also indicate a dependence on stratification. Models AR and ARA have a Greenwich phase of 80°-90° while models BR and BRA have a Greenwich phase of 20°-53°. When the main pycnocline is located above the level of the sill, the Greenwich phase of the K_1 tide, at 33 metres depth, in models AR and ARA is 306°-359° degrees. In models with the main pycnocline at sill depth, the Greenwich phase is 226°-282° degrees. The observed Greenwich phase at this depth (315°±100°) indicates a large degree of variability and the phase of the modelled tides are all within the 95% confidence interval.

Moving further north to M7-97, the model runs agree well with the observed values of the K_1 ellipse orientation. The range of values produced by all of the models for the orientation of the tidal ellipse at 7.5 metres depth is 22°-45° compared to the 27° orientation found in the available data. At 31 metres, the models produce a tidal ellipse that is oriented 3°-18° compared to the observed orientation of 179°. The Greenwich phase at 7.5 metres depth of the statically stratified models agrees with the observed 252° degrees. The Greenwich phase of models A and B is 252° and 263°, respectively. Models that include mixing delay the tide by 20°-30° degrees. The estimate for the Greenwich phase in the mixing models is 275°-301°.

Moving towards the mouth of the inlet at M4-96, the orientation of the tidal ellipses at 10 metres depth is consistent between all models, 13°-15° with the exception of model ARA oriented at 2°. The observed value of the tidal ellipse at this depth is 15°. The observed tidal ellipses rotate slightly counter-clockwise with increasing depth, the orientations at 20 and 45 metres depth is 20° and 25° degrees respectively. Only model BR reproduces this counter-clockwise rotation to 20 metres depth, the other models all rotate clockwise 2°-13° as the depth increases. Although the direction of rotation is incorrect, the values obtained for the orientation of the tidal ellipses (170°-21°) are not unreasonable. There is significantly more variation in the orientation of the tidal ellipses at 45 metres depth where the currents are the weakest.

At 10 metres depth, the models also indicate a consistent Greenwich phase for the K_1. The modeled tides have a phase of 291°-329°. The modelled tides precede the observed tide (Greenwich phase of 354°±71°), however all of the modelled tides are within the 95% confidence interval of the observation. At 20 metres depth, the estimated Greenwich phase from the models is 281°-312°, these values nicely bracket the observed phase of 300°. Even at 45 metres depth the comparison between the modelled phase and observed phase is quite good. However, despite the agreement between the Greenwich phase of the model to the observed Greenwich phase there are some very obvious and significant differences between the model and the observations. The observed tide arrives first at 45 metres depth with a phase lag of 71° between the bottom and surface tide. This behaviour of the K_1 tide is only found in models AR and BRA. In model AR the phase lag between the bottom and top of the water column is 74° almost equal to the observed phase lag, but the phase difference of 57° degrees between the 45 and 20 metre levels is much larger than the observed phase difference of 17°. The observed tide at 20 metres depth is closer in phase with the tide at 45 metres depth. The model reverses this and has the tide at 20 metres depth almost in phase with the surface tide. A similar behaviour is seen in model BRA. In model ARA, the 10 and 20 metre tides arrive almost simultaneously preceding the bottom tide by approximately 40°. In model BR the tide at 20 metres depth arrives slightly ahead (7° phase lag) of the bottom current, the two deeper tides arriving 20°-25° sooner than the surface tide.

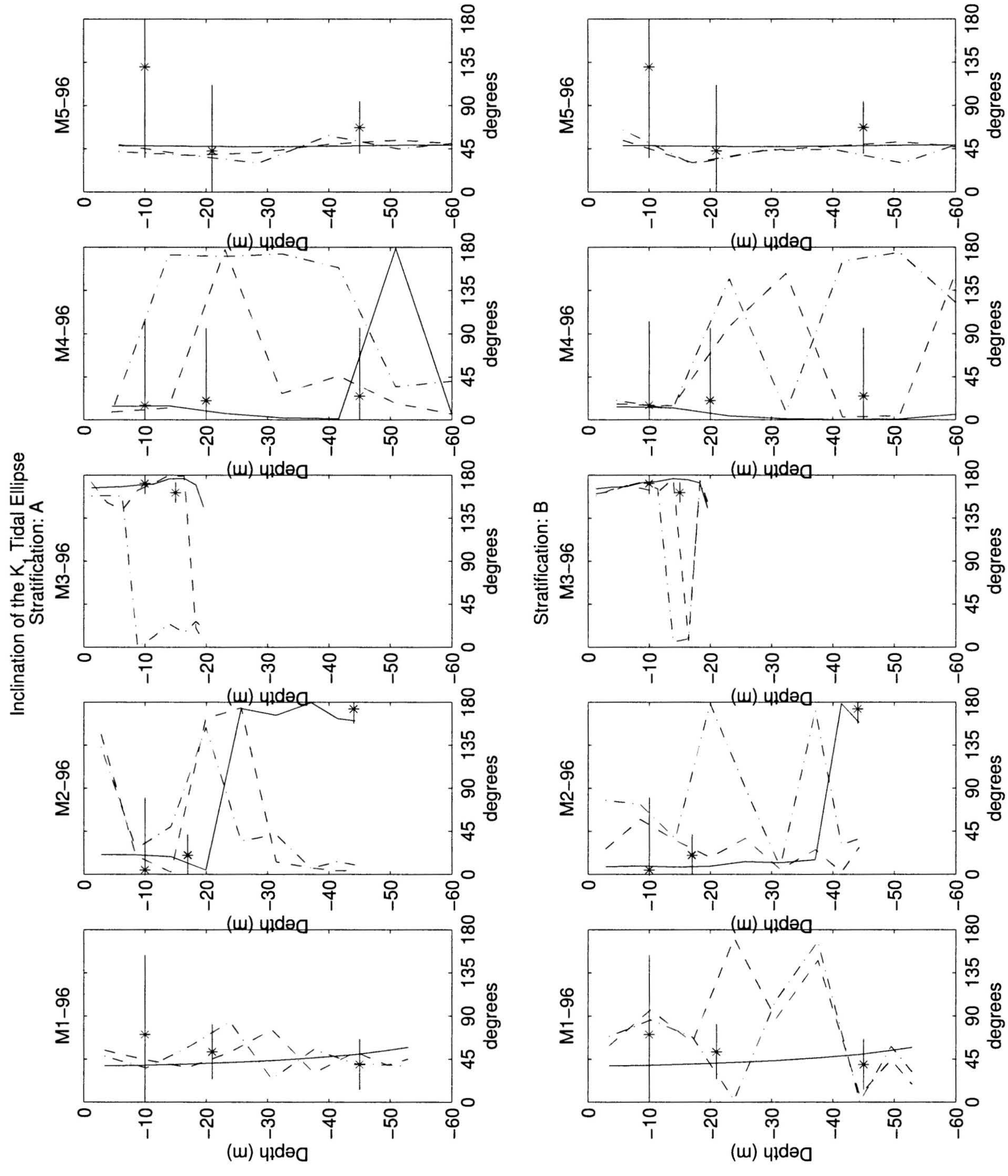

Figure 5.5 Inclination (degrees) of the K_1 tidal ellipse 1996 (mixing models). Stratification A (left): **Model A** (solid line) **Model AR** (dashed line); **Model ARA** (dash dot line). **Stratification B** (right): **Model B** (solid line) **Model BR** (dashed line); **Model BRA** (dash dot line). **Observations (*)** plotted with error bars representing the 95% confidence interval.

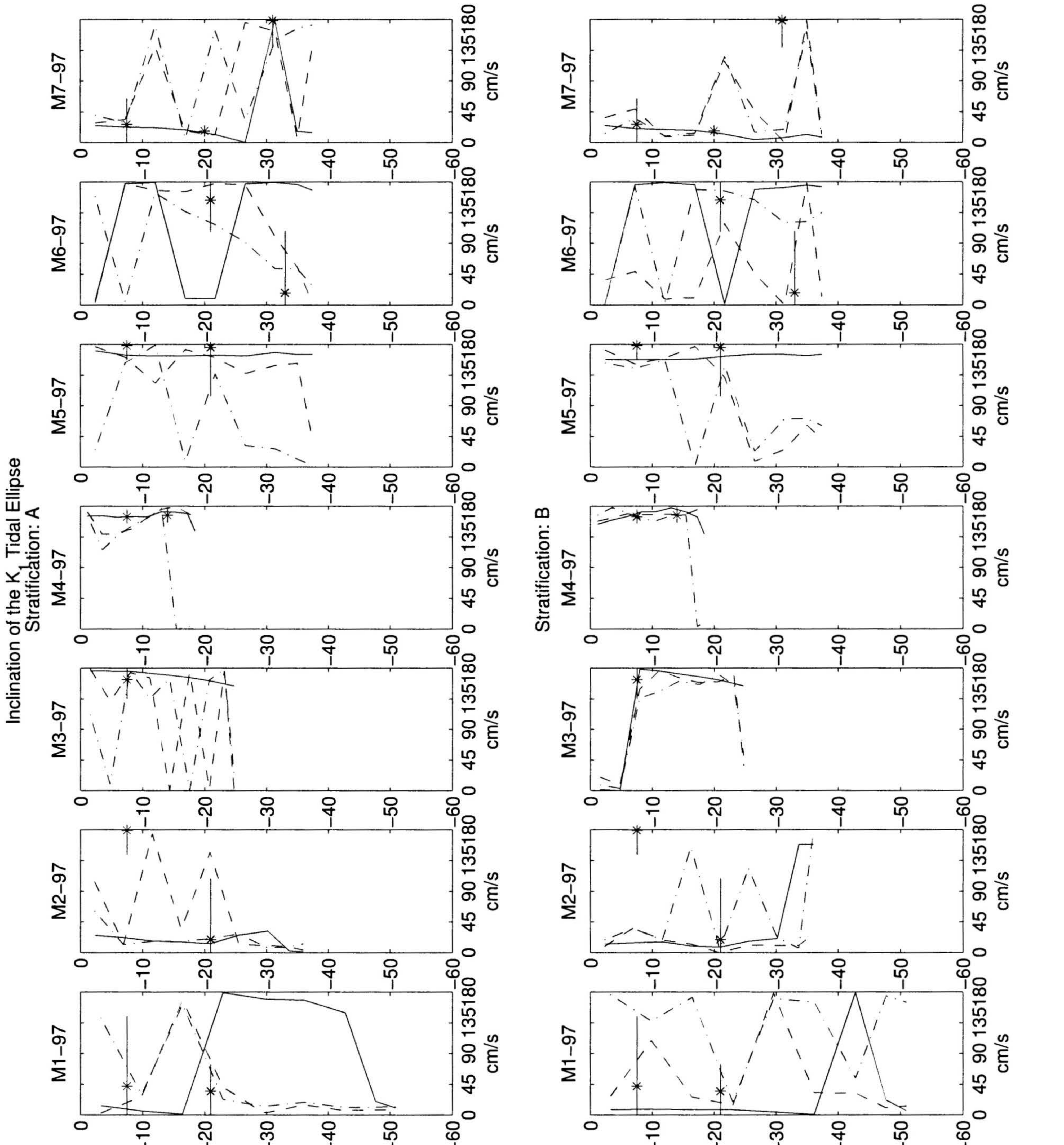

Figure 5.6 Inclination (degrees) of the K_1 tidal ellipse 1997 (mixing models). Stratification A (left): **Model A** (solid line); **Model AR** (dashed line); **Model ARA** (dash dot line). **Stratification B** (right): **Model B** (solid line); **Model BR** (dashed line); **Model BRA** (dash dot line). **Observations** (*) plotted with error bars representing the 95% confidence interval.

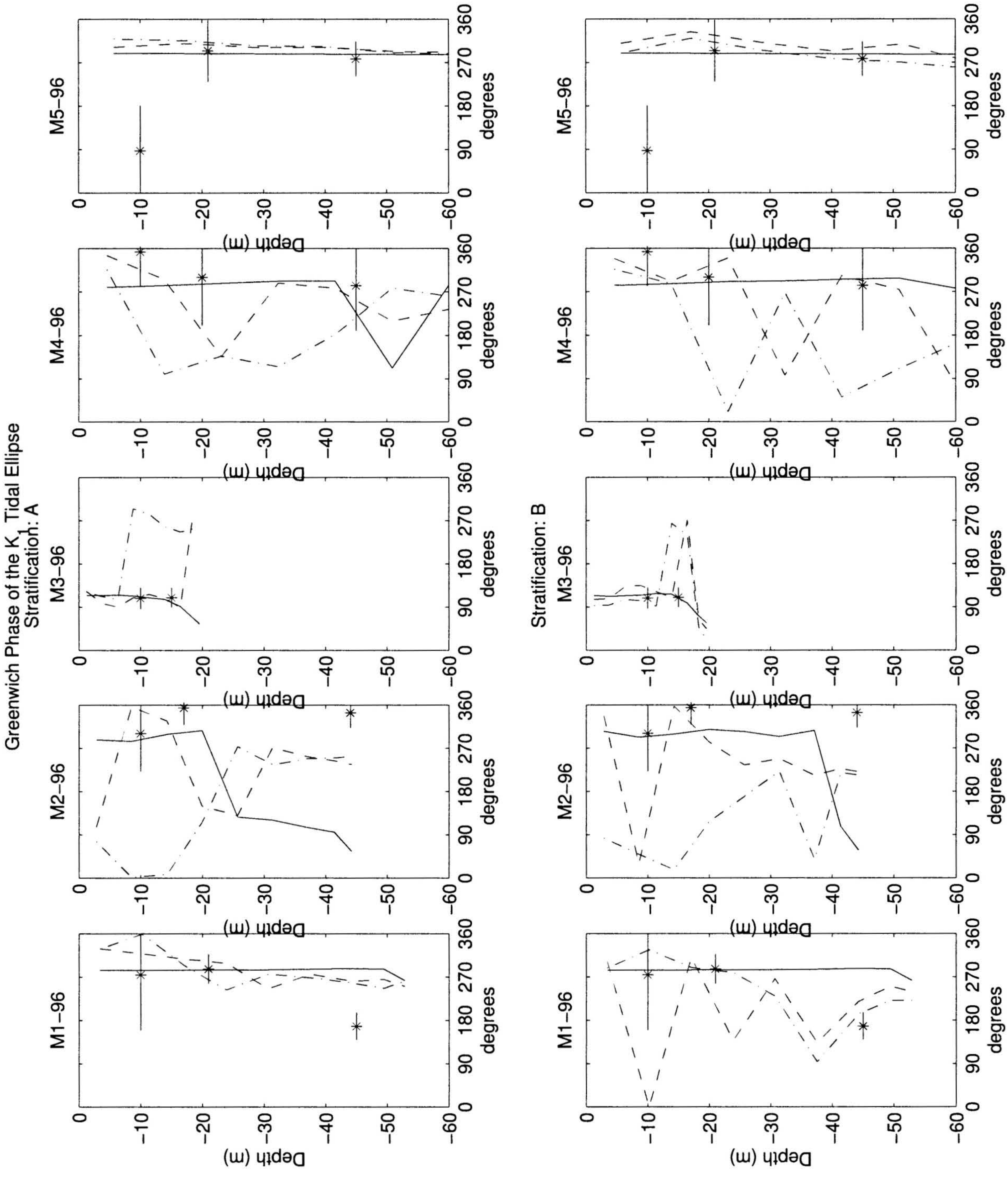

Figure 5.7 Greenwich Phase (degrees) of the K_1 tide 1996 (mixing models). Stratification A (left): **Model A** (solid line); **Model AR** (dashed line); **Model ARA** (dash dot line). **Stratification B** (right): **Model B** (solid line); **Model BR** (dashed line); **Model BRA** (dash dot line). **Observations (*)** plotted with error bars representing the 95% confidence interval.

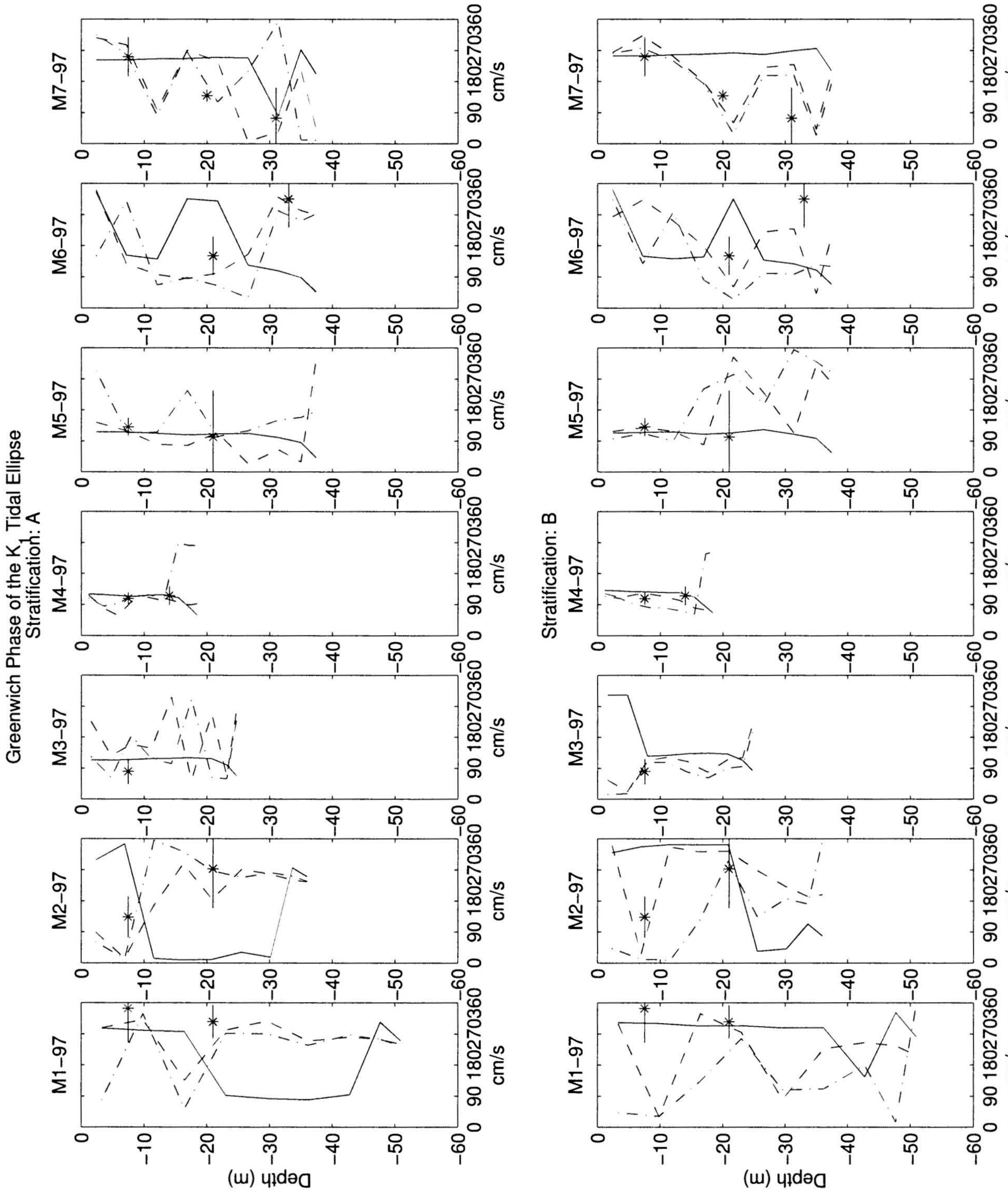

Figure 5.8 Greenwich Phase (degrees) of the K_1 tide ellipse 1997 (mixing models). Stratification A (left): **Model A** (solid line); **Model AR** (dashed line); **Model ARA** (dash dot line). **Stratification B** (right): **Model B** (solid line); **Model BR** (dashed line); **Model BRA** (dash dot line). **Observations (*)** plotted with error bars representing the 95% confidence interval.

Mixing also influence the orientation (Figure 5.9-5.10, Tables C.13 and C.15) and Greenwich phase (Figures 5.11-5.12, Tables C.14 and C.16) of the main semi-diurnal M_2 tide. Within the inner basin, at M1-96, the observed tidal M_2 ellipses at the surface tide are oriented at 52°, there is little variation in the orientation with depth: tidal ellipses at 21 and 45 metres depth have an orientation of 45°. The ellipse orientation is constant in the models A and B but once mixing is introduced into the model the ellipse orientation becomes more variable. Model AR indicates the least amount of variation with the M_2 tidal ellipses oriented between 32° and 43°. The tide at 10 and 21 metres depth was oriented more easterly (32°-36°) than the observed ellipse. In model ARA, the orientation of the tidal ellipse at 21 and 45 metres depth (41° and 53°) agrees with the observed orientation but the surface tide at 10 metres depth is rotated eastward to 14°. With the main pycnocline located near the depth of the sill, models BR and BRA indicate the greatest departure from the observed data. The orientation of the M_2 tidal ellipse at 10 metres depth is 37°-41°. At 21 metres depth, close to the depth of the main pycnocline, the tidal ellipse rotates northward to 61°-63°, while at the bottom (45 metres depth), the M_2 tide is rotated almost due east, 6°-9°. Prior to the introduction of mixing the Greenwich phase of the M_2 tide in models A and B was constant throughout the water column at 155°-157°. This is contrast to the observed phase of the M_2 that indicates a phase lag of approximately 120° between the bottom and surface tide. The phase of the surface M_2 tide in models A and B lags the observed surface tide by 60°. With mixing and with the pycnocline located above the level of the sill, models AR and ARA both have a phase lag between the bottom and surface tides, 25° in model AR and 50° in model ARA. The phase of the surface tide is in good agreement in with the observed value:

model AR has a Greenwich phase of 98° and model ARA has a phase of 113°. Models BR and BRA are similar to models AR and ARA, the phase lag between the bottom and top of the water column in both models is approximately 50° while the Greenwich phase of the surface tide is 114° in model BR and 97° in model BRA. The averaging process used to permit evolution of the background scalar fields appears to have opposite effects in the two models. In model ARA, the averaging process leads to a departure of the Greenwich phase from the observations, while in model BRA it brings the value of the Greenwich phase into closer agreement with the observations. It is not obvious why this occurs, the enhanced mixing resulting from the evolving background density field is expected to lead to a gradual weakening in the density gradient across the main pycnocline. The breakdown of this density gradient appears to be an important factor in the determining the phase of the surface tide.

At M2-96, the orientation of the M_2 tidal ellipse at the surface is consistent with the observed value of 18° in models A, B, AR and ARA at 13°-17° degrees. With the deeper main pycnocline, the tide rotates towards the north to 31°-40° in models BR and BRA. This northward rotation of the tide in models BR and BRA was also found in the orientation of the K_1 tidal ellipses. At 21 metres depth, models AR and ARA that have the greatest departure from the observed M_2 tide. Models AR and ARA have tidal ellipses that lie close to the east-west axis at 6° and 172° degrees, respectively. The observed M_2 tidal ellipse was oriented at 23°; the tidal ellipses in models A, B, BRA are oriented at 15°-16° while model BRA was oriented at 25°. At the bottom of the channel, the observed M_2 tide rotates to within 5° of the east-west axis, this is reasonably consistent in all models (3°-7°) while the observed tide was oriented towards the northwest (175°). The observed phase of the M_2 tide indicates that the bottom tide precedes the surface tide by as much as 160°. All of the models that include mixing indicate the bottom tide preceding the surface tide, however, the phase difference of the tides varies depending upon the depth of the main pycnocline. With the main pycnocline located at 10 metres depth, the bottom tide precedes the surface tide by 70°-80°. With the main pycnocline at sill depth, the phase difference increases to 100°-110°. The Greenwich phase of the surface tide in models AR and ARA lags the observed Greenwich phase by 30°. In models BR and BRA, this phase lag increases to 40° (BR) and 50° (BRA).

The Greenwich phase of the surface tide in the models is dependent upon the choice of mixing algorithm and also on the depth of the main pycnocline. When the background scalar fields evolve over time the phase difference between the observed and modelled tide increases when the main pycnocline is located above the sill. When the main pycnocline is located at sill depth, the evolution of the background scalar fields reduces the phase difference between the model and the observations.

Examining the M_2 tide across the inner basin, the orientation of the M_2 tidal ellipses at moorings M1-97, M2-97 and M3-97 agree very well with the observed values. Prior to the introduction of mixing, the surface M_2 tidal ellipses at M1-97 were oriented more at 18° compared to the 35° ellipse orientation found in the data. Once mixing as been introduced into the model, the tidal ellipses rotate northward to 23°-32°, this rotation also occurs at 21 metres depth where the observed tidal ellipses are orientated at 22°. In the centre of the channel at M2-97, models BR and BRA are rotate the ellipses northwards to 21°-33°, consistent with the rotation of the K_1 tidal ellipses in these models but inconsistent with the 10°-11° ellipse orientation of the observations and other models.

Model ARA departs from the observed tide at 21 metres depth, the orientation of the tidal ellipse is at 19° a significant departure from the east-west orientation found in the observations and other models that include mixing. At M3-97, the range of values for the observed surface tide and all models was 167°-174°.

All of the models that including mixing produced an M_2 tide in which the bottom tide preceded the surface tide consistent with the observed behaviour at this location. This is not found in models A and B where the phase is constant throughout the water column. The phase lag between the tide at 21 metres depth and the tide at 7.5 metres depth is dependent on the depth of the main pycnocline and also on the algorithm used for mixing. The observed phase difference between the two levels was approximately 60°, the greatest phase lag in the models is 40° in model ARA while the smallest phase lag is only 5 ° in model BRA. Model AR has a phase lag of only 7° while model BR has a phase lag of 27°. Similar to the Greenwich phase at mooring M1-96, the addition of an evolving background scalar field into the mixing algorithm produces a later tide in model ARA (123°) compared to model AR (93°). The same algorithm improves the agreement of the Greenwich phase from model BR (114°) to model BRA (66°) which agrees with the observed value of 58°.

At M2-97, the observed tide at 21 metres depth precedes the surface tide with the phase difference approximately 50°. This behaviour is replicated by models that include mixing and was noticeably absent in the models with a static stratification. The difference in phase between the tide at 21 metres depth and the tide at 7.5 metres depth is, again, found to be dependent on the mixing algorithm and the depth of the main pycnocline. In model ARA the, phase difference of approximately 80° is signficantly larger than the observed value, while in model ARA, the phase difference has been reduced to 50°. When the main pycnocline is at sill depth the phase difference increases from 30° in model BR to 40° in model BRA. None of the mixing models produce a tide with the same Greenwich phase as the observed 75°. When the main pycnocline lies above the level of the sill, the modelled Greenwich phase (133°-142°) lags the observed Greenwich phase by approximately 65°; the deeper main pycnocline reduces this difference to approximately 50° (Greenwich phase: 120°-125°) but this is still a significant departure from the observed value. The Greenwich phase of the modelled tide also lags the observed Greenwich phase at M3-97 by approximately 40° in all models to include mixing except model ARA where the modelled tide lags by 84°.

At the sill, the orientation of the tidal ellipses should be controlled by the local bathymetry due to the narrowness of the channel. At M3-96, the M_2 tidal ellipse has an orientation of 170°. All of the models are able to replicate this behaviour with tidal ellipses oriented 167°-176° degrees. At 15 metres depth, the tidal ellipses are rotated clockwise from the tide at surface to 163°, the tidal ellipses in models with mixing all rotate counter-clockwise. At M4-97, the M_2 tidal ellipses at 7.5 and 15 metres depth are oriented at 161° and 168°, respectively. At this location the observed tide rotates in a counter-clockwise direction with increasing depth. Model ARA is able to replicate this characteristic of the tide quite well with tidal ellipses oriented at 159° and 171° at the 7.5 and 14 metres depth. Models AR and BR produce a very small 3° clockwise rotating current while the M_2 tide in model BRA had no rotation. There are two features within the model that may partially account for this behaviour. Firstly the region of the sill was broadened and deepened in order to satisfy the requirement of hydrostatic consistency, as a consequence of this the tide may be more directly influenced by the tidal currents lying to the seaward side of the sill. The second factor that may influence the direction of the tidal ellipses in the region of the sill is friction. In order to achieve numerical stability in the region of the sill, it was necessary to introduce high bottom friction and lateral friction in the region of the sill. The parameterization of friction in the region of the sill was continually increased until numerical stability was achieved so that the model is able to execute a 30-day simulation under conditions of static stratification. The frictional terms were not adjusted once mixing was introduced into the model. It may be possible to re-parameterize the bottom and lateral friction terms used within the model to produce a tidal flow that is more representative of the observed tide.

Adjustment of the bottom friction in the region of the sill would influence the phase of the M_2 as it crosses over the sill. A comparison of the observed Greenwich phase of the M_2 tide between moorings M3-96 and M4-97 shows that in the near surface region (7.5 and 10 metres depth) the Greenwich phase is almost equal ranging from 231°-233°. The Greenwich phase of the deeper current (14 and 15 metres depth) increases from 220° to 229° as the tide moves from mooring M4-97 to M3-96. M4-97 is approximately 250 metres further to the east than mooring M3-96. Examining the Greenwich phase associated with the model runs we find that models AR and BRA produce M_2 tides with phases of 225°-227°. These values agree well with the observed phase at 7.5 metres depth. By the time the M_2 reaches the M3-96 (separated in the model by only 5 grid points), the Greenwich phase has increased to 272° in model AR and to 249° in model BRA. The M_2 tide at 14 metres depth in model AR lags both the surface tide and the observed tide by almost 50° at M4-97 having a Greenwich phase of 271°. In model BRA, there is almost no phase difference between the surface and bottom tides at this location with a Greenwich phase of 229°. Neither model produces a significant phase difference at 14 metres depth between moorings M3-96 and M4-97. There are other differences in the M_2 tide at these locations. At mooring M4-97, the observed M_2 tide indicates that the bottom tide precedes the surface tide by approximately 10°. Model runs AR and ARA produce an M_2 tide in which the surface tide precedes the bottom tide by 50° and 20° degrees, respectively, while models BR and BRA produce almost no phase difference between the surface and bottom tides. At M3-96, only model AR produces an M_2 tide that arrives almost simultaneously through the water column similar to the observed tide. The other mixing models produce a phase difference between the bottom and surface tides between 20° (ARA, BRA) and 30° (BR) degrees with the bottom tide preceding the surface tide.

Seaward of the sill, at mooring M5-97, M6-97 and M7-97 the model performs quite well regarding to the orientation of the M_2 tidal ellipses. On the southern side of the channel, the surface M_2 tide is oriented 155°-167° compared to the observed 174° ellipse orientation. The M_2 tide at 21 metres depth is oriented 15°-20° in models AR and ARA in contrast to the 156°-172° orientation from the observations and produced by the other models. In the centre of the channel at mooring M6-97, models ARA and BRA produce a M_2 tidal ellipse at 21 metres depth oriented at 170°-172°, this agrees very well with the observed value of 168° degrees. Model AR produces a M_2 tidal ellipse oriented to the at 5°, while model BR produces an M_2 tidal ellipse oriented at 158°. This latter value lies just on the edge of the 95% confidence interval of the observed value. The M_2 tidal ellipses at 33 metres depth are not significantly different from the observed orientation of

5°, the 95% confidence interval of 60° found in the observations indicating a large amount of variability in the direction of the M_2 tide at this location. Towards the northern coastline at M7-97, the orientation of the surface M_2 tide is found 25°-32° degrees in all models that included mixing. This is more northward of the observed value of 20° and also significantly different than the orientation of the tidal ellipses (9°-10°) produced by the statically stratified models A and B. At 33 metres depth, the mixing models produce a M_2 tide oriented towards the northwest between 163°-175° in contrast to the observed orientation of 9°s. The statically stratified models had previously been able to replicate the proper tidal orientation for this particular location.

Across the channel, the phase of the M_2 tide lags behind the observed M_2 tide. At M5-97, the surface tide produced in models AR and ARA lags the Greenwich phase of the observed tide by 50°, the phase lag of the model BR is 43° while in model BRA the phase lag is only 23°. There is better agreement between the model Greenwich phase and the observed Greenwich phase at 21 metres depth. The phase lag between models AR and ARA and the observed Greenwich phase is reduced to 30° while there is no significant difference between the Greenwich phase of models BR and BRA (190°-201°) and the observed tide (206°). The tide at 21 metres depth precedes the surface tide in all models and also in the observed tide; the difference in phase between the two levels was larger in the model runs (60°-80°) than observed (34°).

At M6-97, models BR and BRA produce an M_2 tide at 21 metres depth with a Greenwich phase of 209°-226°, this agrees very well with the observed value of 216°. The observed M_2 tide at 33 metres depth precedes the M_2 tide at 21 metres depth by 18° this is not found in either models BR or BRA. In model BR the tides at the two levels are almost simultaneous while in model BRA the tide at 21 metres precedes the deeper tide by 50°. Model AR is the only mixing model in which the tide at 31 metres depth precedes the tide at 21 metres depth. The phase difference of 50° between the two levels is much larger than the observed phase difference, although the Greenwich phase of 200° of the tide at 33 metres depth agrees well with the observed 198° Greenwich phase at this depth.

On the northern boundary at M7-97, model BRA produces the best simulation of the observed M_2 tide. The Greenwich phase of 13° at 31 metres depth produced by the model agrees quite well with the observed Greenwich phase of 359°. The other mixing models produce a tide lagging the observed value by 40°-50°. All of the models produce a bottom tide that precedes the surface tide in agreement with the observations. The phase difference in model BRA was 60°, 20° larger than the observed phase difference of 40°. The other models produce a phase difference of only 50° degrees, however, the phase lag between the model and observations in the surface tide of 50°-60° degrees in models AR, ARA and BR create a tide with an arrival time significantly different throughout the water column.

At M4-96, the surface and bottom M_2 tidal ellipses generated by the model are oriented closer to the east-west axis than those found in the observations. Observed orientations of 30° at the surface and 25° at the bottom are rotated more northerly than the tidal currents produced by the model ellipses oriented at 0°-10°. With the exception of model ARA, which produced a tidal ellipses oriented to the northwest, all models produce an M_2 tide at the 20 metre level with an orientation 4°-12°, agreeing reasonably well with the observed value of 4°. When the model was run with a static stratification, the Greenwich phase of the M_2 tide at M4-96 lagged the observed phase at the surface by

95°. The M_2 tide in these model runs has no variation in the phase of the tide through the water column. With the introduction of mixing, the agreement in phase between the models and the observations is greatly improved. Models AR and ARA produce an M_2 tide with a Greenwich phase, at the surface, of 107°, this lags the observed value by approximately 40°. These models also produce a tide in which the surface tide precedes the tide at 20 metres depth, opposite of the observed behaviour of the M_2 tide. Model BR has a surface M_2 tide that lags the observed tide by 40°, with the surface tide preceding the tide at 21 metres depth. The bottom tide produced by the model also lags the observed tide by approximately 40°. Recalling the good agreement of the M_2 tidal currents (Table 5.5 And Figure 5.2), the M_2 tide produced by model M4-96 is a very good representation of the observed M_2 tide at this location apart from the difference in Greenwich phase the M_2.

Model BRA also produced tidal currents of the same order of magnitude of model BR. It is here where we find that the importance of the enhanced mixing that is achieved through evolution of the background scalar fields of temperature and salinity. The Greenwich phase of the M_2 tide modelled in BRA was 81°, 59° and 3° degrees compared to the observed phases of 65°, 52° and 356° degrees at 10, 20 and 45 metres depth. Considering the simplicity of the algorithm used to permit the background scalar fields to evolve, the agreement of the Greenwich phase of the M_2 tide in model BRA with the observations at M4-96, along with the agreement in the strength of the tidal currents indicates that this evolving background density structure may significantly influence the ability of the model to accurately reflect the observed tides within the inlet.

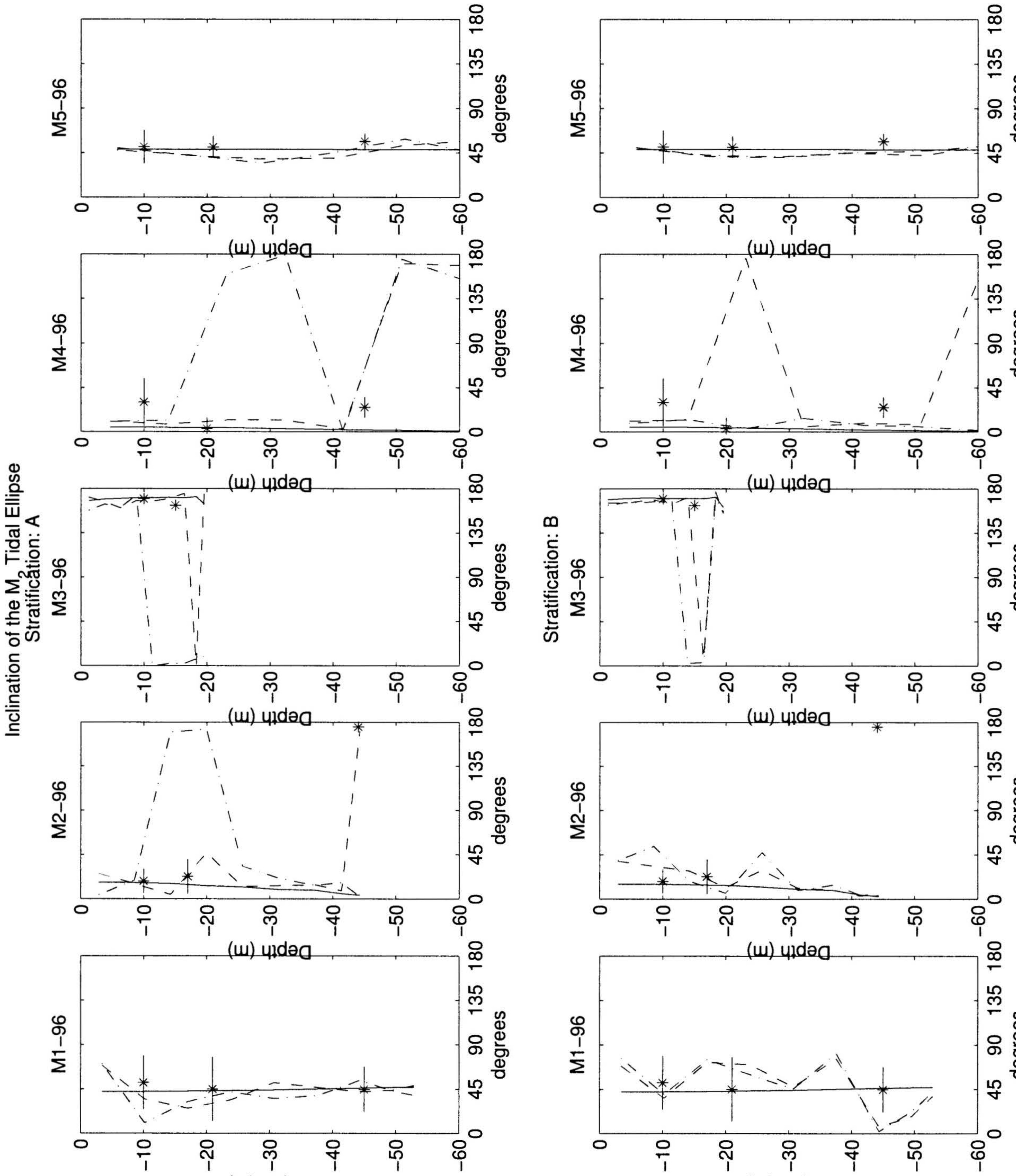

Figure 5.9 Inclination (degrees) of the M_2 tidal ellipse 1996 (mixing models). Stratification A (left): **Model A** (solid line) **Model AR** (dashed line); **Model ARA** (dash dot line). **Stratification B** (right): **Model B** (solid line) **Model BR** (dashed line); **Model BRA** (dash dot line). **Observations (*)** plotted with error bars representing the 95% confidence interval.

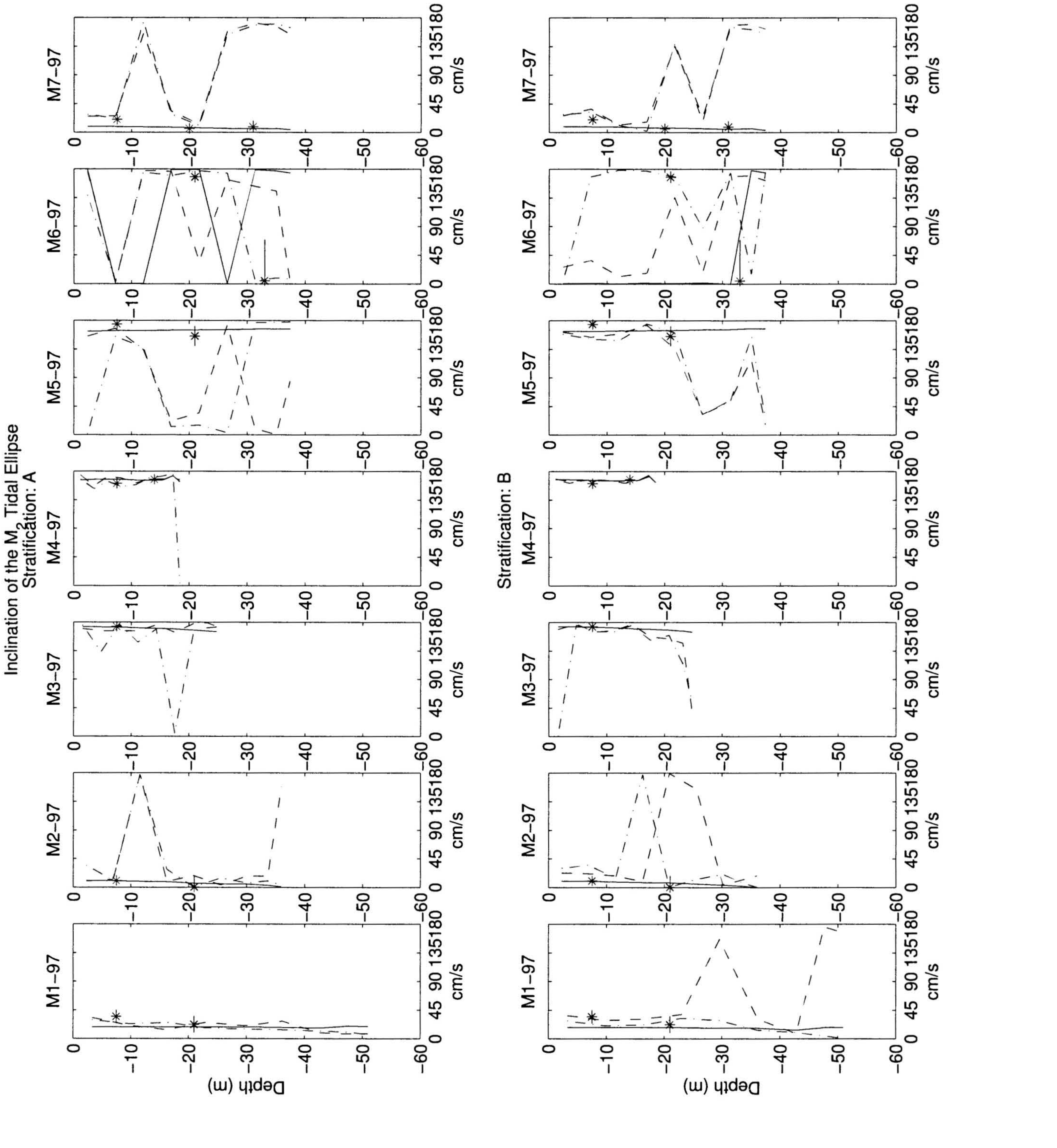

Figure 5.10 Inclination (degrees) of the M_2 tidal ellipse 1997 (mixing models). Stratification A (left): **Model A** (solid line); **Model AR** (dashed line); **Model ARA** (dash dot line). **Stratification B** (right): **Model B** (solid line); **Model BR** (dashed line); **Model BRA** (dash dot line). **Observations (*)** plotted with error bars representing the 95% confidence interval.

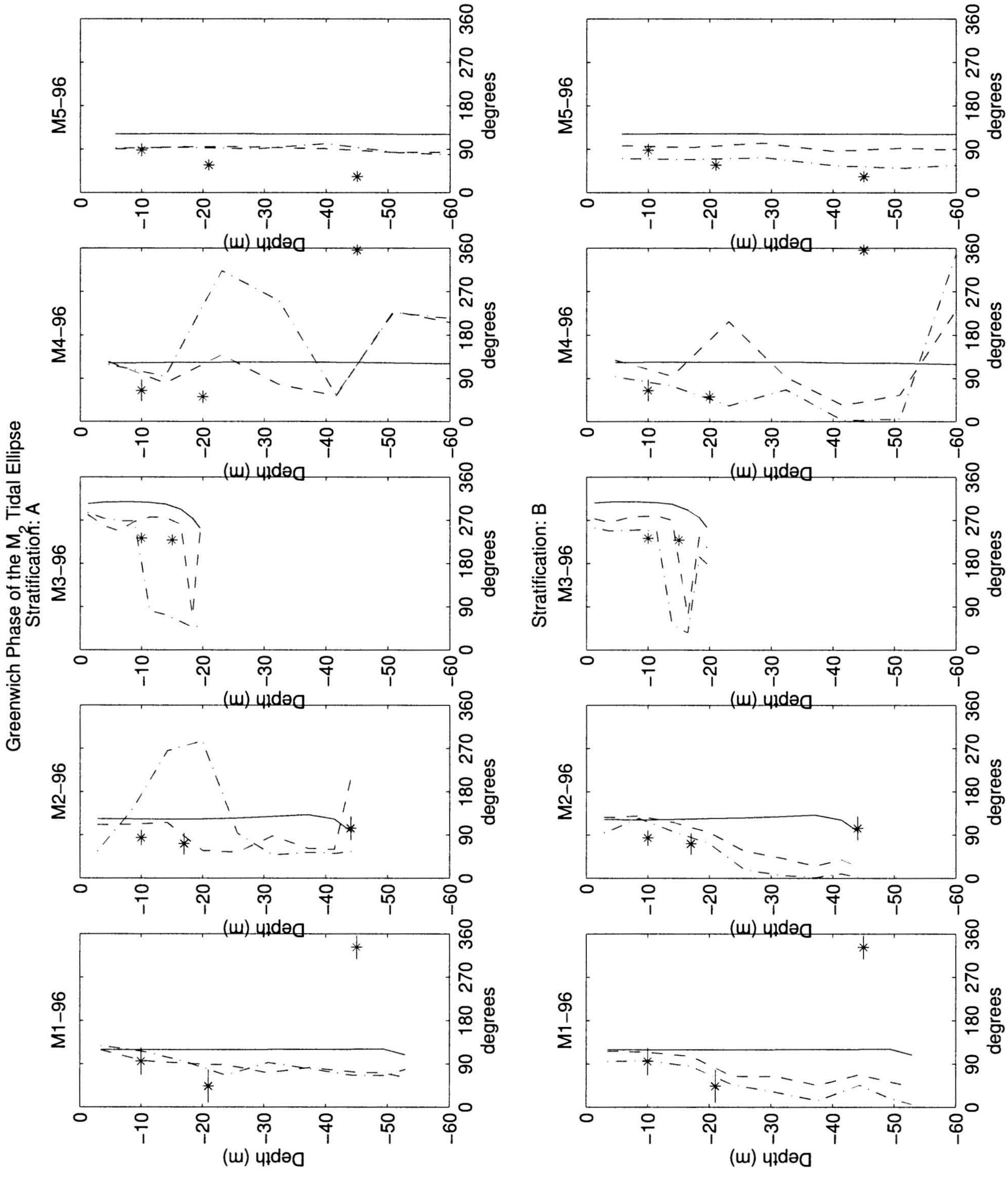

Figure 5.11 Greenwich Phase (degrees) of the M_2 tide 1996 (mixing models). Stratification A (left): **Model A** (solid line); **Model AR** (dashed line); **Model ARA** (dash dot line). **Stratification B** (right): **Model B** (solid line); **Model BR** (dashed line); **Model BRA** (dash dot line). **Observations (*)** plotted with error bars representing the 95% confidence interval.

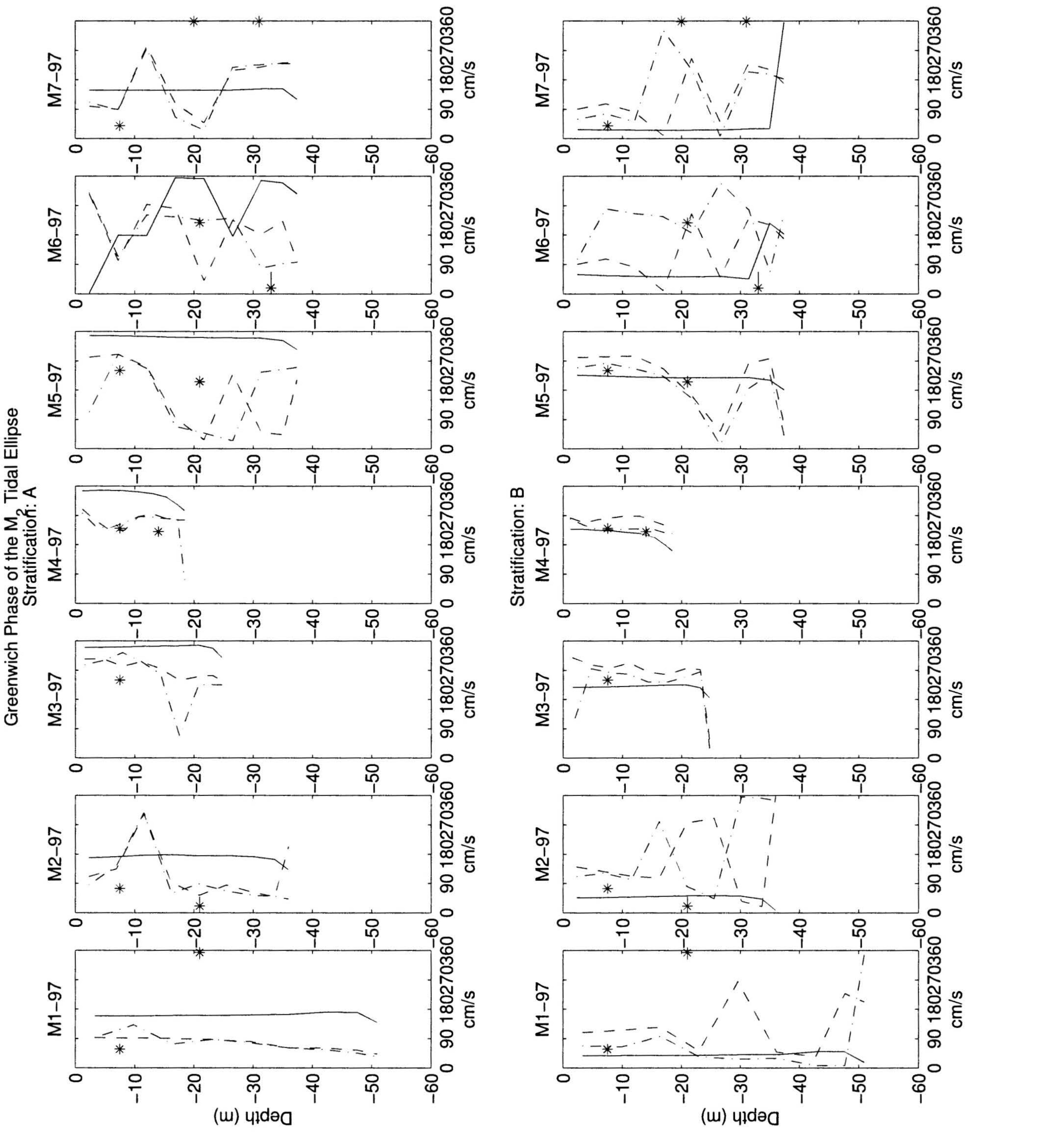

Figure 5.12 Greenwich Phase (degrees) of the M_2 tide 1997 (mixing models). Stratification A (left): **Model A** (solid line); **Model AR** (dashed line); **Model ARA** (dash dot line). **Stratification B** (right): **Model B** (solid line); **Model BR** (dashed line); **Model BRA** (dash dot line). **Observations (*)** plotted with error bars representing the 95% confidence interval.

The results from the models are rather mixed. In the region of the sill, the phase of the tide has been shown depend upon the depth of the main pycnocline and also on the mixing algorithm. Adjustment of bottom friction is unlikely to have much influence except in the lower levels of the model. The phase difference between moorings M3-96 and M4-97 is significant in models AR and ARA. The lateral dissipation introduced in the model may be influencing the phase of the tide in the upper layers; lateral friction becomes stronger as the channel becomes narrower. Ideally, the dissipative term should be replaced with a physically interpreted sidewall friction term. The inability of the model to correctly simulate the flow characteristics at the sill makes use of the model to study the circulation of the inner basin almost impossible. The circulation of the inner basin will depend on the correct tidal forcing. If tidal forces are too weak, the correct balance between tides and wind stress cannot be achieved.

The analysis of the main tidal diurnal and semi-diurnal constituents indicates the evolution of temperature and salinity is a significant factor in determining both the amplitude and phase of the tide. We anticipate that the tidally forced flow will be highly nonlinear and we now turn our attention towards the nonlinear tidal constituents, MS_f and M_4, to determine how well the model is able to reflect the nonlinear nature of the velocity field. Under conditions of a static stratification, the nonlinear tidal constituents in the model were much too weak to represent the true velocity field. When mixing is introduced into the model, the strength of the tidal currents increase, this should increase the nonlinear constituents if the interactions between the tidal constituents is being modelled accurately.

5.1.3 Nonlinear Tidal Constituents

Figures 5.13-5.16 show the vertical structure of the MS_f and M_4 tidal constituents. We begin the comparison by examining the low frequency MS_f tidal constituent. At 10 metres depth for M1-96, the MS_f tidal current was observed at 1.0 cm/s. With the addition of mixing in the model, the MS_f current increases from 0.1 to 0.4 cm/s as the depth of the main pycnocline deepens from 10 metres depth (model AR) to sill depth (model BR). The relaxation of the temperature and salinity fields used in model AR damps the MS_f current. In model ARA the MS_f current increases to 0.6 cm/s from the 0.1 cm/s current in model AR. This is significantly weaker than the observed tidal current at 10 metres depth but the increase in the surface MS_f tide suggests that the enhanced mixing in model ARA and BRA may play a significant role in the nonlinear interactions between M_2 and S_2. It was not possible to determine the MS_f tide in model BRA because the model became numerically unstable after only 20 days. The MS_f tide in all models is weaker than the observed tide. The deeper observations indicate the observed MS_f current is 0.3-0.4 cm/s. The models only produce an MS_f current of 0.1-0.2 cm/s at 21 and 45 metres depth.

At M2-96, mixing increases the MS_f current at 10 metres depth from 0.1-0.2 cm/s in models A and B to 1.1 cm/s in models AR and BR. At the 17 and 45 metre levels, there is a moderate increase in MS_f as mixing is added to the model. Figures 5.13 and 5.14 indicate the vertical profile of the MS_f tide has a maximum current at the surface when mixing is introduced into the models. Without mixing, models A and B both have local maxima of the MS_f near a depth of 30 metres. Figure 5.13 also reveals the enhanced mixing of model ARA results in a distinct maximum in the current near 10 metres depth.

At 10 metres depth, the MS_f tide in model ARA produces s a 1.7 cm/s current agreeing very well with the observed value of 1.6cm/s The observed current was 0.4 and 0.3 cm/s at 21 and 45 metres depth respectively. The MS_f currents in model ARA are 0.7 and 0.3 cm/s at these same depths. The other models produce a weaker tide at both the 17 and 45 metre levels. At 17 metres depth, models AR and BR produce currents of 0.4 cm/s and at 45 metres depth the currents were 0.1-0.2 cm/s. From Figures 5.13 and 5.14 all models appear to fit the observed MS_f tide below 17 metres depth.

Towards the southern coastline, at M1-97, models AR, ARA and BR all produce MS_f tidal currents that are stronger than those found in models A and B. The surface tide increases from 0.2 cm/s in model A to 0.8 cm/s in model AR and to 1.3 cm/s in model ARA. The MS_f current at 21 metres depth increases from 0.2 cm/s to 0.5-0.6 cm/s. At the surface, model AR agrees with the observed value of 0.8 cm/s while model ARA is 50% stronger than the observed current. Both models produce a MS_f current approximately 3 times stronger than observed at 21 metres depth. In model BR, the surface MS_f current increases to 1.6 cm/s; the current at 21 metres depth increases to 0.8 cm/s.

At M2-97, all of the mixing models have a surface MS_f current stronger than the observed tide and a weaker current at 21 metres depth. When the main pycnocline is located about the 10 metre level, the MS_f tide at 7.5 metres depth increases from 0.4 cm/s in model A to 1.9 cm/s in model AR and to 1.5 cm/s in model ARA. At 21 metres depth, the currents decrease from 0.8 cm/s in model A to 0.5 cm/s in both models. The enhanced mixing in model ARA reduces the tidal current at 7.5 metres depth in model AR while having little or no influence on the tidal currents at 21 metres depth. In model BR, the surface MS_f current increases from 0.5 cm/s in model B to 1.7 cm/s; the tidal currents at

21 metres depth are reduced from 0.5 cm/s to 0.1 cm/s. The MS_f currents in the statically stratified models were weaker than the observed 1.0 cm/s. The observed MS_f tidal currents are relatively strong at this location, ranging between 1.0-1.2 cm/s through the water column. None of the models are able to replicate this behaviour. The models also fail to reproduce the strength of the surface MS_f current at mooring M3-97. The greatest current obtained by any model is 0.9 cm/s in model ARA, only 65% of the observed 1.4 cm/s.

At the sill, the strength of the M_2 and S_2 tidal currents produced by the models were significantly weaker than the observed values. The MS_f current is produced through nonlinear interaction between these two semi-diurnal constituents, so the MS_f tidal currents within the model are not expected to bear much resemblance to the observations. A comparison of the mixing models to those with a static stratification clearly indicates that mixing does amplify the nonlinear interaction of the sill. With the main pycnocline located above the sill, mooring M3-96 indicates that model A has a MS_f current of 0.6-0.7 cm/s through the entire water column. With mixing include in the model, the MS_f currents increase to 1.0-1.3 cm/s. However, model ARA, with the enhanced mixing has weaker currents but more variable than those found in model AR. When the main pycnocline is located at the depth of the sill, the greatest increase in the MS_f tidal currents occurs closer to the bottom of the sill region. In model BR, the current at 10 metres depth increases 40% to 0.7 cm/s from the 0.5 cm/s current in model B. At 15 metres depth, the current increases by 160% to 1.3 cm/s.

The response of the tide to mixing at M4-97 differs from that found at M3-96 despite the proximity of these mooring to each other. With the main pycnocline above the sill, model A indicates the MS_f current is 0.8 cm/s at 7.5 metres depth and 0.4 cm/s at 14 metres depth. With the introduction of mixing, model AR has a surface MS_f tidal current of the same magnitude as model A, while the enhanced mixing in model ARA has a tidal current 50% stronger at 1.2 cm/s similar to M3-96. At 14 metres depth, the MS_f current at M4-97 ranges between 1.2-1.4 cm/s similar to the 1.2-1.3 cm/s current at M3-96. Model BR has a weaker surface MS_f current. At 7.5 metres depth, the current decreases from 0.6 cm/s in model B to 0.3 cm/s. At 14 metres depth, the MS_f increases from 0.4 cm/s to 0.7 cm/s in response to mixing. Although this represents an increase of 75%, the MS_f current is still significantly weaker than the 1.2 cm/s current at M3-96 (15 metres depth). In the model, the MS_f current increases from M4-97 to M3-96, suggesting, at least within the model domain, that this region is a location of increasing nonlinear interaction. The increasing MS_f current does appear in the observations at the 7.5-10 metre level but not at the 15 metre level, the tidal currents near the bottom may be effect by frictional forces in the sill region.

Seaward of the sill at M5-97, the observed MS_f tide is stronger, 0.6 cm/s, at 21 metres depth, than at the surface where it is only 0.3 cm/s. All mixing models have a stronger current at the surface. Models AR and ARA both have a surface MS_f tide between 0.8-0.9 cm/s; approximately 3 times stronger than the observed tide. Model BR generates a weaker MS_f current of 0.4 cm/s that is in agreement with the observed value. All models fail to produce MS_f tidal currents that match the observed current at 21 metres depth. Models AR and ARA produce the strongest MS_f currents at 0.3-0.4 cm/s; model BR only generates a current of 0.1 cm/s.

At M6-97, mixing reduces the MS_f current below the sill. Models A and B both have a MS_f tide of 0.5 cm/s, this current is reduced a minimum of 20% to 0.4 cm/s when temperature and salinity mix. The observed MS_f tide at 21 metres depth was 0.8 cm/s; significantly stronger than any of the currents produced by the models.

At mooring M7-97, the MS_f current observed at the surface was 1.3 cm/s. When the main pycnocline was located above the sill (models A, AR and ARA), mixing reduces the MS_f tide from 0.5 cm/s to 0.4 cm/s in model AR, the enhanced mixing of model ARA results in a 60% increase in the tidal current to 0.8 cm/s. At 33 metres depth, the currents decrease from 0.5 cm/s in model A to 0.2-0.3 cm/s in models AR and ARA. Mixing has little influence on the MS_f tidal current at 7.5 metres depth, when the main pycnocline located at sill depth, in models B and BR. At 31 metres depth, mixing reduces the MS_f by 40% to 0.3 cm/s.

Towards the mouth of the inlet at M4-96, mixing increases the MS_f current from the surface down to 45 metres depth in all of the mixing models (Figures 5.13-5.14). Although the strength of the MS_f current increases from 0.1 cm/s to 0.4-0.5 cm/s at 10 metres depth in model AR, it is much weaker than the observed 0.9 cm/s current. Mixing models produce two local maxima in the MS_f currents. The first maximum is found at the surface while the second one occurs just below 30 metres depth. The vertical profiles of model AR and model BR at M4-96 (Figures 5.13 And 5.14) are very similar; the location and strength of the local maxima in the MS_f tide does not appear to depend on the depth of the main pycnocline.

Within the inner basin, the strength of the M_2 tide in the models weakens rapidly as the tide progresses towards the head of the inlet. This weakening current reduces the significance of the nonlinear tidal constituent M_4 that is dependent on the amplitude of the M_2 tide. The weakening of the tide to occurs even in models that include mixing of temperature and salinity. As a result, the M_4 tidal current is less than 0.05 cm/s in almost all models. This prevents a meaningful comparison of the M_4 tide at mooring M1-96.

At M2-96, model ARA is a good representation of the M_2 current at all three observation levels. The increase in M_2 at 10 metres depth appears to be isolated to one sigma level in the model and may not interact with the other sigma levels of the model. The lack of interaction may explain why the M_4 tidal current at 10 metres depth is much weaker, 0.4 cm/s, compared to the observed 0.7 cm/s. At 17 metres depth, both the M_2 tide and the M_4 tide agree well with the observations, the modelled M_4 current and the observed current between 0.1-0.2 cm/s. All models indicate that the M_4 tide has two local maxima, one located near the 10 metres depth and the other located near the bottom at 45 metres depth. The observations also indicate this, however, the observed maximum of 0.7 cm/s at 45 metres depth is much stronger than the 0.3 cm/s produced by model BRA, which has the strongest M_4 current at this depth.

At M1-97, all mixing models have a stronger M_4 current than those models with a static stratification. Models ARA and BRA, with the enhanced mixingm have M_4 tidal currents of 0.3-0.4 cm/s at the 7.5 metres depth; stronger than the observed currents of 0.1 cm/s. At M2-97, the M_4 current also increases when mixing is introduced into the model. At the surface, the strength of M_4 increases from 0.1 cm/s in models A and B to 0.2-0.3 cm/s in models AR, BR and BRA. In model ARA, the M_4 current increases to 0.6 cm/s matching the observed current at 7.5 metres depth. In model BRA, there is a distinct local maximum of, approximately, 0.5 cm/s near 12 metres depth (Figure 5.16). With mixing, the modelled M_4 current increases to 0.2-0.3 cm/s at 21 metres depth. This agrees

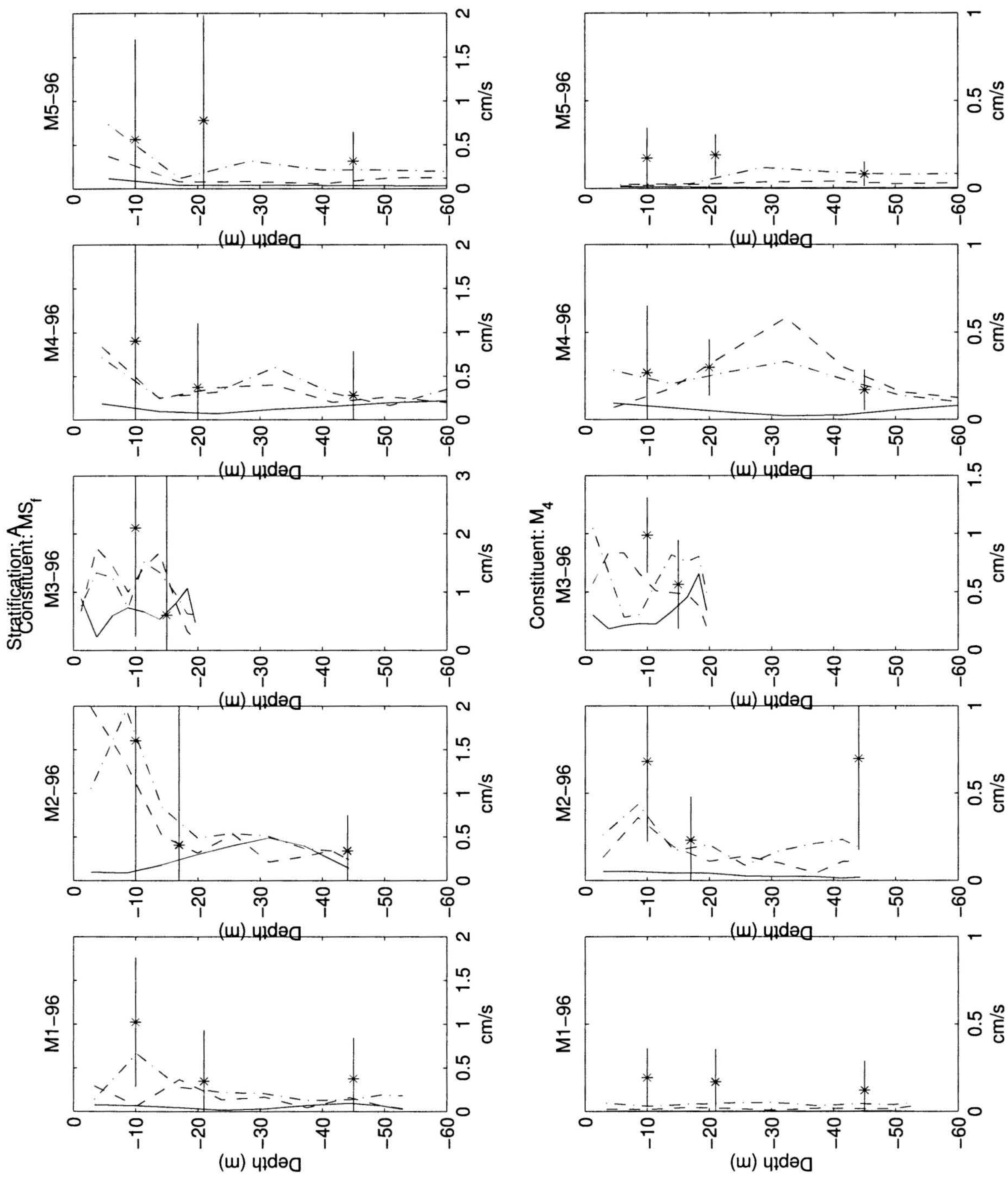

Figure 5.13 Nonlinear Tidal currents (semi-major axis, cm/s) MS_f and M_4 1996, Stratification A: Model A (solid line); **Model AR** (dashed line) and **Model ARA** (dash dot line)

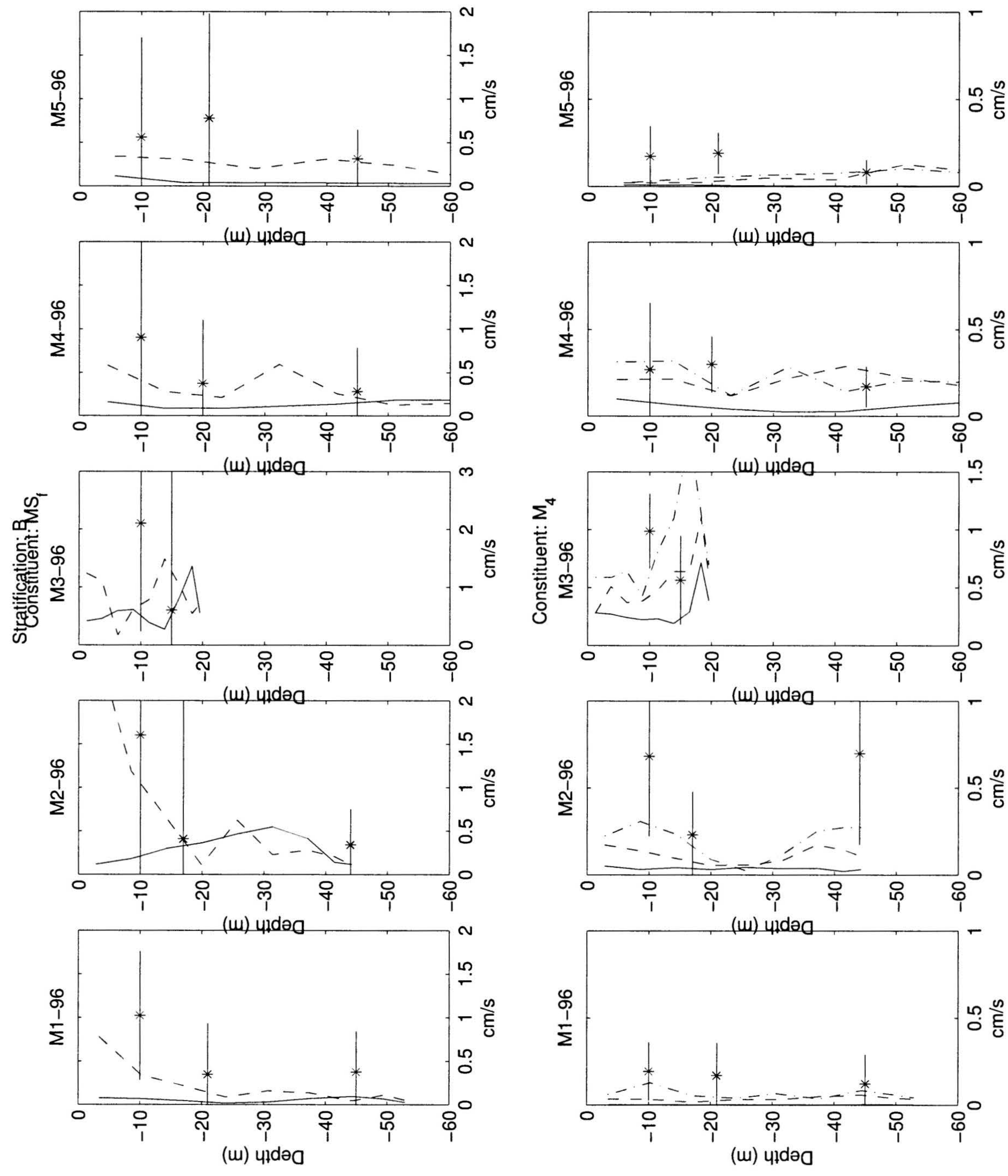

Figure 5.14 Nonlinear Tidal currents (semi-major axis, cm/s) MS$_f$ and M$_4$ 1996, Stratification B: Model B (solid line); **Model BR** (dashed line) and **Model BRA** (dash dot line)

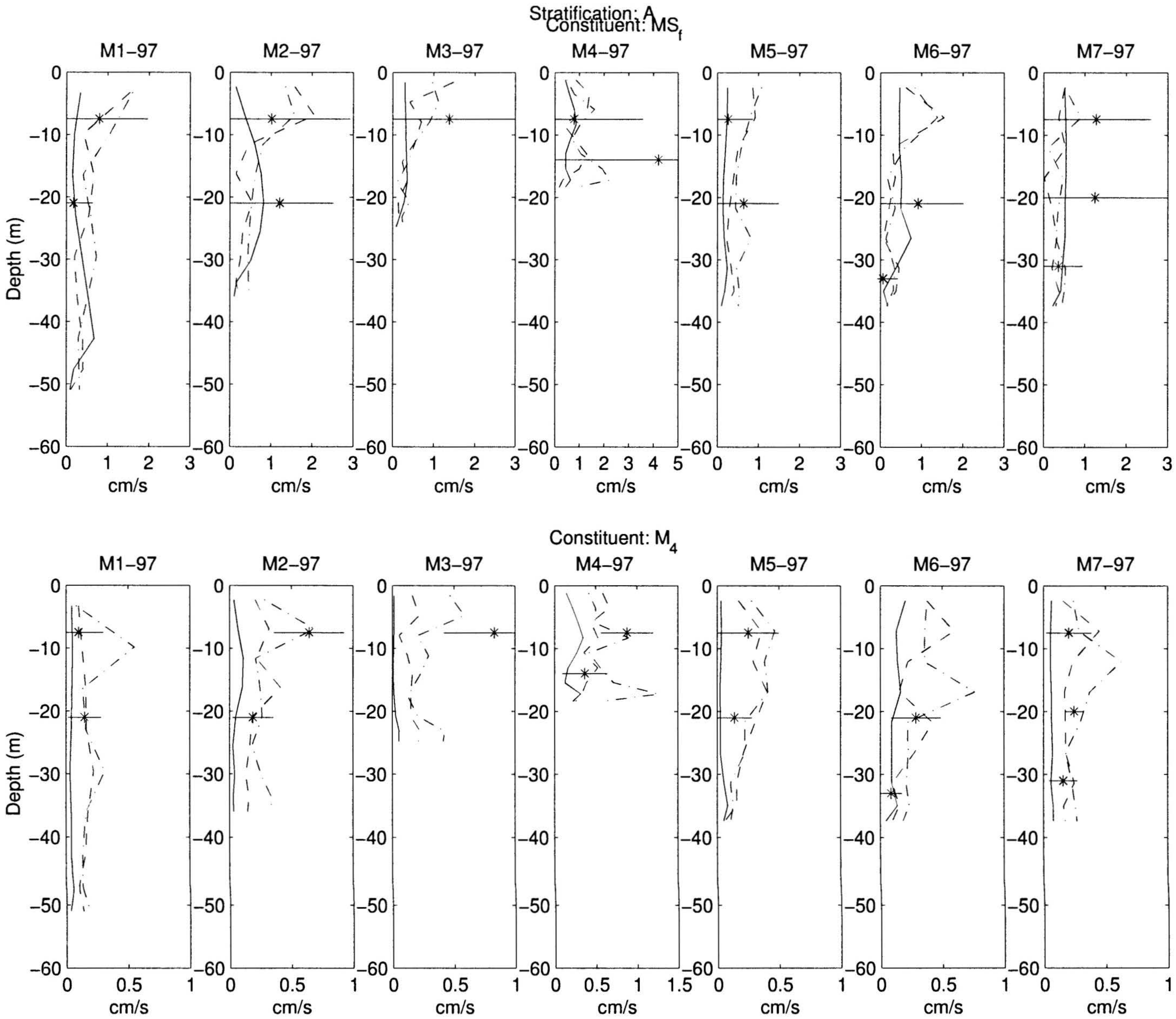

Figure 5.15 Nonlinear Tidal currents (semi-major axis, cm/s) MS_f and M_4 1997, Stratification A: Model A (solid line); **Model AR** (dashed line) and **Model ARA** (dash dot line)

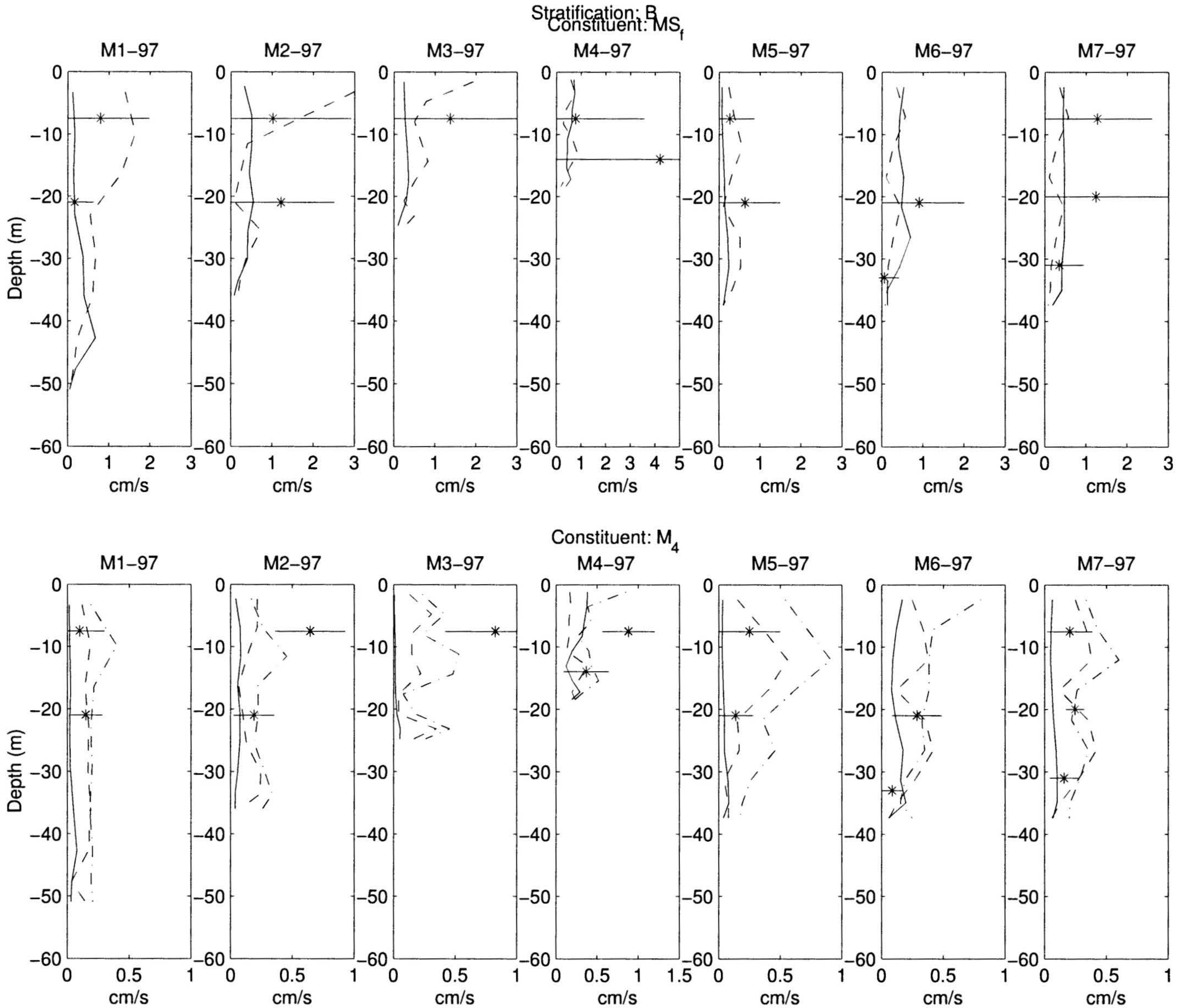

Figure 5.16 Nonlinear Tidal currents (semi-major axis, cm/s) MS$_f$ and M$_4$ 1997, Stratification B: Model B (solid line); **Model BR** (dashed line) and **Model BRA** (dash dot line)

with the observed 0.2 cm/s M_4 current. At M3-97, the M_4 tidal current at the surface also increases with mixing of temperature and salinity. At 7.5 metres depth, the models only produce M_4 currents between 0.1-0.3 cm/s; much weaker than the observed M_4 current of 0.8 cm/s. However, Figures 5.15 and 5.16 indicate a maximum M_4 current of approximately 0.6 cm/s near 5 metres depth in model ARA and between 10 and 15 metres depth in model BRA. Across the inlet, the M_4 current strengthens from south to north in the observed velocity data at moorings M1-97, M2-97 and M3-97. At M1-97, the M_4 current is 0.1 cm/s; at M3-97, the current was 0.8 cm/s. The nonlinear interactions are stronger towards the northern coastline due to the inflow of the tide directed towards this location. Models ARA and BRA indicate that the M_4 current has a local maximum near surface across the inlet from moorings M1-97 to M3-97. In model ARA, the depth at which this maximum occurs becomes shallower moving from south to north. In model BRA, the depth of the maximum becomes deeper from south to north.

At the sill, the observed M_4 current was between 0.9-1.0 cm/s near the surface at both M3-96 and M4-97. The current decreases to 0.4-0.6 cm/s at the 14-15 metres depth. At M3-96, Figure 5.13 indicates that when the main pycnocline is located above the depth of the sill, model AR has a M_4 current of approximately 0.8 cm/s near 5 metres depth that decreases rapidly with depth. Model ARA, has a M_4 current with a completely different vertical profile. In model ARA, there is a distinct local minimum between 5-10 metres depth, the M_4 current increases below 10 metres to produce a local maximum between 15-20 metres depth. At M4-97, model ARA produces two local maxima, one near 7.5 metres depth and the second very close to the bottom. Both models BR and BRA produce local maxima between 15-20 metres depth at M3-96. Model BRA produces a very strong 1.5 cm/s M_4 current near 15 metres depth. This maximum does not appear at M4-97. The strong nonlinear response near the bottom of the sill does not fit the observed M_4 tide.

The bottom maximum is not found in the M_4 current profile of model AR; the vertical profile of M_4 in model ARA may be a transitional state from the vertical profile in model AR to the vertical profiles of model BR. It is possible that the enhanced mixing of model ARA is breaking down the main pycnocline as the water mixes in the region of the sill. The density of the water in this region then becomes more uniform similar to the density profiles of models BR and BRA.

Seaward of the sill moorings at M5-97, M6-97, and M7-97 the M_4 tidal current increases significantly when temperature and salinity mix. At M5-97, compared to models A and B, the M_4 tide at the 7.5 metre level increases from 0.1 cm/s to 0.3-0.6 cm/s in models AR and BR (Figures 5.15-51.6). With enhanced mixing, model ARA differs only slightly from model AR (Figure 5.15) while in model BRA the M_4 current is, approximately, 0.4 cm/s stronger in the top 12 metres than the M_4 current in model BR. Below 12 metres, the M_4 current in model BRA remains 0.2-0.3 cm/s stronger than the current in model BR. Both models BR and BRA produce a local maximum M_4 current near 12 metres depth. This local maximum does not appear when the main pycnocline is located above sill. Of the four mixing models, the M_2 tide in models BR and BRA provide the best fit to the available data (Figure 5.4). Models AR and ARA have a surface M_2 current that is significantly stronger than the observed M_2 tide (Figure 5.3). The large increase in the M_4 current in model BRA must be a consequence of the enhanced mixing as the M_2 currents produced by models BR and BRA are very similar.

At M6-97, the mixing models provide very different vertical profiles for the M_4 current above the level of the sill. The absence of current measurements at this depth, make assessment of the surface M_4 currents impossible. In model ARA, the enhanced mixing produces a maximum M_4 current of 0.8 cm/s between 15 and 20 metres depth. In model AR there is a local minimum in the M_4 current between these levels and a local maximum of 0.6 cm/s near 7.5 metres. In model BR, the maximum surface M_4 current is approximately 0.4 cm/s near 10 metres depth. Unlike model ARA, model BRA raises the depth of the local maximum in the M_4 current towards the surface. Below the depth of the sill all models provide a reasonable fit to the data, however, model ARA produces a M_4 current that is nearly constant from 20 metres depth to the bottom while the other models all produce a current that decreases with depth.

At M7-97, the dependence of the M_4 current on the depth of the pycnocline is very evident. When the main pycnocline is located above the sill, models AR and ARA produce an M_4 current with a single local maximum in the surface region. Both the depth and strength of the maximum M_4 current increase as the background scalar fields evolve in model ARA. In model AR, the maximum M_4 current is approximately 0.5 cm/s located near 7.5 metres depth; in model ARA, the maximum current increases to 0.7 cm/s and deepens to 12 metres depth. Models BR and BRA both produce two local maxima in the vertical profile of the M_4 current. The first maximum occurs just below 10 metres depth while the second local maximum occurs near 25 metres depth. The enhanced mixing of model BRA appears to have little influence on the strength of the M_4 current below the sill. Above 20 metres, model BRA produces a stronger current than model BR, the maximum M_4 current, near 10 metres depth, is approximately 0.7 cm/s compared to the 0.4 cm/s maximum current found in model BR. Below the sill, all models appear to fit the observed M_4 current reasonably well. Above the sill, the models all have M_4 currents of 0.3-0.4 cm/s; stronger than the observed value of 0.2 cm/s.

Previously it was shown that models BR and BRA are able to reproduce the observed M_2 tide at M4-96 (Figure 5.2). With the main pycnocline located at the 10 metre level, models AR and ARA provided an alternative vertical profile of the M_2 tide that did not agree with the observed M_2 tide at M4-96 as well as models BR and BRA but does not seem unreasonable. The M_4 currents at M4-96 show two very distinct vertical profiles that must be a response to the depth of the main pycnocline, the only difference between models AR (ARA) and BR (BRA). When the main pycnocline is located near 10 metres depth the nonlinear interactions within the model produce a very distinct local maximum in the M_4 current just below 30 metres depth. This maximum appears in both AR and ARA. With the enhanced mixing, the strength of the current maximum decreases from 0.6 cm/s in model AR to 0.3 cm/s in model ARA. The M_4 current in model ARA is more uniformly distributed throughout the water column, similar to the vertical structure seen in Figure 5.14 for models BR and BRA. Models BR and BRA produce an M_4 tidal current between 0.2-0.3 cm/s through the entire water column. Model AR produces one local minimum between 20-25 metres depth and one local maximum between 40-45 metres depth. In model BRA, the local maximum rises towards 30-35 metre depth and a second local minimum occurs near 40 metres depth.

MS_4 and S_4 currents are very weak at moorings M1-96. At M2-96, M_4 currents have similar vertical profiles that are independent of the main pycnocline depth. The MS_4 and S_4 currents are strongest when the main pycnocline is located above the sill at the 10 metres depth in models AR and ARA (Figure 5.17). When the main pycnocline is located at sill depth in model BR the MS_4 and S_4 currents are suppressed and the model is unable to match the observed currents (Figure 5.18). Models AR and ARA agree with the observed MS_4 constituent above the 20 metre level. Model ARA produces a maximum S_4 tidal current near 15 metres but is unable to produce the much stronger S_4 current found near 10 metres depth (Figure 5.17).

Across the inner basin, there is a clear dependence on the strength of the nonlinear MS_4 and S_4 currents and the depth of the main pycnocline. These currents are much stronger when the main pycnocline is located above the depth of the sill. Models BR and BRA have currents that are, typically, one half the strength of the currents in models AR and ARA. Near the surface, distinct local maxima in the MS_4 current in model ARA at M1-97 and M2-97 match the observed currents of 0.3 (M1-97) and 0.5 cm/s (M2-97). The model is unable to match the 0.6 cm/s current observed at M3-97 and there is no well defined local maximum in the MS_4 current produced by the model at this location. Below the sill, models AR and ARA produce a MS_4 current at M1-97 between 0.1-0.2 cm/s. At M2-97, model ARA has a second local maximum near 21 metres depth of 0.4 cm/s, double the observed 0.2 cm/s current. In model AR this second local maximum is weaker (0.3 cm/s) and located near 15 metres depth. The current decreases with depth matching the observed current at 21 metres depth.

The observed S_4 currents at M1-97 and M2-97 are very weak, 0.1-0.2 cm/s. At M3-97, the observed surface S_4 current is 0.4 cm/s. The models are not able to replicate the stronger S_4 current at M3-97. Similar to MS_4, the strongest S_4 currents are generated when the main pycnocline is located above the sill. The S_4 currents in model BR are not much stronger than those found in the statically stratified model B. Model ARA produces local maximum in S_4 near the surface not found in any of the other models. Both models AR and ARA produce stronger S_4 currents than the statically stratified model A. In model A, the S_4 currents were less than 0.05 cm/s throughout most of the water column at all three of the inner basin moorings in 1997.

At the sill, nonlinear constituents MS_4 and S_4 are strongest when the main pycnocline lies above the sill. Model BR indicates (Figures 5.18 And 5.20) that the MS_4 current increases from 0.1-0.2 cm/s at M4-97 to 0.4-0.5 cm/s at M3-96. However, the vertical profile of MS_4 at M3-96 indicates that, within the model, the strongest current is located near the bottom of the water column contrary to the observed current which is almost 1 cm/s at the 10 metres depth. At M4-97, the MS_4 current at 7.5 metres depth was 0.7 cm/s.

Model ARA produces the strongest MS_4 currents at both M3-96 and M4-97. At M3-96, the MS_4 current reaches a maximum of approximately 0.7 cm/s just below 10 metres depth and matches the 0.5 cm/s observed at 15 metres depth. However, the M_2 current at M3-96 was only 50-60% of the observed current. At M4-97, where the MS_4 current matches the observed values quite well at both 7.5 and 14 metres depth while the M_2 current decreases towards the surface to only 30% of the observed M_2 tide at 7.5 metres depth (Figure 5.3). The nonlinear interactions, within the model, between M_2 and

S_2 are too strong extracting too much energy from the tide at the sill. The transfer of energy from the main semidiurnal tidal frequencies to higher frequencies will likely produce over-mixing and may be partially responsible for the lack of tidal energy within the inner basin of the model. Constituent S_4 is stronger then expected given the strength of S_2 at the sill. From Tables 5.6 and 5.8 the modelled S_2 tide was only 30-50% of the observed S_2 tide. Despite this, the S_4 tidal currents in model ARA are close to the observed values at the two moorings located at the sill.

Seaward of the sill at M5-97, model ARA provides a very good fit to the observed MS_4 and S_4 constituents (Figure 5.19). Both M_2 and S_2 currents, in models AR and ARA, were stronger than the observed currents at 7.5 metres depth. However, it is only the enhanced mixing in model ARA that is able to produce nonlinear interactions to match those that must exist in the observations. Model BR has M_2 and S_2 currents that provide an, almost, exact match to the observed tides and yet without the enhanced mixing the nonlinear tidal currents are, at best, 50% of the observed currents at 7.5 metres depth. The effect of the enhanced mixing in reproducing the observed nonlinear tidal currents MS_4 and S_4 in model BRA cannot be determined. The shorter currents records produced by model BRA (due to a numerical instability) did not permit separation of the M_2 and S_2 constituents. At M6-97 and M7-97 the M_2 and S_2 currents of all models fit the observations reasonably well. The enhanced mixing of model ARA produces a MS_4 current that is much stronger than the observed MS_4 currents, while S_4 currents at these locations appear to fit the observations.

The influence mixing, within the model, on the nonlinear tidal constituents not only varies with depth of the pycnocline but also appears to vary across the inlet. At M5-

97, the enhanced mixing of model ARA was required for the model to reproduce the observed MS_4 currents while at M6-97 and M7-97, the enhanced mixing of model ARA appears to extract too much energy through the nonlinear interactions of the M_2 and S_2 tides.

At M4-96, model BR that provided a very good match to the observed M_2 tide (Figure 5.2). The S_2 constituent at this location also appears to fit the data reasonably well (Table 5.6), although the surface S_2 current is only 67% of the observed S_2 current. Even though model BR provides a very good fit to the M_2 current throughout the water column, the MS_4 current produced by the model is only 0.2-0.3 cm/s; much weaker than the observed 0.7 cm/s current at 10 metres depth. The models are not able to reproduce the observed 0.7 cm/s MS_4 current. Model ARA produces a maximum MS_4 current near the surface of approximately 0.3 cm/s. A second maximum of 0.3 cm/s near 40 metres depth in model ARA is much stronger than the observed MS_4 current (<0.05 cms) at 45 metres depth. Model AR produces a MS_4 current with a single maximum near 30 metres depth. The MS_4 current in model ARA vanishes as it approaches the surface and decreases to 0.1 cm/s below 45 metres depth. The S_4 tidal currents are much weaker than the observed currents above 20 metres depth with a maximum of 0.1 cm/s compared to the 0.4 cm/s current observed at 10 metres depth.

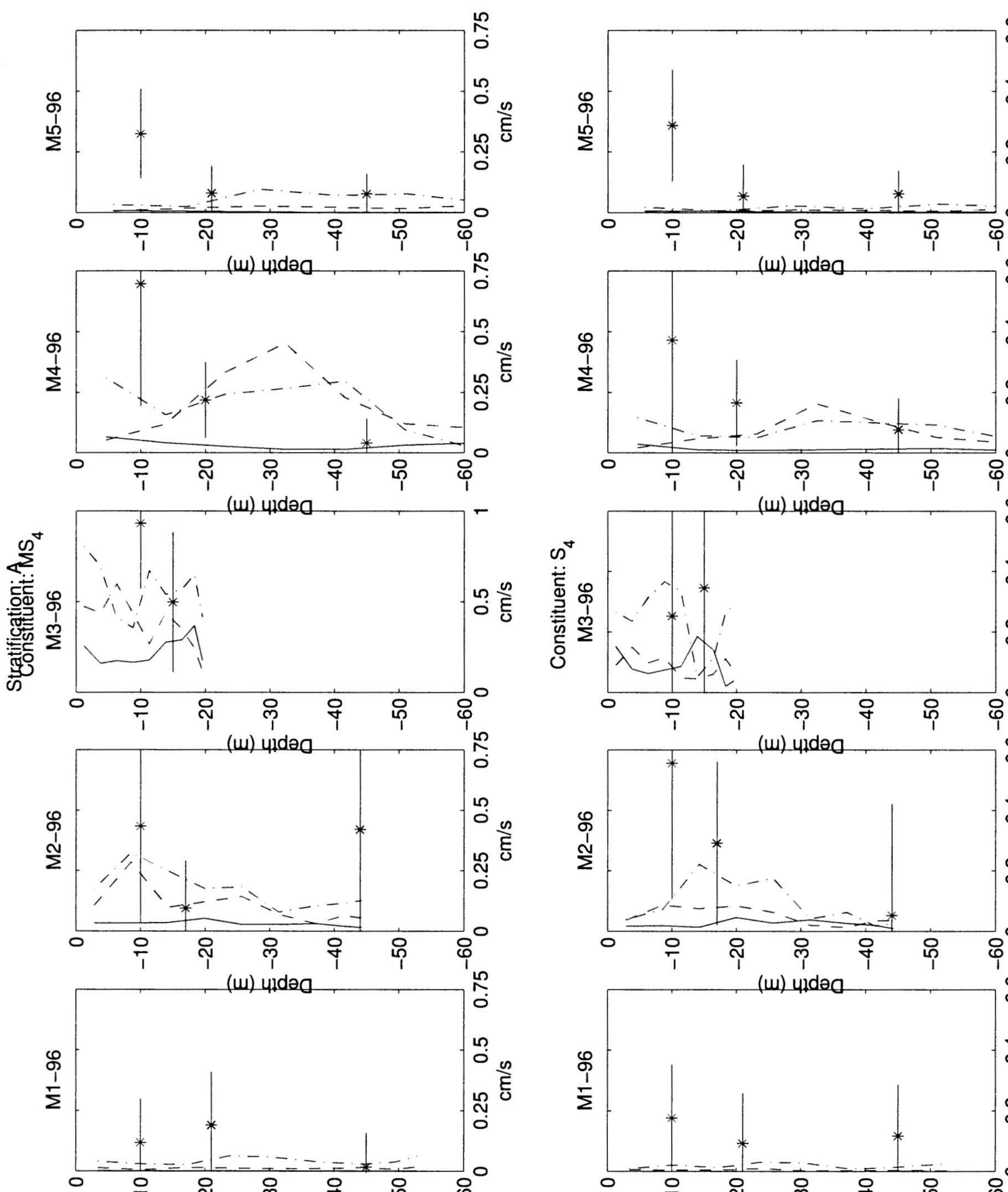

Figure 5.17 Nonlinear Tidal currents (semi-major axis, cm/s) MS_4 and S_4 1996, Stratification A: Model A (solid line); Model **AR** (dashed line) and Model **ARA** (dash dot line)

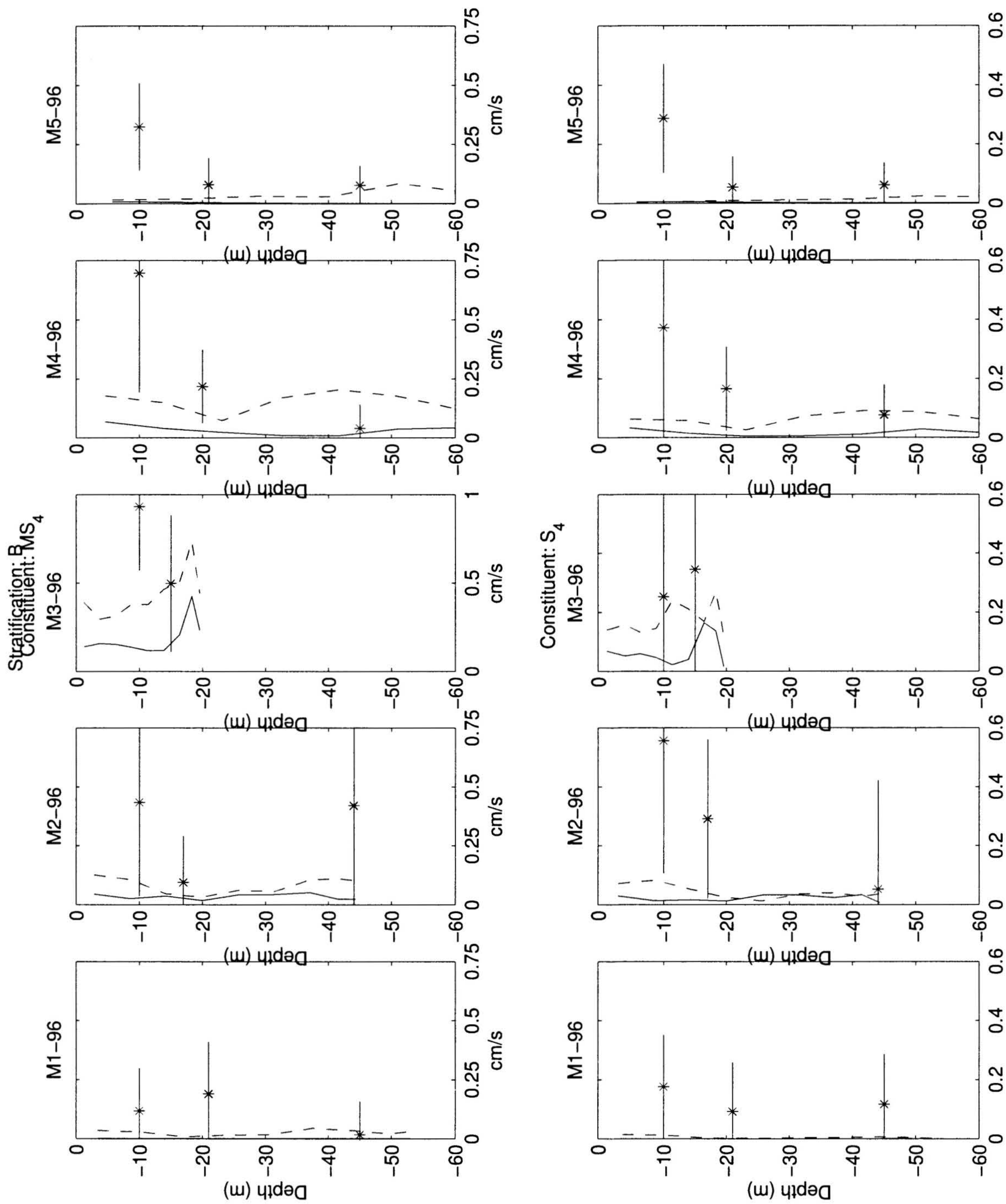

Figure 5.18 Nonlinear Tidal currents (semi-major axis, cm/s) MS_4 and S_4 1996, Stratification B: Model B (solid line); **Model BR** (dashed line) and **Model BRA** (dash dot line)

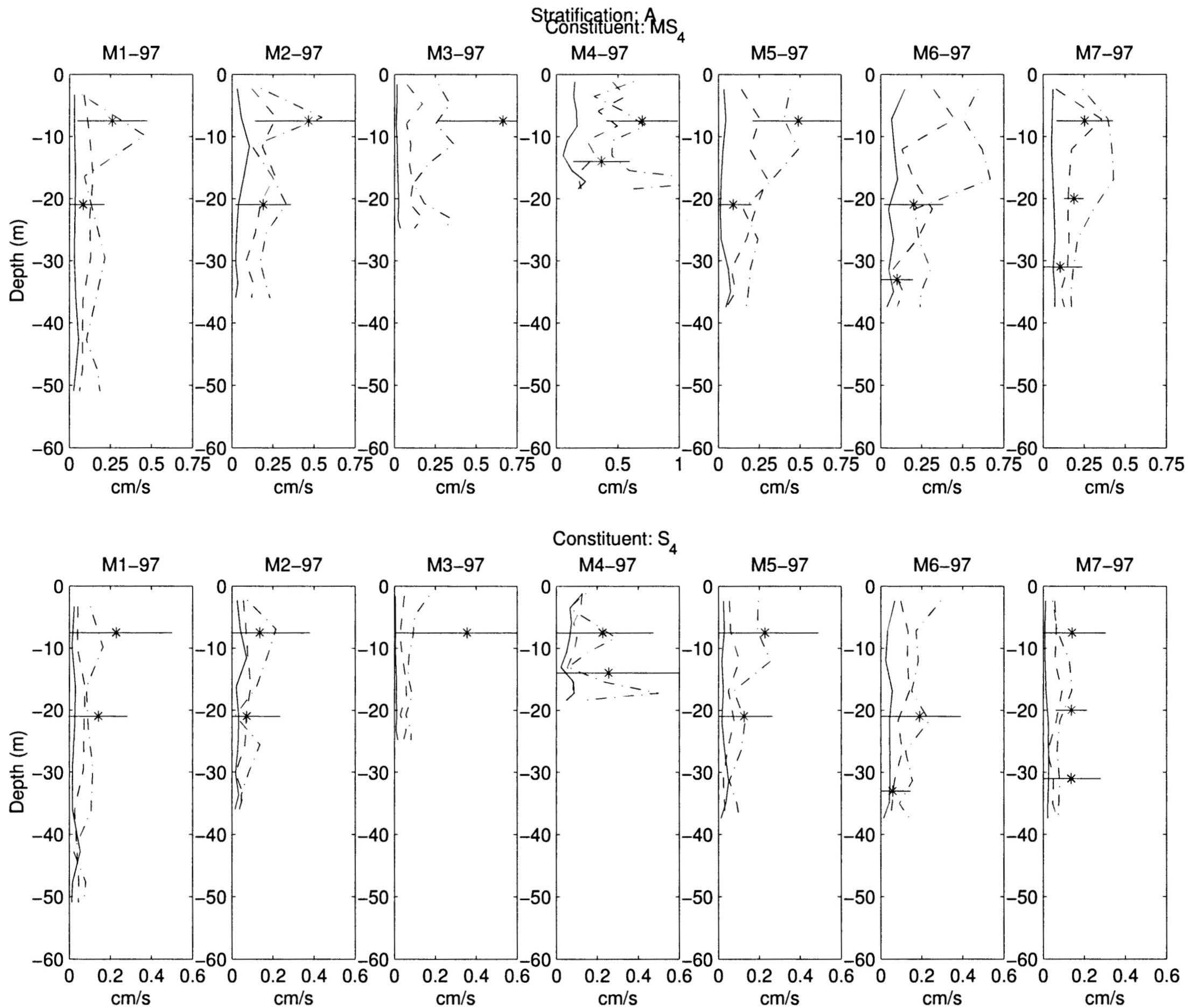

Figure 5.19 Nonlinear Tidal currents (semi-major axis, cm/s) MS_4 and S_4 1997, Stratification A: Model A (solid line); Model AR (dashed line) and **Model ARA** (dash dot line)

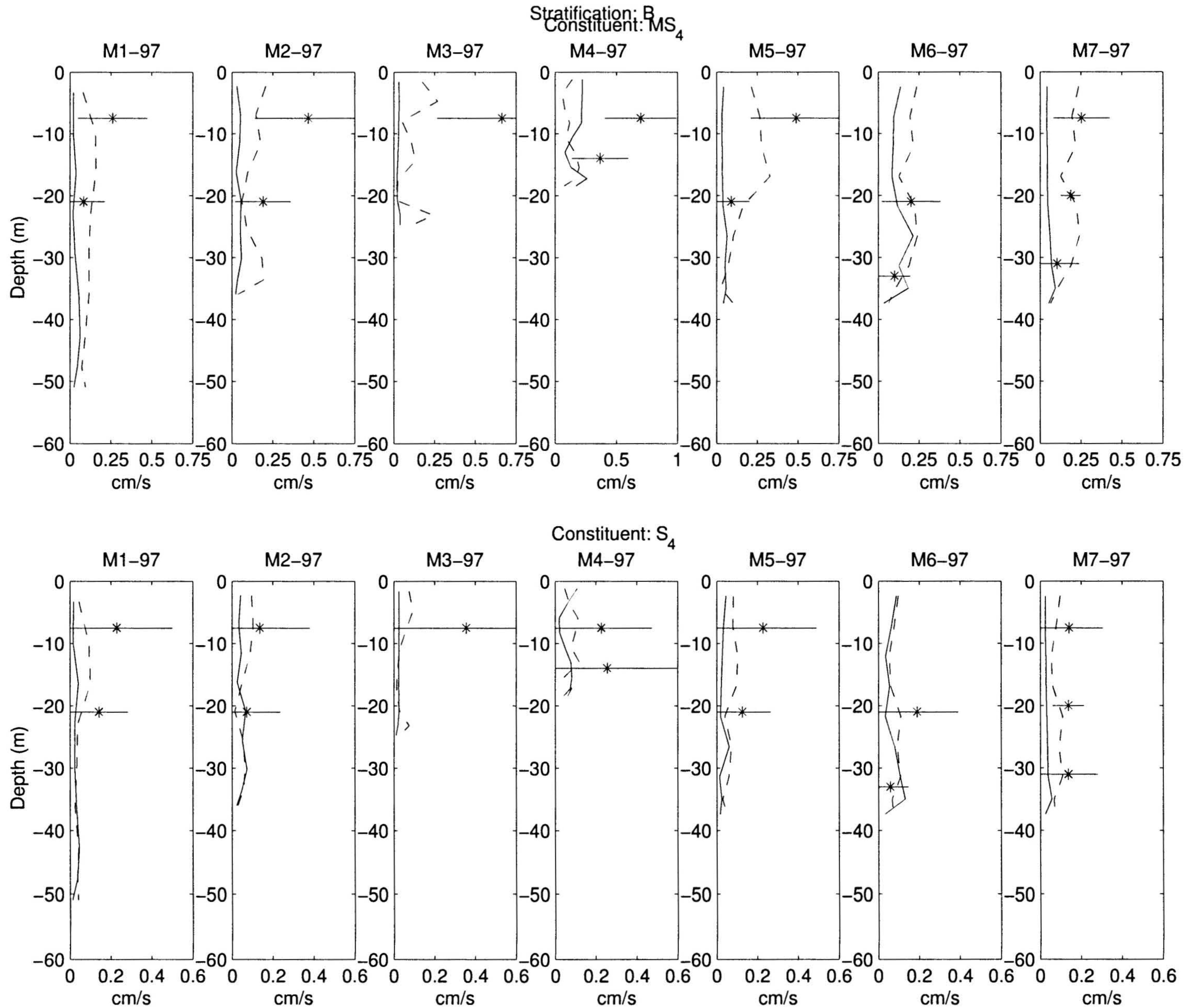

Figure 5.20 Nonlinear Tidal currents (semi-major axis, cm/s) MS_4 and S_4 1997, Stratification B: Model B (solid line); **Model BR** (dashed line) and **Model BRA** (dash dot line)

5.1.4 Frictional Tidal Constituents

We now turn our attention to the influence of mixing on those tidal constituents that are generated through frictional processes: M_6, $2MS_6$ and $2SM_6$ (Figures 5.21-5.24). The statically stratified models produce very weak frictional constituents throughout the model domain. With the introduction of mixing, the lack of tidal energy at M1-96 limits the effect of friction on the tidal signal and all three of the frictional constituents under consideration remain very weak having a typical velocity less than 0.05 cm/s. At M2-96 the three of the frictional constituents are strongest at the bottom of the inner basin where bottom friction has the greatest influence. At 45 metres depth, the observed M_6 current is 0.5 cm/s, while $2MS_6$ and $2SM_6$ were observed to be slightly less than 0.3 cm/s. The mixing models are not able to produce bottom currents greater than 50% of the observed currents at 45 metres depth. Across the inner basin at moorings M1-97, M2-97 and M3-97, the models underestimate the strength of the frictional tidal constituents. What is clear, however, from Figures 5.21-5.24 is that without the mixing of temperature and salinity, the higher frequency tidal constituents have very little variation in the vertical profile. While the mixing models do provide a mechanism by which the higher order tidal constituents are allowed to grow, the constituents M_6, $2MS_6$ and $2SM_6$ are not well represented within the inner basin.

At the sill, both M_2 and S_2 currents in the models are much weaker than those the observations. By normalizing the M_6 tidal currents by the M_2 tidal currents we are able to access if the M_6 tidal current produced by frictional forces at the sill of the model are reflective of the frictional forces within the observations. The normalized M_6 currents from the observations and from the models are listed in Tables 5.1 And 5.2. From the observations in 1996 and 1997 we find that at the sill the ratio of the M_6 currents to the M_2 currents is approximately 1/10. At M3-96, models A and B have normalized M_6 currents that are an order of magnitude weaker than the observed values. With the addition of mixing (models AR and BR) the normalized M_6 current increases to as high as 1/20. It is only with the enhanced mixing of models ARA and BRA that the normalized M_6 currents at 15 metres depth are representative of the observed normalized M_6 current. At M4-97, the normalized M_6 currents are stronger than at M3-96, models A and B having normalized currents of approximately 1/20 and 1.6/20 respectively. Little difference is found in M_6 currents when mixing of temperature and salinity is included (models AR and BR). With enhanced mixing, model BRA produces a normalized M_6 current that almost matches the normalized M_6 current observed. It is only with the enhanced mixing that we are able to achieve a M_6 current in the bottom layers of the model that are representative (proportionally) of the observed M_6 tide generated by frictional forces. If the high frictional forces within the model were responsible for the loss of tidal energy before the tide enters the inner basin, we would expect to see a normalized M_6 current that is significantly larger than the observed M_6 current. From this simple analysis we may conclude that frictional forces are not responsible for the excessive loss of tidal energy over the sill of the model.

Table 5.1 Normalized M_6 current at the sill in 1996

	Ratio of M6/M2 at M3-96						
Depth	**OBS.**	**A**	**AR**	**ARA**	**B**	**BR**	**BRA**
10	0.09	0.01	0.03	0.04	0.01	0.02	0.04
15	0.12	0.01	0.05	0.09	0.01	0.04	0.11

Table 5.2 Normalized M_6 current at the sill in 1997

	Ratio of M6/M2 at M4-97						
Depth	**OBS.**	**A**	**AR**	**ARA**	**B**	**BR**	**BRA**
7.5	0.08	0.04	0.05	0.08	0.08	0.06	0.09
14	0.11	0.06	0.04	0.07	0.08	0.05	0.12

Seaward of the sill, the vertical profile of constituents M_6, $2MS_6$ and $2SM_6$ are clearly dependent on the depth of the main pycnocline (Figures 5.21-5.24). At M5-97, model BRA produces a local minimum near 7.5 metres depth that is not found in model ARA. A local minimum is also found near this level in the vertical profiles of $2MS_6$ and $2SM_6$ in model BRA. In model ARA the top 20 metres of the $2MS_6$ current is nearly constant, while the $2SM_6$ current has a local maximum near 7.5 metres depth. Model ARA appears to provide the best fit to the observed M_6 and $2MS_6$ currents but is too strong at the surface to represent the observed $2SM_6$ current.

At M6-97, model BRA produces a strong (0.5 cm/s) M_6 current at the surface, both models ARA and BRA appear to fit the observations below 20 metres depth, the absence of observations in the surface make it impossible to determine which of the two stratifications is more representative of the true M_6 current. Models AR and ARA produce a surface $2MS_6$ current between 0.2-0.3 cm/s, not found in model BR which has a maximum current of approximately 0.1 cm/s through the water column. The observed $2SM_6$ currents are very weak at M6-97 below 20 metres depth. In model ARA the $2SM_6$ current has a local maximum (0.2 cm/s) near 15 metres depth that does not occur in either model AR or ARA. Both models AR and ARA have a $2SM_6$ current that is stronger than observed at 21 metres depth.

At M7-97, it is only model BRA that matches the observed M_6 current profile. The other models all produce a M_6 tide that is much weaker. The M_2 tide at M7-97 in model BRA was stronger than observed in the surface region while the M_2 tide in models AR and ARA matched the observed M_2 quite well. The relative weakness of the M_6 currents at this location may indicate that frictional forces within the model are weaker than they should be. Model ARA is the only model to produce a local maximum at 10-20 metres depth for $2MS_6$. This local maximum is indicated in the observations at 21 metres depth, deeper than the maximum $2MS_6$ current in the model. The observed $2SM_6$ current is very weak at M7-97 and nearly constant (0.1 cm/s) through the water column. Model ARA indicates a maximum current of 0.2 cm/s near 7.5 metres depth not found in the other models.

At M4-96, models BR and BRA provided a very good fit to the observed M_2 currents (Figure 5.2). Even though the vertical profiles for M_2 produced by the models are very similar, the M_6 tidal currents of the two models are very different. Neither model produces M_6 currents that match the observations. The M_6 tide in model BR is much weaker (0.1 cm/s) compared to the observed M_6 current (0.2-0.3 cm/s). In model BRA, the enhanced mixing produces a M_6 current with a local maximum of 0.5 cm/s near 40 metres depth. Although the M_6 current in model BRA comes close to matching the observed M_6 current at 45 metres depth, it is not clear if this local maximum actually exists as it falls between the observations at 20 and 45 metres depth. The modelled M_6 current at 10 and 20 metres depth is less 50% of the observed tide. Constituents $2MS_6$ and $2SM_6$ are nearly constant at (0.1 cm/s) in the observations at this location. Nearly constant tidal currents are indicated in models AR and BR. Both models provide a reasonable representation of the observed $2MS_6$ tide and a weaker than observed $2SM_6$ tide. Model ARA produces stronger tidal currents for these constituents with both having local maxima of 0.2 cm/s between 20 and 45 metres depth. As with the local maximum of M_6 in model BRA, the observations do not reveal if these local maxima actually exist.

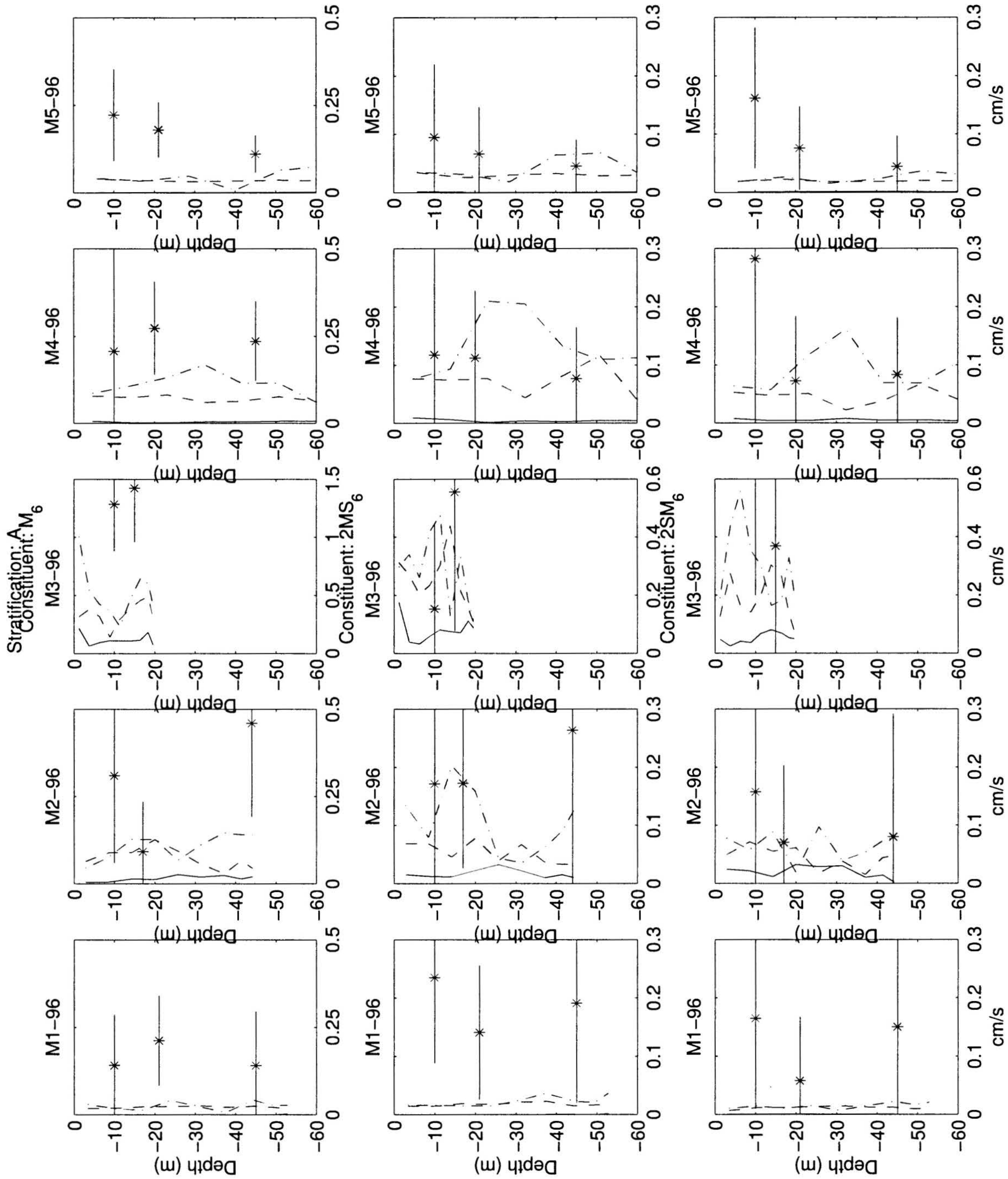

Figure 5.21 Frictional Tidal currents (semi-major axis, cm/s), M_6, $2MS_6$ and $2SM_6$ 1996, Stratification A: Model A (solid line); **Model AR** (dashed line) and **Model ARA** (dash dot line)

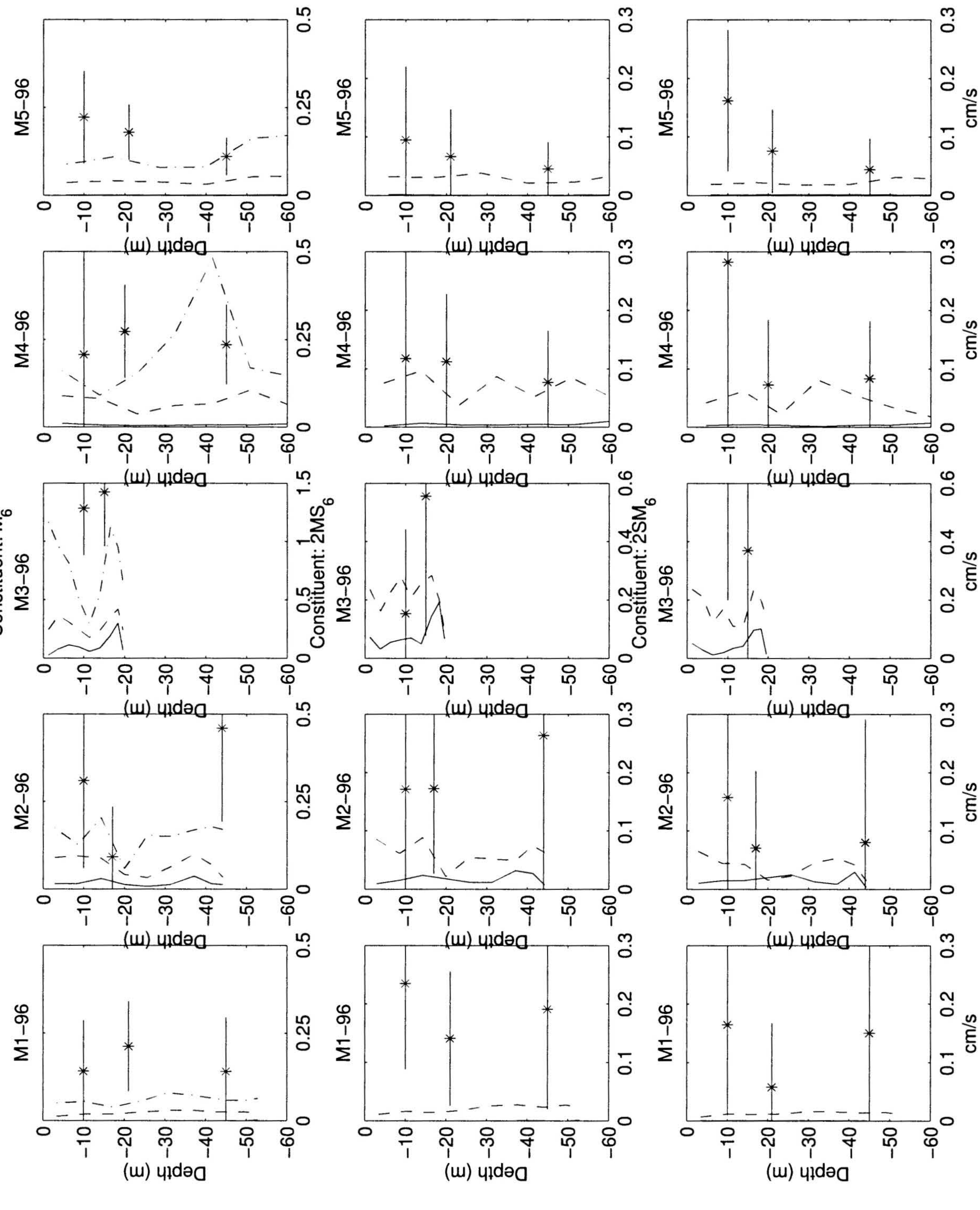

Figure 5.22 Frictional Tidal currents (semi-major axis, cm/s), M_6, $2MS_6$ and $2SM_6$ 1996, Stratification B: Model B (solid line); **Model BR** (dashed line) and **Model BRA** (dash dot line)

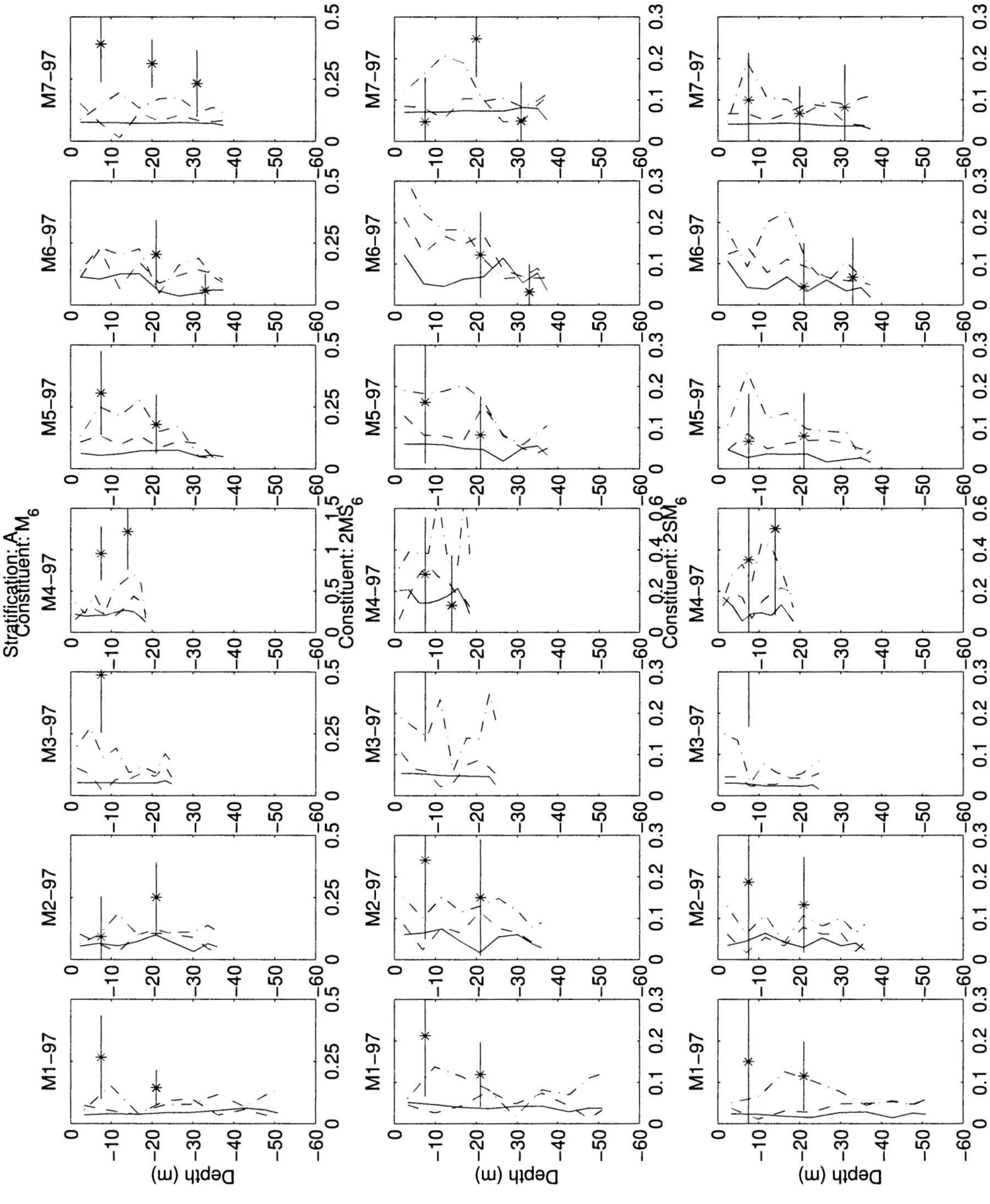

Figure 5.23 Frictional Tidal currents (semi-major axis, cm/s), M_6, $2MS_6$ and $2SM_6$ 1997, Stratification A: Model A (solid line); **Model AR** (dashed line) and **Model ARA** (dash dot line)

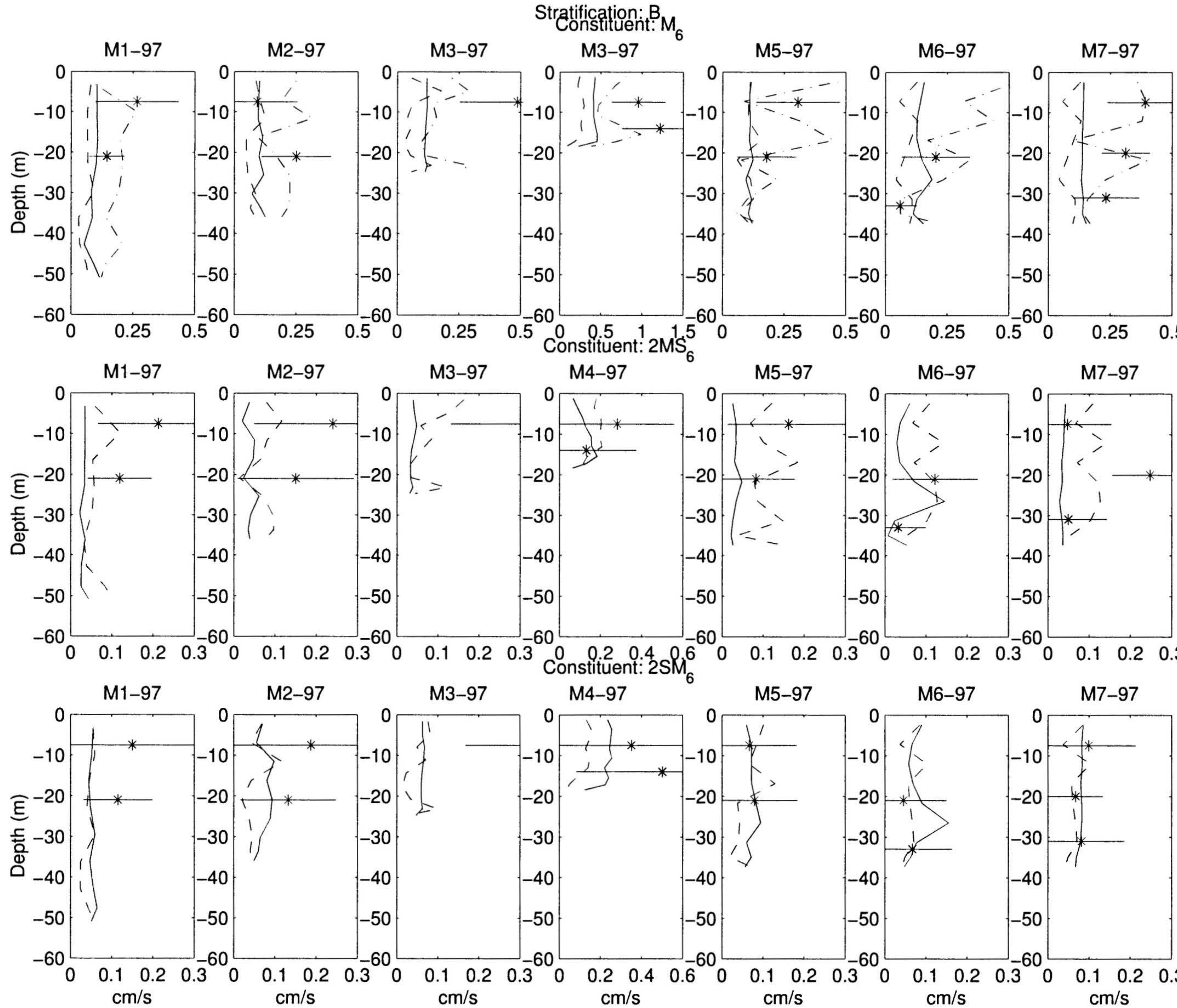

Figure 5.24 Frictional Tidal currents (semi-major axis, cm/s), M_6, $2MS_6$ and $2SM_6$ 1997, Stratification B: Model B (solid line); **Model BR** (dashed line) and **Model BRA** (dash dot line)

5.2 Model Response to Wind Stress

Following the procedure of Chapter 4, wind stress was added to the model in an attempt to validate the model by comparison to the data collected during 1996 and 1997. With the addition of wind stress, the mixing models were became numerically unstable and unable to complete a 30-day simulation over the same period of time used for the statically stratified models. The length of the simulations, before the onset of numerical instability (Table 5.3), varied between 7.5-17 days. The stability of the model was dependent upon the initial stratification and the whether or not the background temperature and salinity fields were held constant or permitted to evolve. Model BRA in the 1997 simulations provided no useful record for analysis (only 31 hours) so it is not included in this following discussion.

Table 5.3: Length of Model Simulations with Tides and Wind. Simulations of 30 days are the maximum record possible. Models with simulations of less than 30 days became numerically unstable, the end time of the simulation is taken two hours from the actual end of the model simulation to reduce the effect of the instability on the analysis of the model output. The specified record length does not include the ramping period (2 days) used to bring the model forcing to 100%.

	1996				1997			
Model	Start Time (Jul. Days)	End time (Jul. Days)	Length of Record (days)	(hours)	Start Time (Jul. Days)	End time (Jul. Days)	Length of Record (days)	(hours)
A	205	235	30	720	195	225	30	720
AR	205	222	17	408	192	202.3	10.3	247
ARA	205	222.13	17.13	411	192	201.54	9.54	229
B	205	225	30	720	195	225	30	720
BR	205	214.66	9.66	232	192	200.5	7.5	204
BRA	205	214.74	9.74	234	192	193.28	1.28	31

The short velocity records available, from the model, make assessment of the distribution of energy difficult. The low frequency band (0-0.1 cpd) cannot be included in this analysis and the period of the meteorological band (0.5-0.1 cpd) is not completely covered by those records with a total length less than 10 days. The velocity records from each mooring location of the model were interpolated to the observation depth and the interpolated velocity was rotated to the principle axis (Tables 5.4-5.5). In the discussion which follows, the description of the orientation assumes that the 0 ° represents the direction east and that positive angles are measured in a counter clockwise direction.

The power spectrum of the primary principle axis was calculated using Welch's method with 5-day windows overlapping by 2.5 days. This provides approximately 6-12 degrees of freedom depending upon the record length. The percentage of energy in the meteorological band (0.1-0.5 cpd), diurnal band (0.8-1.13 cpd) and semi-diurnal band (1.75-2.11 cpd) for each mooring from each of the different models is provided in Tables 5.22-5.33. A subset of the observed velocity field as well as a subset of the model output for models A and B, corresponding to the records of models AR and BR, has been included in the tables.

The orientation of the principle axis for the wind and tidally forced model flows in 1996 (Table 5.4) indicates that the mixing does effect the direction of the flow within the inner basin. The greatest variation within the velocity field is found at the 17 metre level at M2-96. With the addition of mixing, model AR indicates a principle axis oriented at –28°. The coastline of the inner basin area is aligned from southeast to northeast an orientation of -28° aligns the primary direction across the inlet. This cross channel flow also appears at mooring M2-97 at 21 metres depth (Table 5.5). Model ARA indicates a primary axis of 86° which suggests a stronger cross channel velocity field than in either the observed currents or in models A or B which indicate a primary axis oriented 17°-20°. The deeper currents in these two models (AR and ARA) appear to be completely separated from the near surface flow by the main pycnocline, located near 10 metres depth. The surface wind stress is unable to penetrate the main pycnocline within the inner basin of the model. The principle axis in model BR, also depart from the observed velocity field and the statically stratified models. However, the principle axis at 17 metres depth in model BR is nearly aligned with the principle axis at 10 metres depth indicating that the wind stress is able to penetrate the surface layer.

Seaward of the sill, the near surface flow at M4-96 varies significantly over the period of observations. When evaluated over the 17-day period between Julian days 205-222 (model AR) the principle axis from the observed currents are oriented at 69°.

Table 5.4: Orientation of the Principle Axis (degrees). The orientation of the principle axis measured with 0 degrees corresponding to the eastern axis.

Orientation of the Principle Axis 1996 (degrees)

Depth	Data	A	AR	ARA	Depth	Data	B	BR	BRA
				Mooring: M1-96					
Depth	**Data**	**A**	**AR**	**ARA**	**Depth**	**Data**	**B**	**BR**	**BRA**
10	47	43	44	48	**10**	50	51	44	47
21	49	46	27	39	**21**	47	46	54	46
45	46	38	48	44	**45**	46	41	15	16
				Mooring: M2-96					
Depth	**Data**	**A**	**AR**	**ARA**	**Depth**	**Data**	**B**	**BR**	**BRA**
10	17	18	19	29	**10**	21	17	38	46
17	20	17	-28	86	**17**	17	17	35	30
44	-5	8	-5	0	**44**	-8	3	11	1
				Mooring: M3-96					
Depth	**Data**	**A**	**AR**	**ARA**	**Depth**	**Data**	**B**	**BR**	**BRA**
10	-10	-9	-12	-8	**10**	-12	-10	-16	-14
15	-16	-9	-7	-3	**15**	-17	-8	-2	3
				Mooring: M4-96					
Depth	**Data**	**A**	**AR**	**ARA**	**Depth**	**Data**	**B**	**BR**	**BRA**
10	69	6	12	9	**10**	37	5	12	12
20	13	4	10	-8	**20**	1	4	6	10
45	24	1	0	8	**45**	23	1	3	9
				Mooring: M5-96					
Depth	**Data**	**A**	**AR**	**ARA**	**Depth**	**Data**	**B**	**BR**	**BRA**
10	59	49	43	43	**10**	59	54	43	44
21	51	48	44	42	**21**	53	50	43	44
45	52	48	44	43	**45**	56	48	43	44

When the observation period is shortened to days 205-214 (model BR), the principle axis is oriented at only 37°. All of the models produce a current that is oriented between 5°-12° aligning the currents with the coastline near M4-96. This indicates that the wind stress associated with this portion of the numerical grid is much weaker than the true wind stress during the 1996 period and allows the tidal forces to dominate. At M5-97, the

Table 5.5: Orientation of the Principle Axis 1997 (degrees). The orientation of the principle axis measured with 0 degrees corresponding to the eastern axis.

Orientation of the Principle Axis 1997 (degrees)

Mooring: M1-97

Depth	Data	A	AR	ARA	Depth	Data	B	BR
7.5	29	37	35	22	**7.5**	43	55	16
21	32	48	41	25	**21**	31	28	16

Mooring: M2-97

Depth	Data	A	AR	ARA	Depth	Data	B	BR
7.5	15	15	21	3	**7.5**	25	19	3
21	15	3	-25	14	**21**	14	3	14

Mooring: M3-97

Depth	Data	A	AR	ARA	Depth	Data	B	BR
7.5	-19	-14	-13	-8	**7.5**	-22	-11	-13

Mooring: M4-97

Depth	Data	A	AR	ARA	Depth	Data	B	BR
7.5	-23	-9	-12	-12	**7.5**	-21	-13	-12
14	-9	-12	-12	-14	**14**	-6	-17	-19

Mooring: M5-97

Depth	Data	A	AR	ARA	Depth	Data	B	BR
7.5	-6	-15	-16	-19	**7.5**	-10	-28	-40
21	-20	-1	-2	-14	**21**	-22	-33	-21

Mooring: M6-97

Depth	Data	A	AR	ARA	Depth	Data	B	BR
21	23	3	0	-1	**21**	25	-1	-5
33	-4	-27	-8	-3	**33**	-5	88	45

Mooring: M7-97

Depth	Data	A	AR	ARA	Depth	Data	B	BR
7.5	17	27	26	9	**7.5**	17	30	-29
31	10	-3	-11	7	**31**	11	-10	17

surface flow in the model is oriented clockwise from the observed flow, the difference between the model and the observed flow increases as the main pycnocline in the model deepens and, also, with the introduction of mixing. At M7-97, model BR produces a near surface current oriented at –29°, this orientation aligns the surface flow, of this model, towards the northern coastline, this behaviour is not found in either the observations or the other models. At M6-97, the currents at 33 metres depth in model B were oriented at 88° when mixing is introduced the current is oriented at 45°. Neither of these models agrees with the observed orientation of –5°. When the main pycnocline is located above the sill, models AR and ARA are able to produce a current aligned almost east-west (0°) which is a significant improvement to the –27° alignment found in model A at 33 metres depth.

When wind stress is applied to the mixing models, the alignment of the principle axis varies significantly at some locations within the model domain. The variation in the direction of the current should have a direct effect on the nature of the residual circulation within the inlet. If the orientation of the currents disagrees significantly from the observed data it seems unlikely that the model will be able to reproduce the residual circulation found within the observations in 1996 and 1997. A comparison of the residual circulation in the model to the observations will be discussed in the next section. We now focus on the distribution of kinetic energy within the frequency bands.

In the previous section, it was demonstrated that mixing of temperature and salinity enables the model to produce tidal currents that are in closer agreement with the observed tidal currents than the statically stratified models. Within the inner basin, however, the tidal currents are still weaker than expected, with tidal energy being rapidly lost as the tide propagated towards the head of the inlet. As a result of this loss of tidal energy, it is expected that meteorological frequencies will still dominate the circulation of the inner basin. However, the mixing of temperature and salinity should help to redistribute the force of the wind down through the water column.

During the simulations for 1996, the amount of energy located in the meteorological band near the surface (10 metres depth) at M1-96 (Table 5.6) increases as temperature and salinity mix. With the pycnocline located above the sill the proportion of energy associated with meteorological events increases from 28% in model A to between 43% and 34% in models AR and ARA, respectively. The deeper pycnocline in models B, BR and BRA produced an even greater amount of energy in the meteorological band. In model B, 57% of the total energy at 10 metres depth was found in the meteorological frequency band. In models BR and BRA the amount of energy was between 66-69% of the total energy. All of the models have a disproportionate amount of energy in the meteorological frequency band. The tidal forcing at mooring M1-96 in the model is much weaker than the observed tidal forcing. The weakness of the tidal forcing permits wind stress to dominate the near surface region of the inner basin. At 21 metres depth, the energy in the meteorological band in models AR and ARA is 37%-38%, much greater than the amount of energy found at this depth in model A and 3 times the amount of energy observed in this frequency band. Meteorological forces also dominate at 21 metres depth when the pycnocline is located at sill depth. Models B, BR and BRA all indicate that 52%-57% of the total energy found at this location may be due to meteorological forces. At 45 metres depth, the mixing models show a significant decrease in the amount of energy associated with the meteorological band compared to models A and B. Under conditions of static stratification, models A and B indicate that the amount of energy in the meteorological band was 33% and 42%, respectively, of the total energy. With the introduction of mixing, all of the models indicate that only 7%-11% of the total energy at this depth is associated with the meteorological frequency band. This is a significant improvement compared to models A and B but still greater than the 1-4% observed in this frequency band during 1996. The mixing models provide a better dissipative mechanism for the surface wind stress than those models that were statically stratified. At 45 metres depth, it is the semi-diurnal frequency band that contains the largest proportion of the total energy. Models AR and ARA have between 74-75% of the total energy located in this frequency band, this compares very well with the value of 80% calculated from the spectrum of the observed velocity field. Models BR and BRA indicate that 78% of the total energy is found in the semi-diurnal band at 45 metres depth. Over the same time period, the observations indicate that only 46% of the total energy was located in this frequency band.

At M2-96 (Table 5.7), the distribution of the kinetic energy within the mixing models differs significantly from those models with a static density field. With the main pycnocline located near 10 metres depth, the amount of energy located in the meteorological frequency band near the surface in models AR and ARA is 15%-16%. Models BR and BRA indicate that 21%-23% of the total energy is located near the surface in this frequency band. This presents a three-fold increase in the amount of energy located in the meteorological band in model A (5%) and almost double the amount of energy in model B (12%). Models AR and ARA agree very well with the observed 14% of the total energy observed in the meteorological band at 10 metres depth.

Models BR and BRA are higher than the observed value of 16%. At 17 metres depth, the amount of energy associated with wind stress increases to 30% in model BRA. In both model AR and in the observations the proportion of energy in the meteorological band is 16% and 15% respectively. During the period of observations corresponding to models BR and BRA, the meteorological frequency band has 22% of the total energy of the measured currents. This agrees very well with the 20%-21% from models B and BR. All of the models, including those with a static density field agreed well with the observations at 45 metres depth with only 2-7% of the total energy being associated with meteorological events at this depth.

Table 5.6 Distribution of Fluctuating Kinetic Energy, Mooring: M1-96, mixing models. Values represent the percent of the total energy in each frequency band.

Distribution of Energy
Mooring: M1-96

			Met (0.1-0.5 cpd)						
Depth	**Data**	**A**	**AR**	**ARA**	**Depth**	**Data**	**B**	**BR**	**BRA**
10	7	28	43	34	**10**	6	57	69	66
21	12	28	38	37	**21**	19	57	52	56
45	1	33	11	7	**45**	3	42	11	10
			Diurnal (0.8-1.13 cpd)						
Depth	**Data**	**A**	**AR**	**ARA**	**Depth**	**Data**	**B**	**BR**	**BRA**
10	3	1	1	1	**10**	11	3	2	2
21	7	2	1	2	**21**	15	2	4	5
45	1	2	1	1	**45**	5	2	3	4
			Semidiurnal (1.75-2.11 cpd)						
Depth	**Data**	**A**	**AR**	**ARA**	**Depth**	**Data**	**B**	**BR**	**BRA**
10	47	27	21	4	**10**	27	15	21	23
21	13	51	28	26	**21**	12	26	30	29
45	80	33	74	75	**45**	46	16	78	78

Mixing of temperature and salinity also effect the percentage of the total energy in the semi-diurnal frequency band at M2-96. Near the surface, at 10 metres depth, the energy associated with the semi-diurnal band decreased from 65% in model A to 38%-

40% in models AR and ARA. In models BR and BRA, the percentage of energy found in this frequency band decreases to 16%-19% from 67% in model B. Models AR and ARA agree very well with the 35% estimated from the observations corresponding to the model simulation.

Over the period of time associated with model runs BR and BRA, 24% of the total energy was located in the semi-diurnal frequency band. At 17 metres depth, the amount of energy associated with semi-diurnal frequencies is decreases as the amount of mixing increases. In model A, 71% of the total energy at this level was associated with the semi-diurnal frequency band. The introduction of mixing in model AR decreases the percentage to 55% while the enhanced mixing of model ARA decreases the energy of the semi-diurnal frequency band to 16% of the total energy. This is a very significant decrease in the amount of energy associated with the semi-diurnal frequency band and model ARA is in agreement with the observed 13% estimated from the observed currents at this depth. With the pycnocline located at sill depth, there is also a reduction in the amount of energy in the semi-diurnal band as mixing is introduced into the model. However, with the deeper pycnocline, the greatest decrease in energy is found between models B and BR where the percentage of energy located in the semi-diurnal frequency band decreases from 66% to 35%. Enhanced mixing reduces this percentage to 27% but this is more than twice the amount of 11% estimated from the observations. At 44 metres depth, the semi-diurnal tides dominate with 70%-83% of the total energy located at the semi-diurnal frequencies in the models. The observed values of 27%-31% of the total energy at semi-diurnal frequencies suggests that the tidal signal in the model remains more coherent than the actual tidal signal.

Table 5.7 Distribution of Fluctuating Kinetic Energy, Mooring: M2-96, mixing models. Values represent the percent of the total energy in each frequency band.

Distribution of Energy
Mooring: M2-96

Met (0.1-0.5 cpd)

Depth	Data	A	AR	ARA	Depth	Data	B	BR	BRA
10	14	5	16	15	**10**	16	12	21	23
17	15	8	16	30	**17**	22	12	20	21
44	3	3	2	2	**44**	7	6	4	7

Diurnal (0.8-1.13 cpd)

Depth	Data	A	AR	ARA	Depth	Data	B	BR	BRA
10	4	4	2	2	**10**	5	5	5	4
17	4	2	2	2	**17**	6	5	6	5
44	1	2	1	2	**44**	4	6	4	2

Semidiurnal (1.75-2.11 cpd)

Depth	Data	A	AR	ARA	Depth	Data	B	BR	BRA
10	35	65	38	40	**10**	24	67	19	16
17	13	71	55	16	**17**	11	66	35	27
44	31	82	83	82	**44**	27	80	74	70

At mooring M3-96 (Table 5.8), both the observed currents and the models indicate the dominance of the semi-diurnal forcing. From the measured currents at M3-96, it was determined that between 54%-68% of the total energy was located in the semi-diurnal band. The amount of energy associated with the semi-diurnal frequencies in the models is 81%-91%. The amount of energy associated with the meteorological frequencies observed at the sill are 3%-8% this is higher than the 1% found in the model where the wind stress in the region of the sill was intentionally reduced (Chapter 3) to promote numerical stability. There does not appear to be any significant amount of energy in either the diurnal or meteorological bands that would account for the 20-30% difference in the amount of energy located in the semi-diurnal band of the observations and model. The tidal analysis suggests that the weaker currents of the models are unable to transfer of energy into lower frequencies such as MS_f and higher frequency constituents such as M_4. This may partially explain the concentration of kinetic energy in the semi-diurnal band of the models.

Table 5.8 Distribution of Fluctuating Kinetic Energy, Mooring: M3-96, mixing models. Values represent the percent of the total energy in each frequency band.

Distribution of Energy
Mooring: M3-96

Met (0.1-0.5 cpd)

Depth	Data	A	AR	ARA	Depth	Data	B	BR	BRA
10	3	0	0	1	**10**	4	0	1	1
15	4	1	0	0	**15**	8	1	1	1

Diurnal (0.8-1.13 cpd)

Depth	Data	A	AR	ARA	Depth	Data	B	BR	BRA
10	5	2	2	2	**10**	13	5	6	6
15	2	2	2	2	**15**	4	6	5	5

Semidiurnal (1.75-2.11 cpd)

Depth	Data	A	AR	ARA	Depth	Data	B	BR	BRA
10	66	91	89	87	**10**	54	88	85	83
15	68	88	89	88	**15**	56	86	85	81

Seaward of the sill at M4-96 (Table 5.9), meteorological forcing within the model is too weak at this location. With the exception of model B where 7%-10% of the total energy was located in the meteorological band, all of the models indicate that the amount of energy in the meteorological band is less than 5% much less than the 10-14% observed at these frequencies at both 10 and 20 metres depth. It is not immediately obvious why model B is able to achieve the higher distribution of energy into the meteorological band as all of the models were run with identical forcing and grid configurations. The tidal analysis of the previous section indicated that with mixing included in the model, the main diurnal and semi-diurnal tides matched the observed tide quite well, while the nonlinear and frictional constituents generated by the interaction of M_2 and S_2 were generally weaker than expected. Analysis of the entire observation record for 1996 (Table

2.2) indicates that between 62%-74% of the high frequency (> 0.8 cpd) energy at this location is not located in either the diurnal, inertial or semi-diurnal frequency bands. The model is unable to replicate this transfer of energy from the identified frequency bands to the higher frequency bands and the energy remains trapped at semi-diurnal frequencies. Although the diurnal and semi-diurnal tides generated by the model are in good agreement with the observations, the high percentage of energy found in the semi-diurnal bands of the models suggests that the model is unable reflect the amount of mixing that occurs at this location. The most obvious explanation for this is the strong relaxation of temperature and salinity required to promote numerical stability. The averaging technique used to enhance the mixing within the model is also suspect as it coincides with the semi-diurnal frequency band.

At M5-96 (Table 5.10), the distribution of energy within the meteorological frequency band at 10 metres depth agrees quite well with the observed distribution when the main pycnocline is located near 10 metres depth. However, in models A, AR and ARA, the meteorological energy is trapped near the surface; the amount of energy located in the meteorological band at 20 metres depth is only 10-14%, while the observed distribution remains relatively constant. In models B, BR and BRA, when the main pycnocline is located at sill depth, the results are similar. Below the main pycnocline, the distribution of energy into the meteorological frequency band decrease from 31%-36% at 21 metres depth to 5-14% at 45 metres depth in models B (14%), BR and BRA (5-6%) similar to the observations.

Table 5.9 Distribution of Fluctuating Kinetic Energy, Mooring: M4-96, mixing models. Values represent the percent of the total energy in each frequency band.

Distribution of Energy
Mooring: M4-96

Met (0.1-0.5 cpd)

Depth	Data	A	AR	ARA	Depth	Data	B	BR	BRA
10	10	4	2	3	**10**	12	10	2	2
20	12	4	2	4	**20**	14	7	4	4
45	4	3	1	2	**45**	7	7	3	5

Diurnal (0.8-1.13 cpd)

Depth	Data	A	AR	ARA	Depth	Data	B	BR	BRA
10	5	4	5	2	**10**	4	9	6	5
20	7	1	4	5	**20**	16	4	9	8
45	3	2	1	1	**45**	8	5	4	6

Semidiurnal (1.75-2.11 cpd)

Depth	Data	A	AR	ARA	Depth	Data	B	BR	BRA
10	21	81	83	84	**10**	19	69	80	82
20	29	85	83	74	**20**	18	76	77	76
45	34	86	86	81	**45**	26	78	78	65

Table 5.10 Distribution of Fluctuating Kinetic Energy, Mooring: M5-96, mixing models. Values represent the percent of the total energy in each frequency band.

Distribution of Energy
Mooring: M5-96

Met (0.1-0.5 cpd)

Depth	Data	A	AR	ARA	Depth	Data	B	BR	BRA
10	25	20	20	24	**10**	25	35	40	40
21	21	10	14	12	**21**	27	31	36	31
45	13	4	3	5	**45**	13	14	5	6

Diurnal (0.8-1.13 cpd)

Depth	Data	A	AR	ARA	Depth	Data	B	BR	BRA
10	11	8	4	3	**10**	13	14	8	8
21	12	2	2	2	**21**	14	4	1	1
45	10	1	2	1	**45**	20	2	7	6

Semidiurnal (1.75-2.11 cpd)

Depth	Data	A	AR	ARA	Depth	Data	B	BR	BRA
10	12	52	55	50	**10**	7	23	27	26
21	16	75	69	75	**21**	5	44	48	54
45	35	86	84	78	**45**	26	71	76	69

The simulations for 1997 also reveal problems with the distribution of the fluctuating kinetic energy within the model once wind stress is applied. The model was forced with the same tide and wind fields used to create the 30-day simulations for the statically stratified models A and B. When the model was stratified with the main pycnocline located at 10 metres depth (model A), the simulations that included mixing of temperature and salinity (models AR and ARA) were only able to produce 10 days of output before the onset of numerical instability. With the main pycnocline located near sill depth (model B), the mixing of temperature and salinity led to numerical instability after only 7.5 days of simulation in model BR while the enhanced mixing of model BRA failed after less than two days of simulation. Due to the short simulation produced by model BRA it is not possible to assess the distribution of energy in the meteorological band so this particular model is not included in the following analysis.

At M1-97 (Table 5.11), evaluation of the power spectrum of the measured velocity field over the 10 day period corresponding to the model simulations AR and ARA indicates that 26% of the energy at 7.5 metres depth may be due to meteorological forcing. Both the statically stratified model (A) and the enhanced mixing model (ARA) underestimate this distribution indicating that only 8%-11% of the energy may be found in this frequency band. Model AR indicates that 20% of the energy may be due to meteorological forcing. Model BR indicates that only 3% of the energy is located in the meteorological frequency band, compared to the 25% in model B and the 35% calculated from the observed currents over the 7.5 days of simulation used for model BR. At 21 metres depth, the amount of energy associated with meteorological events is found to decrease with increased mixing and also with the deepening of the main pycnocline within the model. Evaluated over 7.5 days for model B and over 10 days for models AR and ARA, the measured currents have 11%-12% of the energy within the meteorological frequency band. The currents in model A indicate that 23% of the energy is associated with meteorological forces. As mixing of temperature and salinity increases, the amount of energy associated with this frequency decreases to 15% in model ARA. With the deeper main pycnocline, models B and BR indicate that only 4%-8% of the energy may be associated with meteorological events.

The semi-diurnal tidal frequencies are found to be the dominant force in models A and ARA containing 63% and 73% of the total kinetic energy at 7.5 metres depth. In model AR only 39% of the total energy was associated with the semi-diurnal tides. The observation indicate that only 21% of the total energy is located at semi-diurnal frequencies within the 10 day period of simulation. Model BR, indicates that 19% of the total energy is associated with the semi-diurnal tides, much less than the 36% found in this frequency band for model B. Over the 7.5 day period of simulation, the observations at 7.5 metres depth indicate that only 11% of the energy at M1-97 is in the semi-diurnal frequency band. At 21 metres depth, the semi-diurnal frequency band contains 60% of the total energy in model ARA while models AR and BR have 13% and 25%, respectively.

The large proportion of energy found in the semi-diurnal band of the enhanced mixing model ARA is also found at M2-97 (Table 5.12) and M3-97 (Table 5.13). This is very different than the distribution of energy found at M2-96 (Table 5.7) where the amount of energy associated with the semi-diurnal tides at 10 metres depth did not change significantly with the addition of the averaging process to enhance the mixing. At

M2-96, models AR and ARA indicated that 38%-40% of the total energy is associated with the semi-diurnal tides, while models BR and BRA indicated that 16%-19% of the total energy is located at semi-diurnal frequencies. Although the distribution of energy into the semi-diurnal frequencies at M2-96 is clearly dependent upon the depth of the main pycnocline, the difference between the mixing models and the corresponding enhanced mixing model was only 2-3%.

In the 1997 simulations the difference in energy distribution into the semi-diurnal frequencies between models AR and ARA is between 33% (M3-97) to 55% (M2-97). It is unlikely that the shortness of the 1997 model simulations is responsible for the appearance of this additional energy in the semi-diurnal band. The 1996 simulations for models BR and BRA were only 10 days long; the same time frame as models AR and ARA in the 1997 simulations. It appears as if the averaging process used to enhance the mixing in model ARA may be creating a numerical resonance on the grid. It should be possible to investigate the possibility of numerical resonance through variation of averaging times used to advance the background scalar fields.

Table 5.11 Distribution of Fluctuating Kinetic Energy, Mooring: M1-97, mixing models. Values represent the percent of the total energy in each frequency band.

Distribution of Energy
Mooring: M1-97

Depth	Data	A	AR	ARA	Depth	Data	B	BR
Met (0.1-0.5 cpd)								
7.5	26	11	20	8	**7.5**	35	25	3
21	12	23	19	15	**21**	11	8	4
Diurnal (0.8-1.13 cpd)								
7.5	8	4	3	2	**7.5**	5	4	9
21	12	2	4	2	**21**	15	4	15
Semidiurnal (1.75-2.11 cpd)								
7.5	21	63	39	73	**7.5**	11	36	19
21	11	39	25	60	**21**	12	49	13

Table 5.12 Distribution of Fluctuating Kinetic Energy, Mooring: M2-97, mixing models. Values represent the percent of the total energy in each frequency band.

Distribution of Energy
Mooring: M2-97

Depth	**Data**	**A**	**AR**	**ARA**	**Depth**	**Data**	**B**	**BR**
Met (0.1-0.5 cpd)								
7.5	24	12	38	3	**7.5**	21	17	2
21	12	6	39	6	**21**	11	21	4
Diurnal (0.8-1.13 cpd)								
7.5	7	9	5	5	**7.5**	3	5	8
21	2	3	4	7	**21**	3	6	15
Semidiurnal (1.75-2.11 cpd)								
7.5	21	49	18	73	**7.5**	13	26	15
21	16	61	22	58	**21**	20	29	4

Table 5.13 Distribution of Fluctuating Kinetic Energy, Mooring: M3-97, mixing models. Values represent the percent of the total energy in each frequency band.

Distribution of Energy
Mooring: M3-97

Depth	**Data**	**A**	**AR**	**ARA**	**Depth**	**Data**	**B**	**BR**
Met (0.1-0.5 cpd)								
7.5	14	25	37	13	**7.5**	17	24	1
Diurnal (0.8-1.13 cpd)								
7.5	3	3	3	3	**7.5**	2	6	5
Semidiurnal (1.75-2.11 cpd)								
7.5	45	40	25	58	**7.5**	37	39	27

At the sill, mooring M4-97 (Table 5.14) indicates that in model BR only 24% of the energy is associated with the semi-diurnal frequency band. This agrees quite well with the observed distribution of energy where 21%-29% of the total energy was located in this frequency band. With the enhanced mixing, model ARA indicates that 82% of the total energy is located in the semi-diurnal frequency band. This is consistent with the model results at M3-96 (Table 5.8) of the 1996 simulations. In model AR, the difference in the proportion of energy in the semi-diurnal frequency band is dependent on if the current lies above or below the main pycnocline. Above the main pycnocline (7.5 metres depth) only 44% of the total energy is associated with the semi-diurnal tides. At 14 metres depth (below the main pycnocline), we find that 71% of the total energy is found in this frequency band. Mooring M4-97 is located closer to the seaward side of the sill than mooring M3-96. Model AR suggests that at this location semi-diurnal tides are lifting over the sill but remain trapped below the main pycnocline. This would contradict the observed behaviour of the tidal energy as the observations indicate that the energy associated with the semi-diurnal tides is relatively constant between 31-34% throughout the water column.

Table 5.14 Distribution of Fluctuating Kinetic Energy, Mooring: M4-97, mixing models. Values represent the percent of the total energy in each frequency band.

Distribution of Energy
Mooring: M4-97

Depth	Data	A	AR	ARA	Depth	Data	B	BR
Met (0.1-0.5 cpd)								
7.5	15	0	1	0	**7.5**	20	1	1
14	15	1	0	0	**14**	14	0	1
Diurnal (0.8-1.13 cpd)								
7.5	8	1	2	4	**7.5**	8	2	2
14	3	3	3	3	**14**	4	3	2
Semidiurnal (1.75-2.11 cpd)								
7.5	31	64	44	82	**7.5**	21	60	24
14	34	79	71	82	**14**	29	65	24

Seaward of the sill, at M5-97, M6-97 and M7-97 (Tables 5.15-5.17) the semi-diurnal band has the majority (50%-80%) of the total energy when the main pycnocline is located above the sill (A, AR, ARA) similar M4-96 (Table 5.9). The models also indicate that the amount of meteorological energy in the near surface (7.5 metres depth) at moorings M5-97 and M7-97 is significantly less (1-15%) than the observed meteorological energy (22%-25%). When the main pycnocline is at sill depth (B, BR, BRA), the proportion of energy located in the semi-diurnal band decreases significantly when temperature and salinity mix. Model BR indicates that only 18-21% of the total energy is located in the semi-diurnal bands near the surface at M5-97 and M7-97, much less than the 58-65% of the total energy associated with the semi-diurnal tides in model B. The energy of the meteorological frequency band remains very weak. In section 5.1, the tidal analysis indicates that the models produce a tidal signal that agrees well with the observations in this region. The tapering of the wind field towards the coastline coupled with the reduction of the surface wind stress in the surface layer of the internal mode result in a model that is unable to properly reflect the transfer of energy from the wind to the surface of the water.

During the simulations for 1997, mixing of temperature and salinity in models AR and BR increase the transfer of energy from the semi-diurnal tide to higher frequencies. Moorings M5-97, M6-97 and M7-97 were located closer to the sill than mooring M4-96 where there was little change in the percentage of energy associated with the semi-diurnal tides when temperature and salinity were allowed to mix compared to the statically stratified models. The decrease of energy in the semi-diurnal band at these locations suggests that the model is able to transfer some energy into mixing in the vicinity of the sill. However, the transfer of energy into mixing by the model appears to be damped very quickly as the distance from the sill increases. If this were not the case, the amount of energy located in the semi-diurnal band at M4-96 would also show a significant reduction when mixing of temperature and salinity were introduced in the model.

Table 5.15 Distribution of Fluctuating Kinetic Energy, Mooring: M5-97, mixing models. Values represent the percent of the total energy in each frequency band.

Distribution of Energy
Mooring: M5-97

Met (0.1-0.5 cpd)

Depth	Data	A	AR	ARA	Depth	Data	B	BR
7.5	25	1	3	15	**7.5**	31	1	3
21	44	28	37	6	**21**	47	29	3

Diurnal (0.8-1.13 cpd)

Depth	Data	A	AR	ARA	Depth	Data	B	BR
7.5	8	4	3	1	**7.5**	8	3	3
21	1	1	1	2	**21**	1	1	1

Semidiurnal (1.75-2.11 cpd)

Depth	Data	A	AR	ARA	Depth	Data	B	BR
7.5	21	80	71	61	**7.5**	13	58	18
21	2	28	12	75	**21**	2	17	22

Table 5.16 Distribution of Fluctuating Kinetic Energy, Mooring: M6-97, mixing models. Values represent the percent of the total energy in each frequency band.

Distribution of Energy
Mooring: M6-97

Met (0.1-0.5 cpd)

Depth	Data	A	AR	ARA	Depth	Data	B	BR
21	36	1	4	1	**21**	42	2	3
33	10	19	5	2	**33**	10	46	3

Diurnal (0.8-1.13 cpd)

Depth	Data	A	AR	ARA	Depth	Data	B	BR
21	1	4	4	3	**21**	1	2	2
33	13	1	1	2	**33**	14	1	1

Semidiurnal (1.75-2.11 cpd)

Depth	Data	A	AR	ARA	Depth	Data	B	BR
21	9	72	53	75	**21**	7	51	20
33	9	23	16	80	**33**	8	0	7

Table 5.17 Distribution of Fluctuating Kinetic Energy, Mooring: M7-97, mixing models. Values represent the percent of the total energy in each frequency band.

Distribution of Energy
Mooring: M7-97
Met (0.1-0.5 cpd)

Depth	Data	A	AR	ARA	Depth	Data	B	BR
7.5	22	1	1	2	**7.5**	22	4	0
31	23	6	5	3	**31**	15	3	4

Diurnal (0.8-1.13 cpd)

Depth	Data	A	AR	ARA	Depth	Data	B	BR
7.5	6	3	3	1	**7.5**	9	3	1
31	7	1	3	1	**31**	10	4	4

Semidiurnal (1.75-2.11 cpd)

Depth	Data	A	AR	ARA	Depth	Data	B	BR
7.5	15	81	72	82	**7.5**	3	65	21
31	8	68	58	82	**31**	12	59	26

5.3 Residual Currents

To determine the mean current direction at each mooring location, the hourly output from the models forced by winds and tides was passed through an 8th order Butterworth filter to remove the diurnal and semi-diurnal tides. The mean and standard deviation were then calculated from the de-tided signal. The results of this analysis are presented in Tables 5.18-5.29. Some of the residual currents are also presented in Figures 5.25-5.30. Generally we find that the model is unable to reproduce the mean circulation observed at the mooring locations. No meteorological data was collected at Clode Sound during either of the observation programs of 1996 and 1997. To compensate for the absence of meteorological data the model was forced with the wind field data collected at Gander International Airport. Based upon the model output when this wind data is applied to the Clode Sound domain, it appears that the wind field at Gander International Airport may not be representative of the true wind field found in Clode Sound. The observation data is included in the tables and figures of this section. However, a comparison of the model output to the actual data does not seem plausible. The following discussion will focus on the differences between the model runs themselves and how the mixing of temperature and salinity is able to influence the residual circulation of the model. As with the orientation of the tidal ellipses, all angular measurements used to describe the orientation of the mean current are measured with the eastern axis equal to 0 degrees.

At M1-96 (Table 5.18), the statically stratified models A and B produced a mean current of 0.7-0.9 cm/s at 10 metres depth directed towards the southwest, 196°-207°. With the addition of mixing, the mean surface current rotates counter clockwise to 228°-232°. Mixing also increases the mean current speed at 10 metres depth. The speed of the mean current increases from 0.7 cm/s in model A to 1.2 cm/s in model ARA. The enhanced mixing of model ARA produces a mean current speed of 2.5 cm/s. With the main pycnocline located at sill depth the enhanced mixing in model BRA appears to have little influence on the current speed compared to model BR. Both models BR and BRA produce a mean current speed between 1.7-1.8 cm/s double the 0.9 cm/s produced in model B. Model ARA also shows a significant increase in the variability of the residual currents at 10 metres depth. This is the only model that is able to match the observed variability of the currents a mooring M1-96.

At 21 metres depth all of the models produce a mean current between 0.7-0.9 cm/s; the currents are directed towards the southwest, between 196°-210° in all of the models except model ARA where the current is directed slightly north of west at 174°. At 45 metres depth, the model produces a mean current between 0.3-0.6 cm/s but the direction of the current varies significantly between the models with static stratification and those that include mixing. Models A and B indicate a mean current that is directed almost due west between 180°-189°. When mixing is included in the models, the mean current rotates to the southwest 198°-236°.

Table 5.18 Mean and Standard Deviation of the Residual Currents (cm/s) Mooring: M1-96. The Observed (Obs.) mean and standard deviations are calculated over Julian days 205-235 coinciding with models A and B (See. Table 5.19 for length of each simulation)

Mooring: M1-96

East-West Velocity (U)

Depth	Obs.	A	AR	ARA	Obs.	B	BR	BRA
10	1.8±1.7	-0.7±0.7	-0.8±0.6	-1.7±1.1	1.5±1.1	-0.8±0.5	-1.1±0.7	-1.1±0.6
21	0.3±1.0	-0.7±0.4	-0.7±0.8	-0.9±0.8	0.1±0.8	-0.7±0.4	-0.6±0.4	-0.6±0.5
45	0.2±1.0	-0.6±0.5	-0.2±0.3	-0.3±0.4	0.9±0.6	-0.5±0.5	-0.3±0.2	-0.2±0.1

North-South Velocity (V)

Depth	Obs.	A	AR	ARA	Obs.	B	BR	BRA
10	0.7±1.5	-0.2±0.7	-0.9±0.7	-1.9±1.3	0.8±1.5	-0.4±0.6	-1.3±0.7	-1.4±0.8
21	0.5±0.9	-0.2±0.4	-0.2±0.5	0.1±0.7	0.3±0.9	-0.4±0.5	-0.2±0.5	-0.3±0.5
45	0.2±0.5	-0.1±0.3	-0.3±0.3	-0.2±0.4	-0.1±0.4	-0.0±0.4	-0.1±0.1	-0.2±0.1

The model indicates a residual current that flows almost directly opposite to that of the observed flow at 10 and 21 metres depth. The observed circulation at M1-96 may be a response to an increase in the availability of fresh water that occurs between Julian Days 185-205 (Figure 2.26). The model does not contain a fresh water source, it may be possible to include a fresh water source into models ARA and BRA to test this hypothesis but this has not been done.

At M2-96 (Table 5.19, Figure 5.25), mixing increases the mean current at 10 metres depth from 0.4-0.5 cm/s to 2.1-2.9 cm/s. With the inclusion of mixing, the current rotates from a nearly southerly direction of 264°-270° in models A and B to a more southwesterly, 215°-234°. The variability of the currents at 10 metres depth also increases significantly when mixing is included in the model. The variability of the east-west and north-south components of the residual velocity in Table 5.19 indicates that without the inclusion of mixing (models A and B), the model suppresses the internal response at both 10 and 17 metres depth. It is very evident from both Tables 5.18 and 5.19 that if the model is to be used to study the dynamics and circulation within the inner basin, than the mixing of temperature and salinity must be included. Without mixing, the model is unable to produce the observed sub-tidal variability observed in the inner basin. The ability of the model to reproduce the observed residual circulation within the inner basin is doubtful (Figures 5.25). However, the model does begin to produce a residual circulation that is able to obtain speeds that are close to the observed current speed even if the direction does not match.

At 10 metres depth at moorings M1-96 and M2-96, the difference in the response of the statically stratified model A and the response of the mixing models is clearly evident between Julian days 210-220 (Figures 5.25). In model A (solid black line), the residual current at 10 metres depth is bounded above and below by speeds of 0.1 cm/s at both M1-96 and M2-96. When mixing is included, the residual currents show a distinct local maximum that occurs at approximately days 215 at M1-96 and days 212-213 at M2-96. There is evidence of this maximum current in the observations (+) although the orientation of the observed current differs significantly from the modelled flow. The orientation of the currents at M1-96 cannot be expected to match the observed flow. Near the surface, the direction of the currents will depend strongly on both the wind field and the tidal forcing. The tidal analysis clearly indicates that the strength of the tide was much weaker than the observed tide at M1-96. The distribution of the fluctuating kinetic energy indicates that, within the model, the near surface currents are dominated by forcing in the meteorological frequency band while the observed currents had the largest proportion of energy in the semi-diurnal frequency band. With the external forcing used by the model to simulate the circulation incorrectly balanced, the model is able to simulate some of the variability observed within the inner basin. However, there is little reason to expect that the model can accurately reflect the cause of this variability.

Table 5.19 Mean and Standard Deviation of the Residual Currents (cm/s) Mooring: M2-96. The Observed (Obs.) mean and standard deviations are calculated over Julian days 205-235 coinciding with models A and B (See. Table 5.19 for length of each simulation)

Mooring: M2-96

East-West Velocity (U)

Depth	Obs.	A	AR	ARA	Obs.	B	BR	BRA
10	-3.2±3.2	-0.1±0.5	-1.7±1.3	-1.8±1.9	-4.2±2.0	-0.0±0.5	-1.8±1.9	-1.7±1.9
17	-0.7±2.4	-0.2±0.6	-0.8±0.7	-0.7±0.6	-0.5±1.1	-0.1±0.5	-0.8±0.7	-1.2±1.0
44	0.1±0.7	-0.4±0.3	0.2±0.3	0.1±0.4	-0.0±0.8	-0.3±0.2	0.1±0.2	0.2±0.3

North-South Velocity (V)

Depth	Obs.	A	AR	ARA	Obs.	B	BR	BRA
10	2.3±2.1	-0.5±0.3	-1.2±0.7	-1.7±1.2	1.9±2.1	-0.4±0.3	-1.9±1.5	-2.3±2.0
17	0.5±1.0	-1.0±0.5	-1.2±1.2	-1.2±1.3	0.7±0.7	-1.0±0.4	-1.1±1.0	-1.2±1.0
44	0.5±0.8	-0.2±0.3	0.1±0.2	-0.1±0.4	0.6±0.8	-0.1±0.3	0.1±0.3	0.2±0.3

At M3-96 (Table 5.36, Figure 5.26), the sill is oriented almost along the east-west axis. Within the model, there is very little variation found in the east-west current of the simulations. It is only after day 210 that there is evidence of any significant difference in the east-west velocity at 10 metres depth. When the main pycnocline is located above the sill, models AR and ARA indicate a mean surface current that flows seaward while models BR and BRA indicate a mean surface flow towards the inner basin. The rapid increase in the east-west velocity at day 215 is more likely to be the onset of numerical instability. At 15 metres depth, the north-south current from the models appear to reflect the observed north-south current quite well. This apparent match coincides with the spring-neap cycle of the tide and may be tidally driven although it does not appear in model A.

Table 5.20 Mean and Standard Deviation of the Residual Currents (cm/s) Mooring: M3-96. The Observed (Obs.) mean and standard deviations are calculated over Julian days 205-235 coinciding with models A and B (See. Table 5.19 for length of each simulation)

Mooring: M3-96

East-West Velocity (U)

Depth	Obs.	A	AR	ARA	Obs.	B	BR	BRA
10	-2.3±4.5	0.3±0.9	0.9±1.2	0.3±1.6	-2.3±4.0	0.4±1.0	0.4±1.1	0.1±1.2
15	-0.9±5.1	0.3±1.2	0.2±1.4	-0.1±1.2	-0.3±3.7	0.5±1.2	0.2±1.1	0.3±1.4

North-South Velocity (V)

Depth	Obs.	A	AR	ARA	Obs.	B	BR	BRA
10	4.6±2.1	0.4±0.4	0.8±0.6	0.4±0.4	5.6±2.0	0.3±0.5	0.6±0.5	0.3±0.6
15	2.6±2.1	-0.2±0.3	1.6±1.2	1.8±1.5	2.4±1.6	-0.2±0.3	1.4±0.8	1.8±0.7

The dominant semi-diurnal tides and weak meteorological forcing at M4-96 (Table 5.21, Figure 5.27), within the model, result in a residual circulation at this location that is almost constant throughout the water column. The K_1 and M_2 tides at this mooring agreed very well with the observed tides in models BR and BRA. The inability of the model to reflect the residual circulation indicates that tidal forcing cannot solely responsible for the mean circulation at this location. Mixing does produce a residual current at 10 metres depth that is 2-4 times stronger than then the residual current in models A and B, however the variability of the surface current increases by a factor of only 1.5.

At M5-96 (Table 5.22), there was more energy located in the meteorological frequency band than at M4-96. There is some evidence of residual currents at 10 metres depth driven by wind stress in the model. However, at this location the tidal forces within the model were much weaker than the observed tide. The current speed at 10 metres depth from 0.7-0.8 cm/s in models A and B increases to 1.3-1.4 cm/s with the mixing of temperature and salinity. This increase occurs in the north-south component of the velocity field and results in a change of orientation from west (180°) in models A and B to southwest (225°) aligning the current with the coastline.

Table 5.21 Mean and Standard Deviation of the Residual Currents (cm/s) Mooring: M4-96. The Observed (Obs.) mean and standard deviations are calculated over Julian days 205-235 coinciding with models A and B (See. Table 5.19 for length of each simulation)

Mooring: M4-96

East-West Velocity (U)

Depth	Obs.	A	AR	ARA	Obs.	B	BR	BRA
10	-4.3±3.0	0.2±0.3	0.9±0.5	0.8±0.5	-5.6±2.8	0.2±0.4	0.5±0.6	0.5±0.6
20	1.2±1.6	-0.4±0.3	0.3±0.6	0.5±0.5	1.4±1.2	-0.3±0.3	-0.1±0.2	-0.1±0.2
45	0.3±0.7	-0.4±0.4	-0.6±0.2	-0.4±0.2	0.0±0.7	-0.2±0.3	-0.1±0.2	-0.0±0.3

North-South Velocity (V)

Depth	Obs.	A	AR	ARA	Obs.	B	BR	BRA
10	1.7±3.8	0.2±0.2	0.2±0.1	0.1±0.1	3.3±2.3	0.3±0.2	0.1±0.3	0.1±0.3
20	0.1±1.1	0.2±0.3	-0.1±0.2	-0.3±0.2	-0.5±0.7	0.1±0.4	0.3±0.3	0.2±0.3
45	0.3±0.6	0.2±0.3	0.0±0.1	0.0±0.2	0.6±0.5	0.1±0.4	0.2±0.3	0.1±0.3

The results of the models from moorings M4-96 and M5-96 indicate that neither the wind stress nor the tides alone can generate the observed residual circulation found seaward of the sill in Clode Sound. At 10 metres depth, the observed currents at both M4-96 and M5-96 indicate that there are numerous oscillations in the residual circulation with a "period" of 1.5-3 days. These oscillations in the residual circulation do not appear to be related to tidal forcing as there is no evidence of this behaviour in the model at M4-96. Although they are found in the meteorological frequency band they do not appear to be generated locally as there is little evidence of this in the model at M5-96. The inability of the model to generate them with either tides or winds as the dominant energy source indicates that the origin of these oscillations may lie beyond the mouth of the inlet or is the result of the interaction of the tides and wind. This oscillatory behaviour is more pronounced at M5-96 than at M4-96 which may indicate that these low frequency waves are being damped out as they propagate up through inlet which supports the hypothesis that they are not generated within the inlet.

Table 5.22 Mean and Standard Deviation of the Residual Currents (cm/s) Mooring: M5-96. The Observed (Obs.) mean and standard deviations are calculated over Julian days 205-235 coinciding with models A and B (See. Table 5.19 for length of each simulation)

Mooring: M5-96

East-West Velocity (U)

Depth	Obs.	A	AR	ARA	Obs.	B	BR	BRA
10	-3.0±1.6	0.8±0.6	0.9±0.8	1.0±0.8	-3.0±1.6	0.7±0.7	1.0±0.9	1.0±0.9
21	0.6±1.3	-0.4±0.3	-0.4±0.4	-0.4±0.4	0.7±1.5	-0.4±0.3	-0.3±0.4	-0.4±0.3
45	0.4±0.7	-0.3±0.2	-0.4±0.3	-0.6±0.5	0.5±0.7	-0.3±0.2	-0.1±0.2	-0.2±0.3

North-South Velocity (V)

Depth	Obs.	A	AR	ARA	Obs.	B	BR	BRA
10	-3.9±2.7	0.1±0.6	0.9±0.7	1.0±0.7	-4.6±2.7	0.2±0.7	0.8±0.7	0.8±0.7
21	-0.1±1.6	-0.0±0.3	-0.4±0.4	-0.4±0.4	0.0±1.8	-0.0±0.4	-0.3±0.4	-0.2±0.4
45	0.7±0.6	-0.1±0.2	-0.2±0.2	-0.3±0.2	0.8±0.6	-0.1±0.3	-0.2±0.2	-0.3±0.3

The ability of the model to match the observations from 1997 is not greatly improved. During the simulations for 1997, the mean current speed at M1-97 (Table 5.23) increases from 0.1-0.2 cm/s when the stratification is held constant to 0.8-1.1 cm/s when temperature and salinity are mixing. The orientation of the near surface current is also found to rotate clockwise from a southeasterly 297°-315° to 248°-275° (south-southwest to south). In model A, circulation after day 200 is directed towards the northwest. Model BR, produces a strong southerly flow after day 197. Although the variability of the residual circulation is found to increase in models ARA and BR, clearly none of the models are able to match the variability found in the observations at M1-97. At 21 metres depth, the mean current speed decreases from 0.9 cm/s with the enhanced mixing of model ARA and also in model BR when the main pycnocline is located at sill depth. The variability of the residual current also decreases in model BR, but with enhanced mixing, model ARA produces greater variability in the residual circulation.

Table 5.23 Mean and Standard Deviation of the Residual Currents (cm/s) Mooring: M1-97. The Observed (Obs.) mean and standard deviations are calculated over Julian days 195-225 coinciding with models A and B (See. Table 5.19 for length of each simulation)

Mooring: M1-97

East-West Velocity (U)

Depth	Obs.	A	AR	ARA	B	BR
7.5	-0.0±2.7	0.1±0.5	-0.1±0.5	-0.4±0.7	0.1±0.3	0.1±0.5
21	1.1±1.0	-0.5±0.5	-0.5±0.5	0.0±0.8	-0.6±0.7	-0.5±0.4

North-South Velocity (V)

Depth	Obs.	A	AR	ARA	B	BR
7.5	1.3±2.2	-0.1±0.4	-0.8±0.6	-1.0±0.7	-0.2±0.5	-1.1±1.2
21	0.1±0.7	-0.8±0.6	-0.7±0.9	-0.3±0.8	-0.7±0.7	-0.2±0.4

At M2-97 (Table 5.24, Figure 5.28), the model exhibits some of the greatest variability found in the residual circulation at any mooring location. The greatest variation in the currents at 7.5 metres occurs when the main pycnocline is located above the sill (AR and ARA). With the model statically stratified, the model produces a mean current of 0.1-0.3 cm/s directed either towards the east (model A) or northeast (model B). With the introduction of mixing, the mean current speed increases 2.1 cm/s (models AR). Models ARA and BR have a mean current speed of 1.1-1.3 cm/s. All of the mixing models produce a southwesterly flow between 202°-225°. This mooring also illustrates one of the most significant differences between the mixing model AR and the enhanced mixing model ARA. At day 195 (Figure 5.28) the mixing models all produce a strong westward component in the residual velocity that is not found in model A (solid black line). The westward component is weakest in model BR (gray dashed line) and strongest in model ARA (black dash dot line). In both models BR and ARA, this westward flow relaxes back towards zero at approximately day 198 while in model AR the westward component of the residual velocity does not begin to relax back towards zero until two days later.

Table 5.24 Mean and Standard Deviation of the Residual Currents (cm/s) Mooring: M2-97. The Observed (Obs.) mean and standard deviations are calculated over Julian days 195-225 coinciding with models A and B (See. Table 5.19 for length of each simulation)

Mooring: M2-97

East-West Velocity (U)

Depth	Obs.	A	AR	ARA	B	BR
7.5	-3.0±3.4	0.3±0.4	-1.8±1.1	-1.2±1.4	0.1±0.5	-0.8±0.8
21	-0.5±2.1	-0.1±0.6	1.7±0.7	1.0±1.1	-0.1±0.3	-0.5±0.5

North-South Velocity (V)

Depth	Obs.	A	AR	ARA	B	BR
7.5	0.3±1.8	0.0±0.4	-1.0±0.6	-0.5±0.6	0.1±0.5	-0.8±0.7
21	0.5±0.7	-1.1±0.7	-0.2±0.7	-0.3±1.0	-0.9±0.6	-0.1±0.1

As can be seen in the observations ("+ " in the figures) at M2-97 (Figure 5.28), most of the events found in the residual circulation have a duration of not more than two days similar to those found in models ARA and BR. The enhanced mixing of model ARA appears to allow the model to respond more quickly to changes in either the wind field or density field. With only ten vertical levels used in the model, one advantage of the enhanced mixing model may be that it permits the depth of the main pycnocline to adjust to external forcing. This may help to explain why model ARA begins to track with the velocity field of model BR in which the main pycnocline was located at sill depth. When the background temperature and salinity fields are held constant the density field of the model will always be relaxed back towards its initial configuration. With the expectation of high mixing rates in the neighbourhood of the sill, the inability of models AR and BR to breakdown the main pycnocline may not be a very good representation of the actual density field as it would artificially impose a certain amount of structure that may not exist. However, it cannot be the breakdown of the main pycnocline that is solely responsible for the ability of model ARA to relax more quickly than model AR. Even in the absence of the main pycnocline, the north-south velocity also demonstrates the ability of the enhanced mixing model to relax more quickly. At 7.5 metres depth both models

AR and BR begin to develop a southern velocity component, while model ARA appears to relax back towards the velocity field produced in model A in which the stratification was held constant.

At M3-97 (Table 5.25) there appears to be very little difference in the east-west components of the velocity fields generated by the models. The mean currents produced by model A and B indicate an east-west velocity in excess of 1.0 cm/s that does not appear in any of the mixing models. However, a closer examination of the time series suggests that this is misleading and may be coincidental with the shorter records of data. Beyond day 200 model A produces a steady westward flow while models AR and ARA begin to develop a strong easterly flow just before the end of the model run (which terminated early due to numerical instability).

Table 5.25 Mean and Standard Deviation of the Residual Currents (cm/s) Mooring: M3-97. The Observed (Obs.) mean and standard deviations are calculated over Julian days 195-225 coinciding with models A and B (See. Table 5.19 for length of each simulation)

Mooring: M3-97

East-West Velocity (U)

Depth	Obs.	A	AR	ARA	B	BR
7.5	-6.2±3.9	1.4±0.9	-0.1±1.0	0.2±1.0	1.2±0.9	-0.1±1.0

North-South Velocity (V)

Depth	Obs.	A	AR	ARA	B	BR
7.5	-6.8±2.8	-0.4±0.5	-0.2±0.3	-0.4±0.3	-0.3±0.5	-0.2±0.4

M4-97 (Table 5.26, Figure 5.29) is located at the sill and, similar to the results of M3-96, we see how poorly the model is able to reproduce the residual circulation at the sill. The mixing models do show significantly different residual flow from the statically stratified models. With mixing, the mean east-west component of the velocity at 7.5 metres depth decreases in magnitude and reverses direction from 0.7-1.0 cm/s in model A and B to –0.5-0.0 cm/s. The north-south component of the velocity reverses direction and increases from 0.2-0.4 cm/s to approximately –1.0 cm/s in models AR and ARA. The explanation of these values is clearly visible in Figure 5.33. At 7.5 metres depth the east-west component of the residual velocity in model A tracks eastward while the mixing models remain very close to zero. The north south component of velocity also identifies significant differences between the model output. Near the surface models AR and ARA show a north-south component that is increasing towards the south while model BR tracks the statically stratified model A. At 14 metres depth all of the models that include mixing exhibit a northward flowing current while the north-south velocity component of the statically stratified model A tracked the observed current between days 195 and 200. These results are indicative of the numerical instabilities that exist in the mixing models. It is in the neighbourhood of the sill that all of the mixing models became numerically unstable.

Table 5.26 Mean and Standard Deviation of the Residual Currents (cm/s) Mooring: M4-97. The Observed (Obs.) mean and standard deviations are calculated over Julian days 195-225 coinciding with models A and B (See. Table 5.19 for length of each simulation)

Mooring: M4-97

East-West Velocity (U)

Depth	Obs.	A	AR	ARA	B	BR
7.5	-3.6±5.1	1.0±0.8	-0.5±0.4	-0.2±0.5	0.7±0.7	0.0±0.7
14	2.4±9.2	0.1±0.5	-0.1±1.1	0.1±1.2	-0.1±0.6	-0.6±1.0

North-South Velocity (V)

Depth	Obs.	A	AR	ARA	B	BR
7.5	2.9±1.9	0.4±0.6	-1.0±0.5	-1.1±0.7	0.2±0.3	-0.0±0.2
14	0.8±2.2	-0.3±0.3	1.2±0.7	1.4±0.7	-0.4±0.3	1.2±0.5

Seaward of the sill at M5-97 (Table 5.27) we find that at 7.5 metres depth the mixing models produce a strong westward component for the mean current that is not found in the statically stratified models. This westward flow is strongest in model ARA with the enhanced mixing scheme. Little difference is found between models AR and BR suggesting that the east-west component of the modeled residual current does not depend on the depth of the main pycnocline but only on the amount of mixing. The north-south component of the residual velocity also reveals a significant difference between the statically stratified models and the mixing models.

The statically stratified model A does appear to be able to track some of the variation of the observed residual flow. Between days 196 and 199 the observed current develops a strong southwesterly direction that also develops in model A at approximately the same time. The southward component in the modeled flow, however relaxes slowly back towards zero, while the westward component is maintained until approximately day 202. This disagrees with the observed current that reverses the direction of the flow within about 2 days of the onset of the southwesterly current. None of the mixing models are able to produce this southwesterly flow. At 21 metres depth, it is the mixing models that appear to be able to produce some of the observed southeasterly flow between days 195 and 198. Models AR and ARA produce a stronger eastward component than model BR, while the southerly component of all three mixing models agree very closely with each other. The source of energy that drives this response within the model is not clear.

The observations at M5-97 indicate that between 44-47% of the total energy belongs to the meteorological frequency band while only 2% of the total energy is located at semi-diurnal frequencies (Table 5.15). Models ARA and BR indicate that only 3-6% of the energy is found in the meteorological frequency band while model AR shows 37% of the total energy to belong to meteorological forcing. Model ARA also indicates that 75% of the total energy is found in the semi-diurnal frequency band which is significantly greater than the 12-22% of the total energy located at semi-diurnal frequencies in models AR and BR. Despite this apparent mismatch in the distribution of energy, models AR and

ARA produce very similar residual currents. As previously mentioned, it is apparent that the averaging of the background scalar fields over a semi-diurnal period may be producing a numerical resonance within the model at some locations on the numerical grid.

Table 5.27 Mean and Standard Deviation of the Residual Currents (cm/s) Mooring: M5-97. The Observed (Obs.) mean and standard deviations are calculated over Julian days 195-225 coinciding with models A and B (See. Table 5.19 for length of each simulation)

Mooring: M5-97

East-West Velocity (U)

Depth	Obs.	A	AR	ARA	B	BR
7.5	1.3±2.3	0.1±0.7	0.8±0.8	1.3±1.0	-0.1±0.7	0.6±0.5
21	2.1±2.8	0.3±0.6	-0.6±1.0	-0.3±1.1	0.2±0.6	-0.0±0.3

North-South Velocity (V)

Depth	Obs.	A	AR	ARA	B	BR
7.5	-0.3±1.2	-0.5±0.6	0.5±0.5	0.6±0.4	-0.5±0.6	-0.1±0.5
21	-0.5±1.2	0.1±0.3	0.1±0.4	-0.1±0.5	0.1±0.3	0.0±0.3

At M6-97 (Table 5.28, Figure 5.30), the mixing models AR and ARA produce a mean current that is directed northward at 21 metres depth, while model A produces a mean current that is directed eastward. The introduction of mixing into the model combined with the lack of energy in the meteorological frequency band (Table 5.16) produces an east-west current that is dominated by the tide. In consequence of this tidal forcing, the principle axis is oriented along the east-west direction (Table 5.5) and produces very little mean flow in either the east or west direction. However, the model also indicates that the variability in the north-south component of the residual circulation increases with mixing when the main pycnocline is located above the sill. It appears that the variability of the cross channel flow (north-south) arises as tidal energy is used to mix across the sigma levels of the model in the cross channel direction. This same effect is found at 33 metres depth in all of the mixing models including model BR, when the main pycnocline is located above this observation level.

Table 5.28 Mean and Standard Deviation of the Residual Currents (cm/s) Mooring: M6-97. The Observed (Obs.) mean and standard deviations are calculated over Julian days 195-225 coinciding with models A and B (See. Table 5.19 for length of each simulation)

Mooring: M6-97

East-West Velocity (U)

Depth	**Obs.**	**A**	**AR**	**ARA**	**B**	**BR**
21	0.4±2.9	0.6±0.4	-0.0±0.3	0.1±0.3	0.5±0.4	-0.1±0.2
33	0.2±1.4	1.0±0.5	-0.4±0.2	-0.3±0.2	0.9±0.3	0.3±0.1

North-South Velocity (V)

Depth	**Obs.**	**A**	**AR**	**ARA**	**B**	**BR**
21	-0.6±2.0	-0.1±0.3	0.7±0.6	0.6±0.7	-0.1±0.3	0.0±0.2
33	0.6±1.2	-0.2±0.3	0.1±0.7	0.1±0.6	-0.2±0.3	0.2±0.6

At M7-97 (Table 5.29), the model is unable to reproduce the strong westerly flow observed at 7.5 metres depth. The statically stratified model A does produce a stronger westward flow after day 200 at both 7.5 and 33 metres depth. The mixing models do not produce this westerly flow at 33 metres depth. The model results are not conclusive at 7.5 metres depth as the model runs terminated just as the flow appears to begin to turn westward.

Table 5.29 Mean and Standard Deviation of the Residual Currents (cm/s) Mooring: M7-97. The Observed (Obs.) mean and standard deviations are calculated over Julian days 195-225 coinciding with models A and B (See. Table 5.19 for length of each simulation)

Mooring: M7-97

East-West Velocity (U)

Depth	**Obs.**	**A**	**AR**	**ARA**	**B**	**BR**
7.5	-5.2±1.9	-1.1±0.6	-0.2±0.4	0.1±0.6	-0.9±0.6	-0.3±0.7
31	0.6±2.9	-1.0±0.6	-0.4±0.4	-0.4±0.3	-1.0±0.6	-0.7±0.3

North-South Velocity (V)

Depth	**Obs.**	**A**	**AR**	**ARA**	**B**	**BR**
7.5	-1.0±0.9	-0.1±0.2	-0.2±0.3	-0.1±0.3	-0.1±0.2	-0.8±0.5
31	0.4±1.0	0.1±0.2	0.4±0.3	0.4±0.3	0.1±0.2	-0.0±0.5

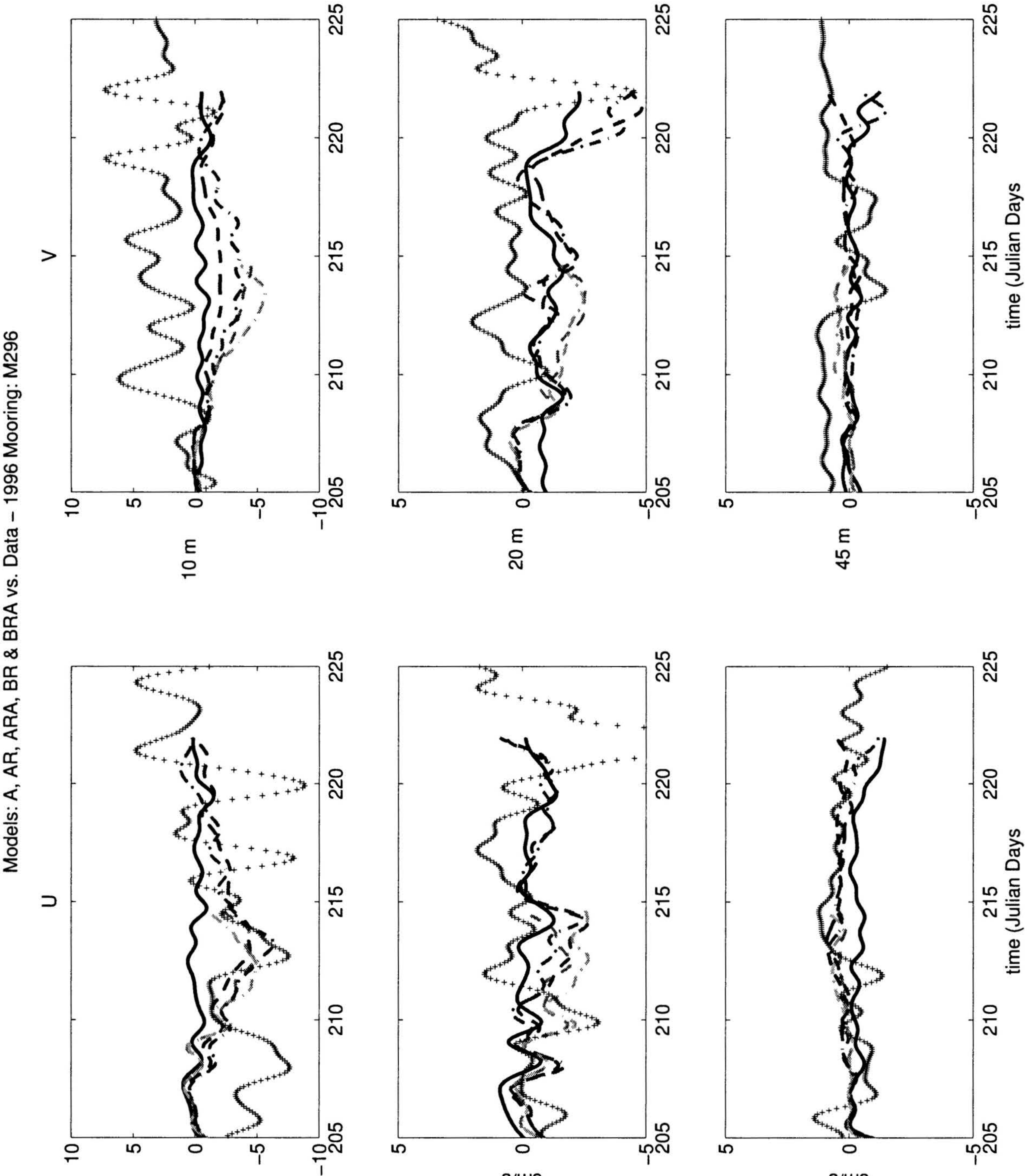

Figure 5.25 Residual Currents at M2-96 - Mixing Models: Model A (solid black line); **Model AR** (dashed black line); **Model ARA** (dash dot black line); **Model BR** (dashed gray line); **Model BRA** (dash dot gray line) and the **observed** residual currents (+).

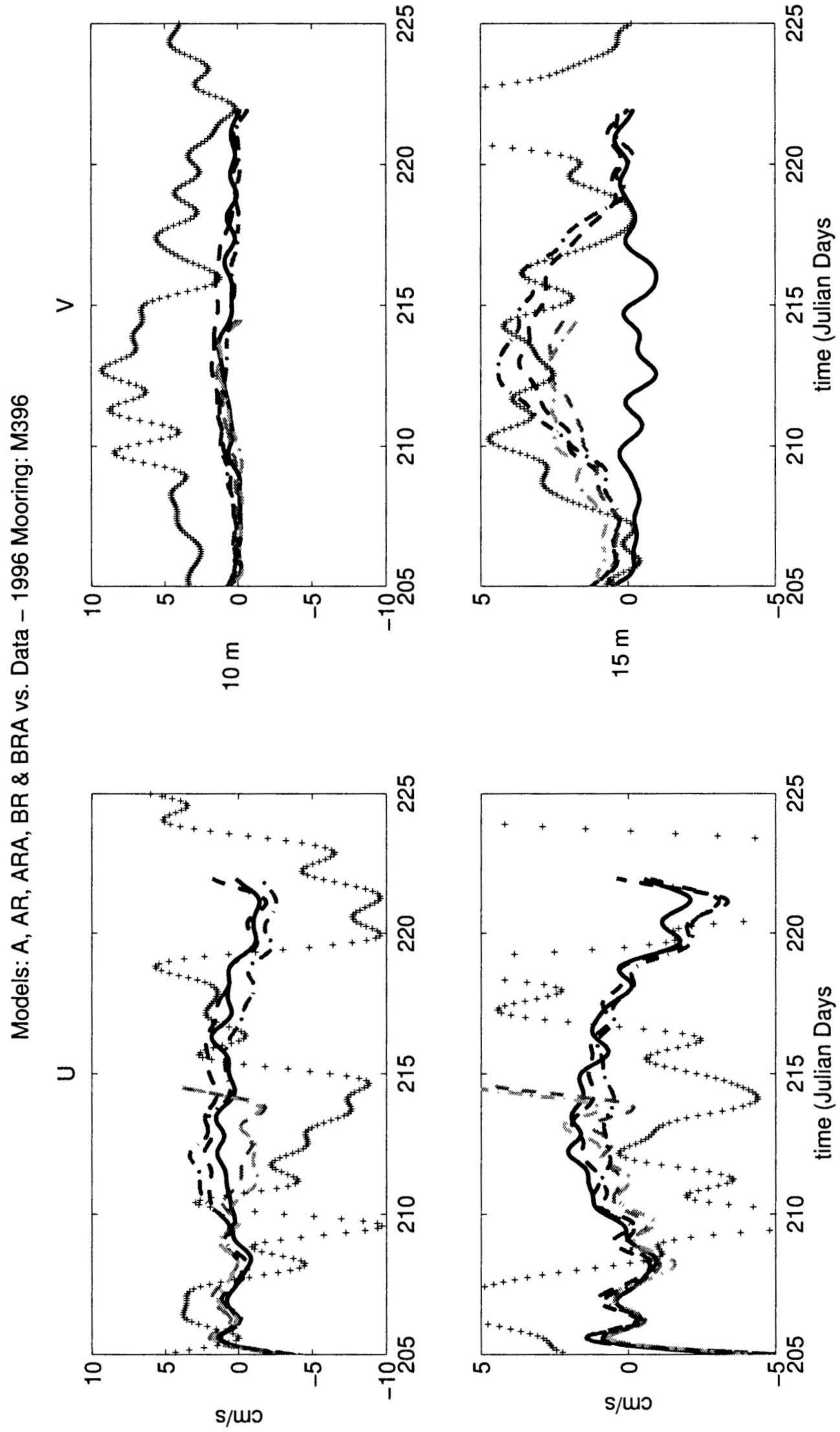

Figure 5.26 Residual Currents at M3-96 - Mixing Models: Model A (solid black line); **Model AR** (dashed black line); **Model ARA** (dash dot black line); **Model BR** (dashed gray line); **Model BRA** (dash dot gray line) and the **observed** residual currents (+).

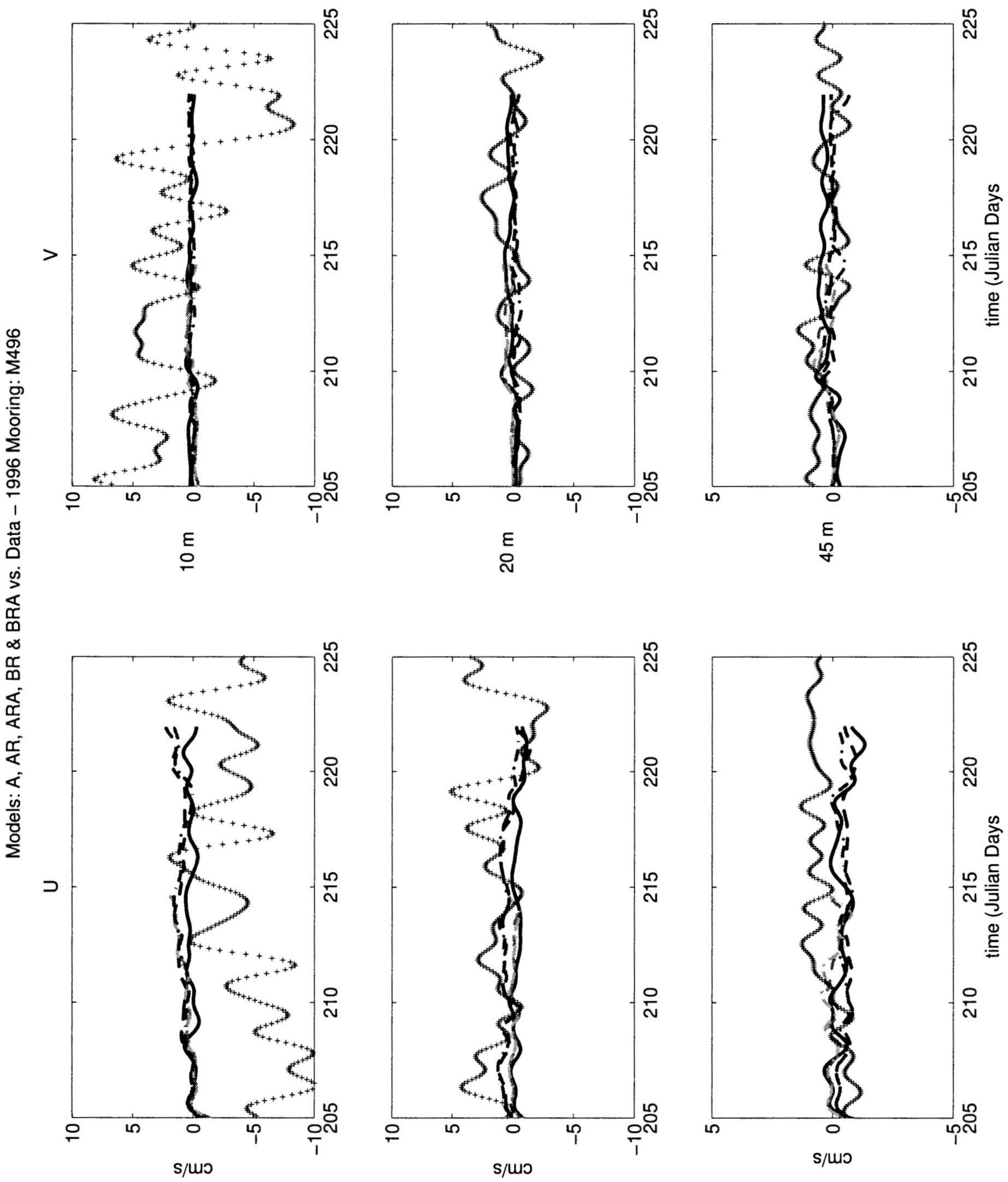

Figure 5.27 Residual Currents at M4-96 - Mixing Models: Model A (solid black line); **Model AR** (dashed black line); **Model ARA** (dash dot black line); **Model BR** (dashed gray line); **Model BRA** (dash dot gray line) and the **observed** residual currents (+).

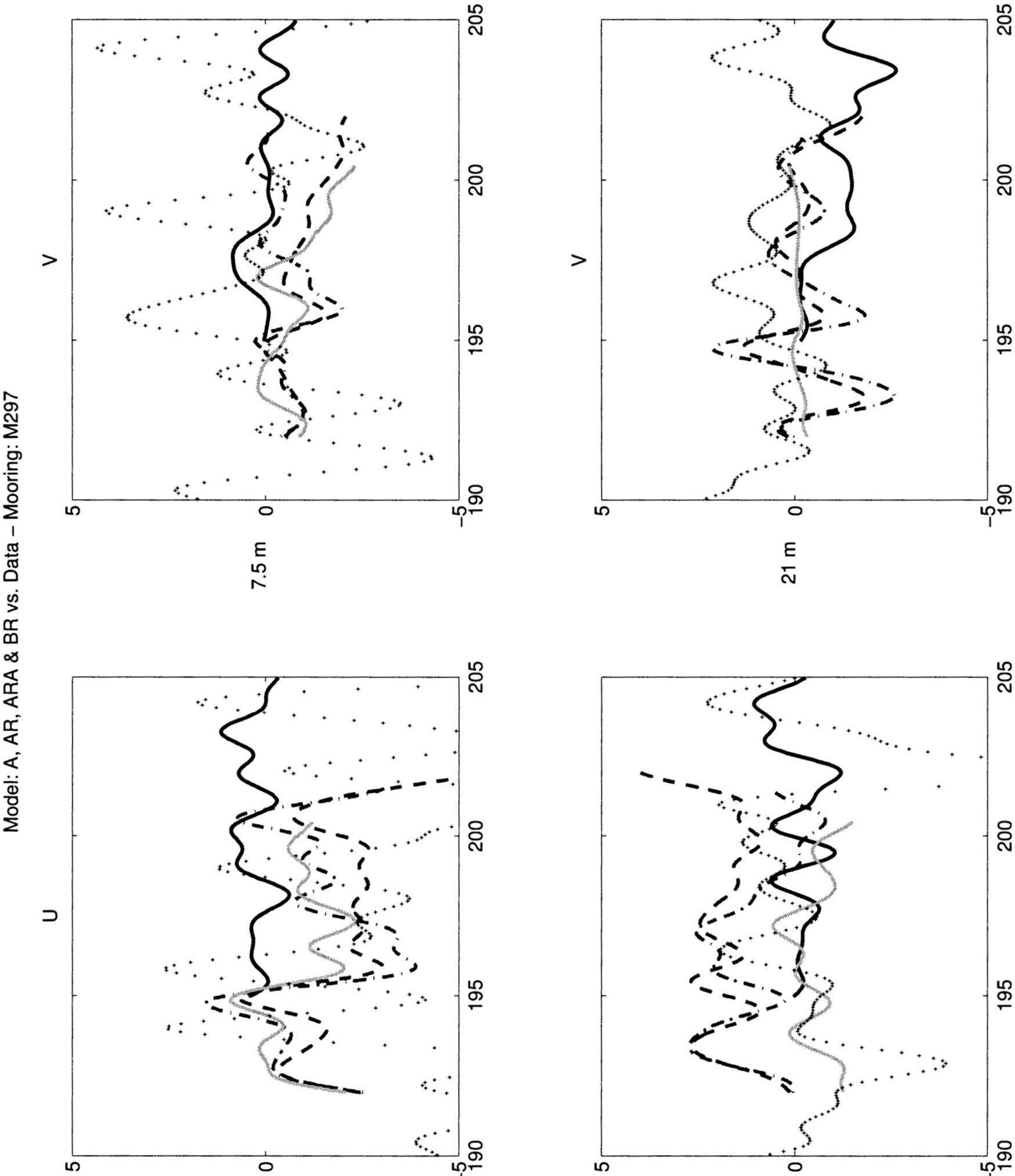

Figure 5.28 Residual Currents at M2-97 - Mixing Models: Model A (solid black line); **Model AR** (dashed black line); **Model ARA** (dash dot black line); **Model BR** (dashed gray line); **Model BRA** (dash dot gray line) and the **observed** residual currents (+).

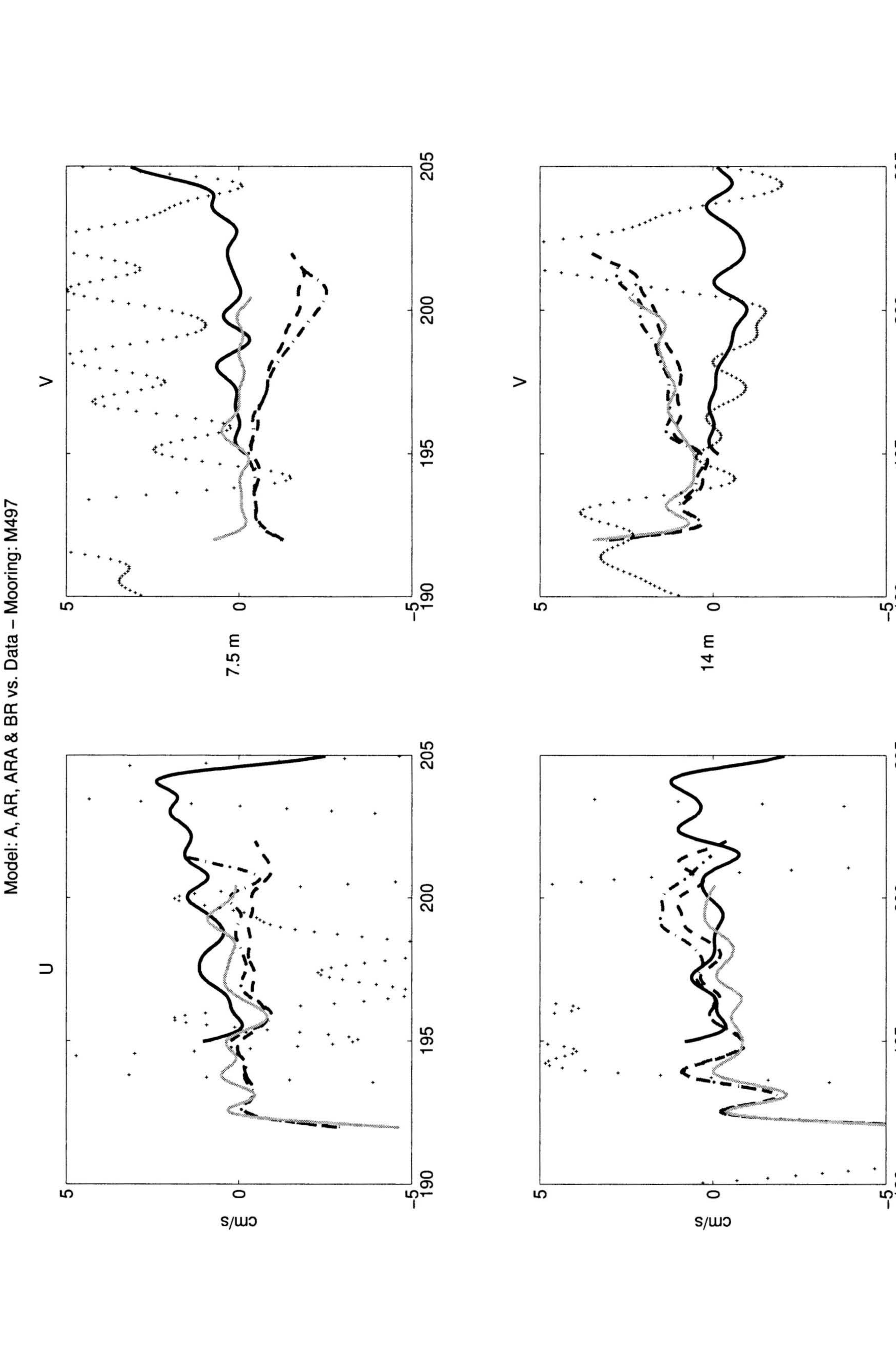

Figure 5.29 Residual Currents at M4-97 - Mixing Models: Model A (solid black line); **Model AR** (dashed black line); **Model ARA** (dash dot black line); **Model BR** (dashed gray line); **Model BRA** (dash dot gray line) and the **observed** residual currents (+).

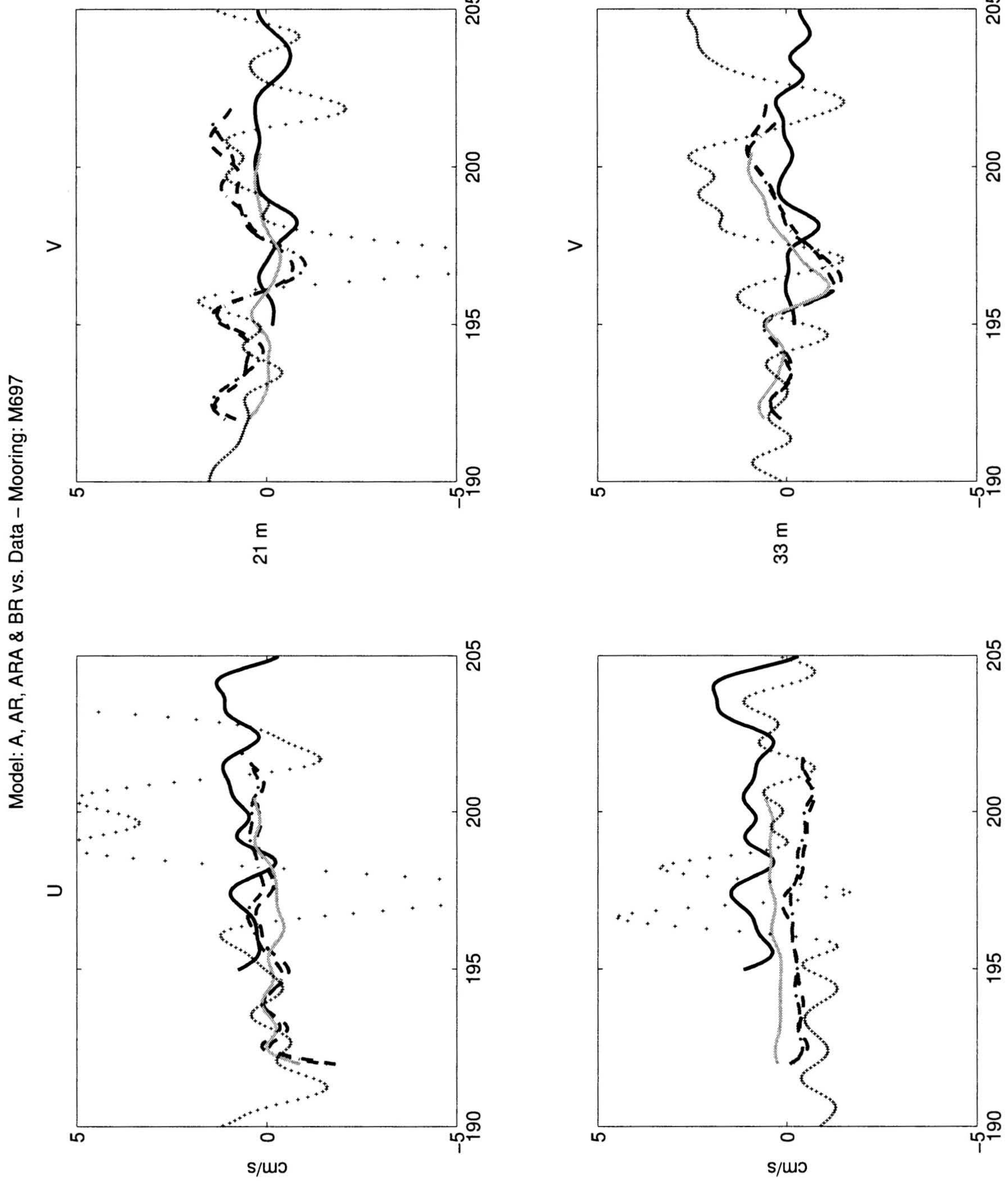

Figure 5.30 Residual Currents at M6-97 - Mixing Models: Model A (solid black line); **Model AR** (dashed black line); **Model ARA** (dash dot black line); **Model BR** (dashed gray line); **Model BRA** (dash dot gray line) and the **observed** residual currents (+).

5.4 Summary

With the introduction of mixing into the model, the tidal analysis indicates that mixing of temperature and salinity play an important role in the development of the tide as it propagates through the inlet. Seaward of the sill the main tidal constituents are reasonably represented at moorings M4-96, M5-97, M6-97 and M7-97. The additional damping and relaxation at the mouth appears to reduce the model performance at M5-96. It may be possible to extend the model domain or reduce the amount of relaxation imposed at the mouth to provide a better tidal simulation at M5-96.

The model output also indicates a large loss of tidal energy as the tide crosses over the sill. Neither friction nor the addition of the dissipative term to smooth the solution would appear to explain this loss of energy. A comparison of the strength of the M_6 tidal currents and the M_2 tidal currents at the sill indicates that the strength of the frictional tidal constituents in the model matches the ratio found in the observations. However, at M3-96 and M4-97, the tide is significantly weaker than the observed tide having an M_2 tidal current which is at best 70% of the observed tide even though the tidal currents were found to match quite well at those moorings located seaward of the sill and away from the mouth of the model domain (such as M4-96).

The strong relaxation, of temperature and salinity, required for numerical stability when the scalar fields evolve suggests that the loss of energy from the tide may be the result of overmixing. The energy from the tide may be transferred into the mixing of temperature and salinity by the turbulence scheme. In the absence of a relaxation scheme the model is unable to maintain numerical stability even over a slow ramping of the tidal force. When relaxation of temperature and salinity is introduced, the turbulence scheme will still remove energy from the tides and transfer it into the mixing of temperature and salinity. However, the relaxation scheme artificially damps the amount of mixing and by doing so removes the energy completely from the model. This may explain the loss of tidal energy in the neighbourhood of the sill.

The averaging process used to enhance mixing, allowing the background scalar fields to evolve, is simplistic. It is a simple approach that permits a slow evolution of the scalar fields as if the temperature fields were evolving on different time scales. A more realistic approach may be to recast the governing equations within the model by applying a multiple scales technique. For such an approach the appropriate time scales for this type of modeling would appear to be the period of the dominant tidal forces although other time scales may be appropriate depending on the processes being studied. The averaging technique used only accounts for the temporal variations at a fixed location, it does not account for the propagation of internal waves or baroclinic fronts within the model domain. It is evident from the results of the tidal analysis that the simplistic approach used in this model does not greatly influence the structure of the main tidal constituents (M_2, K_1) but does appear to have a significant impact on the nonlinear (MS_f, M_4) and frictional tidal constituents (M_6) derived from the main forcing. In some cases the enhanced mixing produced a better match to the nonlinear and frictional tidal constituents while in other case it was found to overestimate the magnitude.

One obvious advantage to allowing some temporal evolution in the background scalar fields is the ability of the model to permit a transfer of thermal energy at the surface and also the possibly of a fresh water source. If the background temperature and salinity fields are held constant the addition of a thermal energy flux at the surface and/or the addition of a fresh water source would be significantly damped by the strong relaxation period required to maintain numerical stability when temperature and salinity are allowed to mix within the model. Without an evolving background scalar field, the addition of a surface heat flux or fresh water will lead to numerical instability.

At present the model is unable to reproduce any of the residual circulation of the inlet when forced by winds and tides. There are numerous possibilities that may explain this. One possibility is that the wind field used was not representative of the true wind field at Clode Sound. The absence of meteorological data collected at the site made this necessary and unavoidable. However, in the absence of an accurate wind field, the model was unable to reproduce the variability of the residual circulation found in the observations. This may be partially accounted for by the reduction of the wind stress in the surface layer of the internal mode. However, without this reduction, the model was unable to produce any simulation as the vertical shear produced in the surface layer was too great.

The addition of a surface wind stress remains a problem at this resolution. With only 10 sigma levels in the model, surface wind stress induces a strong vertical shear in the upper layers of the model. A recent revision of the turbulence scheme (PROFQ) for the POM model (Mellor and Blumberg, 2004) that includes the effects of wave breaking in the surface layers of the model has been proposed. Attempts have been made to implement this latest revision of the turbulence scheme but, at present, the model remains numerically unstable. The cause of the numerical instability in the model with the new turbulence scheme has not been investigated.

Chapter 6 Conclusion

"Oh, I've had such a curious dream!" said Alice. And she told her sister, as well as she could remember them, all these strange Adventures of hers, that you have just been reading about;

- Lewis Carroll
Alice's Adventure in Wonderland

The CTD surveys and submerged moorings deployed in 1996 and 1997 are the first studies of the circulation in Clode Sound. The CTD surveys were conducted along the main axis of the inlet extending from the head to the mouth during both 1996 and 1997. The submerged moorings deployed in 1996 were also located along the axis used for the CTD survey. In 1997, the moorings were placed in an array to measure temperature, salinity and velocity in the vicinity of the sill.

The analysis of the CTD and mooring data in chapter 2, presents a brief description of the temperature and salinity characteristics of Clode Sound during 1996 and 1997 as well as an analysis of the main tidal constituents that act as the primary driving force of the circulation. Other factors that influence the circulation of the inlet are wind stress, solar radiation and fresh water input from the Northwest River. In addition to the description of the temperature, salinity and tides of Clode Sound, chapter 2 also includes an assessment of the proportion of energy associated with the surface wind stress, diurnal and semi-diurnal tidal frequencies at each of the mooring locations. The residual circulation, based upon the mooring data, is also discussed and an attempt to relate selected mixing events to physical causes has been presented.

Analysis of the temperature data measured at the moorings in 1996 and 1997 indicates that average change in temperature above the level of the sill is uniform. In

1996 the temperature of the water at 10 metres depth increased at a rate of 0.16 to 0.17 degrees Celsius per day and in 1997 the rate of increase was 0.08 to 0.09 degrees Celsius per day at 7.5 metres depth. The temperature increases in 1996 are 3 times greater than the average temperature increase calculated from a linear approximation to the annual harmonic at station 27 for the period of observation. The increases in 1997 are 2 times greater than the trend calculated from the harmonic. Below the level of the sill, the mixing rates are different on each side of the sill. Seaward of the sill, the increase of temperature at 30 to 50 metres depth is equal to or greater than the estimate from the annual harmonic in both 1996 and 1997. The deeper water of the inner basin remains much colder, average temperature changes of water trapped by the sill are only ½ those estimated from the annual harmonic at station 27. The difference in the temperature signals indicates that vertical mixing on each side of the sill occurs at different rates.

A comparison of temperature and salinity of the bottom water of the inner basin to the temperature and salinity measured at station 27 indicates that the inner basin water forms between January and April of the preceding winter. It is expected that this inner basin water is not renewed until the following winter although at present there is no data in support of this hypothesis. The inner basin water is trapped by the sill during the summer months when the water column begins to warm and mixing on the seaward side of the sill creates a surface layer that extends below the depth of the sill.

In both 1996 and 1997, the deepening of the surface layer below sill depth occurred between Julian Days 211-220. The timing of this event may be predictable. The main source of fresh water is the Northwest River that flows into the head of the inlet. Flow rates, for this river, are typically very low (5 m^3/s) and the formation of the surface layer is dependent upon the water column becoming thermally stratified. It is reasonable to assume that the amount of heat required to deepen the surface layer below the sill is not available until late July or early August which would make the deepening of the surface layer below the sill an annual event. Based upon only two years of observations, however, it is not possible to draw a strong conclusion.

The enhanced mixing on the seaward side of the sill may result from supercritical flow at the sill during spring tides. Based upon a two-layer model, it was shown that supercritical flow may occur, at the sill, during spring tides. Supercritical flow at the sill may lead to the formation of hydraulic jumps and/or internal bores that may propagate away from the sill and increase the amount of vertical mixing. The inflow of fresh water at the head of the inlet increases the bouyancy of the water column towards the sill and may prevent internal waves from propagating into the inner basin. On the seaward side of the sill, bouyancy decreases and may permit the propagation of such internal structures. This may help to explain the differing rates of vertical mixing on either side of the sill.

Tidal forces at the sill account for 50-60% of the fluctuating kinetic energy. Away from the sill, tidal forces are balanced by wind stress in both the inner basin and outer channel with both representing 20%-30% of the total energy in the surface layer in 1996. Closer to the sill, the velocity data from the mooring array in 1997 indicate that tidal forces account for 30%-40% of the total energy while meteorological forces account for only 15%-20%.

During periods of slack water, the moorings located at the sill indicate a weak exchange flow. Some of this exchange flow may represent estuarine circulation during periods of high fresh water inflow. However, 70% of the exchange flow was reversed with surface waters flowing into the inner basin. Such events were observed to occur during neap tides. Steady easterly winds may drive surface waters across the sill and towards the head of the inner basin. When tidal forcing is weakest, the resulting pressure gradient may be strong enough to drive currents back across the sill. Such an event was found to occur between days Julian days 190 and 192 of the 1996 observations.

Tides are the dominant force driving the circulation across the sill. The dominant tidal frequency is the lunar semi-diurnal constituent, M_2. The amplitude of the M_2 tide is approximately 30 cm that may drive a tidal current of up to 14 cm/s at the sill. Within the inner basin, the phase of the M_2 tidal current indicates that internal tides and friction may have significant influence on the circulation. Across the inner basin, the 1997 data indicates that the tidal currents are not symmetrical with the tide stronger along the northern coastline. This is most likely a consequence of the orientation of the coastline and bathymetric contours and may result in a tidally driven eddy located near the sill.

Analysis of the tides in Clode Sound also revealed a secular behaviour in the tidal forcing across the sill. Two distinct secular behaviours were identified. The strength of the M_2 current was found to decrease coincident with the formation of the surface layer below sill depth. Examination of the kinetic energy associated with the tide across the sill suggests that the tidal energy may be transferred into vertical mixing on the seaward side of the sill once the surface layer reaches below sill depth. Within the inner basin, the tidal signals appear to be modulated, the period of modulation was estimated to be approximately twice the lunar monthly constituent M_M. As the observation periods were quite short it is not possible to determine the cause of this modulation or how "regular" it is.

The residual currents and de-tided temperature and salinity signals from Clode Sound indicate the occurrence of large mixing events. These events may be caused by a sudden increase in the flow of fresh water from the Northwest River or the sudden intrusion of cold saline water from the mouth of the inlet. An increase in fresh water at the surface may result in downwards mixing on the seaward side of the sill. When density is restored in the outer channel, interfacial waves may propagate towards the head of the inner basin. When an intrusion of cold saline water occurs, the sill acts to block the flow. This may result in a large degree of mixing in the outer channel but have minimal effect on the circulation of the inner basin.

Chapter 3 describes coding changes to the Princeton Ocean Model that were necessary to apply this model to the Clode Sound Domain. The necessary changes include: 1.) The introduction of partial cells along the coastline to correct an error in the volume flux used in the calculation of the surface elevation and velocity. 2.) Re-masking of flux calculations in the advection operators to eliminate non-zero fluxes through solid boundaries. 3.) The introduction of a dissipation operator that acts to suppress noise in the nonlinear terms and also as side-wall friction; 4.) A reduction of the surface wind stress applied in the top sigma level to reduce the vertical shear in the velocity field that is a consequence of the surface boundary condition in the calculation of turbulence scheme. An attempt to address the surface boundary condition in the turbulence calculation (subroutine PROFQ) has recently been proposed (Mellor and Blumberg, 2004). Assessment of the new turbulence algorithm has not been included in this thesis. The author is unaware of any existing versions of the POM code that include the other coding changes.

The calculation of temperature and salinity mixing in the model required the inclusion of strong relaxation for the scalar fields. The required relaxation time was equal to ¼ of the period of the dominant M_2 tide used to force the model. To compensate for the strong relaxation that results from the short relaxation time scale (approximately 3.1 hours), an algorithm that permits the background scalar fields to evolve on a slower time scale is also presented in chapter 3. The scalar fields are averaged over a tidal cycle and the background fields are updated with the average value after every complete period of the main M_2 tidal forcing.

The development of the model domain is also described and open boundary conditions used by the model are included in chapter 3. Development of the domain required significant smoothing of the bathymetry to avoid hydrostatic inconsistency within the model domain. Any attempts to execute the model with a hydrostatic inconsistent density field were found to be numerically unstable. An elementary explanation of error propagation on the sigma grid used by the POM model is presented to explain some of the difficulties encountered in the application of the model to Clode Sound.

A nonlinear model was shown to be necessary in chapter 4 to study the circulation in Clode Sound. A linear model was unable to reproduce the formation of a tidal jet in the region of the sill. A comparison of model simulations with a statically stratified fluid to the tidal data was conducted to assess the influence of the depth of the surface layer on the tidally forced flow within the inlet. Based upon the CTD data collected during 1996 and 1997, the depth of the surface layer was chosen to lie above, at and below the level of the sill. With temperature and salinity held constant the simulations revealed that the location of the main pycnocline had very little influence on the structure of the main diurnal and semi-diurnal tidal constituents. The simulations for a stratified fluid did not reveal any significant difference compared to the nonlinear simulation for a barotropic fluid.

The tides calculated by the statically stratified models were, generally, found to be much weaker than those observed in Clode Sound. In particular, the strength of the K_1 and M_2 tidal currents at the sill were found to be equal to no more than 50% of the observed tidal currents at the moorings located in the sill region in 1996 and 1997. The tidal currents of the near surface region of the model (7.5 and 10 metres depth) were also shown to be much weaker than the observed tidal currents. Below the surface region, the orientation of the tidal ellipses, estimated from the model, are found to be in close agreement with the observed orientations. The direction of the tidal currents in Clode Sound is controlled by the orientation of the coastline and bathymetric contours. Differences between the orientations of the main tidal constituents in the surface region is attributed to the influence of wind stress in Clode Sound; wind stress was not included in the model simulations used in comparison of the tidal structure. The Greenwich Phase estimated from the model data was nearly constant throughout the water column at all mooring locations indicating that the tide in the statically stratified models was barotopic in constrast to the baroclinic tidal structure observed within the inner basin. At the sill and seaward of the sill, the agreement between the Greenwich Phase estimated from the data and the Greenwich Phase of the models was reasonable. Shallow water constituents, generated by nonlinearities (MS_f, M_4, MS_4, and S_4) and friction (M_6, $2MS_6$ and $2SM_6$), are suppressed in the model simulations.

The modelled data indicates that the majority (85%-90%) of the energy in the semi-diurnal tide is extracted between the mouth of the model domain and the sill, in contrast to the 80%-90% of energy dissipation observed in the inner basin. The dissipation of energy in the diurnal tidal constituent, K_1, was also higher on the seaward side of the sill of the model (65%) than observed (15%). Only for constituent O_1 was the model able to reproduce the observed rate of energy dissipation in the model domain. The high loss of energy on the seaward side of the sill in the model does not appear to be a consequence of friction. If frictional forces were responsible for the energy loss in the model, the Greenwich Phase of the modelled tide should differ signifcantly from the observed Greenwich Phase.

The lack of tidal energy within the inner basin of the model leads to an imbalance of the physical forces driving the circulation when wind stress is applied. When wind stress was applied to the model, the direction of the principle axis was found to be in good agreement with the principle axis calculated from the mooring data. The agreement between the model and the observation in the surface region appears to correct for the discrepancy between the modelled and observed orientation of the tidal ellipses. A comparison of the energy spectrum of the model and the observed velocities indicates that within the model wind stress dominates the circulation of the inner basin. The meteorological frequency band accounted for almost 50% of the total energy at M1-96 in the model compared to only 10% in the observed energy spectrum. At M2-96, closer to the sill, the model energy spectrum reveals that 70%-80% of the energy is located in the semi-diurnal frequency band compared to the 30% located in this frequency band estimated from the mooring data. The observed velocities M2-96 indicate that 20% of the energy at this location may be attributed to meteorological effects; the models indicated that meteorological forces contributed to less than 10% of the total energy at this location. The difference between the balance of forces at M1-96 and M2-96 may be attributed to several factors. Tidal energy is very weak within the inner basin of the model as indicated by the high dissipation rates seaward of the sill. As discussed in chapter 3, wind stress was tapered towards the coastline and also scaled by a constant Ekman depth to eliminate numerical instabilities. At M2-96, even though the tidal energy is weaker than observed, the wind-stress is also very weak as a consequence of the tapering and scaling. At this particular location in the model domain, tidal forces are the dominant driving force. At M1-96, tidal energy had been further dissipated and wind stress is stronger as the tapering of the wind field has no effect at this location on the grid.

At the sill, 95% of the energy is located in the semi-diurnal frequency band compared to 60%-65% identified at this frequency band in the mooring data. Although semi-diurnal energy dominates, at this location, the model suggests that signal at the sill is more coherent and less energy is being transferred into high frequency energy. Semi-diurnal tidal energy also dominates on the seaward side of this sill, however, the percentage of energy located in the meteorological band at both M4-96 and M-96 in the model agrees reasonably well with the observations. At M4-96, 80% of the energy was located in the semi-diurnal frequency band, much greater than the 20% identified in the observed velocity field. At M5-96, 45%-85% of the energy was concentrated at semi-diurnal frequencies, compared to 15%-35% observed. The difference between the model and observations indicates that the model is unable to transfer energy from the main semi-diurnal tide into higher frequencies. The amount of high frequency energy that remains unexplained in the observations is significantly greater than that found in the model suggesting that the energy is being transferred into these higher frequencies and may be available for mixing. The rate of energy dissipation on the seaward side of the sill is very high in the model. This energy appears to be lost in either the model's turbulence or friction schemes. The energy is not transferred into the nonlinear or frictional tidal constituents, as these remain very weak in the model. The Greenwich Phases of the main tidal constituents of the models are, generally, in agreement with the observed tidal phase seaward of the sill. If frictional forces were too high in the model, agreement between the Greenwich Phase of the model and observations is not expected. It is evident that turbulence closure scheme may require an adjustment of the parameters to work effectively at the high (50 metre) horizontal resolution used by this application.

The residual circulation of the model, generated by tides and winds is discussed at the end of chapter 4. The model indicates the formation of a tidally induced residual circulation in the vicinity of the sill. The variation of the phase of the observed tide across the inner basin and orientation of the principle axis indicates that the formation of an eddy on either side of the sill is probable. However, the formation of the eddy on the sill, as indicated by the model seems unlikely. The smoothing algorithm used to prepare the model bathymetry resulted in a wider and deeper channel in the region of the sill, that does not reflect the true bathymetry of this region. When wind stress is used in the model simulations, the model indicates the formation of a large eddy forming across the inner basin inwards of the sill. Another eddy appears at the head of the inlet. While these structures may possibly form within the inner basin, the imbalance of the driving forces of wind stress and tides within the model makes it impossible to draw a strong conclusion. When the de-tided velocity fields from the model are compared to the de-tided mooring data, the model fails to replicate the observed strength or variability of the residual currents. It is also found that the residual circulation of a stratified fluid in the model does not vary significantly from the residual circulation of the barotropic model.

The results discussed in chapter 4 indicate that when the model is executed with a static density field, the influence of stratification on the velocity fields is minimal when compared to a 3-dimensional barotropic model. Neither the barotropic model nor the stratified models are able to reproduce the tides or correct energy balance of the circulation driven by wind stress and tidal forcing. There is little evidence to justify the imposition of stratification on the model without permitting temperature and salinity to mix.

Chapter 5 examined model simulations that included the mixing of temperature and salinity. The inclusion of mixing for temperature and salinity in the model required very strong relaxation of the scalar fields. The relaxation scheme requires the scalar fields be relaxed at a rate equal to ¼ of the period of dominant tidal forcing (M_2).

Typical relaxation schemes used in larger scale models use a pre-determined climatology for the background scalar fields. With no such climatology available for Clode Sound, the scalar fields were relaxed towards the initial temperature and salinity used by the model. However, in recognition of the strong mixing across the sill, evident in the CTD and mooring data, the relaxation of temperature and salinity towards the initial scalar fields at the time scale required to maintain numerical stability, may inhibit mixing of the scalar fields. To compensate for the strong relaxation, a simplistic averaging scheme is employed by the model that allows the background scalar fields to evolve a temporal average over the period of the dominant M_2 tidal forcing.

Chapter 5 explored the effect of this averaging scheme by comparing the tidal structure of the model with and without the averaging scheme. The resulting simulations are also compared to the case of the statically stratified models presented in chapter 4 and to the mooring observations of 1996 and 1997. Additional simulations with the addition of wind stress attempt to assess the ability of the model to simulate the residual circulation.

At the sill, the tides are much weaker than the observed tides. The inclusion of temperature salinity mixing into the model did not significantly improve the abiltiy of the model to simulate the velocity field at the sill. The mooring data from the sill in 1996 and 1997 indicated that, during a spring tide, the flow at the sill may be supercritical. Velocities at the sill, generated by the model, were always subcritical. The weakness of the velocities generated by the model may be attributed to the disproportionate volume increase at the sill that resulted when the local bathymetry was smoothed to satisfy the condition of hydrostatic consistency. It should be possible to improve model performance, in the region of the sill, by narrowing the modelled sill width so that the volume of the modelled sill is in the correct proportion to the volume of the outer channel and inner basin.

The tidal flow towards the mouth of the model domain was also much weaker than observed. The modelled tides in this region of the model remained barotropic and are most likely influenced by the open boundary conditions that imposed additional relaxation of temperature and salinity at the mouth of the inlet. Within the inner basin, the dissipation of the tidal signal towards the head of the inlet is still very strong. The inclusion of mixing did not significantly improve the ability of the model to simulate the tides towards the head of the inner basin.

Between the sill and the ends of the model domain (the head and mouth of the inlet), the ability of all of the models that include mixing of temperature and salinity indicate a significant improvement compared to the statically stratified models presented in chapter 4. With the inclusion of mixing, K_1 and M_2 tidal currents generated by the model on either side of the sill increased, matching the observed tides at several locations. The modelled tides were baroclinic as opposed to the barotropic tides generated by the models in which the density field was held constant. The modelled tides also indicated a greater variation in the Greenwich Phase. The resulting phase of the tides indicates mixed results when compared to the mooring observations. At some locations the modelled tidal currents provided a very good simulation of the observed tidal behaviour in both strength and phase and in locations the tidal currents were found to be out of phase with the observed tide. The mixing models were run with the same lateral dissipation and bottom friction used in the statically stratified models, some improvement to the phase estimates within the model may be possible by adjustment of the these terms.

The most significant difference between those mixing models that employed the averaging scheme to permit evolution of the background temperature and salinity fields to those that did not was found in the nonlinear and frictional tidal constituents. Both types of models showed a stronger MS_f current. At many locations, there was little difference between the resulting MS_f signal generated by either type of model. Comparison of model MS_f to the observed tide were rather mixed. At some locations the matching of MS_f was found to be very good but was also relatively poor at other locations with the MS_f signal in the model being either too weak or too strong compared to the observed tidal current.

The most significant difference between the two model types was found in the higher frequency nonlinear constituents M_4, MS_4, S_4, and frictional constituents M_6, $2MS_6$ and $2SM_6$. With the strong relaxation used by the model, there is a tendency for higher frequency oscillations to be damped. The statically stratified models in chapter 4 generated almost no significant higher frequency tidal constituents. When temperature and salinity mix, both nonlinear and frictional tidal constituents begin to grow. However, the strong relaxation used in the model damps the growth of these constituents and they are typically weaker than observed. It is only with the inclusion of the averaging scheme, allowing the background scalar fields to evolve, that the model is able to generate nonlinear and frictional tidal constituents that begin to match the strength of the observed tide. However, matching the model to the observations for these tidal constituents is a difficult task. The signal to noise ratio is very low, providing a large degree of uncertainty in any such comparison.

When wind stress was applied to the models that included the mixing of temperature and salinity, numerical instabilities became very difficult to overcome. Most simulations with wind stress became numerically unstable after only 10 days of simulated time. Assessment of the distribution of energy resulting from these simulations contains a large degree of uncertainty. A true assessment of the energy distribution in the meteorological frequency band, 0.1-0.5 cycles per day, is not possible when only 10 days of model output are available for analysis. Some variation in the models was evident but the results are not conclusive.

The residual circulation resulting from the inclusion of temperature and salinity mixing does indicate that the inclusion of mixing into the model does increase the variability and strength of the residual currents compared to the residual circulation generated by the statically stratified models. The variability of the residual flow when background scalar fields evolve over time compared to those in which the background fields are held constant does not consistently increase at all locations. None of the models are unable to match the circulation observed at the moorings in 1996 and 1997. There may be many reasons for this, including uncertainty in the wind field used to force the model and the actual density structure of Clode Sound.

It is clear that temperature and salinity mixing must be included in any attempt to model the circulation of Clode Sound, it is likely that this holds true for simulations of other similar small inlets and bays as well. The results of chapter 5 suggest that the addition of an evolving background scalar field does not significantly effect the ability of the model to simulate the tides. The tidal analysis of the model data reveal some variation in the velocity field with the inclusion of the averaging process but it is not clear the overall performance of the model was either improved or degraded by this feature. However, the inclusion of an evolving background field should enable the model to include surface heating and possibly a fresh water source. If the averaging process is not included, the strong relaxation used by the model would inhibit the transfer of heat and fresh water down through the water column.

The performance, of the model, in simulating the tides of Clode Sound limit its use as a diagnostic tool to study the mixing in the region of the sill. Before a study of the mixing processes may begin, the model domain must be corrected to adjust for the disproportionate volume at the sill. This should increase the strength of the tidal currents at the sill but may lead to an increase in the numerical difficulties. The observed flow across the sill was shown to reach speeds that indicate supercritical flow. This may lead to the formation of hydraulic jumps and internal bores. The Princeton Ocean Model is a hydrostatic model. It is not clear that the use of such a model is appropriate to study the circulation in a region where the hydrostatic assumption may not hold to be true.

Additional numerical issues exist that may or may not be resolvable. The inclusion of wind stress in the model is found to lead to the rapid onset of numerical instability. The recent changes to the turbulence scheme proposed by Mellor and Blumberg (2004) may or may not reduce the instability. Attempts to implement this new algorithm have shown little improvement in the model performance of this particular application. The loss of tidal energy in the model appears to be a consequence of the turbulence scheme. At a 50 metre horizontal resolution it seems very likely that the parameters of turbulence scheme need to be adjusted. Such a study will require a detailed study of the vertical diffusivities and turbulent energy of the model. The complex domain of Clode Sound would only compound the difficulties of the turbulence adjustment. An attempt to adjust and test the turbulence scheme at this fine of a horizontal resolution should be conducted in a much simpler and more idealized domain where changes in geometry and bathymetry may be controlled.

Bibliography

Adcroft, A., C. Hill and J. Marshall, 1997. Representation of topography by shaved cells in a height coordinate ocean model. *Monthly Weather Review* 125: 2293–2315

Afanasyev, Y. D. and W.R. Peltier, 2001a. On breaking internal waves over the sill in Knight Inlet. *Proc. R. Soc. Lond. A* 457: 2799-2825

Afanasyev, Y. D. and W.R. Peltier, 2001b. Reply to comment on the paper 'On breaking internal waves over the sill in Knight Inlet'. *Proc. R. Soc. Lond. A* 457: 2831-2834

Allen G. L. and J. H. Simpson, 2002 The Response of a Strongly Stratified Fjord to Energetic Tidal Forcing, *Estuarine, Coastal and Shelf Science* 55: 629-644

Armi, L., 1986, The hydraulics of two flowing layers with different densities. *J. Fluid Mech.* 163: 27–58

Armi L. and D.M. Farmer, 1986, Maximal two-layer exchange through a contraction with barotropic net flow. *J. Fluid Mech.* 164 : 27-51.

Baines, P.G., 1988.A general method for determining upstream effects in stratified flow of finite depth over long two-dimensional obstacles, *J. Fluid Mech.* 188: 1-22

Beckmann, A. and D.B. Haidvogel, 1993. Numerical Simulation of Flow around a Tall Isolated Seamount. Part1: Problem Formulation and Model Accuracy, *J. Phys. Ocean* 23: 1736-1753

Bell, T.H., 1975. Lee waves in stratified flows with simple harmonic time dependence. *J.F.M.* 67 (1975), pp. 705–722.

Blackford, B.L., 1978. On the generation of internal waves by tidal flow over a sill - a possible nonlinear mechanism, *J Mar Res.* 36: 529-549

Blumberg, A.F. and G.L. Mellor, 1987. A description of a three-dimensional coastal ocean model. In: Heaps, N., (ed.). *Three dimensional Shelf Models Coastal Estuarine Sci.* vol. 5, AGU, Washington, BC, pp. 1–16

Blumberg, A.F., L.A, Khan and J.P. St. John, 1999, Three-dimensional hydrodynamic model of New York Harbor region, *Journal of Hydraulic Engineering* 125: 799-816

Bourgault D. and D.E. Kelley, 2004. A Laterally-Averaged Nonhydrostatic Ocean Model, *Journal Atmos. And Oceanic Tech.*, submitted

Bowden, K.F., 1983. *Physical Oceanography of Coastal Waters*, Ellis Horwood, London, 302pp.

Brooks, D.A., M.W. Baca and Y.-T. Lo, 1999, Tidal Circulation and Residence Time in a Macrotidal Estuary: Cobscook Bay, Maine, *Estuarine, Coastal and Shelf Science,* 49: 647-665

Browning. G.L., W.R. Holland, H.-O. Kreiss and S.J. Worley, 1990. An Accurate Hyperbolic System for Approximately Hydrostatic and Incompressible Oceanographic Flows, Dyn. Atmos. Oceans 14: 303-332

Brown, R.D. and V.R. Swail, 1988. Spatial Correlation of Marine Wind-Speed Observations, *Atmos-Ocean*, 26: 524-540

Cartwright, D.E., 1999, Tides: A Scientific History, Cambridge University Press: New York, 292pp

Casulli, V. and R.T. Cheng, 1992. Semi-implicit finite difference methods for three-dimensional shallow water flow, *International Journal for Numerical Methods in Fluids, Volume* 15: 629-648

Chapman D.C., 1985. Numerical treatment of cross-shelf open boundaries in a barotropic coastal ocean model. *Journal of Physical Oceanography* 15, pp. 1060–1075

Colbourne, E.B., 2004, Decadal Changes in the Ocean Climate in Newfoundland and Labrador Waters from the 1950s to the 1990s, *J. Northw. Atl. Fish. Sci.* 34: 41-59

Craig, P.D., 1987. Solutions for internal tidal generation over coastal topography. *J. Mar. Res.* 45, pp. 83–105.

Cummins, P.F. 2000, Stratified flow over topography: time-dependent comparisons between model solutions and observations. *Dynam. Atmos. Oceans* 33: 43-72

Dietrich D.E., M.G. Marietta and P.J. Roache, 1987. An Ocean Modelling System with Turbulent Boundary Layers and Topography. *Int. J. Numer. Methods Fluids*, 11: 127-150

Darwin, G.H., 1898. The Tides and Kindred Phenomena in the Solar System, London: J. Murray, 342pp

Das, P., P. Marchesiello and J.H. Middleton, 2000. Numerical Modelling of tide-induced residual circulation in Sydney Harbour, *Marine and Freshwater Research* 51: 97-112

Dyer, K.R., 1973. *Estuaries: A Physical Introduction*, Wiley: London

Emery, W.J. and R.E. Thomson, 1998, Data Analysis Methods in Physical Oceanography, Pergamon, 634pp

Farmer, D.M. and L. Armi, 1986. Maximal two-layer exchange over a sill and through the combination of a sill and contraction with barotropic flow. *Journal of Fluid Mechanics* 164: 53–76.

Foreman, M. G. G.,1977. *Manual for tidal heights analysis and prediction* (58 pp.). Pacific Marine Science Report 77-10, Sydney/British Columbia: Institute of Ocean Sciences.

Freeland, H.J. and D.M. Farmer, 1980. Circulation and energetics of a deep, strongly stratified inlet. *Canadian Journal of Fisheries and Aquatic Science* 37: 1398–1410.

Freeland, H.J. and D.M. Farmer, 1983. The physical oceanography of Fjords, *Progress In Oceanography,* 12: 147-194

Gade, H.G. and A. Edwards, 1980. Deep-water renewal in fjords. *In: Freeland, H., Farmer, D., Levings, C. (Eds.), Fjord Oceanography. NATO Conference Series, Vol. 4,* Plenum Press, New York, pp. 453–489

Gargett, A.E. 1980, Turbulence Measurements Through a Train of Breaking Internal Waves in Knight Inlet, B.C. in Fjord Oceanography, ed. Freeland, H.J. and Farmer, D.M, Plenum Publ..

Godin, G., 1972, The Analysis of Tides, Liverpool University Press, 264pp.

Han, G., 2000, Three-dimensional modeling of tidal currents and mixing quantities over the Newfoundland Shelf. *JGR,* 105, C5: 11407-11422

Haney, R.L., 1991. On the pressure-gradient force over step topography in sigma coordinate ocean models. *J. Phys. Oceanogr.* 21:610-619

Hibiya, T., 1986. Generation Mechanism of Internal Waves by Tidal Flow Over a Sill, *JGR* 91 (C6): 7697-7708

Janjić, Z.I., 1977. Pressure gradient force and advection scheme used for forecasting with steep and small scale topography. *Contributions in Atmospheric Physics* 50: 186–199.

Jay D.A and J.D. Musiak, 1996. Internal tidal asymmetry in channel flows: origins and consequences. In: Pattiaratchi, C. (Ed.), Mixing processes in estuaries and coastal seas, an AGU Coastal and Estuarine Series Monograph, Washington, DC, pp. 219–258

Kantha, L.H. and C.A. Clayson, 2000, Numerical Models of Oceans and Oceanic Processes, International Geophysics Series, V.66, London: Academic, 940pp

King, B. and E. Wolanski, 1996. Bottom Friction Reduction in Turbid Estuaries. in: Mixing in Estuaries and Coastal Seas, C. Pattiaratchi (ed.), Coastal and Estuarine Studies, 50: 325-337 American Geophysical Union

Klemp, J.B., R. Rotunno and W.C. Skamarock, 1997. On the propagation of internal bores, *Journal of Fluid Mechanics* 331: 81-106

Lazier, J.R.N., 1982 Seasonal Variability of Temperature and Salinity in the Labrador Current, *J.M.R.* 40, supplement: 341-356

Lazier, J.R.N. and D.G. Wright, 1993, Annual velocity variations in the Labrador Current, *J.P.O.* 23: 659-678

Lear, W.H., 1998, History of fisheries in the Northwest Atlantic: The 500-year perspective, *J. Northw. Atl. Fish. Sci.* 23: 41-73

Lewis, R., 1997. Dispersion in Estuaries and Coastal Waters. Wiley: London , 312pp.
Lynch, D.R., J.T.C. Ip, C.E. Naimie, and F.E. Werner, , 1996. Comprehensive coastal circulation model with application to the Gulf of Maine. *Continental Shelf Research* 16: 875-906

Lu, Y., D. Wright and D. Brickman , *Journal of Atmos. And Oceanic Tech.* 18: 1076-1091

Mahadevan A. and D. Archer, 1998. Modeling a Limited Region of the Ocean, *Journal of Computational Physics*, 145: 555-574

Mellor, G. and A. Blumberg, 2004, Wave Breaking and Ocean Surface Layer Thermal Response, *J. Phys. Ocean* 34: 693-698.

Mellor G.L., T. Ezer and L.-Y. Oey, 1994, The pressure gradient conundrum of sigma coordinate ocean models. *Journal of Atmospheric and Ocean Technology,* 11: 1126–1134.

Mellor, G.L. 1998. User's guide for a three-dimensional, primitive equation numerical ocean model. Program in Atmospheric and Oceanic Sciences, Princeton University Technical Report, Princeton, NJ, 38pp.

Mellor, G.L. and T. Yamada, 1982, Development of a turbulent closure model for geophysical fluid problems. *Review of Geophysics* 20 (1982), pp. 851–875.

Oliger, J. and A. Sundstrom, 1978. Theoretical and Practical Aspects of Some Initial Boundary Value Problems in Fluid Dynamics, *SIAM J Appl Math, Volume* 35: 419-446

Pawlowicz, R., B. Beardsley and S. Lentz, 2002, Classical tidal harmonic analysis including error estimates in MATLAB using T_TIDE, *Computers & Geoscience* 28: 929-937

Petrie, B. and C. Anderson, 1983. Circulation on the Newfoundland continental shelf. *Atmosphere-Ocean* 21: 207–226.

Pickard, G.L. and W.J. Emery, 1990. Descriptive Physical Oceanography: An Introduction. Pergamon Press, Oxford, 320pp

Petrie, B., J.W. Loder, S. Akenhead and J. Lazier, 1991. Temperature and salinity variability on the eastern Newfoundland Shelf: the annual harmonic. *Atmosphere-Ocean* 29: 14–36.

Pritchard, D.W., 1952. Estuarine Hydrography. *Advances in Geophysics* 1: 243-280

Pond, S. and G.L. Pickard, Introductory Dynamical Oceanography, 2nd Edition. Pergamon Press, Oxford, 329pp.

Russell, R.C.H. and D.H. Macmillan, 1954 Waves and Tides, 2nd ed. London: Hutchinson

Sheng, J., D.G. Wright, R.J. Greatbatch and D.E. Dietrich, 1998. CANDIE: A New Version of the DieCAST Ocean Circulation Model, *Journal of Atmos. And Oceanic Tech.* 15: 1414-1432

Stacey, M.W. and Y. Gratton, 2001.The energetics and tidally induced reverse renewal in a two-silled Fjord, *Journal of Physical Oceanography, Volume* 31: 1599-1615

Stacey, M.W., S. Pond and Z.P. Nowak, 1995. A numerical model of the circulation in Knight Inlet, British Columbia, Canada. *Journal of Physical Oceanography* 25: 1037–1062.

Stigebrandt, A., 1976. Vertical diffusion driven by internal waves in a sill fjord. *J. Phys. Oceanogr.* 6, pp. 486–495.

Stigebrandt, A.1980, Some aspects of tidal interaction with Fjord Constrictions. *Estuarine and Coastal Marine Science* 11: 151–166.

Thompson, K.R., R.H. Loucks and R.W. Trites, 1988. Sea Surface Temperature Variability in the Shelf-Slope Region of the Northwest Atlantic. *Atmos.-Ocean*, 26

Timko, P.G., 1995, Msc. Thesis: The Turbulent Dissipation of Internal Solitons in a Stratified Fluid of Finite Depth, University of Alberta, Edmonton, Alberta, Canada.

Timko. P.G., B. de Young, B., J. Foley, K. Forward and J. Helbig, 1998a Observations of Currents Temperature and Salinity in Clode Sound, Newfoundland 1996, *Physics and*

Physical Oceanography Data Report 98-2, Department of Physics, Memorial University of Newfoundland, 45pp.

Timko. P.G., B. de Young, B., J. Foley, K. Forward and J. Helbig, 1998b Observations of Currents Temperature and Salinity in Clode Sound, Newfoundland 1997, *Physics and Physical Oceanography Data Report 98-1, Department of Physics, Memorial University of Newfoundland,* 58pp.

Timko, P.G., and G.E. Swaters, 1997 On the dissipation of internal solitons in coastal seas, *Geophysical and Astrophysical Fluid Dynamics* 85: 163-194

Tinis, S.W. and S. Pond, 2001, Tidal energy dissipation at the sill of Sechelt Inlet, British Columbia, *J. P. O.* 31: 3365-3373

Webber, H.H. and H.V. Thurman (Eds.), 1991, Marine Biology 2nd Edition, Harper Collins, New York.`

Appendix A DataTables for C hapter 2

Table A.1: Seasonal Temperature Trend during 1996 (deg/day)

Depth (m)	M1	M2	M3	M4	M5
10	0.166	0.160	0.167	0.172	0.169
15-20	0.091	0.094	0.122	0.137	0.138
45	0.027	0.032	-	0.071	0.072
75	-	-	-	-	0.022

Table A.2: Seasonal Salinity Trend 1996 (PSU/day)

Depth (m)	M1	M2	M3	M4	M5
10	-	-0.015	-0.025	-0.013	-0.020
15-20	-0.007	-0.009	-0.012	-0.011	-0.011
45	-0.002	-0.003	-	-0.006	-0.003*
75	-	-	-	-	-0.007

(*trend calculated from longest set of continuous observations)

Table A.3: Seasonal Temperature Trend 1997 (deg/day)

Depth (m)	M1	M2	M3	M4	M5	M6	M7
7.5	0.095	0.093	0.090	0.091	0.088	-	0.082
10	-	-	-	0.094	-	-	-
15	-	0.090	0.095	0.092	0.091	0.093	0.088
20	0.045	0.052	-	-	0.089	0.084	0.094
25	-	0.034	-	-	-	0.071	-
30	0.023	0.024	-	-	0.057	0.059	0.075
40	0.017	0.018	-	-	0.041	0.039	-
50	0.015	-	-	-	-	-	-

Table A.4: Seasonal Salinity Trend 1997 (PSU/day)

Depth (m)	M1	M2	M3	M4	M5	M6	M7
7.5	-0.012	-0.013	-0.012	-0.016	-0.006	-	-
15-20	-0.004	-0.005	-	-0.008	-0.0142*	-0.008	-0.012
30	-	-0.004	-	-	-	-0.008	-0.011

(*trend calculated from longest set of continuous observations)

Table A.5: Mean (<*>) and Rates of change of Temperature, M_T (°C/day) and Salinity, M_S (PSU/day) calculated from the annual harmonic at Station 27 during the observation periods in Clode Sound.

Depth (m)	<S-96>	M_{S-96}	<S-97>	M_{S-97}	<T-96>	M_{T-96}	<T-97>	M_{T-97}
0	31.38	-0.009	31.37	-0.008	10.56	0.051	10.31	0.039
10	31.42	-0.010	31.40	-0.008	9.95	0.056	9.75	0.044
20	31.59	-0.010	31.57	-0.008	7.70	0.059	7.62	0.048
30	31.88	-0.009	31.85	-0.008	4.95	0.055	4.99	0.047
50	32.37	-0.007	32.33	-0.007	1.24	0.040	1.38	0.036
75	32.75	-0.004	32.71	-0.004	-0.63	0.022	-0.51	0.020

Table A.6: Average Temperature and Salinity from Observations at Station 27 during the observation periods in Clode Sound in 1996 and 1997.

Depth(m)	<T27-96>	<S27-96>	<T27-97>	<S27-97>
0	11.26	31.73	9.85	31.30
10	10.57	31.77	9.47	31.34
20	7.46	32.14	6.52	31.67
30	4.77	32.14	2.87	32.17
50	1.56	32.44	-0.10	32.56
75	-0.44	32.60	-1.12	32.77

Table A.7: Average Temperature in Clode Sound 1996 (Timko et al, 1998a)

Depth (m)	M1	M2	M3	M4	M5
10	8.78	9.51	8.16	9.19	9.61
15-20	4.86	3.62	5.73	6.16	6.44
45	1.46	1.54	-	2.74	2.77
75	-	-	-	-	0.04

Table A.8: Average Salinity in Clode Sound 1996 (Timko et al, 1998a)

Depth (m)	M1	M2	M3	M4	M5
10	-	29.75**	29.84	29.38	30.72
15-20	31.65	31.75	31.67	30.86	31.64
45	31.86	31.96	-	31.96	31.96*
75	-	-	-	-	32.51

*average calculated over longest set of continuous observations
**data corrected by a constant of -2.5 PSU

Table A.9: Average Temperature in Clode Sound 1997 (Timko et al, 1998b)

Depth (m)	M1	M2	M3	M4	M5	M6	M7
7.5	8.02	8.37	9.07	8.75	8.73	-	9.56
10	-	-	-	7.57	-	-	-
15	-	5.43	6.26	6.27	7.09	6.36	8.15
20	2.63	3.03	-	-	5.72	5.05	6.59
25	-	2.00	-	-	-	4.14	-
30	1.28	0.92	-	-	3.07	3.24	4.28
40	0.64	0.79	-	-	2.11	1.87	-
50	0.44	-	-	-	-	-	-

Table A.10 Average Salinity in Clode Sound 1997 (Timko et al, 1998b)

Depth (m)	M1	M2	M3	M4	M5	M6	M7
7.5	29.94**	29.60	29.43	30.27	31.45	-	-
15-20	32.03	31.75	-	31.11	31.72*	31.55	31.45
30	-	32.22	-	-	-	31.76	31.72

*average calculated over longest set of continuous observations
**data corrected by a constant of -2.5 PSU

Table A.11: Amplitude (A) and Phase (P) of the Temperature Signal at Tidal Frequency M_2 1996

Mooring	M1		M2		M3		M4		M5	
Depth (m)	A (°C)	P (deg)	A (°C)	P (deg)	A (°C)	P (deg)	A (°C)	P (deg)	A (°C)	P (deg)
10	0.195	235	0.335	256	0.713	307	0.381	169	0.186	250
21	0.036	178	0.264	274	0.929	291	0.320	164	0.148	253
45	0.024	151	0.089	293			0.174	153	0.085	235
76									0.028	198

Table A.12: Amplitude (A) and Phase (P) of the Temperature Signal at Tidal Frequency K_1 1996

Mooring	M1		M2		M3		M4		M5	
Depth (m)	A (°C)	P (deg)	A (°C)	P (deg)	A (°C)	P (deg)	A (°C)	P (deg)	A (°C)	P (deg)
10	0.083	252	0.168	176	0.102	97	0.057	335	0.105	33
21	0.022	36	0.053	80	0.178	81	0.112	7	0.078	9
45	0.011	354	0.042	32			0.036	350	0.054	353
76									0.015	120

Table A.13: Amplitude (A) and Phase (P) of the Temperature Signal at Tidal Frequency M_2 1997

M3

Depth (m)	A (°C)	P (deg)
7.5	0.302	159
14	0.403	178

M7

Depth (m)	A (°C)	P (deg)
7.5	0.230	85
14	0.402	66
20	0.434	51
31	0.256	18

M2

Depth (m)	A (°C)	P (deg)
7.5	0.299	158
14	0.403	163
21	0.337	155
25	0.242	155
30	0.173	169
37	0.095	157

M4

Depth (m)	A (°C)	P (deg)
7.5	0.223	139
11	0.385	185
14	0.710	189

M6

Depth (m)	A (°C)	P (deg)
14	0.390	49
21	0.363	36
25	0.297	30
33	0.200	25
39	0.095	33

M1

Depth (m)	A (°C)	P (deg)
7.5	0.328	156
21	0.270	141
30	0.143	169
40	0.044	147
51	0.010	106

M5

Depth (m)	A (°C)	P (deg)
7.5	0.387	66
14	0.430	62
21	0.362	51
30	0.199	41
36	0.122	42

Table A.14: Amplitude (A) and Phase (P) of the Temperature Signal at Tidal Frequency K_1 1997

M3

Depth (m)	A (°C)	P (deg)
7.5	0.152	162
14	0.069	98

M7

Depth (m)	A (°C)	P (deg)
7.5	0.050	21
14	0.131	12
20	0.077	330
31	0.116	317

M2

Depth (m)	A (°C)	P (deg)
7.5	0.103	142
14	0.090	90
21	0.027	33
25	0.052	345
30	0.077	8
37	0.057	357

M4

Depth (m)	A (°C)	P (deg)
7.5	0.085	69
11	0.158	51
14	0.139	49

M6

Depth (m)	A (°C)	P (deg)
14	0.059	317
21	0.083	337
25	0.127	316
33	0.095	322
39	0.083	19

M1

Depth (m)	A (°C)	P (deg)
7.5	0.084	153
21	0.036	339
30	0.065	358
40	0.028	358
51	0.005	299

M5

Depth (m)	A (°C)	P (deg)
7.5	0.101	355
14	0.074	336
21	0.070	321
30	0.107	331
36	0.085	18

Appendix B Data Tables for C hapter 4

Table B.1: Comparison of Main Tidal Constituents (Observed) vs. Model (nonlinear and linear) for a barotropic fluid. The values in the table represent semi-major axis of the tidal ellipse (cm/s) as calculated in Pawlowicz et al. (2002), along with the 95% confidence intervals.

Depth: 10 metres

Tidal Constituent: O_1

Mooring	M1-96	M2-96	M3-96	M4-96	M5-96
Observation	0.10 ± 0.44	0.46 ± 0.59	2.04 ± 1.41	1.08 ± 0.87	0.58 ± 0.61
Nonlinear	0.02 ± 0.01	0.18 ± 0.05	0.67 ± 0.10	0.13 ± 0.02	0.10 ± 0.02
Linear	0.06 ± 0.01	0.13 ± 0.02	0.63 ± 0.07	0.13 ± 0.01	0.09 ± 0.01

Tidal Constituent: K_1

Mooring	M1-96	M2-96	M3-96	M4-96	M5-96
Observation	0.36 ± 0.44	0.86 ± 0.63	3.73 ± 1.41	0.76 ± 0.69	0.53 ± 0.47
Nonlinear	0.10 ± 0.01	0.20 ± 0.05	1.31 ± 0.10	0.26 ± 0.02	0.20 ± 0.02
Linear	0.11 ± 0.01	0.26 ± 0.01	1.26 ± 0.07	0.26 ± 0.01	0.18 ± 0.01

Tidal Constituent: M_2

Mooring	M1-96	M2-96	M3-96	M4-96	M5-96
Observation	1.82 ± 0.96	3.36 ± 0.90	14.38 ± 0.91	2.87 ± 0.76	2.00 ± 0.53
Nonlinear	0.59 ± 0.11	1.42 ± 0.23	6.90 ± 1.60	1.33 ± 0.31	0.96 ± 0.18
Linear	0.57 ± 0.09	1.32 ± 0.18	6.46 ± 0.97	1.34 ± 0.19	0.94 ± 0.14

Tidal Constituent: S_2

Mooring	M1-96	M2-96	M3-96	M4-96	M5-96
Observation	1.52 ± 0.90	1.43 ± 1.04	7.26 ± 1.07	1.57 ± 0.82	1.24 ± 0.54
Nonlinear	0.20 ± 0.11	0.50 ± 0.24	2.39 ± 1.46	0.48 ± 0.29	0.37± 0.18
Linear	0.25 ± 0.08	0.58 ± 0.21	2.86 ± 0.97	0.59 ± 0.19	0.41 ± 0.15

Table B.2: Comparison of Main Tidal Constituents (Observed) vs. Model (nonlinear and linear) for a barotropic fluid. The values in the table represent semi-major axis of the tidal ellipse (cm/s) as calculated in Pawlowicz et al. (2002), along with the 95% confidence intervals.

Depth: 20 metres

Tidal Constituent: O_1

Mooring	M1-96	M2-96	M3-96	M4-96	M5-96
Observation	0.52 ± 0.57	0.20 ± 0.47	1.18 ± 0.95	0.32 ± 0.30	0.13 ± 0.42
Nonlinear	0.06 ± 0.01	0.36 ± 0.11	0.54 ± 0.08	0.11 ± 0.04	0.17 ± 0.02
Linear	0.06 ± 0.01	0.13 ± 0.01	0.62 ± 0.08	0.13 ± 0.01	0.09 ± 0.01

Tidal Constituent: K_1

Mooring	M1-96	M2-96	M3-96	M4-96	M5-96
Observation	1.09 ± 0.58	1.03 ± 0.62	2.36 ± 0.91	0.30 ± 0.34	0.50 ± 0.57
Nonlinear	0.10 ± 0.01	0.12 ± 0.08	0.73 ± 0.07	0.23 ± 0.04	0.20 ± 0.02
Linear	0.11 ± 0.01	0.25 ± 0.01	1.22 ± 0.05	0.26 ± 0.01	0.18 ± 0.01

Tidal Constituent: M_2

Mooring	M1-96	M2-96	M3-96	M4-96	M5-96
Observation	0.74 ± 0.37	1.52 ± 0.59	12.02 ± 0.96	1.32 ± 0.30	1.77 ± 0.44
Nonlinear	0.59 ± 0.10	1.33 ± 0.26	5.31 ± 0.89	1.34 ± 0.30	0.96 ± 0.19
Linear	0.57 ± 0.08	1.30 ± 0.19	6.25 ± 0.92	1.34 ± 0.19	0.95 ± 0.13

Tidal Constituent: S_2

Mooring	M1-96	M2-96	M3-96	M4-96	M5-96
Observation	0.43 ± 0.39	1.01 ± 0.60	5.85 ± 1.03	0.40 ± 0.23	1.05 ± 0.39
Nonlinear	0.20 ± 0.12	0.43 ± 0.25	1.62 ± 0.91	0.46 ± 0.29	0.35 ± 0.19
Linear	0.25 ± 0.09	0.57 ± 0.17	2.76 ± 0.94	0.59 ± 0.19	0.42 ± 0.13

Table B.3: Comparison of Main Tidal Constituents (Observed) vs. Model (nonlinear and linear) for a barotropic fluid. The values in the table represent semi-major axis of the tidal ellipse (cm/s) as calculated in Pawlowicz et al. (2002), along with the 95% confidence intervals.

Depth: 7.5 metres

Tidal Constituent: O_1

Mooring	M1-97	M2-97	M3-97	M4-97	M5-97	M6-97	M7-97
Observation	0.41 ± 0.58	0.84 ± 0.96	0.76 ± 0.63	2.04 ± 0.75	0.54 ± 0.43	-	0.30 ± 0.37
Nonlinear	0.19 ± 0.04	0.43 ± 0.11	0.18 ± 0.02	0.60 ± 0.08	0.21 ± 0.06	0.78 ± 0.09	0.07 ± 0.03
Linear	0.13 ± 0.01	0.15 ± 0.01	0.14 ± 0.01	0.61 ± 0.05	0.14 ± 0.01	0.18 ± 0.02	0.20 ± 0.02

Tidal Constituent: K_1

Mooring	M1-97	M2-97	M3-97	M4-97	M5-97	M6-97	M7-97
Observation	0.41 ± 0.57	1.24 ± 0.96	1.15 ± 0.96	2.49 ± 0.71	0.84 ± 0.42	-	0.51 ± 0.46
Nonlinear	0.34 ± 0.04	0.27 ± 0.10	0.34 ± 0.02	1.17 ± 0.08	0.30 ± 0.07	0.90 ± 0.10	0.27 ± 0.02
Linear	0.24 ± 0.01	0.27 ± 0.01	0.28 ± 0.01	1.15 ± 0.05	0.28 ± 0.01	0.35 ± 0.01	0.37 ± 0.02

Tidal Constituent: M_2

Mooring	M1-97	M2-97	M3-97	M4-97	M5-97	M6-97	M7-97
Observation	2.50 ± 0.58	4.49 ± 0.98	5.29 ± 1.00	12.10 ±1.03	2.98 ± 0.45	-	2.27 ± 0.48
Nonlinear	1.25 ± 0.21	1.28 ± 0.30	1.48 ± 0.23	5.46 ± 0.78	1.55 ± 0.30	1.70 ± 0.41	1.99 ± 0.24
Linear	1.21 ± 0.16	1.42 ± 0.19	1.45 ± 0.20	5.83 ± 0.88	1.53 ± 0.19	1.85 ± 0.25	1.94± 0.28

Tidal Constituent: S_2

Mooring	M1-97	M2-97	M3-97	M4-97	M5-97	M6-97	M7-97
Observation	0.93 ± 0.54	2.25 ± 0.97	1.95 ± 1.04	6.12 ± 1.12	1.25 ± 0.41	-	1.29 ± 0.43
Nonlinear	0.54 ± 0.17	0.58 ± 0.29	0.65 ± 0.26	2.51 ± 0.77	0.71 ± 0.25	0.83 ± 0.48	0.88 ± 0.26
Linear	0.53 ± 0.15	0.62 ± 0.18	0.63 ± 0.21	2.63 ± 0.79	0.67 ± 0.22	0.81 ± 0.25	0.86 ± 0.23

Table B.4: Comparison of Main Tidal Constituents (Observed) vs. Model (nonlinear and linear) for a barotropic fluid. The values in the table represent semi-major axis of the tidal ellipse (cm/s) as calculated in Pawlowicz et al. (2002), along with the 95% confidence intervals.

Depth: 15 - 30 metres

Tidal Constituent: O_1

Mooring	M1-97	M2-97	M3-97	M4-97	M5-97	M6-97	M7-97
Observation	0.26 ± 0.45	0.36 ± 0.40	-	0.84 ± 0.99	0.29 ± 0.35	0.25 ± 0.23	0.32 ± 0.40
Nonlinear	0.12 ± 0.04	0.27 ± 0.10	0.17 ± 0.03	0.43 ± 0.04	0.11 ± 0.03	0.09 ± 0.07	0.62 ± 0.02
Linear	0.13 ± 0.01	0.15 ± 0.01	0.14 ± 0.01	0.57 ± 0.05	0.14 ± 0.01	0.18 ± 0.02	0.19 ± 0.02

Tidal Constituent: K_1

Mooring	M1-97	M2-97	M3-97	M4-97	M5-97	M6-97	M7-97
Observation	0.53 ± 0.48	0.32 ± 0.39	-	1.81 ± 0.96	0.26 ± 0.30	0.19 ± 0.22	0.29 ± 0.34
Nonlinear	0.28 ± 0.03	0.17 ± 0.11	0.34 ± 0.03	0.76 ± 0.04	0.29 ± 0.03	0.30 ± 0.07	0.31 ± 0.01
Linear	0.23 ± 0.01	0.27 ± 0.01	0.27 ± 0.01	1.11 ± 0.05	0.28 ± 0.01	0.35 ± 0.01	0.36 ± 0.02

Tidal Constituent: M_2

Mooring	M1-97	M2-97	M3-97	M4-97	M5-97	M6-97	M7-97
Observation	0.85 ± 0.32	1.18 ± 0.63	-	11.28 ±0.78	1.60 ± 0.60	0.46 ± 0.18	1.38 ± 0.49
Nonlinear	1.24 ± 0.17	1.28 ± 0.31	1.53 ± 0.24	4.36 ± 0.64	1.63 ± 0.24	2.10 ± 0.26	1.99 ± 0.26
Linear	1.20 ± 0.15	1.40 ± 0.18	1.41 ± 0.18	5.64 ± 0.75	1.53 ± 0.17	1.83 ± 0.23	1.92 ± 0.26

Tidal Constituent: S_2

Mooring	M1-97	M2-97	M3-97	M4-97	M5-97	M6-97	M7-97
Observation	0.38 ± 0.32	0.60 ± 0.57	-	5.74 ± 0.68	0.53 ± 0.46	0.23 ± 0.21	0.65 ± 0.41
Nonlinear	0.55 ± 0.16	0.53 ± 0.30	0.71 ± 0.20	1.83 ± 0.60	0.73 ± 0.22	0.93 ± 0.27	0.09 ± 0.29
Linear	0.53 ± 0.17	0.62 ± 0.22	0.61 ± 0.19	2.54 ± 0.76	0.67 ± 0.22	0.80 ± 0.26	0.85 ± 0.26

Table B.5The influence of stratification on the main diurnal constituents of the tide 1996. The magnitude of the semi-major axis of the current ellipse (cm/s) from a tidal analysis of stratified model data. The error associated with each value is the 95% confidence interval as calculated in Pawlowicz et al. (2002). Columns A, B, C represent the model output for each of the test cases in the model. Tidal analysis of the observed tides are included for comparison.

Main Diurnal Constituents 1996 (cm/s)

Constituent: O_1

Mooring: M1-96

Depth	Obs.	A	B	C
10	0.1±0.4	0.1±0.0	0.1±0.0	0.1±0.0
21	0.5±0.5	0.1±0.0	0.1±0.0	0.1±0.0
45	0.4±0.4	0.1±0.0	0.1±0.0	0.1±0.0

Mooring: M4-96

Depth	Obs.	A	B	C
10	1.1±0.9	0.1±0.0	0.1±0.0	0.1±0.0
20	0.3±0.3	0.1±0.0	0.1±0.0	0.1±0.0
45	0.2±0.2	0.2±0.1	0.2±0.1	0.2±0.1

Mooring: M2-96

Depth	Obs.	A	B	C
10	0.5±0.6	0.2±0.1	0.2±0.0	0.2±0.1
17	0.2±0.4	0.2±0.1	0.2±0.1	0.2±0.1
44	0.1±0.2	0.1±0.0	0.1±0.0	0.1±0.0

Mooring: M5-96

Depth	Obs.	A	B	C
10	0.6±0.6	0.1±0.0	0.1±0.0	0.1±0.0
21	0.1±0.4	0.1±0.0	0.1±0.0	0.1±0.0
45	0.3±0.2	0.1±0.0	0.1±0.0	0.1±0.0

Mooring: M3-96

Depth	Obs.	A	B	C
10	2.0±1.5	1.1±0.2	1.1±0.2	1.0±0.2
15	1.2±0.9	1.2±0.3	1.2±0.2	1.3±0.2

Constituent: K_1

Mooring: M1-96

Depth	Obs.	A	B	C
10	0.4±0.4	0.1±0.0	0.1±0.0	0.1±0.0
21	1.1±0.5	0.1±0.0	0.1±0.0	0.1±0.0
45	0.8±0.3	0.1±0.0	0.1±0.0	0.1±0.0

Mooring: M4-96

Depth	Obs.	A	B	C
10	0.8±0.7	0.2±0.0	0.2±0.0	0.2±0.0
20	0.3±0.3	0.2±0.0	0.2±0.0	0.2±0.0
45	0.2±0.2	0.2±0.0	0.2±0.1	0.2±0.1

Mooring: M2-96

Depth	Obs.	A	B	C
10	0.9±0.5	0.3±0.1	0.2±0.0	0.2±0.1
17	1.0±0.6	0.2±0.1	0.1±0.1	0.2±0.1
44	0.4±0.2	0.1±0.0	0.1±0.0	0.2±0.0

Mooring: M5-96

Depth	Obs.	A	B	C
10	0.5±0.5	0.2±0.0	0.2±0.0	0.2±0.0
21	0.5±0.4	0.2±0.0	0.2±0.0	0.2±0.0
45	0.4±0.3	0.2±0.0	0.2±0.0	0.2±0.0

Mooring: M3-96

Depth	Obs.	A	B	C
10	3.7±1.4	1.5±0.2	1.5±0.2	1.3±0.2
15	2.4±0.9	1.5±0.3	1.5±0.2	1.3±0.2

Table B.6: The influence of stratification on the main diurnal constituents of the tide 1997. The magnitude of the semi-major axis of the current ellipse (cm/s) from a tidal analysis of stratified model data. The error associated with each value is the 95% confidence interval as calculated in Pawlowicz et al. (2002). Columns A, B, C represent the model output for each of the test cases in the model. Tidal analysis of the observed tides are included for comparison.

Main Diurnal Constituents 1997 (cm/s)

Constituent: O_1

Mooring: M1-97					Mooring: M5-97				
Depth	**Obs.**	**A**	**B**	**C**	**Depth**	**Obs.**	**A**	**B**	**C**
7.5	0.4±0.6	0.2±0.0	0.2±0.0	0.1±0.0	**7.5**	0.5±0.4	0.1±0.0	0.1±0.0	0.1±0.0
21	0.3±0.3	0.1±0.0	0.1±0.0	0.1±0.0	**21**	0.3±0.2	0.2±0.1	0.1±0.0	0.1±0.0

Mooring: M2-97					Mooring: M6-97				
Depth	**Obs.**	**A**	**B**	**C**	**Depth**	**Obs.**	**A**	**B**	**C**
7.5	0.8±0.8	0.3±0.1	0.3±0.1	0.3±0.1	**21**	0.3±0.3	0.3±0.1	0.3±0.0	0.5±0.1
21	0.4±0.4	0.5±0.2	0.3±0.1	0.3±0.1	**33**	0.3±0.2	0.3±0.1	0.3±0.1	0.5±0.1

Mooring: M3-97					Mooring: M7-97				
Depth	**Obs.**	**A**	**B**	**C**	**Depth**	**Obs.**	**A**	**B**	**C**
7.5	0.8±0.7	0.2±0.0	0.2±0.0	0.2±0.0	**14**	0.3±0.4	0.1±0.0	0.1±0.0	0.1±0.0
					31	0.3±0.4	0.1±0.0	0.1±0.0	0.0±0.0

Mooring: M4-97				
Depth	**Obs.**	**A**	**B**	**C**
7.5	2.0±0.8	0.6±0.2	0.7±0.1	0.6±0.1
14	0.8±1.1	0.8±0.4	0.8±0.3	0.6±0.2

Constituent: K_1

Mooring: M1-97					Mooring: M5-97				
Depth	**Obs.**	**A**	**B**	**C**	**Depth**	**Obs.**	**A**	**B**	**C**
7.5	0.4±0.5	0.3±0.1	0.3±0.0	0.3±0.0	**7.5**	0.8±0.4	0.3±0.0	0.2±0.0	0.2±0.0
21	0.5±0.4	0.2±0.0	0.3±0.0	0.3±0.0	**21**	0.1±0.3	0.3±0.1	0.3±0.0	0.3±0.0

Mooring: M2-97					Mooring: M6-97				
Depth	**Obs.**	**A**	**B**	**C**	**Depth**	**Obs.**	**A**	**B**	**C**
7.5	1.2±1.0	0.2±0.1	0.2±0.1	0.2±0.1	**21**	0.5±0.4	0.4±0.1	0.5±0.0	0.6±0.1
21	0.3±0.4	0.3±0.2	0.2±0.1	0.3±0.1	**33**	0.2±0.2	0.4±0.1	0.5±0.1	0.6±0.1

Mooring: M3-97					Mooring: M7-97				
Depth	**Obs.**	**A**	**B**	**C**	**Depth**	**Obs.**	**A**	**B**	**C**
7.5	1.1±0.6	0.3±0.0	0.3±0.0	0.3±0.0	**14**	0.5±0.5	0.2±0.0	0.3±0.0	0.2±0.0
					31	0.3±0.4	0.3±0.0	0.3±0.0	0.3±0.0

Mooring: M4-97				
Depth	**Obs.**	**A**	**B**	**C**
7.5	2.5±0.8	0.9±0.1	1.2±0.1	0.9±0.1
14	1.8±0.7	0.9±0.3	1.1±0.3	0.8±0.2

Table B.7: The influence of stratification on the main semi diurnal constituents of the tide 1996. The magnitude of the semi-major axis of the current ellipse (cm/s) from a tidal analysis of stratified model data. The error associated with each value is the 95% confidence interval as calculated in Pawlowicz et al. (2002). Columns A, B, C represent the model output for each of the test cases in the model. Tidal analysis of the observed tides are included for comparison.

Main Semi Diurnal Constituents 1996 (cm/s)

Constituent: M_2

Mooring: M1-96				
Depth	**Obs.**	**A**	**B**	**C**
10	1.8±0.8	0.6±0.1	0.6±0.1	0.6±0.1
21	0.7±0.3	0.6±0.1	0.6±0.1	0.6±0.1
45	2.4±1.1	0.5±0.1	0.5±0.1	0.5±0.1

Mooring: M4-96				
Depth	**Obs.**	**A**	**B**	**C**
10	2.9±0.9	1.2±0.2	1.2±0.2	1.2±0.3
20	1.3±0.3	1.2±0.2	1.2±0.2	1.2±0.2
45	1.0±0.2	1.3±0.3	1.2±0.2	1.2±0.2

Mooring: M2-96				
Depth	**Obs.**	**A**	**B**	**C**
10	3.4±1.0	1.2±0.2	1.2±0.2	1.2±0.2
17	1.5±0.5	1.2±0.2	1.2±0.2	1.2±0.2
44	1.1±0.4	1.0±0.2	1.0±0.2	1.0±0.2

Mooring: M5-96				
Depth	**Obs.**	**A**	**B**	**C**
10	2.0±0.5	1.0±0.1	1.0±0.1	1.0±0.1
21	1.8±0.4	1.0±0.1	1.0±0.1	1.0±0.1
45	1.0±0.2	1.0±0.1	1.0±0.1	1.0±0.1

Mooring: M3-96				
Depth	**Obs.**	**A**	**B**	**C**
10	14.4±1.0	7.9±1.5	8.0±1.9	7.6±1.4
15	12.0±0.7	7.5±1.5	7.6±1.2	7.6±1.5

Constituent: S_2

Mooring: M1-96				
Depth	**Obs.**	**A**	**B**	**C**
10	1.5±0.9	0.2±0.1	0.2±0.1	0.2±0.1
21	0.4±0.3	0.2±0.1	0.2±0.1	0.2±0.1
45	1.5±1.0	0.2±0.1	0.2±0.1	0.2±0.1

Mooring: M4-96				
Depth	**Obs.**	**A**	**B**	**C**
10	1.6±1.0	0.5±0.2	0.5±0.2	0.5±0.3
20	0.4±0.2	0.5±0.2	0.5±0.2	0.5±0.2
45	0.5±0.2	0.5±0.3	0.5±0.3	0.5±0.3

Mooring: M2-96				
Depth	**Obs.**	**A**	**B**	**C**
10	1.4±0.8	0.5±0.2	0.5±0.2	0.5±0.2
17	1.0±0.5	0.5±0.2	0.5±0.2	0.5±0.2
44	0.6±0.5	0.4±0.2	0.4±0.2	0.4±0.2

Mooring: M5-96				
Depth	**Obs.**	**A**	**B**	**C**
10	1.2±0.5	0.4±0.1	0.4±0.2	0.4±0.1
21	1.0±0.4	0.4±0.1	0.4±0.1	0.4±0.1
45	0.6±0.2	0.4±0.1	0.4±0.1	0.4±0.1

Mooring: M3-96				
Depth	**Obs.**	**A**	**B**	**C**
10	7.3±1.2	3.2±1.8	3.3±1.6	3.0±1.4
15	5.8±0.8	2.8±1.8	2.9±1.5	3.1±1.5

Table B.8: The influence of stratification on the main diurnal constituents of the tide 1997. The magnitude of the semi-major axis of the current ellipse (cm/s) from a tidal analysis of stratified model data. The error associated with each value is the 95% confidence interval as calculated in Pawlowicz et al. (2002). Columns A, B, C represent the model output for each of the test cases in the model. Tidal analysis of the observed tides are included for comparison.

Main Semi Diurnal Constituents 1997 (cm/s)
Constituent: M_2

Mooring: M1-97

Depth	Obs.	A	B	C
7.5	2.5±0.4	1.3±0.3	1.2±0.2	1.3±0.2
21	0.9±0.3	1.3±0.3	1.2±0.1	1.3±0.2

Mooring: M5-97

Depth	Obs.	A	B	C
7.5	3.0±0.4	1.6±0.3	1.5±0.2	1.6±0.3
21	1.4±0.4	1.6±0.3	1.6±0.2	1.7±0.3

Mooring: M2-97

Depth	Obs.	A	B	C
7.5	4.5±0.9	1.5±0.3	1.3±0.2	1.5±0.3
21	1.2±0.6	1.4±0.2	1.3±0.3	1.5±0.2

Mooring: M6-97

Depth	Obs.	A	B	C
21	1.9±0.6	1.9±0.4	1.8±0.3	1.9±0.3
33	0.5±0.2	2.1±0.5	2.0±0.3	2.1±0.3

Mooring: M3-97

Depth	Obs.	A	B	C
7.5	5.3±0.9	1.5±0.3	1.5±0.2	1.5±0.3

Mooring: M7-97

Depth	Obs.	A	B	C
14	2.3±0.5	2.1±0.5	2.1±0.3	2.1±0.4
31	1.4±0.4	2.0±0.5	2.0±0.2	2.0±0.4

Mooring: M4-97

Depth	Obs.	A	B	C
7.5	12.1±0.9	5.5±1.2	5.2±0.7	5.1±0.9
14	11.3±0.7	5.2±1.0	5.0±0.6	5.0±0.9

Constituent: S_2

Mooring: M1-97

Depth	Obs.	A	B	C
7.5	0.9±0.5	0.4±0.3	0.5±0.2	0.4±0.2
21	0.4±0.3	0.4±0.2	0.5±0.2	0.4±0.2

Mooring: M5-97

Depth	Obs.	A	B	C
7.5	1.3±0.4	0.5±0.3	0.7±0.2	0.6±0.3
21	0.4±0.3	0.5±0.3	0.7±0.2	0.6±0.3

Mooring: M2-97

Depth	Obs.	A	B	C
7.5	2.2±0.8	0.5±0.3	0.5±0.3	0.5±0.3
21	0.6±0.5	0.5±0.2	0.6±0.3	0.5±0.2

Mooring: M6-97

Depth	Obs.	A	B	C
21	0.7±0.6	0.7±0.4	0.8±0.3	0.7±0.3
33	0.2±0.2	0.7±0.5	0.9±0.3	0.7±0.4

Mooring: M3-97

Depth	Obs.	A	B	C
7.5	1.9±0.9	0.5±0.3	0.7±0.2	0.5±0.3

Mooring: M7-97

Depth	Obs.	A	B	C
14	1.3±0.5	0.7±0.4	0.9±0.3	0.7±0.4
31	0.6±0.4	0.7±0.5	0.9±0.3	0.7±0.4

Mooring: M4-97

Depth	Obs.	A	B	C
7.5	6.1±1.0	1.9±1.1	2.4±0.7	1.7±1.0
14	5.7±0.7	1.7±1.2	2.1±0.7	1.7±1.0

Table B.9 Inclination of the tidal ellipse 1996. The inclination of the tidal ellipses as calculated during the tidal analysis for K_1 and M_2. Values in the table represent degrees with 0 degrees representing the eastern axis. The error associated with the values represent 95% confidence intervals.

Inclination of the Tidal Ellipse 1996 (degrees)
Constituent: K_1

Mooring: M1-96					Mooring: M4-96				
Depth	**Obs.**	**A**	**B**	**C**	**Depth**	**Obs.**	**A**	**B**	**C**
10	71±89	39±5	39±5	39±4	**10**	15±91	15±6	13±10	10±8
21	53±29	41±5	41±4	41±5	**20**	20±69	10±5	7±7	10±6
45	40±23	51±5	51±5	50±5	**45**	25±70	1±2	1±4	3±4

Mooring: M2-96					Mooring: M5-96				
Depth	**Obs.**	**A**	**B**	**C**	**Depth**	**Obs.**	**A**	**B**	**C**
10	5±87	20±7	9±15	10±34	**10**	130±88	48±5	48±5	48±5
17	20±20	12±18	8±20	9±35	**21**	43±60	48±5	48±5	48±5
44	173±15	160±18	159±15	154±14	**45**	67±27	48±5	48±5	48±5

Mooring: M3-96				
Depth	**Obs.**	**A**	**B**	**C**
10	171±11	170±4	173±5	168±3
15	162±11	177±3	176±3	174±4

Constituent: M_2

Mooring: M1-96					Mooring: M4-96				
Depth	**Obs.**	**A**	**B**	**C**	**Depth**	**Obs.**	**A**	**B**	**C**
10	52±26	43±7	43±8	43±8	**10**	30±20	5±3	5±3	5±3
21	45±32	43±8	43±8	43±8	**20**	4±11	4±2	5±2	4±2
45	45±26	46±8	46±7	46±9	**45**	25±14	2±2	2±2	2±2

Mooring: M2-96					Mooring: M5-96				
Depth	**Obs.**	**A**	**B**	**C**	**Depth**	**Obs.**	**A**	**B**	**C**
10	18±12	17±6	15±3	15±4	**10**	51±14	49±8	49±9	49±8
17	23±17	15±4	15±3	14±5	**21**	51±10	49±9	49±8	49±8
44	175±6	4±3	3±2	4±4	**45**	57±8	48±8	48±8	48±8

Mooring: M3-96				
Depth	**Obs.**	**A**	**B**	**C**
10	170±4	171±3	170±3	170±2
15	163±3	171±3	170±3	169±3

Table B.10: Inclination of the tidal ellipse 1997. The inclination of the tidal ellipses as calculated during the tidal analysis for K_1 and M_2. Values in the table represent degrees with 0 degrees representing the eastern axis. The error associated with the values represent 95% confidence intervals.

Inclination of the Tidal Ellipse 1997 (degrees)
Constituent: K_1

	Mooring: M1-97					Mooring: M5-97			
Depth	**Obs.**	**A**	**B**	**C**	**Depth**	**Obs.**	**A**	**B**	**C**
7.5	42±93	9±14	9± 6	13±11	**8**	178±23	164± 9	158± 7	167±19
21	35±41	180±12	8± 6	12± 4	**21**	176±61	164± 6	162± 4	160± 9

	Mooring: M2-97					Mooring: M6-97			
Depth	**Obs.**	**A**	**B**	**C**	**Depth**	**Obs.**	**A**	**B**	**C**
7.5	179±35	22±35	15± 9	12± 9	**21**	150±46	10±10	179± 2	5± 3
21	19±81	13±14	8±16	17± 9	**33**	18±97	179±20	172± 4	3± 6

	Mooring: M3-97					Mooring: M7-97			
Depth	**Obs.**	**A**	**B**	**C**	**Depth**	**Obs.**	**A**	**B**	**C**
7.5	163±28	176± 3	179± 2	178± 2	**14**	27±37	24± 5	22± 4	29± 6
					31	179±43	5± 5	7± 2	10± 4

	Mooring: M4-97			
Depth	**Obs.**	**A**	**B**	**C**
7.5	165±10	165± 8	170± 3	167± 5
14	167±13	172±10	176± 6	166± 9

Constituent: M_2

	Mooring: M1-97					Mooring: M5-97			
Depth	**Obs.**	**A**	**B**	**C**	**Depth**	**Obs.**	**A**	**B**	**C**
7.5	35±10	18± 5	18± 5	19± 5	**8**	174± 6	164± 4	163± 3	164± 5
21	22±14	18± 5	18± 4	19± 5	**21**	156±17	166± 4	165± 3	166± 4

	Mooring: M2-97					Mooring: M6-97			
Depth	**Obs.**	**A**	**B**	**C**	**Depth**	**Obs.**	**A**	**B**	**C**
7.5	10± 7	10± 3	10± 4	9± 4	**21**	168± 9	179± 2	1± 1	180± 2
21	1±15	7± 3	8± 3	8± 3	**33**	5±66	180± 3	1± 1	179± 2

	Mooring: M3-97					Mooring: M7-97			
Depth	**Obs.**	**A**	**B**	**C**	**Depth**	**Obs.**	**A**	**B**	**C**
7.5	173± 7	172± 3	173± 2	173± 2	**14**	20± 5	10± 3	9± 2	9± 3
					31	9± 9	7± 3	7± 2	7± 3

	Mooring: M4-97			
Depth	**Obs.**	**A**	**B**	**C**
7.5	161± 3	167± 4	166± 2	167± 4
14	168± 2	166± 4	166± 3	167± 4

Table B.11 Greenwich Phase of the main tidal constituents 1996. Calculated greenwich phase for the model and observations in 1996. The error associated with the values represents the 95% confidence intervals. Comparison of the stated values below must take into account the orientation of the tidal ellipse as the phase is measured from the semi-major axis always assumed to lie in a northerly direction.

Greenwich Phase 1996 (degrees)
Constituent: K_1

Mooring: M1-96

Depth	Obs.	A	B	C
10	274±116	296±6	296±5	296±5
21	286±29	296±5	296±5	296±5
45	168±28	300±5	300±6	300±5

Mooring: M4-96

Depth	Obs.	A	B	C
10	354±82	294±9	297±11	290±13
20	300±91	298±10	301±7	298±9
45	283±93	305±12	309±16	300±15

Mooring: M2-96

Depth	Obs.	A	B	C
10	301±85	300±13	307±17	300±30
17	355±34	315±18	315±34	302±34
44	344±35	71±10	75±11	75±13

Mooring: M5-96

Depth	Obs.	A	B	C
10	88±87	301±4	301±5	301±5
21	294±76	301±6	301±5	301±5
45	278±38	300±5	300±5	300±5

Mooring: M3-96

Depth	Obs.	A	B	C
10	109±21	124±6	128±6	121±10
15	110±19	112±11	122±8	114±10

Constituent: M_2

Mooring: M1-96

Depth	Obs.	A	B	C
10	95±27	80±8	80±7	80±8
21	44±35	80±8	80±8	80±8
45	332±23	81±7	81±7	81±8

Mooring: M4-96

Depth	Obs.	A	B	C
10	65±20	83±11	84±11	81±12
20	52±13	84±10	84±10	83±11
45	356±12	83±11	83±11	85±10

Mooring: M2-96

Depth	Obs.	A	B	C
10	84±16	83±9	82±11	85±9
17	72±18	83±11	84±8	87±10
44	104±26	59±12	59±11	57±13

Mooring: M5-96

Depth	Obs.	A	B	C
10	88±13	82±8	82±8	82±7
21	58±11	83±7	83±7	83±8
45	33±10	82±7	82±7	82±7

Mooring: M3-96

Depth	Obs.	A	B	C
10	233±4	268±12	268±12	266±11
15	229±4	260±11	259±9	263±10

Table B.12: Greenwich Phase of the main tidal constituents 1997. Calculated greenwich phase for the model and observations in 1996. The error associated with the values represents the 95% confidence intervals. Comparison of the stated values below must take into account the orientation of the tidal ellipse as the phase is measured from the semi-major axis always assumed to lie in a northerly direction.

Greenwich Phase 1997 (degrees)

Constituent: K_1

Mooring: M1-97					Mooring: M5-97				
Depth	**Obs.**	**A**	**B**	**C**	**Depth**	**Obs.**	**A**	**B**	**C**
7.5	344±109	283±12	301± 8	287± 9	**8**	131±30	116± 7	115±11	108±10
21	305±47	93±10	294± 7	278± 7	**21**	102±140	110±10	113± 6	95± 7

Mooring: M2-97					Mooring: M6-97				
Depth	**Obs.**	**A**	**B**	**C**	**Depth**	**Obs.**	**A**	**B**	**C**
7.5	134±51	349±25	338±19	332±20	**21**	158±58	313±12	141± 5	322± 6
21	273±105	11±34	344±35	344±16	**33**	315±87	112±11	131± 6	315±12

Mooring: M3-97					Mooring: M7-97				
Depth	**Obs.**	**A**	**B**	**C**	**Depth**	**Obs.**	**A**	**B**	**C**
7.5	81±36	114± 4	124± 5	114± 5	**14**	252±59	243± 5	253± 3	255± 9
					31	74±91	249± 8	260± 3	256± 5

Mooring: M4-97				
Depth	**Obs.**	**A**	**B**	**C**
7.5	108±18	115±10	127± 4	114± 7
14	116±29	116±22	120±13	111±11

Constituent: M_2

Mooring: M1-97					Mooring: M5-97				
Depth	**Obs.**	**A**	**B**	**C**	**Depth**	**Obs.**	**A**	**B**	**C**
7.5	58±11	79±13	318± 8	81±11	**8**	240± 9	267± 9	144± 8	267±10
21	354±20	81±11	319± 7	83±10	**21**	206±19	262±11	139± 9	261±11

Mooring: M2-97					Mooring: M6-97				
Depth	**Obs.**	**A**	**B**	**C**	**Depth**	**Obs.**	**A**	**B**	**C**
7.5	75±12	93±10	328±11	92± 9	**21**	216±16	275±10	332± 8	277±10
21	21±30	95± 8	333±11	93±10	**33**	18±54	269±13	327± 7	275± 9

Mooring: M3-97					Mooring: M7-97				
Depth	**Obs.**	**A**	**B**	**C**	**Depth**	**Obs.**	**A**	**B**	**C**
7.5	239±10	262±12	139± 8	262±10	**14**	39±12	68±12	307± 8	70±13
					31	359±17	69±14	307± 7	70±14

Mooring: M4-97				
Depth	**Obs.**	**A**	**B**	**C**
7.5	231± 4	267±11	144± 9	262±11
14	220± 4	253±11	130± 7	256±11

Table B.13 Amplitude (semi-major axis) of the Nonlinear Tidal Current MS_f 1996. Table values represent the semi-major axis (cm/s) of the tidal ellipse and 95% confidence intervals. Values of 0.0 in the table indicate velocities less than 0.05 cm/s.

Nonlinear Tidal Constituents 1996
Constituent: MS_f

Mooring: M1-96

Depth	Obs.	A	B	C
10	1.0±0.7	0.1±0.1	0.1±0.1	0.1±0.1
21	0.3±0.6	0.0±0.0	0.0±0.0	0.0±0.0
45	0.4±0.5	0.1±0.1	0.1±0.1	0.1±0.1

Mooring: M4-96

Depth	Obs.	A	B	C
10	0.9±1.6	0.1±0.1	0.1±0.1	0.1±0.1
20	0.4±0.7	0.1±0.1	0.1±0.1	0.1±0.1
45	0.3±0.5	0.2±0.1	0.2±0.1	0.2±0.1

Mooring: M2-96

Depth	Obs.	A	B	C
10	1.6±2.0	0.1±0.1	0.2±0.2	0.4±0.5
17	0.4±1.5	0.2±0.2	0.3±0.3	0.5±0.4
44	0.3±0.4	0.2±0.1	0.1±0.1	0.1±0.1

Mooring: M5-96

Depth	Obs.	A	B	C
10	0.6±1.0	0.1±0.2	0.1±0.2	0.1±0.2
21	0.8±1.1	0.0±0.1	0.0±0.1	0.0±0.1
45	0.3±0.4	0.0±0.1	0.0±0.1	0.0±0.1

Mooring: M3-96

Depth	Obs.	A	B	C
10	2.1±1.8	0.7±0.3	0.5±0.2	0.5±0.2
15	0.6±2.6	0.6±0.5	0.5±0.2	0.4±0.2

Table B.14 Amplitude (semi-major axis) of the Nonlinear Tidal Current MS_f 1997. Table values represent the semi-major axis (cm/s) of the tidal ellipse and 95% confidence intervals. Values of 0.0 in the table indicate velocities less than 0.05 cm/s.

Nonlinear Tidal Constituents 1997
Constituent: MS_f

Mooring: M1-97

Depth	Obs.	A	B	C
7.5	0.8±1.2	0.2±0.1	0.2±0.2	0.2±0.2
21	0.2±0.4	0.2±0.3	0.2±0.1	0.2±0.2

Mooring: M5-97

Depth	Obs.	A	B	C
7.5	0.3±0.5	0.2±0.2	0.1±0.1	0.3±0.2
21	0.6±0.8	0.1±0.1	0.1±0.1	0.2±0.1

Mooring: M2-97

Depth	Obs.	A	B	C
7.5	1.0±2.0	0.4±0.3	0.5±0.2	0.2±0.2
21	1.2±1.3	0.8±0.4	0.5±0.3	0.5±0.2

Mooring: M6-97

Depth	Obs.	A	B	C
21	0.8±0.9	0.5±0.2	0.5±0.4	0.7±0.4
33	0.1±0.4	0.5±0.2	0.5±0.4	0.7±0.3

Mooring: M3-97

Depth	Obs.	A	B	C
7.5	1.4±2.3	0.3±0.3	0.3±0.2	0.3±0.1

Mooring: M7-97

Depth	Obs.	A	B	C
14	1.3±1.3	0.5±0.2	0.5±0.3	0.5±0.2
31	0.4±0.6	0.5±0.2	0.5±0.2	0.5±0.2

Mooring: M4-97

Depth	Obs.	A	B	C
7.5	0.8±2.6	0.8±0.3	0.6±0.4	0.6±0.3
14	4.2±4.9	0.4±0.2	0.4±0.2	0.4±0.1

Table B.15: Nonlinear Tidal Constituents at the sill 1996: Table values represent the semi-major axis (cm/s) of the tidal ellipse and 95% confidence intervals. Values of 0.0 in the table indicate velocities less than 0.05 cm/s.

Nonlinear Tidal Constituents: M3-96

Constituent: M_4

Depth	Obs.	A	B	C
10	1.0±0.3	0.2±0.1	0.2±0.1	0.2±0.1
15	0.6±0.4	0.4±0.3	0.2±0.1	0.2±0.1

Constituent: MS_4

Depth	Obs.	A	B	C
10	0.9±0.3	0.2±0.1	0.1±0.1	0.1±0.1
15	0.5±0.4	0.3±0.2	0.1±0.1	0.1±0.1

Constituent: S_4

Depth	Obs.	A	B	C
10	0.3±0.3	0.1±0.1	0.0±0.1	0.0±0.1
15	0.3±0.4	0.2±0.2	0.1±0.1	0.0±0.1

Table B.16: Nonlinear Tidal Constituents at the sill 1997: Table values represent the semi-major axis (cm/s) of the tidal ellipse and 95% confidence intervals. Values of 0.0 in the table indicate velocities less than 0.05 cm/s.

Nonlinear Tidal Constituents: M4-97

Constituent: M_4

Depth	Obs.	A	B	C
7.5	0.9±0.3	0.3±0.2	0.3±0.1	0.2±0.1
14	0.4±0.2	0.1±0.1	0.1±0.1	0.1±0.1

Constituent: MS_4

Depth	Obs.	A	B	C
7.5	0.7±0.3	0.2±0.2	0.2±0.1	0.1±0.1
14	0.4±0.2	0.0±0.1	0.1±0.1	0.1±0.1

Constituent: S_4

Depth	Obs.	A	B	C
7.5	0.2±0.2	0.1±0.1	0.0±0.1	0.0±0.1
14	0.3±0.3	0.0±0.1	0.1±0.1	0.0±0.1

Table B.17 Frictional Tidal Constituents at the sill 1996: The amplitude (cm/a) of the semi-major axis and 95% confidence intervals. Values of 0.0 in the table indicate velocities less than 0.05 cm/s.

Frictional Tidal Constituents: M3-96

Constituent: M_6

Depth	Obs.	A	B	C
10	1.3±0.4	0.1±0.1	0.1±0.1	0.0±0.0
15	1.4±0.5	0.1±0.1	0.1±0.1	0.1±0.1

Constituent: $2MS_6$

Depth	Obs.	A	B	C
10	0.2±0.3	0.1±0.1	0.1±0.1	0.0±0.0
15	0.6±0.5	0.1±0.1	0.1±0.1	0.1±0.1

Constituent: $2SM_6$

Depth	Obs.	A	B	C
10	0.6±0.4	0.1±0.1	0.0±0.1	0.0±0.0
15	0.4±0.4	0.1±0.1	0.1±0.1	0.0±0.1

Table B.18 Frictional Tidal Constituents at the sill 1997: The amplitude (cm/s) of the semi-major axis and 95% confidence intervals. Values of 0.0 in the table indicate velocities less than 0.05 cm/s.

Fictional Tidal Constituents: M4-97

Constituent: M_6

Depth	Obs.	A	B	C
7.5	1.0±0.3	0.2±0.3	0.4±0.4	0.2±0.3
14	1.2±0.4	0.3±0.3	0.4±0.4	0.2±0.3

Constituent: $2MS_6$

Depth	Obs.	A	B	C
7.5	0.3±0.3	0.1±0.3	0.1±0.3	0.2±0.3
14	0.1±0.2	0.2±0.3	0.2±0.4	0.2±0.4

Constituent: $2SM_6$

Depth	Obs.	A	B	C
7.5	0.4±0.3	0.1±0.3	0.2±0.3	0.1±0.3
14	0.5±0.4	0.1±0.3	0.2±0.4	0.1±0.3

Table B.19 Time Averaged Velocity and Standard Deviation. Units are in cm/s. Values of the observations represent subsets of the total observation record extracted to correspond to the model runs to the right of the observed (Obs.) value.

Mooring: M1-96

	East-West Velocity (U)						North-South Velocity (V)					
Depth	**Obs.**	**Baro.**	**Obs.**	**A**	**B**	**C**	**Obs.**	**Baro.**	**Obs.**	**A**	**B**	**C**
10	1.8±1.5	0.2±0.6	1.5±2.1	-0.5±0.9	-0.5±0.8	-0.6±0.8	0.6±1.5	-0.1±0.6	0.7±1.5	-0.1±0.8	-0.1±0.8	-0.1±0.7
21	0.7±1.1	-0.9±0.7	0.0±1.3	-0.5±0.6	-0.5±0.6	-0.7±0.6	0.1±1.2	-0.4±0.7	0.5±0.8	-0.1±0.6	-0.2±0.6	-0.2±0.5
45	0.0±1.0	-1.1±0.9	0.3±1.1	-0.5±0.6	-0.5±0.6	-0.5±0.6	0.0±0.7	-0.3±0.9	0.4±0.5	-0.0±0.5	-0.0±0.5	-0.0±0.5

Mooring: M2-96

	East-West Velocity (U)						North-South Velocity (V)					
Depth	**Obs.**	**Baro.**	**Obs.**	**A**	**B**	**C**	**Obs.**	**Baro.**	**Obs.**	**A**	**B**	**C**
10	-3.7±3.8	-0.3±1.0	-2.7±3.7	-0.1±1.2	-0.1±1.2	-0.1±1.2	0.9±2.8	-0.3±0.8	2.2±2.1	-0.3±0.6	-0.3±0.7	-0.2±0.6
17	-0.7±1.6	-0.3±0.9	-0.1±2.3	-0.2±1.2	-0.2±1.2	-0.3±1.2	0.6±1.1	-0.8±0.6	0.5±1.2	-0.8±0.7	-0.8±0.7	-0.7±0.7
44	0.1±0.8	-0.5±0.7	0.0±0.6	-0.4±0.9	-0.3±0.9	-0.3±1.0	0.4±0.7	-0.3±0.6	0.7±0.7	-0.1±0.4	-0.2±0.4	-0.2±0.5

Mooring: M3-96

	East-West Velocity (U)						North-South Velocity (V)					
Depth	**Obs.**	**Baro.**	**Obs.**	**A**	**B**	**C**	**Obs.**	**Baro.**	**Obs.**	**A**	**B**	**C**
10	-3.3±4.8	0.0±5.1	-1.6±4.7	0.4±6.9	0.2±6.9	0.5±6.5	4.3±2.2	0.0±1.0	4.8±2.0	0.4±1.3	0.4±1.4	0.1±1.3
15	-1.9±4.7	-0.1±4.4	0.7±5.7	0.3±6.6	0.1±6.6	0.1±6.7	2.6±1.7	-0.2±1.0	2.2±2.1	-0.1±1.2	-0.1±1.2	0.1±1.3

Mooring: M4-96

	East-West Velocity (U)						North-South Velocity (V)					
Depth	**Obs.**	**Baro.**	**Obs.**	**A**	**B**	**C**	**Obs.**	**Baro.**	**Obs.**	**A**	**B**	**C**
10	-4.9±3.6	0.4±0.9	-4.4±3.1	0.0±1.1	0.0±1.1	0.1±1.1	0.2±4.4	0.2±0.5	0.2±3.9	0.1±0.3	0.1±0.3	0.1±0.3
20	0.8±1.5	-0.2±0.9	1.0±1.8	-0.3±1.1	-0.3±1.1	-0.3±1.1	0.1±1.0	0.0±0.3	0.3±1.3	0.2±0.4	0.2±0.4	0.2±0.4
45	-0.3±0.8	-0.4±1.0	0.5±0.6	-0.2±1.2	-0.2±1.2	-0.2±1.2	0.1±0.7	0.0±0.6	0.3±0.6	0.2±0.3	0.2±0.3	0.2±0.4

Mooring: M5-96

	East-West Velocity (U)						North-South Velocity (V)					
Depth	**Obs.**	**Baro.**	**Obs.**	**A**	**B**	**C**	**Obs.**	**Baro.**	**Obs.**	**A**	**B**	**C**
10	-3.2±2.1	1.0±0.9	-3.4±2.9	0.7±0.9	0.6±0.9	0.6±0.9	-4.1±2.4	0.4±1.3	-4.3±3.1	-0.0±1.0	-0.0±1.0	-0.0±1.0
21	-0.1±1.7	-0.1±0.6	0.7±1.7	-0.3±0.7	-0.3±0.7	-0.3±0.7	-0.8±2.5	0.0±0.7	-0.1±2.4	0.1±0.7	0.1±0.8	0.0±0.7
45	0.3±0.8	-0.5±0.6	0.4±0.8	-0.2±0.6	-0.2±0.6	-0.2±0.6	0.4±0.8	-0.2±0.7	0.7±0.8	-0.0±0.7	-0.0±0.7	-0.0±0.7

Table B.20: Time Average Velocity and Standard Deviations. Units are in cm/s. Values of the observations represent subsets of the total observation record extracted to correspond to the model runs to the right of the observed (Obs.) value.

Mooring: M1-97

	East-West Velocity (U)							North-South Velocity (V)						
Depth	**Obs.**	**Baro.**	**Obs.**	**A**	**B**	**Obs.**	**C**	**Obs.**	**Baro.**	**Obs.**	**A**	**B**	**Obs.**	**C**
7.5	-0.2±3.3	0.0±1.3	-1.1±3.4	0.1±1.2	0.1±1.3	1.5±2.1	0.1±1.4	0.8±2.3	-0.3±1.0	0.5±2.5	-0.2±0.7	-0.3±0.7	1.6±1.5	-0.2±0.9
21	0.8±1.0	-0.5±1.3	1.1±1.0	-0.5±1.2	-0.5±1.3	0.6±0.6	-0.7±1.3	0.0±0.9	-0.9±0.7	0.3±0.9	-0.9±0.8	-0.9±0.7	-0.2±0.5	-0.8±0.7

Mooring: M2-97

	East-West Velocity (U)							North-South Velocity (V)						
Depth	**Obs.**	**Baro.**	**Obs.**	**A**	**B**	**Obs.**	**C**	**Obs.**	**Baro.**	**Obs.**	**A**	**B**	**Obs.**	**C**
7.5	-3.5±4.3	-0.0±1.7	-4.6±4.2	0.5±1.6	0.5±1.5	-3.7±4.5	0.8±1.8	-0.2±2.2	-0.2±0.8	-0.2±2.3	-0.2±0.7	-0.1±0.8	-0.1±1.9	-0.0±1.0
21	0.0±2.1	-0.1±1.7	-0.5±2.3	0.2±1.5	0.1±1.6	0.8±1.0	-0.4±1.7	0.1±1.2	-0.9±0.8	0.3±1.2	-1.1±0.9	-1.0±0.8	-0.2±0.7	-0.9±0.8

Mooring: M3-97

	East-West Velocity (U)							North-South Velocity (V)						
Depth	**Obs.**	**Baro.**	**Obs.**	**A**	**B**	**Obs.**	**C**	**Obs.**	**Baro.**	**Obs.**	**A**	**B**	**Obs.**	**C**
7.5	-6.4±4.0	1.1±1.8	-8.1±3.1	1.5±1.7	1.5±1.6	-6.1±3.9	1.4±1.8	-5.5±3.0	-0.2±0.7	-4.7±2.9	-0.5±0.7	-0.4±0.7	-5.8±3.2	-0.1±0.6

Mooring: M4-97

	East-West Velocity (U)							North-South Velocity (V)						
Depth	**Obs.**	**Baro.**	**Obs.**	**A**	**B**	**Obs.**	**C**	**Obs.**	**Baro.**	**Obs.**	**A**	**B**	**Obs.**	**C**
7.5	-1.6±6.8	0.5±5.3	-3.7±6.8	0.8±4.9	0.7±4.8	0.2±6.4	0.7±5.2	2.7±1.9	0.2±1.2	3.2±2.0	0.2±1.2	0.1±1.2	2.6±1.7	0.1±1.2
14	1.5±9.5	0.1±4.5	-1.2±9.8	0.1±4.6	0.0±4.6	3.9±8.5	0.2±5.3	0.7±2.1	-0.4±1.2	1.3±2.2	-0.3±1.3	-0.4±1.3	-0.2±1.6	0.0±1.4

Mooring: M5-97

	East-West Velocity (U)							North-South Velocity (V)						
Depth	**Obs.**	**Baro.**	**Obs.**	**A**	**B**	**Obs.**	**C**	**Obs.**	**Baro.**	**Obs.**	**A**	**B**	**Obs.**	**C**
7.5	1.0±2.6	0.4±1.8	1.0±2.8	-0.2±1.5	-0.2±1.5	0.8±1.9	0.2±1.8	-0.6±1.1	-0.3±0.9	-0.5±1.0	-0.4±0.6	-0.4±0.6	-0.5±1.2	-0.5±0.9
21	1.2±2.6	-0.1±1.7	0.9±2.7	0.3±1.5	0.3±1.6	1.0±2.9	0.2±1.8	-0.6±1.2	-0.0±0.6	-0.6±1.1	-0.1±0.6	-0.1±0.6	-0.5±1.4	-0.1±0.7

Mooring: M6-97

	East-West Velocity (U)							North-South Velocity (V)						
Depth	**Obs.**	**Baro.**	**Obs.**	**A**	**B**	**Obs.**	**C**	**Obs.**	**Baro.**	**Obs.**	**A**	**B**	**Obs.**	**C**
21	2.3±3.2	0.3±1.9	1.8±3.2	0.4±1.9	0.3±1.9	2.7±3.0	0.7±2.4	0.4±1.6	-0.0±0.5	0.3±1.8	-0.1±0.4	-0.1±0.4	0.5±1.2	-0.2±0.6
33	0.9±1.7	-0.1±2.1	0.5±1.4	0.9±2.0	0.9±2.0	1.2±2.1	1.1±2.5	0.7±1.2	0.0±0.5	0.7±1.1	-0.2±0.5	-0.2±0.5	0.8±1.4	-0.2±0.6

Mooring: M7-97

	East-West Velocity (U)							North-South Velocity (V)						
Depth	**Obs.**	**Baro.**	**Obs.**	**A**	**B**	**Obs.**	**C**	**Obs.**	**Baro.**	**Obs.**	**A**	**B**	**Obs.**	**C**
7.5	-5.1±2.6	-0.5±1.9	-5.5±2.5	-0.8±1.9	-0.8±1.9	-5.5±1.9	-1.0±2.1	-0.9±0.9	-0.0±0.7	-1.0±1.0	-0.1±0.4	-0.1±0.4	-0.9±0.6	-0.0±0.5
31	-0.1±2.1	-0.7±2.0	0.2±2.3	-0.7±1.9	-0.7±1.9	-0.6±1.1	-1.0±2.1	0.5±0.9	0.1±0.4	0.6±0.9	0.1±0.3	0.1±0.4	0.1±0.9	0.0±0.4

Appendix C Data Tables for Chapter 5

Table C.1 Semi Major Axis of the O_1 Tidal Ellipse (cm/s) at Mooring Locations in 1996. All models evaluated over a 30-day simulation with the exception of BRA which is evaluated over a 13 day simulation. Observed tide is evaluated over the entire observation period (60 days).

Constituent: O_1 (cm/s)

Mooring: M1-96

Depth	Data	A	AR	ARA	B	BR	BRA
10	0.1±0.4	0.1±0.0	0.1±0.0	0.1±0.0	0.1±0.0	0.1±0.0	-
21	0.5±0.5	0.1±0.0	0.1±0.0	0.1±0.0	0.1±0.0	0.1±0.0	-
45	0.4±0.3	0.1±0.0	0.1±0.0	0.1±0.0	0.1±0.0	0.1±0.0	-

Mooring: M2-96

Depth	Data	A	AR	ARA	B	BR	BRA
10	0.5±0.5	0.2±0.1	0.3±0.1	0.4±0.2	0.2±0.1	0.7±0.1	-
17	0.2±0.4	0.2±0.1	0.2±0.1	0.2±0.2	0.2±0.1	0.3±0.0	-
44	0.1±0.2	0.1±0.0	0.2±0.0	0.1±0.0	0.1±0.0	0.1±0.0	-

Mooring: M3-96

Depth	Data	A	AR	ARA	B	BR	BRA
10	2.0±1.4	1.1±0.2	0.9±0.1	1.0±0.2	1.2±0.2	1.0±0.1	-
15	1.2±0.9	1.2±0.3	0.6±0.1	0.6±0.1	1.2±0.2	0.7±0.1	-

Mooring: M4-96

Depth	Data	A	AR	ARA	B	BR	BRA
10	1.1±0.9	0.1±0.0	0.3±0.0	0.3±0.1	0.1±0.0	0.3±0.0	-
20	0.3±0.3	0.1±0.0	0.4±0.0	0.2±0.1	0.1±0.0	0.1±0.0	-
45	0.2±0.2	0.2±0.1	0.1±0.0	0.2±0.1	0.2±0.1	0.1±0.0	-

Mooring: M5-96

Depth	Data	A	AR	ARA	B	BR	BRA
10	0.6±0.6	0.1±0.0	0.1±0.0	0.1±0.0	0.1±0.0	0.1±0.0	-
21	0.1±0.4	0.1±0.0	0.1±0.0	0.1±0.0	0.1±0.0	0.1±0.0	-
45	0.3±0.2	0.1±0.0	0.1±0.0	0.1±0.0	0.1±0.0	0.1±0.0	-

Table C.2 Semi Major Axis of the K_1 Tidal Ellipse (cm/s) at Mooring Locations in 1996. All models evaluated over a 30-day simulation with the exception of BRA which is evaluated over a 13 day simulation. Observed tide is evaluated over the entire observation period (60 days).

Constituent: K_1

Mooring: M1-96

Depth	Data	A	AR	ARA	B	BR	BRA
10	0.4±0.5	0.1±0.0	0.1±0.0	0.2±0.0	0.1±0.0	0.2±0.0	0.2±0.1
21	1.1±0.4	0.1±0.0	0.1±0.0	0.1±0.0	0.1±0.0	0.1±0.0	0.1±0.1
45	0.8±0.4	0.1±0.0	0.1±0.0	0.1±0.0	0.1±0.0	0.1±0.0	0.1±0.1

Mooring: M2-96

Depth	Data	A	AR	ARA	B	BR	BRA
10	0.9±0.6	0.3±0.1	0.3±0.1	0.6±0.2	0.2±0.0	0.5±0.1	0.7±0.5
17	1.0±0.6	0.2±0.1	0.2±0.1	0.2±0.2	0.1±0.1	0.2±0.0	0.4±0.3
44	0.4±0.2	0.1±0.0	0.2±0.0	0.2±0.0	0.1±0.0	0.1±0.0	0.1±0.1

Mooring: M3-96

Depth	Data	A	AR	ARA	B	BR	BRA
10	3.7±1.3	1.5±0.2	1.5±0.1	1.4±0.2	1.5±0.2	1.4±0.1	2.0±0.8
15	2.4±0.8	1.5±0.3	1.6±0.1	1.0±0.1	1.5±0.2	1.4±0.1	1.7±0.5

Mooring: M4-96

Depth	Data	A	AR	ARA	B	BR	BRA
10	0.8±0.8	0.2±0.0	0.4±0.0	0.6±0.1	0.2±0.0	0.6±0.0	0.7±0.3
20	0.3±0.3	0.2±0.0	0.5±0.0	0.4±0.1	0.2±0.0	0.2±0.0	0.3±0.1
45	0.2±0.2	0.2±0.0	0.1±0.0	0.1±0.0	0.2±0.1	0.1±0.0	0.1±0.1

Mooring: M5-96

Depth	Data	A	AR	ARA	B	BR	BRA
10	0.5±0.5	0.2±0.0	0.2±0.0	0.2±0.0	0.2±0.0	0.2±0.0	0.2±0.1
21	0.5±0.4	0.2±0.0	0.2±0.0	0.2±0.0	0.2±0.0	0.2±0.0	0.2±0.1
45	0.4±0.3	0.2±0.0	0.2±0.0	0.2±0.0	0.2±0.0	0.2±0.0	0.2±0.1

Table C.3: Semi Major Axis of the O_1 Tidal Ellipse (cm/s) at 1997 Mooring Locations. All models evaluated over a 30-day simulation with the exception of BRA which is evaluated over a 13 day simulation. Observed tide is evaluated over the entire observation period (100 days).

Constituent: O_1

Mooring: M1-97

Depth	Data	A	AR	ARA	B	BR	BRA
7.5	0.4±0.5	0.2±0.1	0.2±0.1	0.2±0.1	0.2±0.0	0.3±0.2	-
21	0.3±0.3	0.1±0.0	0.1±0.1	0.2±0.1	0.1±0.0	0.3±0.0	-

Mooring: M2-97

Depth	Data	A	AR	ARA	B	BR	BRA
7.5	0.8±1.0	0.3±0.1	0.4±0.2	0.6±0.3	0.3±0.1	0.8±0.0	-
21	0.4±0.4	0.5±0.2	0.2±0.1	0.2±0.1	0.3±0.1	0.1±0.0	-

Mooring: M3-97

Depth	Data	A	AR	ARA	B	BR	BRA
7.5	0.8±0.7	0.2±0.0	0.2±0.1	0.5±0.1	0.2±0.0	0.3±0.0	-

Mooring: M4-97

Depth	Data	A	AR	ARA	B	BR	BRA
7.5	2.0±0.8	0.6±0.1	0.5±0.1	0.4±0.1	0.7±0.1	0.6±0.1	-
14	0.8±1.0	0.8±0.3	0.7±0.1	0.9±0.1	0.8±0.3	0.5±0.1	-

Mooring: M5-97

Depth	Data	A	AR	ARA	B	BR	BRA
7.5	0.5±0.4	0.1±0.0	0.5±0.1	0.5±0.1	0.1±0.0	0.3±0.1	-
21	0.3±0.3	0.2±0.1	0.1±0.0	0.1±0.0	0.1±0.0	0.1±0.0	-

Mooring: M6-97

Depth	Data	A	AR	ARA	B	BR	BRA
21	0.3±0.3	0.3±0.1	0.3±0.0	0.2±0.1	0.3±0.0	0.1±0.0	-
33	0.3±0.2	0.3±0.1	0.0±0.0	0.1±0.1	0.3±0.1	0.1±0.0	-

Mooring: M7-97

Depth	Data	A	AR	ARA	B	BR	BRA
7.5	0.3±0.5	0.1±0.0	0.3±0.0	0.2±0.1	0.1±0.0	0.4±0.1	-
31	0.3±0.4	0.1±0.0	0.1±0.0	0.1±0.1	0.1±0.0	0.1±0.0	-

Table C.4: Semi-Major Axis of the K_1 Tidal Ellipse (cm/s) at 1997 Mooring Locations. All models evaluated over a 30-day simulation with the exception of BRA which is evaluated over a 13 day simulation. Observed tide is evaluated over the entire observation period (100 days).

Constituent: K_1

Mooring: M1-97

Depth	Data	A	AR	ARA	B	BR	BRA
7.5	0.4±0.5	0.3±0.1	0.3±0.1	0.5±0.1	0.3±0.0	0.4±0.1	0.4±0.2
21	0.5±0.3	0.2±0.0	0.2±0.0	0.2±0.1	0.3±0.0	0.2±0.1	0.4±0.2

Mooring: M2-97

Depth	Data	A	AR	ARA	B	BR	BRA
7.5	1.2±0.9	0.2±0.1	0.5±0.2	0.8±0.2	0.2±0.1	0.8±0.0	0.8±0.6
21	0.3±0.3	0.3±0.2	0.2±0.1	0.3±0.2	0.2±0.1	0.2±0.0	0.4±0.2

Mooring: M3-97

Depth	Data	A	AR	ARA	B	BR	BRA
7.5	1.1±0.7	0.3±0.0	0.2±0.1	0.5±0.1	0.3±0.0	0.5±0.0	0.6±0.4

Mooring: M4-97

Depth	Data	A	AR	ARA	B	BR	BRA
7.5	2.5±0.7	0.9±0.2	0.4±0.1	0.6±0.1	1.2±0.1	0.8±0.1	1.0±0.3
14	1.8±1.0	0.9±0.3	1.4±0.1	1.5±0.1	1.1±0.3	1.1±0.1	1.3±0.4

Mooring: M5-97

Depth	Data	A	AR	ARA	B	BR	BRA
7.5	0.8±0.4	0.3±0.0	1.0±0.1	1.3±0.1	0.2±0.0	0.5±0.0	0.7±0.3
21	0.1±0.2	0.3±0.0	0.2±0.0	0.2±0.0	0.3±0.0	0.1±0.0	0.1±0.1

Mooring: M6-97

Depth	Data	A	AR	ARA	B	BR	BRA
21	0.5±0.3	0.4±0.1	0.3±0.0	0.3±0.1	0.5±0.0	0.2±0.0	0.3±0.2
33	0.2±0.2	0.4±0.1	0.1±0.0	0.1±0.1	0.5±0.1	0.2±0.1	0.1±0.1

Mooring: M7-97

Depth	Data	A	AR	ARA	B	BR	BRA
7.5	0.5±0.5	0.2±0.0	0.6±0.0	0.5±0.1	0.3±0.0	0.7±0.1	0.9±0.2
31	0.3±0.3	0.3±0.0	0.2±0.0	0.1±0.1	0.3±0.0	0.2±0.1	0.2±0.1

Table C.5: Semi Major Axis of the M_2 Tidal Ellipse (cm/s) at 1996 Mooring Locations. All models evaluated over a 30-day simulation with the exception of BRA which is evaluated over a 13 day simulation. Observed tide is evaluated over the entire observation period (60 days).

Constituent: M_2

Mooring: M1-96

Depth	Data	A	AR	ARA	B	BR	BRA
10	1.8±0.8	0.6±0.1	0.5±0.0	0.3±0.1	0.6±0.1	0.7±0.0	0.9±0.3
21	0.7±0.3	0.5±0.1	0.5±0.0	0.6±0.0	0.5±0.1	0.6±0.0	0.7±0.2
45	2.4±0.9	0.5±0.1	0.8±0.0	0.9±0.0	0.5±0.1	0.7±0.0	0.9±0.3

Mooring: M2-96

Depth	Data	A	AR	ARA	B	BR	BRA
10	3.4±1.1	1.2±0.2	1.6±0.1	2.4±0.2	1.2±0.2	2.2±0.1	2.2±0.7
17	1.5±0.5	1.2±0.2	1.1±0.1	1.0±0.1	1.2±0.2	1.4±0.1	1.6±0.5
44	1.1±0.4	1.0±0.2	1.5±0.1	1.5±0.2	1.0±0.2	0.7±0.0	0.8±0.3

Mooring: M3-96

Depth	Data	A	AR	ARA	B	BR	BRA
10	14.4±0.9	7.9±1.5	7.8±0.3	8.2±0.4	8.0±1.7	8.1±0.3	9.4±3.3
15	12.0±0.9	7.5±1.4	8.0±0.3	5.7±0.4	7.5±1.4	7.1±0.2	7.5±2.7

Mooring: M4-96

Depth	Data	A	AR	ARA	B	BR	BRA
10	2.9±1.0	1.2±0.2	1.8±0.1	2.0±0.1	1.2±0.3	2.8±0.1	3.1±1.3
20	1.3±0.3	1.2±0.2	2.0±0.1	1.6±0.1	1.2±0.2	1.3±0.1	1.8±0.8
45	1.0±0.2	1.3±0.2	1.1±0.0	0.8±0.1	1.2±0.3	0.9±0.0	1.1±0.4

Mooring: M5-96

Depth	Data	A	AR	ARA	B	BR	BRA
10	2.0±0.4	1.0±0.1	1.0±0.0	1.0±0.0	1.0±0.1	1.0±0.0	1.0±0.3
21	1.8±0.4	1.0±0.1	1.0±0.0	1.0±0.0	1.0±0.1	1.0±0.0	1.1±0.3
45	1.0±0.2	1.0±0.1	0.9±0.0	1.1±0.0	1.0±0.1	0.9±0.0	1.1±0.3

Table C.6: Semi Major Axis of the S_2 Tidal Ellipse (cm/s) at 1996 Mooring Locations. All models evaluated over a 30-day simulation with the exception of BRA which is evaluated over a 13 day simulation. Observed tide is evaluated over the entire observation period (60 days).

Constituent: S_2

Mooring: M1-96

Depth	Data	A	AR	ARA	B	BR	BRA
10	1.5±0.8	0.2±0.1	0.2±0.0	0.2±0.1	0.2±0.1	0.3±0.0	-
21	0.4±0.3	0.2±0.1	0.2±0.0	0.3±0.0	0.2±0.1	0.2±0.0	-
45	1.5±1.0	0.2±0.1	0.3±0.0	0.3±0.0	0.2±0.1	0.3±0.0	-

Mooring: M2-96

Depth	Data	A	AR	ARA	B	BR	BRA
10	1.4±0.8	0.5±0.2	0.7±0.1	1.2±0.3	0.5±0.2	1.0±0.1	-
17	1.0±0.6	0.5±0.2	0.5±0.1	0.3±0.1	0.5±0.2	0.6±0.1	-
44	0.6±0.5	0.4±0.2	0.6±0.1	0.5±0.2	0.4±0.2	0.3±0.0	-

Mooring: M3-96

Depth	Data	A	AR	ARA	B	BR	BRA
10	7.3±1.0	3.2±1.6	3.1±0.3	3.3±0.4	3.2±1.8	3.0±0.3	-
15	5.8±0.9	2.8±1.6	2.8±0.3	1.9±0.4	2.9±1.4	2.7±0.2	-

Mooring: M4-96

Depth	Data	A	AR	ARA	B	BR	BRA
10	1.6±1.0	0.5±0.2	0.7±0.1	0.8±0.1	0.5±0.3	1.1±0.1	-
20	0.4±0.3	0.5±0.2	0.7±0.1	0.5±0.1	0.5±0.2	0.5±0.1	-
45	0.5±0.2	0.5±0.2	0.5±0.1	0.3±0.1	0.5±0.2	0.3±0.0	-

Mooring: M5-96

Depth	Data	A	AR	ARA	B	BR	BRA
10	1.2±0.5	0.4±0.1	0.4±0.0	0.4±0.0	0.4±0.1	0.3±0.0	-
21	1.0±0.4	0.4±0.1	0.4±0.0	0.4±0.0	0.4±0.1	0.4±0.0	-
45	0.6±0.2	0.4±0.1	0.4±0.0	0.4±0.0	0.4±0.1	0.4±0.0	-

Table C.7: Semi Major Axis of the M_2 Tidal Ellipse (cm/s) at 1997 Mooring Locations. All models evaluated over a 30-day simulation with the exception of BRA which is evaluated over a 13 day simulation. Observed tide is evaluated over the entire observation period (100 days).

Constituent: M_2

Mooring: M1-97

Depth	Data	A	AR	ARA	B	BR	BRA
7.5	2.5±0.5	1.3±0.3	1.6±0.1	1.9±0.2	1.2±0.2	1.7±0.1	1.8±0.5
21	0.9±0.3	1.3±0.3	1.1±0.1	1.1±0.2	1.2±0.1	1.2±0.1	1.4±0.4

Mooring: M2-97

Depth	Data	A	AR	ARA	B	BR	BRA
7.5	4.5±0.9	1.5±0.3	2.2±0.2	3.0±0.3	1.3±0.3	2.6±0.2	3.0±1.5
21	1.2±0.6	1.4±0.2	1.2±0.2	1.8±0.2	1.3±0.3	1.1±0.1	1.8±0.8

Mooring: M3-97

Depth	Data	A	AR	ARA	B	BR	BRA
7.5	5.3±0.9	1.5±0.3	1.7±0.1	2.6±0.2	1.5±0.2	2.3±0.1	2.7±1.1

Mooring: M4-97

Depth	Data	A	AR	ARA	B	BR	BRA
7.5	12.1±0.8	5.5±1.0	4.0±0.3	3.6±0.2	5.2±0.8	5.1±0.2	5.5±1.7
14	11.3±0.8	5.2±0.9	7.7±0.2	9.8±0.4	5.0±0.7	6.0±0.2	6.9±2.5

Mooring: M5-97

Depth	Data	A	AR	ARA	B	BR	BRA
7.5	3.0±0.4	1.6±0.3	4.3±0.2	5.9±0.2	1.5±0.2	2.8±0.1	3.6±1.1
21	1.4±0.4	1.6±0.3	1.3±0.1	1.4±0.3	1.6±0.2	0.9±0.0	0.9±0.3

Mooring: M6-97

Depth	Data	A	AR	ARA	B	BR	BRA
21	1.9±0.6	1.9±0.3	1.8±0.1	1.3±0.3	1.8±0.3	1.4±0.0	1.8±0.7
33	0.5±0.2	2.1±0.4	0.7±0.1	0.8±0.2	2.0±0.3	1.1±0.1	0.4±0.2

Mooring: M7-97

Depth	Data	A	AR	ARA	B	BR	BRA
7.5	2.3±0.5	2.1±0.5	3.2±0.1	3.0±0.1	2.1±0.3	3.2±0.1	4.3±1.4
31	1.4±0.4	2.0±0.4	1.6±0.0	1.3±0.1	2.0±0.2	1.6±0.1	1.4±0.5

Table C.8: Semi Major Axis of the S_2 Tidal Ellipse (cm/s) at 1997 Mooring Locations. All models evaluated over a 30-day simulation with the exception of BRA which is evaluated over a 13 day simulation. Observed tide is evaluated over the entire observation period (100 days).

Constituent: S_2

Mooring: M1-97

Depth	Data	A	AR	ARA	B	BR	BRA
7.5	0.9±0.6	0.4±0.2	0.7±0.1	0.8±0.2	0.5±0.2	0.6±0.2	-
21	0.4±0.3	0.4±0.2	0.4±0.1	0.4±0.2	0.5±0.1	0.4±0.1	-

Mooring: M2-97

Depth	Data	A	AR	ARA	B	BR	BRA
7.5	2.2±0.9	0.5±0.3	1.0±0.2	1.3±0.2	0.5±0.2	1.3±0.2	-
21	0.6±0.5	0.5±0.2	0.6±0.3	0.8±0.2	0.6±0.3	0.4±0.0	-

Mooring: M3-97

Depth	Data	A	AR	ARA	B	BR	BRA
7.5	1.9±0.9	0.5±0.3	0.7±0.1	1.1±0.2	0.7±0.2	0.9±0.1	-

Mooring: M4-97

Depth	Data	A	AR	ARA	B	BR	BRA
7.5	6.1±0.9	1.9±1.1	1.6±0.3	1.5±0.2	2.4±0.8	2.0±0.2	-
14	5.7±0.7	1.7±1.0	2.8±0.2	3.8±0.5	2.1±0.7	2.2±0.2	-

Mooring: M5-97

Depth	Data	A	AR	ARA	B	BR	BRA
7.5	1.3±0.5	0.5±0.3	1.8±0.2	2.3±0.2	0.7±0.2	1.1±0.2	-
21	0.4±0.4	0.5±0.3	0.5±0.1	0.6±0.3	0.7±0.2	0.4±0.0	-

Mooring: M6-97

Depth	Data	A	AR	ARA	B	BR	BRA
21	0.7±0.6	0.7±0.4	0.7±0.1	0.6±0.3	0.8±0.3	0.6±0.0	-
33	0.2±0.2	0.7±0.4	0.3±0.1	0.3±0.1	0.9±0.3	0.4±0.1	-

Mooring: M7-97

Depth	Data	A	AR	ARA	B	BR	BRA
7.5	1.3±0.5	0.7±0.4	1.2±0.1	1.3±0.1	0.9±0.3	1.2±0.1	-
31	0.6±0.4	0.7±0.5	0.7±0.1	0.4±0.1	0.9±0.3	0.6±0.1	-

Table C.9 Inclination of the K_1 Tidal Ellipse (degrees) at 1996 Mooring Locations. All models evaluated over a 30-day simulation with the exception of BRA which is evaluated over a 13 day simulation. Observed tide is evaluated over the entire observation period (60 days).

Inclination Constituent: K_1

Mooring: M1-96

Depth	Data	A	AR	ARA	B	BR	BRA
10	71± 97	39± 5	45± 5	36± 21	39± 4	95± 9	85± 32
21	53± 31	41± 5	47± 4	71± 10	41± 4	24± 9	29± 67
45	40± 27	51± 5	51± 2	40± 6	51± 5	17± 5	9± 22

Mooring: M2-96

Depth	Data	A	AR	ARA	B	BR	BRA
10	5± 82	20± 7	18± 15	31± 21	9± 14	56± 7	68± 56
17	20± 19	12± 18	175± 18	9± 28	8± 20	33± 17	33± 73
44	173± 15	160± 18	4± 7	10± 11	159± 16	26± 13	37± 56

Mooring: M3-96

Depth	Data	A	AR	ARA	B	BR	BRA
10	171± 11	170± 4	168± 2	4± 6	173± 5	164± 3	170± 10
15	162± 11	177± 3	1± 4	22± 12	176± 3	1± 3	7± 17

Mooring: M4-96

Depth	Data	A	AR	ARA	B	BR	BRA
10	15± 85	15± 6	14± 5	2± 11	13± 11	14± 4	14± 8
20	20± 75	10± 5	1± 5	170± 19	7± 6	21± 3	12± 22
45	25± 71	1± 2	43± 13	164± 46	1± 4	0± 16	167± 42

Mooring: M5-96

Depth	Data	A	AR	ARA	B	BR	BRA
10	130± 82	48± 4	45± 3	41± 16	48± 5	47± 3	55± 18
21	43± 72	48± 6	40± 2	35± 7	48± 6	36± 4	36± 34
45	67± 31	48± 5	52± 2	52± 3	48± 6	49± 3	39± 21

Table C.10: Greenwich Phase of the K_1 Tidal Current (degrees) at 1996 Mooring Locations. All models evaluated over a 30-day simulation with the exception of BRA which is evaluated over a 13 day simulation. Observed tide is evaluated over the entire observation period (60 days).

Phase Constituent: K_1

Mooring: M1-96

Depth	Data	A	AR	ARA	B	BR	BRA
10	274±116	293± 5	319± 5	359± 24	293± 5	358± 11	325± 41
21	286± 27	294± 5	302± 5	264± 13	294± 5	316± 9	289± 71
45	168± 30	297± 5	262± 2	256± 6	297± 6	229± 6	202± 35

Mooring: M2-96

Depth	Data	A	AR	ARA	B	BR	BRA
10	301± 85	297± 12	354± 15	4± 18	304± 19	26± 7	46± 62
17	355± 31	313± 22	142± 23	328± 79	313± 33	348± 13	8± 76
44	344± 34	69± 9	238± 7	254± 6	72± 12	221± 10	215± 51

Mooring: M3-96

Depth	Data	A	AR	ARA	B	BR	BRA
10	109± 23	121± 6	114± 5	291± 7	126± 6	129± 4	98± 22
15	110± 19	110± 9	281± 3	254± 8	119± 8	282± 5	256± 18

Mooring: M4-96

Depth	Data	A	AR	ARA	B	BR	BRA
10	354± 71	291± 9	329± 3	304± 11	294± 11	314± 3	298± 24
20	300± 81	296± 10	312± 5	125± 11	299± 7	289± 3	281± 33
45	283±101	302± 14	255± 11	168± 37	306± 13	296± 17	64± 55

Mooring: M5-96

Depth	Data	A	AR	ARA	B	BR	BRA
10	88±100	298± 5	306± 3	318± 18	298± 5	317± 4	297± 22
21	294± 76	298± 5	307± 2	312± 8	298± 5	326± 3	311± 33
45	278± 36	297± 6	298± 2	297± 3	297± 5	302± 3	276± 19

Table C.11: Inclination of the K_1 Tidal Ellipse (degrees) at 1997 Mooring Locations. All models evaluated over a 30-day simulation with the exception of BRA which is evaluated over a 13 day simulation. Observed tide is evaluated over the entire observation period (100 days).

Inclination Constituent: K_1

Mooring: M1-97

Depth	Data	A	AR	ARA	B	BR	BRA
7.5	42± 97	9± 14	14± 14	26± 10	9± 6	110± 29	157± 44
21	35± 38	180± 11	27± 12	21± 35	8± 7	16± 9	172± 47

Mooring: M2-97

Depth	Data	A	AR	ARA	B	BR	BRA
7.5	179± 38	22± 38	10± 21	12± 13	15± 9	36± 3	34± 50
21	19± 82	13± 15	148± 46	22± 73	8± 17	0± 3	4± 29

Mooring: M3-97

Depth	Data	A	AR	ARA	B	BR	BRA
7.5	163± 32	176± 3	159± 27	176± 17	179± 2	148± 5	135± 48

Mooring: M4-97

Depth	Data	A	AR	ARA	B	BR	BRA
7.5	165± 10	165± 8	146± 8	150± 10	170± 3	168± 2	164± 11
14	167± 14	172± 11	177± 2	178± 3	176± 6	169± 2	167± 9

Mooring: M5-97

Depth	Data	A	AR	ARA	B	BR	BRA
7.5	178± 22	164± 8	161± 1	154± 7	158± 7	152± 5	146± 24
21	176± 64	164± 5	170± 11	146± 11	162± 4	174± 36	7±166

Mooring: M6-97

Depth	Data	A	AR	ARA	B	BR	BRA
21	150± 44	10± 9	171± 6	129± 26	179± 2	163± 8	156± 38
33	18±102	179± 20	55± 25	45± 68	172± 4	19± 9	134± 53

Mooring: M7-97

Depth	Data	A	AR	ARA	B	BR	BRA
7.5	27± 41	24± 5	34± 3	29± 12	22± 4	45± 5	32± 15
31	179± 43	5± 6	3± 4	16± 88	7± 3	18± 11	163± 25

Table C.12: Greenwich Phase of the K_1 Tidal Current (degrees) at 1997 Mooring Locations. All models evaluated over a 30-day simulation with the exception of BRA which is evaluated over a 13 day simulation. Observed tide is evaluated over the entire observation period (100 days).

Phase Constituent: K_1

Mooring: M1-97

Depth	Data	A	AR	ARA	B	BR	BRA
7.5	344± 97	293± 14	299± 8	323± 10	311± 8	28± 30	37± 27
21	305± 43	103± 10	290± 14	270± 20	303± 7	312± 13	114± 47

Mooring: M2-97

Depth	Data	A	AR	ARA	B	BR	BRA
7.5	134± 55	359± 23	11± 21	12± 15	348± 20	24± 3	11± 59
21	273±109	21± 36	184± 44	267± 72	353± 35	324± 8	296± 43

Mooring: M3-97

Depth	Data	A	AR	ARA	B	BR	BRA
7.5	81± 36	124± 4	150± 16	191± 15	134± 6	122± 6	114± 50

Mooring: M4-97

Depth	Data	A	AR	ARA	B	BR	BRA
7.5	108± 16	124± 8	91± 12	116± 12	137± 3	121± 7	85± 15
14	116± 31	126± 21	106± 3	97± 4	130± 13	96± 5	69± 19

Mooring: M5-97

Depth	Data	A	AR	ARA	B	BR	BRA
7.5	131± 26	126± 6	120± 3	114± 6	124± 10	129± 6	112± 32
21	102±134	119± 10	103± 9	96± 11	123± 6	38± 32	214±120

Mooring: M6-97

Depth	Data	A	AR	ARA	B	BR	BRA
21	158± 53	323± 12	91± 5	80± 27	151± 5	20± 9	53± 43
33	315±100	122± 12	359± 20	306± 70	141± 7	226± 19	102±131

Mooring: M7-97

Depth	Data	A	AR	ARA	B	BR	BRA
7.5	252± 53	252± 5	292± 3	279± 10	263± 3	301± 5	275± 11
31	74± 83	259± 8	219± 6	257± 79	270± 3	213± 21	17± 21

Table C.13 Inclination of the M_2 Tidal Ellipse (degrees) at 1996 Mooring Locations. All models evaluated over a 30-day simulation with the exception of BRA which is evaluated over a 13 day simulation. Observed tide is evaluated over the entire observation period (60 days).

Inclination Constituent: M_2

Mooring: M1-96

Depth	Data	A	AR	ARA	B	BR	BRA
10	52± 25	43± 8	36± 2	14± 13	43± 8	37± 4	41± 24
21	45± 31	43± 8	32± 2	41± 4	43± 8	63± 2	61± 15
45	45± 22	46± 8	43± 1	53± 2	46± 8	9± 2	6± 15

Mooring: M2-96

Depth	Data	A	AR	ARA	B	BR	BRA
10	18± 11	17± 4	13± 2	16± 4	15± 4	31± 3	40± 30
17	23± 18	15± 4	6± 3	172± 7	15± 4	25± 3	16± 10
44	175± 5	4± 3	173± 2	4± 3	3± 2	7± 2	4± 17

Mooring: M3-96

Depth	Data	A	AR	ARA	B	BR	BRA
10	170± 4	171± 3	167± 1	176± 3	170± 3	167± 1	167± 7
15	163± 3	171± 3	172± 1	2± 2	170± 3	179± 1	4± 5

Mooring: M4-96

Depth	Data	A	AR	ARA	B	BR	BRA
10	30± 21	5± 2	10± 1	10± 3	5± 3	10± 2	10± 7
20	4± 10	4± 2	12± 2	171± 5	5± 2	4± 1	9± 5
45	25± 11	2± 2	179± 3	180± 10	2± 2	9± 3	7± 11

Mooring: M5-96

Depth	Data	A	AR	ARA	B	BR	BRA
10	51± 16	49± 8	47± 2	46± 2	49± 8	47± 1	48± 16
21	51± 13	49± 8	41± 1	41± 1	49± 7	41± 2	42± 13
45	57± 9	48± 8	45± 2	50± 2	48± 7	44± 2	46± 15

Table C.14: Greenwich Phase of the K_1 Tidal Current (degrees) at 1996 Mooring Locations. All models evaluated over a 30-day simulation with the exception of BRA which is evaluated over a 13 day simulation. Observed tide is evaluated over the entire observation period (60 days).

Phase Constituent: M_2

Mooring: M1-96

Depth	Data	A	AR	ARA	B	BR	BRA
10	95± 27	155± 8	98± 2	115± 13	155± 8	114± 4	97± 23
21	44± 38	155± 7	88± 2	76± 4	155± 8	88± 2	65± 20
45	332± 22	157± 8	73± 2	67± 2	157± 8	65± 3	43± 21

Mooring: M2-96

Depth	Data	A	AR	ARA	B	BR	BRA
10	84± 16	159± 9	113± 4	138± 7	158± 10	126± 4	113± 30
17	72± 20	159± 9	107± 4	276± 9	160± 8	111± 3	92± 19
44	104± 26	135± 12	222± 3	56± 7	135± 13	26± 3	3± 25

Mooring: M3-96

Depth	Data	A	AR	ARA	B	BR	BRA
10	233± 4	344± 12	272± 2	266± 3	344± 13	279± 2	249± 23
15	229± 4	335± 11	270± 2	68± 4	335± 10	262± 2	47± 20

Mooring: M4-96

Depth	Data	A	AR	ARA	B	BR	BRA
10	65± 22	159± 11	107± 2	108± 4	160± 11	107± 2	81± 24
20	52± 13	160± 11	128± 2	301± 5	160± 12	75± 3	59± 26
45	356± 10	159± 11	233± 2	234± 10	158± 11	37± 3	3± 19

Mooring: M5-96

Depth	Data	A	AR	ARA	B	BR	BRA
10	88± 14	158± 8	92± 2	93± 2	158± 7	96± 1	69± 14
21	58± 11	158± 8	95± 1	93± 1	158± 7	98± 2	70± 14
45	33± 10	157± 8	88± 2	95± 2	157± 7	89± 2	54± 14

Table C.15: Inclination of the M_2 Tidal Ellipse (degrees) at 1997 Mooring Locations. All models evaluated over a 30-day simulation with the exception of BRA which is evaluated over a 13 day simulation. Observed tide is evaluated over the entire observation period (100 days).

Inclinination Constituent: M_2

Mooring: M1-97

Depth	Data	A	AR	ARA	B	BR	BRA
7.5	35± 11	18± 6	26± 2	25± 3	18± 4	32± 8	23± 30
21	22± 14	18± 5	23± 3	20± 7	18± 4	32± 4	31± 20

Mooring: M2-97

Depth	Data	A	AR	ARA	B	BR	BRA
7.5	10± 6	10± 4	11± 4	10± 4	10± 4	21± 5	33± 22
21	1± 17	7± 3	19± 11	1± 7	8± 3	180± 1	1± 4

Mooring: M3-97

Depth	Data	A	AR	ARA	B	BR	BRA
7.5	173± 7	172± 3	168± 2	174± 3	173± 2	167± 2	167± 11

Mooring: M4-97

Depth	Data	A	AR	ARA	B	BR	BRA
7.5	161± 3	167± 4	170± 1	159± 3	166± 3	167± 1	166± 6
14	168± 2	166± 3	168± 1	171± 1	166± 3	164± 2	166± 8

Mooring: M5-97

Depth	Data	A	AR	ARA	B	BR	BRA
7.5	174± 7	164± 4	167± 2	155± 2	163± 3	155± 2	152± 13
21	156± 16	166± 4	19± 3	14± 6	165± 3	160± 4	172± 19

Mooring: M6-97

Depth	Data	A	AR	ARA	B	BR	BRA
21	168± 10	179± 2	5± 3	172± 6	1± 1	158± 2	170± 10
33	5± 59	180± 3	162± 3	179± 8	1± 1	179± 3	172± 43

Mooring: M7-97

Depth	Data	A	AR	ARA	B	BR	BRA
7.5	20± 6	10± 3	27± 1	25± 2	9± 2	32± 2	31± 14
31	9± 10	7± 3	175± 1	163± 2	7± 1	171± 2	170± 19

Table C.16: Greenwich Phase of the M_2 Tidal Current (degrees) at 1997 Mooring Locations. All models evaluated over a 30-day simulation with the exception of BRA which is evaluated over a 13 day simulation. Observed tide is evaluated over the entire observation period (100 days).

Phase Constituent: M_2

Mooring: M1-97

Depth	Data	A	AR	ARA	B	BR	BRA
7.5	58± 10	196± 12	93± 3	123± 4	74± 7	114± 6	66± 25
21	354± 18	197± 11	86± 4	83± 10	75± 7	87± 4	61± 21

Mooring: M2-97

Depth	Data	A	AR	ARA	B	BR	BRA
7.5	75± 12	209± 10	133± 5	142± 6	84± 11	125± 6	120± 29
21	21± 28	211± 9	55± 11	89± 8	89± 11	276± 3	82± 31

Mooring: M3-97

Depth	Data	A	AR	ARA	B	BR	BRA
7.5	239± 10	18± 11	286± 3	323± 3	255± 7	278± 3	265± 30

Mooring: M4-97

Depth	Data	A	AR	ARA	B	BR	BRA
7.5	231± 4	23± 11	225± 5	244± 3	260± 8	262± 2	227± 18
14	220± 4	9± 9	271± 2	264± 3	246± 7	262± 2	229± 22

Mooring: M5-97

Depth	Data	A	AR	ARA	B	BR	BRA
7.5	240± 8	23± 9	290± 3	290± 2	260± 8	283± 3	263± 18
21	206± 17	18± 11	53± 5	54± 13	255± 9	201± 3	190± 22

Mooring: M6-97

Depth	Data	A	AR	ARA	B	BR	BRA
21	216± 17	31± 11	73± 3	234± 14	88± 10	226± 2	209± 24
33	18± 41	26± 13	200± 4	250± 10	84± 9	229± 4	258± 36

Mooring: M7-97

Depth	Data	A	AR	ARA	B	BR	BRA
7.5	39± 14	185± 11	93± 1	96± 2	63± 7	101± 2	72± 21
31	359± 16	185± 14	219± 2	221± 4	63± 8	231± 3	193± 21